BEILSTEIN JOURNAL OF NANOTECHNOLOGY

Recent advances in synthesis and applications of organometallic nanomaterials

Edited by Thanh-Danh Nguyen, Bui The Huy and Trinh-Duy Nguyen

Generated on 08 November 2026, 00:14

Imprint

Beilstein Journal of Nanotechnology
www.bjnano.org
ISSN 2190-4286
Email: journals-support@beilstein-institut.de

The *Beilstein Journal of Nanotechnology* is published by the Beilstein-Institut zur Förderung der Chemischen Wissenschaften.

Beilstein-Institut zur Förderung der Chemischen Wissenschaften
Trakehner Straße 7–9
60487 Frankfurt am Main
Germany
www.beilstein-institut.de

The copyright to this document as a whole, which is published in the *Beilstein Journal of Nanotechnology*, is held by the Beilstein-Institut zur Förderung der Chemischen Wissenschaften. The copyright to the individual articles in this document is held by the respective authors, subject to a Creative Commons Attribution license.

BEILSTEIN JOURNAL OF NANOTECHNOLOGY

In situ magnesiothermic reduction synthesis of a Ge@C composite for high-performance lithium-ion batterie anodes

Ha Tran Huu[1], Ngoc Phi Nguyen[1], Vuong Hoang Ngo[1], Huy Hoang Luc[2], Minh Kha Le[3], Minh Thu Nguyen[3], My Loan Phung Le[3], Hye Rim Kim[4], In Young Kim[4], Sung Jin Kim[4], Van Man Tran[*3] and Vien Vo[*1]

Full Research Paper

Open Access

Address:
[1]Faculty of Natural Science, Quy Nhon University, 170 An Duong Vuong, Quy Nhon, Binh Dinh, 55000, Vietnam, [2]Faculty of Physics, Hanoi National University of Education, 136 Xuan Thuy, Cau Giay, 11300, Hanoi, Vietnam, [3]Applied Physical Chemistry Laboratory, University of Science, Viet Nam National University Ho Chi Minh City, 70000, Vietnam and [4]Department of Chemistry and Nanoscience, Ewha Womans University, Seoul 120-750, South Korea

Email:
Van Man Tran[*] - tvman@hcmus.edu.vn;
Vien Vo[*] - vovien@qnu.edu.vn

* Corresponding author

Keywords:
Ge anode; in situ synthesis; lithium-ion batteries; magnesiothermic reduction

Beilstein J. Nanotechnol. **2023,** *14,* 751–761.
https://doi.org/10.3762/bjnano.14.62

Received: 27 March 2023
Accepted: 14 June 2023
Published: 26 June 2023

This article is part of the thematic issue "Recent advances in synthesis and applications of organometallic nanomaterials".

Guest Editor: D. T. Nguyen

© 2023 Tran Huu et al.; licensee Beilstein-Institut.
License and terms: see end of document.

Abstract

Metallothermic, especially magnesiothermic, solid-state reactions have been widely applied to synthesize various materials. However, further investigations regarding the use of this method for composite syntheses are needed because of the high reactivity of magnesium. Herein, we report an in situ magnesiothermic reduction to synthesize a composite of Ge@C as an anode material for lithium-ion batteries. The obtained electrode delivered a specific capacity of 454.2 mAh·g^{-1} after 200 cycles at a specific current of 1000 mA·g^{-1}. The stable electrochemical performance and good rate performance of the electrode (432.3 mAh·g^{-1} at a specific current of 5000 mA·g^{-1}) are attributed to the enhancement in distribution and chemical contact between Ge nanoparticles and the biomass-based carbon matrix. A comparison with other synthesis routes has been conducted to demonstrate the effectiveness of contact formation during in situ synthesis.

Introduction

The significantly increasing energy consumption leads to the exhaustion of fossil fuel sources such as coal, oil, and natural gas. Additionally, there are various negative environmental consequences of using fossil fuel energy, such as water pollution, increasing emissions of greenhouse gases, and air pollution [1]. Therefore, research regarding eco-friendly and renew-

able energy resources has emerged [2]. One of the best alternatives to fossil fuels are solar and wind energy [3]. However, high-power, high-energy, and long-lasting energy storage systems are necessary to utilize these energy resources effectively [4]. Moreover, to reduce greenhouse gas emissions, various governments have committed themselves to develop strategies for increasing the number of electric vehicles (EVs) [5,6]. The most important component of EVs are suitable energy storage systems, the further development of which will be key to a more widespread use of this kind of transportation [7].

Commercialized first by Sony company, lithium-ion batteries (LIBs) and related systems have become the most popular energy storage systems, with applications from mobile devices to EVs and grid-scale storage [8,9]. However, the low specific theoretical capacity of graphite limits the energy density of the commercial LIBs [10-13]. Germanium, as a lithium alloying material, is a possible alternative for graphite electrodes due to its high theoretical capacity of 1623 $mAh \cdot g^{-1}$ (four times higher than that of graphite) and good rate performance due to high electronic (2.1 $S \cdot m^{-1}$, 1×10^4 times higher than that of silicon) and ionic (6.51×10^{-12} $cm^2 \cdot s^{-1}$, 400 times higher than Si at room temperature) conductivity [14]. However, electrodes based on alloying suffer from deterioration during repeated lithiation/delithiation because of the large variation in volume. Despite the lower volume change ratio compared to Si (370% for Ge and 400% for Si) and the structural robustness, for example, a higher resistance to pulverization than Si, the durability of Ge-based anode is not sufficient for practical applications [14]. To overcome this limitation, nanoscale control and composite design are two effective strategies [15-19].

In addition to various Ge preparation routes, such as sputtering deposition [20], wet-chemical reduction [21,22], thermal reduction [23], colloidal synthesis [24], and molten-salt synthesis [25], metallothermic, especially magnesiothermic reduction, has been widely applied in the synthesis of group-IV elements to control the nanostructures of the obtained products because of its simplicity in operation and the applicability for pseudomorphic transformations [26-28]. For instance, in our previous study, a magnesiothermic reaction was applied for the reduction of GeO_2 to Ge nanoparticles [29]. In addition to improving the cycling performance of Ge-based anodes, a carbon matrix is the most popular choice to disperse nanoparticles, avoiding their aggregation and reducing the internal stress induced by volume variation, because of its flexible structure and high conductivity [30-32]. In our recent study, the combination of Ge nanoparticles and a carbon matrix using a hydrothermal route has been reported, and the enhancement in the electrochemical performance of Ge@C electrodes was demonstrated [33]. In this work, a one-pot synthesis route has been followed to prepare a Ge@C composite using an in situ magnesiothermic reduction of GeO_2 and biomass-derived carbon as precursor. A series of experiments using other methods to combine Ge and biomass carbon was also conducted for comparison. The in situ synthesized electrode exhibits superior electrochemical performance in lithium storage. This is attributed to a better contact between the components obtained via this route.

Results and Discussion

Physicochemical characterization

The synthesis of Ge/C-iM750 (see Experimental section for sample denominations) was carried out through a one-pot in situ generation of Ge nanoparticles in the presence of a carbon matrix. In this synthesis route, the newly formed nanoparticles are deposited uniformly inside the carbon matrix, which is favorable for the formation of good chemical contacts between the components. The magnesiothermic reduction of GeO_2 to form Ge is given in Equation 1. Accordingly, the stoichiometric molar ratio of Mg and GeO_2 should be 2:1. However, in the previous report [29], up to a molar ratio of 2.5, the GeO_2 phase still remained. Therefore, in this work, Mg and GeO_2 powders were mixed at a mass ratio of 5:4 (approximately a molar ratio of 3.5:1) to ascertain the formation of the pure Ge phase. The XRD patterns of pure Ge, biomass-derived activated carbon, and as-synthesized Ge@C composites are shown in Figure 1a. The pattern of Ge pattern exhibits reflections at $2\theta = 27.3°$, 45.3°, 53.7°, 66.0°, and 72.8°, corresponding to the (111), (220), (311), (400), and (331) crystal planes of cubic Ge (space group F*d*−3*m*, JCPDS card No. 04-0545). There is no observable signal related to the GeO_2 precursor. The XRD pattern of the BC-800 carbon material exhibits a diffraction signal at $2\theta = 26.3°$ attributed to the (002) plane of disordered graphite-like carbon. The peaks at $2\theta = 28.1°$ and 44.0° correspond to the (104) and (100) planes of the hexagonal structure in graphite [34,35]. However, the intensity of the diffraction peaks in the XRD pattern of BC-800 is mostly weak, which indicates the poor graphitic structure with small crystallite sizes of biomass carbon [36]. In the Ge@C composite sample, signals related to the Ge phase are observable, while those of the carbon phase do not appear. There are no significant differences between the XRD patterns of pure Ge and the composites, which implies that the presence of carbon does not alter the structure of Ge.

$$2Mg + GeO_2 \xrightarrow{\Delta} 2MgO + Ge \quad (1)$$

Chemical bonds and the carbon phases in the composites were determined using FTIR spectroscopy, as shown in Figure 1b.

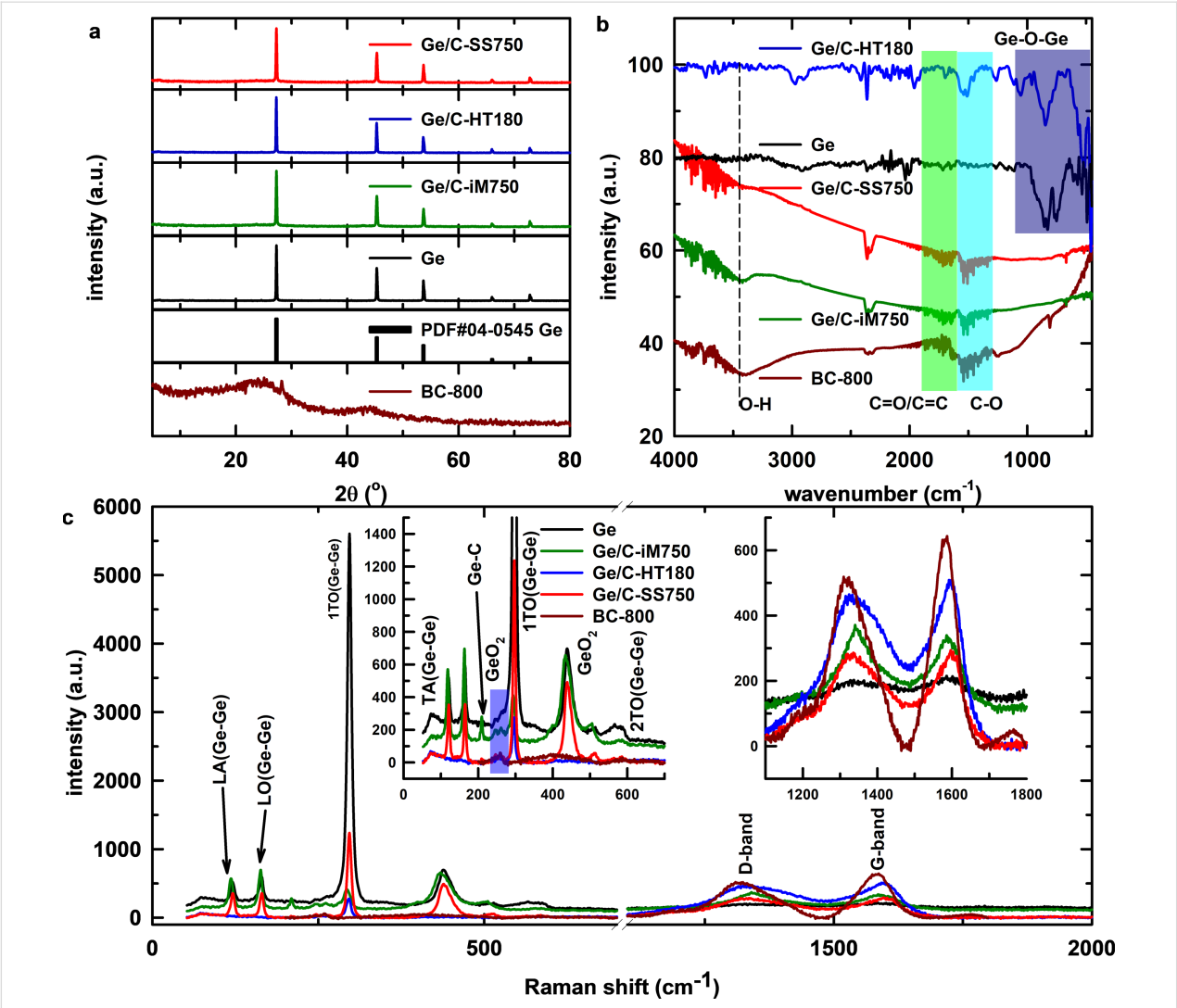


Figure 1: (a) XRD patterns, (b) FTIR spectra, and (c) Raman spectra of pure Ge, Ge/C-iM750, Ge/C-HT180, Ge/C-SS750, and BC-800 (see Experimental section for sample denominations).

The FTIR spectra of pure Ge consist of two broad bands in the wavenumber ranges of 500–600 and 800–1000 cm^{-1}. The former band corresponds to the bending modes, and the latter band is attributed to the stretching modes of Ge–O–Ge bonds [37] from the oxidized outer layer of the Ge nanoparticles. The FTIR spectrum of BC-800 exhibits absorption bands at ca. 3500, 1400–1600, and 1000–1300 cm^{-1}. The band in the high-wavenumber region is ascribed to the vibration of hydroxy O–H bonds [38]. The medium-wavenumber signals are assigned to the stretching motions of C=O and C=C groups. The remaining band are stretching vibrations of alkoxy C–O or aromatic bonds [39].

Further analysis of the structure of pure Ge, biomass-derived carbon, and chemical contact between Ge and carbon matrix in the composites was conducted using Raman spectra. As shown in Figure 1c, the Raman spectrum of pure Ge exhibits a signal at 83 cm^{-1}, attributed to the transverse acoustic phonon mode, and two peaks at 127 and 169 cm^{-1} ascribed, respectively, to the longitudinal acoustic and longitudinal optic phonon modes of Ge–Ge bonds [40,41]. The sharp peak at 296 cm^{-1} and a low-intensity band around 550 cm^{-1} are assigned to the first-order and second-order transverse optic phonon modes of crystalline Ge [41-43]. Moreover, the broadband detected at 449 cm^{-1} corresponds to the customary Raman-active motion of α-GeO_2 [44]. The presence of characteristic signals in the Ge@C composite is similar to that of the samples prepared through other direct coupling methods (Ge/C-HT180 and Ge/C-SS750), except for the emergence of two bands at 1354 and 1608 cm^{-1}, D band and G band, respectively, which signify disordered and graphitic phases of carbon-based materials [45,46]. The difference in Raman signals between Ge/C-iM750

and pure Ge is more notable. New peaks appear at 252, 264, 438 and 509 cm^{-1}, indicating further in situ surface oxidation of newly formed Ge and functional groups containing oxygen on the carbon material [47].

The intensity ratio of the Ge–Ge (ca. 300 cm^{-1}) and Ge–O (ca. 440 cm^{-1}) signals can be used to assess the thickness of the oxide layer [48]. The I_{Ge-O}/I_{Ge-Ge} ratio shows a significant increase from 0.134 (pure Ge) to 1.68 (Ge/C-iM750). The ratio of Ge/C-SS750 is I_{Ge-O}/I_{Ge-Ge} = 0.721, which may be explained by the fact that oxygen-containing functional groups of biomass carbon induce the oxidation of Ge [47]. However, the lower ratio observed in Ge/C-SS750 suggests a less tight contact between Ge and carbon matrix than in Ge/C-iM750. In addition, the emergence of a new signal at 208 cm^{-1} and the decreased intensity of the transverse optic mode of crystalline Ge suggest the development of a novel Ge–C bond, akin to what has been observed in earlier studies on Ge–Sn and Ge–graphene [49,50]. Upon closer inspection of the Raman spectra between 1200 and 1800 cm^{-1}, it can be observed that the I_D/I_G intensity ratio increases from 0.79 for BC-800 to 1.07 for Ge/C-iM750. This indicates that the graphite structure has undergone deformation, resulting in a highly disordered carbon matrix. Such a transformation is anticipated to enhance the conductivity and to increase the number of active sites for binding lithium ions [51,52]. These results demonstrate the enhanced contact between the in situ formed Ge and the carbon matrix, which promotes conductivity, accommodates volume variation, and ultimately improves the electrochemical performance of the material.

The morphology of the materials was observed using FE-SEM and HR-TEM. As shown in Figure 2a, the spherical Ge nanoparticles are quite uniform, with dimensions of several nanometers. In Figure 2b, the composite Ge/C-iM750 combines Ge nanoparticles with porous activated carbon. The texture of Ge@C composites was observed using TEM. According to Figure 2d–f, the Ge nanoparticles in Ge/C-iM750 are well dispersed in the porous carbon matrix, while they seem to be aggregated on the carbon surface in Ge/C-HT180 or unevenly distributed in Ge/C-SS750.

Electrochemical characterization

The electrochemical behavior during lithiation/delithiation of Ge and Ge@C electrodes was investigated using CV curves. As shown in Figure 3a, the first cathodic process of the Ge electrode yielded a reduction peak at 0.17 V vs Li/Li^+ and a broad band from 1.0 to 0.6 V vs Li/Li^+. The lower-potential peak with stronger intensity can be attributed to the lithiation of Ge to form Li_xGe alloys with various compositions such as Li_7Ge_2, Li_9Ge_4, and $Li_{22}Ge_2$ [53-55]. The remaining shoulder can be ascribed to the decomposition of the electrolyte and the formation of solid–electrolyte interface (SEI) layers [55,56]. In the following cycles, the signal of the SEI layer formation at a potentials of 0.3 V vs Li/Li^+ remains, demonstrating the continuous loss of lithium in this irreversible process. This is consistent with the fact that the alloying electrodes suffer from damages caused by the volume variation during lithiation/delithiation, leading to the continuous exposure of new active material and electrolyte [57,58]. In the first anodic process, the peaks at 0.30 and 0.56 V vs Li/Li^+ correspond to the dealloying

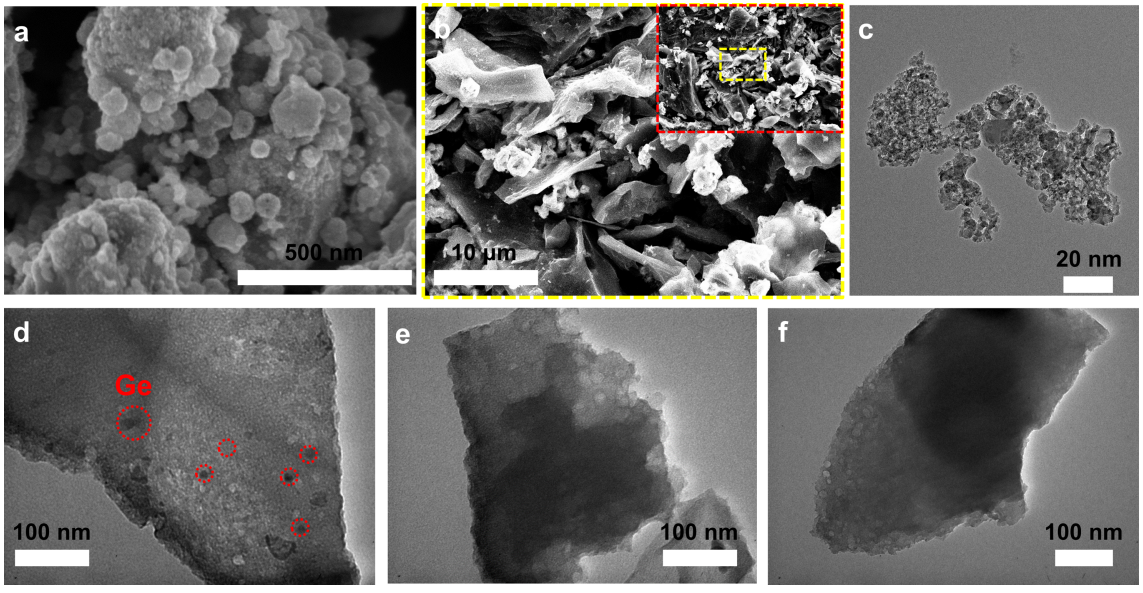


Figure 2: SEM images of (a) Ge and (b) Ge/C-iM750; TEM images of (c) Ge, (d) Ge/C-iM750, (e) Ge/C-HT180, and (f) Ge/C-SS750.

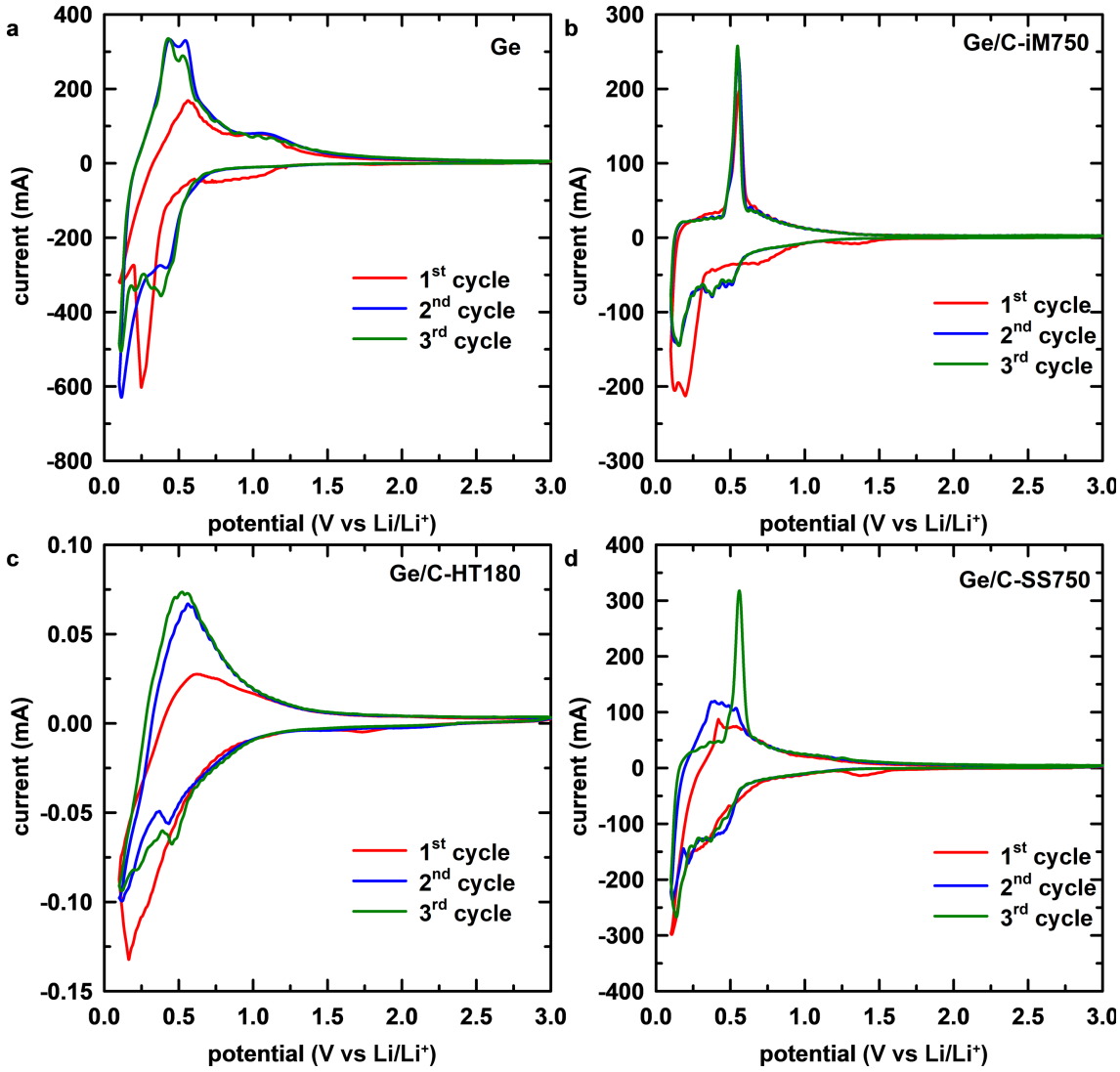


Figure 3: CV measurements of (a) pure Ge, (b) Ge/C-iM750, (c) Ge/C-HT180, and (d) Ge/C-SS750 electrodes.

reaction of Li_xGe alloys. This multistep delithiation correlates to the stepwise alloying observed by the splitting of cathodic peaks in the following cycles. Compared to the signals in the first cycle, the subsequent cycles yield broad and low-intensity peaks caused by the electrochemical milling of the active material, leading to reduced size and amorphous structures [59,60].

For the Ge@C electrodes, the first cathodic peaks in the potential range of 0.5–1.5 V vs Li/Li^+, are assigned to the formation of the SEI layer. They mostly disappear in the subsequent cycles, which demonstrates the buffering role of the carbon matrix in accommodating volume variation and stabilizing the SEI layer [61]. Besides the peak at 0.2 V vs Li/Li^+ in the first cycle, corresponding to the alloying of lithium ions, a new signal was observed at 0.1 V vs Li/Li^+, ascribed to the intercalation of the carbon structure [55]. In the following cycles, multistep alloying processes of Ge appear in the range of 0.1–0.8 V vs Li/Li^+. In the anodic process, the deintercalation of lithium ions from carbon (0.1 V vs Li/Li^+) and from Li_xGe alloys (0.3–0.6 V vs Li/Li^+) is similar in all three Ge@C electrodes. However, the CV curve of Ge/C-iM750 exhibits the highest repeatability. This demonstrates the high stability and reversibility during lithiation/delithiation of this electrode, which could be explained by the better chemical contact between two components, as previously discussed. Noticeably, compared to the Ge component, the reversibly electrochemical signals of carbon (0.1 V for carbon and 0.56 V for Ge) are much lower. This partly indicates that the contribution of the carbon matrix to the total capacity of the electrode is negligible.

The galvanostatic cycling with potential limitation (GCPL) profiles of all electrodes in the first three cycles are shown in Figure 4. The first discharge curve of the Ge electrode consists of two plateaus at 0.20 and 0.40 V vs Li/Li$^+$, corresponding to the alloying of Li and Ge and the formation of the SEI layer. In the first charge process, the plateau at 0.52 V vs Li/Li$^+$ is attributed to the dealloying of Li_xGe. The long plateau from 0.65 to 0.25 V vs Li/Li$^+$ illustrates the continuous irreversible SEI formation in the subsequent cycles. Meanwhile, the signal of SEI formation (plateau at 0.75 V vs Li/Li$^+$) in the first cycle vanished in the next discharge, consistent with the CV observations. Compared to the pure Ge electrode, the Ge@C electrodes exhibit lower specific discharge capacity and Coulombic efficiency (CE) values in the first cycle. As summarized in Table 1, the pure Ge electrode delivers specific discharge/charge capacities of 601.7/430.1 mAh·g^{-1}, corresponding to a value of the first CE of 71.5%, while the values of Ge/C-HT180 and Ge/C-SS750 are 795.6/307.7 and 946.7/441.2 mAh·g^{-1}, with values of the first CE of 38.7% and 46.6%, respectively. The increase in the first specific discharge capacities and the decrease in the initial CE values of Ge@C electrodes can be attributed to the large contribution of the irreversible SEI formation because of the large surface area of biomass-derived activated carbon [62-64], which is electrochemically inactive, as observed in the CV results.

The first discharge/charge capacities of the Ge/C-iM-750 electrode are 1008.5/791.7 mAh·g^{-1}, accounting for value of the

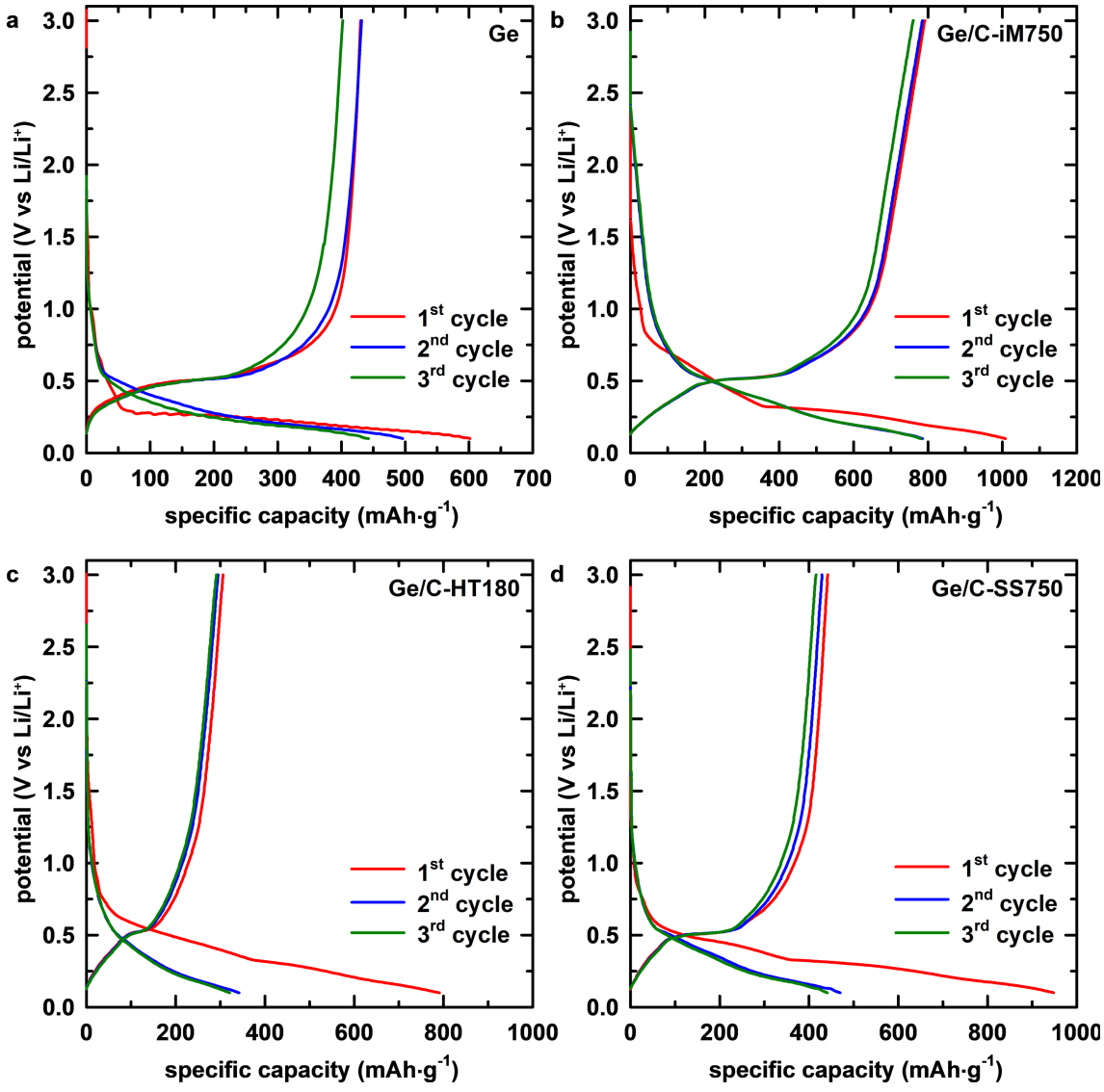


Figure 4: GCPL profiles for the three first cycles of (a) pure Ge, (b) Ge/C-iM750, (c) Ge/C-HT180, and (d) Ge/C-SS750 electrodes.

Table 1: Summarized results of the electrochemical performance of all electrodes (the specific current was 100 mA·g^{-1} for the first five cycles and 1000 mA·g^{-1} for the subsequent cycles).

Electrode	First specific discharge capacity (mAh·g^{-1})	First Coulombic efficiency (%)	Specific discharge capacity at the 200th cycle (mAh·g^{-1})	Retention at 200th cycle (%)
Ge	601.7	71.5	74.8	41.7
Ge/C-iM750	1008.5	78.5	454.2	95.2
Ge/C-HT180	795.6	38.8	168.3	86.2
Ge/C-SS750	946.7	46.6	204.8	90.2

first CE of 78.5%. The improved initial CE of Ge/C-iM750 could be attributed to the effect of the in situ magnesiothermic reduction on the carbon structure, as observed in Raman results, as well as the enhanced chemical contact between Ge and carbon matrix. In the subsequent cycles, the CE of all samples increases and reaches approximately 100%, demonstrating the good reversibility of these electrodes. Nevertheless, the slower increase in CE of Ge in the first few cycles is indicative of the unstable SEI of this electrode.

The specific capacity values as function of the number of cycles are shown in Figure 5a. After increasing the specific current to 1000 mA·g^{-1}, the Ge electrode exhibits a rapid capacity fading to 74.8 mAh·g^{-1}, with a retention of 41.7% (compared to the

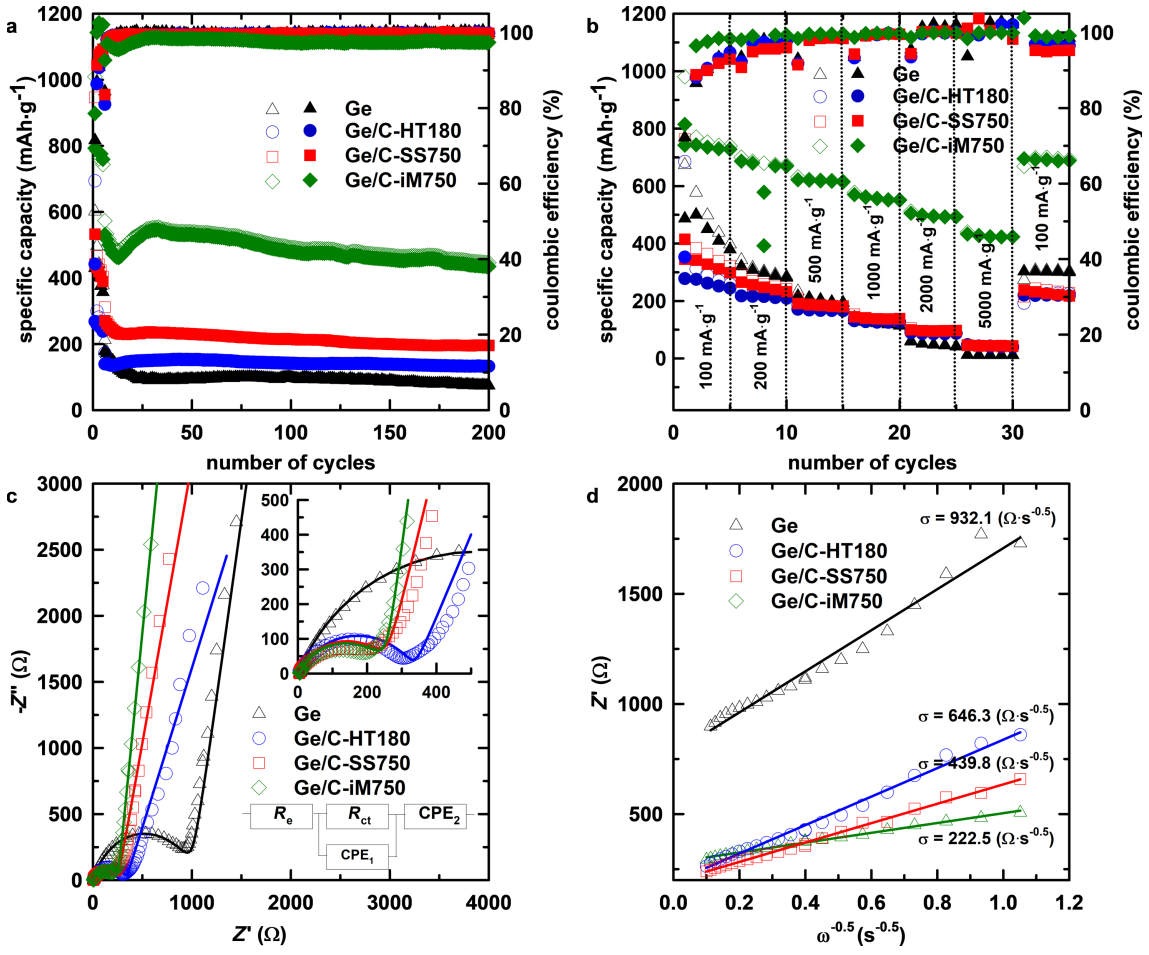


Figure 5: (a) Cycling, (b) rate performance, (c) Nyquist plots of pure Ge, Ge/C-iM750, Ge/C-HT180, and Ge/C-SS750 electrodes, and (d) fit results of the real part of the impedance (Z', Ω) as a function of the angular frequency to the power of −0.5 ($\omega^{-0.5}$, $s^{-0.5}$).

sixth cycle) after 200 cycles. This is explained by the breakdown of Ge particles during continuous lithiation/delithiation, which causes high structural stress and leads to the loss of electrical contact between active material and the current collector. The Ge@C electrodes, after a short period of fading after the change of specific current, deliver a stable specific capacity for almost 200 cycles with retention values of 90.2, 86.2, and 95.2% for Ge/C-SS750, Ge/C-HT180, and Ge/C-iM750, respectively. This observation demonstrates that the presence of a carbon matrix is useful in stabilizing the electrode by alleviating the stress caused by volume change. Amongst the composites, the electrochemical performance increases in the order of Ge/C-HT180 < Ge/C-SSS750 < Ge/C-iM750. The origin of this improvement is the better chemical contact between Ge and the carbon matrix. The Raman results indicate that this chemical contact is enhanced by the high-temperature treatment, which is in agreement with the improved behavior of Ge/C-SSS750 compared to Ge/C-HT180. In addition, the in situ synthesis induces an improved contact between Ge and the carbon matrix, leading to enhanced electronic and ionic conductivity, which was further analyzed using rate performance and EIS results. Figure 5b shows the rate performance of the Ge@C electrodes at different specific currents. The common phenomenon of capacity reduction at increasing specific currents is observed in all electrodes. However, the higher specific capacity (432.3 mAh·g^{-1}) of Ge@C-iM750 indicates an improvement in the kinetics of lithium storage reactions, even under the harshest condition of 5000 mA·g^{-1}.

The Nyquist plots of all electrodes (Figure 5c) contain a semicircle in the high-to-medium frequency range and a sloping tail in the low-frequency region. The former component is characteristic of charge transfer resistance, while the latter presents the diffusion of ions in the solid phase. Compared to the pure Ge electrode, the diameters of the semicircle are smaller in the Ge@C electrodes because of the higher electrical conductivity of the additional carbon matrix, indicating the decrease in charge transfer resistance of the composite electrodes. The EIS results were fitted using an equivalent circuit model, including an internal or electrolyte resistance (R_e), a charge transfer resistance (R_{ct}), and two constant phase elements (CPE) [65]. According to Table 2, the charge transfer resistances of all Ge@C electrodes are much lower than the values of the pure Ge electrode, and Ge/C-iM750 exhibits the lowest value. The ionic conductivity was evaluated using the lithium-ion diffusion coefficient (D_{Li^+}) using the following equation:

$$D_{Li^+} = \frac{R^2T^2}{2A^2n^2F^4C^2\sigma^2}, \quad (2)$$

in which, R (8.314 J·mol^{-1}·K^{-1}) is the molar gas constant, T (289.15 K) is the temperature, A (cm^2) is the effective surface area of the electrodes, n is the number of electrons related to the redox reaction, F (96485 C·mol^{-1}) is the Faraday constant, C (mol·cm^{-3}) is the lithium concentration, and σ (Ω·s$^{-0.5}$) is the Warburg coefficient derived from the linear fit of the real part of the impedance (Z′, Ω) as a function of the angular frequency to the power of −0.5 (ω$^{-0.5}$, s$^{-0.5}$):

$$Z = R_e + R_{ct} + \sigma \cdot \omega^{-0.5}. \quad (3)$$

As shown in Table 2, the D_{Li^+} value of Ge/C-iM750 is 2.37 × 10^{-16} cm^2·s^{-1}, 17.7 times higher than that of pure Ge. Therefore, the presence of the carbon matrix, especially in the in situ synthesized composite, plays a key role by not only accommodating the volume variation but also significantly improving the electrical and ionic conductivity of the electrode.

Conclusion

In this work, one-pot in situ synthesis of Ge@C composites using magnesiothermic reduction was reported. Structural characterization indicates a good binding between Ge and carbon matrix after the in situ synthesis, which alleviates the structural stress induced by volume change and increases the conduction of electrons and ions in the composite electrodes. These observations are supported by the superior electrochemical performance of the Ge/C-iM750 electrode with a specific capacity of 454.2 mAh·g^{-1} after 200 cycles at a specific current of 1000 mA·g^{-1}, which accounted for a retention of 95.2%, and an acceptable rate capacity of 432.3 mAh·g^{-1} at a higher specific

Table 2: Impedance parameters obtained from EIS fitting.

Electrode	R_e (Ω)	R_{ct} (Ω)	σ (Ω·s$^{-0.5}$)	D_{Li^+} (cm^2·s^{-1})
Ge	7.3	1023.7	932.1	1.34 × 10^{-17}
Ge/C-iM750	10.4	221.4	222.5	2.37 × 10^{-16}
Ge/C-HT180	5.2	335.2	646.3	2.79 × 10^{-17}
Ge/C-SS750	6.8	267.1	439.8	6.03 × 10^{-17}

current of 5000 mA·g^{-1}. Other composites were also prepared using hydrothermal and direct solid-state coupling. However, these routes did not provide such a good chemical contact between the components, as demonstrated by their low specific capacity and poor rate performance.

Experimental

Chemicals

The chemicals, including germanium oxide (GeO_2) (99.99%) from Sigma-Aldrich and hydrochloric acid (HCl) (35–37%), magnesium powder (Mg) (99.95%), ethanol (C_2H_5OH) (99.5%), and potassium hydroxide (KOH) (85%) from Xilong, China, were used without further purification. Banana peels were collected from Binh Dinh province, Vietnam.

Fabrication of activated carbon from banana peel

A procedure similar to our previous work [33] has been used to prepare carbon materials from banana peels. An appropriate amount of banana peels was dried at 80 °C overnight in a vacuum oven and ground into small pieces, then placed in a ceramic crucible and heated to 800 °C for 5 h under argon gas flow with a heating rate of 10 °C·min^{-1}. The obtained solid was washed with potassium hydroxide solution (KOH 20%) at 70 °C for 2 h, then leached with 2 M HCl at 70 °C for 15 h and washed several times with de-ionized (DI) water, before being dried in a vacuum oven at 110 °C for 12 h. The product was further heated under air at 300 °C for 3 h. The activated carbon was obtained after washing with 2 M HCL and DI water. It was dried under vacuum and denoted as BC-800.

In situ fabrication of Ge/C-iM750 composite material

A mixture of germanium dioxide, magnesium, and activated carbon at a mass ratio of 5:4:10, was ground well and transferred into a ceramic crucible. The solid was heated to 750 °C under Ar gas flow for 3 h. The obtained powder was rinsed with 1 M HCl to remove by-products. The sample, obtained after rinsing with DI water and drying at 70 °C for 12 h, was denoted as Ge/C-iM750.

An analogous route to our previous work [29] without adding activated carbon was applied to synthesize pure germanium (denoted as Ge).

Hydrothermal coupling to synthesize Ge/C-HT180 composite

The hydrothermal synthesis was carried out according to our previous work [33]. Ge and BC-800 at a mass ratio of 2:5 (approximate to that estimated from the Ge/C-750 precursor) were added to a mixture of ethanol and DI water at a ratio of 1:1 (v/v). The dispersion was well stirred in a Teflon beaker, transferred into an autoclave, and held at 180 °C for 12 h. After cooling to room temperature, the solid was collected and rinsed with DI water to neutral pH. The dried solid was denoted as Ge/C-HT180.

Solid-state reaction coupling to synthesize Ge/C-SS750 composite

Relevant amounts of Ge and BC-800 at a mass ratio of 2:5 were well ground and transferred to a ceramic crucible. The mixture was heated at 750 °C in argon gas flow for 3 h. The obtained solid was re-ground and denoted as Ge/C-SS750.

Material characterization

X-ray diffraction measurements (XRD, Bruker D8 Advance with Cu Kα radiation (λ = 1.5406 Å) at 40 kV and 40 mA) were carried out for structural and phase information. Infrared (IR, Shimadzu IRAffinity-1S) and Raman (LabRAM HR evolution confocal Raman microscope) spectra were measured for bond analysis. Field-emission scanning electron microscopy (FE-SEM, Hitachi S-4800) and high-resolution transmission electron microscopy (HR-TEM, JEOL JEM-2100F) were conducted for morphology and particle size investigation.

A well-blended mixture of active material, conductive carbon C65, and polyvinylidene fluoride (PVDF) binder with a mass ratio of 75:15:10 in *N*-methyl-2-pyrrolidone solvent was used for fabricating the working electrodes. The obtained slurry was cast onto copper foil using an automatic film coater and dried in a vacuum oven at 80 °C for 10 h. Discs (diameter of 12 mm with a mass loading of the active material of around 1.2 mg·cm^{-2}) punched from the film were used as a working electrodes. CR2032 coin cells, in half-cell configuration, were assembled in an argon-filled glovebox (MB 20 G, MBRAUN), with oxygen content and moisture below 1.0 ppm. A disc-shaped lithium metal foil was used as counter electrode, and a glassy carbon fiber pad soaked in 1 M electrolyte of $LiPF_6$ in ethylene carbonate/dimethyl carbonate/diethyl carbonate (1:1:1, v/v) with 5% of fluoroethylene carbonate (by mass) was used as separator.

Galvanostatic cycling with potential limitation (GCPL) was performed on a LAND battery testing system CT-2001A in a potential window of 0.1–3.0 V vs Li/Li$^+$ at specific currents of 100 mA·g^{-1} for the initial five cycles and 1000 mAh·g^{-1} for the following cycles. The rate performance was measured under the same conditions with different specific currents from 100 to 5000 mA·g^{-1}. Cyclic voltammetry (CV) was carried out in the above potential window at a scan rate of 0.1 mV·s^{-1} on a Biologic-MPG2 instrument. Electrochemical impedance spectroscopy (EIS) was carried out at the open-circuit voltage of the

assembled cells after 6 h of resting on a Biologic VSP3 potentiostat. A sinusoidal signal with an amplitude of 10.0 mV and a frequency varying exponentially from 10 mHz to 100 kHz was used.

Funding

This research was funded by The Vietnamese Ministry of Education and Training under grant B2021-DQN-04.

ORCID® iDs

Ha Tran Huu - https://orcid.org/0000-0002-2153-1076
Ngoc Phi Nguyen - https://orcid.org/0009-0002-3763-8799
Huy Hoang Luc - https://orcid.org/0009-0006-4836-3531
In Young Kim - https://orcid.org/0000-0003-4150-1306
Vien Vo - https://orcid.org/0000-0002-7197-0923

References

1. Lelieveld, J.; Klingmüller, K.; Pozzer, A.; Burnett, R. T.; Haines, A.; Ramanathan, V. *Proc. Natl. Acad. Sci. U. S. A.* **2019,** *116,* 7192–7197. doi:10.1073/pnas.1819989116
2. Khare, V.; Nema, S.; Baredar, P. *Renewable Sustainable Energy Rev.* **2016,** *58,* 23–33. doi:10.1016/j.rser.2015.12.223
3. Panwar, N. L.; Kaushik, S. C.; Kothari, S. *Renewable Sustainable Energy Rev.* **2011,** *15,* 1513–1524. doi:10.1016/j.rser.2010.11.037
4. Olabi, A. G. *Energy* **2017,** *136,* 1–6. doi:10.1016/j.energy.2017.07.054
5. Vidhi, R.; Shrivastava, P. *Energies (Basel, Switz.)* **2018,** *11,* 483. doi:10.3390/en11030483
6. Peng, M.; Liu, L.; Jiang, C. *Renewable Sustainable Energy Rev.* **2012,** *16,* 1508–1515. doi:10.1016/j.rser.2011.12.009
7. Hannan, M. A.; Hoque, M. M.; Mohamed, A.; Ayob, A. *Renewable Sustainable Energy Rev.* **2017,** *69,* 771–789. doi:10.1016/j.rser.2016.11.171
8. Tian, Y.; Zeng, G.; Rutt, A.; Shi, T.; Kim, H.; Wang, J.; Koettgen, J.; Sun, Y.; Ouyang, B.; Chen, T.; Lun, Z.; Rong, Z.; Persson, K.; Ceder, G. *Chem. Rev.* **2021,** *121,* 1623–1669. doi:10.1021/acs.chemrev.0c00767
9. Kamran, M.; Raugei, M.; Hutchinson, A. *Resour., Conserv. Recycl.* **2021,** *167,* 105412. doi:10.1016/j.resconrec.2021.105412
10. Xu, W.; Welty, C.; Peterson, M. R.; Read, J. A.; Stadie, N. P. *J. Electrochem. Soc.* **2022,** *169,* 010531. doi:10.1149/1945-7111/ac4b87
11. Asenbauer, J.; Eisenmann, T.; Kuenzel, M.; Kazzazi, A.; Chen, Z.; Bresser, D. *Sustainable Energy Fuels* **2020,** *4,* 5387–5416. doi:10.1039/d0se00175a
12. Yan, C.; Liu, Q.; Gao, J.; Yang, Z.; He, D. *Beilstein J. Nanotechnol.* **2017,** *8,* 222–228. doi:10.3762/bjnano.8.24
13. Ma, F.; Guan, S.; Liu, D.; Liu, Z.; Qiu, Y.; Sun, C.; Wang, Y.-J. *J. Alloys Compd.* **2023,** *940,* 168777. doi:10.1016/j.jallcom.2023.168777
14. Liu, X.; Wu, X.-Y.; Chang, B.; Wang, K.-X. *Energy Storage Mater.* **2020,** *30,* 146–169. doi:10.1016/j.ensm.2020.05.010
15. Lee, H.; Kim, H.; Doo, S.-G.; Cho, J. *J. Electrochem. Soc.* **2007,** *154,* A343. doi:10.1149/1.2437059
16. Xue, D.-J.; Xin, S.; Yan, Y.; Jiang, K.-C.; Yin, Y.-X.; Guo, Y.-G.; Wan, L.-J. *J. Am. Chem. Soc.* **2012,** *134,* 2512–2515. doi:10.1021/ja211266m
17. Park, M.-H.; Cho, Y.; Kim, K.; Kim, J.; Liu, M.; Cho, J. *Angew. Chem., Int. Ed.* **2011,** *50,* 9647–9650. doi:10.1002/anie.201103062
18. Song, T.; Cheng, H.; Choi, H.; Lee, J.-H.; Han, H.; Lee, D. H.; Yoo, D. S.; Kwon, M.-S.; Choi, J.-M.; Doo, S. G.; Chang, H.; Xiao, J.; Huang, Y.; Park, W. I.; Chung, Y.-C.; Kim, H.; Rogers, J. A.; Paik, U. *ACS Nano* **2012,** *6,* 303–309. doi:10.1021/nn203572n
19. Chen, H.; Zheng, Y.; Wu, Q.; Zhou, W.; Wei, Q.; Wei, M. *Electrochim. Acta* **2022,** *417,* 140337. doi:10.1016/j.electacta.2022.140337
20. Kim, S.-J.; Park, H.-C.; Kim, M.-C.; Kim, D.-M.; Lee, Y.-W.; Park, K.-W. *J. Power Sources* **2015,** *273,* 707–715. doi:10.1016/j.jpowsour.2014.09.162
21. Park, M.-H.; Kim, K.; Kim, J.; Cho, J. *Adv. Mater. (Weinheim, Ger.)* **2010,** *22,* 415–418. doi:10.1002/adma.200901846
22. Xiao, Y.; Cao, M. *ACS Appl. Mater. Interfaces* **2014,** *6,* 12922–12930. doi:10.1021/am502867f
23. Henderson, E. J.; Hessel, C. M.; Veinot, J. G. C. *J. Am. Chem. Soc.* **2008,** *130,* 3624–3632. doi:10.1021/ja710286a
24. Vaughn, D. D., II; Bondi, J. F.; Schaak, R. E. *Chem. Mater.* **2010,** *22,* 6103–6108. doi:10.1021/cm1015965
25. Liu, H.; Wu, T.; Zhang, L.; Wang, X.; Li, H.; Liu, S.; Zhang, Q.; Zhang, X.; Yu, H. *ACS Nano* **2022,** *16,* 14402–14411. doi:10.1021/acsnano.2c04748
26. Jia, H.; Kloepsch, R.; He, X.; Badillo, J. P.; Gao, P.; Fromm, O.; Placke, T.; Winter, M. *Chem. Mater.* **2014,** *26,* 5683–5688. doi:10.1021/cm5025124
27. Yoo, J.-K.; Kim, J.; Jung, Y. S.; Kang, K. *Adv. Mater. (Weinheim, Ger.)* **2012,** *24,* 5452–5456. doi:10.1002/adma.201201601
28. Petrack, J.; Jost, S.; Boenigk, J.; Epple, M. *Beilstein J. Nanotechnol.* **2014,** *5,* 554–560. doi:10.3762/bjnano.5.65
29. Nhung Thi Nguyen, H.; Nguyen Ngoc, P.; Tran Huu, H.; Thuy Trang Phan, T.; Nhan Nguyen, D.; Huong Thi Nguyen, T.; Nguyen Van, T.; Nguyen Thi, L.; Kha Le, M.; Man Tran, V.; Loan Phung Le, M.; Vo, V. *Chem. Phys. Lett.* **2022,** *801,* 139747. doi:10.1016/j.cplett.2022.139747
30. Ruttert, M.; Holtstiege, F.; Hüsker, J.; Börner, M.; Winter, M.; Placke, T. *Beilstein J. Nanotechnol.* **2018,** *9,* 2381–2395. doi:10.3762/bjnano.9.223
31. Zhang, H.; Zong, P.; Chen, M.; Jin, H.; Bai, Y.; Li, S.; Ma, F.; Xu, H.; Lian, K. *ACS Nano* **2019,** *13,* 3054–3062. doi:10.1021/acsnano.8b08088
32. Yoon, S.; Jung, S.-H.; Jung, K.-N.; Woo, S.-G.; Cho, W.; Jo, Y.-N.; Cho, K. Y. *Electrochim. Acta* **2016,** *188,* 120–125. doi:10.1016/j.electacta.2015.11.132
33. Le Thi, T.; Phan Thi Thuy, T.; Tran Thi Thu, P.; Nguyen Thi, L.; Nguyen Van, T.; Vo, V. *Vietnam J. Catal. Adsorpt.* **2022,** *11,* 26–30. doi:10.51316/jca.2022.065
34. Zhang, Y.; Huang, Y.; Feng, C.; Zhang, Y.; Wu, H. *Ionics* **2019,** *25,* 6051–6059. doi:10.1007/s11581-019-03136-9
35. Palanisamy, S.; Shyma, A. P.; Srinivasan, S.; Venkatachalam, R. *J. Energy Storage* **2019,** *22,* 283–294. doi:10.1016/j.est.2019.02.006
36. Li, W.; Zhu, Y. *Energy Fuels* **2014,** *28,* 3645–3654. doi:10.1021/ef500300r
37. Ardyanian, M.; Rinnert, H.; Vergnat, M. *J. Lumin.* **2009,** *129,* 729–733. doi:10.1016/j.jlumin.2009.02.013
38. Li, D.-C.; Ding, J.-W.; Qian, T.-T.; Zhang, S.; Jiang, H. *RSC Adv.* **2016,** *6,* 12226–12234. doi:10.1039/c5ra22870k

39. Li, G.; Zhu, W.; Zhang, C.; Zhang, S.; Liu, L.; Zhu, L.; Zhao, W. *Bioresour. Technol.* **2016,** *206,* 16–22. doi:10.1016/j.biortech.2015.12.087
40. Bermejo, D.; Cardona, M. *J. Non-Cryst. Solids* **1979,** *32,* 405–419. doi:10.1016/0022-3093(79)90085-1
41. Zanatta, A. R. *Results Phys.* **2020,** *19,* 103500. doi:10.1016/j.rinp.2020.103500
42. Parker, J. H., Jr.; Feldman, D. W.; Ashkin, M. *Phys. Rev.* **1967,** *155,* 712–714. doi:10.1103/physrev.155.712
43. Sui, Z.; Herman, I. P. *Phys. Rev. B* **1993,** *48,* 17938–17953. doi:10.1103/physrevb.48.17938
44. Sato, T.; Suda, J. *J. Phys. Soc. Jpn.* **1998,** *67,* 3809–3815. doi:10.1143/jpsj.67.3809
45. Boncel, S.; Pattinson, S. W.; Geiser, V.; Shaffer, M. S. P.; Koziol, K. K. K. *Beilstein J. Nanotechnol.* **2014,** *5,* 219–233. doi:10.3762/bjnano.5.24
46. Venosta, L.; Bajales, N.; Suárez, S.; Bercoff, P. G. *Beilstein J. Nanotechnol.* **2018,** *9,* 2708–2717. doi:10.3762/bjnano.9.253
47. Xu, R.; Wu, S.; Du, Y.; Zhang, Z. *Chem. Eng. J.* **2016,** *296,* 349–355. doi:10.1016/j.cej.2016.03.126
48. Giri, P.; Dhara, S. *J. Nanomater.* **2012,** 905178. doi:10.1155/2012/905178
49. Sorb, Y. A.; Subramanian, N.; Ravindran, T. R.; Sahu, P. C. *AIP Conf. Proc.* **2012,** *1447,* 145–146. doi:10.1063/1.4709923
50. Sorb, Y. A.; Subramanian, N.; Ravindran, T. R.; Sahu, P. C. *AIP Conf. Proc.* **2011,** *1349,* 1305–1306. doi:10.1063/1.3606347
51. Guo, R.; Liu, X.; Wen, B.; Liu, F.; Meng, J.; Wu, P.; Wu, J.; Li, Q.; Mai, L. *Nano-Micro Lett.* **2020,** *12,* 148. doi:10.1007/s40820-020-00481-7
52. Sun, N.; Guan, Z.; Liu, Y.; Cao, Y.; Zhu, Q.; Liu, H.; Wang, Z.; Zhang, P.; Xu, B. *Adv. Energy Mater.* **2019,** *9,* 1901351. doi:10.1002/aenm.201901351
53. Zhang, C.; Lin, Z.; Yang, Z.; Xiao, D.; Hu, P.; Xu, H.; Duan, Y.; Pang, S.; Gu, L.; Cui, G. *Chem. Mater.* **2015,** *27,* 2189–2194. doi:10.1021/acs.chemmater.5b00218
54. Ren, J.-G.; Wu, Q.-H.; Tang, H.; Hong, G.; Zhang, W.; Lee, S.-T. *J. Mater. Chem. A* **2013,** *1,* 1821–1826. doi:10.1039/c2ta01286c
55. Gao, C.; Kim, N. D.; Villegas Salvatierra, R.; Lee, S.-K.; Li, L.; Li, Y.; Sha, J.; Silva, G. A. L.; Fei, H.; Xie, E.; Tour, J. M. *Carbon* **2017,** *123,* 433–439. doi:10.1016/j.carbon.2017.07.081
56. Fang, S.; Shen, L.; Zheng, H.; Zhang, X. *J. Mater. Chem. A* **2015,** *3,* 1498–1503. doi:10.1039/c4ta04350b
57. Li, N.-W.; Yin, Y.-X.; Yang, C.-P.; Guo, Y.-G. *Adv. Mater. (Weinheim, Ger.)* **2016,** *28,* 1853–1858. doi:10.1002/adma.201504526
58. Shen, C.; Hu, G.; Cheong, L.-Z.; Huang, S.; Zhang, J.-G.; Wang, D. *Small Methods* **2018,** *2,* 1700298. doi:10.1002/smtd.201700298
59. Kim, J. K.; Park, G. D.; Kang, Y. C. *J. Korean Ceram. Soc.* **2019,** *56,* 65–70. doi:10.4191/kcers.2019.56.1.07
60. Tran Huu, H.; Im, W. B. *ACS Appl. Mater. Interfaces* **2020,** *12,* 35152–35163. doi:10.1021/acsami.0c11862
61. Liu, L.; Wang, X.; Zhang, X.; Zhang, X.; Chen, S. *Ionics* **2020,** *26,* 2225–2231. doi:10.1007/s11581-019-03398-3
62. Muraleedharan Pillai, M.; Kalidas, N.; Zhao, X.; Lehto, V.-P. *Front. Chem. (Lausanne, Switz.)* **2022,** *10,* 882081. doi:10.3389/fchem.2022.882081
63. Xie, F.; Xu, Z.; Guo, Z.; Titirici, M.-M. *Prog. Energy* **2020,** *2,* 042002. doi:10.1088/2516-1083/aba5f5
64. Zhu, Y.; Chen, M.; Li, Q.; Yuan, C.; Wang, C. *Carbon* **2018,** *129,* 695–701. doi:10.1016/j.carbon.2017.12.103
65. Nguyen, H. T.; Tran, T. L.; Nguyen, D. T.; Shin, E.-C.; Kang, S.-H.; Lee, J.-S. *J. Korean Ceram. Soc.* **2018,** *55,* 244–260. doi:10.4191/kcers.2018.55.3.11

License and Terms

This is an open access article licensed under the terms of the Beilstein-Institut Open Access License Agreement (https://www.beilstein-journals.org/bjnano/terms), which is identical to the Creative Commons Attribution 4.0 International License (https://creativecommons.org/licenses/by/4.0). The reuse of material under this license requires that the author(s), source and license are credited. Third-party material in this article could be subject to other licenses (typically indicated in the credit line), and in this case, users are required to obtain permission from the license holder to reuse the material.

The definitive version of this article is the electronic one which can be found at:
https://doi.org/10.3762/bjnano.14.62

BEILSTEIN JOURNAL OF NANOTECHNOLOGY

Silver nanoparticles loaded on lactose/alginate: in situ synthesis, catalytic degradation, and pH-dependent antibacterial activity

Nguyen Thi Thanh Tu[1], T. Lan-Anh Vo[2], T. Thu-Trang Ho[2], Kim-Phuong T. Dang[2], Van-Dung Le[2], Phan Nhat Minh[*2], Chi-Hien Dang[2,3], Vinh-Thien Tran[*4], Van-Su Dang[5], Tran Thi Kim Chi[6], Hieu Vu-Quang[7], Radek Fajgar[8], Thi-Lan-Huong Nguyen[9], Van-Dat Doan[10] and Thanh-Danh Nguyen[*2,3]

Full Research Paper

Open Access

Address:
[1]Faculty of Applied Technology, School of Technology, Van Lang University, Ho Chi Minh City, Vietnam, [2]Institute of Chemical Technology, Vietnam Academy of Science and Technology, 1A TL29 Street, District 12, Ho Chi Minh City 700000, Vietnam, [3]Graduate University of Science and Technology, Vietnam Academy of Science and Technology, 18 Hoang Quoc Viet, Cau Giay, Hanoi 11000, Vietnam, [4]Faculty of Environment Ho Chi Minh City University of Natural Resources and Environment, 236B Le Van Sy Street, Tan Binh District, Ho Chi Minh City 700000, Vietnam, [5]Department of Chemical Technology, Ho Chi Minh City University of Food Industry, Ho Chi Minh City 700000, Vietnam, [6]Institute of Materials Science, Vietnam Academy of Science and Technology, 18 Hoang Quoc 14 Viet, Cau Giay District, Hanoi 11000, Vietnam, [7]NTT Hi-Tech Institute, Nguyen Tat Thanh University, Ho Chi Minh City 700000, Vietnam, [8]Institute of Chemical Process Fundamentals of the AS CR Prague, Czech Republic, [9]Institute of Biotechnology and Food Technology, Industrial University of Ho Chi Minh City, Ho Chi Minh City, Vietnam and [10]Faculty of Chemical Engineering, Industrial University of Ho Chi Minh City, Ho Chi Minh City, Vietnam

Email:
Phan Nhat Minh[*] - phannhatminh@gmail.com; Vinh-Thien Tran[*] - tvthien@hcmunre.edu.vn; Thanh-Danh Nguyen[*] - ntdanh@ict.vast.vn

* Corresponding author

Keywords:
alginate; bacterial activity; catalysis; lactose; silver nanoparticles; synthesis

Beilstein J. Nanotechnol. **2023,** *14,* 781–792.
https://doi.org/10.3762/bjnano.14.64

Received: 11 March 2023
Accepted: 20 June 2023
Published: 04 July 2023

This article is part of the thematic issue "Recent advances in synthesis and applications of organometallic nanomaterials".

Associate Editor: A. Salvati



© 2023 Tu et al.; licensee Beilstein-Institut.
License and terms: see end of document.

Abstract

We present the in situ synthesis of silver nanoparticles (AgNPs) through ionotropic gelation utilizing the biodegradable saccharides lactose (Lac) and alginate (Alg). The lactose reduced silver ions to form AgNPs. The crystallite structure of the nanocomposite

AgNPs@Lac/Alg, with a mean size of 4–6 nm, was confirmed by analytical techniques. The nanocomposite exhibited high catalytic performance in degrading the pollutants methyl orange and rhodamine B. The antibacterial activity of the nanocomposite is pH-dependent, related to the alterations in surface properties of the nanocomposite at different pH values. At pH 6, the nanocomposite demonstrated the highest antibacterial activity. These findings suggest that this nanocomposite has the potential to be tailored for specific applications in environmental and medicinal treatments, making it a highly promising material.

Introduction

Silver nanoparticles (AgNPs) have raised significant interest for their wide range of applications in biomedicine [1,2], treatment of wastewater [3,4], and catalysis [5,6]. The utilization of eco-friendly sources, such as plant extracts [7,8], fungi [9,10], and bacteria [11], for synthesizing AgNPs is an important topic in the field of nanotechnology. However, AgNPs synthesized in that way have a number of drawbacks such as high cost and low stability. Typically, AgNPs are loaded onto polymers/composites in order to enhance their performance in usage [4,10,12]. Among polymers, polysaccharides have shown significant improvement in stabilization because of the hydroxy groups in the sugar molecules of the polysaccharide chain, which can form strong associations with AgNPs [13-15]. Previous studies have reported that metallic nanoparticles can be easily incorporated into polysaccharides by an in situ reduction process that requires no additional chemicals [16,17]. This technique using polysaccharides such as alginate [18] or chitosan [19] in conjunction with reducing agents enhanced cost efficiency and reduced the amounts of impurities or toxic compounds.

AgNPs are widely used as antibacterial agents. One of the advantages of AgNPs over bulk metal or salts is their ability to controllably release silver as ions or particles, resulting in prolonged protection against bacteria [20]. While the specific mechanism of their antibacterial properties is not fully understood, mechanisms such as release of silver ions or electrostatic interaction between AgNPs and microbial cells, have been proposed [21,22]. The AgNPs might release silver ions capable of binding to nucleic acids, thereby, exhibiting antibacterial activity [23,24]. Consequently, any silver-containing composite material with antibacterial properties can serve as a source of silver ions. Another mechanism involves the electrostatic attraction between negatively charged microbial cells and positively charged AgNPs [25]. Because of their affinity to sulfur proteins and through electrostatic attraction, silver ions can bind to both cytoplasm and cell wall, leading to increased permeability and, eventually, disruption of the bacterial cell wall [26]. This disruption can deactivate respiratory enzymes, resulting in the generation of reactive oxygen species [27] and the inhibition of adenosine triphosphate release [26]. The antibacterial properties of AgNPs can be influenced by factors such as size, pH value, and ionic strength of the medium [28-31]. Extensive research has been dedicated to control the size and shape of AgNPs through the application of various capping agents. In addition to their antimicrobial properties, AgNPs are also valuable catalysts for the removal of environmental contaminants in aqueous solutions. The high surface-to-volume ratio of AgNPs provides many active sites, thereby, enhancing their catalytic activity [32]. The catalytic activity of AgNPs is also influenced by the morphology and the use of capping agents [33]. The efficiency of the catalyst can be improved by studying different carrier materials [34,35]. Interface factors, including morphology and capping agents, play a significant role in the catalytic activity of AgNPs. The ionotropic gelation mechanism has been recently employed to create nanocomposites using saccharides, such as alginate, cyclodextrin, and lactose. This method allows for the loading of metallic ions onto the nanocomposite, followed by their reduction to nanoparticles [36,37]. The nanocomposite matrix can release silver in appropriate environments, exhibiting pH-dependent antibacterial activity [38].

In this study, we prepared a nanocomposite, Lac/Alg, to stabilize AgNPs without any additives, utilizing lactose as a reducing agent. The resulting nanocomposite AgNPs@Lac/Alg was used for the catalytic degradation of toxic dyes and investigated regarding its pH-dependent antibacterial activity.

Results and Discussion

Synthesis of AgNPs@Lac/Alg

Our recent work has demonstrated the successful synthesis of AgNPs using a two-step process involving loading and reduction, resulting in nanocomposites composed of alginate and cyclodextrins [36,38]. In the first step, silver ions were loaded onto the nanocomposite [37,39], followed by reduction using plant extract [36,38]. In the present work, we have developed an in situ synthesis method for AgNPs using an alginate composite with lactose as reducing sugar. This method involves the use of lactose as a negatively charged compound that disrupts the cross-linking between Ca^{2+} ions and COO^{-} groups of sugar molecules in the alginate chains, leading to the formation of soluble nanoparticles (Figure 1).

To obtain the nanocomposite AgNPs@Lac/Alg, Ag^{+}@Lac/Alg was reduced through a heating process, without the use of additional additives. The formation of AgNPs was confirmed by a change in the color of the colloidal solution. To find the optimal

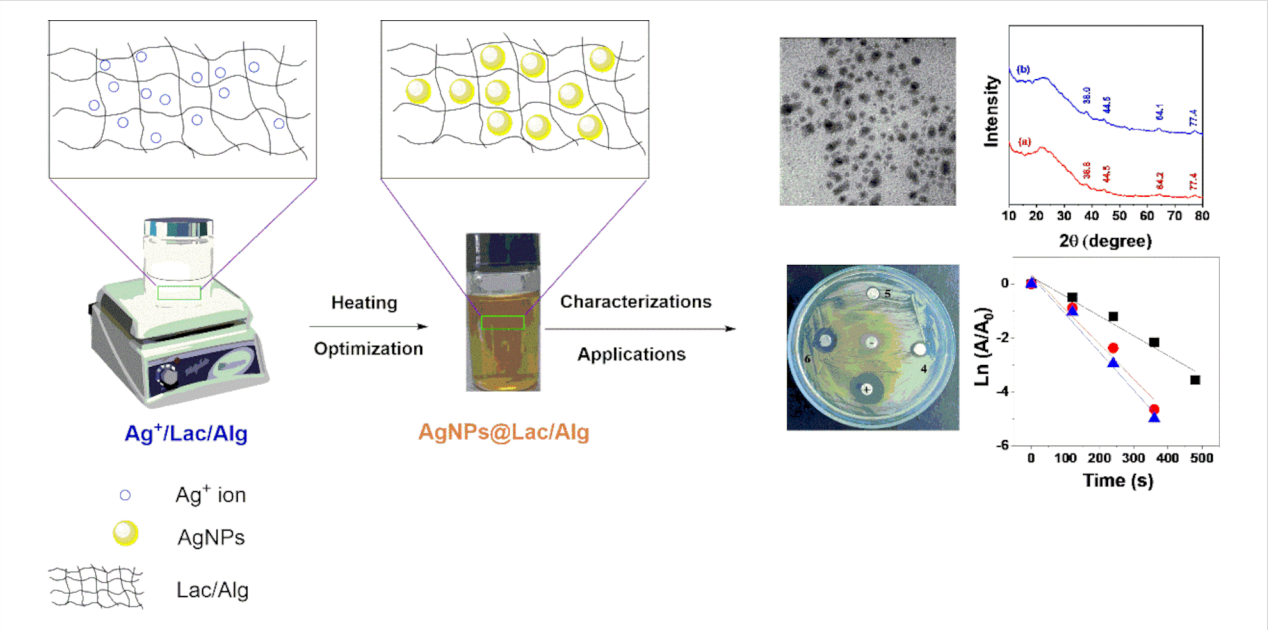


Figure 1: Schematic illustration for route study on AgNPs@Lac/Alg.

reaction conditions, the synthesis of the nanocomposite was carried out while varying the reaction conditions, such as temperature, reaction time, and ratio of Ag^+ to blank composite. Subsequently, AgNPs@Lac/Alg was characterized using various analytical techniques and applied for the catalytic degradation of contaminants and in bacterial activity assays. Absorption spectra were analyzed to monitor changes in physicochemical properties at the maximum peak region of surface plasmon resonance (SPR) of the AgNPs, which falls in the range of 400–450 nm.

The synthesis of stable AgNPs was performed at solution temperatures ranging from 30 to 90 °C. The results are shown in Figure 2A and Figure 2B. Below 70 °C, the SPR peak in the UV–vis spectra disappeared, indicating that no AgNPs were formed at lower solution temperatures. Increasing the reaction temperature resulted in a high concentration of AgNPs in the colloidal solution, with the highest intensity observed at a temperature of 90 °C. However, the increase in temperature did not significantly affect the morphology of the formed AgNPs, as evidenced by the absence of any notable change in λ_{max} values.

To investigate the influence of the reaction time, the gel Ag^+@Lac/Alg was heated at a solution temperature of 90 °C and the UV–vis spectra were measured every 20 min. As seen in Figure 2C and Figure 2D, the formation of AgNPs in the colloidal solution was significantly influenced by the reaction time. The SPR band of AgNPs was not clearly observed within the initial 60 min, indicating a slow formation of the nanocomposite. However, after this period, AgNPs were rapidly produced, leading to a substantial increase in the absorbance values up to 140 min. Throughout the synthesis process, the λ_{max} values showed a slight increase, which confirms the critical role of reaction time in the synthesis of stable nanocomposites.

To assess the impact of silver ion concentration, ratios of silver ions to gel in the range of 0.1–0.7 (w/w) were optimized at 90 °C and 140 min. As shown in Figure 2E and Figure 2F, the concentration of silver ions strongly influenced the formation of AgNPs. A clear absorption peak was not observed at a ratio of 0.1 (w/w), indicating no formation of AgNPs. However, the increase in silver ions resulted in an increase in the absorbance value in the UV–vis spectra. Minor changes in λ_{max} values were noted from the absorption data, indicating a slight influence of the silver-ion-to-nanocomposite ratio on the physicochemical properties of the synthesized AgNPs. Considering these findings, two ratios of silver ions to Lac/Alg, namely 0.3 (AgNPs@Lac/Alg-0.3) and 0.7 (AgNPs@Lac/Alg-0.7), were selected for further physicochemical characterizations.

Physicochemical characterizations

The stability and size of the nanocomposites in the colloidal solution were evaluated through zeta potential and DLS measurements at a temperature of 25 °C. The results are presented in Figure 3, demonstrating that all the synthesized nanocomposites were stable. The zeta potential values of AgNPs@Lac/Alg-0.3 and AgNPs@Lac/Alg-0.7 were −61.6 mV and −41.0 mV, respectively. These values were lower than that of the blank Lac/Alg nanocomposite (−102.7 mV) [37]. The decrease in zeta potential suggests that the presence of AgNPs reduced the nega-

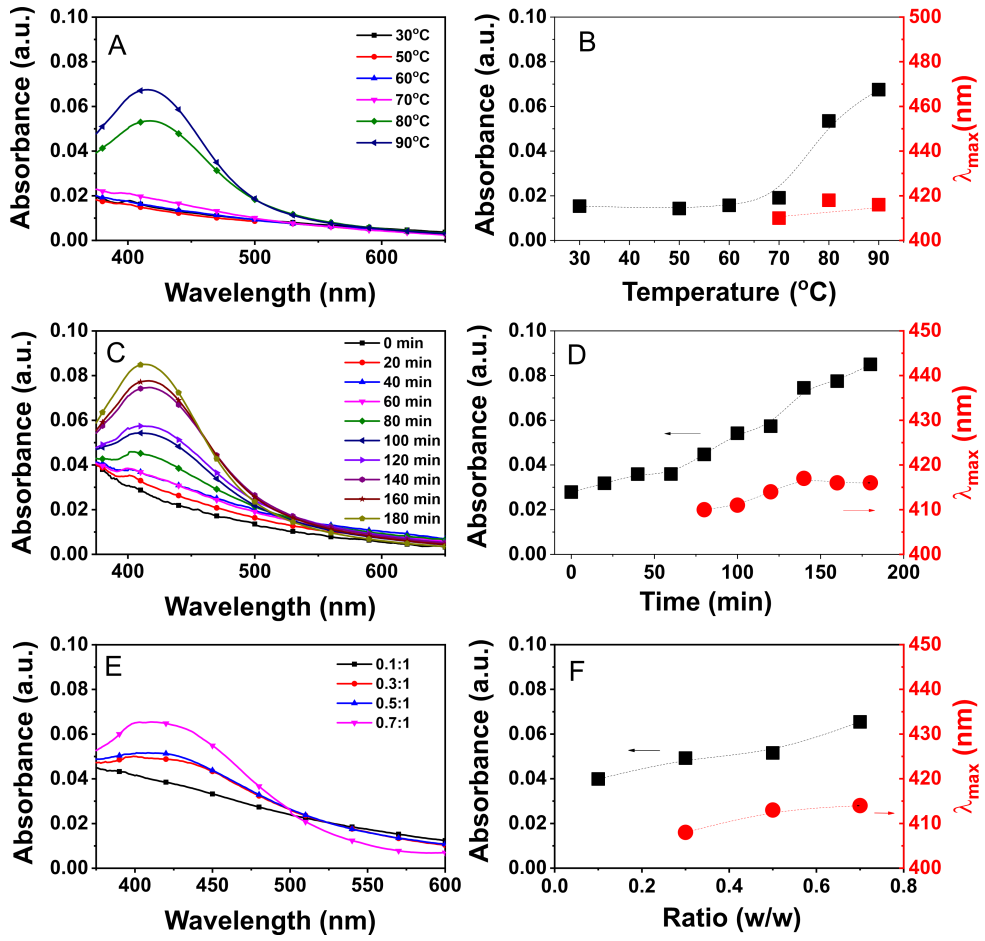


Figure 2: UV–vis spectra of AgNPs@Lac/Alg (left) and plots of absorbance and wavelength (λ_{max}) data (right) recorded as a function of temperature (A and B), reaction time (C and D) and the ratio of silver ion to blank Lac/Alg (E and F).

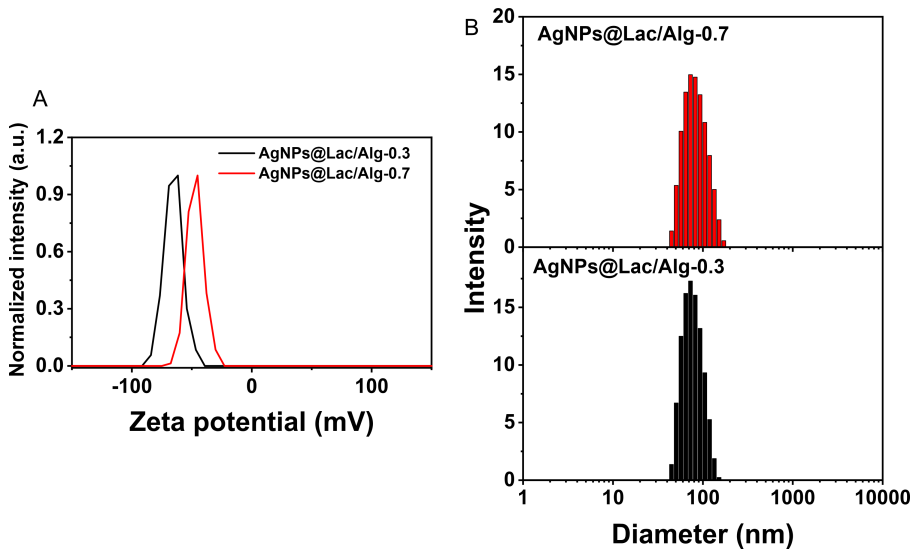


Figure 3: Zeta potentials (A) and size distribution obtained from DLS measurements (B) of AgNPs@Lac/Alg with different amount of AgNPs.

tive charge of the nanocomposites, resulting in a decrease in their stability. The DLS data indicated that both nanocomposites exhibited wide size distributions ranging from 40–150 nm, with mean sizes of 73.9 ± 19.2 nm and 80.2 ± 24.1 nm for AgNPs@Lac/Alg-0.3 and AgNPs@Lac/Alg-0.7, respectively. These findings are consistent with a previous study on the synthesis of gold nanoparticles using this nanocomposite [37].

Figure 4 presents the FTIR spectra of the AgNPs@Lac/Alg nanocomposites. Both spectra exhibit similar signals, including broad band at around 3400 and 2900 cm^{-1}, attributed, respectively, to the –OH and –CH stretching vibrations of the sugar units of polysaccharides [40]. Furthermore, single peaks at 1600 and 1436 cm^{-1} are observed, corresponding to the symmetric and asymmetric stretching vibrations of COO^- groups, respectively [41]. Additionally, the peaks at 1034 and 826 cm^{-1} are attributed to the stretching vibration of C–OH groups and the bending vibration of –CH groups [42]. Based on these data, it can be inferred that the primary components of the nanocomposites are polysaccharides.

To determine the crystalline structure of the nanocomposites, powder XRD patterns are evaluated and displayed in Figure 4B. Both nanocomposites exhibit feature peaks of AgNPs crystals at 2θ angles of about 38°, 44°, 64°, and 77°, indicating, respectively, the (111), (200), (220), and (311) planes of face-centered cubic silver (card number 00-004-0783). The XRD pattern of AgNPs@Lac/Alg-0.7 exhibits more intensive peaks compared to AgNPs@Lac/Alg-0.3, likely because of the different contents of AgNPs in the samples. The calculated XRD parameters are shown in Supporting Information File 1, Table S1. Using the Scherrer equation, the crystallite sizes of AgNPs in the nanocomposites were estimated to be 17.3 ± 2.7 nm for AgNPs@Lac/Alg-0.3 and 14.8 ± 2.5 nm for AgNPs@Lac/Alg-0.7. The mean lattice parameter and the cell volume of AgNPs in AgNPs@Lac/Alg-0.3 were determined to be 4.09 ± 0.02 Å and 68.5 ± 1.0 $Å^3$, respectively, while those of AgNPs@Lac/Alg-0.7 were 4.09 ± 0.2 Å and 68.4 ± 0.8 $Å^3$, respectively [43]. Thus, the XRD data provide evidence for the presence of AgNPs in the nanocomposites.

To evaluate the thermal properties of the AgNPs@Lac/Alg nanocomposites, TGA and DSC measurements were performed on both the blank composite and the nanocomposites in an air flow of 20 mL/min at a heating rate of 10 °C/min. The TGA curve of AgNPs@Lac/Alg closely resembles that of the blank composite. Between 37 and 200 °C, the nanocomposite AgNPs@Lac/Alg-0.3 exhibited a significantly higher thermal loss (28%) compared to the other compounds (ca. 10%), which can be attributed to the presence of hydrate and volatile compo-

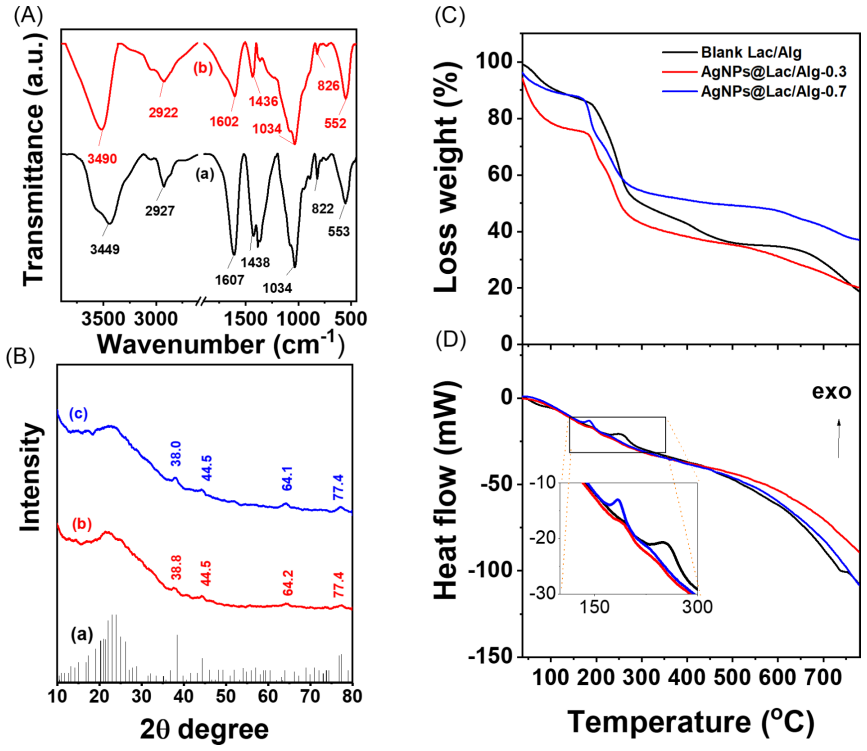


Figure 4: FTIR spectra (A) of AgNPs@Lac/Alg-0.3 (a) and AgNPs@Lac/Alg-0.7 (b); XRD patterns (B) of card number 00-004-0783 (a), AgNPs@Lac/Alg-0.3 (b), and AgNPs@Lac/Alg-0.7 (c); TGA (C) and DSC (D) curves of the different nanocomposites (the colors are the same as in panel (C)).

nents. In the range of 200–800 °C, the binding between the alginate chain and the AgNPs significantly stabilized the weight loss of Lac/Alg [37]. The weight losses of AgNPs@Lac/Alg-0.3 and AgNPs@Lac/Alg-0.7 were approximately 52 and 48%, respectively, while the blank nanocomposite underwent a weight loss of about 68%. The presence of similar quality of ashes remaining after the heating process confirms the presence of inorganic components in the nanocomposites that are comparable to those in the blank nanocomposite.

DSC analysis revealed weakly exothermic peaks in the range of 150–300 °C, corresponding to the oxidation of organic components in the nanocomposites. The temperature peak for the blank sample was found at 248 °C, while for the nanocomposites AgNPs@Lac/Alg-0.3 and AgNPs@Lac/Alg-0.7, the peaks occurred at 187 and 183 °C, respectively. These results suggest that the nanocomposites should be used in temperature regions below 200 °C.

TEM images and size distributions of AgNPs@Lac/Alg are displayed in Figure 5. The TEM images demonstrate the presence of uniformly shaped spherical AgNPs. The size distribution analysis of AgNPs@Lac/Alg-0.3 and AgNPs@Lac/Alg-0.7 indicates that the highest frequency for AgNPs@Lac/Alg-0.3 is at 6 nm while for AgNPs@Lac/Alg-0.7, it is at 4 nm, with sizes ranging from 2 to 8 nm. The results show the similarity in physicochemical properties of the AgNPs@Lac/Alg nanocomposites. Thus, AgNPs@Lac/Alg-0.7 was selected for assessment of its catalytic and antibacterial properties in this study.

Catalytic degradation of contaminants

Toxic organic dyes pose a serious threat to the environment, and their non-biodegradability in aqueous media has led to the consideration of various methods for their treatment [44,45]. In recent years, catalytic degradation using oxidizing and reducing agents such as H_2O_2 and $NaBH_4$ has been frequently reported [46-48]. Plasmonic nanoscale metal particles have demonstrated enhanced catalytic performance in conjunction with $NaBH_4$. The surface of the nanoscale metal particles served as an absorbent of dyes and BH_4^- ions. Subsequently, an electron transfer process occurs from BH_4^- (electron donor) to the dyes (electron acceptor) (Figure 6). As a result, the catalytic efficacy of metal NPs is significantly influenced by factors such as the surface characteristics and concentration of nanocatalyst, which directly impact the binding/adsorption capability of the reactant and the release/desorption of the reaction products [49]. This study aims to investigate the catalytic activity of the nanocomposite AgNPs@Lac/Alg for the degradation of two toxic dyes, methyl orange (MO) and rhodamine B (RhB), using various doses of the nanocomposite.

The degradation of toxic dyes using a nanocomposite catalyst was monitored in situ by measuring UV–vis absorption at ambient temperature, with the concentration changing in a time-dependent manner. The effectiveness of the reactions is confirmed by discoloration of the pollutant solution and a reduction in absorbance values in the UV–vis spectra. In a separate study [45], it was shown that the dyes degraded weakly in the absence of a catalyst. As seen in Figure 7 and Figure 8, the

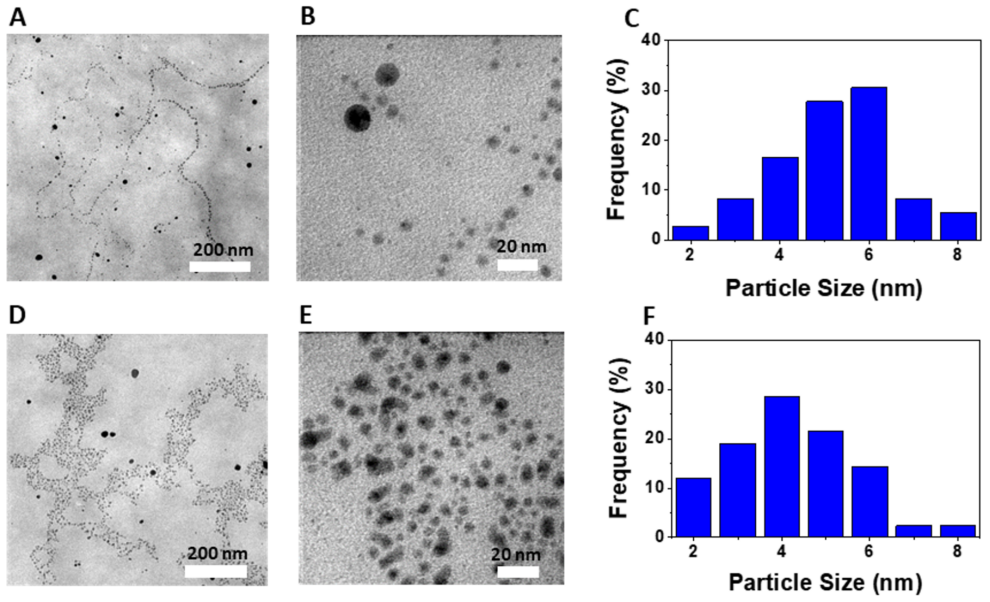


Figure 5: TEM images at different magnifications and particle size distributions of AgNPs@Lac/Alg-0.3 (A, B and C) and AgNPs@Lac/Alg-0.7 (D, E and F).

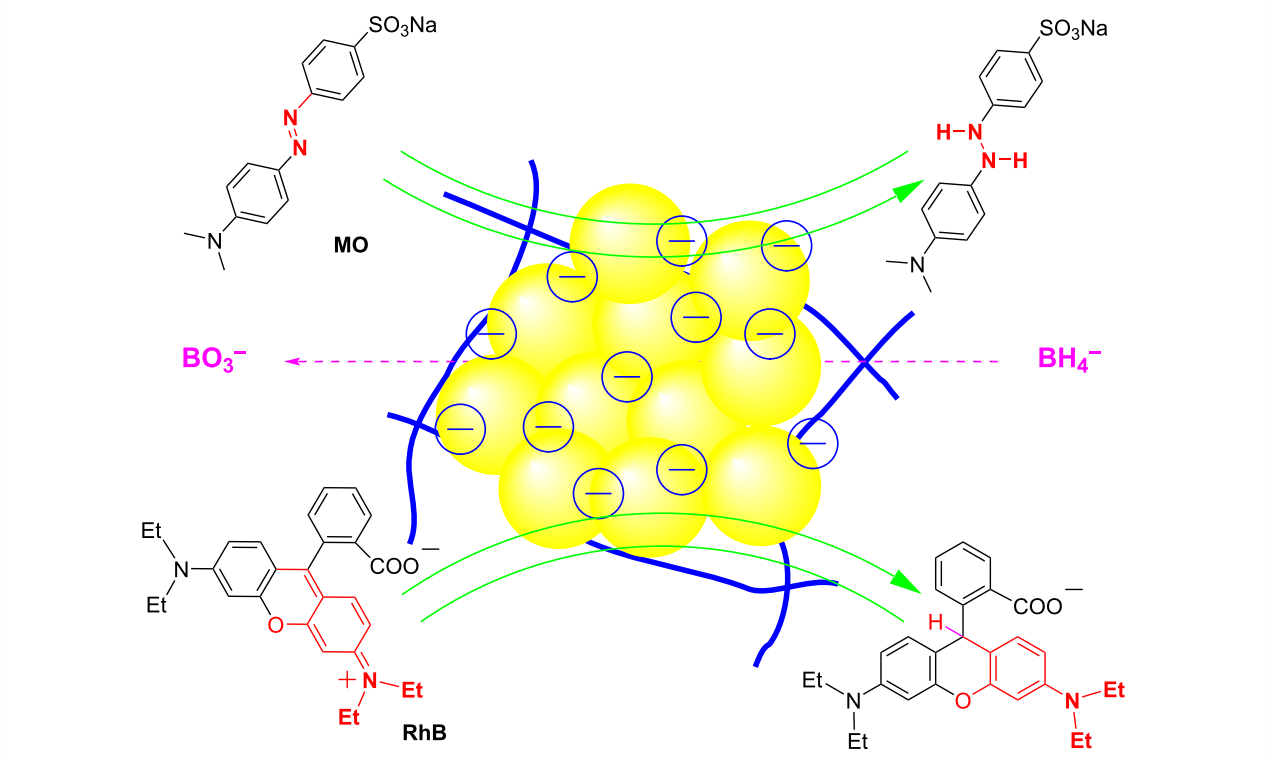


Figure 6: Proposed mechanism of AgNPs@Lac/Alg catalysis in reduction of methyl orange and rhodamine B using $NaBH_4$.

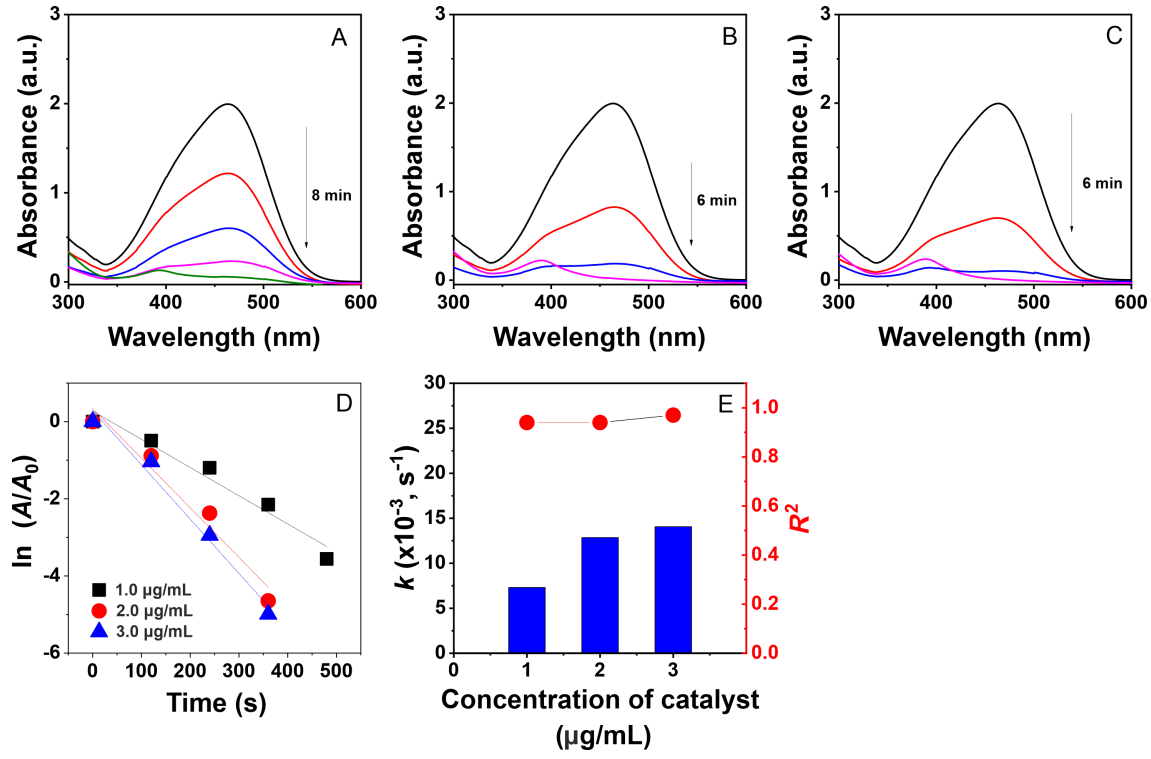


Figure 7: UV–vis spectra of the catalyst at concentrations of 1.0 μg/mL (A), 2.0 μg/mL (B), and 3.0 μg/mL (C); plots of first-order kinetics (D) and rate constants (E) for the catalytic degradation of methyl orange.

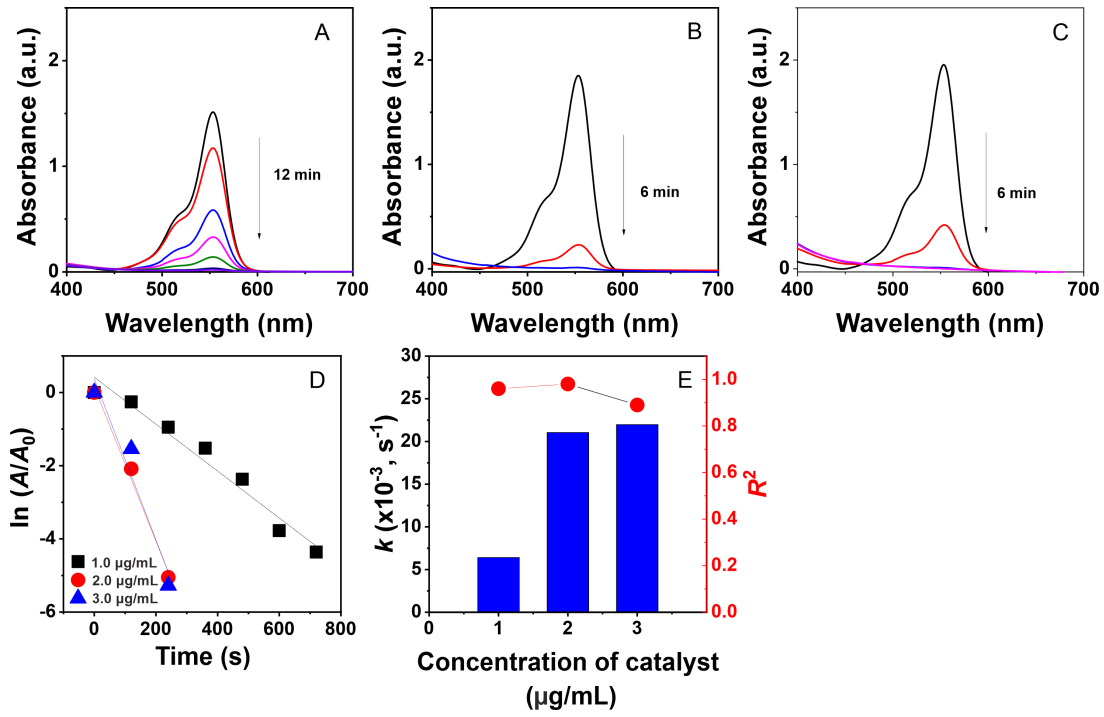


Figure 8: UV–vis spectra of the catalyst at concentrations of 1.0 µg/mL (A), 2.0 µg/mL (B), and 3.0 µg/mL (C); plots of first order kinetic (D) and rate constants (E) for the catalytic degradation of rhodamine B.

reduction of MO and RhB is achieved using different doses of the AgNPs@Lac/Alg solution (1.0–3.0 µg/mL), resulting in the reduction of the absorption peaks at 467 and 553 nm, respectively. The reaction rate increases with the catalyst dose as evidenced by a decrease in the reaction time. For instance, the degradation of MO at a dose of the colloidal solution of 1.0 µg/mL was completed in 8 min, while it took only 6 min in the presence of 2.0 µg/mL and 3.0 µg/mL of the nanocatalyst. The addition of the nanocatalyst also facilitated the degradation of RhB, with complete reaction times of 12 min for 1.0 µg/mL and 6 min for 2.0 µg/mL and 3.0 µg/mL of the nanocatalyst.

For the reaction kinetics, the plots of $\ln(A_0/A_t)$ values versus reaction time show good linear correlation with high determination coefficients for the degradation of the organic dyes, indicating a pseudo-first-order reaction (Figure 7E and Figure 8E). Furthermore, the calculated rate constants increase with higher concentrations of the nanocatalyst. Specifically, the rate constant for MO degradation increases from 7.31×10^{-3} s^{-1} (R^2 = 0.94) for 1.0 µg/mL of AgNPs@Lac/Alg to 14.07×10^{-3} s^{-1} (R^2 = 0.97) for 3.0 µg/mL of AgNPs@Lac/Alg. For RhB degradation, the calculated values at 1.0 µg/mL, 2.0 µg/mL, and 3.0 µg/mL of AgNPs@Lac/Alg are 6.41×10^{-3} s^{-1} (R^2 = 0.96), 21.05×10^{-3} s^{-1} (R^2 = 0.98), and 21.98×10^{-3} s^{-1} (R^2 = 0.89), respectively. The rate constants of AgNPs@Lac/Alg are found to be higher than the values of metal NPs loaded on alginate-based nanocomposites used in the solid state [36-38]. These results suggest that amount and carrier property of the metal NPs play a significant role in the catalytic degradation of organic dyes.

Antibacterial activity

The effectiveness of AgNPs@Lac/Alg in inhibiting the growth of bacteria was tested on the two microbial strains *S. aureus* (Gram-positive) and *S. typhi* (Gram-negative) using the disk diffusion method at different pH values. To establish the bioactivity of the nanocomposite, antibacterial assays were also conducted in media with different pH values without the nanocomposite. These resulted in no bioactivity against either of the strains, indicating that the observed bioactivity was due to the nanocomposite alone (Supporting Information File 1, Figure S1). Inhibition images and inhibition zone plots of AgNPs@Lac/Alg at different pH values are presented in Figure 9. The results show that the antibacterial activity of the nanocomposite is pH-dependent, and the ability to inhibit bacterial growth can be attributed to the leaching of silver (ions or nanoparticles) from the nanocomposite into the medium. The nanocomposite exhibited the highest antibacterial activity at weakly acidic and basic pH values, with the highest inhibition zone diameters recorded at pH 6 against *S. aureus* (10.8 ± 0.57 mm) and *S. typhi* (9.3 ± 1.34 mm). In contrast, the

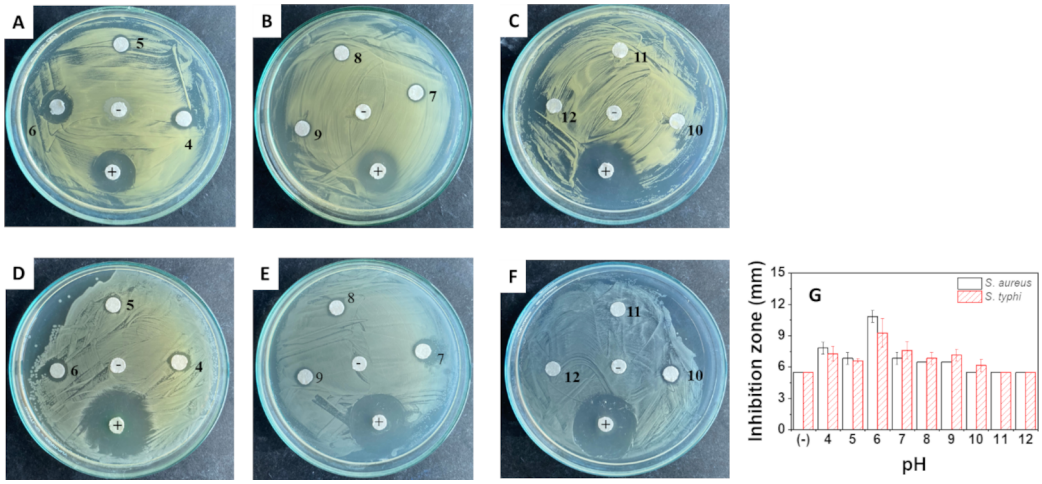


Figure 9: Antibacterial activity of AgNPs@Lac/Alg tested with various pH (4–12) against *S. aureus* (A, B and C) and *S. typhi* (D, E and F) and inhibition zone diameters as functions of the pH value (G).

nanocomposite showed no inhibition in highly basic media (pH 11 and 12) because of the aggregation of nanoparticles, which hindered the leaching of silver into the medium. The antibacterial effectiveness of the nanocomposite varied among the bacterial strains and pH values, which may be related to the antibacterial mechanism of AgNPs and the cell wall and membrane structure of each bacterial strain [50]. These findings suggest that the antibacterial activity of the nanocomposite could be tailored to specific pharmaceutical applications, such as drug delivery, by adjusting the release medium.

To investigate the pH-dependent antibacterial effectiveness, zeta potential and morphology of the nanocomposite were examined at pH 4, 6, and 12, as shown in Figure 10. The zeta potentials of the nanocomposite were −23.3, −27.5, and −13.3 mV at pH 4, 6, and 12, respectively, indicating that the stability of the nanocomposite was low in highly acidic and basic media, leading to the aggregation of nanoparticles. TEM images demonstrated significant variations in the morphology of the nanocomposite in different media. At pH 4, AgNPs aggregated to form larger particles compared to those formed at pH 6. In contrast, at pH 12, the nanocomposite was disrupted, leading to the aggregation of gel and a reduced interaction between AgNPs and the bacterial cell wall. This accounts for the low activity of the nanocomposite in highly basic media.

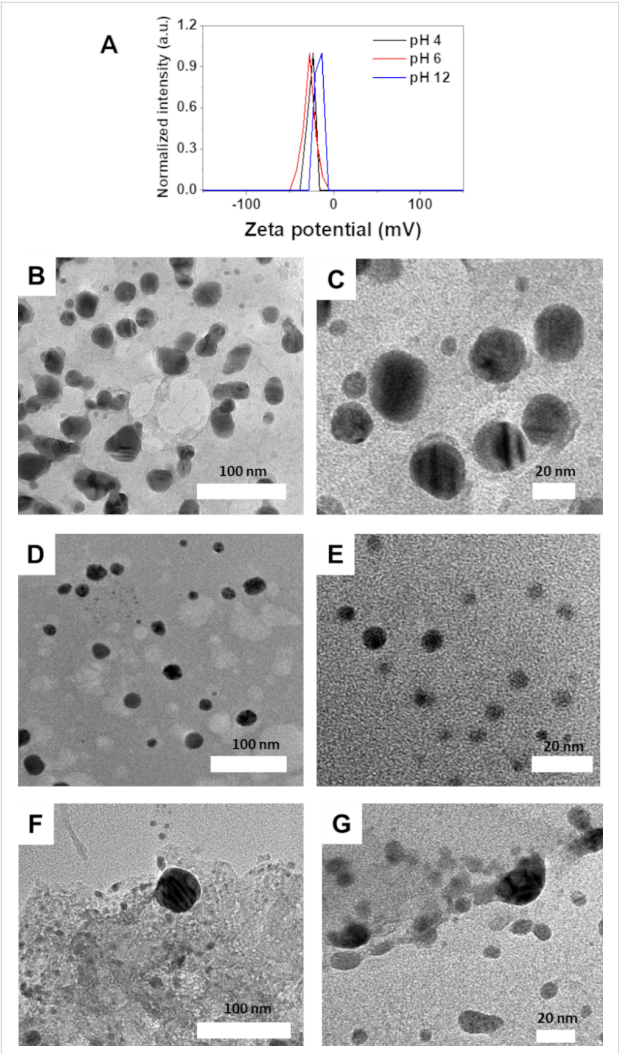


Figure 10: Zeta potential (A) and TEM images of the nanocomposite solutions at pH 4 (B and C), pH 6 (D and E) and pH 12 (F and G).

Conclusion

A lactose/alginate nanocomposite was successfully employed for the in situ synthesis of AgNPs. This study presents a novel polysaccharide-based nanocomposite with a straightforward synthesis approach. The AgNPs@Lac/Alg synthesized under optimal conditions had an average size in the range of 4–6 nm. Remarkable catalytic performance was demonstrated regarding

the degradation of two contaminants. The antibacterial activity of the nanocomposite was found to be pH-dependent, which can be attributed to the varying surface properties of silver nanoparticles. The highest bioactivity was observed at pH 6. These findings suggest that the nanocomposite may be customized for specific applications in environmental and medicinal treatments, making it a promising material.

Experimental

Materials

The following chemicals and reagents were purchased from Acros (Belgium): silver nitrate ($AgNO_3$), methyl orange (MO), rhodamine B (RhB), calcium acetate hydrate, sodium alginate, and sodium tetrahydroborate ($NaBH_4$). Lactose was obtained from Yong Da (China). The chemicals were used without additional purification. Distilled water was utilized throughout the experiments.

Synthesis of AgNPs@Lac/Alg

The AgNPs@Lac/Alg composite was produced by in situ reduction of silver ions to form AgNPs with the aid of the Lac/Alg nanocomposite. The Lac/Alg nanocomposite was synthesized using an ionic gelation method as previously reported [37]. Briefly, an aqueous solution of calcium acetate (14.36 mL; 6.5 mg·mL^{-1}) was slowly added dropwise into an aqueous solution of sodium alginate (40 mL; 7 mg·mL^{-1}) under stirring for 1 h at 1200 rpm. The mixture was allowed to equilibrate overnight. Subsequently, the Alg/Ca^{2+} spheres were separated by centrifugation at 3000 rpm for 10 min and washed three times with distilled water (20 mL each) to remove impurities. Next, an aqueous solution of lactose (16.06 mL, 1.5 mg·mL^{-1}) was added to the Alg/Ca^{2+} spheres and stirred for 1 h at 1200 rpm. To ensure the formation of a stable gel, the Lac/Alg gel solution was ultrasonically treated for 30 min and left to reach equilibrium overnight. After purification, the resulting gel was freeze-dried at −80 °C for 24 h using an EYELA FDU-2110 (Japan) instrument. Next, an aqueous solution of $AgNO_3$ (15 mL) with different concentrations in the range of 7.9–55.6 μg·mL^{-1} was mixed with 3 mL of an aqueous solution containing Lac/Alg nanocomposite (4.37 mg·mL^{-1}) and stirred for 1 h. The mixture was heated, and the formation of AgNPs was confirmed by a change in color of the mixture. The influence of the reaction parameters, namely temperature (30–90 °C), reaction time (0–180 min), and weight ratio of silver to Lac/Alg composite (0.1:1 to 0.7:1 (w/w)), was scrutinized using UV–vis measurements (UV-5100, Shanghai Metash Intruments Co. Ltd) in the range of 350–600 nm. For investigating the influence of temperature, a ratio of silver to Lac/Alg composite of 0.6:1 was used for a reaction time of 120 min. The influence of the reaction time was investigated with a ratio of silver to Lac/Alg composite of 0.6:1 and a solution temperature of 90 °C. The optimal ratio of silver to Lac/Alg composite was determined in reactions at 90 °C for 120 min. The AgNPs@Lac/Alg nanocomposite was then centrifuged and washed with distilled water. The purified nanocomposite was stored at 4 °C for further experiments.

Characterizations of AgNPs@Lac/Alg nanocomposite

The size distribution and stability of the nanocomposites were determined using dynamic light scattering (DLS) and zeta potential measurements, which were measured on a nanoPartica Horiba SZ-100 (Japan). Fourier-transform infrared (FTIR) spectra were obtained using a Bruker Tensor 27 FTIR spectrophotometer (Germany). X-ray diffraction (XRD) patterns were collected using a Bruker D8 Advance X-ray diffractometer. The morphology of the nanocomposites was investigated using transmission electron microscopy (TEM) with a JEOL JEM-1400 instrument. Thermal analysis, including thermogravimetry analysis (TGA) and differential scanning calorimetry (DSC), was conducted using a LabSys Evo 1600 thermal analyzer (SETARAM, France) under atmospheric conditions from 25 to 800 °C with a heating rate of 10 °C/min.

Catalytic activity for degradation of contaminants

Catalytic activity of the synthetic nanocomposite was evaluated through the degradation of pollutants (MO and RhB) in the presence of excess amounts of $NaBH_4$ [51]. In a quartz cell with a path length of 1 cm, 2.5 mL of a solution containing 0.1 mM of the contaminants and an aqueous nanocomposite solution of catalyst (AgNPs@Lac/Alg-0.7, in which the ratio of Ag^+ to Lac/Alg was 0.7:1, w/w) at concentrations ranging from 1.0 to 3.0 μg/mL were added. Subsequently, 0.5 mL of $NaBH_4$ solution (0.05 M) was introduced into the cell. Using a UV–vis spectrophotometer, the catalytic degradation of the contaminants was monitored at ambient temperature in 2 min intervals. The reaction kinetics were determined by measuring the reduction in absorption intensity at the corresponding absorption peak. It is important to note that the catalytic degradation of these contaminants in the presence of excess amount of $NaBH_4$ is a pseudo-first-order reaction, which can be expressed by the equation $\ln(A/A_0) = -kt$. Here, k is reaction rate constant, and $[A_0]$ and $[A]$ are initial and current absorbance of the contaminant, respectively [43]. The catalytic efficiency of the nanocomposite was determined by calculating the rate constant from the slope of the straight line obtained from plots of $\ln(A/A_0)$ versus reaction time.

Effect of pH value and antibacterial assay

The impact of pH value on the stability of the nanocomposite was analyzed under various acidic and alkaline conditions

within the pH range of 4 to 12. An aqueous solution of the nanocomposite AgNPs@Lac/Alg-0.7 (1 mL) was added to HCl or NaOH solutions, resulting in 3 mL solution with the corresponding pH values. The solutions were used to experiment antibacterial activity. The solutions with pH 4, 6, and 12 were also used to determine stability of the nanocomposite through zeta potential measurements and TEM.

The disk diffusion method was employed to assay the antibacterial activity of the samples [52]. In order to conduct the antibacterial tests, the nanocomposite solution (0.3 mL) at various pH values was diluted in DMSO (10 mL) to obtain a composite solution (0.87 μg/mL) prior to the experiment. *Staphylococcus aureus* (a Gram-positive bacterium) and *Salmonella typhi* (a Gram-negative bacterium) were used for the tests. Each aliquot (20 μL) was placed on paper disks with a diameter of 5.5 mm. These disks were then placed on agar plates that were previously inoculated with bacterial cultures (1.0 mL, 10^6 CFU/mL). The antibiotic ampicillin (0.01 mg/mL) and Luria Bertani broth were utilized as positive and negative controls, respectively. The same protocol was applied to evaluate media with the corresponding pH values and without the nanocomposite. The inhibition zone diameter including the paper disk, was measured to determine the activity.

Supporting Information

Supporting Information features physical parameters calculated from XRD patterns and antibacterial activity of controls without nanocomposite.

Supporting Information File 1

Additional experimental data.
[https://www.beilstein-journals.org/bjnano/content/supplementary/2190-4286-14-64-S1.pdf]

Funding

The authors are thankful to Vietnam Academy of Science and Technology (QTCZ01.01/22-23) and to Czech academy of Sciences (Mobility Plus Programme No. VAST-22-02) for funding this work.

ORCID® iDs

Nguyen Thi Thanh Tu - https://orcid.org/0000-0002-8299-4429
Chi-Hien Dang - https://orcid.org/0000-0002-4284-563X
Vinh-Thien Tran - https://orcid.org/0000-0001-7762-4207
Van-Su Dang - https://orcid.org/0000-0002-1458-1307
Hieu Vu-Quang - https://orcid.org/0000-0002-3468-5816
Van-Dat Doan - https://orcid.org/0000-0003-1838-1836
Thanh-Danh Nguyen - https://orcid.org/0000-0001-6330-8916

References

1. Pasparakis, G. *Wiley Interdiscip. Rev.: Nanomed. Nanobiotechnol.* **2022,** *14,* e1817. doi:10.1002/wnan.1817
2. Huq, M. A.; Ashrafudoulla, M.; Rahman, M. M.; Balusamy, S. R.; Akter, S. *Polymers (Basel, Switz.)* **2022,** *14,* 742. doi:10.3390/polym14040742
3. Ahmed, T.; Ogulata, R. T. *J. Nat. Fibers* **2022,** *19,* 8463–8484. doi:10.1080/15440478.2021.1964135
4. Sana, S. S.; Haldhar, R.; Parameswaranpillai, J.; Chavali, M.; Kim, S.-C. *Cleaner Mater.* **2022,** 100161. doi:10.1016/j.clema.2022.100161
5. Garg, R.; Rani, P.; Garg, R.; Khan, M. A.; Khan, N. A.; Khan, A. H.; Américo-Pinheiro, J. H. P. *Environ. Pollut.* **2022,** *310,* 119830. doi:10.1016/j.envpol.2022.119830
6. Shaker Ardakani, L.; Surendar, A.; Thangavelu, L.; Mandal, T. *Synth. Commun.* **2021,** *51,* 1516–1536. doi:10.1080/00397911.2021.1894450
7. Logambal, S.; Thilagavathi, T.; Chandrasekar, M.; Inmozhi, C.; Belle Ebanda Kedi, P.; Bassyouni, F. A.; Uthrakumar, R.; Muthukumaran, A.; Naveenkumar, S.; Kaviyarasu, K. *J. King Saud Univ., Sci.* **2023,** *35,* 102455. doi:10.1016/j.jksus.2022.102455
8. Rodríguez-Félix, F.; Graciano-Verdugo, A. Z.; Moreno-Vásquez, M. J.; Lagarda-Díaz, I.; Barreras-Urbina, C. G.; Armenta-Villegas, L.; Olguín-Moreno, A.; Tapia-Hernández, J. A. *J. Nanomater.* **2022,** *2022,* 1–37. doi:10.1155/2022/8874003
9. Alavi, M. *Expert Rev. Anti-Infect. Ther.* **2022,** *20,* 897–906. doi:10.1080/14787210.2022.2045194
10. Roy, S.; Rhim, J.-W. *Food Biosci.* **2022,** *49,* 101867. doi:10.1016/j.fbio.2022.101867
11. Mustapha, T.; Misni, N.; Ithnin, N. R.; Daskum, A. M.; Unyah, N. Z. *Int. J. Environ. Res. Public Health* **2022,** *19,* 674. doi:10.3390/ijerph19020674
12. de Souza, M. G. M.; Batista, J. P.; de Faria, E. H.; Ciuffi, K. J.; Rocha, L. A.; Nassar, E. J.; da Silva, J. V. L.; Oliveira, M. F.; Maia, I. A. *J. Sol-Gel Sci. Technol.* **2022,** *102,* 219–228. doi:10.1007/s10971-021-05693-w
13. Alavi, M.; Varma, R. S. *Cellulose* **2021,** *28,* 8295–8311. doi:10.1007/s10570-021-04067-3
14. Irshad, A.; Sarwar, N.; Sadia, H.; Malik, K.; Javed, I.; Irshad, A.; Afzal, M.; Abbas, M.; Rizvi, H. *Int. J. Biol. Macromol.* **2020,** *145,* 189–196. doi:10.1016/j.ijbiomac.2019.12.089
15. Emam, H. E.; Ahmed, H. B. *Carbohydr. Polym.* **2016,** *135,* 300–307. doi:10.1016/j.carbpol.2015.08.095
16. Yang, X.; Jia, M.; Li, Z.; Ma, Z.; Lv, J.; Jia, D.; He, D.; Zeng, R.; Luo, G.; Yu, Y. *Int. J. Biol. Macromol.* **2022,** *215,* 550–559. doi:10.1016/j.ijbiomac.2022.06.131
17. Shahid-ul-Islam; Butola, B. S.; Kumar, A. *Int. J. Biol. Macromol.* **2020,** *152,* 1135–1145. doi:10.1016/j.ijbiomac.2019.10.202
18. ALSamman, M. T.; Sánchez, J. *Arabian J. Chem.* **2021,** *14,* 103455. doi:10.1016/j.arabjc.2021.103455
19. Yuan, W.; Fu, J.; Su, K.; Ji, J. *Colloids Surf., B* **2010,** *76,* 549–555. doi:10.1016/j.colsurfb.2009.12.017
20. Xu, L.; Yi-Yi, W.; Huang, J.; Chun-Yuan, C.; Zhen-Xing, W.; Xie, H. *Theranostics* **2020,** *10,* 8996–9031. doi:10.7150/thno.45413
21. Tang, S.; Zheng, J. *Adv. Healthcare Mater.* **2018,** *7,* 1701503. doi:10.1002/adhm.201701503
22. Agnihotri, S.; Mukherji, S.; Mukherji, S. *Nanoscale* **2013,** *5,* 7328–7340. doi:10.1039/c3nr00024a

23. Zhang, C.; Hu, Z.; Deng, B. *Water Res.* **2016,** *88,* 403–427. doi:10.1016/j.watres.2015.10.025
24. Mijnendonckx, K.; Leys, N.; Mahillon, J.; Silver, S.; Van Houdt, R. *BioMetals* **2013,** *26,* 609–621. doi:10.1007/s10534-013-9645-z
25. Abbaszadegan, A.; Ghahramani, Y.; Gholami, A.; Hemmateenejad, B.; Dorostkar, S.; Nabavizadeh, M.; Sharghi, H. *J. Nanomater.* **2015,** *2015,* 720654. doi:10.1155/2015/720654
26. Yin, I. X.; Zhang, J.; Zhao, I. S.; Mei, M. L.; Li, Q.; Chu, C. H. *Int. J. Nanomed.* **2020,** *15,* 2555–2562. doi:10.2147/ijn.s246764
27. Banerjee, M.; Mallick, S.; Paul, A.; Chattopadhyay, A.; Ghosh, S. S. *Langmuir* **2010,** *26,* 5901–5908. doi:10.1021/la9038528
28. Martínez-Castañón, G. A.; Niño-Martínez, N.; Martínez-Gutierrez, F.; Martínez-Mendoza, J. R.; Ruiz, F. *J. Nanopart. Res.* **2008,** *10,* 1343–1348. doi:10.1007/s11051-008-9428-6
29. Qiao, Z.; Yao, Y.; Song, S.; Yin, M.; Luo, J. *J. Mater. Chem. B* **2019,** *7,* 830–840. doi:10.1039/c8tb02917b
30. Chambers, B. A.; Afrooz, A. R. M. N.; Bae, S.; Aich, N.; Katz, L.; Saleh, N. B.; Kirisits, M. J. *Environ. Sci. Technol.* **2014,** *48,* 761–769. doi:10.1021/es403969x
31. Hsueh, Y.-H.; Tsai, P.-H.; Lin, K.-S. *Int. J. Mol. Sci.* **2017,** *18,* 793. doi:10.3390/ijms18040793
32. Naz, M.; Rafiq, A.; Ikram, M.; Haider, A.; Ahmad, S. O. A.; Haider, J.; Naz, S. *J. Mater. Sci.* **2021,** *56,* 15572–15608. doi:10.1007/s10853-021-06279-1
33. Beyene, H. D.; Werkneh, A. A.; Bezabh, H. K.; Ambaye, T. G. *Sustainable Mater. Technol.* **2017,** *13,* 18–23. doi:10.1016/j.susmat.2017.08.001
34. Chakhtouna, H.; Benzeid, H.; Zari, N.; Qaiss, A. e. k.; Bouhfid, R. *Environ. Sci. Pollut. Res.* **2021,** *28,* 44638–44666. doi:10.1007/s11356-021-14996-y
35. Salama, A.; Abouzeid, R. E.; Owda, M. E.; Cruz-Maya, I.; Guarino, V. *Biomolecules* **2021,** *11,* 1684. doi:10.3390/biom11111684
36. Nguyen, T.-D.; Dang, C.-H.; Mai, D.-T. *Carbohydr. Polym.* **2018,** *197,* 29–37. doi:10.1016/j.carbpol.2018.05.077
37. Ho, T. T.-T.; Dang, C.-H.; Huynh, T. K.-C.; Hoang, T. K.-D.; Nguyen, T.-D. *Carbohydr. Polym.* **2021,** *251,* 116998. doi:10.1016/j.carbpol.2020.116998
38. Nguyen, T.-D.; Vo, T.-T.; Huynh, T. T.-T.; Nguyen, C.-H.; Doan, V.-D.; Nguyen, D.-T.; Nguyen, T.-D.; Dang, C.-H. *New J. Chem.* **2019,** *43,* 16841–16852. doi:10.1039/c9nj04730a
39. Nguyen, T.-D.; Hong-Ngan Tran, T.; Nguyen, C.-H.; Im, C.; Dang, C.-H. *Chem. Biochem. Eng. Q.* **2015,** *29,* 429–435.
40. Wathoni, N.; Yuan Shan, C.; Yi Shan, W.; Rostinawati, T.; Indradi, R. B.; Pratiwi, R.; Muchtaridi, M. *Heliyon* **2019,** *5,* e02299. doi:10.1016/j.heliyon.2019.e02299
41. Thinh, P. D.; Hang, C. T. T.; Trung, D. T.; Nguyen, T.-D. *Processes* **2023,** *11,* 1054. doi:10.3390/pr11041054
42. Santos, M. I.; Araujo-Andrade, C.; Tymczyszyn, E. E.; Gómez-Zavaglia, A. *Food Res. Int.* **2014,** *64,* 514–519. doi:10.1016/j.foodres.2014.07.040
43. Doan, V.-D.; Pham, Q.-H.; Huynh, B.-A.; Nguyen, T.-L.-H.; Nguyen, A.-T.; Nguyen, T.-D. *J. Environ. Chem. Eng.* **2021,** *9,* 106590. doi:10.1016/j.jece.2021.106590
44. Shahid, M.; Farooqi, Z. H.; Begum, R.; Arif, M.; Wu, W.; Irfan, A. *Crit. Rev. Anal. Chem.* **2020,** *50,* 513–537. doi:10.1080/10408347.2019.1663148
45. Shalla, A. H.; Bhat, M. A.; Yaseen, Z. *J. Environ. Chem. Eng.* **2018,** *6,* 5938–5949. doi:10.1016/j.jece.2018.08.063
46. Samarghandi, M. R.; Dargahi, A.; Zolghadr Nasab, H.; Ghahramani, E.; Salehi, S. *Water Environ. Res.* **2020,** *92,* 1173–1183. doi:10.1002/wer.1312
47. De, A.; Kalita, D.; Jain, P. *ChemistrySelect* **2021,** *6,* 10776–10787. doi:10.1002/slct.202101987
48. Al-Shehri, A. S.; Zaheer, Z.; Alsudairi, A. M.; Kosa, S. A. *ACS Omega* **2021,** *6,* 27510–27526. doi:10.1021/acsomega.1c04501
49. Tran, M.-T.; Nguyen, L.-P.; Nguyen, D.-T.; Le Cam-Huong, T.; Dang, C.-H.; Chi, T. T. K.; Nguyen, T.-D. *Res. Chem. Intermed.* **2021,** *47,* 4613–4633. doi:10.1007/s11164-021-04548-x
50. Ploux, L.; Ponche, A.; Anselme, K. *J. Adhes. Sci. Technol.* **2010,** *24,* 2165–2201. doi:10.1163/016942410x511079
51. Dang, V.-S.; Tran, H.-H.; Dieu, P. T. T.; Tran, M.-T.; Dang, C.-H.; Mai, D.-T.; Doan, V.-D.; Nguyen, T.-L.-H.; Chi, T. T. K.; Nguyen, T.-D. *Res. Chem. Intermed.* **2022,** *48,* 2047–2067. doi:10.1007/s11164-022-04687-9
52. Loo, Y. Y.; Rukayadi, Y.; Nor-Khaizura, M.-A.-R.; Kuan, C. H.; Chieng, B. W.; Nishibuchi, M.; Radu, S. *Front. Microbiol.* **2018,** *9,* 10.3389/fmicb.2018.01555. doi:10.3389/fmicb.2018.01555

License and Terms

This is an open access article licensed under the terms of the Beilstein-Institut Open Access License Agreement (https://www.beilstein-journals.org/bjnano/terms), which is identical to the Creative Commons Attribution 4.0 International License (https://creativecommons.org/licenses/by/4.0). The reuse of material under this license requires that the author(s), source and license are credited. Third-party material in this article could be subject to other licenses (typically indicated in the credit line), and in this case, users are required to obtain permission from the license holder to reuse the material.

The definitive version of this article is the electronic one which can be found at:
https://doi.org/10.3762/bjnano.14.64

BEILSTEIN JOURNAL OF NANOTECHNOLOGY

Silver-based SERS substrates fabricated using a 3D printed microfluidic device

Phommachith Sonexai[1], Minh Van Nguyen[1], Bui The Huy[1] and Yong-Ill Lee[*1,2]

Full Research Paper

Open Access

Address:
[1]Anastro Laboratory, Institute of Basic Science, Changwon National University, Changwon 51140, Republic of Korea and [2]Department of Pharmacy, Pharmaceutical Technical University, Tashkent 100084, Uzbekistan

Email:
Yong-Ill Lee[*] - yilee@changwon.ac.kr

* Corresponding author

Keywords:
3D printing; microfluidic droplet; SERS substrate; silver nanoparticle; smartphone detection

Beilstein J. Nanotechnol. **2023,** *14,* 793–803.
https://doi.org/10.3762/bjnano.14.65

Received: 20 April 2023
Accepted: 21 June 2023
Published: 21 July 2023

This article is part of the thematic issue "Recent advances in synthesis and applications of organometallic nanomaterials".

Guest Editor: D. T. Nguyen

© 2023 Sonexai et al.; licensee Beilstein-Institut.
License and terms: see end of document.

Abstract

The detection of harmful chemicals in the environment and for food safety is a crucial requirement. While traditional techniques such as GC–MS and HPLC provide high sensitivity, they are expensive, time-consuming, and require skilled labor. Surface-enhanced Raman spectroscopy (SERS) is a powerful analytical tool for detecting ultralow concentrations of chemical compounds and biomolecules. We present a reproducible method for producing Ag nanoparticles that can be used to create highly sensitive SERS substrates. A microfluidic device was employed to confine the precursor reagents within the droplets, resulting in Ag nanoparticles of uniform shape and size. The study investigates the effects of various synthesis conditions on the size distribution, dispersity, and localized surface plasmon resonance wavelength of the Ag nanoparticles. To create the SERS substrate, the as-synthesized Ag nanoparticles were assembled into a monolayer on a liquid/air interface and deposited onto a porous silicon array prepared through a metal-assisted chemical etching approach. By using the developed microfluidic device, enhancement factors of the Raman signal for rhodamine B (at 10^{-9} M) and melamine (at 10^{-7} M) of 8.59×10^6 and 8.21×10^3, respectively, were obtained. The detection limits for rhodamine B and melamine were estimated to be 1.94×10^{-10} M and 2.8×10^{-8} M with relative standard deviation values of 3.4% and 4.6%, respectively. The developed SERS substrate exhibits exceptional analytical performance and has the potential to be a valuable analytical tool for monitoring environmental contaminants.

Introduction

Surface-enhanced Raman spectroscopy (SERS) has emerged as a powerful optical trace detection technique in various biochemical applications because of its exceptional sensitivity and the capabilities of real-time analysis and label-free detection [1,2]. SERS has been used to identify targets for single molecules in chemical and biological systems [3,4] since its discovery by

Martin Fleischmann in 1974 [5]. Electromagnetic and chemical mechanisms are attributed to the SERS enhancement. In electromagnetic theory, the excitation of metal particles through light leads to localized surface plasmon resonance due to the collective oscillation of free electrons in the confined space of the metal particles. The electric field is enhanced, and the Raman enhancement factor (EF) can reach 10^6 [6]. The induced amplification of the local field by plasmonic coupling occurs in nanometer-scale regions around the metal particles, the so-called electromagnetic "hot spots". The chemical mechanism suggests the formation of a charge-transfer complex between chemisorbed species and matrix material, which yields enhancement when the excitation frequency resonates with a charge-transfer transition [7].

Noble metal nanoparticles (NPs) have gained much popularity in various fields, such as analytical chemistry and catalytic chemistry, where they have been used to develop localized surface plasmon resonance (LSPR) and SERS substrates [8]. For example, Ag NPs yield a strong SERS effect at relatively low cost. However, an issue often encountered in synthetic approaches is the non-uniformity of the Ag NPs. Homogeneous Ag NPs are necessary for Ag-based SERS substrates to function well. The microfluidic approach is a technique for the fine control and manipulation of fluids, in which capillary penetration is limited to the micrometer scale and mass transport dominates [9,10]. Microfluidic devices are used in various fields in industry and laboratories, such as chemical synthesis and microreactors [11,12], drug screening [13], and clinical trials [14]. They can create homogeneous reaction environments with controllable parameters for synthesizing homogeneous colloidal nanoparticles with a narrow size distribution [15-17]. Two types of microfluidic devices are commonly used, namely droplet-based and continuous devices. Continuous microfluidic devices have several disadvantages when applied for chemical syntheses, such as laminar flow formation due to the low Reynolds number of fluids, which leads to a lack of uniform mixing [18]. In addition, nanoparticles tend to accumulate on the sidewalls of the microfluidic channel, thus limiting the reuse of the device [8,19]. In contrast, droplet-based microfluidic devices are based on the formation of microdroplets using two or more immiscible fluids with reactants in segmented flow and oil in continuous flow. They can control the reaction rates by mass transfer through convection and diffusion [20,21]. Furthermore, droplet-based microfluidic devices are frequently utilized to synthesize complex materials of uniform size, as each droplet can function as a separate microreactor [12,22].

A traditional approach to producing microfluidic devices involves a three-step microfabrication process of (i) creating a channel mold using photolithography, (ii) fabricating the channels by casting the mold through soft lithography, and (iii) bonding the channel device to a substrate [23]. This procedure typically requires a clean room and expensive facilities such as a photolithography machine, a spin-coater, and photoresist agents, as well as long processing times and well-trained technical staff. Additionally, the photolithography process is limited to planar fabrication, resulting in a low aspect ratio of the achieved features.

Because 3D printing enables the creation and testing of objects in short periods of time, it provides a new tool for constructing microfluidic devices. This has led to fast and dynamic developments in chemical synthesis and analytical systems at low cost [24-26]. There are two techniques for producing 3D-printed microfluidic devices. In the first approach, monolithic microfluidic devices are 3D printed [27,28]. Although this one-step process offers the benefits of quick development and ease of fabrication, reducing the channel dimension to a scale smaller than a millimeter remains challenging [29]. In the second approach, 3D printing can replace photolithography to fabricate a mold. This approach can achieve a better lateral resolution of printed features down to 100 μm with a higher aspect ratio of the printed channel features [30]; also, it does not require a clean room. The stereolithography (SLA) technique is an additive manufacturing technique in which a photopolymer resin is cured and converted from a liquid to a solid by an ultraviolet laser. The resolution of SLA printers is determined by the radial beam scattering and the type of resin [31]. With particular resins, SLA can fabricate features with lateral dimensions of 100 μm and a mold-printed resolution of 50 μm.

Over the past decade, numerous SERS substrates based on various materials, including paper [32,33], polymers [34,35], fibers [36], dielectrics [37], porous aluminum oxide [38], and semiconductors [39] have been reported. Dielectric and semiconductor substrates, such as ZnO nanowires, silicon nanowires, and porous silicon (PS), are particularly popular because of their larger contribution to the amplification of the Raman signal and longer shelf life [40-42]. Silicon nanostructures with high specific areas are especially popular because they have no fluorescence properties.

In this work, we report on the synthesis of a highly sensitive SERS substrate for detecting rhodamine B (RhB) and melamine (MLM) and on the analytical properties of the developed system. The substrate was prepared from Ag NPs by decorating the surface of porous silicon with Ag NPs using self-assembled monolayers (SAMs). The SAM method offers precise control, versatility, simplicity, stability, and compatibility, making it a valuable technique for surface modification in various scientific and technological applications. The Ag NPs were synthe-

sized using a droplet-based microfluidic device and a stereolithographic 3D printing method. The microfluidic device was optimized to produce uniform droplets, within which silver nitrate was reduced by sodium borohydride. This method limits the amount of precursor chemicals and enables the sequential flow of droplets, resulting in silver nanoparticles of uniform shape and size. We investigated the effects of different synthesis conditions on the size distribution, dispersity, and LSPR wavelength of the silver nanoparticles.

Experimental

Chemicals and apparatus

Silver nitrate ($AgNO_3$, 99.9%) was purchased from Kojima Chemical (Japan). Sodium borohydride ($NaBH_4$, 98%) and melamine (99%) were obtained from Sigma-Aldrich (Republic of Korea). Hydrofluoric acid (48–51%), sulfuric acid (98%), nitric acid (65–70%), rhodamine B (pure), mineral oil (light molecular biology grade), sorbitan monooleate (SPAN 80), and trisodium citrate dehydrate (TCD) (99%) were purchased from Alfa Aesar (Republic of Korea). Sylgard 184 A&B was obtained from Sewang Hitech (Republic of Korea), and the XL-1500 UV cross-linker used for UV curing was purchased from Krackeler Scientific (USA). Methyl alcohol, hydrogen peroxide (35%), sodium hydroxide (<97%), ammonia water (25–29%), acetone (99.5%), ethyl alcohol (95%), and 2-propanol (99.5%) were bought from Daejung (Republic of Korea). The Formlabs 3D printer and clear V4 resin were purchased from Formlabs (USA). Deionized water with a resistivity of 18 $M\Omega \cdot cm^{-1}$, provided by a Milli-Q water purification system (Millipore Corp., MA, USA), was used throughout all the experiments.

The morphologies of Ag NPs and SERS substrates were examined using a field-emission scanning electron microscope (FE-SEM, Mira II, TESCAN). A UV–vis spectrometer (Agilent 8453, Agilent, USA) and a micro-Raman spectrometer (NS200, Nanoscope System, Republic of Korea) were used to record the absorption spectra and Raman spectra, respectively.

Fabrication of the droplet-based microfluidic device

The fabrication process of the microfluidic device is illustrated in Scheme S1 (Supporting Information File 1). The 3D model of the microfluidic device mold was designed using Solidworks Professional 2022 SP3.1 software and printed on a Formslab 3 SLA 3D printer (Formlabs Inc., Somerville, MA, USA) using Clear V4 resin. The mold was post-treated by being soaked for 20 min in a 90% (v/v) isopropanol solution, followed by 10 min in deionized water, and then gently dried in a nitrogen flow. After that, the mold was exposed to UV light at an energy level of 120 $mJ \cdot cm^{-2}$ for 30 s and then annealed at 60 °C for 12 h in an oven for slow evaporative drying (Scheme S1a, Supporting Information File 1). Before casting into the printed mold, polydimethylsiloxane (PDMS) Sylgard^{TM} 184 and curing agent (10:1, w/w) were mixed for 10 min and de-bubbled in vacuum for 30 min. The PDMS cast was dried for 18 h to cure after being dried in air for 24 h (Scheme S1b, Supporting Information File 1). After that, the cast was peeled off from the mold and was immersed for 24 h in 1 M NaOH solution (Scheme S1c, Supporting Information File 1). Finally, the cast was carefully adhered to the surface of a glass plate (Scheme S1d, Supporting Information File 1) and treated at 90 °C for 5 min on a hot plate. Following this step, silicon tubes were joined to the inlets of the microfluidic device using Loctite superglue.

Synthesis of silver nanoparticles

The droplet-based microfluidic device was used to synthesize Ag NPs. These droplets enable the uniform distribution of nanoparticles. Ag NPs were created by reducing $AgNO_3$ solution with $NaBH_4$ as a reducing agent and TCD as a stabilizer [43,44]. Mineral oil served as a continuous phase when combined with the surfactant Span 80 (2% w/v). To prevent droplets from coalescing in the microchannel, Span 80 was added to lower the interfacial tension between oil and aqueous phase.

For the synthesis of Ag NPs, 20 mL of $AgNO_3$ and 20 mL of TCD were mixed in a 1:3 molar ratio to form the reactant solution, designated as solution (a). 20 mL of $NaBH_4$ and NaOH were mixed in a 1:3 molar ratio, designated as solution (b). Two syringe pumps (NE-300 InfusionONE Syginge Pump, USA) were used to inject mineral oil mixed with the surfactant Span 80 (2% w/v), solution (a), and solution (b) into the droplet-based microfluidic system at flow rates of 20 and 80 $\mu L \cdot min^{-1}$, respectively.

The as-synthesized colloidal solution of Ag NPs was centrifuged at 12,000 rpm for 5 min to separate the Ag NPs solution and remove the oil phase. Finally, the Ag NPs suspension was stored in a dark vial at room temperature for further experiments.

Fabrication of porous silicon (PS) substrate

A p-type Si(100) wafer with a resistivity of 0.01–0.09 Ω·cm was used in this work. The wafer was divided into 1 × 1 cm^2 pieces, which were then cleaned with an ultrasonic cleaner in acetone (20 min), ethanol (15 min), and deionized water (10 min). The wafer pieces were oxidized in hot Piranha solution (45 mL of H_2SO_4/15 mL of H_2O_2) for 5 min. To perform metal-assisted chemical etching (MACE), the wafer pieces were placed in a beaker containing an etchant solution made up of 5 mL of 4.6 M HF and 5 mL of 0.02 M $AgNO_3$. The etching

timings were 0, 5, 10, 20, 40, and 80 min. After the etching process, to remove the as-generated Ag dendrites, the substrates were immediately submerged in concentrated HNO_3, rinsed with deionized water, and then dried at room temperature to produce the PS substrates.

Fabrication of the SERS substrate

The deposition of Ag particles on the substrates is based on the SAM method. Colloidal Ag NPs solutions were generated at the methanol/air interface by adapting the method described in [45]. Briefly, 5 mL of the colloidal solution of Ag NPs and 5 mL of acetone were mixed in a 50 mL glass vial. This mixture was quickly poured into another glass vial containing 5 mL of hexane. The vial was shaken for 30 s and then stabilized for 10 min. The Ag NPs moved from water to hexane with the aid of acetone. The porous silicon (PS) template substrate was placed at the bottom of a beaker containing methanol. A pipette was then used to gradually transfer the Ag NPs suspension in hexane to the surface of methanol. After the hexane evaporated, a tightly packed monolayer of Ag NPs appeared at the methanol/air interface. The PS@Ag substrates were created by depositing a monolayer of Ag NPs on the substrate surface after allowing the methanol to slowly evaporate under ambient conditions.

SERS substrate characterization

Raman spectra were obtained using a 24 mW laser and an integration time of 1000 ms. Asymmetric least-squares baseline subtraction was utilized to remove the SERS spectrum background. Each Raman spectrum represents the mean of three readings. Aqueous solutions of RhB and MLM were prepared at varying concentrations, and the SERS substrate was loaded with the analyte solution (30 µL) and air-dried at room temperature. SERS signals were then collected from random locations.

Results and Discussion

Fabrication of droplet-based microfluidic device using 3D printing

SLA 3D printing is an additive manufacturing technology that employs a laser to transform a liquid resin into a solid plastic. When exposed to laser radiation with an appropriate wavelength, the short molecular chains in photocurable resins polymerize to form rigid or flexible solid geometries. As the printing limit of the 3D line dimension suggested by the Formlabs 3 printer manufacturer is 100 µm × 100 µm, a mold with line features was created instead of printing the microfluidic device directly. To minimize defects during the printing of the mold, the microchannel was designed with larger dimensions. Three inlets for the mixing channel were made with a width and a depth of 200 µm × 150 µm, respectively, while the mixing channel had dimensions of 400 µm × 200 µm. The total length of the serpentine-shaped microchannel, which is the reaction length, was 605.6 mm, as shown in Figure S1 (Supporting Information File 1). The photograph of the prepared microfluidic device is given in Figure 1. The droplet-based microfluidic device was constructed with three inlets for introducing reactants and oil, a long serpentine-shaped microchannel for combining chemical solutions, and one outlet for collecting suspended Ag NPs.

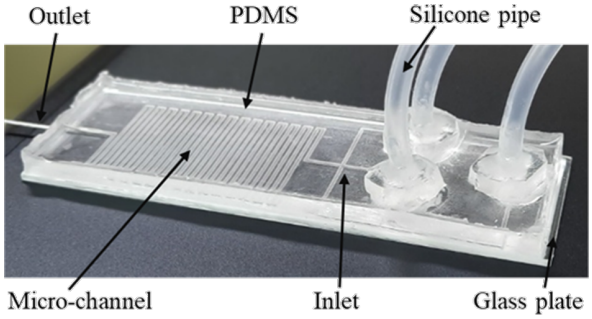


Figure 1: Photograph of the as-fabricated droplet-based microfluidic device.

The PDMS cast was bound to a glass plate after peeling off from the mold. There are various surface treatment methods available, including oxygen plasma, UV/ozone, corona oxidizer, and plasma pen [46,47]. In this study, we employed a previously reported chemical treatment method that uses 1 M NaOH solution for 24 h [48]. Although this method takes longer, it is more cost-effective, straightforward, and accessible. The chemical treatment of PDMS and the glass plate aims to decorate their surfaces with silanol groups (Si–OH), enabling the two surfaces to bond chemically at the atomic level [49]. To determine the droplet size, we used two dye solutions and captured images of the observed droplets (Figure S2, Supporting Information File 1). Figures S3–S7 in Supporting Information File 1 show data on the droplet size as functions of the flow rates of aqueous solutions and oil. Our investigation revealed that the optimal flow rates are 20 and 80 µL/min for the aqueous solutions and oil, respectively.

Synthesis of silver nanoparticles

Different molar ratios of silver nitrate to sodium borohydride were used to produce Ag nanoparticles in the microfluidic device at room temperature, with flow rates of 20 and 80 µL/min for the aqueous solutions and oil, respectively, as described in detail in Supporting Information File 1. The use of high concentrations of $AgNO_3$ resulted in the formation of numerous Ag nuclei due to a rapid reduction process. The collision frequency of these nuclei increases significantly with

higher concentrations of silver nitrate, promoting the formation of larger particles. This phenomenon explains the observed color change from yellow to greenish after three weeks, as illustrated in Figure S8 (Supporting Information File 1) [50,51]. $NaBH_4$ is a relatively potent reducing agent that can reduce Ag^+. At higher concentrations of $NaBH_4$, the formation of silver nanoparticles occurs more rapidly [52]. When the concentrations of silver nitrate and trisodium citrate were kept constant and the concentration of sodium borohydride was varied from 5–20 mM, the relative amount of capping agent decreased, resulting in a color change of the obtained solution from yellowish to bright yellow after three weeks, as shown in Figure S9 (Supporting Information File 1). The Ag NPs remained almost unchanged after three weeks when the ratio of silver nitrate to sodium borohydride was kept constant, especially with a molar ratio of 10:10 (in mM) (Figure 2).

FE-SEM micrographs of the samples are shown in Figure 3. The average sizes of Ag nanoparticles were estimated to be 24.10 ± 0.15, 27.07 ± 0.16, 28.07 ± 0.17, and 30.88 ± 0.31 nm by using the ImageJ program. Based on the calculated data, it is evident that the average size of Ag NPs increases with an increase in the concentration of reactants.

Structural characterization of the SERS substrate

In Supporting Information File 1, Figure S10a shows the SEM image of the SAM of Ag NPs on the surface of methanol, while Figure S10b displays the image of the PS substrate after covering with the Ag NPs. The SEM image of PS@Ag reveals the presence of nanoscale gaps between the Ag NPs, which act as hot spots with a high electric field intensity when exposed to laser irradiation (Figure S10c). To confirm the distribution of

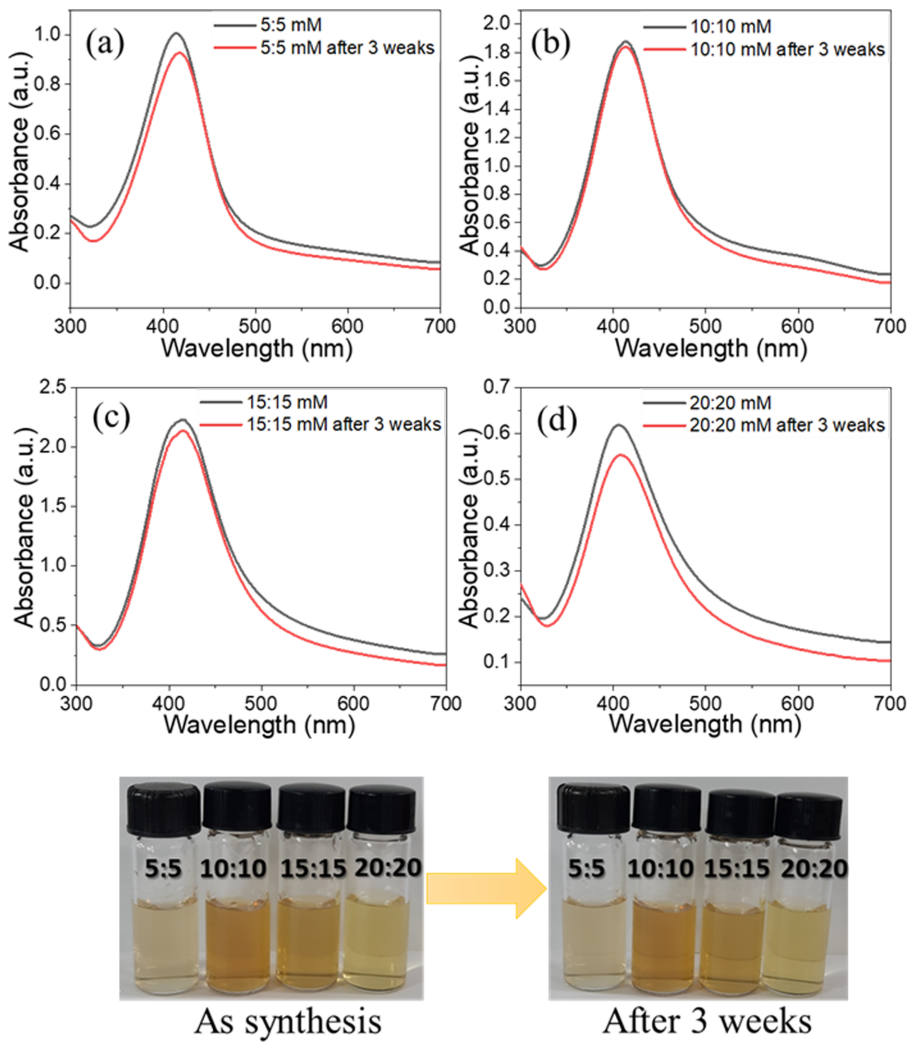


Figure 2: Images and absorbance spectra of Ag NPs synthesized using silver nitrate and sodium borohydride with molar ratios of (a) 5:5, (b) 10:10, (c) 15:15, and (d) 20:20 (in mM).

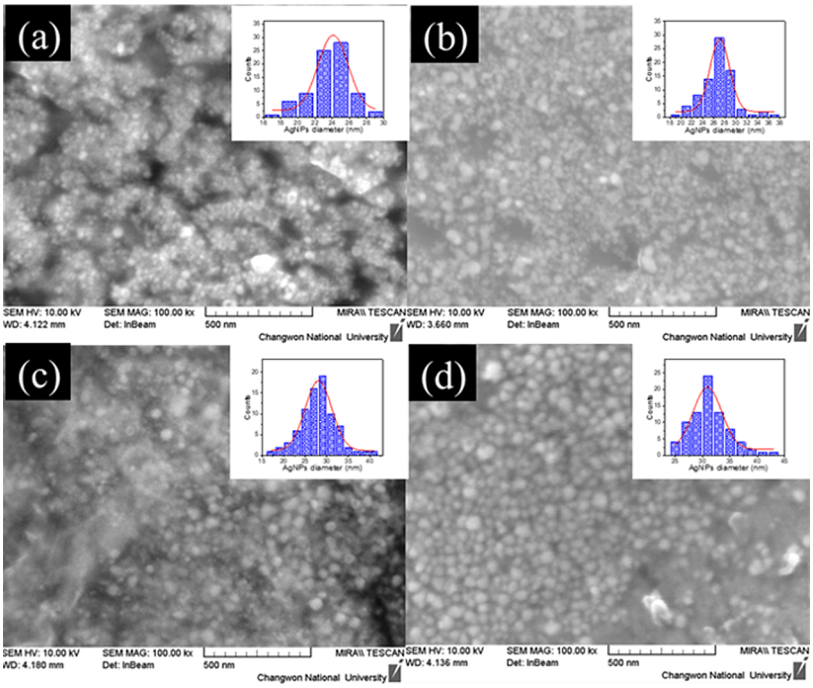


Figure 3: FE-SEM images of the synthesized Ag NPs with the molar ratios of $AgNO_3$ and $NaBH_4$ of (a) 1:1 mM, (b) 5:5 mM, (c) 10:10 mM, and (d) 15:15 mM. Insets of the figures are size distributions obtained from the ImageJ software.

chemical elements on the SERS substrate, energy-dispersive X-ray spectroscopy (EDS) was carried out, as illustrated in Figure S11 (Supporting Information File 1). The EDS mapping results indicate the uniformly distributed signal of the silicon wafer, while oxygen and silver are discontinuously distributed because of the space between PS and Ag NPs on the PS@Ag substrate.

Optimization of the PS@Ag SERS substrate fabrication

To optimize the etching time of PS on the wafers, a RhB solution (10^{-5} M) was chosen for estimating the SERS signal. The wafer pieces were etched for 0, 5, 10, 20, 40, and 80 min. The corresponding substrates were denoted PS0min@Ag, PS5min@Ag, PS10min@Ag, PS20min@Ag, PS40min@Ag, and PS80min@Ag, respectively. The SEM images revealed that the SAM of Ag NPs on the substrate without etching is not uniform, as shown in Figure S12 (Supporting Information File 1). The SAMs of the substrates with etching times of 5 and 10 min exhibited some islands that were not continuous, as shown in Figure S12b,c (Supporting Information File 1). When the etching time was extended to 20 and up to 80 min, the silver nanoparticles were well ordered, especially after an etching time of 40 min (Figure S12d–f, Supporting Information File 1).

Figure 4a shows the SERS spectra of RhB on substrates with different etching times. The spectra exhibit peaks at 621, 1199, 1279, 1358, 1508, 1528, and 1647 cm^{-1}. The peaks at 621, 1199, and 1279 cm^{-1} are related to deformation vibrations of the xanthene ring, the stretching of the C–C bridge bands, and the bending of the aromatic C–H bonds, respectively. The peaks at 1358, 1508, and 1528 cm^{-1} are linked to the aromatic C–C bending, while the peak at 1647 cm^{-1} is determined by the bending and stretching of the C–C bonds [53].

The SERS intensity increases with an extension of the etching time of the PS substrate from 0 to 40 min, and it decreases quickly when longer etching times are applied. The longer etching results in the expansion of pores in the silicon (100) wafer. These pores retain the Ag particles. As the pores become deeper and larger, the distances between the Ag particles increase, thereby reducing the hot spot effect on the Raman signal. The intensities of the peaks from the sample PS0min@Ag are significantly lower than those of the other samples. In comparison with the PS40min@Ag sample, the intensity of the peak at 621 cm^{-1} is approximately sixty times lower (Figure 4b). This confirms that the etching time of PS is a critical parameter for the fabrication of the SERS substrate. The substrate with an etching time of 40 min (PS40min@Ag) exhibited the best SERS performance and thus was chosen as the optimal substrate for the subsequent tests.

The influence of the Ag NP size on the SERS signals was studied. Four different sizes of Ag NPs (24, 27, 28, and 30 nm)

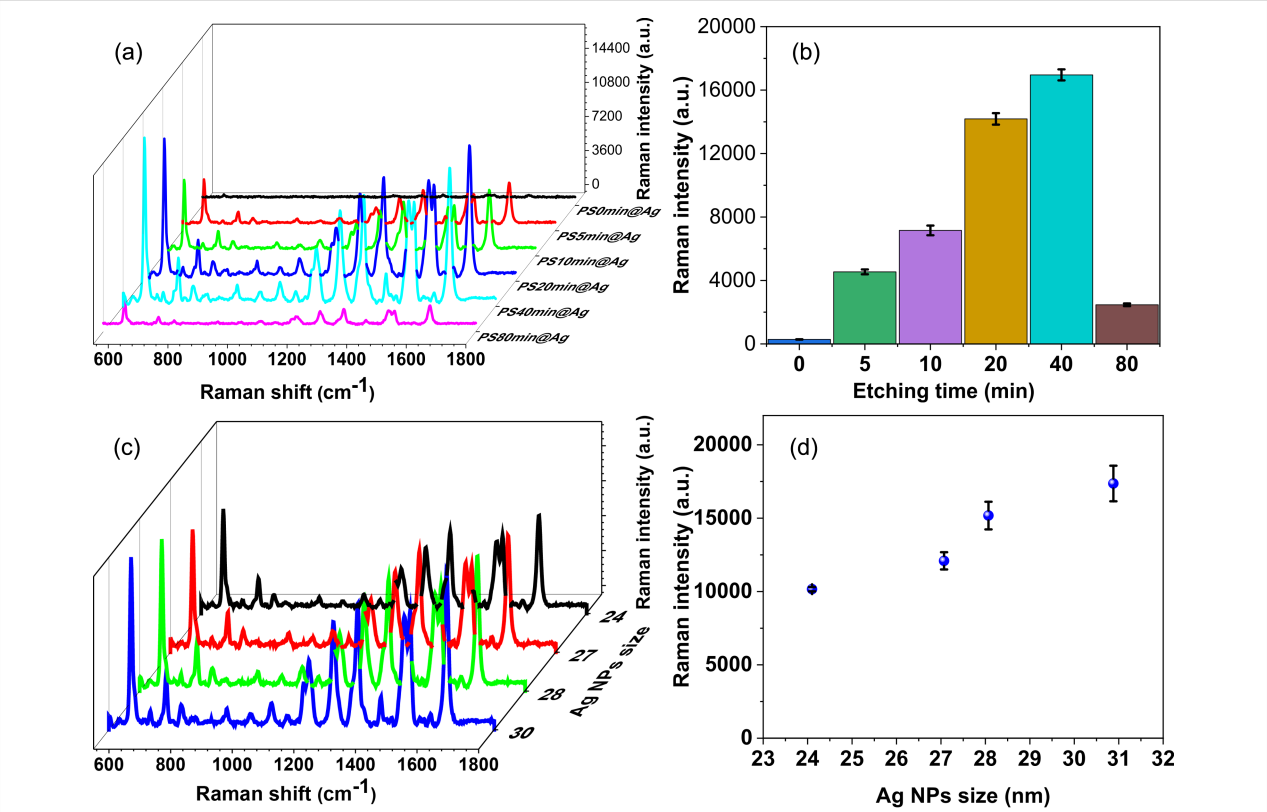


Figure 4: (a) SERS spectra based as a function of the PS etching time. (b) Intensity of the 621 cm^{-1} SERS speak as a function of the PS etching time. (c) SERS spectra of RhB on Ag NPs with different diameters on the PS40min@Ag substrate. (d) Intensity of the 621cm^{-1} SERS peak as a function of the size of the Ag NPs.

were self-assembled on the PS40min@Ag substrate, and the SERS spectra of RhB (10^{-5} M) were collected, as shown in Figure 4c. A slight increase in intensity was observed as the diameter of Ag NPs increased from 24 to 30 nm (Figure 4d). This is because the gaps between the Ag particles become smaller when the size of the particles increases, resulting in a stronger hot spot effect. However, when the particle size exceeds a critical threshold, the Ag particles come into contact with each other, causing the hot spots to dissipate. Based on these findings, we selected Ag NPs with a diameter of 28 nm as the optimal choice for the SERS substrate and used them for subsequent experiments.

Relationship between RhB concentration and Raman intensity

The SERS spectra of RhB samples with different concentrations, ranging from 10^{-9} to 10^{-5} M, were collected using the PS40min@Ag substrate (Figure 5a). The SERS intensity of RhB increased as the concentration increased. Figure 5b illustrates the correlation between RhB concentration and the peak intensity at 621 cm^{-1}, which was used to create a linear calibration with a high regression coefficient of R^2 = 0.99968. By applying the 3σ/*s* method, where σ is the standard deviation of the blank and *s* is the slope of the linear regression equation, the limit of detection was found to be 1.94×10^{-10} M. The SERS substrates showed an enhancement factor (EF) of 8.59×10^6 for the 621 cm^{-1} peak at an RhB concentration of 10^{-9} M. The calculation details for the EF can be found in the "Enhancement factor calculation" section of Supporting Information File 1.

To investigate the uniformity of the SERS substrate, Raman mapping was performed at 16 measuring positions in an area of 100 μm × 100 μm . RhB with a concentration of 10^{-5} M was added to the PS40min@Ag substrate. Figure 5c displays the SERS spectra collected from each position, while Figure 5d shows the SERS peak intensity at 621 cm^{-1} for the different positions. The relative standard deviation (RSD) was calculated to be 8%, indicating that the PS@Ag structure yielded homogeneous results because of the even deposition of the self-assembled monolayer of Ag NPs on the PS substrate.

Detection of melamine using PS@Ag SERS substrate

SERS spectra of MLM solutions at different concentrations (10^{-7} to 10^{-3} M) on the PS@Ag substrates were recorded, as

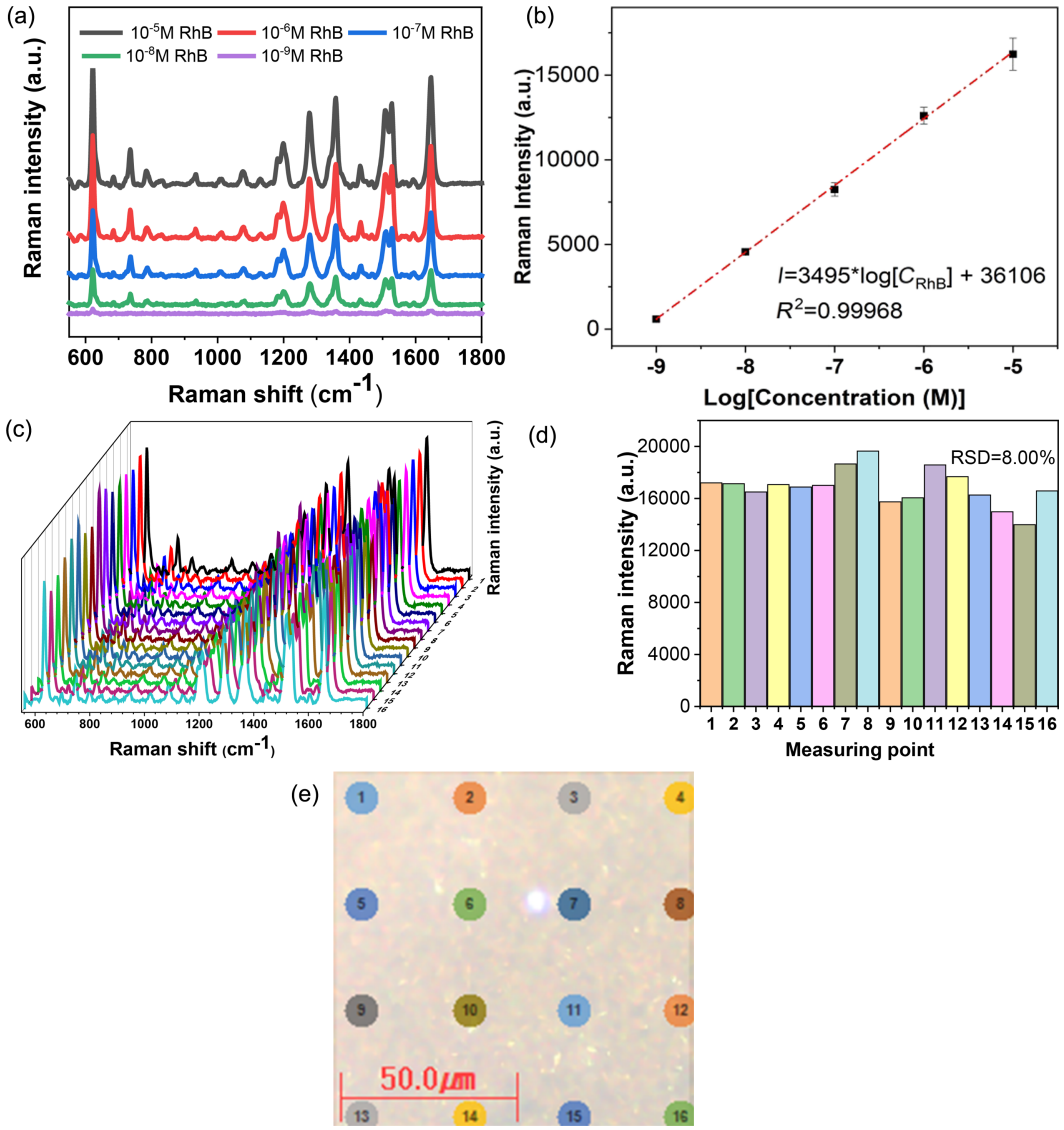


Figure 5: (a) Raman spectra of RhB solutions in the range from 10^{-9} to 10^{-5} M. (b) Intensity of the Raman peak at 621 cm^{-1} as a function of the RhB concentration. (c) SERS spectra and (d) SERS intensity of the 621 cm^{-1} peak at 16 positions of the SERS substrate, which are given in (e).

shown in Figure 6a. The Raman spectrum of MLM exhibits strong peaks at 583, 676, and 983 cm^{-1}. The peak at 583 cm^{-1} is related to a mixed mode of N–C–N bending and NH_2 twisting vibrations. The peak at 676 cm^{-1} is attributed to the plane deformation modes of the triazine ring, and the peak at 983 cm^{-1} is ascribed to C–N–C bending vibrations [54,55]. The Raman spectra of MLM on the PS@Ag SERS substrate shows peaks at 585, 679, and 985 cm^{-1}, which are shifted compared to those in the Raman spectrum of MLM because of the interaction between MLM and the Ag surface.

The SERS intensity at the fingerprint peak of 682 cm^{-1} as a function of the MLM concentration is displayed in Figure 6b. The calculated limit of detection for MLM was found to be 2.8×10^{-8} M, which is significantly below the safety limit established by the US Food and Drug Administration [56]. The SERS substrates displayed an impressive EF of 8.21×10^3 at the 682 cm^{-1} peak for an MLM concentration of 10^{-7} M. Further information on the calculation of the EF can be found in the "Enhancement factor calculation" section of Supporting Information File 1.

Conclusion

Using 3D printing, a droplet-based microfluidic device was successfully fabricated without the need for expensive and time-consuming photolithography. The resulting devices were

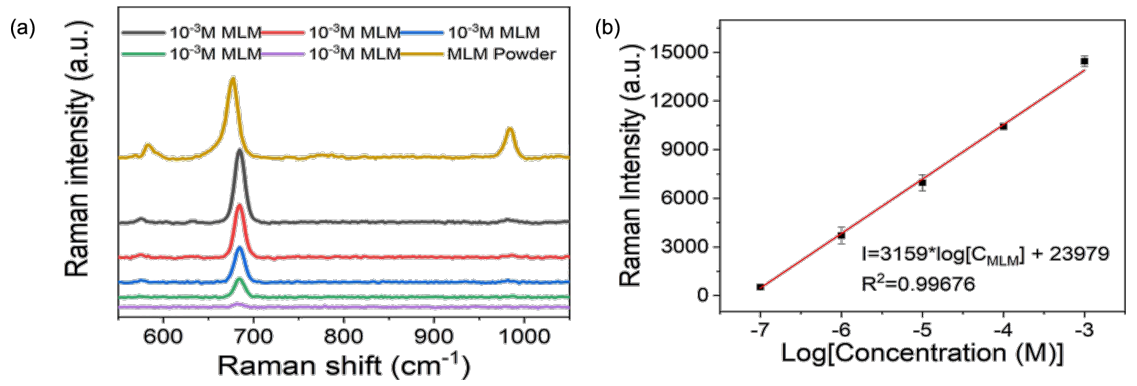


Figure 6: (a) Raman spectra of powder and trace concentrations of MLM (10^{-7} to 10^{-3} M). (b) SERS intensity of the 682 cm^{-1} peak as a function of the MLM concentration.

utilized to produce uniformly distributed silver nanoparticles that were then applied to the surface of a porous silicon substrate via a self-assembly technique. This created SERS substrates detecting RhB and MLM with detection limits of 1.94×10^{-10} and 2.8×10^{-8} M, respectively. Enhancement factors of 8.59×10^6 and 8.21×10^3 were achieved for RhB and MLM, respectively. SERS mapping showed the substrate to have good homogeneity with a relative standard deviation of the peak intensities of 8%. These results demonstrate the excellent analytical performance of the PS@Ag SERS substrate, making it a promising tool for detecting environmental pollutants and ensuring food safety.

Supporting Information

The Supporting Information features the following: four steps of the fabrication process of a microfluidic device; design of the mold; optimization of droplet generation; synthesis of silver nanoparticles in the droplet-based microfluidic device; FESEM images and EDX spectra of the SERS substrate; SEM images of the SERS substrate with RhB; and calculation of the enhancement factors for RhB and MLM.

Supporting Information File 1

Additional experimental data.
[https://www.beilstein-journals.org/bjnano/content/supplementary/2190-4286-14-65-S1.pdf]

Funding

This work was supported by the National Research Foundation of Korea (NRF) grant funded by the Korea government (MSIT) (NRF-2023R1A2C1004414).

ORCID® iDs

Phommachith Sonexai - https://orcid.org/0009-0005-3541-2878
Minh Van Nguyen - https://orcid.org/0009-0001-5770-0249
Bui The Huy - https://orcid.org/0000-0002-1218-3073
Yong-Ill Lee - https://orcid.org/0000-0001-5383-9801

Preprint

A non-peer-reviewed version of this article has been previously published as a preprint: https://doi.org/10.3762/bxiv.2023.16.v1

References

1. Fan, M.; Andrade, G. F. S.; Brolo, A. G. *Anal. Chim. Acta* **2020,** *1097,* 1–29. doi:10.1016/j.aca.2019.11.049
2. Langer, J.; Jimenez de Aberasturi, D.; Aizpurua, J.; Alvarez-Puebla, R. A.; Auguié, B.; Baumberg, J. J.; Bazan, G. C.; Bell, S. E. J.; Boisen, A.; Brolo, A. G.; Choo, J.; Cialla-May, D.; Deckert, V.; Fabris, L.; Faulds, K.; García de Abajo, F. J.; Goodacre, R.; Graham, D.; Haes, A. J.; Haynes, C. L.; Huck, C.; Itoh, T.; Käll, M.; Kneipp, J.; Kotov, N. A.; Kuang, H.; Le Ru, E. C.; Lee, H. K.; Li, J.-F.; Ling, X. Y.; Maier, S. A.; Mayerhöfer, T.; Moskovits, M.; Murakoshi, K.; Nam, J.-M.; Nie, S.; Ozaki, Y.; Pastoriza-Santos, I.; Perez-Juste, J.; Popp, J.; Pucci, A.; Reich, S.; Ren, B.; Schatz, G. C.; Shegai, T.; Schlücker, S.; Tay, L.-L.; Thomas, K. G.; Tian, Z.-Q.; Van Duyne, R. P.; Vo-Dinh, T.; Wang, Y.; Willets, K. A.; Xu, C.; Xu, H.; Xu, Y.; Yamamoto, Y. S.; Zhao, B.; Liz-Marzán, L. M. *ACS Nano* **2020,** *14,* 28–117. doi:10.1021/acsnano.9b04224
3. Almehmadi, L. M.; Curley, S. M.; Tokranova, N. A.; Tenenbaum, S. A.; Lednev, I. K. *Sci. Rep.* **2019,** *9,* 12356. doi:10.1038/s41598-019-48650-y
4. Keshavarz, M.; Kassanos, P.; Tan, B.; Venkatakrishnan, K. *Nanoscale Horiz.* **2020,** *5,* 294–307. doi:10.1039/c9nh00590k
5. Fleischmann, M.; Hendra, P. J.; McQuillan, A. J. *Chem. Phys. Lett.* **1974,** *26,* 163–166. doi:10.1016/0009-2614(74)85388-1
6. McCall, S. L.; Platzman, P. M.; Wolff, P. A. *Phys. Lett. A* **1980,** *77,* 381–383. doi:10.1016/0375-9601(80)90726-4
7. Strommen, D. P.; Nakamoto, K. *J. Chem. Educ.* **1977,** *54,* 474. doi:10.1021/ed054p474

8. Nie, Y.; Jin, C.; Zhang, J. X. J. *ACS Sens.* **2021,** *6,* 2584–2592. doi:10.1021/acssensors.1c00117
9. Kuo, J. S.; Chiu, D. T. *Annu. Rev. Anal. Chem.* **2011,** *4,* 275–296. doi:10.1146/annurev-anchem-061010-113926
10. Zhao, C.-X.; He, L.; Qiao, S. Z.; Middelberg, A. P. J. *Chem. Eng. Sci.* **2011,** *66,* 1463–1479. doi:10.1016/j.ces.2010.08.039
11. Elvira, K. S.; i Solvas, X. C.; Wootton, R. C. R.; deMello, A. J. *Nat. Chem.* **2013,** *5,* 905–915. doi:10.1038/nchem.1753
12. Abalde-Cela, S.; Taladriz-Blanco, P.; de Oliveira, M. G.; Abell, C. *Sci. Rep.* **2018,** *8,* 2440. doi:10.1038/s41598-018-20754-x
13. Kwapiszewska, K.; Michalczuk, A.; Rybka, M.; Kwapiszewski, R.; Brzózka, Z. *Lab Chip* **2014,** *14,* 2096–2104. doi:10.1039/c4lc00291a
14. Iyer, V.; Yang, Z.; Ko, J.; Weissleder, R.; Issadore, D. *Lab Chip* **2022,** *22,* 3110–3121. doi:10.1039/d2lc00024e
15. Wang, J.; Jin, M.; Gong, Y.; Li, H.; Wu, S.; Zhang, Z.; Zhou, G.; Shui, L.; Eijkel, J. C. T.; van den Berg, A. *Lab Chip* **2017,** *17,* 1970–1979. doi:10.1039/c7lc00081b
16. Thu, V. T.; Mai, A. N.; Le The, T.; Van Trung, H.; Thu, P. T.; Tien, B. Q.; Thuat, N. T.; Lam, T. D. *J. Electron. Mater.* **2016,** *45,* 2576–2581. doi:10.1007/s11664-016-4424-6
17. Choi, J. W.; Kim, Y. J.; Lee, J. M.; Choi, J.-H.; Choi, J.-W.; Chung, B. G. *BioChip J.* **2020,** *14,* 298–307. doi:10.1007/s13206-020-4307-z
18. Xia, H. M.; Wan, S. Y. M.; Shu, C.; Chew, Y. T. *Lab Chip* **2005,** *5,* 748–755. doi:10.1039/b502031j
19. Höhn, E.-M.; Panneerselvam, R.; Das, A.; Belder, D. *Anal. Chem. (Washington, DC, U. S.)* **2019,** *91,* 9844–9851. doi:10.1021/acs.analchem.9b01514
20. Wang, J.; Li, Y.; Wang, X.; Wang, J.; Tian, H.; Zhao, P.; Tian, Y.; Gu, Y.; Wang, L.; Wang, C. *Micromachines* **2017,** *8,* 22. doi:10.3390/mi8010022
21. Sahin, S.; Bliznyuk, O.; Rovalino Cordova, A.; Schroën, K. *Sci. Rep.* **2016,** *6,* 26407. doi:10.1038/srep26407
22. Cheng, Y.; Ling, S. D.; Geng, Y.; Wang, Y.; Xu, J. *Nanoscale Adv.* **2021,** *3,* 2180–2195. doi:10.1039/d0na00933d
23. Damodara, S.; Shahriari, S.; Wu, W.-I.; Rezai, P.; Hsu, H.-H.; Selvaganapathy, R. Materials and methods for microfabrication of microfluidic devices. *Microfluidic Devices for Biomedical Applications,* 2nd ed.; Woodhead Publishing, 2021; pp 1–78. doi:10.1016/b978-0-12-819971-8.00008-1
24. Li, Y.; Bøtker, J.; Rantanen, J.; Yang, M.; Bohr, A. *Int. J. Pharm.* **2020,** *583,* 119388. doi:10.1016/j.ijpharm.2020.119388
25. Duarte, L. C.; Pereira, I.; Maciel, L. I. L.; Vaz, B. G.; Coltro, W. K. T. *Anal. Chim. Acta* **2022,** *1190,* 339252. doi:10.1016/j.aca.2021.339252
26. Bressan, L. P.; Robles-Najar, J.; Adamo, C. B.; Quero, R. F.; Costa, B. M. C.; de Jesus, D. P.; da Silva, J. A. F. *Microchem. J.* **2019,** *146,* 1083–1089. doi:10.1016/j.microc.2019.02.043
27. Xu, Q.; Lo, J.; Lee, S.-W. *Appl. Sci.* **2020,** *10,* 3384. doi:10.3390/app10103384
28. Litti, L.; Trivini, S.; Ferraro, D.; Reguera, J. *ACS Appl. Mater. Interfaces* **2021,** *13,* 34752–34761. doi:10.1021/acsami.1c09771
29. Wang, L.; Pumera, M. *TrAC, Trends Anal. Chem.* **2021,** *135,* 116151. doi:10.1016/j.trac.2020.116151
30. Mohamed, M.; Kumar, H.; Wang, Z.; Martin, N.; Mills, B.; Kim, K. *J. Manuf. Mater. Process.* **2019,** *3,* 26. doi:10.3390/jmmp3010026
31. Gross, B. C.; Erkal, J. L.; Lockwood, S. Y.; Chen, C.; Spence, D. M. *Anal. Chem. (Washington, DC, U. S.)* **2014,** *86,* 3240–3253. doi:10.1021/ac403397r
32. Thuy, T. T.; Sharipov, M.; Lee, Y.; Huy, B. T.; Lee, Y.-I. *Nano Sel.* **2020,** *1,* 499–509. doi:10.1002/nano.202000081
33. Lin, S.; Hasi, W.; Han, S.; Lin, X.; Wang, L. *Anal. Methods* **2020,** *12,* 2571–2579. doi:10.1039/d0ay00483a
34. Xing, L.; Xiahou, Y.; Zhang, X.; Du, W.; Zhang, P.; Xia, H. *ACS Appl. Mater. Interfaces* **2022,** *14,* 13480–13489. doi:10.1021/acsami.1c23638
35. Yang, N.; You, T.-T.; Gao, Y.-K.; Zhang, C.-M.; Yin, P.-G. *J. Agric. Food Chem.* **2018,** *66,* 6889–6896. doi:10.1021/acs.jafc.8b01702
36. Ge, F.; Chen, Y.; Liu, A.; Guang, S.; Cai, Z. *Cellulose* **2019,** *26,* 2689–2697. doi:10.1007/s10570-018-2209-1
37. Shanthil, M.; Fathima, H.; George Thomas, K. *ACS Appl. Mater. Interfaces* **2017,** *9,* 19470–19477. doi:10.1021/acsami.6b12478
38. Chen, J.; Feng, S.; Gao, F.; Grant, E.; Xu, J.; Wang, S.; Huang, Q.; Lu, X. *J. Food Sci.* **2015,** *80,* N834–N840. doi:10.1111/1750-3841.12825
39. Zhang, C.; Jiang, S. Z.; Huo, Y. Y.; Liu, A. H.; Xu, S. C.; Liu, X. Y.; Sun, Z. C.; Xu, Y. Y.; Li, Z.; Man, B. Y. *Opt. Express* **2015,** *23,* 24811–24821. doi:10.1364/oe.23.024811
40. Kara, S. A.; Keffous, A.; Giovannozzi, A. M.; Rossi, A. M.; Cara, E.; D'Ortenzi, L.; Sparnacci, K.; Boarino, L.; Gabouze, N.; Soukane, S. *RSC Adv.* **2016,** *6,* 93649–93659. doi:10.1039/c6ra20323j
41. Rani, S.; Shukla, A. K. *Thin Solid Films* **2021,** *723,* 138595. doi:10.1016/j.tsf.2021.138595
42. Lai, Y.-C.; Ho, H.-C.; Shih, B.-W.; Tsai, F.-Y.; Hsueh, C.-H. *Appl. Surf. Sci.* **2018,** *439,* 852–858. doi:10.1016/j.apsusc.2018.01.092
43. Hao, N.; Nie, Y.; Xu, Z.; Zhang, J. X. J. *J. Colloid Interface Sci.* **2019,** *542,* 370–378. doi:10.1016/j.jcis.2019.02.021
44. Sarjuna, K. *ECS Trans.* **2022,** *107* (1), 4113. doi:10.1149/10701.4113ecst
45. Leiterer, C.; Zopf, D.; Seise, B.; Jahn, F.; Weber, K.; Popp, J.; Cialla-May, D.; Fritzsche, W. *J. Nanopart. Res.* **2014,** *16,* 2467. doi:10.1007/s11051-014-2467-2
46. Solis-Tinoco, V.; Marquez, S.; Sepulveda, B.; Lechuga, L. M. *RSC Adv.* **2016,** *6,* 85666–85674. doi:10.1039/c6ra15485a
47. Natarajan, S.; Chang-Yen, D. A.; Gale, B. K. *J. Micromech. Microeng.* **2008,** *18,* 045021. doi:10.1088/0960-1317/18/4/045021
48. Hoek, I.; Tho, F.; Arnold, W. M. *Lab Chip* **2010,** *10,* 2283–2285. doi:10.1039/c004769d
49. Maji, D.; Lahiri, S. K.; Das, S. *Surf. Interface Anal.* **2012,** *44,* 62–69. doi:10.1002/sia.3770
50. Sobczak-Kupiec, A.; Malina, D.; Wzorek, Z.; Zimowska, M. *Micro Nano Lett.* **2011,** *6,* 656. doi:10.1049/mnl.2011.0152
51. Fu, L.-M.; Hsu, J.-H.; Shih, M.-K.; Hsieh, C.-W.; Ju, W.-J.; Chen, Y.-W.; Lee, B.-H.; Hou, C.-Y. *Micromachines* **2021,** *12,* 1123. doi:10.3390/mi12091123
52. Zhang, Q.; Li, N.; Goebl, J.; Lu, Z.; Yin, Y. *J. Am. Chem. Soc.* **2011,** *133,* 18931–18939. doi:10.1021/ja2080345
53. Sun, Y.; Li, W.; Zhao, L.; Li, F.; Xie, Y.; Yao, W.; Liu, W.; Lin, Z. *Food Chem.* **2021,** *357,* 129741. doi:10.1016/j.foodchem.2021.129741
54. Huy, B. T.; Pham, Q.-T.; An, N. T. T.; Conte, E.; Lee, Y.-I. *J. Lumin.* **2017,** *188,* 436–440. doi:10.1016/j.jlumin.2017.05.009
55. An, N. T. T.; Dao, D. Q.; Nam, P. C.; Huy, B. T.; Nhung Tran, H. *Spectrochim. Acta, Part A* **2016,** *169,* 230–237. doi:10.1016/j.saa.2016.06.043
56. Dao, D. Q.; Ngo, T. C.; Le, T. T. H.; Trinh, Q. T.; Nguyen, T. L. A.; Huy, B. T.; Tri, N. N.; Trung, N. T.; Nguyen, M. T. *J. Phys. Chem. A* **2021,** *125,* 8529–8541. doi:10.1021/acs.jpca.1c04957

License and Terms

This is an open access article licensed under the terms of the Beilstein-Institut Open Access License Agreement (https://www.beilstein-journals.org/bjnano/terms), which is identical to the Creative Commons Attribution 4.0 International License (https://creativecommons.org/licenses/by/4.0). The reuse of material under this license requires that the author(s), source and license are credited. Third-party material in this article could be subject to other licenses (typically indicated in the credit line), and in this case, users are required to obtain permission from the license holder to reuse the material.

The definitive version of this article is the electronic one which can be found at:
https://doi.org/10.3762/bjnano.14.65

BEILSTEIN JOURNAL OF NANOTECHNOLOGY

Ni, Co, Zn, and Cu metal-organic framework-based nanomaterials for electrochemical reduction of CO_2: A review

Ha Huu Do[1] and Hai Bang Truong[*2,3]

Review

Open Access

Address:
[1]VKTech Research Center, NTT Hi-Tech Institute, Nguyen Tat Thanh University, Ho Chi Minh City, 700000, Vietnam, [2]Optical Materials Research Group, Science and Technology Advanced Institute, Van Lang University, Ho Chi Minh City, Vietnam and [3]Faculty of Applied Technology, School of Technology, Van Lang University, Ho Chi Minh City, Vietnam

Email:
Hai Bang Truong[*] - truonghaibang@vlu.edu.vn

* Corresponding author

Keywords:
carbon capture; CO_2 reduction; electrocatalysis; metal-organic frameworks; nanomaterials

Beilstein J. Nanotechnol. **2023,** *14,* 904–911.
https://doi.org/10.3762/bjnano.14.74

Received: 23 June 2023
Accepted: 17 August 2023
Published: 31 August 2023

This article is part of the thematic issue "Recent advances in synthesis and applications of organometallic nanomaterials".

Associate Editor: C. T. Yavuz



© 2023 Do and Truong; licensee Beilstein-Institut.
License and terms: see end of document.

Abstract

The combustion of fossil fuels has resulted in the amplification of the greenhouse effect, primarily through the release of a substantial quantity of carbon dioxide into the atmosphere. The imperative pursuit of converting CO_2 into valuable chemicals through electrochemical techniques has garnered significant attention. Metal-organic frameworks (MOFs) have occured as highly prospective materials for the reduction of CO_2, owing to their exceptional attributes including extensive surface area, customizable architectures, pronounced porosity, abundant active sites, and well-distributed metallic nodes. This article commences by elucidating the mechanistic aspects of CO_2 reduction, followed by a comprehensive exploration of diverse materials encompassing MOFs based on nickel, cobalt, zinc, and copper for efficient CO_2 conversion. Finally, a meticulous discourse encompasses the challenges encountered and the prospects envisioned for the advancement of MOF-based nanomaterials in the realm of electrochemical reduction of CO_2.

Introduction

The emission of carbon dioxide resulting from the utilization of fossil fuels has been identified as a primary cause of the greenhouse effect, ultimately contributing to the severity of climate change [1]. To mitigate these detrimental consequences, numerous strategies have been implemented to address the issue of CO_2 emissions. Among these, the carbon capture and storage (CCS) technique plays a crucial role in curtailing the release of CO_2 into the air. By capturing and containing approximately 90% of the CO_2 gas generated through the combustion of conventional fuels utilized for human energy consumption [2,3], this method proves instrumental in abating the pollution caused by CO_2. Nevertheless, CO_2 storage and transportation

are expensive, necessitating the development of efficient adsorbents [3]. An auspicious avenue to tackle these challenges is the conversion of CO_2 into valuable compounds through electrochemical reduction. The electrocatalytic process for CO_2 reduction reactions (CO_2RR) encounters a persistent obstacle in the activation of CO_2 [4]. The formation of $CO_2^{\bullet-}$ necessitates a high thermodynamic potential of −1.90 V vs the standard hydrogen electrode. Subsequently, multiple electron transfers occur, leading to the generation of diverse products such as ethanol, methanol, and methane [5-7]. Therefore, to reduce the activation energy and to improve selectivity, the meticulous consideration of catalysts becomes imperative [8-16]. The first work on electrocatalytic CO_2 reduction was published in 1870 using a Zn material to produce HCOOH [17,18]. Subsequent investigations have yielded numerous studies focusing on the development of electrocatalysts for CO_2RR. In 1994, Hori et al. highlighted that the selectivity of products exhibited considerable variation depending on the elemental composition of pure metal catalysts [19]. Notably, Au, Ag, and Zn catalysts exhibit preferential CO generation, while Sn, In, and Pb catalysts prove effective in producing formate ions ($HCOO^-$) [20].

Metal-organic frameworks (MOFs) are established from metal ions and organic linkers, and have been identified as prospective materials for CO_2RR [21]. Therefore, a multitude of MOFs structures have been explored in experimental studies [22,23], exhibiting diverse applications such as gas storage [24], electrocatalysis [25-27], glucose sensing [28-30], and biomedical [31] applications. These materials are distinguished by their exceptional attributes, including a substantial specific surface area, pronounced porosity, and modifiable chemical structures [32]. Within the catalytic domain, MOFs demonstrate catalytic activity stemming from both their metal sites and organic components. Furthermore, their catalytic properties can be readily modified through functionalization. For instance, Fu et al. grafted $–NH_2$ groups onto MIL-125(Ti) material to enhance CO_2RR for the production of $HCOO^-$ [33]. The outcome indicated that NH_2-MIL-125(Ti) indicated superior catalytic activity compared to MIL-125(Ti). Notably, MOF-210 has established a remarkable record in CO_2 adsorption among all porous materials, boasting an adsorption capacity of 2870 $mg \cdot g^{-1}$ [34]. Such properties facilitate favorable interactions between CO_2 molecules and catalytic sites within MOFs, thereby enhancing the CO_2RR process. Besides, MOFs could be used as ideal precursors for the controlled dispersion of metal nanoparticles within organic frameworks, either through operational conditions or via the pyrolysis technique, thereby promoting efficient CO_2 reduction [35,36]. The augmentation of MOF properties can be accomplished by converting pristine MOFs into nanoscale materials. A diverse array of MOF nanomaterials has been reported, encompassing single-atom nanocatalysts (SACs), hetero-atom-doped nanomaterials, and MOF nanofiber-based aerogels, among others, as highlighted by Behera et al. in 2022 [37]. These derived nanomaterials showcase enhanced stability, favorable morphologies, advanced functionalities, and precisely controlled textural characteristics in comparison to their original MOF counterparts.

Herein, we provide a comprehensive overview of the latest literature pertaining to the implementation of MOF-based nanomaterials for the electrochemical conversion of CO_2. First, the reaction pathway of the CO_2 reduction is described for the production of different chemicals. Then, various structures, including Ni-, Co-, Zn-, and Cu-based MOFs for electrochemical CO_2RR are presented. Finally, we present the potential pathways and current problems in progressing MOF-based nanomaterials for CO_2 conversion.

Review

Mechanism of CO_2RR

The process of CO_2 reduction consists of three steps. First, the CO_2 molecules are adsorbed on the active sites of catalysts. Second, charge transfer processes take place to create intermediates such as *CHO, *CO, and *COO. The process could include many electrons attending in the electrochemical reaction, and orientate the formed products. Finally, these species are desorbed from the active sites of electrocatalysts to generate various products, as shown in Figure 1. In addition to the properties of the catalyst material, other parameters, such as potential, pH, solvent, and temperature, also determine the formation of desired products.

MOFs nanomaterials for electrocatalytic reduction of CO_2

Ni-based MOFs nanomaterials

Two-dimensional (2D) MOFs represent a novel addition to the family of 2D materials. Particularly, 2D MOF nanolayers with several outstanding characteristics, such as high surface area and abundant exposed active sites, have been studied for CO_2RR. As a case in point, Wu et al. prepared 2D Ni-based zeolitic imidazole framework (ZIF) nanosheets as efficient material for electrochemical CO_2 conversion [39]. 2D $Ni(Im)_2$ materials with various thicknesses were fabricated through varying centrifugation speeds (Figure 2a). The outcome revealed that the optimal sample, possessing a thickness of 5 nm, yielded the highest performance of CO production (FE_{CO} = 78.8% at −0.85 V vs RHE), compared to its bulk counterpart with a value of 33.7% (Figure 2b). The optimal sample also showed a high turnover frequency (TOF) and outstanding stability after a testing period of 14 h (Figure 2c,d). The high catalytic activity can be ascribed to the enhanced number of active sites achieved through the transition from the bulk state to the nano-

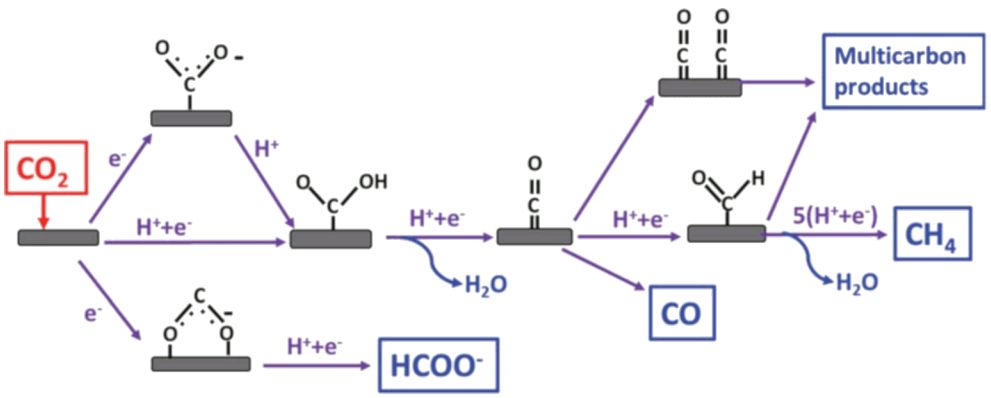


Figure 1: Schematic illustration of CO_2RR for various chemicals production. Republished with permission of The Royal Society of Chemistry, from [38], ("CO_2 electrochemical reduction on metal-organic framework catalysts: current status and future directions" by D. Narváez-Celada and A. S. Varela, J. Mater. Chem. A, Vol. 10, Issue 11, © 2022); permission conveyed through Copyright Clearance Center, Inc. This content is not subject to CC BY 4.0.".

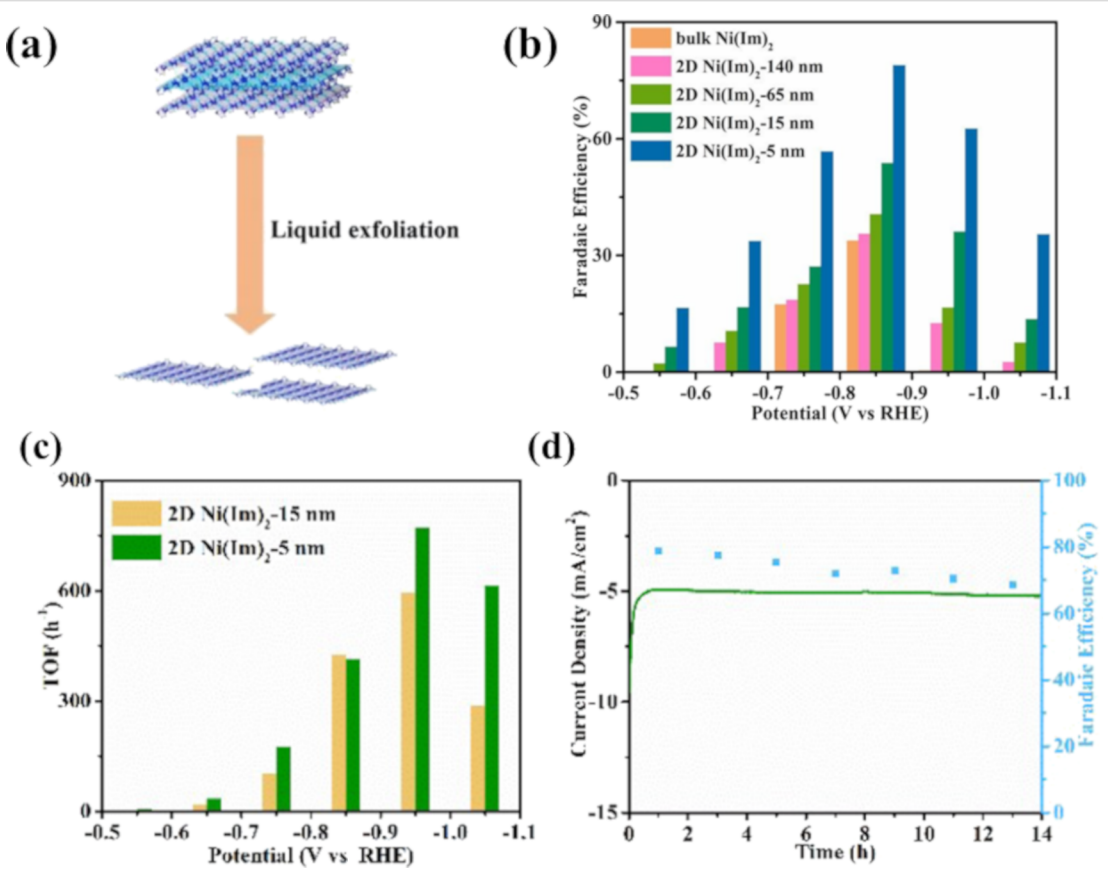


Figure 2: (a) Graphic representation of the synthesis of 2D $Ni(Im)_2$, (b) Faradaic efficiency of 2D $Ni(Im)_2$ with various thicknesses, (c) TOF of 2D $Ni(Im)_2$-5 nm and 2D $Ni(Im)_2$-15 nm, (d) durability test and FE of 2D $Ni(Im)_2$-5 nm at –0.85 V vs RHE for 14 h. Figure 2 was adapted with permission of The Royal Society of Chemistry, from [39], ("Ultrathin 2D nickel zeolitic imidazolate framework nanosheets for electrocatalytic reduction of CO_2" by J.-X. Wu et al., Chemical Communications, Vol. 55, Issue 77, © 2019); permission conveyed through Copyright Clearance Center, Inc. This content is not subject to CC BY 4.0.

material form. The optimal condition for the fabrication of 2D $Ni(Im)_2$ was determined to be the utilization of 5 mL of NH_4OH.

Co-based MOFs nanomaterials

Cobalt materials provide a diversity of reduction–oxidation states and are, thus, considered potential candidates in electro-

catalysis. Co-related MOFs have been extensively investigated for their applicability in CO_2 conversion processes. Wang et al. introduced an interesting work based on four distinct structures, including Co-PMOF, Ni-PMOF, Fe-PMOF, and Zn-PMOF (P: polyoxometalate) for CO_2 conversion. Co-PMOF displayed the highest catalytic activity for CO_2RR among the investigated MOFs, as illustrated in Figure 3a,b. Moreover, this catalyst also showed remarkable durability, with the current density remaining stable after 35 h of testing. To gain insights into the reaction pathway and to provide explanations for the observed outcome, the research team employed computational science techniques. Density functional theory (DFT) calculations implied that Co-PMOF possessed the lowest total free energy leading to its superiority as a catalyst for CO_2RR. The author postulated that Co(II) is converted into Co(I), which acts as a redox center for the reduction of CO_2 into CO (Figure 3c,d). Because of their poor conductivity, Co-MOFs are typically grown on conductive templates, such as fluorine-doped tin oxide (FTO), carbon cloth, and carbon pastes, which serve as cathodes for CO_2RR. To illustrate, Kornienko et al. deposited a Co-based MOF material onto an FTO substrate as a working electrode for CO_2 conversion [40]. This material exhibited good performance in CO generation, achieving a faradaic efficiency (FE) of 76% (at −0.7 V vs RHE). The authors attributed the active center for CO_2 conversion to Co(I) species generated through the reduction of Co(II).

Zn-based MOFs nanomaterials

Zinc (Zn) metal-based electrocatalysts have been identified as outstanding candidates for CO_2 conversion into CO because of their low cost, nontoxic nature, and high efficiency. Therefore, considerable interest has been directed towards exploring the potential of Zn-based MOFs in CO_2RR applications. Wang and co-workers successfully prepared ZIF-8 from different metal salts for CO_2RR [42]. ZIF-8 derived from $ZnSO_4$ yielded the best performance for the electrochemical reduction of CO_2 into CO, with an FE of 65%. The research group also revealed that the Zn^{2+} species operate as active sites in the catalytic process.

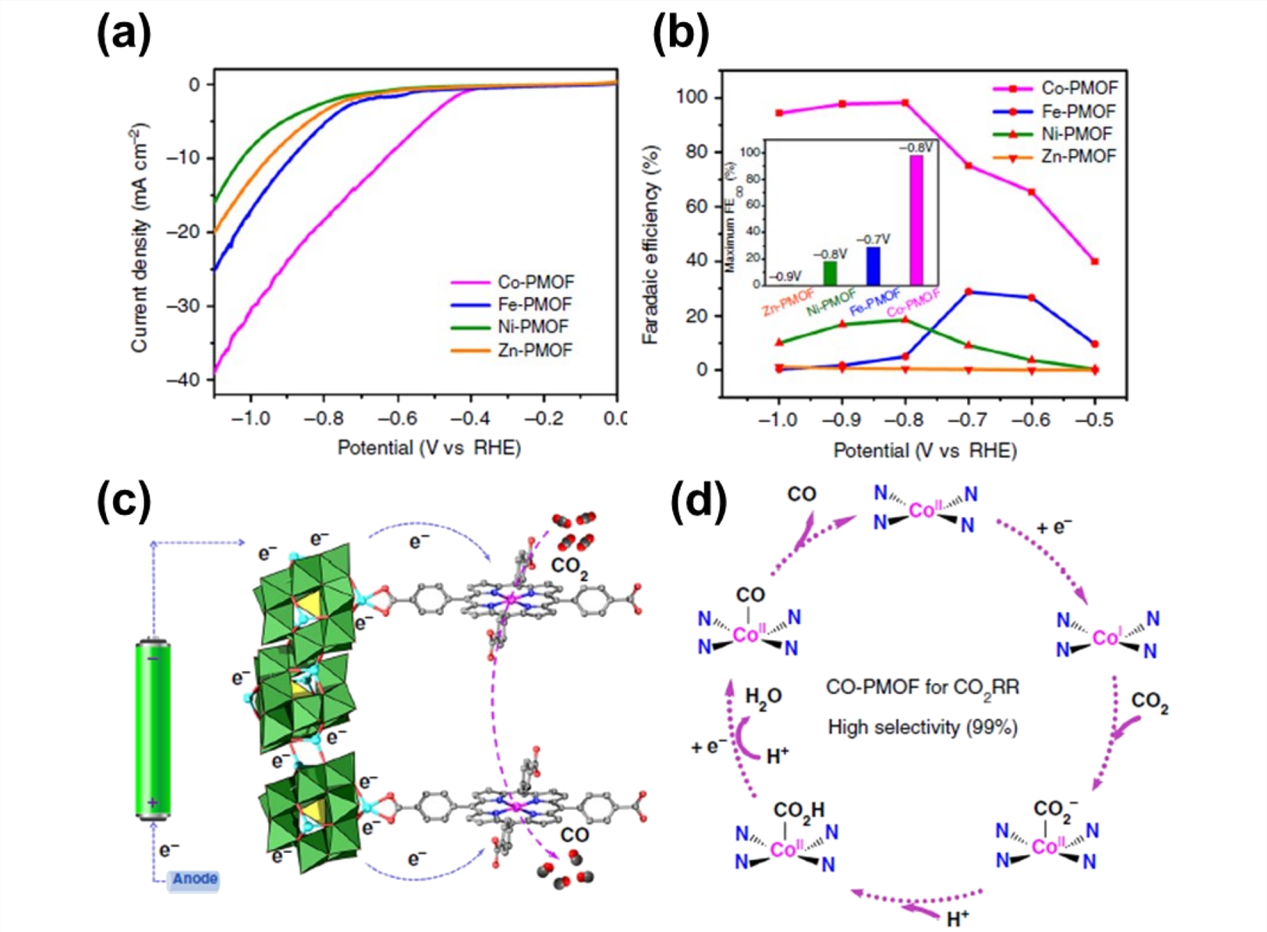


Figure 3: (a) Polarization curves of various M-PMOFs (M = Co, Ni, Fe, Zn) for CO formation, (b) Faradaic efficiency for CO product on different materials, (c, d) proposed reaction pathway for the electrochemical CO_2 conversion with Co-PMOF. Figure 3 was adapted from [41]; (© 2018 Y.-R. Wang et al., published by Springer Nature, distributed under the terms of the Creative Commons Attribution 4.0 International License (CCBY 4.0), http://creativecommons.org/licenses/by/4.0/).

Another investigation shed light on the significance of organic ligands within Zn-based MOF architectures for CO_2RR. Jiang et al. prepared four Zn-based ZIFs, including ZIF-7, ZIF-108, ZIF-8, and SIM-1, employing various ligands while utilizing the same Zn-containing salt [43]. These architectures were evaluated under identical conditions to determine the role of ligands in CO_2 conversion. The ZIF-8 variant with the 2-methylimidazole ligand exhibited the highest activity for CO_2RR to carbon monoxide (FE = 81% at −1.1 V vs RHE). This can be explained by the fact that ZIF-8 has the smallest adsorption energy of hydrogen, facilitating the desired CO_2RR process. The outcomes of this study serve as a foundation for the exploration of transition metal ion doping in ZIF-8, aiming to enhance the performance of CO_2 conversion, as recently reported (Figure 4a). Cho et al. revealed that Cu-doped ZIF-8 exhibited the highest catalytic activity, surpassing both Fe- and Ni-doped ZIF-8 [44]. Specifically, $Cu_{0.5}Zn_{0.5}$/ZIF-8 yielded a large FE_{CO} of 88.5% at −1.0 V (RHE), whereas the values were 48.8% and 34.7% for Fe-doped ZIF-8 and Ni-doped ZIF-8 at −1.2 V (RHE), respectively (Figure 4b). These results were confirmed

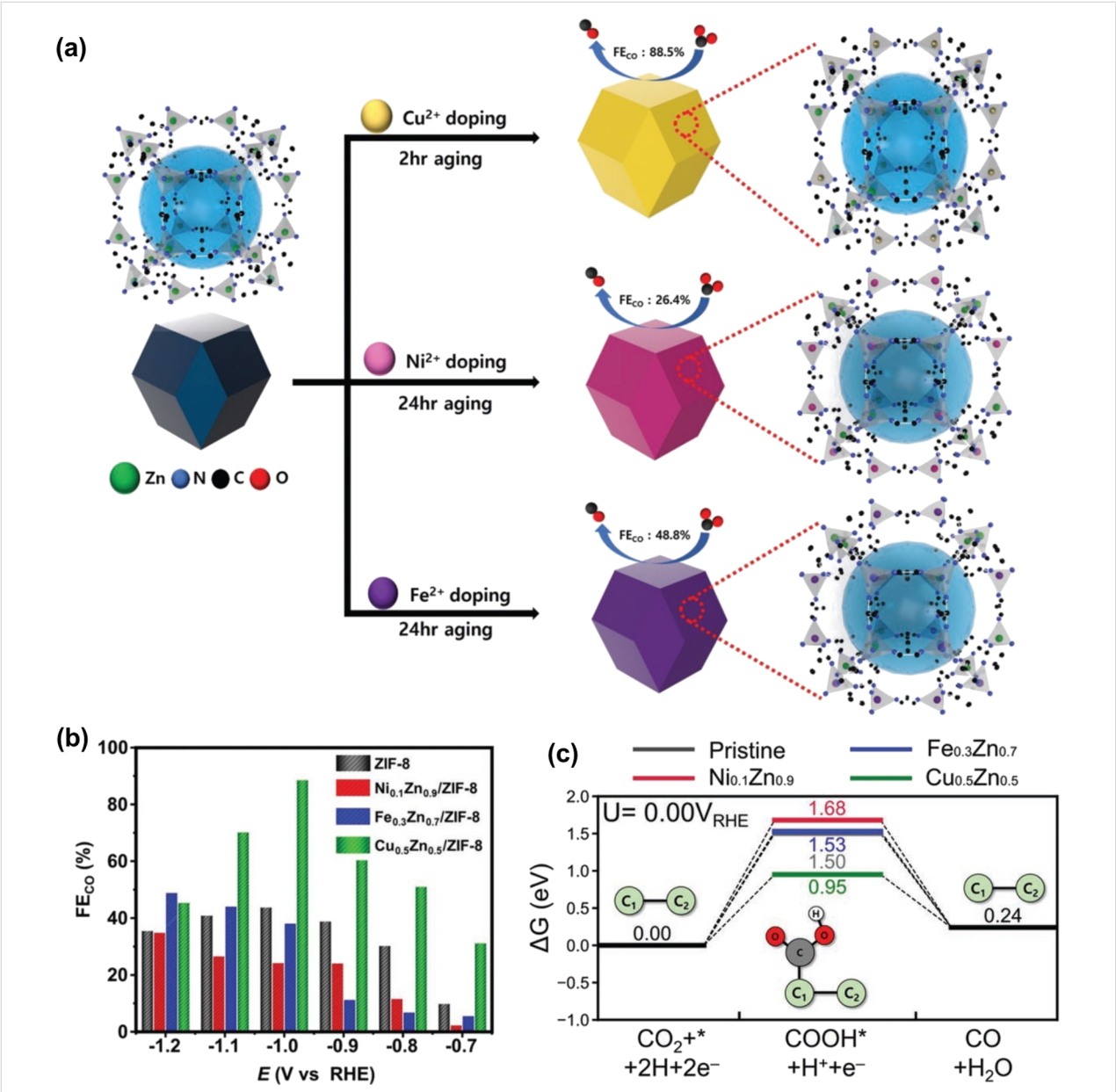


Figure 4: (a) A graphic representation of the preparation of M_2Zn_y/ZIF-8, (b) Faradaic efficiency for the CO production using different materials, (c) diagram of free energy for CO_2RR. Figure 4 was adapted from [44], J. H. Cho et al., "Transition Metal Ion Doping on ZIF-8 Enhances the Electrochemical CO_2 Reduction Reaction", Advanced Materials, with permission from John Wiley and Sons. Copyright © 2022 Wiley-VCH GmbH. This content is not subject to CC BY 4.0.

by theoretical calculations, which indicated the lowest COOH adsorption energy of Cu-doped ZIF-8 (Figure 4c).

Cu-based MOF nanomaterials

Cu-based MOFs are high-potential materials for the electrochemical CO_2 reduction because of their cost-effectiveness, nontoxicity, and diversity of active sites. Hinogami et al. reported that a copper rubeanate MOF has a higher catalytic activity than Cu metal for the CO_2 conversion into formic acid, primarily because of the weak adsorption of CO_2 on the MOF surface [45]. Solvents also play a vital role in CO_2 reduction, as highlighted in Kumar's study [46], where the dimethylformamide solvent supplied protons for HCOOH formation with high purity. Albo et al. assessed the catalytic activity of different Cu-MOFs for CO_2 reduction [47]. The study revealed that HKUST-1 showed the highest performance with a FE of 15.9% at a current density of 10 $mA{\cdot}cm^{-2}$ for methanol and ethanol formation. In particular, $FE_{(methanol)}$ is 5.6% and $FE_{(ethanol)}$ is 10.3%. This result can be explained by two reasons. On the one hand, HKUST-1 contains open metal sites (Cu^{2+}), which are not hindered by surrounding linkers, facilitating interaction with intermediates and, thus, increasing CO_2 reduction. On the other hand, the largest surface area also partially contributes to improving the performance of CO_2 reduction. Later, the authors improved the CO_2 reduction performance by mixing HKUST-1 with a Bi-based MOF (CAU-17) [48]. The optimized sample demonstrated a considerably elevated FE for alcohol production, reaching 36.9%. This enhancement was attributed to the synergistic effects between Cu- and Bi-MOFs, which played a pivotal role in promoting interactions between active species and transition states. Notably, Bi centers in CAU-17 are the main active sites in the generation of HCOO–, after which these intermediates would move to open Cu metal sites (HKUST-1), thus improving activity. In an interesting study by Wu et al., Cu-based MOF nanosheets were utilized for CO_2 reduction to formate and acetate (Figure 5a,b) [49]. The authors observed

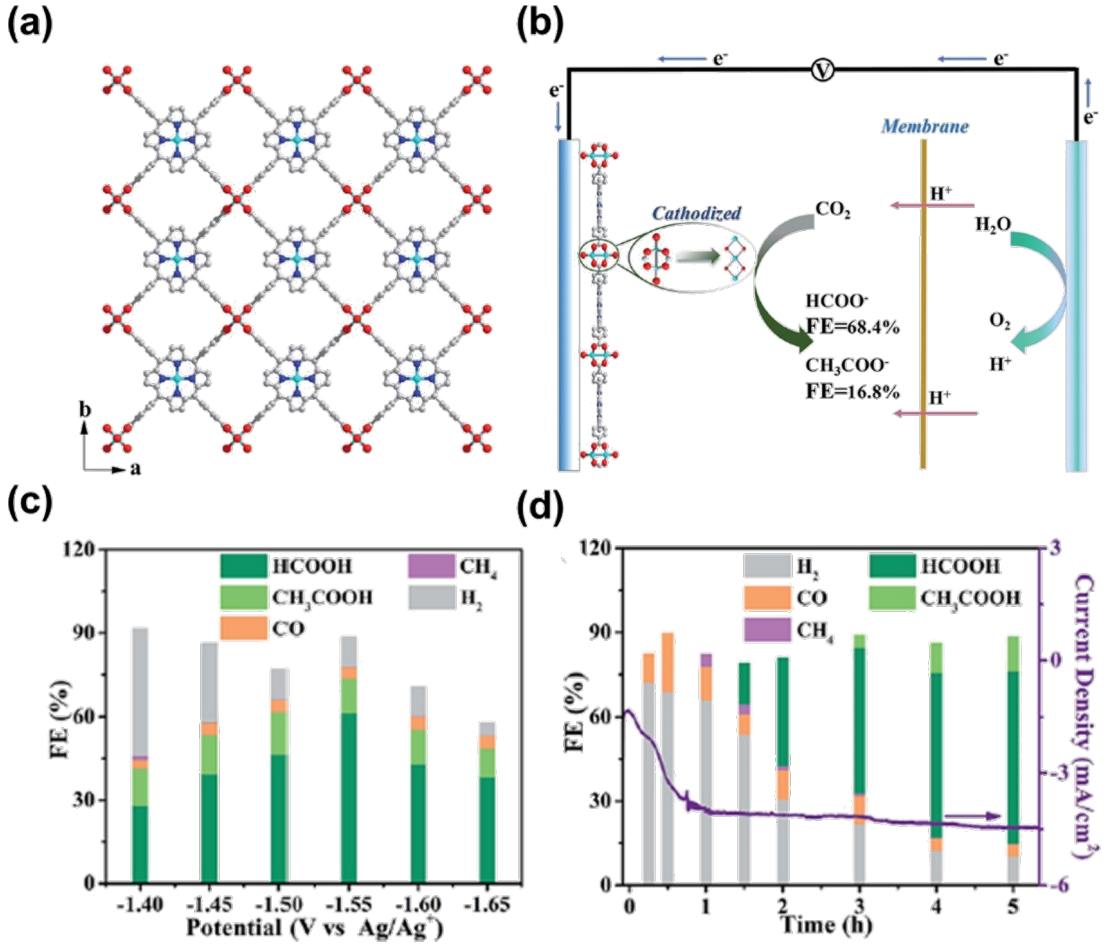


Figure 5: (a) Crystal architecture of 2D Cu_2(CuTCPP) nanosheets, (b) graphic illustration of the electrochemical CO_2 reduction, (c) Faradaic efficiency of catalysts at various potentials, (d) Faradaic efficiency of catalysts as functions of the time. Figure 5 was adapted from [49]. ("Cathodized copper porphyrin metal–organic framework nanosheets for selective formate and acetate production from CO_2 electroreduction", © 2019 J.-X. Wu et al., published by The Royal Society of Chemistry, distributed under the terms of the Creative Commons Attribution-Non Commercial 3.0 Unported Licence, https://creativecommons.org/licenses/by-nc/3.0/). This content is not subject to CC BY 4.0.

that Cu^{2+} nodes underwent conversion to copper oxides under operational conditions. The presence of these species, along with a porphyrin–Cu(II) complex, resulted in an enhancement of CO_2 reduction. As a result, this material exhibited a substantial FE of 68.4% for formate generation at a voltage of −1.55 V (Figure 5c,d). However, the performance decreased after 5 h of testing, attributed to a restructuring of the Cu-based MOF. In addition, methane and ethylene were also considered as useful compounds in specific applications. However, the utilization of MOFs as electrocatalysts for the conversion of CO_2 into hydrocarbons remains relatively limited. A recent study by Yang et al. presented a potential MOF for the reduction of CO_2 to methane and ethylene [36]. Cu nanoparticles were created during when the Cu^{II}/ade-MOFs reconstructed and act as active centers for CO_2 reduction to CH_4 and C_2H_4.

Conclusion and Outlook

MOFs were recognized as promising nanomaterials for the transformation of CO_2 into valuable products through electrochemical processes. This interest arises from their advantageous properties, including high surface area, customizable morphological structures, well-defined metal sites, facile modification, and compositional diversity. Overall, the catalytic generation of diverse products from the electrochemical reduction of CO_2 is governed by the inherent characteristics of metal sites and organic linkers within the MOF structure. Notably, MOF nanomaterials based on Zn, Co, and Ni have demonstrated potential for CO_2 reduction to CO, whereas Cu-related MOFs are favorable for the conversion of CO_2 to formate, formic acid, alcohol, and hydrocarbons. Numerous studies have proposed reaction mechanisms based on the calculation of Gibbs energy for intermediate species, providing insights into the underlying processes involved in CO_2 electrocatalysis. However, they also encounter some difficulties in the field of CO_2 reduction. In particular, the low conductivity of MOFs hampers electron transport, leading to sluggish electrochemical reaction kinetics. To alleviate this problem, highly conductive materials such as graphene, and carbon nanotubes were combined with MOFs to improve overall conductivity. Additionally, the usage of pristine MOFs as sacrificial agents to create metal or metal compounds embedded in carbon matrices was considered a potential direction in CO_2RR application. Systematic studies should be conducted to control morphological structure and composition by changing reaction conditions (time, temperature, and pressure) when converting individual MOFs into MOF-derived carbon-support nanomaterials. Another issue is the durability of the working electrodes. Many studies have employed drop casting and the use of binders to affix MOFs onto the substrate for electrode fabrication. This approach presents drawbacks such as reduced accessibility to active sites and unstable MOFs/substrate interfaces. Therefore, further studies are required to develop binder-free electrodes by in situ synthesis of MOFs on conductive substrates, such as nickel foam, copper foil, and carbon cloth, to overcome the aforementioned limitations and advancing the field of CO_2RR.

ORCID® iDs

Hai Bang Truong - https://orcid.org/0000-0003-2906-7658

References

1. Xiang, S.; He, Y.; Zhang, Z.; Wu, H.; Zhou, W.; Krishna, R.; Chen, B. *Nat. Commun.* **2012,** *3,* 954. doi:10.1038/ncomms1956
2. Grant, T.; Guinan, A.; Shih, C. Y.; Lin, S.; Vikara, D.; Morgan, D.; Remson, D. *Int. J. Greenhouse Gas Control* **2018,** *72,* 175–191. doi:10.1016/j.ijggc.2018.03.012
3. Vikara, D.; Shih, C. Y.; Lin, S.; Guinan, A.; Grant, T.; Morgan, D.; Remson, D. *J. Sustainable Energy Eng.* **2017,** *5,* 307–340. doi:10.7569/jsee.2017.629523
4. Chhowalla, M.; Shin, H. S.; Eda, G.; Li, L.-J.; Loh, K. P.; Zhang, H. *Nat. Chem.* **2013,** *5,* 263–275. doi:10.1038/nchem.1589
5. Melchionna, M.; Fornasiero, P. *ACS Catal.* **2020,** *10,* 5493–5501. doi:10.1021/acscatal.0c01204
6. Chu, S.; Majumdar, A. *Nature* **2012,** *488,* 294–303. doi:10.1038/nature11475
7. Chu, S.; Cui, Y.; Liu, N. *Nat. Mater.* **2017,** *16,* 16–22. doi:10.1038/nmat4834
8. Zhao, S.; Yang, Y.; Tang, Z. *Angew. Chem., Int. Ed.* **2022,** *61,* 202110186. doi:10.1002/anie.202110186
9. Wu, Z.; Liu, X.; Li, H.; Sun, Z.; Cao, M.; Li, Z.; Fang, C.; Zhou, J.; Cao, C.; Dong, J.; Zhao, S.; Chen, Z. *Nat. Commun.* **2023,** *14,* 2574. doi:10.1038/s41467-023-38285-z
10. Zhang, S.; Tan, C.; Yan, R.; Zou, X.; Hu, F.-L.; Mi, Y.; Yan, C.; Zhao, S. *Angew. Chem., Int. Ed.* **2023,** *62,* 202302795. doi:10.1002/anie.202302795
11. Peng, J.-X.; Yang, W.; Jia, Z.; Jiao, L.; Jiang, H.-L. *Nano Res.* **2022,** *15,* 10063–10069. doi:10.1007/s12274-022-4467-3
12. Shah, S. S. A.; Najam, T.; Wen, M.; Zang, S.-Q.; Waseem, A.; Jiang, H.-L. *Small Struct.* **2022,** *3,* 2100090. doi:10.1002/sstr.202100090
13. Jiao, L.; Zhu, J.; Zhang, Y.; Yang, W.; Zhou, S.; Li, A.; Xie, C.; Zheng, X.; Zhou, W.; Yu, S.-H.; Jiang, H.-L. *J. Am. Chem. Soc.* **2021,** *143,* 19417–19424. doi:10.1021/jacs.1c08050
14. Zhang, Y.; Jiao, L.; Yang, W.; Xie, C.; Jiang, H.-L. *Angew. Chem., Int. Ed.* **2021,** *60,* 7607–7611. doi:10.1002/anie.202016219
15. Gong, Y.-N.; Jiao, L.; Qian, Y.; Pan, C.-Y.; Zheng, L.; Cai, X.; Liu, B.; Yu, S.-H.; Jiang, H.-L. *Angew. Chem., Int. Ed.* **2020,** *59,* 2705–2709. doi:10.1002/anie.201914977
16. Jiao, L.; Yang, W.; Wan, G.; Zhang, R.; Zheng, X.; Zhou, H.; Yu, S.-H.; Jiang, H.-L. *Angew. Chem., Int. Ed.* **2020,** *59,* 20589–20595. doi:10.1002/anie.202008787
17. Royer, M. *Compt. Rend.* **1870,** *70,* 731–732.
18. Augustynski, J.; Kedzierzawski, P.; Jermann, B. Electrochemical reduction of CO_2 at metallic electrodes. *Studies in Surface Science and Catalysis,;* Elsevier: Amsterdam, Netherlands, 1998; Vol. 114, pp 107–116. doi:10.1016/s0167-2991(98)80731-3
19. Hori, Y.; Wakebe, H.; Tsukamoto, T.; Koga, O. *Electrochim. Acta* **1994,** *39,* 1833–1839. doi:10.1016/0013-4686(94)85172-7

20. Ponnurangam, S.; Chernyshova, I. V.; Somasundaran, P. *Adv. Colloid Interface Sci.* **2017,** *244,* 184–198. doi:10.1016/j.cis.2016.09.002
21. Zhou, H.-C.; Long, J. R.; Yaghi, O. M. *Chem. Rev.* **2012,** *112,* 673–674. doi:10.1021/cr300014x
22. Li, X.; Wen, J.; Low, J.; Fang, Y.; Yu, J. *Sci. China Mater.* **2014,** *57,* 70–100. doi:10.1007/s40843-014-0003-1
23. Ma, Y.; Wang, X.; Jia, Y.; Chen, X.; Han, H.; Li, C. *Chem. Rev.* **2014,** *114,* 9987–10043. doi:10.1021/cr500008u
24. Maity, D. K.; Halder, A.; Bhattacharya, B.; Das, A.; Ghoshal, D. *Cryst. Growth Des.* **2016,** *16,* 1162–1167. doi:10.1021/acs.cgd.5b01686
25. Duan, J.; Chen, S.; Zhao, C. *Nat. Commun.* **2017,** *8,* 15341. doi:10.1038/ncomms15341
26. Wang, W.; Xu, X.; Zhou, W.; Shao, Z. *Adv. Sci.* **2017,** *4,* 1600371. doi:10.1002/advs.201600371
27. Zhong, G.; Liu, D.; Zhang, J. *J. Mater. Chem. A* **2018,** *6,* 1887–1899. doi:10.1039/c7ta08268a
28. Xiao, X.; Zheng, S.; Li, X.; Zhang, G.; Guo, X.; Xue, H.; Pang, H. *J. Mater. Chem. B* **2017,** *5,* 5234–5239. doi:10.1039/c7tb00180k
29. Sun, Y.; Li, Y.; Wang, N.; Xu, Q. Q.; Xu, L.; Lin, M. *Electroanalysis* **2018,** *30,* 474–478. doi:10.1002/elan.201700629
30. Kumar, P.; Deep, A.; Kim, K.-H. *TrAC, Trends Anal. Chem.* **2015,** *73,* 39–53. doi:10.1016/j.trac.2015.04.009
31. Horcajada, P.; Serre, C.; Vallet-Regí, M.; Sebban, M.; Taulelle, F.; Férey, G. *Angew. Chem., Int. Ed.* **2006,** *45,* 5974–5978. doi:10.1002/anie.200601878
32. Tekalgne, M. A.; Do, H. H.; Hasani, A.; Van Le, Q.; Jang, H. W.; Ahn, S. H.; Kim, S. Y. *Mater. Today Adv.* **2020,** *5,* 100038. doi:10.1016/j.mtadv.2019.100038
33. Fu, Y.; Sun, D.; Chen, Y.; Huang, R.; Ding, Z.; Fu, X.; Li, Z. *Angew. Chem., Int. Ed.* **2012,** *51,* 3364–3367. doi:10.1002/anie.201108357
34. Furukawa, H.; Ko, N.; Go, Y. B.; Aratani, N.; Choi, S. B.; Choi, E.; Yazaydin, A. Ö.; Snurr, R. Q.; O'Keeffe, M.; Kim, J.; Yaghi, O. M. *Science* **2010,** *329,* 424–428. doi:10.1126/science.1192160
35. Lamagni, P.; Miola, M.; Catalano, J.; Hvid, M. S.; Mamakhel, M. A. H.; Christensen, M.; Madsen, M. R.; Jeppesen, H. S.; Hu, X.-M.; Daasbjerg, K.; Skrydstrup, T.; Lock, N. *Adv. Funct. Mater.* **2020,** *30,* 1910408. doi:10.1002/adfm.201910408
36. Yang, F.; Chen, A.; Deng, P. L.; Zhou, Y.; Shahid, Z.; Liu, H.; Xia, B. Y. *Chem. Sci.* **2019,** *10,* 7975–7981. doi:10.1039/c9sc02605c
37. Behera, P.; Subudhi, S.; Tripathy, S. P.; Parida, K. *Coord. Chem. Rev.* **2022,** *456,* 214392. doi:10.1016/j.ccr.2021.214392
38. Narváez-Celada, D.; Varela, A. S. *J. Mater. Chem. A* **2022,** *10,* 5899–5917. doi:10.1039/d1ta10440c
39. Wu, J.-X.; Yuan, W.-W.; Xu, M.; Gu, Z.-Y. *Chem. Commun.* **2019,** *55,* 11634–11637. doi:10.1039/c9cc05487a
40. Kornienko, N.; Zhao, Y.; Kley, C. S.; Zhu, C.; Kim, D.; Lin, S.; Chang, C. J.; Yaghi, O. M.; Yang, P. *J. Am. Chem. Soc.* **2015,** *137,* 14129–14135. doi:10.1021/jacs.5b08212
41. Wang, Y.-R.; Huang, Q.; He, C.-T.; Chen, Y.; Liu, J.; Shen, F.-C.; Lan, Y.-Q. *Nat. Commun.* **2018,** *9,* 4466. doi:10.1038/s41467-018-06938-z
42. Wang, Y.; Hou, P.; Wang, Z.; Kang, P. *ChemPhysChem* **2017,** *18,* 3142–3147. doi:10.1002/cphc.201700716
43. Jiang, X.; Li, H.; Xiao, J.; Gao, D.; Si, R.; Yang, F.; Li, Y.; Wang, G.; Bao, X. *Nano Energy* **2018,** *52,* 345–350. doi:10.1016/j.nanoen.2018.07.047
44. Cho, J. H.; Lee, C.; Hong, S. H.; Jang, H. Y.; Back, S.; Seo, M.-g.; Lee, M.; Min, H.-K.; Choi, Y.; Jang, Y. J.; Ahn, S. H.; Jang, H. W.; Kim, S. Y. *Adv. Mater. (Weinheim, Ger.)* **2022,** 2208224. doi:10.1002/adma.202208224
45. Hinogami, R.; Yotsuhashi, S.; Deguchi, M.; Zenitani, Y.; Hashiba, H.; Yamada, Y. *ECS Electrochem. Lett.* **2012,** *1,* H17–H19. doi:10.1149/2.001204eel
46. Senthil Kumar, R.; Senthil Kumar, S.; Anbu Kulandainathan, M. *Electrochem. Commun.* **2012,** *25,* 70–73. doi:10.1016/j.elecom.2012.09.018
47. Albo, J.; Vallejo, D.; Beobide, G.; Castillo, O.; Castaño, P.; Irabien, A. *ChemSusChem* **2017,** *10,* 1100–1109. doi:10.1002/cssc.201600693
48. Albo, J.; Perfecto-Irigaray, M.; Beobide, G.; Irabien, A. *J. CO2 Util.* **2019,** *33,* 157–165. doi:10.1016/j.jcou.2019.05.025
49. Wu, J.-X.; Hou, S.-Z.; Zhang, X.-D.; Xu, M.; Yang, H.-F.; Cao, P.-S.; Gu, Z.-Y. *Chem. Sci.* **2019,** *10,* 2199–2205. doi:10.1039/c8sc04344b

License and Terms

This is an open access article licensed under the terms of the Beilstein-Institut Open Access License Agreement (https://www.beilstein-journals.org/bjnano/terms), which is identical to the Creative Commons Attribution 4.0 International License (https://creativecommons.org/licenses/by/4.0). The reuse of material under this license requires that the author(s), source and license are credited. Third-party material in this article could be subject to other licenses (typically indicated in the credit line), and in this case, users are required to obtain permission from the license holder to reuse the material.

The definitive version of this article is the electronic one which can be found at:
https://doi.org/10.3762/bjnano.14.74

BEILSTEIN JOURNAL OF NANOTECHNOLOGY

Metal-organic framework-based nanomaterials for CO_2 storage: A review

Ha Huu Do[1], Iqra Rabani[2] and Hai Bang Truong[*3,4]

Review

Open Access

Address:
[1]VKTech Research Center, NTT Hi-Tech Institute, Nguyen Tat Thanh University, Ho Chi Minh City 700000, Vietnam, [2]Department of Nanotechnology and Advanced Materials Engineering, Sejong University, Seoul 05006, Republic of Korea, [3]Optical Materials Research Group, Science and Technology Advanced Institute, Van Lang University, Ho Chi Minh City, Vietnam and [4]Faculty of Applied Technology, School of Technology, Van Lang University, Ho Chi Minh City, Vietnam

Email:
Hai Bang Truong[*] - truonghaibang@vlu.edu.vn

* Corresponding author

Keywords:
CO_2 storage; metal-organic frameworks; nanomaterials; open metal sites; pore size

Beilstein J. Nanotechnol. **2023,** *14,* 964–970.
https://doi.org/10.3762/bjnano.14.79

Received: 09 July 2023
Accepted: 12 September 2023
Published: 20 September 2023

This article is part of the thematic issue "Recent advances in synthesis and applications of organometallic nanomaterials".

Associate Editor: K. Ariga



© 2023 Do et al.; licensee Beilstein-Institut.
License and terms: see end of document.

Abstract

The increasing recognition of the impact of CO_2 emissions as a global concern, directly linked to the rise in global temperature, has raised significant attention. Carbon capture and storage, particularly in association with adsorbents, has occurred as a pivotal approach to address this pressing issue. Large surface area, high porosity, and abundant adsorption sites make metal-organic frameworks (MOFs) promising contenders for CO_2 uptake. This review commences by discussing recent advancements in MOFs with diverse adsorption sites, encompassing open metal sites and Lewis basic centers. Next, diverse strategies aimed at enhancing CO_2 adsorption capabilities are presented, including pore size manipulation, post-synthetic modifications, and composite formation. Finally, the extant challenges and anticipated prospects pertaining to the development of MOF-based nanomaterials for CO_2 storage are described.

Introduction

One of the major issues associated with CO_2 emissions is the heightened risk of climate change faced by our planet. Furthermore, there is an alarming issue of elevated levels of air pollution affecting human population [1]. One potential solution to address this problem involves increased government funding for the maintenance of existing renewable energy sources and the development of new green energies [2,3]. However, the widespread implementation of these solutions is hindered by the challenges posed by nascent technology [4,5]. Another feasible approach to tackle this issue is the advancement of carbon capture and storage (CCS) methods, particularly those involving highly efficient adsorbents [6,7]. The CCS process has the capability to effectively treat substantial volumes of CO_2 emissions originating from conventional fossil fuel sources [8-10]. Therefore, identification and development of durable and efficient adsorbents are critical to the successful implementation of

CCS. Until now, various classes of materials have been investigated for CO_2 adsorption, such as covalent organic frameworks, molecular sieves, activated carbon, and metal-organic frameworks (MOFs) [11-13]. Notably, MOFs constructed from metal ions and organic linkers are expected to be alternative materials to the organic alcohol amines in CCS [14]. These nanosized materials posess unique properties such as ultrahigh surface area, tunable pore size, open metal sites (OMSs), and facile post-synthetic modifications, which allow for diverse strategies towards efficient adsorption and separation of gas molecules [15]. Among the nanosized MOFs, MOF-210 has demonstrated a remarkable ability to adsorb CO_2 (54.5 mmol·g^{-1} at 50 bar, 298 K) owing to its large surface area of 6240 m^2·g^{-1} [16-19]. However, several studies have indicated that the surface area is not the sole determining factor in CO_2 storage at low pressure. For instance, despite having a lower surface area than MOF-177, HKUST-1 exhibited a greater CO_2 adsorption capacity of 4.16 mmol·g^{-1} at 298 K and 1 bar [20]. This discrepancy can be attributed to the presence of unsaturated Cu metal centers within the MOF structure, which facilitate interactions with CO_2 molecules. Additionally, the MOF-74 family, built from metal(II) oxide chains linked by 2,5-dioxido-1,4-benzenedicarboxylate, exhibited a high CO_2 adsorption ability with OMSs ranging from 5.5 to 8.0 mmol·g^{-1} at 296 K and 1 bar [21]. Moreover, acid Lewis sites within these MOFs effectively interact with CO_2, leading to increased adsorption. The pore size plays a vital role in the adsorption and separation of CO_2 from gas mixtures because of the different kinetic diameters of gas molecules.

Herein, we present a comprehensive examination of the current scientific literature pertaining to the utilization of metal-organic framework (MOF)-based nanomaterials in the context of CO_2 storage and conversion. This account focuses on the introduction of MOFs featuring chemical sites, such as open metal sites (OMSs) and Lewis acid sites, for CO_2 adsorption applications. Furthermore, we explore several approaches that have been employed to enhance CO_2 storage capabilities, including pore size control, post-synthetic modification, and the development of composites. Finally, the expected direction and existing challenges in progressing MOF-based nanomaterials for CO_2 storage are discussed.

Review

Nanosized MOFs with adsorption centers for CO_2 capture

MOFs with open metal sites

OMSs are a fundamental characteristic of MOF-based nanomaterials, generating strong interactions with other chemical species. Extensive literature has been devoted to the investigation of MOFs with OMSs. Notably, HKUST-1, featuring copper OMSs, displayed a CO_2 uptake of 4.1 mmol·g^{-1} at 298 K and 1 bar [22]. The effectiveness of OMSs has been exemplified in a study conducted by Caskey and coworkers [21]. Under conditions of 296 K and 1 bar, the authors observed that Mg-MOF-74 exhibited the highest CO_2 absorption capacity, reaching 8.0 mmol·g^{-1}, followed by Co-MOF-74 with 7.0 mmol·g^{-1}. In contrast, Zn-MOF-74 demonstrated the lowest performance, displaying an adsorption capacity of 5.5 mmol·g^{-1}. This discrepancy was attributed to the shorter length of the Mg–O bonds, which facilitated enhanced electrostatic interactions between the Mg sites and CO_2 molecules. Moreover, Mg-MOF-74 exhibited a higher heat of adsorption than other variants. Kim et al. synthesized bimetallic MOFs, specifically Mg/Zn-MOF-74 and Ni/Zn-MOF-74, for CO_2 storage [23]. The presence of different metal ions in bimetallic MOFs generated a synergistic effect, leading to a higher CO_2 adsorption capacity compared to Zn-MOF-74.

Also, several theoretical computations have been implemented to elucidate the adsorption mechanism of CO_2 on MOFs featuring OMSs. Wu et al. revealed that the interactions between the OMSs of Mg-MOF-74 and HKUST-1 and CO_2 molecules are primarily of physical nature [24]. This type of adsorption mechanism offers the advantage of low energy requirements in material regeneration. Another significant contribution in the field of mechanism studies was made by Valenzano and coworkers [25]. The recorded an adsorption angle of 129° for CO_2 adsorption on Mg-MOF-74, which is smaller than the corresponding angles observed for N_2 and CO, implying a stronger interaction between Mg-MOF-74 and CO_2 (Figure 1).

MOFs with Lewis basic centers

N-containing linkers serve as secondary units in the construction of MOFs with Lewis basic centers (LBCs), producing strong interactions with CO_2 gas [26]. An illustrative example of this is demonstrated by Peikert et al., who employed 1,3,5-benzenetricarboxylic acid (BTC) to prepare Cu-based MOF nanoparticles (UHM-30) for gas storage, as depicted in Figure 2 [27]. The benefit of this strategy is the generation of both OMSs and LBCs, resulting in an enhanced CO_2 adsorption capacity for UHM-30 (5.26 mmol·g^{-1}) compared to HKUST-1 (4.69 mmol·g^{-1}). The effectiveness of amino groups in facilitating CO_2 adsorption has been further demonstrated by Si and coworkers [28]. The authors used 2-amino-1,4-benzenedicarboxylate to fabricate an amine-containing MOF, which exhibited a high CO_2 adsorption capacity of 7.2 mmol·g^{-1}. Moreover, MOFs constructed by N-containing aromatic ring linkers have been examined for CO_2 capture. For instance, Shimizu et al. used 3-amino-1,2,4-triazolate as a linker to create Zn-based MOF nanomaterials, yielding a high efficiency in CO_2 storage

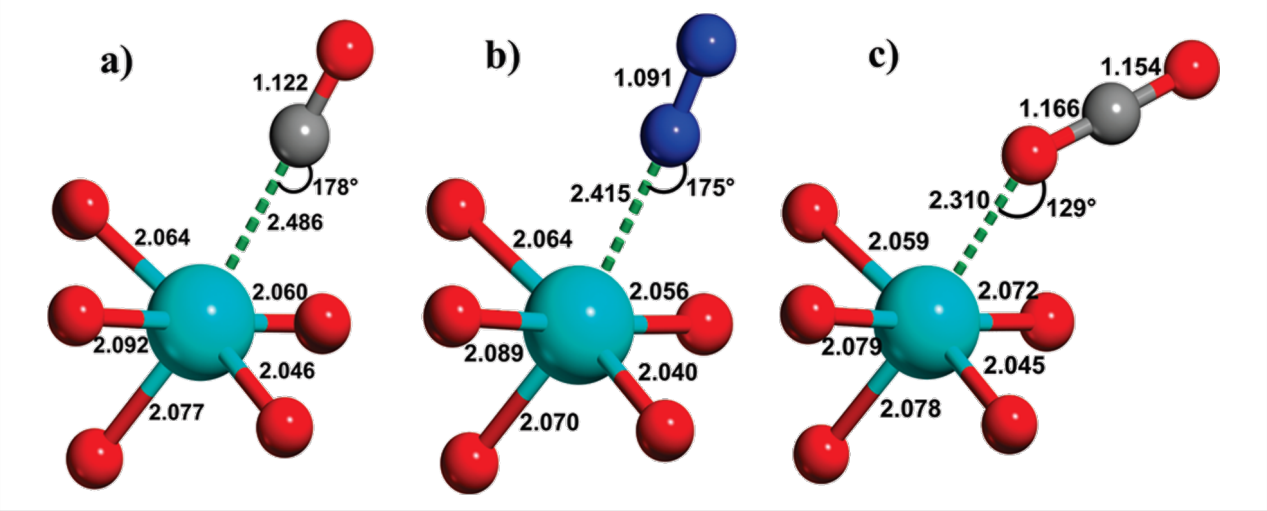


Figure 1: Distances (Å) and angles of interaction between Mg-MOF-74, [Mg/DOBCD] (DOBCD: 2,5-dioxido-1,4-benzenedicarboxylate), with (a) CO, (b) N_2, and (c) CO_2. Figure 1 was reprinted with permission from [25]. Copyright 2010 American Chemical Society. This content is not subject to CC BY 4.0.

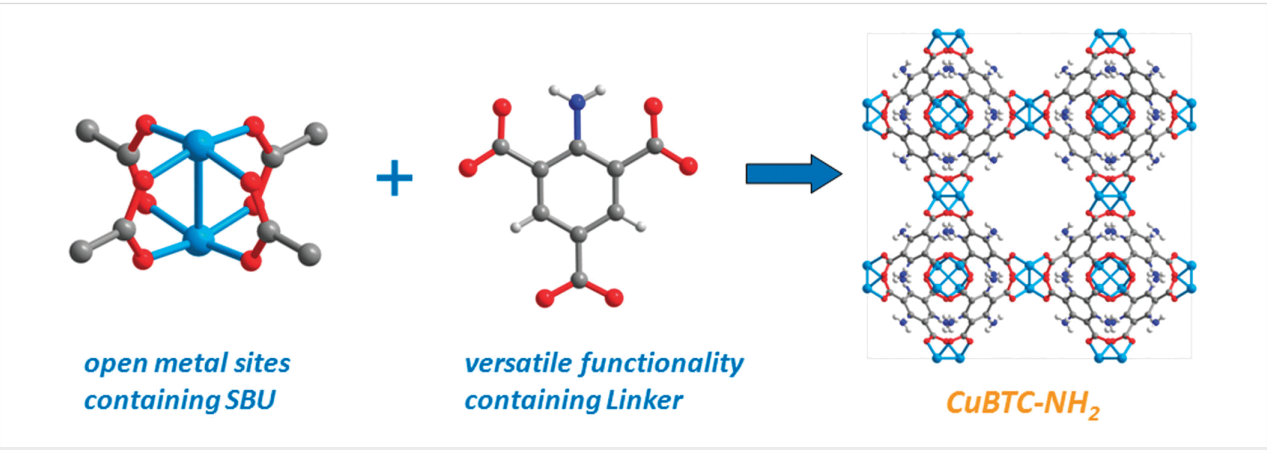


Figure 2: Schematic illustration for the preparation of a CuBTC-NH_2 nanomaterial. Figure 2 was republished with permission of The Royal Society of Chemistry, from [27] ("Amino substituted $Cu_3(btc)_2$: a new metal–organic framework with a versatile functionality" by K. Peikert et al., Chem. Commun., vol. 48, © 2012); permission conveyed through Copyright Clearance Center, Inc. This content is not subject to CC BY 4.0.

[29]. The result was attributed to the favorable interaction between CO_2 and NH_2 groups. Likewise, Panda utilized 5-aminotetrazole to synthesize ZTF-1, a MOF nanomaterial featuring LBCs [30]. This approach offered the advantage of creating a synergistic effect, leading to a noteworthy CO_2 adsorption capacity of 5.6 mmol·g^{-1}.

Strategies for enhanced CO_2 storage in MOF-based nanomaterials

Pore size control

Individual MOFs displayed promising capacities for CO_2 adsorption. Nevertheless, to meet industrial criteria, it is necessary to enhance the CO_2 capture performance of MOFs. Therefore, various methods were applied to modify the physical and chemical properties of MOFs, leading to improved performance. The manipulation of pore size by modifying the size of the ligands is an effective approach for accelerating CO_2 adsorption. For instance, Yao et al. used different ligands to fabricate various Zn-based MOF nanomaterials with distinct pore volumes for CO_2 adsorption applications [31]. Notably, SUMOF-2, characterized by the smallest pore diameter (5.9 Å), displayed the highest CO_2 adsorption capacity at 273 K. The interpenetrated linkers contribute to the expansion of the cavity and the creation of an electric field gradient, enhancing the affinity for CO_2. Prasad et al. employed 4-(2-carboxyvinyl)benzoic acid to create nanosized SNU-70, which possesses a pore size of 9 Å, whereas SNU-71, with a 4-(2-carboxyethyl)benzoic acid linker has a pore size of 2.5 Å [32]. The outcomes revealed that SNU-71 displayed a greater CO_2 uptake than SNU-70, attributing to its smaller pore size.

Pore space partition (PSP) is an intriguing strategy for enhancing gas storage and gas separation, encompassing species such as CH_4, CO_2, and N_2. This approach involves the introduction of additional linkers to divide large pores into smaller compartments [33]. PSP not only offers an increased number of active sites but also enhances the efficiency of the cavity space. To exemplify this, Zhao et al. used a 2,4,6-tri(4-pyridyl)-1,3,5-triazine linker to split the pores of MIL-88, as shown in Figure 3 [34]. Consequently, a substantial CO_2 adsorption capacity of 5.6 mmol·g^{-1} was recorded at 273 K and 1 bar, comparable to that of MOF-74 under the same conditions. The efficacy of the pore space partition strategy has also been indicated in a report of Zheng and coworkers [35]. By combining building units of $[In(CO_2)_4]^-$ and $[In_3O]^+$, a core–shell kind of In-based MOF was created, exhibiting a remarkable CO_2 adsorption capacity of approximately 3.6 mmol·g^{-1} at 273 K and 1 bar.

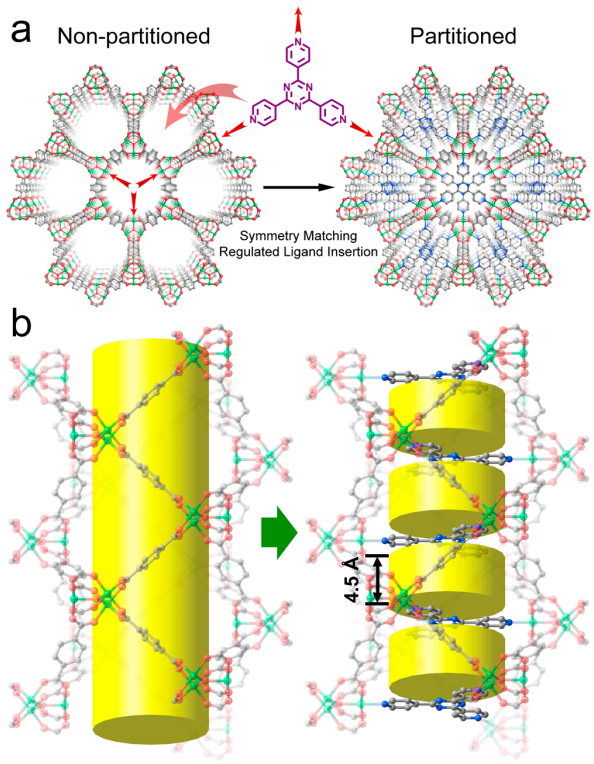


Figure 3: Graphic illustration of pore space partition by inserting TPT in MIL-88 structure. (a) View along the *c* axis and (b) side view of the channels displaying the cylindrical pores. Figure 3 was reprinted with permission from [34]. Copyright 2015 American Chemical Society. This content is not subject to CC BY 4.0.

Post-synthetic functionalization

Amino groups, which have been widely recognized as LBCs in MOFs for the purpose of capturing CO_2, can be grafted onto MOFs through a post-synthetic process. Several studies adopted this strategy to modify the properties of MOFs for gas storage. For instance, Zhang et al. used ethylenediamine to functionalize ZIF-8, resulting in enhanced CO_2 adsorption and selectivity [36]. A benefit of this approach is that the surface area was improved (nearly 40%), while ED-ZIF-8 yielded a two-fold higher amount of adsorbed CO_2 than pure ZIF-8. In a recent study, Gaikwad et al. modified MOF-177 nanoparticles using three different amines to enhance the amount of absorbed CO_2 [37]. The optimally functionalized MOF-177, employing tetraethylenepentamine (TEPA), exhibited a remarkably higher amount of absorbed CO_2 than bare MOF-177 under the same conditions. This enhancement was attributed to the favorable distribution of the relatively small-sized TEPA within the pore space of MOF-177, allowing for more favorable interactions between CO_2 molecules and the amine centers. It is noteworthy that modifications to MOFs have not been limited to the linker molecules but have also involved the metal ions. For example, Lau et al. used an ion exchange strategy to boost the amount of adsorbed CO_2 in UiO-66 (Figure 4) [38]. After replacing approximately 50% of the Zr^{4+} ions in UiO-66 with Ti^{4+}, a significant increase in CO_2 adsorption capacity (81%) was achieved. Several explanations can be considered for this observation. First, the substitution of heavy metal ions (Zr^{4+}) with lighter ones (Ti^{4+}) could result in an increased specific surface area of UiO-66 (BET surface area: 1844 m^2·g^{-1}). Second, the shorter Ti–O bond lengths compared to Zr–O bonds lead to a

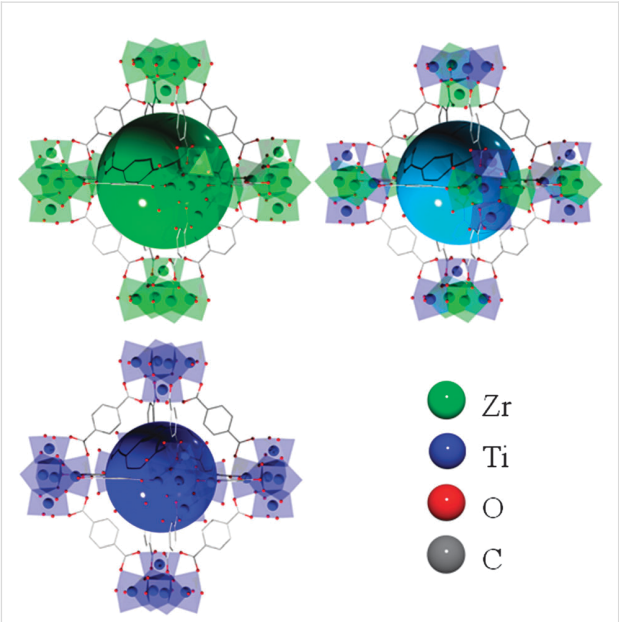


Figure 4: Graphic illustration of the ion exchange by Ti(IV) in UiO-66. Figure 4 was republished with permission of The Royal Society of Chemistry, from [38] ("A route to drastic increase of CO_2 uptake in Zr metal organic framework UiO-66" by C. H. Lau et al., Chem. Commun., vol. 49, © 2013); permission conveyed through Copyright Clearance Center, Inc. This content is not subject to CC BY 4.0.

reduced pore size in UiO-66(Zr/Ti), thereby facilitating improved interactions between the MOF and CO_2 molecules.

MOF composites

Post-synthetic functionalization was recognized as an effective strategy for enhancing the adsorption ability of nanosized MOF structures. However, it demands chemical sites or an appropriate pore size for agent insertion. Many MOFs lack these properties, rendering them unsuitable for post-synthetic strategies. Fortunately, the development of MOF composites is a promising solution to augment the quantity of CO_2 that can be absorbed. As a case in point, Eshraghi et al. fabricated various composites of Cr- and Cu-based nanosized MOFs and multi-walled carbon nanotubes (MWCNTs) [39]. The authors found that the amount of absorbed CO_2 increased significantly by 64% (at 298 K and 18 bar) for MIL-100(Cr) following modification. Similarly, for $Cu_3(BTC)_2$, there was a dramatic growth of 3.46 mmol·g^{-1} in the amount of absorbed CO_2 after the modification, ascribed to the improved pore space by MWCNTs. In another work, MOF/carbon-based composites were reported by Liu and coworkers [40]. The authors used graphene oxides as templates for growing Cu-MOF nanograins for gas storage. A benefit of this strategy was that surface area was enhanced, resulting in a significant 30% increase in the amount of CO_2 adsorbed for the optimal Cu-MOFs/GO composites. Likewise, Kumar et al. employed graphene-based materials to reinforce MOF structures for the improvement of CO_2 uptake [41]. The authors used carboxylic acids to modify graphene nanolayers, and then performed in situ synthesis of different MOF-74 materials on the graphene matrix via a solvothermal method (Figure 5). Although the surface area of composites was only slightly increased compared to the initial materials, the amount of absorbed CO_2 was significantly improved. Notably, the optimal Mg-MOF-74/graphene-based composite yielded a high CO_2 adsorption capacity of 8.4 mmol·g^{-1} at 298 K and 1 bar.

Grand canonical Monte Carlo simulation for CO_2 storage prediction

Grand canonical Monte Carlo (GCMC) simulation is an effective method to predict the gas adsorption ability of porous materials. For instance, Tao et al. used the GCMC method to evaluate CO_2 adsorption on various materials, including MOF-5, ZIF-8, and Mg-MOF-74 [42]. The authors found that the computational results were in agreement with experimental investigations under 10 bar and 298 K. At pressures higher than 10 bar, computational and experimental results were significantly different because of the unsuitable force field under high pressure conditions. Recently, Stanton et al. also used the GCMC technique to predict the CO_2 adsorption of various MOF structures that were modified with amino groups [43]. This study could provide adequate information for further experiments in CO_2 storage areas.

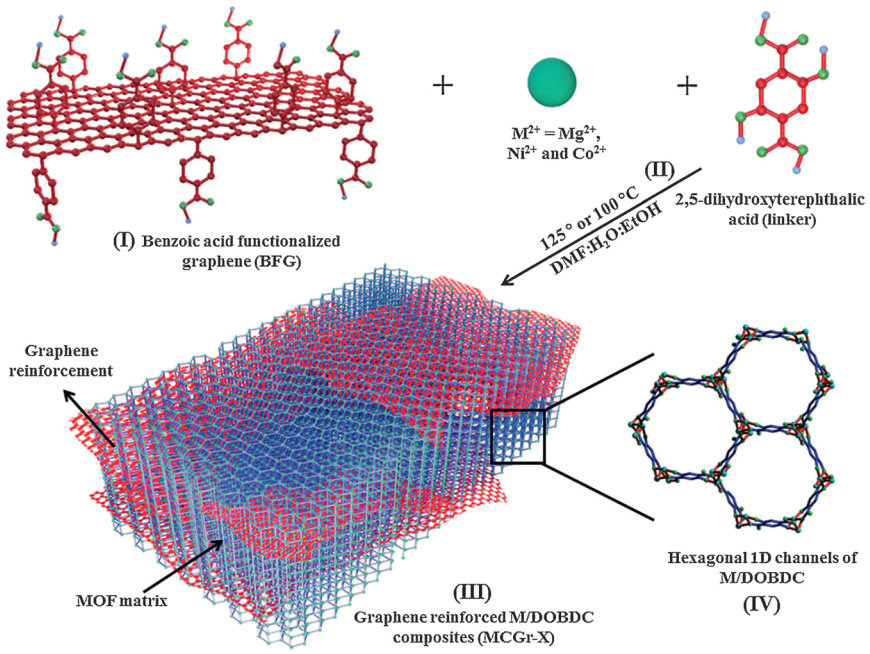


Figure 5: Graphic illustration of the fabrication of MOF/graphene-based composites. Figure 5 was reproduced from [41], R. Kumar et al., "Remarkable Improvement in the Mechanical Properties and CO_2 Uptake of MOFs Brought About by Covalent Linking to Graphene", Angew. Chem., Int. Ed., with permission from John Wiley and Sons. Copyright © 2016 WILEY-VCH Verlag GmbH & Co. KGaA, Weinheim. This content is not subject to CC BY 4.0.

Conclusion

Undoubtedly, MOFs have been widely recognized as promising nanomaterials for CO_2 adsorption, offering potential mitigiation of the impact of CO_2 gas on global warming. However, despite the considerable research efforts dedicated to MOFs in the context of CO_2 adsorption, certain drawbacks still need to be addressed. Primarily, a large number of MOFs have poor CO_2 selectivity in the presence of water and acid gases. These species have higher polarities, which promotes their interaction with OMSs within the MOF structures. In this regard, MOFs tend to exhibit instability under such conditions. Therefore, design and selection of MOFs are imperative for effective CO_2 adsorption, such as in the case of MOF-808. Furthermore, CO_2 storage at low pressure is still limited due to poor CO_2/MOF interaction. Although this challenge can be addressed by modifying the ligand components of MOFs with hydrophilic groups, such modifications result in a substantial increase in the cost of adsorbent production. Finally, it is crucial to explore low-cost and environmentally friendly methods for the synthesis of nanosized MOFs to cater to specific applications.

ORCID® iDs

Ha Huu Do - https://orcid.org/0000-0002-9483-4393
Hai Bang Truong - https://orcid.org/0000-0003-2906-7658

References

1. Chen, P.; Wu, Y.; Rufford, T. E.; Wang, L.; Wang, G.; Wang, Z. *Mater. Today Chem.* **2023,** *27,* 101328. doi:10.1016/j.mtchem.2022.101328
2. Yin, Z.; Liu, X.; Chen, S.; Ma, T.; Li, Y. *Energy Environ. Mater.* **2023,** *6,* e12310. doi:10.1002/eem2.12310
3. Isikgor, F. H.; Zhumagali, S.; Merino, L. V. T.; De Bastiani, M.; McCulloch, I.; De Wolf, S. *Nat. Rev. Mater.* **2023,** *8,* 89–108. doi:10.1038/s41578-022-00503-3
4. Pandey, S.; Karakoti, M.; Bhardwaj, D.; Tatrari, G.; Sharma, R.; Pandey, L.; Lee, M.-J.; Sahoo, N. G. *Nanoscale Adv.* **2023,** *5,* 1492–1526. doi:10.1039/d3na00005b
5. Xu, H.; Li, J.; Chu, X. *Chem. Rec.* **2023,** *23,* e202200244. doi:10.1002/tcr.202200244
6. Li, J.-R.; Ma, Y.; McCarthy, M. C.; Sculley, J.; Yu, J.; Jeong, H.-K.; Balbuena, P. B.; Zhou, H.-C. *Coord. Chem. Rev.* **2011,** *255,* 1791–1823. doi:10.1016/j.ccr.2011.02.012
7. Xiang, S.; He, Y.; Zhang, Z.; Wu, H.; Zhou, W.; Krishna, R.; Chen, B. *Nat. Commun.* **2012,** *3,* 954. doi:10.1038/ncomms1956
8. Grant, T.; Guinan, A.; Shih, C. Y.; Lin, S.; Vikara, D.; Morgan, D.; Remson, D. *Int. J. Greenhouse Gas Control* **2018,** *72,* 175–191. doi:10.1016/j.ijggc.2018.03.012
9. Leung, D. Y. C.; Caramanna, G.; Maroto-Valer, M. M. *Renewable Sustainable Energy Rev.* **2014,** *39,* 426–443. doi:10.1016/j.rser.2014.07.093
10. Vikara, D.; Shih, C. Y.; Lin, S.; Guinan, A.; Grant, T.; Morgan, D.; Remson, D. *J. Sustainable Energy Eng.* **2017,** *5,* 307–340. doi:10.7569/jsee.2017.629523
11. Mahajan, S.; Lahtinen, M. *J. Environ. Chem. Eng.* **2022,** *10,* 108930. doi:10.1016/j.jece.2022.108930
12. Wang, X.; Liu, H.; Li, Y.; Yang, X.; Gao, F.; Wang, X.; Kang, Z.; Fan, W.; Sun, D. *Coord. Chem. Rev.* **2023,** *482,* 215093. doi:10.1016/j.ccr.2023.215093
13. Wang, P.; Teng, Y.; Zhu, J.; Bao, W.; Han, S.; Li, Y.; Zhao, Y.; Xie, H. *Renewable Sustainable Energy Rev.* **2022,** *167,* 112807. doi:10.1016/j.rser.2022.112807
14. Zhou, H.-C.; Long, J. R.; Yaghi, O. M. *Chem. Rev.* **2012,** *112,* 673–674. doi:10.1021/cr300014x
15. Tekalgne, M. A.; Do, H. H.; Hasani, A.; Van Le, Q.; Jang, H. W.; Ahn, S. H.; Kim, S. Y. *Mater. Today Adv.* **2020,** *5,* 100038. doi:10.1016/j.mtadv.2019.100038
16. Furukawa, H.; Ko, N.; Go, Y. B.; Aratani, N.; Choi, S. B.; Choi, E.; Yazaydin, A. Ö.; Snurr, R. Q.; O'Keeffe, M.; Kim, J.; Yaghi, O. M. *Science* **2010,** *329,* 424–428. doi:10.1126/science.1192160
17. Farha, O. K.; Eryazici, I.; Jeong, N. C.; Hauser, B. G.; Wilmer, C. E.; Sarjeant, A. A.; Snurr, R. Q.; Nguyen, S. T.; Yazaydın, A. Ö.; Hupp, J. T. *J. Am. Chem. Soc.* **2012,** *134,* 15016–15021. doi:10.1021/ja3055639
18. Li, R.; Zhang, W.; Zhou, K. *Adv. Mater. (Weinheim, Ger.)* **2018,** *30,* 1705512. doi:10.1002/adma.201705512
19. Li, D.; Kassymova, M.; Cai, X.; Zang, S.-Q.; Jiang, H.-L. *Coord. Chem. Rev.* **2020,** *412,* 213262. doi:10.1016/j.ccr.2020.213262
20. Chen, C.; Li, B.; Zhou, L.; Xia, Z.; Feng, N.; Ding, J.; Wang, L.; Wan, H.; Guan, G. *ACS Appl. Mater. Interfaces* **2017,** *9,* 23060–23071. doi:10.1021/acsami.7b08117
21. Caskey, S. R.; Wong-Foy, A. G.; Matzger, A. J. *J. Am. Chem. Soc.* **2008,** *130,* 10870–10871. doi:10.1021/ja8036096
22. Millward, A. R.; Yaghi, O. M. *J. Am. Chem. Soc.* **2005,** *127,* 17998–17999. doi:10.1021/ja0570032
23. Kim, D.; Coskun, A. *Angew. Chem.* **2017,** *129,* 5153–5158. doi:10.1002/ange.201702501
24. Wu, H.; Simmons, J. M.; Srinivas, G.; Zhou, W.; Yildirim, T. *J. Phys. Chem. Lett.* **2010,** *1,* 1946–1951. doi:10.1021/jz100558r
25. Valenzano, L.; Civalleri, B.; Chavan, S.; Palomino, G. T.; Areán, C. O.; Bordiga, S. *J. Phys. Chem. C* **2010,** *114,* 11185–11191. doi:10.1021/jp102574f
26. Kim, Y.; Huh, S. *CrystEngComm* **2016,** *18,* 3524–3550. doi:10.1039/c6ce00612d
27. Peikert, K.; Hoffmann, F.; Fröba, M. *Chem. Commun.* **2012,** *48,* 11196–11198. doi:10.1039/c2cc36220a
28. Si, X.; Jiao, C.; Li, F.; Zhang, J.; Wang, S.; Liu, S.; Li, Z.; Sun, L.; Xu, F.; Gabelica, Z.; Schick, C. *Energy Environ. Sci.* **2011,** *4,* 4522–4527. doi:10.1039/c1ee01380g
29. Vaidhyanathan, R.; Iremonger, S. S.; Dawson, K. W.; Shimizu, G. K. H. *Chem. Commun.* **2009,** 5230–5232. doi:10.1039/b911481e
30. Panda, T.; Pachfule, P.; Chen, Y.; Jiang, J.; Banerjee, R. *Chem. Commun.* **2011,** *47,* 2011–2013. doi:10.1039/c0cc04169f
31. Yao, Q.; Su, J.; Cheung, O.; Liu, Q.; Hedin, N.; Zou, X. *J. Mater. Chem.* **2012,** *22,* 10345–10351. doi:10.1039/c2jm15933c
32. Prasad, T. K.; Suh, M. P. *Chem. – Eur. J.* **2012,** *18,* 8673–8680. doi:10.1002/chem.201200456
33. Hong, A. N.; Yang, H.; Bu, X.; Feng, P. *EnergyChem* **2022,** *4,* 100080. doi:10.1016/j.enchem.2022.100080
34. Zhao, X.; Bu, X.; Zhai, Q.-G.; Tran, H.; Feng, P. *J. Am. Chem. Soc.* **2015,** *137,* 1396–1399. doi:10.1021/ja512137t
35. Zheng, S.-T.; Bu, J. T.; Li, Y.; Wu, T.; Zuo, F.; Feng, P.; Bu, X. *J. Am. Chem. Soc.* **2010,** *132,* 17062–17064. doi:10.1021/ja106903p
36. Zhang, Z.; Xian, S.; Xia, Q.; Wang, H.; Li, Z.; Li, J. *AIChE J.* **2013,** *59,* 2195–2206. doi:10.1002/aic.13970

37. Gaikwad, S.; Kim, Y.; Gaikwad, R.; Han, S. *J. Environ. Chem. Eng.* **2021,** *9,* 105523. doi:10.1016/j.jece.2021.105523
38. Lau, C. H.; Babarao, R.; Hill, M. R. *Chem. Commun.* **2013,** *49,* 3634–3636. doi:10.1039/c3cc40470f
39. Eshraghi, F.; Anbia, M.; Salehi, S. *J. Environ. Chem. Eng.* **2017,** *5,* 4516–4523. doi:10.1016/j.jece.2017.08.040
40. Liu, S.; Sun, L.; Xu, F.; Zhang, J.; Jiao, C.; Li, F.; Li, Z.; Wang, S.; Wang, Z.; Jiang, X.; Zhou, H.; Yang, L.; Schick, C. *Energy Environ. Sci.* **2013,** *6,* 818–823. doi:10.1039/c3ee23421e
41. Kumar, R.; Raut, D.; Ramamurty, U.; Rao, C. N. R. *Angew. Chem., Int. Ed.* **2016,** *55,* 7857–7861. doi:10.1002/anie.201603320
42. Tao, Y. R.; Zhang, G. H.; Xu, H. J. *Sustainable Mater. Technol.* **2022,** *32,* e00383. doi:10.1016/j.susmat.2021.e00383
43. Stanton, R.; Trivedi, D. J. *J. Phys. Chem. Lett.* **2023,** *14,* 5069–5076. doi:10.1021/acs.jpclett.3c00998

License and Terms

This is an open access article licensed under the terms of the Beilstein-Institut Open Access License Agreement (https://www.beilstein-journals.org/bjnano/terms), which is identical to the Creative Commons Attribution 4.0 International License (https://creativecommons.org/licenses/by/4.0). The reuse of material under this license requires that the author(s), source and license are credited. Third-party material in this article could be subject to other licenses (typically indicated in the credit line), and in this case, users are required to obtain permission from the license holder to reuse the material.

The definitive version of this article is the electronic one which can be found at:
https://doi.org/10.3762/bjnano.14.79

BEILSTEIN JOURNAL OF NANOTECHNOLOGY

Modification of graphene oxide and its effect on properties of natural rubber/graphene oxide nanocomposites

Nghiem Thi Thuong*[1], Le Dinh Quang[1], Vu Quoc Cuong[1], Cao Hong Ha[1], Nguyen Ba Lam[1,2] and Seiichi Kawahara[2]

Full Research Paper

Open Access

Address:
[1]School of Chemical Engineering, Hanoi University of Science and Technology, No 1 Dai co Viet, Hanoi, Vietnam and [2]Faculty of Engineering, Nagaoka University of Technology, 1603-1, Kamitomioka-machi, Nagaoka, Niigata 940-2188, Japan

Email:
Nghiem Thi Thuong* - thuong.nghiemthi@hust.edu.vn

* Corresponding author

Keywords:
graft copolymerization; graphene oxide; natural rubber; vinyltriethoxysilane

Beilstein J. Nanotechnol. **2024,** *15,* 168–179.
https://doi.org/10.3762/bjnano.15.16

Received: 22 November 2023
Accepted: 17 January 2024
Published: 05 February 2024

This article is part of the thematic issue "Recent advances in synthesis and applications of organometallic nanomaterials".

Guest Editor: B. T. Huy

© 2024 Thuong et al.; licensee Beilstein-Institut.
License and terms: see end of document.

Abstract

Modification of graphene oxide (GO) by vinyltriethoxysilane (VTES) was investigated to study the effect of silanized GO on radical graft copolymerization of GO onto deproteinized natural rubber (DPNR). The modified GO, GO-VTES (a and b), was characterized by X-ray diffraction (XRD), Fourier-transform infrared spectroscopy, contact angle, thermal gravimetric analysis, and scanning electron microscopy. The XRD results showed the appearance of an amorphous region of silica particles at a diffraction angle of 22°. The formation of silica was investigated by ^{29}Si NMR, and it was found that the hydrolysis and condensation of VTES proceed more completely in basic conditions than in acidic conditions. The silica content of GO-VTES(b) was 43%, which is higher than that of GO-VTES(a) (8%). Morphology of silica was observed by SEM. The DPNR/GO-VTES nanocomposites prepared with the same amount of GO, GO-VTES(a), and GO-VTES(b) were characterized with tensile tests and dynamic mechanical tests. The stress at break of DPNR/GO-VTES(a) and DPNR/GO-VTES(b) was 5.2 MPa and 4.3 MPa, respectively, which were lower than that of DPNR/GO. However, it exhibited higher stress at small strains and higher storage modulus than DPNR/GO.

Introduction

The graft copolymerization of natural rubber (NR) has gained significant interest for an extended period. This interest derives from the desire to enhance the green strength of NR to achieve the comparable mechanical properties of vulcanized natural rubber (VNR) [1-3]. VNR is commonly utilized for NR commercial products. However, due to its crosslinked structure, VNR products cannot be recycled or degraded after diposal [4,5]. Therefore, new approaches have been introduced to process NR into eco-friendly commercial products [6,7]. Since the discovery of the island nanomatrix structure of NR [8] and

the development of effective methods to prepare deproteinized natural rubber (DPNR) [9,10], graft copolymerization of NR has had significant impacts on improving the mechanical properties of NR. Numerous studies have utilized suitable monomers to graft onto NR via radical routes. For instance, graft copolymerization of styrene [11,12], methyl methacrylate [13,14], and hydroxyethyl methacrylate [15,16] onto NR enhances the green strength for NR. On the other hand, the grafting of nanofiller onto NR to prepare NR nanocomposites has been recently discovered.

Nanofillers, such as nanosilica and derivates of nanocarbon, are the most well-known fillers that have been used in rubber technology. Nanosilica has been known to reduce the rolling resistance and enhance the wet grip of rubber materials. Recently, the usage of silane coupling agents as monomers to generate in situ nanosilica into NR has been found to enhance the mechanical properties of NR. Kawahara et al. [17] used vinyltriethoxysilane (VTES) as a silane monomer for grafting on NR to form an in situ nanosilica nanomatrix. The formation of nanosilica particles improved the thermal and mechanical properties of the graft copolymer. Furthermore, a well-controlled nanosilica nanomatrix structure in NR has been achieved in our previous work [18], where VTES was grafted onto NR grafted PS, gaining the best tensile strength at 19.23 MPa. This result highlights the advantage of a nanosilica nanomatrix on the improvement of mechanical properties of NR. On the other hand, graft copolymerization of nanocarbon materials, such as graphene and graphene oxide (GO) [19,20], has also attracted significant interest. This material with exceptionally high specific surface area, high mechanical properties, and high thermal conductivity is expected to prepare high-performance rubber composites [21-23]. In our recent work [24], we successfully designed a DPNR/GO composite by grafting GO onto DPNR. The results show that the tensile strength of DPNR/GO increased compared to that of DPNR, which proved the successful grafting of GO onto NR by the radical route. However, GO possesses a highly hydrophilic character, which is the opposite of the highly hydrophobic nature of NR. Thus, GO has quite poor compatibility with NR. It is necessary to modify GO to have a better interaction with the NR matrix.

Various researchers have attempted to functionalize GO with silane coupling agents to prepare hybrid GO/silica fillers [25,26]. The concept is based on the hydrolysis and condensation reaction of VTES to form nanosilica on GO membranes, using both acidic and basic conditions to catalyze these reactions. The hybrid GO/silica fillers could enhance the interaction, dispersion, and properties of various composites. For example, GO/3-aminopropyltriethoxysilane and GO/3-glycidyloxypropyltrimethoxysilane used in epoxy nanocomposites [27] or reduced GO/vinyltrimethoxy silane used in low-density polyethylene nanocomposites [28]. Additionally, Charoenchai et al. [29] prepared a hybrid silica/graphene oxide, GO/VTES, catalyzed under basic conditions. The hybrid filler was introduced into the NR matrix through conventional mixing on a two-roll mill. Mainly, GO/VTES was expected to improve its interaction with NR, thus enhancing the mechanical properties of NR at low deformation, along with other compressive and abrasive properties.

Until now, the application of hybrid silica/GO fillers has been limited to vulcanized NR. Moreover, nanoscale carbon-derived materials such as graphene and GO pose limitations in traditional NR vulcanization due to their associated high production costs. However, when ultilized in small quantities, nanoscale carbon-derived materials demonstrate potential in graft copolymerization of NR. Hence, the functionalization of GO with a silane coupling agent significantly contributes to exploring the most optimal methods and conditions for preparing NR/GO nanocomposites through graft copolymerization. Despite this, research involving the hybrid filler GO/silica for grafting onto NR remains unexplored. Therefore, applying this potential hybrid filler to enhance the green strength of NR through grafting techniques, forming a fine nanocomposite between NR and GO/silica hybrid filler, could be necessary. This approach may play a pivotal role in furthering the development of eco-friendly NR products.

In the present research, we modified GO with VTES and investigated the possibility of grafting GO-VTES onto NR through a radical route using tetraethylenepentamine (TEPA) and TBHPO as initiators. Exceptionally, GO-VTES was prepared by modifying GO with VTES under acidic and basic conditions to determine the ideal condition to modify GO for grafting onto NR. The GO-VTES products were characterized using X-ray diffraction (XRD), contact angle, ^{29}Si NMR, Fourier-transform infrared spectroscopy (FTIR), and morphology analysis. The GO-VTES was expected to improve the mechanical properties of NR composite. The usage of GO-VTES may be suitable for the preparation of NR composites for tire applications as the composite may reduce water permeability and enhance the abrasion resistance of commercial products [30].

Experimental

Materials

The natural rubber used in this work is high-ammonia natural rubber latex (HANR, dry rubber content (DRC) 60%) supplied by Dau-Tieng rubber company. Sodium dodecyl sulfate (SDS, 97%) was bought from Nacalai Tesque, Japan. Graphite flake powder (>99% purity) was obtained from Yen-Bai province, Vietnam. The compounds $KMnO_4$, $NaNO_3$ (analytical grade),

and TEPA were purchased from Sigma-Aldrich. Vinyltriethoxysilanes, tert-butyl hydroperoxide (TBHPO), and urea were purchased from Tokyo Chemical Industry, Japan.

Removal of proteins from natural rubber

According to the method reported in [24], deproteinization of HANR was carried out using urea as a denaturing agent and SDS as a surfactant. About 80 g of HANR (60% DRC) was incubated with 80 g of water containing 1.6 g of SDS and 0.16 g of urea for 1 h before the 1st centrifugation at 10,000 rpm at 15 °C for 30 min. The cream recovered after centrifugation was redispersed in 80 g of water containing 0.8 g SDS and subjected to a 2nd centrifugation under the same condition. The cream fraction was again redispersed in water containing 0.16 g of SDS before the 3rd centrifugation. The final cream was diluted in a certain amount of SDS solution to obtain deproteinized natural rubber (DPNR) with DRC (20%) and SDS (0.2%).

Preparation of graphene oxide and silanization with VTES

The graphene oxide used in this work was synthesized from graphite flakes using a modified version of Hummers' method [31], similar to those reported in [24]. About 1 g of graphite powder was put into 23 mL of concentrated H_2SO_4, and 0.5 g of $NaNO_3$ and 3 g of $KMnO_4$ were added to the mixture. The temperature was maintained between 0–5 °C, and the system was kept for 2 h before heating up to 35 °C and kept for 1 h. After that, water was added to increase the temperature to 90 °C for 30 min, and 10 mL of H_2O_2 was dropped into the flask. After 15 min, 100 mL of water was used to dilute the reaction. The powder was filtered and washed with distilled water until it had a neutral pH. The GO powder was then dispersed in water and centrifuged at 10,000 rpm for 30 min to obtain the suspended solution. The purified GO powder was collected after drying the solution in a heating oven.

Vinyltriethoxysilane was used to modify GO [25,32] and it was bonded on the GO surface by the sol–gel method, as shown in Figure 1. Firstly, GO (0.4 g) was thoroughly dispersed in distilled water. After that, VTES (1.8 g) was added to the mixture, followed by the addition of concentrated HCl (1 mL) or NH_4OH (1.5 mL) as catalysts. When using HCl, the mixture was stirred for 2 h under a temperature of 75 °C. Conversely, when NH_4OH was used, the mixture was stirred at 40 °C for 4 h. The solid mixture, obtained after centrifugation, was rinsed and filtered until neutral. The collected solid was entirely dried in an oven at 50 °C to obtain the final GO-VTES(a) and GO-VTES(b).

Preparation of DPNR/GO-VTES composite

The DPNR/GO-VTES composite was prepared via graft copolymerization technique using TEPA/TBHPO redox initiators, similar to our previous work [24]. The experimental steps are illustrated in Figure 2. First, GO-VTES powder (0.2 g) was dispersed into 50 g of a 0.2% SDS solution followed by homogenization for 1 h to obtain a homogeneous GO-VTES disper-

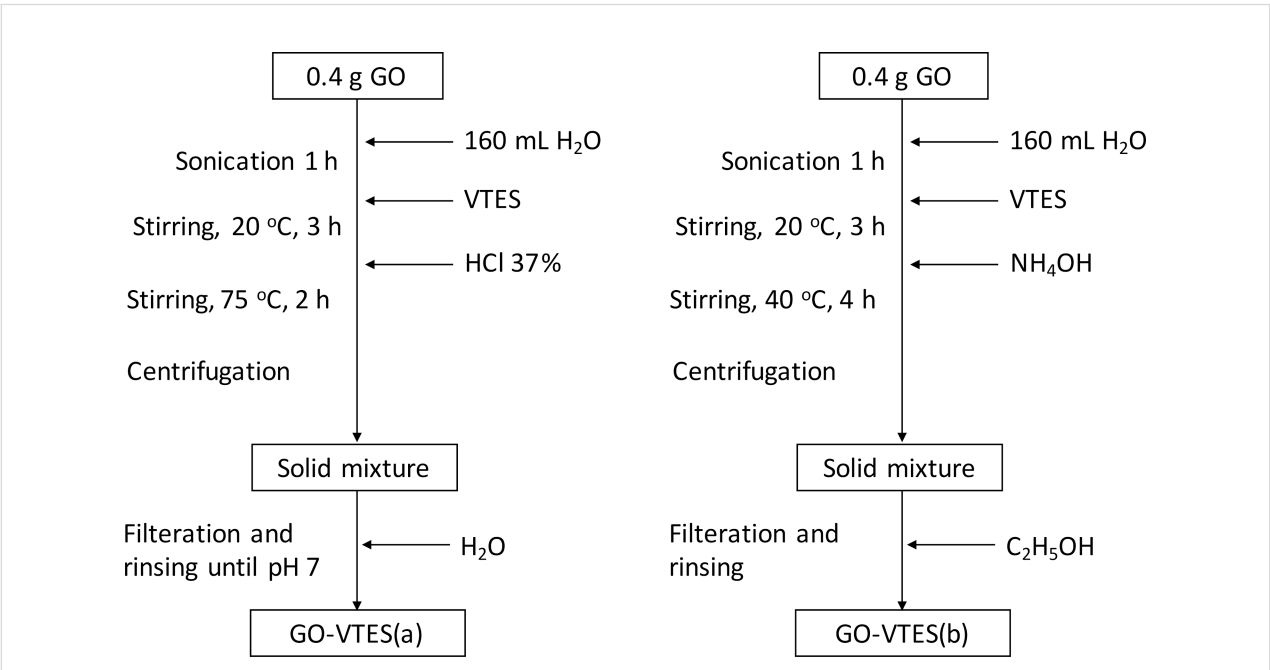


Figure 1: Silanization of graphene oxide in acidic condition (left) and in basic condition (right).

sion. After that, approx. 200 g of DPNR (DRC 20%, SDS 0.2%) was mixed with the GO-VTES dispersion, and the system was bubbled with N_2 gas for 1 h to remove residual dissolved oxygen. Then, 0.51 g of TEPA and 0.34 g of TBHPO initiators were added to the reaction to initiate the radical reaction between GO-VTES and the rubber particles. The reaction was carried out for 3 h with constant stirring under N_2 atmosphere at 30 °C. The reacted latex was subjected to rotary evaporation for 40 min to remove impurities. The resulting latex was cast on a petri dish and dried in an oven at 50 °C, then in a vacuum to obtain a DPNR/GO-VTES composite film. A similar procedure was carried out with 0.2 g of GO, 200 g of DPNR (DRC 20%, SDS 0.2%), and with the same amount of TEPA/TBHPO as in the preparation of DPNR/GO-VTES.

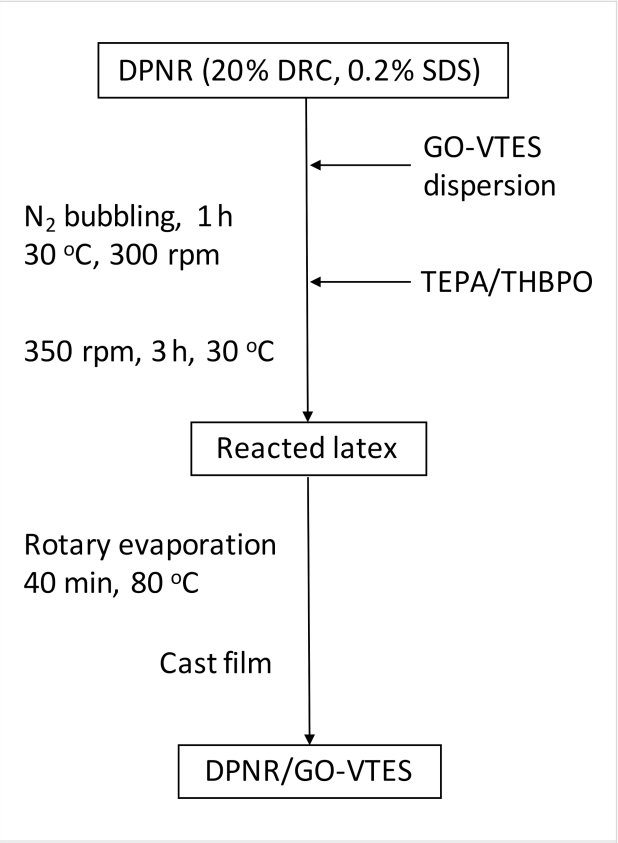


Figure 2: Preparation of DPNR/GO-VTES composite.

Characterizations

X-ray diffraction patterns of graphite and GO were acquired by using a Panalytical X'Pert Pro X-ray diffractometer. The measurements were performed at room temperature with the diffraction angle (2-theta) ranging from 5 to 80°.

Solid-state ^{29}Si NMR spectra were recorded with a JNM ECA-400 (JEOL, Japan) spectrometer operating at a magnetic field of 400 MHz. A suitable amount of rubber sample was inserted in an NMR tube and injected into an NMR system equipped with a CP-MAS probe. The number of scans was 1000.

Contact angles of the samples were measured by taking a photo of a drop of distilled water on the sample surface by a CCD camera. The determination of the contact angle was monitored by the SCA20 software using the Data-physic OCA20 system.

Thermal gravimetric analysis (TGA) of the samples was performed on a TA Q500 instrument. The temperature was increased at a heating rate of 10 °C /min from room temperature to 900 °C in air atmosphere.

The morphology of the DPNR/GO-VTES was observed with field-emission scanning electron microscopy (FE-SEM) performed with HITACHI S-4800. The measurement was performed at room temperature.

The tensile properties of the composite samples were measured with a Tokyo Instron 5300 (Japan). The graft copolymer films (thickness of 1 mm) were cut in a dumbbell shape described in JIS K6251. Tensile measurements were done at room temperature with a speed test of 200 mm/min.

Dynamic mechanical analysis (DMA) of the graft copolymer was measured with a MCR 301 (Anton Paar Physica, Japan) analyzer using a 12 mm parallel plate (PP12) measuring system. First, the samples were heated to 80 °C in gaseous N_2 and kept for 40 min for the attachment of the sample to the measuring system. The frequency-dependent measurement was performed at an initial strain of 1% and at an angular frequency of 0.1–100 rad/s at 30 °C. The number of data points collected was 31.

Results and Discussion

Characterization of GO-VTES

XRD

Figure 3 shows XRD patterns for GO and silanized GO using acid and base catalysts. The sharp peak at 2θ = 11° is a diffraction pattern for GO [33]. This peak is evidence of the exfoliation of the GO sheet synthesized by the modified Hummers' method. After modification with VTES, two diffracting patterns appeared in the XRD spectra for GO-VTES(a) and GO-VTES(b). The peak at 2θ = 11° belongs to the GO sheet, and a new peak that appeared at 2θ = 22° was assigned to the amorphous silica. The broad peak of GO in GO-VTES may be explained to be due to the intercalation of the GO sheet during modification. Silica was formed after the hydrolysis and condensation of VTES. It is noted that the intensity ratio of the silica region and the GO peak for GO-VTEs(a) was lower than that of GO-VTES(b). This evidence may suggest that silica is

more favorably formed in basic conditions than in acidic conditions. These results are a clear evidence for the formation of a silica layer on the surface of GO as a result of the reaction between GO and VTES.

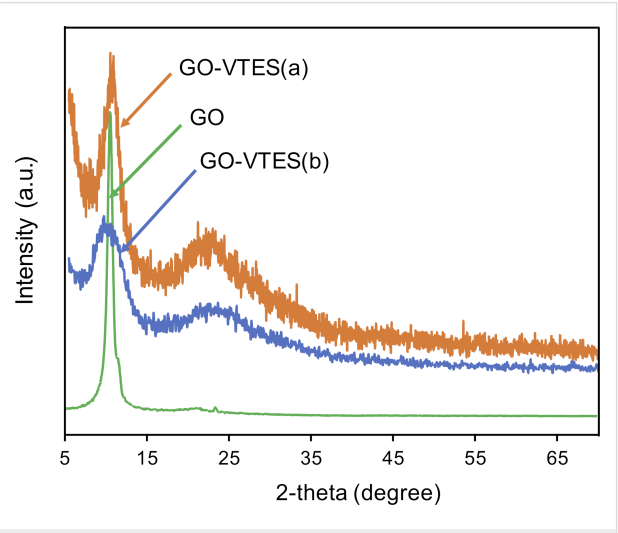


Figure 3: XRD patterns of GO, GO-VTES(a) and GO-VTES(b).

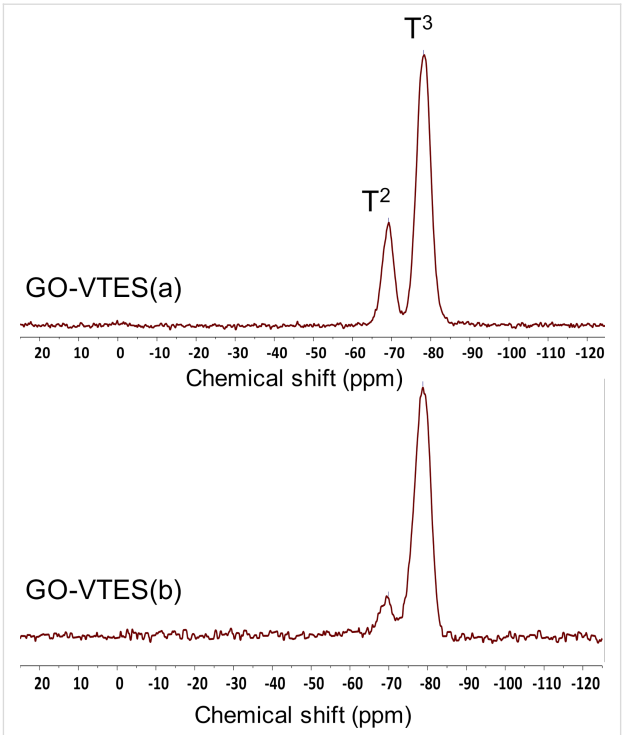


Figure 4: ^{29}Si NMR CP/MAS for GO-VTES(a) and GO-VTES(b).

^{29}Si NMR spectroscopy

To understand the degree of hydrolysis and condensation of VTES to form silica during GO modification, ^{29}Si NMR spectra of GO-VTES(a) and GO-VTES(b) were recorded with a solid CP/MAS probe. In ^{29}Si NMR spectra, the complete hydrolysis and condensation of VTES will result in the signal T_3, corresponding to the R-Si(OSi)$_3$ structure, and the incomplete hydrolysis and condensation of VTES will be accompanied by the T_2 signal, which corresponds to R–Si(OSi)$_2$OC$_2$H$_5$ or R–Si(OSi)$_2$OH. As shown in Figure 4, two signals appeared at chemical shifts −69 and −79 ppm. The signal at −69 ppm was assigned to the Si atom in the T_2 structure (i.e., CH$_2$=CH–Si(O–Si)$_2$(OC$_2$H$_5$) or CH$_2$=CH–Si(O–Si)$_2$(OH)). On the other hand, the signal at −79 ppm was assigned to the Si atom in the T_3 structure (i.e., CH$_2$=CH–Si(O–Si)$_3$) [17]. It was noted that the intensity ratios of T_3 to T_2 signals for GO-VTES(b) were higher than that of GO-VTES(a). The higher intensity ratios of the T_3 to T_2 signals demonstrated that hydrolysis and condensation were more completed in GO-VTES(b) than in GO-VTES(a).

Attenuated total reflection–Fourier-transform infrared spectroscopy results

The attenuated total reflection–Fourier-transform infrared spectroscopy (ATR–FTIR) results of GO, GO-VTES(a), and GO-VTES(b) are shown in Figure 5. The absorption values ranging from 3100 to 3700 cm^{-1} corresponded to –OH and –COOH groups on the GO surfaces and –OH group on silica particle surfaces [33]. However, the intensities of these signals decreased in the FTIR spectra of GO-VTES(a) and GO-VTES(b). This may be attributed to a decrease in the number of –OH groups of GO due to the reaction with VTES and the presence of the vinyl group on the surface of silica particles. The peak at the wavenumber of 1720 cm^{-1} in the GO spectrum corresponds to the C=O bond in the carboxylic group –COOH. However, after modification with VTES, the intensity of the 1720 cm^{-1} signal significantly decreased. It may be due to the removal of the –COOH group during GO modification. In the spectrum of GO, the absorption peak at 1624 cm^{-1} was ascribed to vibration of the C=O bonds on the ketone group [33]. Nevertheless, for GO-VTES(a) and GO-VTES(b), this absorption peak overlapped with the absorption peaks at 1600 cm^{-1}, which appeared due to the appearance of C=C bonds in VTES [17]. In the fingerprint region, the absorption peaks at approx. 950 to 1300 cm^{-1} for GO were due to the vibration of C–O and C–OH bonds in GO. These absorption peaks decreased for GO-VTES(a) and increased for GO-VTES(b) after modification. The increased in these peaks for GO-VTES(b) was due to the asymmetrical vibration of Si–O–Si linkages in silica particles during modification. This suggested that the silica particles were more efficiently formed in basic conditions than in acidic conditions. Note that the absorption at 780 cm^{-1} was due to the symmetrical vibration of Si–O and Si–C linkages. This absorption was due to the formation of silica particles on the GO layer during modification.

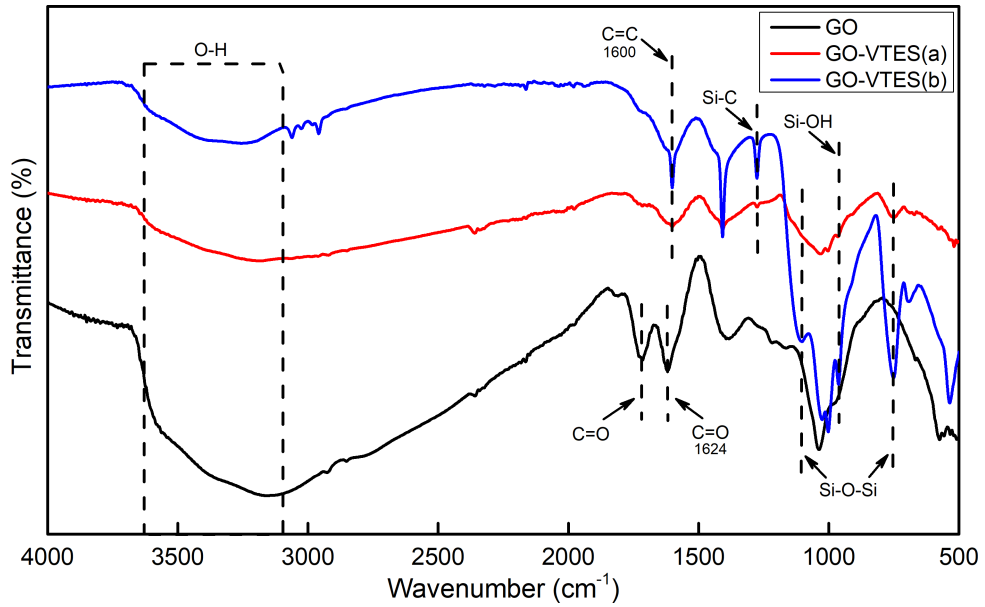


Figure 5: ATR–FTIR spectra of GO, GO-VTES(a) and GO-VTES(b).

Contact angle

The effect of GO modification with VTES on GO surface characteristics was investigated by measuring the contact angle. Figure 6 shows images of distilled water that was dropped onto GO and GO-VTES surfaces. The value of the contact angle elucidates the hydrophilicity or hydrophobicity of the surface. The higher the contact angle, the higher the hydrophobicity. The contact angle of GO is about 67°, and those of GO-VTES(a) and GO-VTES(b) are 91 and 80°, respectively. The excellent hydrophilicity of GO may be due to various hydrophilic functional groups (i.e., hydroxyl group, carboxyl group, and epoxy group) that exist on the GO surface. However, after modification with VTES, the contact angle increased. This suggests that the formation of silica particles enhanced the hydrophobicity of GO. Note that GO-VTES(a) has a higher contact angle than that of GO-VTES(b), which indicates that GO-VTES(a) exhibited higher hydrophobicity than GO-VTES(b). It may be due to a vinyl group (–CH=CH_2) or ethoxy group (–OC_2H_5) attached to

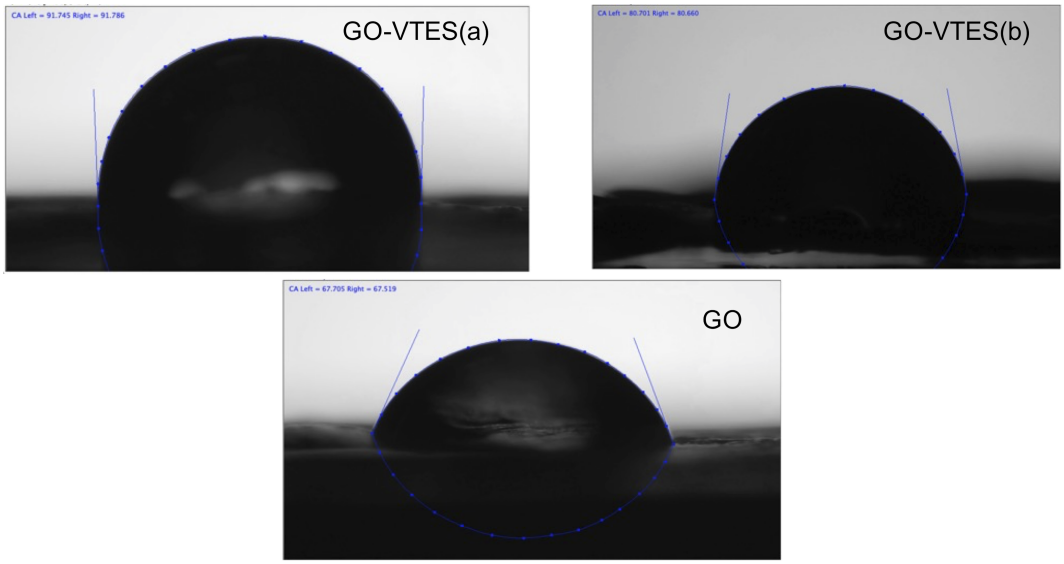


Figure 6: Contact angles of GO, GO-VTES(a) and GO-VTES(b).

the silica surface. However, in the case of GO-VTES(a), the hydrolysis was not completed. Thus, there were fewer –OH groups on the silica and GO surfaces. This result is in agreement with the ^{29}Si NMR and ATR FTIR analysis.

Thermal gravimetric analysis results

The degradation behavior of GO-VTES was investigated with TGA. Figure 7 shows TGA and dTGA curves for GO-VTES(a), and GO-VTES(b) and the weight loss percentage at three temperature ranges and residual ash are given in Table 1. The weight loss percentage from 30 to 100 °C for GO-VTES(a) and GO-VTES(b) was approx. 6% and 4%, respectively. This weight loss was attributed to absorbed water in GO-VTES. At higher temperatures ranging from 150 to 250 °C, the weight loss was due to the decomposition of oxygenous organic functional groups present in GO-VTES. The weight loss percentage in this temperature range was approx. 34% for GO-VTES(a) and 12% for GO-VTES(b). The higher weight loss percentage for GO-VTES(a) may be due to the higher amount of combustible functional groups derived from incomplete hydrolysis of VTES. These results confirmed that silica formation is more favorable in a basic medium than in an acidic medium. From 500 to 800 °C, the combustion of carbon-containing compounds occurs. The weight loss of GO-VTES(a) and GO-VTES(b) were quite similar, approx. 52% and 42%, respectively. After 800 °C, the residual ash was silica. The ash content was 8% for GO-VTES(a) and 42% for GO-VTES(b). From the ash content, it could be confirmed that the VTES was efficiently attached to GO, and the attachment was more efficient in basic conditions rather than acidic conditions.

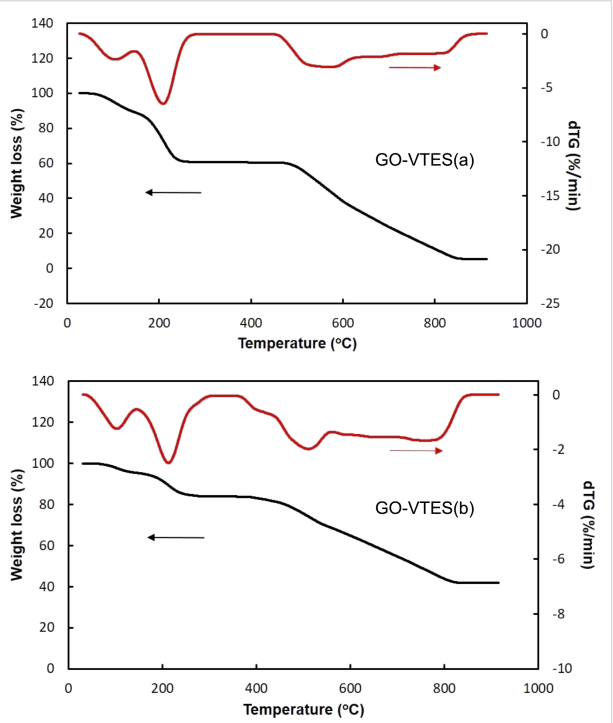


Figure 7: TGA curve of GO-VTES(a) and GO-VTES(b).

Scanning electron microscopy images

Figure 8 shows SEM images for GO-VTES(a) and GO-VTES(b). As can be seen, silica was produced with a size of approx. 50 nm for GO-VTES(a) and GO-VTES(b). It proved that VTES was hydrolyzed and condensed to generate the nanosilica particles. Moreover, more silica particles were found in SEM images of GO-VTES(b) than in GO-VTES(a). At the same time, GO sheets were more visible in the case of GO-VTES(a) but entirely invisible in GO-VTES(b). Nanosilica was generated and covered most of the GO surface in GO-VTES(b), and there was some small agglomerates of silica.

Illustration of GO modification with VTES

Figure 9 illustrates GO modification with VTES. First, VTES is hydrolyzed to form –OH groups. These –OH groups will be attached to the GO surface at the hydroxyl group by hydrogen or chemical bonding. The formation of silica particles from hydrolysis and condensation of VTES may occur on the GO surface and in water. The unreacted vinyl group in GO-VTES may have possible interactions with rubber particles through radical graft copolymerization, same as those reported on graft copolymerization of VTES onto NR [17,18].

Properties of DPNR/GO-VTES

Stress–strain curves

Figure 10 shows stress–strain curves for DPNR/GO-VTES(a), GO-VTES(b), and DPNR/GO as a control sample. The amount of GO, GO-VTES(a), and GO-VTES(b) used in graft copolymerization was 0.5 phr. The tensile strength of the unmodified

Table 1: Weight loss percentage of GO-VTES(a) and GO-VTES(b) at different temperatures.

Sample	Weight loss (%)			
	30 to 100 °C	150 to 250 °C	500 to 800 °C	Residual amount
GO-VTES(a)	6	34	52	8
GO-VTES(b)	4	12	42	42

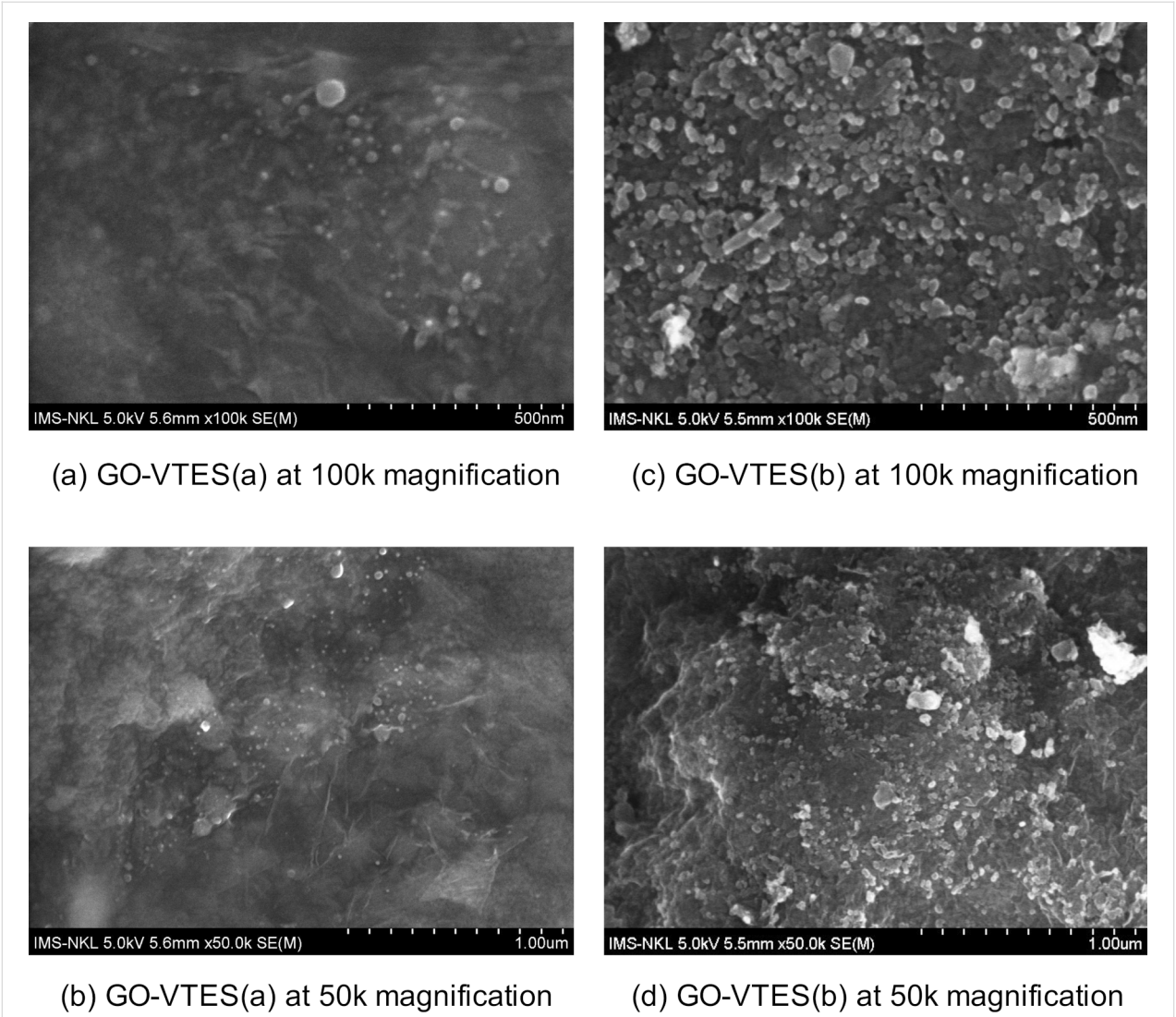


Figure 8: FE-SEM images for GO-VTES(a) and GO-VTES(b) at 100k and 50k magnifications.

DPNR was approx. 2.2 MPa. It increased to 5.2 MPa for DPNR/GO-VTES(a) and to 4.3 MPa for DPNR/GO-VTES(b). However, these tensile strength values were slightly lower than that of DPNR/GO, which was 5.9 MPa. This observation may indicate that GO, after modification with VTES, was not well chemically linked to rubber particles, resulting in a decrease in the reinforcement effect for NR. The giant silica structure on the GO surface, as proposed in Figure 9, may hinder the mobility of GO to interact with rubber particles during radical graft copolymerization. Table 2 shows the value of stress at strain of 100%, 300%, 500%, stress at break, and strain at break for DPNR/GO-VTES(a), DPNR/GO-VTES(b), and DPNR/GO. The samples DPNR/GO-VTES(a) and DPNR/GO-VTES(b) have higher stress values at 100%, 300%, and 500% than those of DPNR/GO. This was due to silica particles on the GO surface, providing the stiffness for DPNR/GO-VTES. Furthermore, tensile strength for DPNR/GO-VTES(a) was slightly higher than that of DPNR/GO-VTES(b), which suggested that GO-VTES(a) may have better interaction with NR than GO-VTES(b). The silica particles on the GO layer may hinder the chemical interaction between GO and NR.

Dynamic mechanical properties

Dynamic mechanical properties of composite samples reveal how much energy is stored or lost during applied cyclic shearing force. Figure 11 shows the dependence of the storage modulus (G'), loss modulus (G''), and loss tangent (tan δ) of DPNR, DPNR/GO, DPNR/GO-VTES(a), and DPNR/GO-VTES(b) as a function of frequency at 30 °C. The G' value of DPNR was 0.13 MPa. This value was much higher than that of DPNR/GO0.5 (0.036 MPa). However, it was lower than those of DPNR/GO-VTES(a) (0.284 MPa) and that of DPNR/GO-

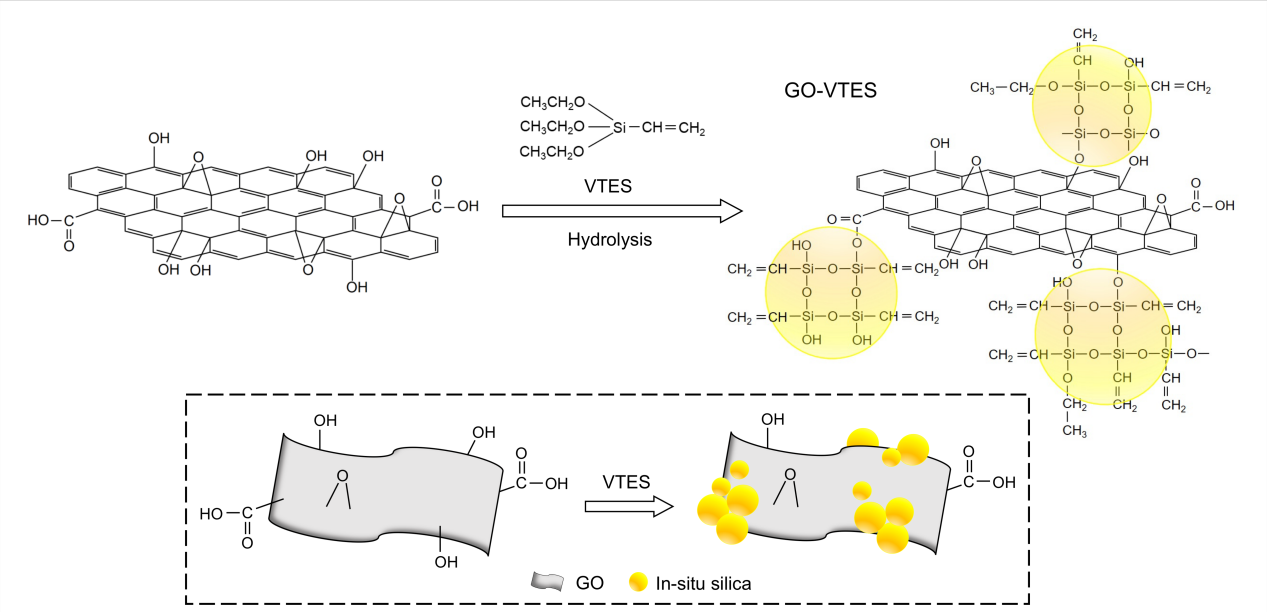


Figure 9: Schematic for modification of GO-VTES.

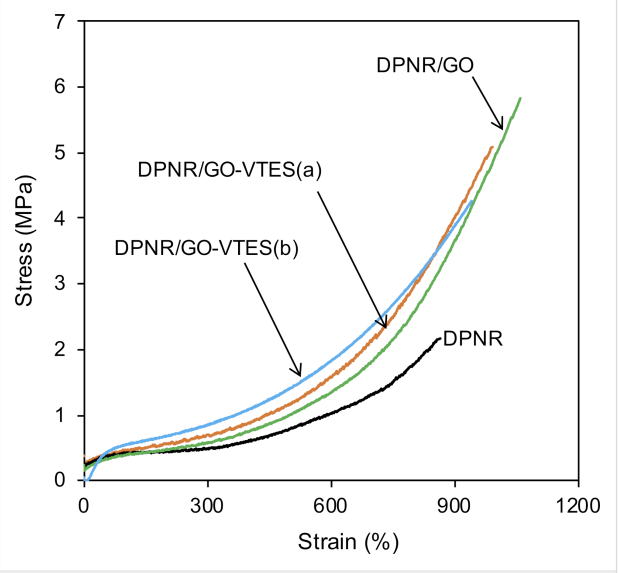


Figure 10: Stress–strain curves of DPNR, DPNR/GO, DPNR/GO-VTES(a), and DPNR/GO-VTEs(b).

VTES(b) (0.334 MPa). The lower G' value of DPNR/GO could be explained by thin and large surface GO layers. The GO sheet could not withstand large shearing force, causing the rubber particles to slip. The high G' value of DPNR/GO-VTES(a) and DPNR/GO-VTES(b) may be due to hard silica particles, which may contribute to higher energy storage for composite materials. The G' values seemed to depend on the silica content; the higher the silica content, the higher the storage modulus.

The dependence of loss modulus (G") on frequency for DPNR, DPNR/GO, DPNR/GO-VTES(a), and DPNR/GO-VTES(b) exhibited a little difference as shown in Figure 11. The G" values of DPNR and DPNR/GO-VTES(a) slightly decreased with frequency. However, the G" values for the DPNR/GO and DPNR/GO-VTES(b) samples slightly increased as frequency increased. These distinguishable behaviors suggested that DPNR/GO and DPNR/GO-VTES(b) may have higher energy dissipation while applying force than DPNR/GO-VTES(a) and DPNR.

Table 2: Tensile stress at break, strain at break, tensile stress at strain of 100%, 300%, 500% of DPNR, DPNR/GO and DPNR/GO-VTES samples.

Sample	Tensile stress at a strain of (MPa)			Tensile stress at break (MPa)	Strain at break (%)
	100%	300%	500%		
DPNR	0.39	0.47	0.77	2.2	864
DPNR/GO	0.39	0.59	1.00	5.8	1060
DPNR/GO-VTES(a)	0.47	0.69	1.16	5.1	1006
DPNR/GO-VTES(b)	0.55	0.86	1.40	4.2	941

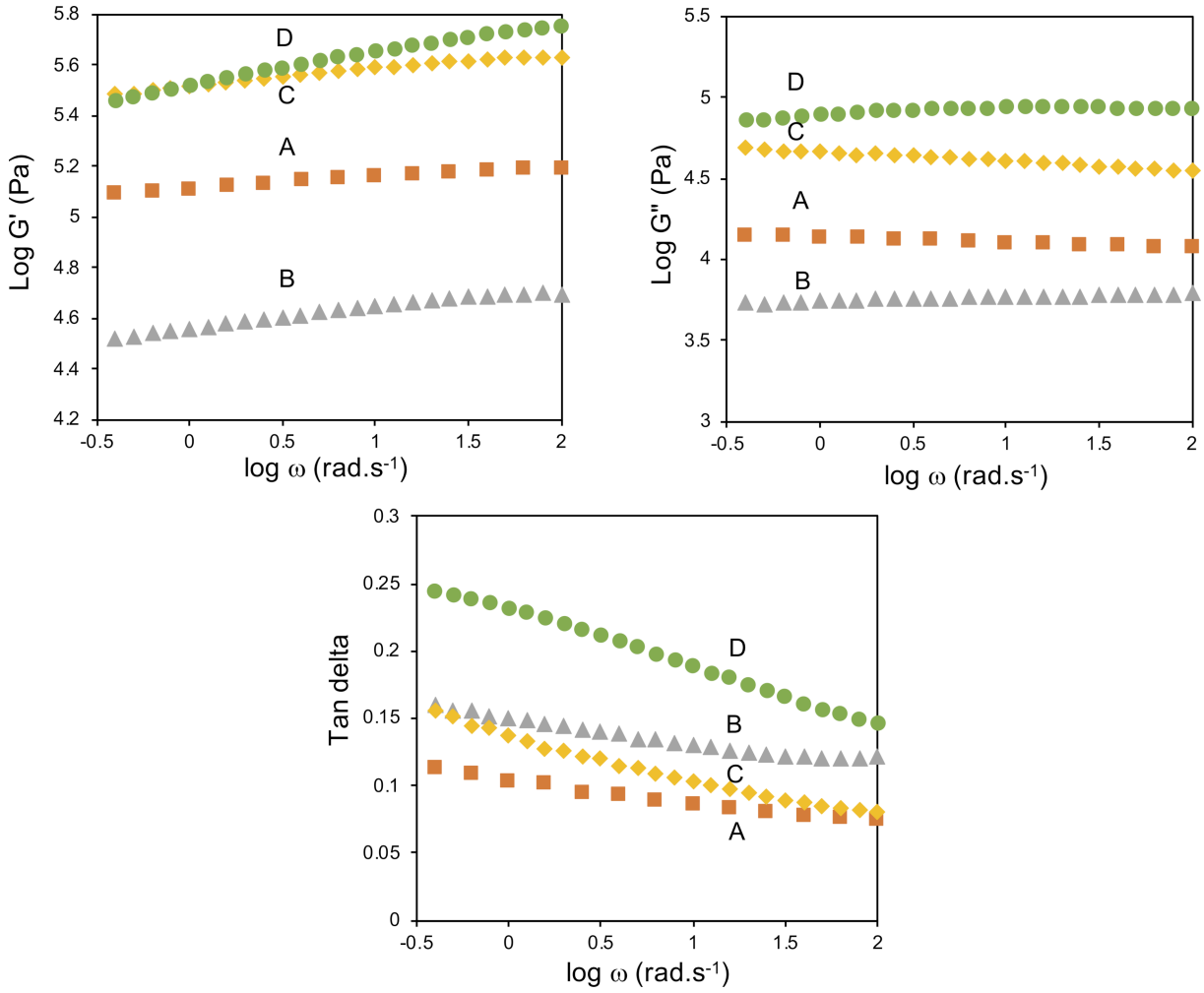


Figure 11: Dependence of storage modulus (G'), loss modulus (G"), and loss tangent (tan δ) of (A) DPNR, (B) DPNR/GO, (C) DPNR/GO-VTES(a), and (D) DPNR/GO-VTES(b) as a function of frequency.

The loss tangent (tan δ) is defined as a G"/G' ratio. The dependence of tan δ with frequency for DPNR/GO samples was quite similar to that of DPNR, in which tan δ decreased as frequency decreased. This phenomenon is appointed to the pure entropic elasticity of NR. Notably, values of tan δ for DPNR/GO-VTES(a) and DPNR/GO-VTES(b) sharply decreased with frequency. This suggests that the energy may be dissipated faster in DPNR/GO-VTES(a) and DPNR/GO-VTES(b) than in DPNR and DPNR/GO. The absence of chemical interactions between NR and GO-VTES in DPNR/GO-VTES(a) and DPNR/GO-VTES(b) may be responsible for a fast energy dissipation. Consequently, DPNR/GO0.5 which uses unmodified GO, shows both entropic and energetic elastic properties, as evidenced by the dependence of loss tangent versus frequency [34].

Conclusion

Graphene oxide was modified by VTES under acidic and basic conditions to produce GO-VTES(a) and GO-VTES(b), respectively. The GO-VTES(a) and GO-VTES(b) samples were then used for the preparation of nanocomposites with deproteinized natural rubber via the graft copolymerization route. The DPNR/GO-VTES(a) and DPNR/GO-VTES(b) samples exhibited lower tensile strength values than that of DPNR/GO. However, they showed higher stress values at small strain values than those of DPNR/GO. This demonstrates that GO-VTES may have poorer chemical interaction with DPNR than GO. From DMA analysis, DPNR/GO-VTES(a) and DPNR/GO-VTES(b) may have more viscous characteristics than DPNR/GO. The silica particles in GO may decrease the chemical interaction between GO and NR via graft copolymerization. However, it contributed to a higher

storage modulus for DPNR/GO-VTES(a) and DPNR/GO-VTES(b), which were approx. two or three times higher than that of DPNR/GO. Our work provided insight into how modified GO interacts with rubber particles during radical graft copolymerization compared to unmodified GO. Then, a suitable approach could be made in the future to fabricate NR/silica/GO composite for abrasion resistance.

Acknowledgements

We acknowledge the Center for Rubber Science and Technology (Hanoi University of Science and Technology, Vietnam) for kindly providing us with experimental equipments and measurement of tensile test. We also thank the Falculty of Engineering (Nagaoka University of Technology, Japan) for the DMA measurements.

Funding

We acknowledge the financial support from Vietnam Ministry of Education and Training (MOET) with grant number B2022-BKA-19.

ORCID® iDs

Nghiem Thi Thuong - https://orcid.org/0000-0003-1484-5437
Cao Hong Ha - https://orcid.org/0000-0002-0206-3182

References

1. Mishra, S. N.; Lenka, S.; Nayak, P. L. *Eur. Polym. J.* **1991,** *27,* 1319–1322. doi:10.1016/0014-3057(91)90228-g
2. Fukuhara, L.; Kado, N.; Thuong, N. T.; Loykulant, S.; Suchiva, K.; Kosugi, K.; Yamamoto, Y.; Ishii, H.; Kawahara, S. *Rubber Chem. Technol.* **2015,** *88,* 117–124. doi:10.5254/rct.14.85992
3. Kawahara, S.; Kawazura, T.; Sawada, T.; Isono, Y. *Polymer* **2003,** *44,* 4527–4531. doi:10.1016/s0032-3861(03)00415-4
4. Akca, E.; Gursel, A.; Sen, N. *Period. Eng. Nat. Sci.* **2018,** *6,* 154–160. doi:10.21533/pen.v6i1.167
5. Chittella, H.; Yoon, L. W.; Ramarad, S.; Lai, Z.-W. *Polym. Degrad. Stab.* **2021,** *194,* 109761. doi:10.1016/j.polymdegradstab.2021.109761
6. Mohd Sani, N. F.; Majid, N. A.; Rehman, A.; Hayeemasae, N.; Radhakrishnan, S.; Kulkarni, M. B.; Khimi, R. *Prog. Rubber, Plast. Recycl. Technol.* **2023,** 10.1177/14777606231200952. doi:10.1177/14777606231200952
7. Fukushima, Y.; Kawahara, S.; Tanaka, Y. *J. Rubber Res. (Singapore, Singapore)* **1998,** *1,* 3.
8. Kawahara, S. *Polym. J.* **2023,** *55,* 1007–1021. doi:10.1038/s41428-023-00797-2
9. Kawahara, S.; Klinklai, W.; Kuroda, H.; Isono, Y. *Polym. Adv. Technol.* **2004,** *15,* 181–184. doi:10.1002/pat.465
10. Chaikumpollert, O.; Yamamoto, Y.; Suchiva, K.; Nghia, P. T.; Kawahara, S. *Polym. Adv. Technol.* **2012,** *23,* 825–828. doi:10.1002/pat.1965
11. Thi Nghiem, T.; Yusof, N. H.; Kawahara, S. *Polym. J.* **2023,** *55,* 631–637. doi:10.1038/s41428-022-00753-6
12. Pukkate, N.; Yamamoto, Y.; Kawahara, S. *Colloid Polym. Sci.* **2008,** *286,* 411–416. doi:10.1007/s00396-007-1787-5
13. George, B.; Maiti, S. N.; Varma, I. K. *J. Elastomers Plast.* **2006,** *38,* 319–331. doi:10.1177/0095244306067129
14. Nghiem Thi, T.; Cao Hong, H.; Nurul Hayati, Y.; Kawahara, S. *J. Polym. Res.* **2021,** *28,* 246. doi:10.1007/s10965-021-02606-x
15. Promdum, Y.; Klinpituksa, P.; Ruamcharoen, J. *Songklanakarin J. Sci. Technol.* **2009,** *31,* 453–457.
16. Mizote, N.; Katakai, A.; Tamada, M. *J. Appl. Polym. Sci.* **2012,** *123,* 2172–2176. doi:10.1002/app.34736
17. Nghiem, T.; Nguyen, L.; Phan, N.; Yusof, N.; Kawahara, S. *Polym. Adv. Technol.* **2020,** *31,* 482–491. doi:10.1002/pat.4785
18. Thuong, N. T.; Dung, T. A.; Yusof, N. H.; Kawahara, S. *Polymer* **2020,** *195,* 122444. doi:10.1016/j.polymer.2020.122444
19. Fu, X.; Lin, J.; Liang, Z.; Yao, R.; Wu, W.; Fang, Z.; Zou, W.; Wu, Z.; Ning, H.; Peng, J. *Surf. Interfaces* **2023,** *37,* 102747. doi:10.1016/j.surfin.2023.102747
20. Shah, R.; Kausar, A.; Muhammad, B.; Shah, S. *Polym.-Plast. Technol. Eng.* **2015,** *54,* 173–183. doi:10.1080/03602559.2014.955202
21. Hernández, M.; del Mar Bernal, M.; Verdejo, R.; Ezquerra, T. A.; López-Manchado, M. A. *Compos. Sci. Technol.* **2012,** *73,* 40–46. doi:10.1016/j.compscitech.2012.08.012
22. Murugesan, A.; Lakshmanan Saraswathy, J.; Chandran, R. *Int. Polym. Process.* **2022,** *37,* 505–522. doi:10.1515/ipp-2022-0008
23. Mensah, B.; Kang, S. I.; Wang, W.; Nah, C. *Mech. Adv. Mater. Mod. Process.* **2018,** *4,* 1. doi:10.1186/s40759-017-0034-0
24. Thuong, N. T.; Manh, N. D.; Ha, C. H.; Anh, N. V. *JST: ETSD* **2023,** *33,* 9–15. doi:10.51316/jst.165.etsd.2023.33.2.2
25. Wang, J.; Xu, C.; Hu, H.; Wan, L.; Chen, R.; Zheng, H.; Liu, F.; Zhang, M.; Shang, X.; Wang, X. *J. Nanopart. Res.* **2011,** *13,* 869–878. doi:10.1007/s11051-010-0088-y
26. Yan, H.; Li, S.; Jia, Y.; Ma, X. Y. *RSC Adv.* **2015,** *5,* 12578–12582. doi:10.1039/c4ra13134g
27. Li, Z.; Wang, R.; Young, R. J.; Deng, L.; Yang, F.; Hao, L.; Jiao, W.; Liu, W. *Polymer* **2013,** *54,* 6437–6446. doi:10.1016/j.polymer.2013.09.054
28. Abbas, S. S.; Rees, G. J.; Patias, G.; Dancer, C. E. J.; Hanna, J. V.; McNally, T. *ACS Appl. Polym. Mater.* **2020,** *2,* 1897–1908. doi:10.1021/acsapm.0c00115
29. Charoenchai, M.; Tangbunsuk, S.; Keawwattana, W. *J. Polym. Res.* **2020,** *27,* 230. doi:10.1007/s10965-020-02209-y
30. Park, K. T.; Choi, J.; Sung, S. J.; Park, J.; Kim, T.; Park, C. R. *Synth. Met.* **2021,** *277,* 116770. doi:10.1016/j.synthmet.2021.116770
31. Hummers, W. S., Jr.; Offeman, R. E. *J. Am. Chem. Soc.* **1958,** *80,* 1339. doi:10.1021/ja01539a017
32. Chen, C.; Wei, S.; Xiang, B.; Wang, B.; Wang, Y.; Liang, Y.; Yuan, Y. *Coatings* **2019,** *9,* 587. doi:10.3390/coatings9090587
33. Surekha, G.; Krishnaiah, K. V.; Ravi, N.; Padma Suvarna, R. *J. Phys.: Conf. Ser.* **2020,** *1495,* 012012. doi:10.1088/1742-6596/1495/1/012012
34. Yamamoto, Y.; Endo, K.; Tévenot, Q.; Kosugi, K.; Nakajima, K.; Kawahara, S. *Langmuir* **2020,** *36,* 11341–11348. doi:10.1021/acs.langmuir.0c02111

License and Terms

This is an open access article licensed under the terms of the Beilstein-Institut Open Access License Agreement (https://www.beilstein-journals.org/bjnano/terms), which is identical to the Creative Commons Attribution 4.0 International License (https://creativecommons.org/licenses/by/4.0). The reuse of material under this license requires that the author(s), source and license are credited. Third-party material in this article could be subject to other licenses (typically indicated in the credit line), and in this case, users are required to obtain permission from the license holder to reuse the material.

The definitive version of this article is the electronic one which can be found at:
https://doi.org/10.3762/bjnano.15.16

BEILSTEIN JOURNAL OF NANOTECHNOLOGY

Nanocarrier systems loaded with IR780, iron oxide nanoparticles and chlorambucil for cancer theragnostics

Phuong-Thao Dang-Luong[1], Hong-Phuc Nguyen[1], Loc Le-Tuan[1], Xuan-Thang Cao[2], Vy Tran-Anh[3] and Hieu Vu Quang[*4,§]

Full Research Paper

Open Access

Address:
[1]NTT Hi-tech institute, Nguyen Tat Thanh University, Ho Chi Minh City, 700000, Vietnam, [2]Faculty of Chemical Engineering, Industrial University of Ho Chi Minh City, Ho Chi Minh City, 700000, Vietnam, [3]Institute of Applied Technology and Sustainable Development, Nguyen Tat Thanh University, Ho Chi Minh City 700000, Vietnam and [4]Department of Biotechnology, NTT Hi-tech institute, Nguyen Tat Thanh University, Ho Chi Minh City, 700000, Vietnam

Email:
Phuong-Thao Dang-Luong - thaodangluong@gmail.com;
Hong-Phuc Nguyen - nhphuc@ntt.edu.vn;
Loc Le-Tuan - ltloc@ntt.edu.vn;
Xuan-Thang Cao - caoxuanthang@iuh.edu.vn;
Vy Tran-Anh - tavy@ntt.edu.vn;
Hieu Vu Quang* - vqhieu@ntt.edu.vn

* Corresponding author
§ Tel: +84 869974364

Keywords:
cancer; chlorambucil; F127-folate; IR780; iron oxide nanoparticles; PLGA; theragnostics

Beilstein J. Nanotechnol. **2024,** *15,* 180–189.
https://doi.org/10.3762/bjnano.15.17

Received: 07 August 2023
Accepted: 22 January 2024
Published: 06 February 2024

This article is part of the thematic issue "Recent advances in synthesis and applications of organometallic nanomaterials".

Associate Editor: A. Salvati

© 2024 Dang-Luong et al.; licensee Beilstein-Institut.
License and terms: see end of document.

Abstract

Theragnostics has become a popular term nowadays, since it enables both diagnosis and therapy at the same time while only using one carrier platform. Therefore, formulating a nanocarrier system that could serve as theragnostic agent by using simple techniques would be an advantage during production. In this project, we aimed to develop a nanocarrier that can be loaded with the chemotherapeutic medication chlorambucil and magnetic resonance imaging agents (e.g., iron oxide nanoparticles and near-infrared fluorophore IR780) for theragnostics. Poly(lactic-*co*-glycolic acid) was combined with the aforementioned ingredients to generate poly(vinyl alcohol)-based nanoparticles (NPs) using the single emulsion technique. Then the NPs were coated with F127 and F127-folate by simple incubation for five days. The nanoparticles have the hydrodynamic size of approx. 250 nm with negative charge. Similar to chlorambucil and IR780, iron oxide loadings were observed for all three kinds of NPs. The release of chlorambucil was quicker at pH 5.4 than at pH 7.4 at 37 °C. The F127@NPs and F127-folate@NPs demonstrated much greater cell uptake and toxicity up to 72 h after incubation. Our in vitro results of F127@NPs and F127-folate@NPs have demonstrated the ability of these systems to serve as medication and imaging agent carriers for cancer treatment and diagnostics, respectively.

Introduction

Theragnostic nanoparticles (NPs) are a diagnostic and therapeutic delivery system. The delivery system is comprised of three components: the carrier, the imaging agent, and the therapeutic drug, all of which need clinical approval before being used in humans.

Poly(lactic-*co*-glycolic acid) (PLGA) is an approved biodegradable and biocompatible material for clinical use [1]. Particularly, PLGA is widely used for nanoparticle formulation because it is a versatile material that can serve multiple functions, including transporting of therapeutic drugs and imaging agents [2,3]. In addition, PLGA can be altered in numerous ways to increase the half-life of nanoparticles in the blood and target efficacy. To increase the blood half-life, stealth materials have been attached to the nanoparticle surface to prevent protein adsorption and immune cell phagocytosis [4]. Most sheath materials are hydrophilic polymers such as poly(vinyl alcohol), poly(ethylene glycol), and poly(ethylene oxide) (PEO). To improve the targeting ability of nanoparticles, ligands are typically designed to be located on the exterior of nanoparticles. Typically, ligands are cell-type-specific monoclonal antibodies, RGD peptides for the overexpression of the asialoglycoprotein receptor on cancer cells [5], mannose for the mannose receptor on activated macrophages [6,7], and folic acid for the overexpression of the folate receptor on the surface of cancer cells and activated macrophages [8]. Thus, in this study, PLGA was chosen for NP formulation since it is a biocompatible and biodegradable material.

Clinical use of superparamagnetic oxide nanoparticles (SPIONs) has been authorized [9]. SPIONs have been utilized in magnetic particle imaging (MPI), magnetic resonance imaging (MRI), computer tomography (CT), and additional imaging models [9-11]. SPIONs have been modified to be applicable to a variety of fields. However, SPIONs typically serve as the core of nanoparticles, while the outer shell is composed of stabilization coating materials such as chitosan, mannan, poly(ethylene glycol) (PEG), Pluronic™ F-127, or PLGA [7,12,13]. SPIONs stabilized with PLGA have attracted interest due to their high potential applications in various fields, including theragnostics. The PLGA SPION nanoparticles were modified to carry siRNA for silencing the inflammatory cytokine Cox-2 in activated macrophages and to serve as a tracer for locating activated macrophages in a mouse model of intra-uterine urinary obstruction [14]. In another study, PLGA SPIONs could transport chemotherapeutic agents for cancer treatment and diagnosis [15]. Therefore, the combination of PLGA and SPIONs promises a useful theragnostic system in our study.

In addition to the encapsulation of SPIONs in PLGA employed for diagnostics, near-infrared (NIR) fluorescent dyes are a potential alternative for the diagnosis and excision of residual malignant cancer, which is invisible by conventional visual examination and palpation [16-18]. Indocyanine green is the only NIR dye permitted for clinical use [19]. Dyes such as IR780 and IR783 are also promising diagnostic choices. Encapsulation of IR780 in nanoparticles can be used for imaging and photothermal, photodynamic, and combinatorial cancer therapies [20-22]. IR780 is also utilized in PEG-PLA nanoparticles for photodynamic therapy of human breast cancer cells [23,24]. Thus, using IR780 in our NPs would bring advantages for local imaging and treatment.

Chemotherapy medications assist in inhibiting the development of tumors. Chemotherapeutic agents such as doxorubicin attach to chromosomes and inhibit DNA replication, while paclitaxel depolymerizes the cytoskeleton and chlorambucil (CHL) inhibits DNA synthesis. These drugs can be encapsulated inside nanoparticles for administration to increase the stability of the medication in circulation and therapeutic efficacy. For example, doxorubicin can be inserted into liposomes and paclitaxel attaches to the protein particle [25,26]. PLGA is one of the finest materials for transporting chemotherapy drugs. PLGA transports not only hydrophobic but also hydrophilic drugs. The encapsulation of chemotherapeutics in PLGA nanoparticles has been extensively studied. PLGA has been loaded with doxorubicin, for instance, for tumor treatment [27], and PLGA-chlorambucil nanoparticles have been developed for the treatment of breast cancer [28]. Due to the efficiency of CHL in cancer treatment, CHL has been used as a drug model in order to evaluate our formulated NPs.

Therefore, in this study, we propose to develop a carrier system capable of transporting NPs that could carry iron oxide (IO) nanoparticles, IR780, and CHL for cancer theragnostic applications.

Materials and Methods

Chlorambucil (C0253), PLGA 504H (719900), IR780 (425311), $FeSO_4{\cdot}7H_2O$ (215422), $FeCl_3{\cdot}6H_2O$ (236489), NaOH (221465), oleic acid (364525), Pluronic™ F-127 (P2443), poly(vinyl alcohol) (PVA) (P8136), phosphate buffered saline (PBS) (P4417), dimethyl sulfoxide (DMSO) (472301), dichloromethane (DCM), 3-[4,5-dimethylthiazol-2-yl]-2,5 diphenyl-2*H*-tetrazolium bromide (MTT) (M2128), and coumarin-6 (442631), $K_3[Fe(CN)_6]$ (1049730100) were purchased from Sigma-Aldrich. Dulbecco's Modified Eagle Medium (DMEM) (11965092), fetal bovine serum (FBS) (MT35010CV), antibiotic (15-240-062), and trypsin (25-200-

056) were purchased from Gibco, Fisher Scientific. All other solvents and reagents were of chemical grade.

Synthesis of iron oxide nanoparticles

Iron oxide NPs were synthesized using a modified coprecipitation method [13]. Firstly, 10 mmol of $FeSO_4{\cdot}7H_2O$ and 5 mmol of $FeCl_3{\cdot}6H_2O$ were dissolved in 50 mL of deionized water in a N_2 atmosphere. Then, 1 M of NaOH was carefully added into the solution while swirling until the pH reached 14. Next, 1 mL of oleic acid was added to the solution and heated to 70 °C for 30 min. The synthesized IO NPs were washed three times with 50 mL of DCM and stored at −80 °C for further experiments.

Synthesis of folate-F127

The synthesis was done as previously described [13]. The Fourier-transform infrared spectroscopy (FTIR) results were displayed in the Supporting Information File 1 (Supplementary data 1) and Figure S1.

Formulation of nanoparticles F127-folate@PLGA/IO/CHL/IR780 and others

In 2 mL of DCM, 20 mg of PLGA, 40 µg of IO, 2 mg of CHL, and 0.1 mg of IR780 were mixed. The organic solvent was then added to the aqueous phase, which contained 10 mL of 1.5% PVA. The mixture was then emulsified by vortexing at 1000 rpm for 1 min, followed by sonication (Sonics, Vnibra cells, USA) over an ice bath for 1 min at 40 W, 40%, 10 s pulse, and 2 s rest. Then, the organic phase was magnetically stirred at 200 rpm and allowed to evaporate overnight in a dark area at room temperature. In the next day, the nanoparticles were centrifuged at 12,000 rpm for 30 min, then resuspended in 600 µL of distilled water. The nanoparticles were then separated into three 200 µL suspension tubes. Then, 2 mg of F127-folate or 2 mg of F127 was separately added to the tubes, and the ligand exchange was performed at 4 °C for one week. The tube without added polymer was designated as PVA@PLGA/IO/CHL/IR780 (PVA@NP). Then, the nanoparticles were centrifuged for 30 min at 12,000 rpm and resuspended in distilled water. The final formulations of the three nanoparticles were F127-folate@PLGA/IO/CHL/IR780 (F127-folate@NP), F127@PLGA/IO/CHL/IR780 (F127@NP), and PVA@PLGA/IO/CHL/IR780 (PVA@NP).

Coumarin-6 (0.2 mg) was added to the organic phase to create F127-folate@NP/Cou-6, F127@NP/Cou-6, and PVA@NP/Cou-6 for the fluorescence assay in cells.

Hydrodynamic size and zeta potential

Dynamic light scattering (DLS) and zeta potential spectra were obtained for three replicates on a nanoPartical Horiba SZ-100 (Japan) with the scattering angle of 90° to determine the size distribution and stability of the nanoparticles. The DLS measurements were performed in both 0.1× PBS (13.7 mM of NaCl, 0.27 mM of KCl, 1 mM of Na_2HPO_4, and 0.18 mM of KH_2PO_4, pH 7.4) and animal cell culture media containing DMEM and 10% FBS.

Scanning electron microscopy

For scanning electron microscopy (SEM) experiments, 10 µL of F127-folate@NP was loaded on the silica film for 1 min, and water was allowed to evaporate. Then, the NPs were coated with titanium and SEM images were acquired using a FE-SEM S4800 HITACHI, Japan.

Loading capacity

Entrapment and release of CHL and IR780 in the NPs were measured by the absorbance of CHL at 256 nm and IR780 at 780 nm using HPLC 1200 and NanoDrop One^C (Thermoscientific, USA).

In brief, a small amount of freeze-dried NPs was weighted and dissolved in 20 µL of acetonitrile. Then, 80 µL of methanol was added to extract the drug. The mixture was centrifuged at 12,000 rpm for 30 min, and the supernatant was kept for drug entrapment calculation.

Chlorambucil release

The NPs were kept in 0.1× PBS at pH 7.4 and pH 5.4 for 24, 48, 72, and 168 h at 37 °C. The NPs were then centrifuged at 12,000 rpm for 30 min. The pellet was collected and freeze-dried. The remaining CHL concentration in NPs was calculated as previously described.

Determination of iron content with the Prussian blue protocol

The iron content was determined by measuring absorption of Prussian blue at 562 nm (Biotek ELX800, Agilent, USA). Briefly, the material was initially reduced for 10 min in 4% HCl. Then, 4% $K_3[Fe(CN)_6]$ was added and the mixture was incubated for an additional 10 min.

Cell culture

The cell lines HepG2, MCF-7, 3T3, and Hek were cultured in DMEM, 10% FBS, and 1% antibiotic at 37 °C and 5% CO_2.

Cell uptake estimation

The cells were seeded onto 6-well plates at 100,000 cells/well and were cultured overnight. On the next day, the cells were incubated with 0.5 mg of F127-folate@NP/Cou-6, F127@NP/Cou-6, and PVA@NP/Cou-6 in 1 mL of cell culture media for 4 h. The cells were then washed with PBS three times and trypsinized. The harvested cells were counted and

20,000 cells/well were added to a black 96-well plate in triplicates. The culture medium and cells without treatment were used as controls. Fluorescent signals were obtained at an excitation wavelength of 460 nm and emission wavelength of 510 nm (Victor Nivo, Perkin Elmer, USA). After the measurements, the cell signal was subtracted from the signal from the cells that did not receive treatment. Then, the signals were normalized to the signal of PVA@NP/Cou-6 for comparison.

The fluorescence image of the NPs in the cells were displayed in Supporting Information File 1, Supplementary data 2 and Figure S2.

Cytotoxicity effects of nanoparticles

The cells were seeded onto 96-well plates at 5,000 cells/well one day prior to the tests. Then, the cells were treated with various particle concentrations (0.5 mg/ mL, 1 mg/mL, and 1.5 mg/mL). Cells treated with CHL and untreated cells were used as controls. Cells were incubated with NPs for 48 and 72 h. The cell viability was evaluated by the MTT assay, and the absorbance was read at 562 nm (Biotek ELX800, Agilent, USA).

Results

The morphology, size, and zeta potential of the particles

The hydrodynamic size of the three types of NPs (Figure 1A) ranged from 245 ± 11 nm to 246 ± 2 nm with the polydispersity index (PDI) smaller than 0.12, which shows the similarity in size and highly homogeneity among the NPs (Table 1). The zeta potential values of the nanoparticles were: PVA@NP: −46 ± 0.7 mV; F127-folate@NP: −67.4 ± 2.3 mV, and F127@NP: −81.13 ± 2.4 mV (Table 1). It was also showed that when the NPs were in cell culture media, their values of DLS and PDI increased to approx. 280 nm and 0.24, respectively.

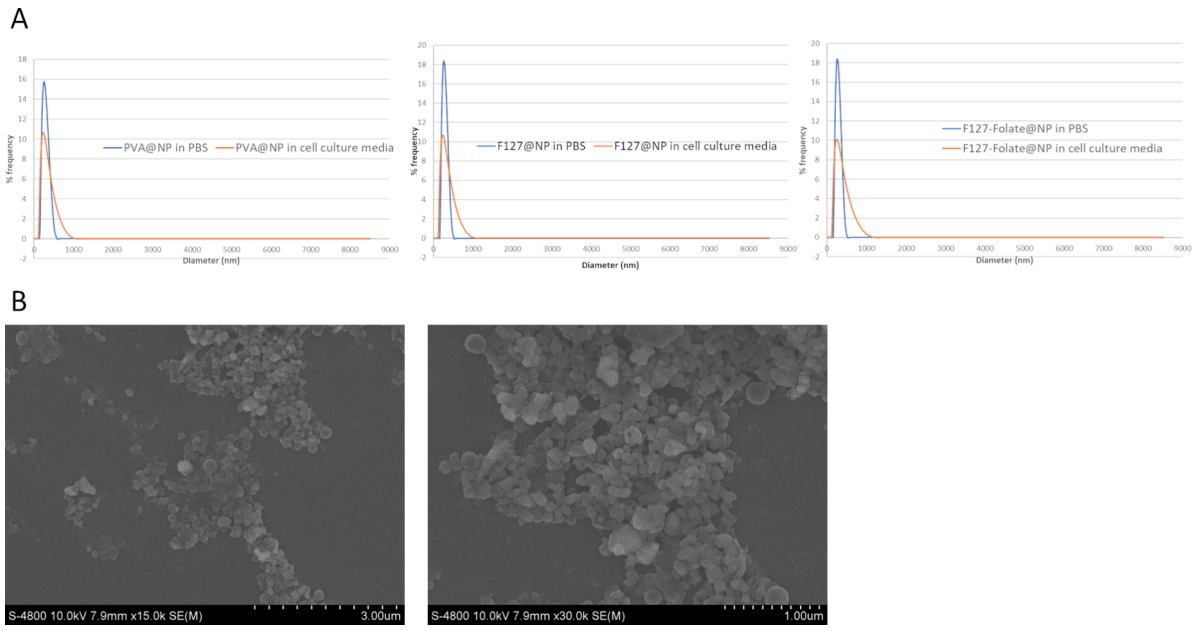


Figure 1: (A) DLS results for the NPs. (B) SEM images of F127-folate@NP at 15k× and 30k× magnifications.

Table 1: Hydrodynamic size and polydispersity index of the NPs in PBS and cell culture medium.

	DLS (nm)	PDI	Zeta potential (mV)
F127@NP in 0.1× PBS	256 ± 11	0.12 ± 0.03	–67.4 ± 2.3
F127-folate@NP in 0.1× PBS	245 ± 2	0.09 ± 0.06	–81.13 ± 2.4
PVA@NP in 0.1× PBS	246 ± 1	0.115 ± 0.03	–46 ± 0.7
F127@NP in cell culture media	290 ± 19	0.464 ± 0.07	–
F127-folate@NP in cell culture media	285 ± 18	0.459 ± 0.06	–
PVA@NP in cell culture media	275 ± 14	0.476 ± 0.04	–

The NPs were still well dispersed in cell culture media; however, the size increase suggested the adsorption of FBS proteins onto the NPs.

The SEM results (Figure 1B) showed the actual size of the nanoparticles, which had a round shape of approx. 150 nm. However, there was a polymer layer covering the outside of the NPs, which made the spherical shape of the NPs not clear.

Drug loading and release

Entrapment of chlorambucil

The entrapment of chlorambucil in the NPs was calculated by measuring the OD absorption of CHL in NPs after purification and freeze-drying. The results showed that there was approx. 0.5% of CHL in the NPs (Table 2). The encapsulation efficiency of the single emulsion was approx. 5%. However, it was reported that the encapsulation efficiency could be increased up to 92% using the double emulsion method [28] or to 70% using the nanoprecipitation method [29].

Table 2: The entrapment of chlorambucil, IR780, and iron oxide nanoparticles into NPs.

	Drug loading capacity
chlorambucil	0.5%
IR780	0.9%
iron oxide nanoparticles	1.11%

The loading of iron oxide nanoparticles

The entrapment of iron oxide NPs into PLGA nanoparticles was estimated by measuring the absorbance at 562 nm through the Prussian blue reaction. The entrapment of IO was approx. 1.11% of the total weight of nanoparticles (Table 2).

The loading of IR780 into nanoparticles

The IR780 loading capacity of the nanoparticles was evaluated by measuring the absorbance at 780 nm. Approximately 0.9% of IR780 was composed of PLGA nanoparticles (Table 2).

The release of chlorambucil from the nanoparticles

The release of chlorambucil from the NPs was monitored during seven days of incubation in media with pH values of 7.4 and 5.4 at 37 °C, which mimicked physiological and endosomal conditions (Figure 2). After seven days of incubation, the CHL concentration in nanoparticles was maintained between 6% and 10%. The CHL remained in the NPs at 57.6 ± 2.4% and 35.26 ± 5.2% during incubation at pH 7.4 and pH 5.4, respectively, over the first 24 h. After 48 h, the concentration decreased to 49.2 ± 4.5% at pH 7.4 and 16.3 ± 4.2 at pH 5.4. On day three, the CHL concentration in the NPs was 32.9 ± 5.7% at pH 7.4 and 13 ± 5.1% at pH 5.4. After 24, 48, and 72 h, the CHL levels in the NPs were significantly lower when incubated in pH 5.4 medium compared to that in pH 7.4 medium. The faster CHL drug release at pH 5.4 was due to a faster degradation of PLGA at pH 5.4 than that at pH 7.4 [30].

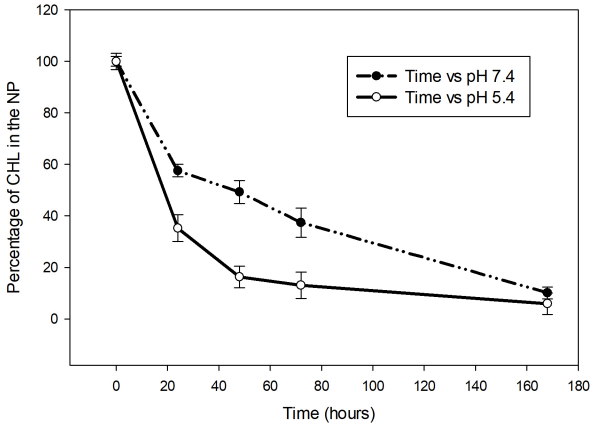


Figure 2: The release of chlorambucil from F127@NP at pH 7.4 and pH 5.4 after seven days of incubation at 37 °C. $n = 3$.

Targeting of nanoparticles to the cells

The NPs encapsulated with Cou-6 were utilized to demonstrate the capacity of our NPs to target cells. In a 6-well plate, cells were treated with 0.2 mg/mL of F127-folate@NP/Cou-6, F127-folate@NP/Cou-6, and PVA@NP/Cou-6 for 3 h at 37 °C and 5% CO_2. Cells treated with F127-folate@NP/Cou-6 and F127-folate@NP/Cou-6 had stronger fluorescence signals than cells treated with PVA@NP/Cou-6 (Figure 3). This was true for all four types of cells. In 3T3, HEK, and MCF-7 cells, the signal of F127-folate@NP/Cou-6 and F127@NP/Cou-6 was 1.4 times stronger than that of PVA@NP/Cou-6. However, in HepG2 cells, it was only 1.2 times stronger. There was no significant difference between the fluorescence signals of F127-folate@NP/Cou-6 and F127@NP/Cou-6 in any cell type. The appearance of F127-folate@NP/Cou-6 and F127@NP/Cou-6 to MCF7 and HepG2 was also confirmed (Supporting Information File 1, Figure S2). The F127-folate@NP did not show a superior targeting effect to cancer cells, which might be due to the fact that cancer cells were cultured in normal cell culture media. Therefore, the expression of folate receptor was not as high compared to that of cancer cells that grew in folic-acid-free cell culture media.

Cytotoxicity of the nanoparticles

This experiment was conducted to assess the toxicity of CHL nanoparticles to four distinct cell types (Figure 4).

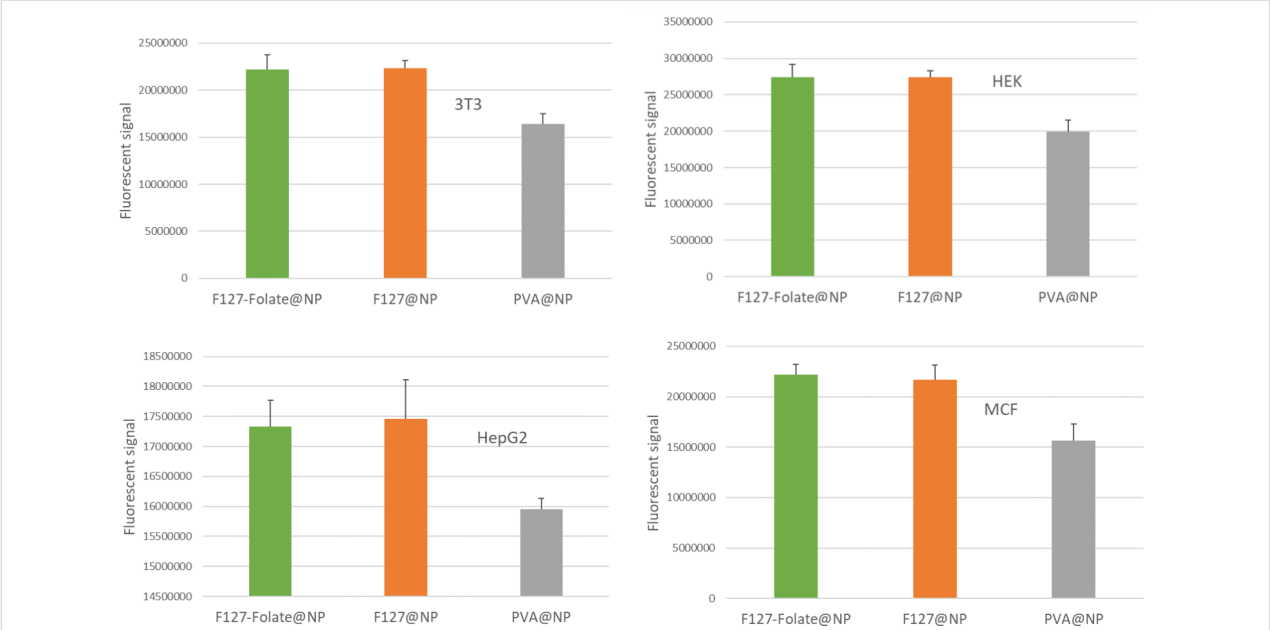


Figure 3: The fluorescence signal of F127-folate@NP/Cou-6, F127-folate@NP/Cou-6, and PVA@NP/Cou-6 in 3T3, HEK, HEPG2, and MCF-7 after background subtraction (n = 3).

After 72 h of incubation, the IC50 of CHL for HepG2 was 0.45 µg/mL. After 72 h of NP exposure to HepG2, the cell viability at the highest dose (1.50 µg/mL) was reduced to approximately 60%. At 72 h, the viability was lower than that at 48 hours. The cellular toxicity at concentrations of 1 mg/mL and 1.5 mg/mL at 48 and 72 h was the same. At 72 h, the concentration of F127@NP and F127-folate@NP was significantly lower than that of PVA-NP. No significant differences existed between F127@NP and F127-folate@NP.

The IC50 of CHL for MCF-7 was 0.4 µg/mL. After 72 h of incubation, the NPs had some impact on the MCF-7 cells. At a dosage of 1.5 mg/mL, the cell viability of both F127@NP and F127-folate@NP decreased to approximately 50%. These results were below PVA@NP (75%). Similar cell viability results were observed with F127-folate@NP and F127@NP.

Chlorambucil was very toxic to 3T3 cells, with an IC50 of 0.4 µg/mL at 48 h and 0.35 mg/mL at 72 h. At the lowest nanoparticle concentration (0.5 mg/mL), the cell viability was approx. 50% for all NPs tested. At a concentration of 0.5 mg/mL, the concentrations of F127 and F127-folate@NP were approx. 50% after 48 and 72 h, whereas the concentrations of PVA@NP were 71% and 55.6% after 48 and 72 h, respectively. The cell viability decreased when the concentration of used NP increased.

In the HepG2 cell line, the IC50 of CHL was 0.45 µg/mL at 72 h. However, cell viability even at the highest concentration of NPs (1.5 mg/mL) was only about 60%. The cytotoxicity of the NPs was significantly lower after 72 h of incubation than that at 48 h. The toxicity effect was similar for both NP concentrations of 1.0 and 1.5 mg/mL at both 48 and 72 h. The cytotoxicity results for F127@NP and F127-folate@NP was significantly lower at 72 h than that for PVA@NP. There were no statistically significant differences between F127@NP and F127-folate@NP.

Discussion

Nanomedicines have their applications in a number of cancer treatments and diagnoses, including tumor-targeted drug delivery, hyperthermia, photodynamic therapy, and imaging. Nanomedicines can be made from a variety of inert, biodegradable, and in vivo biocompatible materials. Poly(lactic-*co*-glycolic acid) is one of the most biodegradable and biocompatible copolymers owing to its nontoxic breakdown products [3]. It has been encapsulated with a variety of drugs. One of the contemporary concerns is theragnostics, in which PLGA nanoparticles have dual diagnostic and therapeutic roles. Various imaging agents and medications have been encapsulated in PLGA for this purpose. For theragnostic applications, we have produced PLGA nanoparticles that carry chlorambucil as the chemotherapeutic medication and iron oxide nanoparticles as the imaging agent.

Li et al., 2023, published similar results on F127@PLGA nanoparticles and claimed that the F127 polymer flocculates over the PVA layer when incubated with PVA@PLGA nanoparticles

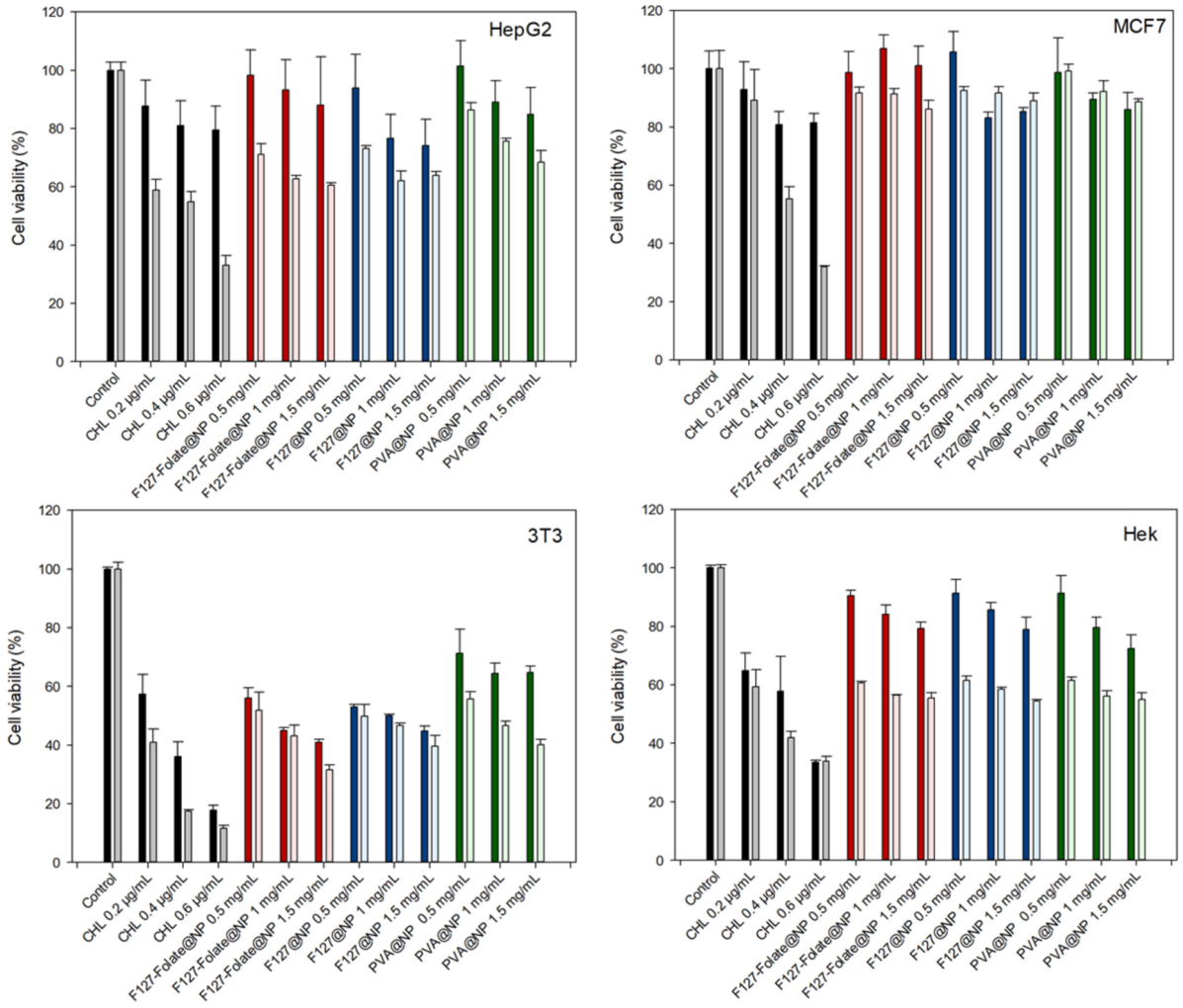


Figure 4: MTT assays of the nanoparticles incubated with HepG2, MCF7, 3T3, and HEK for 48 h (dark color) and 72 h (light color). Cells (5,000 cells/well) were treated with CHL 0.2 µg/mL, 0.4 µg/mL and 0.6 µg/mL (black), F127-folate@NP (red), F127@NP (blue), and PVA@NP (green) at 0.5 mg/mL, 1 mg/mL, 1.5 mg/mL.

[31]. Their research yielded similar findings to our own results. First, F127 could briefly switch the ligand between PVA and F127, or F127 PPO block could stick to the hydrophobic outer shell of PLGA nanoparticles. The presence of F127 on PLGA@NP decreases their charge (Table 1). The alteration of NPs following the hardening of PLGA NPs apparently had no effect on the loading of drugs (CHL) and imaging agents (IR780 and IO) into NPs (Table 2).

Two criteria were necessary for the successful transport of a nanoparticle to a target spot. One is the half-life of NPs in circulation, and the other is nanoparticle targeting. The size, charge, and coating materials of NPs have a considerable influence on the half-life of NPs. It has been observed that nanomedicines with a size of approximately 100 nm have a longer half-life in the bloodstream, but those with a size over 200 nm activate the lymphatic system and are more quickly removed from circulation [32,33]. The core size and hydrodynamic size of our nanoparticles were around 100 nm and 245 ± 3 nm, respectively, making them suitable for intravenous delivery. Thus, the single emulsion/evaporation approach employing 3% PVA as the surfactant was suitable for encapsulating iron oxide nanoparticles, CHL, and IR780, which created stable nanoparticles with the desired size. Additionally, it was documented that nanoparticles with a hydrodynamic size above 100 nm are incapable of traversing the endothelium and the glomerular basement membrane during glomerular filtration in the kidney [34]. Thus, it may be assumed that the half-life of our NPs in the bloodstream is longer than that of smaller NPs.

In addition to the size of nanoparticles, negatively charged NPs are more likely to have an extended half-life. When NPs are administered, they come into contact with blood cells and plasma proteins, which may cause adsorption or opsonization by serum proteins [35]. However, these proteins will have a reduced probability of interacting with our negatively charged nanoparticles, as most proteins are likewise negatively charged. Another element influencing NP elimination is glomerular filtration. However, endothelial cell surfaces are negatively charged [35], therefore less NPs will be excreted through the kidneys.

In regard to extending the half-life of NPs in the bloodstream, the stealth surface of NPs also helps to maintain its stability. Poly(ethylene glycol) (PEG) on the surface of NPs would serve as a brush to inhibit serum protein adsorption [4]. The PEO block of F127 shares the same core structure as PEG; hence, the emergence of a form of PEG would likewise improve the pharmacokinetics of our NPs.

Second, the ligand attached to the nanoparticles would aid in the accumulation of nanoparticles within the cells. Numerous studies have employed different ligands to target overexpressed receptors on cancer cells, including folate receptors [13,37], integrins [36,37], and vascular endothelial growth factor (VEGF) receptors [38,39]. The folate receptor was selected as a targeting modality in our investigation. The findings of the uptake assays (Figure 3), fluorescent assay (Supporting Information File 1, Figure S2) and the cytotoxicity testing (Figure 4) revealed that F127-folate@NP and F127@NP had the same impact. However, both NPs produced superior outcomes than those for PVA@NP control. It has been demonstrated that F127 can enhance the cellular uptake of NPs in vitro via clathrin-mediated endocytosis and caveolae-mediated endocytosis [31,40]. The absorption of F127 onto nanoparticle surfaces would assist the NPs to enter the cells. Therefore, F127 has been used as a nanoparticle component for drug delivery. For example, doxorubicin-loaded L61/F127 NPs (SP1049C, Supratek Pharma Inc., Montreal, Canada) have reached phase three in clinical trials [41,42].

The F127-folate@NP has not shown a substantial increase in cell uptake, probably because of the excess of folate moiety on the NP surface. Due to its hydrophobicity, the folate moiety may bind to itself, reducing the targeting impact. In a recent investigation of PLGA nanoparticles, we discovered that PLGA nanoparticles did not develop when 100% PLGA-PEG-folate was employed [22]. When the weight ratio of PLGA-PEG and PLGA-PEG-folate was decreased from 50 to 1, the nanoparticles exhibited significantly improved uptake capabilities. The combination of F127 and F127-folate may thus be investigated in our next work. Another explanation could be that the cell culture media in the study was not suitable for the targeting of NPs due to the presence of folic acid in it. Therefore, using folic-acid-free cell culture media would be the option for targeting evaluation.

The uptake of both F127-folate@NP and F127@NP into the cells has shown the potential application not only for cancer therapy but also for diagnosis. First, the NPs are internalized into the cells and gradually degrade in the low pH of the endosomes releasing CHL to interrupt the cell cycle. Second, the NPs carry both imaging agents, IR780 and IO, which are suitable for near-infrared imaging and MRI. IR780 is used as the tracer during operation and also in phototherapy [23,24]. The IO NPs have been used as a contrast agent in MRI for diagnosis. Since MRI is a noninvasive and nonradiation technique, it could be used multiple times to follow therapy stages.

Conclusion

We have formulated F127@NP and F127-folate@NP nanoparticles coated with F127 and F127-folate, respectively, using the emulsion/evaporation technique. The synthesized NPs showed the appropriate size and charge for systematic applications. The NPs also showed the ability to carry therapeutic drugs and deliver them into cells. Besides, they also showed the potential to be used as imaging agents for tracing and diagnosis.

Supporting Information

Supporting Information File 1

Supplementary data.
[https://www.beilstein-journals.org/bjnano/content/supplementary/2190-4286-15-17-S1.pdf]

Funding

This research is funded by Vietnam National Foundation for Science and Technology Development (NAFOSTED) under grant number 104.01-2019.50.

Conflict of Interest

The authors confirm that there is no conflict of interest related to the article.

ORCID® iDs

Hieu Vu Quang - https://orcid.org/0000-0002-3468-5816

Data Availability Statement

All data that supports the findings of this study is available in the published article and/or the supporting information to this article.

References

1. Sarkar, C.; Kommineni, N.; Butreddy, A.; Kumar, R.; Bunekar, N.; Gugulothu, K. PLGA Nanoparticles in Drug Delivery. In *Nanoengineering of Biomaterials;* Jana, S.; Jana, S., Eds.; 2022; pp 217–260. doi:10.1002/9783527832095.ch8
2. Ruirui, Z.; He, J.; Xu, X.; Li, S.; Peng, H.; Deng, Z.; Huang, Y. *Mater. Res. Express* **2021,** *8,* 122002. doi:10.1088/2053-1591/ac3f5e
3. Bala, I.; Hariharan, S.; Kumar, M. N. V. R. *Crit. Rev. Ther. Drug Carrier Syst.* **2004,** *21,* 387–422. doi:10.1615/critrevtherdrugcarriersyst.v21.i5.20
4. Li, S.-D.; Huang, L. *J. Controlled Release* **2010,** *145,* 178–181. doi:10.1016/j.jconrel.2010.03.016
5. Yadav, B.; Chauhan, M.; Shekhar, S.; Kumar, A.; Mehata, A. K.; Nayak, A. K.; Dutt, R.; Garg, V.; Kailashiya, V.; Muthu, M. S.; Sonali; Singh, R. P. *Int. J. Pharm.* **2023,** *633,* 122587. doi:10.1016/j.ijpharm.2023.122587
6. Vu-Quang, H.; Yoo, M. K.; Cho, C. S.; Jeong, H. J.; Jeong, Y. Y.; Park, I. K. Immune Cells-Specific Delivery of Mannan-Coated Superparamagnetic Iron Oxide Nanoparticles for the Detection of Metastatic Lymph Node. In *2010 IEEE International Conference on Nano/Molecular Medicine and Engineering,* IEEE NANOMED 2010; 2010. doi:10.1109/nanomed.2010.5749825
7. Muthiah, M.; Vu-Quang, H.; Kim, Y.-K.; Rhee, J. H.; Kang, S. H.; Jun, S. Y.; Choi, Y.-J.; Jeong, Y. Y.; Cho, C.-S.; Park, I.-K. *Carbohydr. Polym.* **2013,** *92,* 1586–1595. doi:10.1016/j.carbpol.2012.11.011
8. Lu, Y.; Sega, E.; Leamon, C. P.; Low, P. S. *Adv. Drug Delivery Rev.* **2004,** *56,* 1161–1176. doi:10.1016/j.addr.2004.01.009
9. Thakor, A. S.; Jokerst, J. V.; Ghanouni, P.; Campbell, J. L.; Mittra, E.; Gambhir, S. S. *J. Nucl. Med.* **2016,** *57,* 1833–1837. doi:10.2967/jnumed.116.181362
10. Wu, L. C.; Zhang, Y.; Steinberg, G.; Qu, H.; Huang, S.; Cheng, M.; Bliss, T.; Du, F.; Rao, J.; Song, G.; Pisani, L.; Doyle, T.; Conolly, S.; Krishnan, K.; Grant, G.; Wintermark, M. *Am. J. Neuroradiol.* **2019,** *40,* 206–212. doi:10.3174/ajnr.a5896
11. Alphandéry, E. *RSC Adv.* **2019,** *9,* 40577–40587. doi:10.1039/c9ra08612a
12. Vu-Quang, H.; Muthiah, M.; Kim, Y.-K.; Cho, C.-S.; Namgung, R.; Kim, W. J.; Rhee, J. H.; Kang, S. H.; Jun, S. Y.; Choi, Y.-J.; Jeong, Y. Y.; Park, I.-K. *Carbohydr. Polym.* **2012,** *88,* 780–788. doi:10.1016/j.carbpol.2012.01.067
13. Vu-Quang, H.; Vinding, M. S.; Nielsen, T.; Ullisch, M. G.; Nielsen, N. C.; Nguyen, D.-T.; Kjems, J. *Polymers (Basel, Switz.)* **2019,** *11,* 743. doi:10.3390/polym11040743
14. Yang, C.; Vu-Quang, H.; Husum, D. M. U.; Tingskov, S. J.; Vinding, M. S.; Nielsen, T.; Song, P.; Nielsen, N. C.; Nørregaard, R.; Kjems, J. *Nanomedicine (N. Y., NY, U. S.)* **2017,** *13,* 2451–2462. doi:10.1016/j.nano.2017.08.007
15. Schleich, N.; Sibret, P.; Danhier, P.; Ucakar, B.; Laurent, S.; Muller, R. N.; Jérôme, C.; Gallez, B.; Préat, V.; Danhier, F. *Int. J. Pharm.* **2013,** *447,* 94–101. doi:10.1016/j.ijpharm.2013.02.042
16. Yi, X.; Yan, F.; Wang, F.; Qin, W.; Wu, G.; Yang, X.; Shao, C.; Chung, L. W. K.; Yuan, J. *Med. Sci. Monit.* **2015,** *21,* 511–517. doi:10.12659/msm.892437
17. Hoogstins, C. E. S.; Tummers, Q. R. J. G.; Gaarenstroom, K. N.; de Kroon, C. D.; Trimbos, J. B. M. Z.; Bosse, T.; Smit, V. T. H. B. M.; Vuyk, J.; van de Velde, C. J. H.; Cohen, A. F.; Low, P. S.; Burggraaf, J.; Vahrmeijer, A. L. *Clin. Cancer Res.* **2016,** *22,* 2929–2938. doi:10.1158/1078-0432.ccr-15-2640
18. Zhang, E.; Luo, S.; Tan, X.; Shi, C. *Biomaterials* **2014,** *35,* 771–778. doi:10.1016/j.biomaterials.2013.10.033
19. Ahmed, T.; Pai, M. V.; Mallik, E.; Varghese, G. M.; Ashish, S.; Acharya, A.; Krishna, A. *Ann. Med. Surg.* **2022,** *77,* 103602. doi:10.1016/j.amsu.2022.103602
20. Hou, K.-T.; Liu, T.-I.; Chiu, H.-C.; Chiang, W.-H. *Eur. Polym. J.* **2019,** *110,* 283–292. doi:10.1016/j.eurpolymj.2018.11.038
21. Yue, C.; Liu, P.; Zheng, M.; Zhao, P.; Wang, Y.; Ma, Y.; Cai, L. *Biomaterials* **2013,** *34,* 6853–6861. doi:10.1016/j.biomaterials.2013.05.071
22. Vu-Quang, H.; Vinding, M. S.; Nielsen, T.; Ullisch, M. G.; Nielsen, N. C.; Kjems, J. *Nanomedicine (N. Y., NY, U. S.)* **2016,** *12,* 1873–1884. doi:10.1016/j.nano.2016.04.010
23. Machado, M. G. C.; de Oliveira, M. A.; Lanna, E. G.; Siqueira, R. P.; Pound-Lana, G.; Branquinho, R. T.; Mosqueira, V. C. F. *Biomed. Pharmacother.* **2022,** *145,* 112464. doi:10.1016/j.biopha.2021.112464
24. Alves, C. G.; Lima-Sousa, R.; de Melo-Diogo, D.; Louro, R. O.; Correia, I. J. *Int. J. Pharm.* **2018,** *542,* 164–175. doi:10.1016/j.ijpharm.2018.03.020
25. Blair, H. A.; Deeks, E. D. *Drugs* **2015,** *75,* 2017–2024. doi:10.1007/s40265-015-0484-9
26. Barenholz, Y. (Chezy). *J. Controlled Release* **2012,** *160,* 117–134. doi:10.1016/j.jconrel.2012.03.020
27. Pieper, S.; Langer, K. *Mater. Today: Proc.* **2017,** *4,* S188–S192. doi:10.1016/j.matpr.2017.09.185
28. Dias, D. J. S.; Joanitti, G. A.; Azevedo, R. B.; Silva, L. P.; Lunardi, C. N.; Gomes, A. J. *J. Biophys. Chem.* **2015,** *6,* 1–13. doi:10.4236/jbpc.2015.61001
29. Costa, A. O.; Lunardi, C. N.; Gomes, A. J. *Curr. Nanomed.* **2020,** *10,* 63–75. doi:10.2174/2468187309666190823153341
30. Baiti, R. N.; Ardhyananta, H.; El Kirat, K. *Adv. Mater. Res.* **2015,** *1123,* 213–216. doi:10.4028/www.scientific.net/amr.1123.213
31. Li, M.; Tang, H.; Xiong, Y.; Yuan, Z.; He, L.; Han, L. *Colloids Surf., B* **2023,** *226,* 113328. doi:10.1016/j.colsurfb.2023.113328
32. Prokop, A.; Davidson, J. M. *J. Pharm. Sci.* **2008,** *97,* 3518–3590. doi:10.1002/jps.21270
33. Rizvi, S. A. A.; Saleh, A. M. *Saudi Pharm. J.* **2018,** *26,* 64–70. doi:10.1016/j.jsps.2017.10.012
34. Du, B.; Yu, M.; Zheng, J. *Nat. Rev. Mater.* **2018,** *3,* 358–374. doi:10.1038/s41578-018-0038-3
35. Longmire, M.; Choyke, P. L.; Kobayashi, H. *Nanomedicine (London, U. K.)* **2008,** *3,* 703–717. doi:10.2217/17435889.3.5.703
36. Graf, N.; Bielenberg, D. R.; Kolishetti, N.; Muus, C.; Banyard, J.; Farokhzad, O. C.; Lippard, S. J. *ACS Nano* **2012,** *6,* 4530–4539. doi:10.1021/nn301148e
37. Desgrosellier, J. S.; Cheresh, D. A. *Nat. Rev. Cancer* **2010,** *10,* 9–22. doi:10.1038/nrc2748
38. Golub, J. S.; Kim, Y.-t.; Duvall, C. L.; Bellamkonda, R. V.; Gupta, D.; Lin, A. S.; Weiss, D.; Robert Taylor, W.; Guldberg, R. E. *Am. J. Physiol.: Heart Circ. Physiol.* **2010,** *298,* H1959–H1965. doi:10.1152/ajpheart.00199.2009
39. Verheul, H. M. W.; Pinedo, H. M. *Clin. Breast Cancer* **2000,** *1,* S80–S84. doi:10.3816/cbc.2000.s.015
40. Arranja, A.; Denkova, A. G.; Morawska, K.; Waton, G.; van Vlierberghe, S.; Dubruel, P.; Schosseler, F.; Mendes, E. *J. Controlled Release* **2016,** *224,* 126–135. doi:10.1016/j.jconrel.2016.01.014

41. Armstrong, A.; Brewer, J.; Newman, C.; Alakhov, V.; Pietrzynski, G.; Campbell, S.; Corrie, P.; Ranson, M.; Valle, J. W. *J. Clin. Oncol.* **2006,** *24,* 4080. doi:10.1200/jco.2006.24.18_suppl.4080
42. Zhang, W.; Shi, Y.; Chen, Y.; Ye, J.; Sha, X.; Fang, X. *Biomaterials* **2011,** *32,* 2894–2906. doi:10.1016/j.biomaterials.2010.12.039

License and Terms

This is an open access article licensed under the terms of the Beilstein-Institut Open Access License Agreement (https://www.beilstein-journals.org/bjnano/terms), which is identical to the Creative Commons Attribution 4.0 International License (https://creativecommons.org/licenses/by/4.0). The reuse of material under this license requires that the author(s), source and license are credited. Third-party material in this article could be subject to other licenses (typically indicated in the credit line), and in this case, users are required to obtain permission from the license holder to reuse the material.

The definitive version of this article is the electronic one which can be found at:
https://doi.org/10.3762/bjnano.15.17

BEILSTEIN JOURNAL OF NANOTECHNOLOGY

Potential of a deep eutectic solvent in silver nanoparticle fabrication for antibiotic residue detection

Le Hong Tho[1,2,3], Bui Xuan Khuyen[4], Ngoc Xuan Dat Mai[2,3] and Nhu Hoa Thi Tran[*1,2]

Full Research Paper

Open Access

Address:
[1]Faculty of Materials Science and Technology, University of Science, Ho Chi Minh City, Vietnam, [2]Vietnam National University, Ho Chi Minh City, Vietnam, [3]Center for Innovative Materials and Architectures (INOMAR), Ho Chi Minh City, Viet Nam and [4]Institute of Materials Science, Vietnam Academy of Science and Technology, Hanoi, Vietnam

Email:
Nhu Hoa Thi Tran[*] - ttnhoa@hcmus.edu.vn

* Corresponding author

Keywords:
Ag NPs; antibiotic residue; deep eutectic solvents; potential; SERS

Beilstein J. Nanotechnol. **2024,** *15,* 426–434.
https://doi.org/10.3762/bjnano.15.38

Received: 22 December 2023
Accepted: 19 March 2024
Published: 16 April 2024

This article is part of the thematic issue "Recent advances in synthesis and applications of organometallic nanomaterials".

Guest Editor: T.-D. Nguyen

© 2024 Tho et al.; licensee Beilstein-Institut.
License and terms: see end of document.

Abstract

Deep eutectic solvents (DESs) have recently emerged as an alternative solvent for nanoparticle synthesis. There have been numerous advancements in the fabrication of silver nanoparticles (Ag NPs), but the potential of DESs in Ag NP synthesis was neither considered nor studied carefully. In this study, we present a novel strategy to fabricate Ag NPs in a DES (Ag NPs-DES). The DES composed of D-glucose, urea, and glycerol does not contain any anions to precipitate with Ag^+ cations. Our Ag NPs-DES sample is used in a surface-enhanced Raman scattering (SERS) sensor. The two analytes for SERS quantitation are nitrofurantoin (NFT) and sulfadiazine (SDZ) whose residues can be traced down to 10^{-8} M. The highest enhancement factors (EFs) are competitive at 6.29×10^7 and 1.69×10^7 for NFT and SDZ, respectively. Besides, the linearity coefficients are extremely close to 1 in the range of 10^{-8} to 10^{-3} M of concentration, and the SERS substrate shows remarkable uniformity along with great selectivity. This powerful SERS performance indicates that DESs have tremendous potential in the synthesis of nanomaterials for biosensor substrate construction.

Introduction

Surface-enhanced Raman scattering (SERS) is a ubiquitous technology for detecting and tracing substances, applied in various kinds of sensors. The spectra of SERS-based biosensors are simple but powerful results, in which every single component of the analytes can be recognized via characteristic vibrations of identical groups [1]. In particular, SERS is an advantageous and practical choice for biosensors in clinical settings thanks to fast response [2], the ability of real-time measurements [3], extremely high sensitivity [4], remarkable selectivity [5], and tremendous versatility [4,6,7]. Many scholars have taken advantage of these properties in cancer diagnosis [8], detection of hazardous chemicals [9], tracing of microor-

ganisms [7,10,11], and other analytical measurements regarding food, medical, and environmental issues [12-14]. Undeniably, SERS is the future for sensor design.

So far, most achievements regarding SERS rely on the development of plasmonic materials. Noble metals (e.g., Au, Ag, and Cu) are the most important group of plasmonic materials, which extensively respond to electromagnetic waves with proper wavelengths in terms of free electrons resonating to the incident waves [9,15]. This is the fundamental principle of surface plasmon resonance (SPR). Moreover, plasmons are easily controlled at the nanoscale through different sizes, shapes, and surface morphologies of nanoparticles [16]. At the contacts among adjacent nanoparticles, so-called "hot spots" form; here, electromagnetic fields are effectively enlarged, leading to localized surface plasmon resonance (LSPR) [1,17]. Crucial parts of SERS-based biosensors are commonly made of LSPR materials [17]. With the development of synthesis techniques, numerous nanostructures of noble metals have been extensively studied to improve the intrinsic parameters of sensors.

Silver nanoparticles (Ag NPs) exhibit great performance in sensing applications owing to the best LSPR properties among the noble metals [18]. One of the decisive factors regarding the SERS performance of Ag NP-based platforms is the agglomeration state of the nanoparticles [19], which directly affects the "hot spots". There have been many studies in which agglomeration of Ag NPs was adjusted by different kinds of surfactants such as cetyltrimethylammonium bromide [20,21], polyvinylpyrrolidone [18], and sodium dodecyl sulfate [21,22]. However, these chemicals have many negative effects on the environment including microbial, plant, soil, and marine ecosystems as reported by Rebello and co-workers [23]. This restricts the applicability of Ag NPs in the biomedical field and leads to the requirement for more eco-friendly products.

Recently, deep eutectic solvents (DESs) have been introduced to the chemical synthesis of nanomaterials. DESs show superior properties including high thermal stability, high polarity, low vapor pressure, and low toxicity, which makes DESs promising candidates for the replacement of thousands of industrial solvents [24,25]. DESs are so versatile that they have been used for nanomaterials synthesis [26,27]. Regarding plasmonic materials, gold nanoparticles (Au NPs) were the first to be fabricated in DESs [28,29]. SERS platforms based on Au NPs-DES whose sensitivity and durability are competitive to the other materials were successfully constructed [29,30]. However, no attention has been paid to the potential of DESs in the fabrication of Ag NPs. The similarities between Ag NPs and Au NPs, with the higher LSPR and SERS performance of Ag NPs [18,31], led to the innovative idea of Ag NPs synthesis in DESs.

In this work, we present a novel strategy to fabricate Ag NPs and demonstrate our hypothesis about the application of DESs in stabilizing Ag NPs. The resulting Ag NPs-DES is used for SERS detection of toxic antibiotics such as nitrofurantoin (NFT) and sulfadiazine (SDZ). These substances have been widely used since the 1970s because of rapid and absolute results against microbes [32], but they are also responsible for hormonal disruptions, methemoglobinemia, allergy, damaged liver, nausea, and cancer [33-36]. Despite these side effects, they are illegally overused in the food industry and medicine, which threatens the human food chain and negatively affects public health [37]. By evaluating the SERS parameters of the Ag NPs-DES substrate regarding the detection of NFT and SDZ, we demonstrate application aspects of our product, showing the great potential of DESs in sensing and biomedical applications.

Results and Discussion

Formation of Ag NPs-DES

We have developed new and simple strategy to fabricate Ag NPs-DES in which ascorbic acid was used as reducing agent. The synthesis protocol is summarily presented in Figure 1. Also, to characterize our material, UV–vis and XRD measurements were carried out. Figure 2A shows the broad adsorption

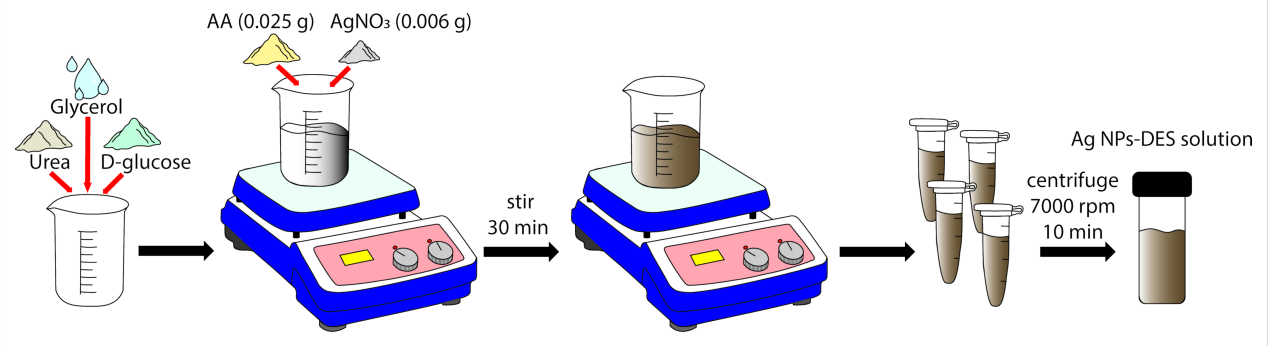


Figure 1: Schematic of the Ag NPs-DES synthesis.

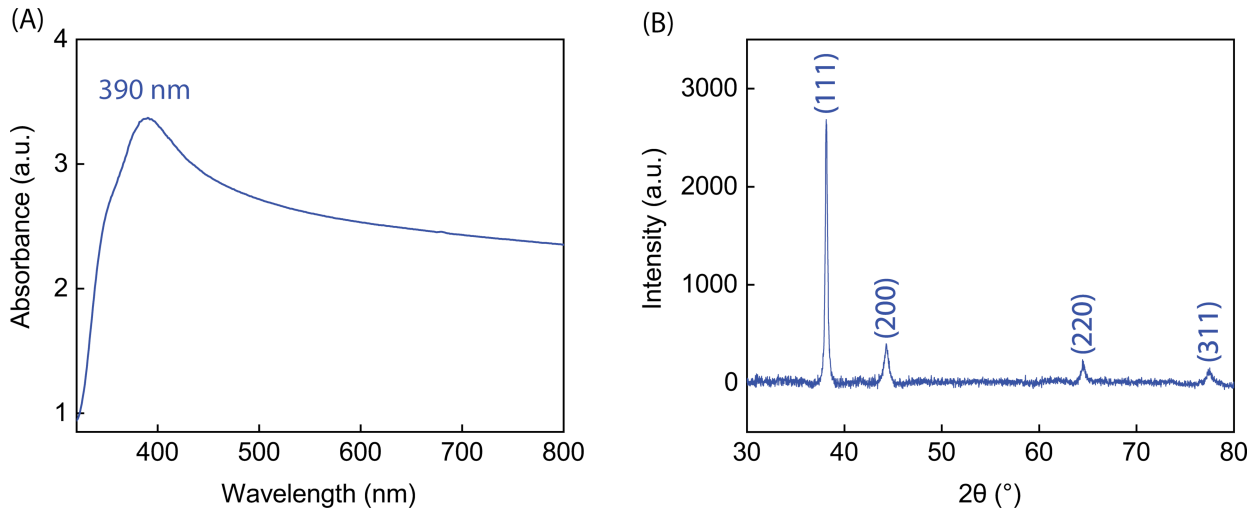


Figure 2: (A) UV–vis spectrum of the Ag NPs-DES solution. (B) XRD pattern of the Ag NPs-DES thin film.

band indicating the high number of excitons [38] on the surface of Ag NPs due to SPR. The SPR peak is located at 390 nm, which is suitable for SERS applications with 532 nm laser excitation. Besides, the shape of the UV–vis spectrum is in accordance with Mie scattering theory calculations, as reported in [39], proving the existence of Ag NPs in the solution. Moreover, the XRD pattern of the thin film (Figure 2B) shows four characteristic peaks at 38.2°, 44.3°, 64.4°, and 77.6°, corresponding to the (111), (200), (220), and (311) planes of face-centered cubic (fcc) Ag, respectively. The crystallite size is 30.61 nm, calculated from the most characteristic (111) peak of the Ag NPs [40]. From the presence of the fcc Ag lattice planes, we claim that Ag NPs-DES have been successfully synthesized [41].

The development of clusters into nanoparticles following our strategy is supported by the DES. DESs have been reported to be potential shape-controlling agents, and highly branched nanostructures were the most common [30]. In our procedure, $AgNO_3$ was added right after L-ascorbic acid was dissolved in the DES at room temperature. The color of the mixture gradually turned from yellow-orange to dark brown, indicating the crystallization of Ag NPs. The synthesized Ag NPs-DES exhibits rod-like shapes of the NPs as well as a high aggregation state (Figure 3A). This is because of the high viscosity of the DES, which directly affected the stirring and yielded nonspherical NP shapes. The aggregated Ag NPs are supported by pure DES in which oxygen and hydrogen atoms of D-glucose, urea, and glycerol tend to form hydrogen bonds. The DES acts as a surfactant helping to stabilize Ag NPs. The rod-like appearance with 122.6 nm average length and small crystals on the surface of Ag NPs crucially contribute to strengthening the LSPR phenomenon thanks to the lightning rod effect [42]. As reported by other scholars, the rod-like morphology is better than a spherical one at increasing the extinction coefficient, about 10^9 to 10^{11} $M^{-1}{\cdot}cm^{-1}$ higher [43,44], which proves the applicability of

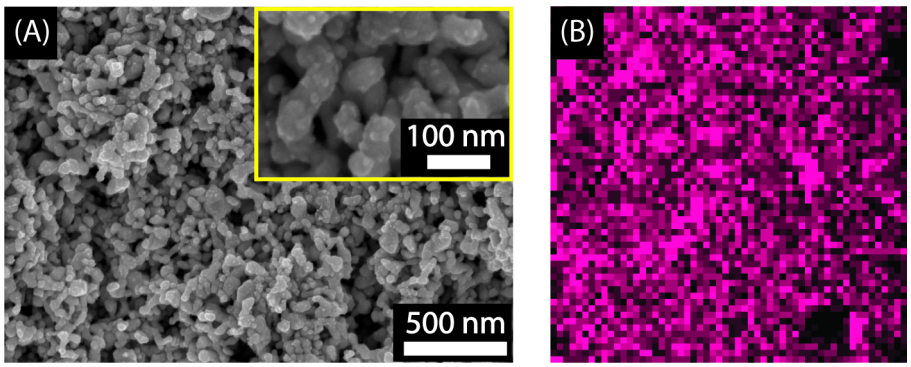


Figure 3: (A) SEM images of Ag NPs-DES. (B) XRF mapping of the Ag NPs-DES thin film with pink dots representing silver.

Ag NPs-DES in SERS biosensors. Furthermore, X-ray fluorescence mapping was used to evaluate the presence of silver in the thin film (Figure 3B). The uniform distribution of silver shows the uniformity of Ag NPs-DES thin film on the glass substrate, which is crucial for the applicability of this material.

NFT detection

The most fundamental component of a SERS-based biosensor is its SERS substrate. It directly affects the SERS performance of the biosensor [6]. Herein, the Ag NPs-DES thin film with the superiorly uniform Ag NPs-DES coating can be used as a SERS substrate for the analysis of antibiotics. First, residue tracing of nitrofurantoin (NFT) has been conducted in the range from 10^{-3} M down to 10^{-8} M (Figure 4A). At the limit of detection (LOD) of 10^{-8} M, the SERS spectrum clearly shows emerging peaks, the highest enhancement factor (EF) of which reaches 6.29×10^7, proving the NFT residue tracing capability of the Ag NPs-DES substrate. These peaks correspond to vibrations of characteristic groups of NFT as reported in Table 1 with the most intense ones at 1580 and 1321 cm^{-1}. Consequently, these two peaks were used to construct the calibration curves as shown in Figure 4B. The R^2 values for 1580 and 1321 cm^{-1} are 0.9956 and 0.9993, respectively, which is close to the ideal value of 1. This indicates that the Ag NPs-DES substrate is sensitive and can be used for quantitative analysis of NFT following the two linear fitting equations:

$$I_{1580} = 3265.6 \log[\mathrm{NFT}] + 29828 \quad (1)$$

$$I_{1321} = 2067.6 \log[\mathrm{NFT}] + 19071 \quad (2)$$

Table 1: Vibrational modes assigned to specific peaks in Raman spectra of selected antibiotics.

Chemicals	Frequency (cm^{-1})	Assignment[a]	Ref.
NFT	1580	ν N–N=C, ν $–NO_2$	[45,46]
	1321	ω N–H	
	1162	ρ (furan ring)	
	998	ρ (hydantoin ring)	
	787	ν C–H	
SDZ	1567	ω N–H, ν (benzene ring)	[47]
	1356	ν C–N	
	1055	ν S=O	
	856	τ (pyrimidine ring)	
	610	ω (benzene ring)	

[a]ν: streching; ω: bending; τ: torsion; ρ: deformation.

For further investigations on the SERS performance of the Ag NPs-DES thin film, NFT was again selected to test the stability. In practice, a stable SERS substrate is not only able to withstand the conditions of storage but also exhibits consistent Raman signals over the surface of the coating. Drops of 10^{-6} M NFT were placed on six different spots of the Ag NPs-DES substrate (Figure 5A). Then, the SERS spectra were analyzed by considering the variation of peak intensity of the two Raman peaks at 1580 and 1321 cm^{-1}. In the diagram shown in Figure 5B, the yellow lines indicate the average intensity, while the areas covering all points represent the deviation. The peaks show a comparatively low relative standard deviation (RSD), namely 11.95% for 1580 cm^{-1} and 4.69% for 1321 cm^{-1}. In addition, SERS mapping of 10^{-6} M NFT investigated on the sub-

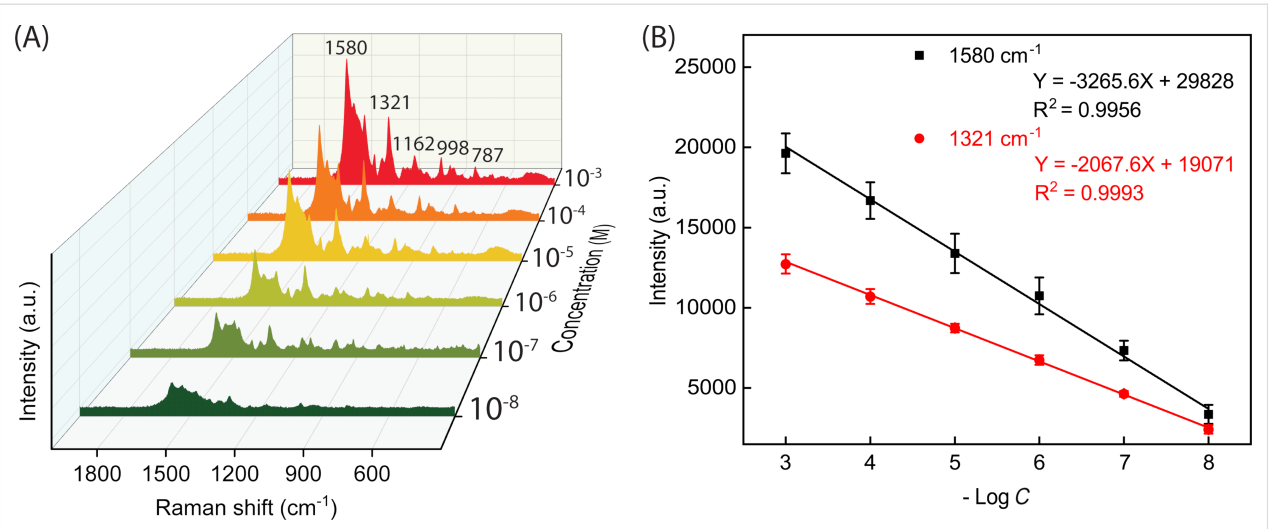


Figure 4: (A) SERS performance of the Ag NPs-DES substrate in detecting different concentrations of NFT. (B) Linear fit of –log *C* and peak intensities at 1580 and 1321 cm^{-1} (*C* stands for the concentration of NFT).

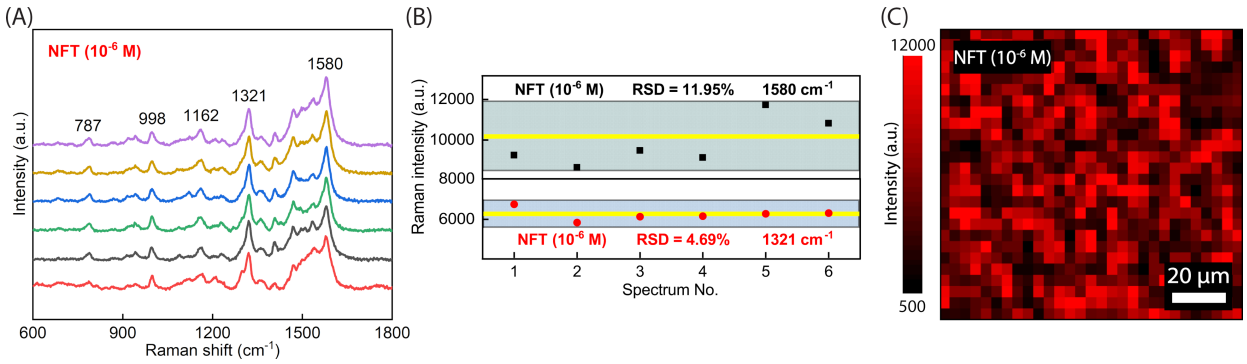


Figure 5: (A) SERS spectra at different points of the Ag NPs-DES substrate. (B) Variation of peak intensity at the two chosen wavenumbers. (C) SERS mapping of NFT (10^{-6} M) detected on the Ag NPs-DES substrate.

strate also helps to provide a larger scope on the uniformity of SERS signals. As shown in Figure 5C, there are plenty of high-intensity dots corresponding to signal enhancement by the Ag NPs-DES substrate, and the very even distribution indicates good uniformity, that is, satisfactory stability. These results can be explained by the LSPR of the rod-like Ag NPs synthesized in DES, which plays an important role in the high intensity [48] and the uniformity of the Ag NPs-DES coating proven in Figure 3B.

SDZ detection and selectivity of Ag NPs-DES substrate

Another antibiotic commonly used in infectious disease treatment is sulfadiazine (SDZ). Both NFT and SDZ are effective antimicrobial substances, but their overuse statuses were reported to be hazardous as mentioned above. Since their molecular structures are partially different [36,49], SERS analysis is meaningful for the selectivity test of the Ag NPs-DES substrate. In our study, different concentrations of SDZ were measured on the substrate to find out the LOD (Figure 6A). Collected peak intensity data were also used to construct the calibration curves shown in Figure 6B. The substrate shows a linear range from 10^{-3} to 10^{-8} M, in which the LOD value is 10^{-8} M, and the highest EF reaches 1.69×10^7. The vibrational modes of the assigned peaks are listed in Table 1. There are two clearly enhanced peaks at 1567 and 1055 cm^{-1}, whose correlation factors R^2 are equal to 0.9984 and 0.9904, respectively. Along with the parameters of NFT SERS analysis obtained previously, these high R^2 values help to provide undeniable proof of the remarkable quantity ability of our Ag NPs-DES substrate in antibiotic residue tracing. The linear regressions of the two chosen analytical peaks of SDZ are as follows:

$$I_{1567} = 3340.5 \log[\mathrm{SDZ}] + 29771 \quad (3)$$

$$I_{1055} = 2006.6 \log[\mathrm{SDZ}] + 16562 \quad (4)$$

Although the consistency in SERS signals recorded on the Ag NPs-DES substrate has been investigated with 10^{-6} M NFT, we need to evaluate the SERS mapping image of SDZ to ensure the

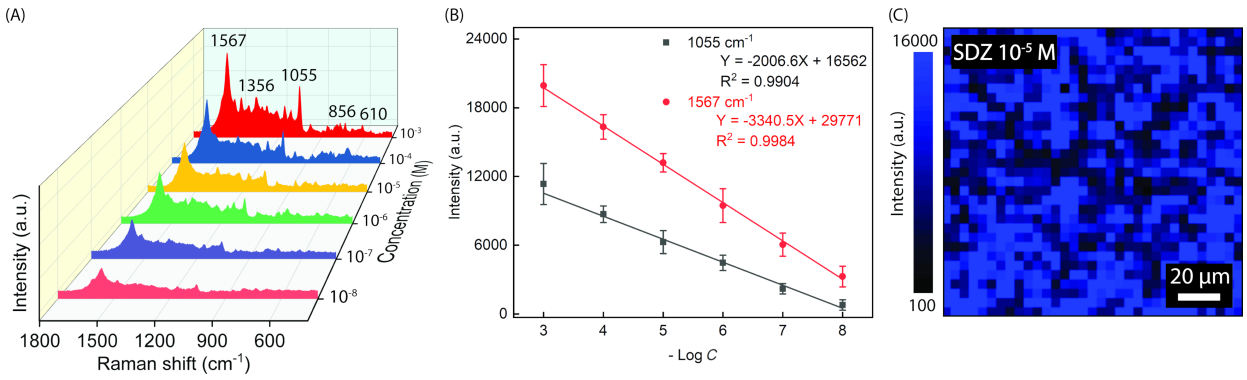


Figure 6: (A) SERS spectra of SDZ in the concentration range from 10^{-3} to 10^{-8} M. (B) Linear fit of SDZ concentrations and intensity of the peaks at 1055 and 1567 cm^{-1}. (C) SERS mapping of 10^{-5} M SDZ on the Ag NPs-DES substrate.

stability of our substrate when analytes are changed. Hence, 10^{-5} M of SDZ was added dropwise and let dry naturally before the laser excitation. The SERS mapping shown in Figure 6C shows an even distribution of high intensity over the entire considered surface. This shows that the Ag NPs-DES coating has good consistency despite the different analytes. DES is supposed to play a crucial role in dispersing the Ag NP suspension via its hydrogen bonding networks [30], which increases the possibility of linkage formation between $-NH_2$ groups of 3-aminopropyl)triethoxysilane (APTES) and Ag NPs. This eventually explains the evenness of the Ag NPs-DES thin film.

Another type of selectivity test was carried out with a solution containing 10^{-5} M NFT and 10^{-5} M SDZ. The SERS spectrum in Figure 7A verifies the difference in Raman shifts among the characteristic peaks of the two analytes. Here, the blue diamonds represent SDZ's key peaks, whereas the red arrows stand for the ones of NFT. With the presence of all characteristic peaks, NFT is effortless to detect in the solution thanks to the high intensity. In contrast, the SERS spectrum of SDZ shows solely three peaks instead of the common five. Additionally, the two most intense peaks of NFT at 1580 cm^{-1} and SDZ at 1567 cm^{-1} overlap, which makes it difficult to ascertain the intensity for quantitative determination (Figure 7B). Therefore, we propose the peaks at 1321 cm^{-1} of NFT and 1055 cm^{-1} of SDZ as alternatives. Their intensity is comparable to the base of the SERS spectrum, and they are separated from each other as well as from the others. Based on the data experimentally collected and the correlation between $-\log C$ and peak intensity as given in Equation 2 and Equation 4, the concentrations of NFT and SDZ can be determined. This surely can be applied to other solutions of various substances, indicating that the Ag NPs-DES substrate has a good selectivity. Moreover, compared to other studies on NFT and SDZ detection (Table 2), the Ag NPs-DES material shows competitive LOD values and a linear range. Thus, Ag NPs-DES is a promising candidate in SERS applications along with the tremendous potential of DES in Ag NPs fabrication.

Conclusion

In this study, we have proposed a novel strategy for Ag NP synthesis in a DES composed of D-glucose, glycerol, and urea. The Ag NPs-DES sample was prepared successfully through chemical reduction, in which DES acts as solvent and shape-controlling agent. Using NFT and SDZ as probe molecules, the SERS performance of Ag NPs-DES was discussed. The LOD value is 10^{-8} M for the detection of NFT and SDZ. The EF values are relatively high, 6.29×10^7 for NFT and 1.69×10^7 for SDZ, and the linearity coefficients are very close to 1, proving the quantitative residue tracing capabilities of the synthesized Ag NPs-DES substrate. Besides the high sensitivity, the sensor exhibits also uniformity of the coating, consistency in SERS signals, and good selectivity. Overall, Ag NPs-DES is a promising candidate for SERS-based biosensor applications. This work hopefully provides useful information about the potential of DES in nanomaterials fabrication and a possible guidance for low-cost and effective SERS substrate construction in biosensors.

Experimental

Chemicals

L-Ascorbic acid (AA, $C_6H_8O_6$, 99%), silver nitrate ($AgNO_3$, 99%), (3-aminopropyl)triethoxysilane (APTES, 99%), NFT

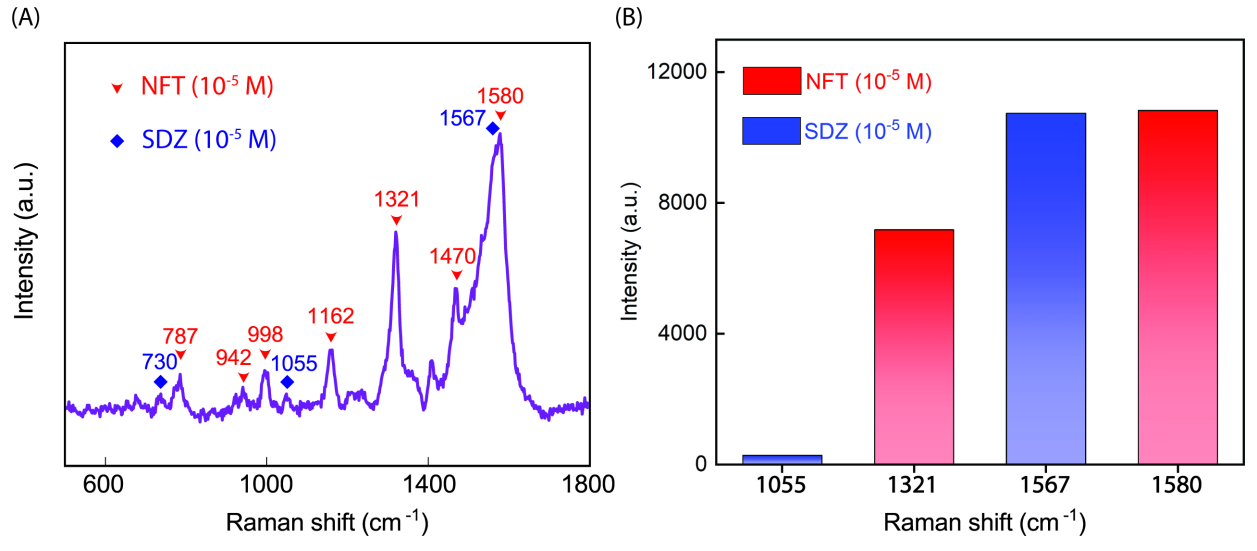


Figure 7: (A) SERS spectrum of NFT (10^{-5} M) and SDZ (10^{-5} M) solution. (B) Specific peak intensity identification corresponding to NFT and SDZ.

Table 2: An overview of reported studies on NFT and SDZ detection.

Analyte	Material	Year	LOD	Linear range	Ref.
NFT	Au NPs/GO	2021	5 ng/mL	5–500 ng/mL	[46]
	BT/CNF/GCE	2021	5×10^{-9} M	4.5×10^{-4} to 6×10^{-8} M	[50]
	N-CQD@Co_3O_4/MWCNT	2020	4.4×10^{-8} M	1.22×10^{-3} to 5×10^{-8} M	[51]
	NiO/BCN	2019	10^{-8} M	2.3×10^{-4} to 5×10^{-8} M	[52]
	Ag NPs-DES	2023	10^{-8} M	10^{-3} to 10^{-8} M	this work
SDZ	$SrWO_4$	2021	9×10^{-9} M	2.35×10^{-4} to 5×10^{-8} M	[53]
	Au NPs	2021	1 µg/L	1–100 µg/L	[49]
	RGO/Ag - coated alloy fiber	2019	1.9 ng/cm^3	0.01–100 µg/cm^3	[54]
	MIP - QDs	2019	6.7×10^{-7} M	4×10^{-6} to 2×10^{-5} M	[55]
	Ag NPs-DES	2023	10^{-8} M	10^{-3} to 10^{-8} M	this work

($C_8H_6N_4O_5$, 98%), and SDZ ($C_{10}H_{10}N_4O_2S$, 99%) were purchased from Sigma-Aldrich Co., MO, USA. Urea (CH_4N_2O, 99%) was obtained from ACS, Reag. Ph Eur, Merck Co., Germany, whereas glycerol ($C_3H_8O_3$, 99%) was supplied by Daejung Ltd., Korea. D-glucose ($C_6H_{12}O_6$, 99%) was purchased from Fisher Ltd., UK. The microscope glass slides (SiO_2, Na_2O, CaO, and MgO) were manufactured by ISOLAB Laborgeräte GmbH, Eschau, Germany.

Fabrication of DES and Ag NPs-DES

The most ubiquitous DES studied vastly in recent years is reline, composed of urea and choline chloride in a 2:1 molar ratio [24]. However, this substance is not appropriate for Ag NPs synthesis because of the Cl^- anions in choline chloride, which may unintentionally cause AgCl precipitation. Here, we chose an alternative DES [56] without any anions precipitating with Ag^+ cations. D-glucose, urea, and glycerol (molar ratio 1:1:2) were mixed and magnetically stirred at relatively high temperature until a homogenous liquid formed. Then, the mixture was cooled down gradually to room temperature while keeping the vigorous stirring. 0.025 g of AA was dissolved in 10.195 g of fabricated DES, and 0.006 g of $AgNO_3$ was added later, which helped the reaction to occur. After 30 min of constant stirring, the obtained Ag NPs-DES were washed with DI water several times, and the pellets were re-dispersed in DI water for further use.

The Ag NPs-DES thin film was prepared following the procedure for self-assembly monolayer construction. A clean glass substrate was treated with oxygen plasma to form reactive –OH groups on the surface. The substrate was then soaked in a 3% ethanolic solution of APTES for 2 h, which helped to stabilize the $–NH_2$ groups. A total of 2 mL of Ag NPs-DES solution was used to deposit Ag NPs on the glass substrate via Ag–NH_2 linkage by fully immersing the treated glass for 2 h. At last, the product was dried naturally at room temperature, resulting in the successful fabrication of the Ag NPs-DES substrate.

NFT and SDZ detection on the Ag NPs-DES substrate

Various concentrations from 10^{-3} to 10^{-8} M of NFT and SDZ were added dropwise on the Ag NPs-DES substrate (20 µL for each measurement). The analyte was then dried at room temperature, and the Raman spectra were recorded via laser excitation at 532 nm. Other investigations on the SERS performance of our sample were also carried out, including Raman mapping, signal consistency, uniformity, and selectivity.

Instrument characterization and apparatus

The absorbance properties of the sample were recorded using a V-730 UV–vis–NIR spectrophotometer supplied by JASCO, Japan. The crystallinity of the Ag NPs-DES thin film was determined using a D8 Advance diffractometer, Bruker, UK, with a Ni-filtered Cu Kα X-ray source. To evaluate the nanostructure and surface morphology of the nanoparticles, as well as the elemental distribution of silver on the substrate, a S4800 field-emission scanning electron microscope purchased from Hitachi, Japan, and an M4 TORNADO^{Plus} Micro X-ray fluorescence spectrometer with a Rh tube at 30 W micro-focus light element from Bruker, UK, were used. Raman spectra were collected with a XploRA ONE spectroscope (HORIBA, Japan), with a laser wavelength of 532 nm, 1 mW power, and an accumulation number of 60.

Funding

This research was funded by University of Science, VNU-HCM under grant number T2023-149.

Conflict of Interest

The authors declare that they have no known competing financial interests or personal relationships that could have influenced the work reported in this paper.

Author Contributions

Le Hong Tho: data curation; methodology; software; validation; writing – original draft. Bui Xuan Khuyen: methodology; software; validation; visualization. Ngoc Xuan Dat Mai: data curation; formal analysis; validation. Nhu Hoa Thi Tran: conceptualization; data curation; resources; supervision; writing – original draft; writing – review & editing.

ORCID® iDs

Ngoc Xuan Dat Mai - https://orcid.org/0000-0001-6752-4173
Nhu Hoa Thi Tran - https://orcid.org/0000-0002-1530-2402

Data Availability Statement

The data that supports the findings of this study is available from the corresponding author upon reasonable request.

Preprint

A non-peer-reviewed version of this article has been previously published as a preprint: https://doi.org/10.3762/bxiv.2023.65.v1

References

1. Alvarez-Puebla, R. A.; Liz-Marzán, L. M. *Small* **2010,** *6,* 604–610. doi:10.1002/smll.200901820
2. Zhao, B.; Yang, T.; Qu, Y.; Mills, A. J.; Zhang, G.; He, L. *Sci. Total Environ.* **2020,** *716,* 137097. doi:10.1016/j.scitotenv.2020.137097
3. Liu, J.; Zheng, T.; Tian, Y. *Angew. Chem., Int. Ed.* **2019,** *58,* 7757–7761. doi:10.1002/anie.201902776
4. Arabi, M.; Ostovan, A.; Wang, Y.; Mei, R.; Fu, L.; Li, J.; Wang, X.; Chen, L. *Nat. Commun.* **2022,** *13,* 5757. doi:10.1038/s41467-022-33448-w
5. Lin, D.; Dong, R.; Li, P.; Li, S.; Ge, M.; Zhang, Y.; Yang, L.; Xu, W. *Talanta* **2020,** *218,* 121157. doi:10.1016/j.talanta.2020.121157
6. Liang, X.; Li, N.; Zhang, R.; Yin, P.; Zhang, C.; Yang, N.; Liang, K.; Kong, B. *NPG Asia Mater.* **2021,** *13,* 8. doi:10.1038/s41427-020-00278-5
7. Saviñon-Flores, F.; Méndez, E.; López-Castaños, M.; Carabarin-Lima, A.; López-Castaños, K. A.; González-Fuentes, M. A.; Méndez-Albores, A. *Biosensors* **2021,** *11,* 66. doi:10.3390/bios11030066
8. Li, L.; Jiang, R.; Shan, B.; Lu, Y.; Zheng, C.; Li, M. *Nat. Commun.* **2022,** *13,* 5249. doi:10.1038/s41467-022-32975-w
9. La Ngoc Tran, N.; Van Hoang, D.; Tuan Thanh Pham, A.; Tran Truc Phuong, N.; Xuan Dat Mai, N.; Chi, T. T. K.; Hien, B. T. T.; Bach Phan, T.; Tran, N. H. T. J. *J. Sci.: Adv. Mater. Devices* **2023,** *8,* 100584. doi:10.1016/j.jsamd.2023.100584
10. Eskandari, V.; Sahbafar, H.; Zeinalizad, L.; Hadi, A. *ISSS J. Micro Smart Syst.* **2022,** *11,* 363–382. doi:10.1007/s41683-022-00103-x
11. Xia, J.; Li, W.; Sun, M.; Wang, H. *Nanomaterials* **2022,** *12,* 3572. doi:10.3390/nano12203572
12. Lin, D. Y.; Yu, C. Y.; Ku, C. A.; Chung, C. K. *Micromachines* **2023,** *14,* 1343. doi:10.3390/mi14071343
13. Schlücker, S. *ChemPhysChem* **2009,** *10,* 1344–1354. doi:10.1002/cphc.200900119
14. Nguyen, D.-K.; Dinh, V.-P.; Dang, N. T.; Khan, D. T.; Hung, N. T.; Thi Tran, N. H. *RSC Adv.* **2023,** *13,* 20565–20574. doi:10.1039/d3ra02552g
15. Chegel, V. I.; Lopatynskyi, A. M., Eds. *Molecular Plasmonics;* Jenny Stanford Publishing: New York City, NY, U.S.A., 2020. doi:10.1201/9780429295119
16. Nickelson, L. *Electromagnetic Theory and Plasmonics for Engineers;* Springer: Singapore, 2018. doi:10.1007/978-981-13-2352-2
17. Xu, T.; Geng, Z. *Biosens. Bioelectron.* **2021,** *174,* 112850. doi:10.1016/j.bios.2020.112850
18. Truc Phuong, N. T.; Dang, V. Q.; Van Hieu, L.; Bach, T. N.; Khuyen, B. X.; Thi Ta, H. K.; Ju, H.; Phan, B. T.; Thi Tran, N. H. *RSC Adv.* **2022,** *12,* 31352–31362. doi:10.1039/d2ra06074d
19. Zook, J. M.; Rastogi, V.; MacCuspie, R. I.; Keene, A. M.; Fagan, J. *ACS Nano* **2011,** *5,* 8070–8079. doi:10.1021/nn202645b
20. Iqbal, N.; Iqubal, S. M. S.; Khan, A. A.; Mohammed, T.; Alshabi, A. M.; Aazam, E. S.; Rafiquee, M. Z. A. *J. Mol. Liq.* **2021,** *329,* 115537. doi:10.1016/j.molliq.2021.115537
21. AL-Thabaiti, S. A.; Al-Nowaiser, F. M.; Obaid, A. Y.; Al-Youbi, A. O.; Khan, Z. *Colloids Surf., B* **2008,** *67,* 230–237. doi:10.1016/j.colsurfb.2008.08.022
22. Naseem, K.; Ali, F.; Tahir, M. H.; Afaq, M.; Yasir, H. M.; Ahmed, K.; Aljuwayid, A. m.; Habila, M. A. *J. Mol. Struct.* **2022,** *1262,* 132996. doi:10.1016/j.molstruc.2022.132996
23. Rebello, S.; Asok, A. K.; Mundayoor, S.; Jisha, M. S. *Environ. Chem. Lett.* **2014,** *12,* 275–287. doi:10.1007/s10311-014-0466-2
24. Smith, E. L.; Abbott, A. P.; Ryder, K. S. *Chem. Rev.* **2014,** *114,* 11060–11082. doi:10.1021/cr300162p
25. Hikmawanti, N. P. E.; Ramadon, D.; Jantan, I.; Mun'im, A. *Plants* **2021,** *10,* 2091. doi:10.3390/plants10102091
26. Abo-Hamad, A.; Hayyan, M.; AlSaadi, M. A. H.; Hashim, M. A. *Chem. Eng. J.* **2015,** *273,* 551–567. doi:10.1016/j.cej.2015.03.091
27. Das, N.; Kumar, A.; Rayavarapu, R. G. *Beilstein J. Nanotechnol.* **2021,** *12,* 924–938. doi:10.3762/bjnano.12.69
28. Liao, H.-G.; Jiang, Y.-X.; Zhou, Z.-Y.; Chen, S.-P.; Sun, S.-G. *Angew. Chem., Int. Ed.* **2008,** *47,* 9100–9103. doi:10.1002/anie.200803202
29. Raghuwanshi, V. S.; Ochmann, M.; Hoell, A.; Polzer, F.; Rademann, K. *Langmuir* **2014,** *30,* 6038–6046. doi:10.1021/la500979p
30. Mahyari, F. A.; Tohidi, M.; Safavi, A. *Mater. Res. Express* **2016,** *3,* 095006. doi:10.1088/2053-1591/3/9/095006
31. Lismont, M.; Dreesen, L. *Mater. Sci. Eng., C* **2012,** *32,* 1437–1442. doi:10.1016/j.msec.2012.04.023
32. Zhang, Y.; Yu, Z.; Yue, Z.; Gao, J.; Wu, S.; Zhang, Z.; Li, G. *J. Raman Spectrosc.* **2019,** *50,* 1094–1102. doi:10.1002/jrs.5636
33. Kabbara, W. K.; Kordahi, M. C. *J. Infect. Publ. Health* **2015,** *8,* 309–313. doi:10.1016/j.jiph.2015.01.007
34. Lewkowski, J.; Rogacz, D.; Rychter, P. *Chemosphere* **2019,** *222,* 381–390. doi:10.1016/j.chemosphere.2019.01.144
35. Wu, W.; Mehedi Hassan, M.; Ding, X.; Wu, J.; Ouyang, Q.; Chen, Q. *Microchem. J.* **2023,** *191,* 108765. doi:10.1016/j.microc.2023.108765

36. Mariyappan, V.; Keerthi, M.; Chen, S.-M.; Jeyapragasam, T. *J. Colloid Interface Sci.* **2021,** *600,* 537–549. doi:10.1016/j.jcis.2021.05.035
37. Ezhil Vilian, A. T.; Hwang, S.-K.; Bhaskaran, G.; Alhammadi, M.; Kim, S.; Tiwari, J. N.; Suk Huh, Y.; Han, Y.-K. *Chem. Eng. J.* **2023,** *454,* 139980. doi:10.1016/j.cej.2022.139980
38. Hou, Y.; Zhang, W.; Li, S.; Wang, Z.; Zhong, H.; Liu, Z.; Guo, Z. *Analyst* **2018,** *143,* 3677–3685. doi:10.1039/c8an00405f
39. Perkampus, H.-H. *UV-VIS Spectroscopy and Its Applications;* Springer Lab Manuals; Springer: Berlin Heidelberg, 1992. doi:10.1007/978-3-642-77477-5
40. Sharbaf Moghadas, M. R.; Motamedi, E.; Nasiri, J.; Naghavi, M. R.; Sabokdast, M. *Heliyon* **2020,** *6,* E04730. doi:10.1016/j.heliyon.2020.e04730
41. Tran Truc Phuong, N.; Xoan Hoang, T.; La Ngoc Tran, N.; Gia Phuc, L.; Phung, V.-D.; Kieu Thi Ta, H.; Ngoc Bach, T.; Hoa Thi Tran, N.; The Loan Trinh, K. *Spectrochim. Acta, Part A* **2021,** *263,* 120179. doi:10.1016/j.saa.2021.120179
42. He, L.; Rahaman, M.; Madeira, T. I.; Zahn, D. R. T. *Nanomaterials* **2021,** *11,* 376. doi:10.3390/nano11020376
43. Murphy, C. J.; Gole, A. M.; Hunyadi, S. E.; Stone, J. W.; Sisco, P. N.; Alkilany, A.; Kinard, B. E.; Hankins, P. *Chem. Commun.* **2008,** *8,* 544–557. doi:10.1039/b711069c
44. Xia, Y. *Anal. Bioanal. Chem.* **2016,** *408,* 2813–2825. doi:10.1007/s00216-015-9203-3
45. Chen, J.; Li, S.; Yao, F.; Xu, W.; Li, Y.; Chen, Q.; Liang, P. *Chemosensors* **2023,** *11,* 232. doi:10.3390/chemosensors11040232
46. Wang, Y.; Chen, H.; Jiang, L. *Analyst* **2021,** *146,* 5740–5746. doi:10.1039/d1an01185e
47. Shen, X.-R.; Zheng, H.; Pang, R.; Liu, G.-K.; Wu, D.-Y.; Tian, Z.-Q. *J. Phys. Chem. A* **2019,** *123,* 9199–9208. doi:10.1021/acs.jpca.9b07346
48. Francis, M. K.; Sahu, B. K.; Bhargav, P. B.; C, B.; Ahmed, N.; Das, A.; Dhara, S. *Phys. E (Amsterdam, Neth.)* **2022,** *137,* 115080. doi:10.1016/j.physe.2021.115080
49. Zhou, Z.-m.; Zheng, H.; Liu, T.; Xie, Z.-z.; Luo, S.-h.; Chen, G.-y.; Tian, Z.-q.; Liu, G.-k. *Anal. Chem. (Washington, DC, U. S.)* **2021,** *93,* 8603–8612. doi:10.1021/acs.analchem.1c01530
50. Nataraj, N.; Chen, S.-M. *J. Electroanal. Chem.* **2021,** *887,* 115152. doi:10.1016/j.jelechem.2021.115152
51. Muthusankar, G.; Devi, R. K.; Gopu, G. *Biosens. Bioelectron.* **2020,** *150,* 111947. doi:10.1016/j.bios.2019.111947
52. Kokulnathan, T.; Wang, T.-J. *Composites, Part B* **2019,** *174,* 106914. doi:10.1016/j.compositesb.2019.106914
53. Kokulnathan, T.; Kumar, E. A.; Wang, T.-J.; Cheng, I.-C. *Ecotoxicol. Environ. Saf.* **2021,** *208,* 111516. doi:10.1016/j.ecoenv.2020.111516
54. Cui, J.; Chen, S.; Ma, X.; Shao, H.; Zhan, J. *Microchim. Acta* **2019,** *186,* 19. doi:10.1007/s00604-018-3105-y
55. Shi, T.; Tan, L.; Fu, H.; Wang, J. *Mar. Pollut. Bull.* **2019,** *146,* 591–597. doi:10.1016/j.marpolbul.2019.07.010
56. Zdanowicz, M. *Int. J. Biol. Macromol.* **2021,** *176,* 387–393. doi:10.1016/j.ijbiomac.2021.02.039

License and Terms

This is an open access article licensed under the terms of the Beilstein-Institut Open Access License Agreement (https://www.beilstein-journals.org/bjnano/terms), which is identical to the Creative Commons Attribution 4.0 International License (https://creativecommons.org/licenses/by/4.0). The reuse of material under this license requires that the author(s), source and license are credited. Third-party material in this article could be subject to other licenses (typically indicated in the credit line), and in this case, users are required to obtain permission from the license holder to reuse the material.

The definitive version of this article is the electronic one which can be found at:
https://doi.org/10.3762/bjnano.15.38

BEILSTEIN JOURNAL OF NANOTECHNOLOGY

Photocatalytic degradation of methylene blue under visible light by cobalt ferrite nanoparticles/graphene quantum dots

Vo Chau Ngoc Anh[1,2], Le Thi Thanh Nhi[3,4], Le Thi Kim Dung[1], Dang Thi Ngoc Hoa[1], Nguyen Truong Son[1], Nguyen Thi Thao Uyen[2], Nguyen Ngoc Uyen Thu[2], Le Van Thanh Son[5], Le Trung Hieu[2], Tran Ngoc Tuyen[*2] and Dinh Quang Khieu[*2]

Full Research Paper

Open Access

Address:
[1]University of Pharmacy and Medicine, Hue University, Vietnam, [2]University of Sciences, Hue University, Vietnam, [3]Center for Advanced Chemistry, Institute of Research & Development, Duy Tan University, Vietnam, [4]Faculty of Natural Sciences, Duy Tan University, Vietnam and [5]University of Education and Science, The University of Danang, Vietnam

Email:
Tran Ngoc Tuyen[*] - tntuyen@hueuni.edu.vn;
Dinh Quang Khieu[*] - dqkhieu@hueuni.edu.vn

* Corresponding author

Keywords:
cobalt ferrite; graphene quantum dots; methylene blue

Beilstein J. Nanotechnol. **2024,** *15,* 475–489.
https://doi.org/10.3762/bjnano.15.43

Received: 28 January 2024
Accepted: 26 March 2024
Published: 29 April 2024

This article is part of the thematic issue "Recent advances in synthesis and applications of organometallic nanomaterials".

Guest Editor: T.-D. Nguyen



© 2024 Anh et al.; licensee Beilstein-Institut.
License and terms: see end of document.

Abstract

A simple approach was developed to synthesize cobalt ferrite nanoparticles/graphene quantum dots (CF/GQDs). The material was prepared from a homogeneous mixture of iron nitrate, cobalt nitrate, and starch at 140, 180 and 200 °C in a 24 h thermal hydrolysis process. The obtained materials were characterised by using X-ray diffraction, scanning electron microscopy, transmission electron microscopy, ultraviolet–visible diffuse reflectance spectroscopy, Fourier-transform infrared spectroscopy, photoluminescence spectroscopy, vibrating-sample magnetometry, and nitrogen adsorption/desorption isotherms. Cobalt ferrite crystals of around 8–10 nm and graphene quantum dots formed directly at 200 °C. Stacking GQDs sheets onto the CF nanoparticles resulted in CF/GQDs nanoparticles. The nanocomposite exhibits satisfactory fluorescent and superparamagnetic properties, which are vital for catalytic applications. The CF/GQDs catalyse significantly the degradation of methylene blue (MB) under visible light. The catalyst can be recycled with an external magnetic field and displays suitable stability. Also, it was reused in three successive experiments with a loss of efficiency of about 5%. The CF/GQDs are considered as an efficient photocatalyst for MB degradation and other dyes.

Introduction

Graphene quantum dots (GQDs) have unique properties, including photoluminescence, biocompatibility, slight chemical toxicity, inertness, and excellent photostability [1,2]. Graphene quantum dots consist of graphene sheets that are single-, double-, or multilayered, all smaller than 10 nm in thickness and 100 nm in width. Therefore, GQDs possess an ultralarge specific

surface area thanks to nanometre-sized graphene sheets. Graphene quantum dots are fabricated via two techniques, that is, by breaking graphene sheets or from molecules with aromatic structure (fullerenes, starch, and carbohydrates) [3]. However, often GQDs are only stable in solvents, which limits their application in fields that require their solid form, such as in adsorption and photocatalytic, or electrochemical applications [4].

Several magnetic nanomaterials that can be recycled and reused have been developed for catalysis or adsorption [5]. Among them are ferrites with the general formula of MFe_2O_4 (M: Mn, Fe, Co, Ni, Cu, and Zn). They are important magnetic materials. Among the spinel ferrites, $CoFe_2O_4$ (CF) is one of the most important soft-magnetic ferrite materials because of its ferromagnetic properties, high magnetic and thermal stability, low conductivity, and anisotropy [6]. The controllable synthesis of spherical CF nanoparticles from corresponding salts and Arabic gum as surfactant agent using a hydrothermal method was reported [7]. The effect of oleylamine concentration on the physicochemical properties of CF synthesized via a solvothermal process has been presented [8]. However, ferrites exhibit self-agglomeration due to their magnetic nature. Combining different functional materials to prepare multiple-component photocatalysts is a common way to overcome the issues of single-phase photocatalysts [9].

Stacking GQDs sheets onto CF nanoparticles not only prevents CF from agglomeration but also forms heterojunction contacts, which possibly reduce the recombination of the photo-induced electron–hole pairs in photocatalytic processes. Ramachandran et al. reported the synthesis of a CF/GQDs nanocomposite by co-precipitating cobalt ferrite nanoparticles on graphene quantum dots prepared from citric acid [10]. Naghshbandi et al. synthesized CF/GQDs from a mixture of GQDs, prepared by carbonising citric acid in a controlled manner, and CF; the material was used to reduce 4-nitrophenol with a very high rate constant compared to the individual components [11].

Despite various advancements in preparation techniques for nanocatalysts, the development of a well-controlled method remains a challenge. In this study, we describe an eco-friendly facile hydrothermal method to prepare magnetic CF/GQDs nanocomposites. The CF nanoparticles, 8–10 nm in diameter, were highly dispersed in a graphene quantum dot matrix and directly formed at 200 °C. Stacking GQDs sheets onto the CF nanoparticles resulted in CF/GQDs nanoparticles. Magnetic properties, morphology, structure, and fluorescence of the nanocomposites were studied, and the photocatalytic degradation of methylene blue as a dye model and the mechanism of methylene degradation were also addressed.

Experimental

Materials

Cobalt(II) nitrate hexahydrate ($Co(NO_3)_2{\cdot}6H_2O$, 98%), iron(III) nitrate nonahydrate ($Fe(NO_3)_3{\cdot}9H_2O$, 98%), and starch ($(C_6H_{10}O_5)_n$, 98%) were purchased from Merck, Germany. Methylene blue trihydrate ($C_{16}H_{18}ClN_3S{\cdot}3H_2O$), isopropanol ($C_3H_8O$), potassium iodide (KI), and potassium bromate ($KBrO_3$) were also purchased from Merck, and benzoquinone ($C_6H_4O_2$) was provided by Sigma-Aldrich, USA. Sodium hydroxide (NaOH, ≥96%) and hydrogen chloride (HCl, 38%) were purchased from Xilong, China.

Instruments

X-ray diffraction (XRD) patterns were recorded by using a D8 Advance (Bruker, Germany) with Cu Kα radiation (λ = 0.154 nm). Fourier-transform infrared (FTIR) spectra were recorded on a IR-Prestige-21 (Shimadzu). Raman spectra were recorded on an Xplora Plus instrument (Horiba, Japan) in a frequency range from 200 to 2000 cm^{-1} and with an excitation wavelength of 785 nm. The nitrogen adsorption/desorption isotherms were recorded by using a Tristar-3030 system (Micromeritics, USA). The magnetic properties were measured on a Micro Sense vibrating-sample magnetometer (VSM) at room temperature. Scanning electron microscopy (SEM) observations and energy-dispersive X-ray elemental mapping (EDX mapping) were carried out on a Hitachi S-4800 FESEM (Japan). High-resolution transmission electron microscopy (HR-TEM) observation was performed with a JEM 1010. The intermediates in the MB degradation were determined by using an Agilent 1100 LC/MS-MS system with an electron spray ionization source combined with an ion trap.

Synthesis of $CoFe_2O_4$, $CoFe_2O_4$/GQDs, and GQDs

Cobalt ferrite was synthesized through a thermal hydrolysis method according to the literature [12]. Briefly, mixtures of $Co(NO_3)_2{\cdot}6H_2O$, $Fe(NO_3)_3{\cdot}9H_2O$, and starch $(C_6H_{10}O_5)_n$ with different compositions were prepared (Table 1). Each mixture was heated to 80–85 °C for 1 h in a flask to hydrolyse the starch. Then, the mixture was transferred to a 100 mL Teflon-lined autoclave and heated at 200 °C for 24 h. After hydrolysis, the product was cooled to room temperature. The brown solid was centrifuged, washed several times with distilled water, and calcinated at 700 °C for 3 h to obtain cobalt ferrite. The products were denoted as CF0.5, CF0.67, CF1.0, and CF2.0, where the numeral is the initial Fe/Co molar ratio.

$CoFe_2O_4$/GQDs were synthesized in a similar manner. A mixture of $Co(NO_3)_2{\cdot}6H_2O$ (4.95 g), $Fe(NO_3)_3{\cdot}9H_2O$ (3.44 g), and starch $(C_6H_{10}O_5)_n$ (6.20 g) with a nCo/nFe/starch/$n$$H_2O$ molar ratio of 2:1:4.5:540 was dissolved in a flask and heated to

Table 1: Precursor compositions for cobalt ferrite samples from different Fe/Co molar ratios.

	$Co(NO_3)_2{\cdot}6H_2O$ (g)	$Fe(NO_3)_3{\cdot}9H_2O$ (g)	$(C_6H_{10}O_5)_n$ (g)	H_2O (g)
CF0.5	4.95	3.44	6.20	82.7
CF0.67	3.71	3.44	5.17	68.9
CF1.0	2.48	3.44	4.14	55.1
CF2.0	1.24	3.44	3.10	41.4

80–85 °C for 1 h to hydrolyse the starch. Then, the mixture was transferred to a 100 mL Teflon-line autoclave and heated at 140, 180, and 200 °C for 24 h. The brown solid was centrifuged, washed several times with distilled water, and dried at 100 °C for 24 h to obtain $CoFe_2O_4$/GQDs. The material was denoted as CF/GQDs-140, CF/GQDs-180, and CF/GQDs-200, where the numeral symbol presents the hydrolysis temperature.

For the sake of comparison, GQDs were synthesized similarly at 200 °C without cobalt and iron. The product mixture was evaporated at 100 °C for 48 h and dried to obtain GQDs.

Photocatalysic studies

Kinetic study

The photochemical activity of the material was evaluated through the photochemical decomposition of MB solution under simulated sunlight conditions (160 W bulb, Osram, Germany). 0.05 g of the sample material was dispersed in 100 mL of 10 ppm MB solution in a 250 mL Erlenmeyer flask. Before illumination, the solution was placed in the dark for 1 h under stirring to achieve an adsorption–desorption equilibrium. Aliquots of 2 mL were taken at certain time intervals during irradiation and separated by centrifuging. In the supernatant, the MB concentration was determined via absorption spectroscopy at a wavelength of 664 nm. The photochemical degradation efficiency of MB was calculated according to formula $F = \frac{C_0 - C_t}{C_0}$, where C_0 and C_t are the MB concentration at the beginning and at time t, respectively.

Effect of pH value

The $CoFe_2O_4$/GQDs composite material was placed in flasks sealed with aluminium foil and containing 20 mL of 10 ppm MB solution at pH 3–11, adjusted with 0.01 M HCl or 0.01 M NaOH. After 60 min of adsorption and photodegradation, the tubes were placed in a photocatalytic cabinet for illumination for 120 min. Then, the material was separated from the solution, and the MB concentration was determined to evaluate the MB decomposition efficiency.

Reusability

Reusability and stability of the $CoFe_2O_4$/GQDs were assessed in three cycles of 120 min. After each cycle, the catalyst was separated from the MB solution with a magnet and dried at 100 °C for 2 h for use in the subsequent cycle. The photocatalytic reaction in each cycle was conducted under the same conditions.

Scavengers

1,4-Benzoquinone (BQ, 10 mM), isopropanol (IPA), potassium iodide (KI, 10 mM), and potassium bromate ($KBrO_3$, 10 mM) were used as scavengers for $^{\bullet}O_2^-$, $^{\bullet}OH$, h^+, and e^- species in the reaction. After adding 0.05 g of $CoFe_2O_4$/GQDs material to 100 mL of a 10 ppm MB solution, the mixture was kept in the dark and stirred continuously for 60 min. Then, 10 mL of each scavenger solution was added, and the illuminator was switched on. After specified time intervals, 10 mL of the sample was taken and centrifuged to separate the material from the solution. The concentration of remaining MB in the solution was determined by using UV–vis spectroscopy.

Identification of intermediates

Intermediate products and mineralization level of the MB photodegradation were evaluated by using dual liquid chromatography–mass spectrometry (LC/MS-MS) after the MB solution samples were illuminated for 0, 60, 120, and 180 min. The chemical oxygen demand (COD) of MB solution samples was assessed after 0, 30, 60, 90, 120, and 150 min of light exposure.

Result and Discussion

Materials characterisation

The XRD patterns of cobalt ferrite with decreasing Fe/Co molar ratio from 2 to 0.5 are presented in Figure 1a. The XRD patterns of CF confirm that cobalt ferrite has a spinel structure, and all main peaks correspond to the standard pattern of bulk $CoFe_2O_4$ (JCPDS 00-022-1086). It is notable that the XRD pattern of cobalt ferrite with the initial Fe/Co ratio of 2 (stoichiometric ratio) exhibits the diffraction of iron oxides at 2θ of 24.2°, 33.2°, 40.8°, and 49.6° (JCPDS no. 33-0664). This means that a part of cobalt ions goes to the liquid phase during synthesis. Therefore, it is necessary to ensure a higher amount of cobalt than its theoretical ratio to achieve stoichiometric cobalt ferrite. Cobalt ferrite with the initial Fe/Co molar ratio of 0.5 has also spinel structure, and no additional and intermediate phase are observed, indicating that a single-phase spinel was obtained.

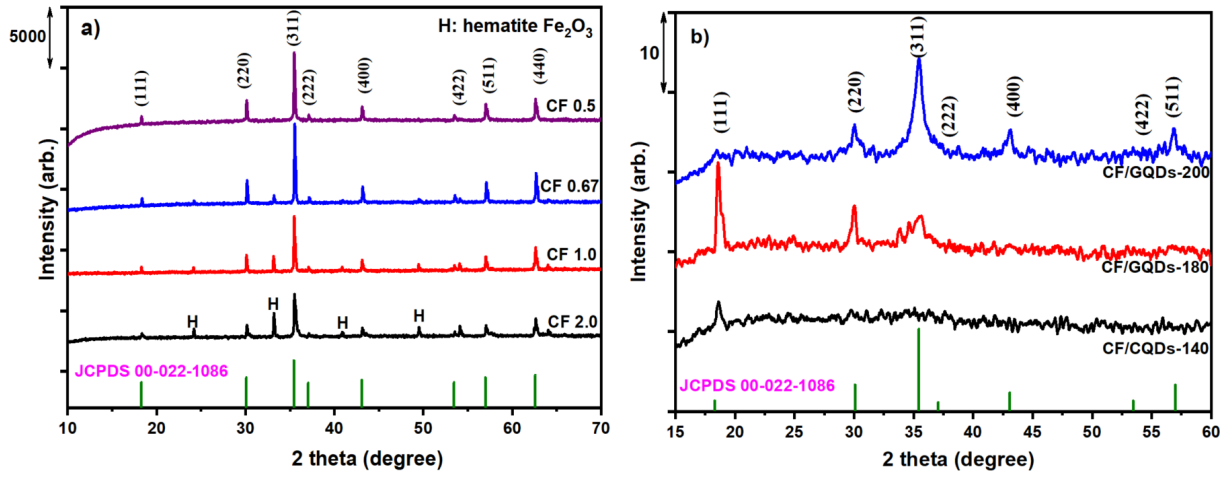


Figure 1: XRD patterns of (a) CF and (b) CF/GQDs.

Therefore, the initial Fe/Co molar ratio of 0.5 was used to prepare CF/GQDs. Figure 1b presents XRD patterns of CF/GQDs prepared at different temperatures. No diffraction peaks of CF/GQDs prepared at 140 °C are observed; the characteristic peaks of cobalt ferrite spinel appear for the samples prepared at 180 and 200 °C. No signals for GQDs can be observed because of the low crystallinity, high dispersion, and small amount of GQDs in CF/GQDs.

The peak of the (222) plane is related to the octahedral sites, while the peaks at the (220) and (422) planes are attributed to the tetrahedral sites [13]. The ratio of the peak intensities between the (220) and the (222) planes as well as between the (422) and the (222) planes are used to estimate the distribution of cobalt ions in the tetrahedral sites or octahedral sites. The values of the intensity ratios (I_{220}/I_{222}) and (I_{422}/I_{222}) for CF and CF-GQDs-200 are 1.25 and 1.05, and 1.09 and 1.00, respectively. The ratios in CF are higher than those in CF-GQDs, indicating that the number of cobalt ions at tetrahedral sites in CF is higher than that in CF/GQDs-200.

The crystallite size of the as-prepared $CoFe_2O_4$ ferrite particles was calculated from the (311) peak of the XRD pattern by using the Scherrer equation [14], $D_{hkl} = \frac{k\lambda}{\beta\cos\theta}$, where D_{hkl} is the crystallite size; k is the shape factor (0.89); θ is the diffraction angle; β is the full width at half maximum of the (311) peak, and λ is the X-ray wavelength (1.54 Å). The average crystallite sizes of the as-synthesized $CoFe_2O_4$ and CF/GQDs-200 are, respectively, about 17.2 and 9.2 nm. Since cobalt ferrite possesses an inverse spinel structure (space group $Fd\bar{3}m$) [13], the ferrite lattice parameter of CF and CF/GQDs-200 is 8.394 Å, agreeing well with the bulk value of 8.377 Å [15].

The suspension of CF/GQDs-200 after thermal hydrolysis was filtered by centrifuging and divided into two parts, that is, solution and solid. The optical properties of the solution are shown in Figure 2a. The inset in Figure 2a presents the 100 mL beaker containing the GQD solution. The sample on the left was exposed to white light, and it has a yellow-brown colour, characteristic of GQDs prepared from the natural polymer starch [16]. The solution on the right was exposed to 254 nm UV light, and the colour changed to green. The typical absorption peak at 287 nm in the UV–vis spectrum of the aqueous GQD solution (Figure 2a) can be attributed to the n–π* transition of graphitic sp^2 domains, which is the characteristic band of a polyaromatic structure [16,17]. Figure 2b presents the maximum emission at a wavelength of 498 nm (blue line) with an excitation wavelength of 410 nm (red line). The exact PL behaviour of GQDs is still unclear. It is possible that electron–hole recombination, quantum effects, and surface defects in the functional groups of the GQDs are involved [18]. The XRD pattern of GQDs prepared from starch without iron and cobalt salts is presented in Figure 2c. The diffraction peaks of the GQDs are centred at 2θ of 23°, 30.9°, and 39.6°, corresponding to d-spacing values of 0.52, 0.45, and 0.21 nm, respectively. A larger d-spacing value manifests that GQDs contain oxygen functional groups. This could be assigned to the size of GQDs. The broad nature of the diffraction peaks is attributed to GQDs with nanoscale size composed of few-layer graphene. These results confirm that the supernatant contains GQDs. Similarly, the supernatants from the CF/GQDs suspensions synthesized at 140 and 180 °C (Figure 2c) also contain graphene quantum dots (Figure 2c).

Figure 3 presents some characterisations of the solid part extracted from the suspension of CF/GQDs-200. The FTIR

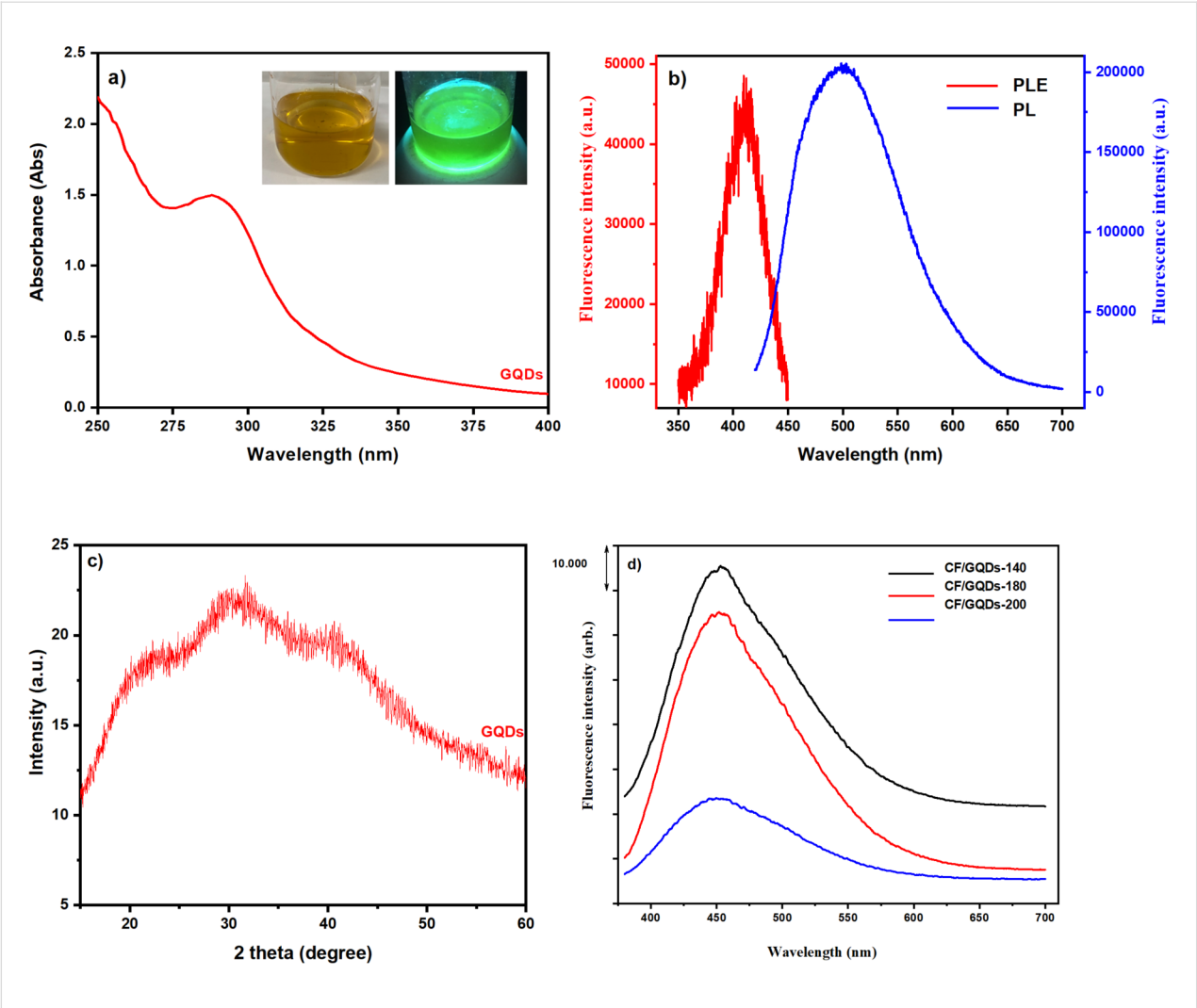


Figure 2: (a) UV–vis absorption spectra of the GQD solution; inset: GQD solution under white light (left) and ultraviolet light (254 nm, right); (b) photoluminescence excitation (PL) and photoluminescence emission spectra (PLE) of the GQDs; (c) XRD pattern of GQDs; (d) PL spectra of supernatants from prepared CF/GQD suspensions.

spectra of CF and CF/GQDs-200 are shown in Figure 3a. CF has two broad bands at 387 and 580 cm^{-1}, attributed to the characteristic stretching vibrations of the iron and cobalt bonds at the tetrahedral and octahedral sites, respectively [19]. For CF/GQDs, the broad bands from 750–400 cm^{-1} possibly involve the vibrations of metal and oxygen in cobalt ferrite. The bands at 3408–3450 cm^{-1} are attributed to stretching vibrations of O–H groups, while the bands at 1622, 1375, 1233, and 1080 cm^{-1} are assigned to C=C vibrations of aromatic carbons, O–H bending in carboxylic and carbonyl groups, C=O vibrations in epoxy groups, and stretching vibrations of C–O in alkoxy groups, respectively [20,21]. These functional groups prove the existence of GQDs in CF/GQDs. The Raman spectra of CF and CF/GQDs are presented in Figure 3b,c. CF exhibits four peaks at 469, 550, 614, and 690 cm^{-1}, corresponding to the $T_{1g(2)}$, $T_{1g(1)}$, $A_{1g(2)}$, and $A_{1g(1)}$ Raman modes, respectively [22]. For CF/GQDs, these modes are broad and weak, but these results also confirm the existence of CF in GQDs.

In contrast to the spectra of pure CF, there are obvious vibrations at 1200–2000 cm^{-1} with two characteristic peaks of graphitic carbon (G band) and disordered carbon (D band), appearing at 1590 and 1298 cm^{-1}, respectively. The I_D/I_G ratio is 1.03, which is higher than that of graphene oxide (GO), which is 0.93. The strong band in the Raman spectra at 690 cm^{-1} is attributed to the $A_{1g(1)}$ symmetry (tetrahedral sites) [22], and the band at 469 cm^{-1} is assigned to the $T_{1g(2)}$ symmetry at the octahedral sites [19]. The ratio of intensities of these two peaks at 469 and 690 cm^{-1} also reveals the distribution of Co^{2+} between the tetrahedral and octahedral sites [13]. This peak intensity ratio for CF is higher than that for CF/GQDs-200. These results from Raman spectra are consistent

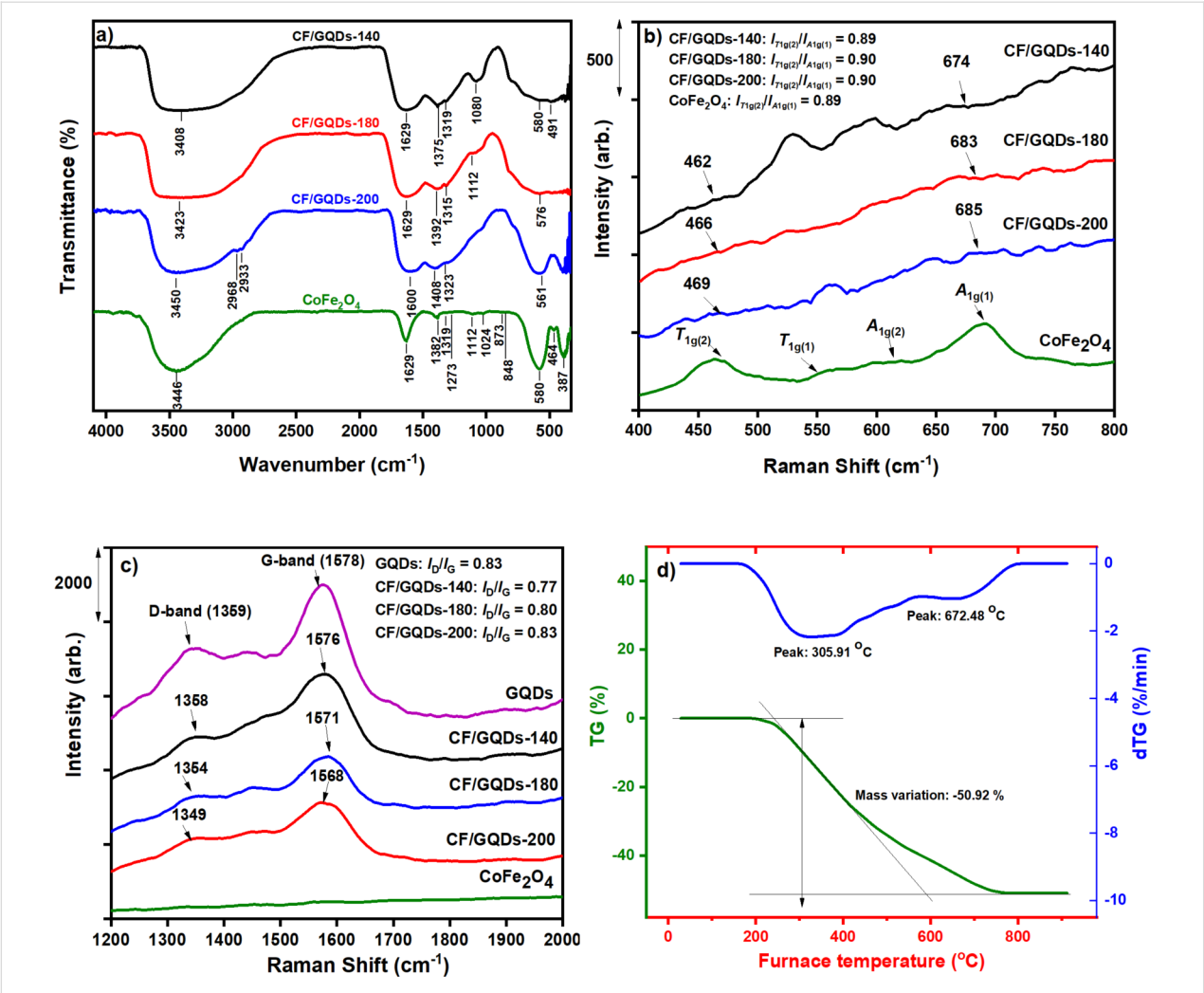


Figure 3: (a) FTIR spectra of CF/GQDs and $CoFe_2O_4$; (b, c) Raman spectra; (d) TG/dTG curves of CF/GQDs-200.

with XRD analysis, indicating that Co^{2+} in CF has a tendency to settle at tetrahedral sites, while Co^{2+} in CF/GQDs-200 does not.

The TG-dTG curves of CF/GQDs-200 is presented in Figure 3d. Weight losses are observed between 200 and 800 °C, and the material remains stable at higher temperatures. The significant loss from 200 to 700 °C of around 50.92% is attributed to GQDs. These results show that the equation illustrating the synthesis of CF/GQDs can be written as follows:

$$Co^{2+} + Fe^{3+} + \text{starch} \rightarrow CoFe_2O_4/\text{GQDs} + \text{GQDs}$$

SEM images of CF/GQDs synthesized at hydrothermal temperatures of 140, 180 and 200 °C are shown in Figure 4a–c. The morphology reveals that CF/GQDs consist of heavily agglomerated particles, several hundreds of nanometers in diameter, because of their magnetic nature. Figure 4d and Figure 4e present the TEM images of CF and CF/GQDs-200, respectively, and the corresponding particle size distribution. CF has very fine particles of around 15–20 nm. The intimate interfacial contact between GQDs sheets and the CF nanoparticle is further depicted in the TEM image (Figure 4e). In this image, the deposited nanoparticles of around 9.2 nm are obvious on the GQDs. Such a good interfacial contact between CF and GQDs is favourable for the separation of the photogenerated charge carriers in the CF/GQDs.

The elemental distribution of CF/GQDs was studied by EDX mapping. The elements Fe, Co, O, and C are present, as expected. Figure 5 shows that the elements, such as iron and cobalt, are evenly distributed in the GQDs matrix. No other elements were found, indicating no impurities in CF/GQDs. The Fe/Co molar ratio of 2.05 in CF/GQDs is very close to 2, the Fe/Co initial ratio.

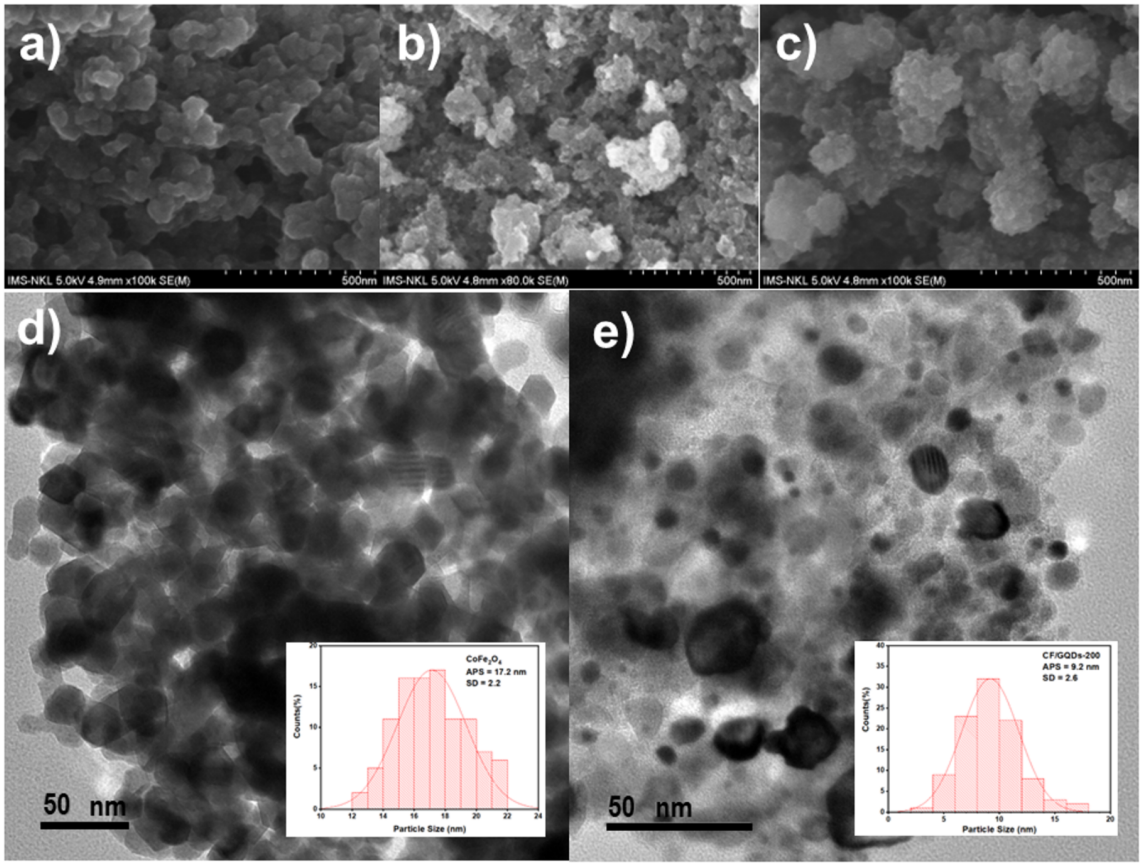


Figure 4: SEM images of (a) CF/GQD-140, (b) CF/GQD-180, and (c) CF/GQD-200; TEM observations and corresponding particle size distribution of (d) CF and (e) CF/GQDs-200.

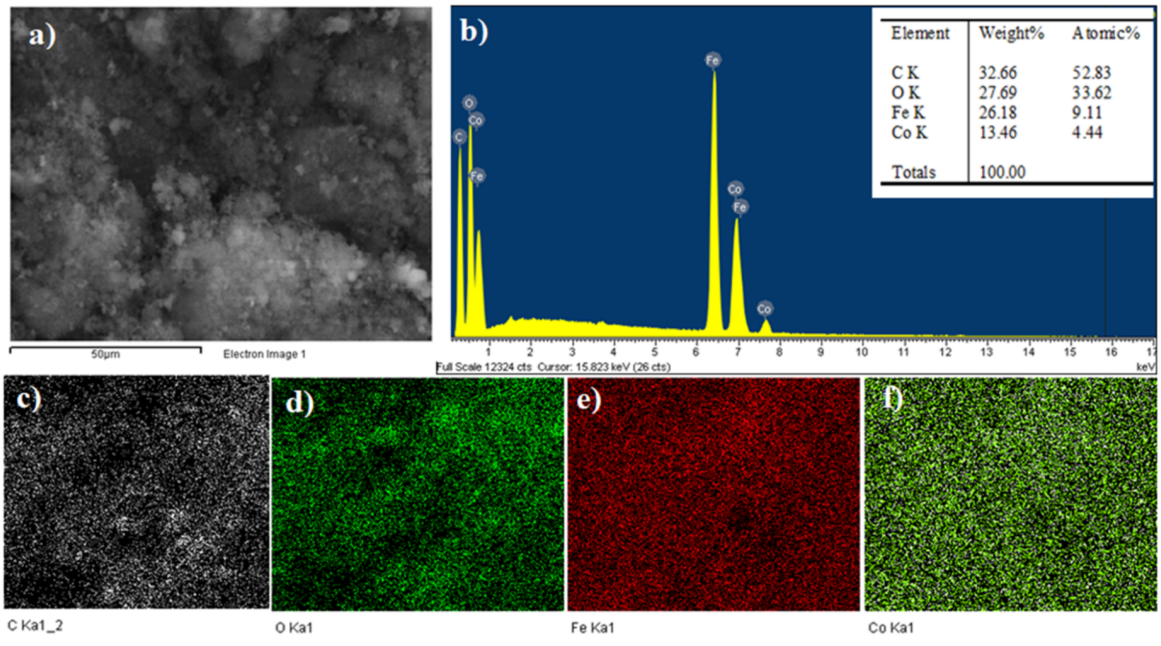


Figure 5: EDX-mapping of CF/GQDs-200. (a) Electron microscopy image, (b) EDX spectrum, (c) carbon mapping, (d) oxygen mapping, (e) iron mapping, and (f) cobalt mapping.

As depicted in Figure 6a, the CF/GQDs nanoparticles exhibit a significantly lower PL emission intensity than CF alone because of the higher separation efficiency of charge carriers of the CF/GQDs sample. The UV–vis DRS spectra of CF and CF/GQDs (Figure 6b) show that the absorption intensity becomes stronger after grafting the GQDs on CF, indicating that the resulting composite can enhance the absorption capacity [11]. This observation is an agreement with previous works [11]. In addition, a slight shift of the PL emission peak is also observed because of the blue shift in the UV–vis spectrum, which is consistent with their bigger bandgap energy.

The magnetic characteristics of the CF/GQDs nanocomposite were identified by using VSM. The magnetic parameters, including the saturation magnetization (M_s), coercivity (H_c), and remanence (M_r), are presented in Table 2. As can be seen in Figure 6c, the hysteresis characteristics of $CoFe_2O_4$ show hard ferrites with high coercive field and magnetization, while the

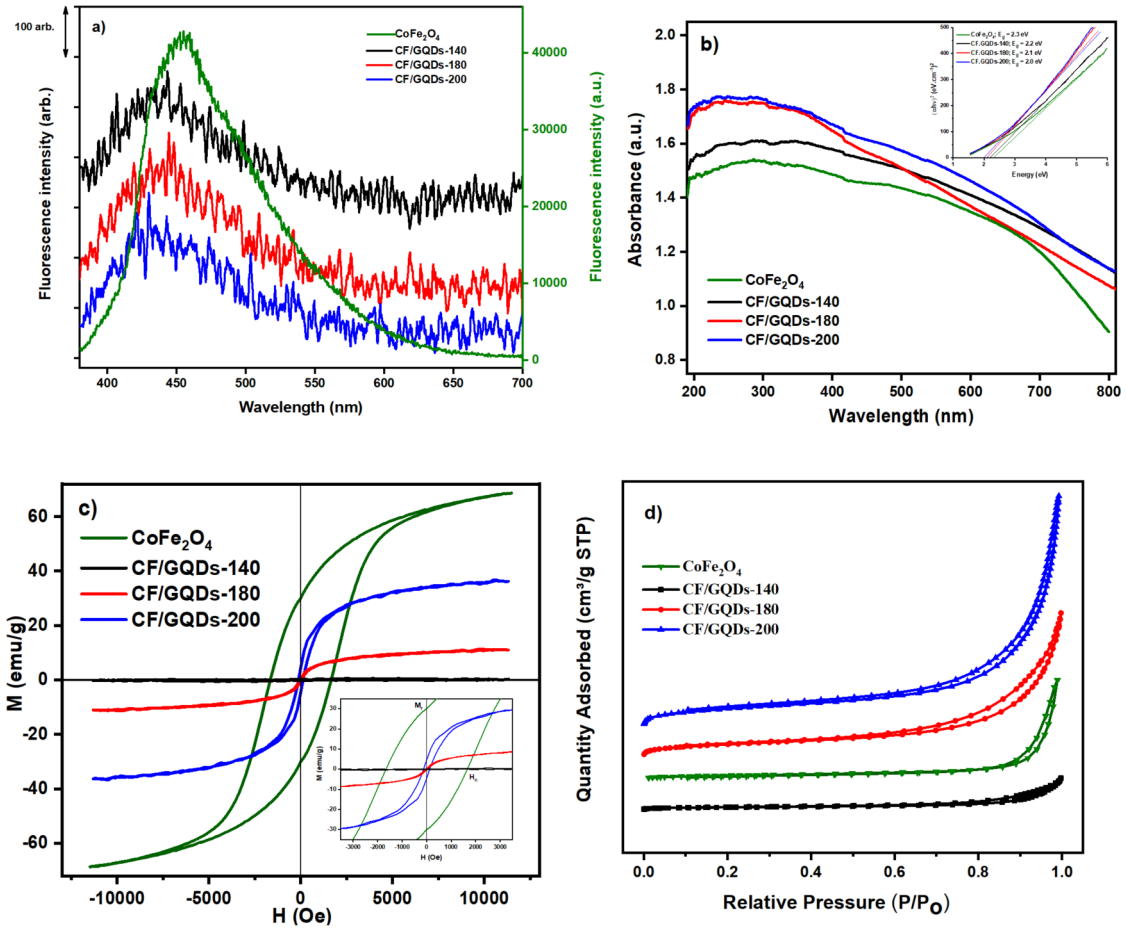


Figure 6: (a) PL spectra, (b) UV–vis diffuse reflectance spectra with Tauc's plots in the inset, (c) magnetization curves, and (d) nitrogen adsorption/desorption isotherms of CF/GQDs prepared at different temperatures.

Table 2: Physical properties of CF/GQDs.

Sample	S_{BET} ($m^2 \cdot g^{-1}$)	Porous volume ($cm^3 \cdot g^{-1}$)	Crystallite size (nm)	M_s ($emu \cdot g^{-1}$)	M_r ($emu \cdot g^{-1}$)	H_c (Oe)
$CoFe_2O_4$	21.0	0.17	32.5	65.8	30.0	1654.9
CF/GQDs-140	11.3	0.05	—	—	—	—
CF/GQDs-180	59.3	0.24	—	11.1	0.6	38.4
CF/GQDs-200	85.2	0.41	9.2	36.3	4.6	146.6

hysteresis loops of CF/GQDs are reversible, indicating that CF/GQDs exhibit superparamagnetic characteristics. The magnetic saturation values of the CF/GQDs-140, -180 and -200 samples are 0, 11.1, and 36.3 emu/g, respectively, at room temperature. They are much smaller than the bulk value (65.8 emu/g). The decrease in the saturation magnetization of the CF/GQDs is attributed to the presence of the nonmagnetic GQDs. The particles' high magnetic permeability shows that they could be separated with an external magnetic field. The M_r values of 0.6 emu/g for CF/GQDs-180 and 4.6 emu/g for CF/GQDs-200 are taken from the inset in Figure 6c. The obtained H_c value (146.6 Oe) for our sample is much lower than that in the literature [23]. Generally, the $CoFe_2O_4$ ferrite particles may have a multidomain structure. The formation of multiple domains and the easy movement of the domain walls can result in a decrease in coercivity. The reduced particle size leads to reduced coercivity, which could be expressed as a transformation from a ferrimagnetic to a superparamagnetic state [15].

Figure 6d presents the nitrogen adsorption/desorption isotherms of $CoFe_2O_4$ and CF/GQDs. All isotherm curves belong to type V according to IUPAC. At a high relative pressure (above 0.8), the hysteresis sloop indicates that the materials have micro-meso structures. The surface area of $CoFe_2O_4$ is small because of heavy agglomeration (21.0 $m^2 \cdot g^{-1}$). However, CF/GQDs have a significantly larger surface area compared with that of $CoFe_2O_4$ (11.3 $m^2 \cdot g^{-1}$ for CF/GQDs-140, 59.3 $m^2 \cdot g^{-1}$ for CF/GQDs-180, and 85.2 $m^2 \cdot g^{-1}$ for CF/GQDs-200). This is possibly due to stacked GQDs in $CoFe_2O_4$ crystals, making the structure of CF/GQDs more porous. The surface area increases with increasing hydrolysis temperature because the higher the temperature, the more the $CoFe_2O_4$ crystals form, making it less agglomerated. The CF/GQDs-200 sample with the largest surface area was selected for further studies.

Photocatalytic studies

Figure 7a presents the decolourisation kinetics over different CF/GQDs samples as catalysts. The decolourisation occurs in

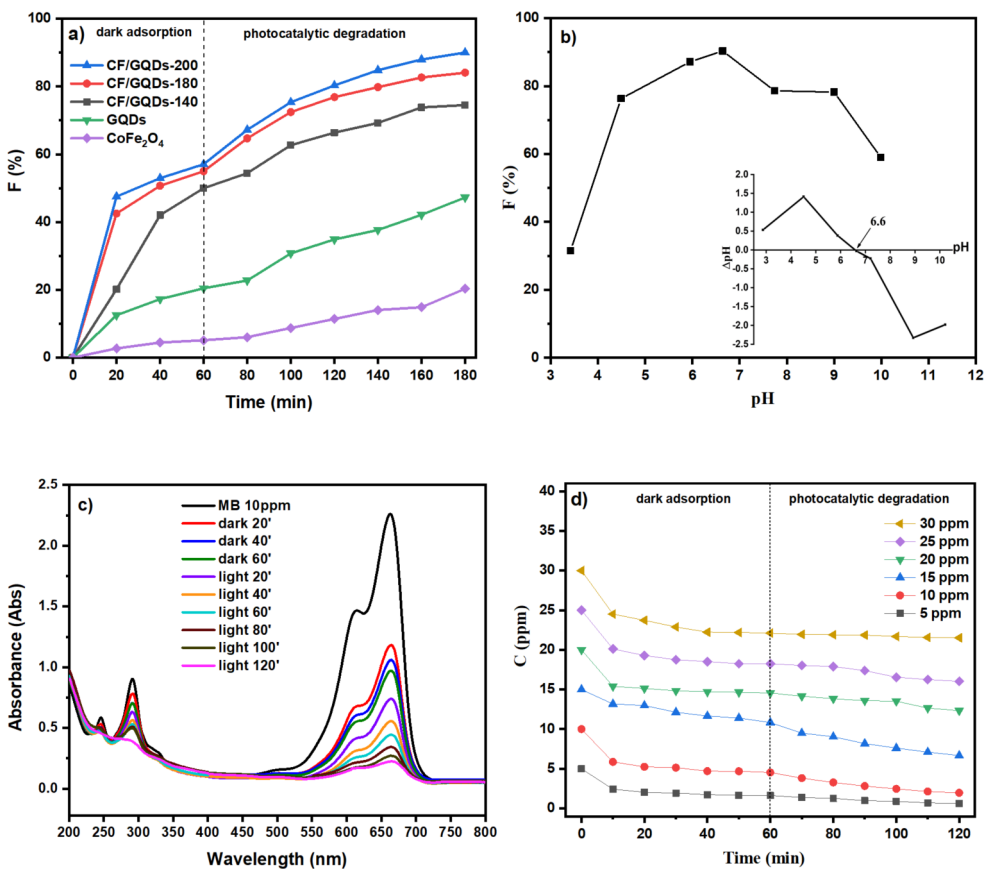


Figure 7: (a) MB decolourisation over different catalysts (V = 100 mL, $C_{0(MB)}$ = 10 ppm, m = 0.05 g, time of darkness adsorption: 60 min; time of light irradiation: 120 min). (b) Effect of pH value on the MB decolourisation over CF/GQDs-200; the inset presents the point of zero charge (V = 20 mL, $C_{0(MB)}$ = 10 ppm, m = 0.02 g, time of light irradiation: 120 min). (c) UV–vis spectra of MB and the treated solution (V = 100 mL, $C_{0(MB)}$ = 10 ppm, m = 0.05 g, time of darkness adsorption: 60 min, time of light irradiation: 120 min). (d) Decolourisation kinetics (V = 100 mL, $C_{0(MB)}$ = 5–30 ppm, m = 0.05 g, time of darkness adsorption: 60 min, time of light irradiation: 60 min).

two steps. First, the catalyst was mixed with the MB solution in the dark for 60 min to ensure the adsorption/desorption equilibrium; second, the lamp was turned on to irradiate the MB solution under mechanical stirring. It is found that the rate constant increases in the following order: CF/GQDs-200 (k = 0.0123 min^{-1}) > CF/GQDs-180 (k = 0.0087 min^{-1}) > CF/GQDs-140 (k = 0.0059 min^{-1}) > GQDs (k = 0.0034 min^{-1}) > CF (k = 0.0014 min^{-1}).

The $CoFe_2O_4$ particles agglomerate heavily because of their magnetic nature, as expected, and they exhibit slight MB adsorption and decolourisation. The combination of GQDs and $CoFe_2O_4$ improves the decolourisation capacity significantly. Stacking $CoFe_2O_4$ crystals onto GQDs sheets not only prevents agglomeration but also creates heterojunction contacts or intermediate steps in the electronic structure. These heterojunctions limit the recombination of photo-induced electron–hole pairs and, thus, enhance catalytic decolourisation. Therefore, the CF/GQDs-200 sample was selected for further studies.

The point of zero charge (pzc) of CF/GQDs-200 obtained by the pH drift method is 6.6 (see the inset of Figure 7b). Therefore, the surface of CF/GQDs-200 is negatively charged at pH > 6.6 and positively charged when pH < 6.6. Methylene blue possesses three basic sites, whose pK_a values are 2.6 (pK_{a1}), 11.2 (pK_{a2}), and 11.2 (pK_{a3}) [24]. Based on the average pK_a value of MB, the point of zero charge for MB is calculated as 8.33 [25]. The MB dye can exist in several chemical forms, namely MBH_3^{2+} (the tri-protonated form), MBH_2^+ (diprotonated form), MBH (monoprotonated form), and MB^- (deprotonated form) [25].

With increasing pH, the decolourisation efficiency increases, reaches its maximum at pH ca. 7, and decreases afterwards (Figure 7b). This could possibly be due to the fact that at low pH, the increase in pH makes the surface of CF/GQDs and MB become less positive, and the attractive interaction increases. In contrast, at high pH, the increasing pH makes the surface of CF/GQDs and MB become more negative; as a result, the repulsion force of these species comes into play, reducing adsorption.

UV–vis spectroscopy was used to study MB decolourisation (Figure 7c). The UV–vis spectra of MB present a strong adsorption band at 664 nm, corresponding to functional groups (n–π* electron transition), and two adsorption bands at 246 and 292 nm corresponding to aromatic rings (π–π* electron transition). The colour intensity of the MB solution decreases only slightly in the absence of catalysts (0 to 10 h), indicating that MB is stable and exhibits weak self-degradation under incident radiation. However, when CF/GQDs-200 was added, the peak magnitude for MB at 246, 292, and 664 nm decreased remarkably. The colour disappearance and the cleavage of aromatic rings were completed after 120 min of irradiation (Figure 7c). The decolourisation kinetics of MB over CF/GQDs-200 is shown in Figure 7d. The Langmuir–Hinshelwood first-order kinetic model is widely employed to assess the kinetic data of photocatalytic degradation. This model is as follows: $\ln\frac{C_t}{C_0} = -k_1 t$, where C_t and C_0 are the MB concentration at the beginning and at the time t, respectively; k_1 is the first-order kinetic rate constant. The slope of the linear plot of $\ln\frac{C_t}{C_0}$ vs t provides the value of k_1. The values of k_1, along with others from the literature, are presented in Table 3. However, because the reactions were conducted under different conditions, the comparison is arbitrary.

To clarify the mechanism of MB photocatalytic degradation, 10 mM isopropyl (IPA), potassium iodide (KI), potassium bromate ($KBrO_3$), and p-benzoquinone (BQ) were used as scavengers to capture hydroxyl radicals ($^{\bullet}OH$), photo-induced holes

Table 3: A comparison of the rate constant of the present work with other values from literature.

Materials	Mass of catalyst (mg)/mass of dye (mg)	Light source	k (min^{-1})	Ref
$Co_{0.5}Zn_{0.5}Fe_2O_4$	0.5/1	visible light	0.064	[26]
$CoFe_2O_4$	1/1	visible light	0.01	[27]
$ZnFe_2O_4$	200/1	UV–vis light	0.032	[28]
$Co_{0.5}Mg_{0.5}Fe_2O_4$	200/1	UV–vis light	0.072	[28]
$Zn_{0.25}Co_{0.375}Mg_{0.375}Fe_2O_4$	200/1	UV–vis light	0.108	[28]
$ZnFe_2O_4/Fe_2O_3$	100/1	75 W mercury lamp	0.019	[29]
$MnFe_2O_4$/rGO	30/1	UV–vis light	0.0586	[30]
γ-Fe_2O_3/Fe_3O_4/ SiO_2	2/1	UV light	0.01836	[31]
g-$C_3N_4/Ca_2Fe_2O_5$	156/1	natural sunlight	0.058	[32]
$Co_{0.1}Mg_{0.9}Fe_2O_4$	20/1	halogen lamp	0.005	[33]
CF/GQDs	50/1	160 W Osram bulb	0.0123	this work

(h^+), photo-induced electrons (e^-), and superoxide anions $^{\bullet}O_2^-$, respectively. As can be seen, IPA exhibits a strong interaction with the hydroxyl radical through a simple electron transfer process [34].

$$\text{isopropyl–OH} + {}^{\bullet}\text{OH} \rightarrow \text{isopropyl–O}^{\bullet} + H_2O$$

If the $^{\bullet}$OH radicals play a crucial role in the MB degradation, the reaction rate is expected to decrease significantly. As depicted in Figure 8a, adding an excess amount of 10 mM IPA to the reaction mixture significantly suppresses the MB degradation (by ca. 28.5%). The rate constant of MB degradation decreases to 0.0015 min^{-1} from 0.0123 min^{-1}. This result indicates that the $^{\bullet}$OH degradation pathway plays a critical role in the MB photocatalytic degradation.

Iodide ions (I^-) are strong scavengers that react with valence band holes (h^+_{VB}) [35].

$$I^- + h^+_{VB} \rightarrow \text{heat}$$

Bromate ions (BrO_3^-) capture photoinduced electrons (e_{CB}), which leads to a reduction to form bromide ions [36].

$$BrO_3^- + 6e^-_{CB} + 6H^+ \rightarrow Br^- + 3H_2O$$

Figure 8a presents the effect of adding an excess of 10 mM KI or 10 mM $KBrO_3$ on the MB degradation. The rate constant decreases to 0.0059 min^{-1} for KI and 0.0074 min^{-1} for $KBrO_3$, and the decolourisation efficiency decreases by 9.9% for KI and by 4.2% for $KBrO_3$ compared with the absence of scavenger. This means that the MB photocatalytic degradation is moderately affected by KI or $KBrO_3$, which indicates the role of h^+ and e^-_{CB} in the MB photocatalytic degradation.

p-Benzochinone reacts as a scavenger with superoxide anions through a simple electron transfer process [37].

$$BQ + {}^{\bullet}O_2^- \rightarrow BQ^{\bullet -} + O_2$$

The photocatalytic degradation of MB is mildly affected by BQ (decolourisation efficiency drops by 13.5%, indicating the influence of $^{\bullet}O_2^-$ during the photocatalytic degradation of MB [37].

The mineralisation of MB was estimated with COD measurements (Figure 8b). The value of COD decreases with increasing reaction time. The initial COD value is 87.4 $mg{\cdot}L^{-1}$ and decreases to 6.5 $mg{\cdot}L^{-1}$ after 150 min of reaction, indicating that the mineralisation was almost complete. Furthermore, LC-MS was used to explore the MB degradation pathway. Detailed data is provided in Supporting Information File 1. The mass spectra of the oxidized MB solutions at different residue times show the various intermediates due to demethylation and hydroxylation processes [38]. Low-bond-energy intermediates and ring-breaking products were obtained in the MB degradation (acetates, oxalates, and sulfates, Scheme 1). Finally, MB could be mineralized to CO_2, H_2O, SO_4^{2-}, and NO_3^- [38].

In order to check the stability of the materials, the prepared CF/GQDs-200 catalysts were reused in three cycles (Figure 9b). After each run, the catalyst was separated with an external magnetic field. It was found that the present photocatalyst exhibits

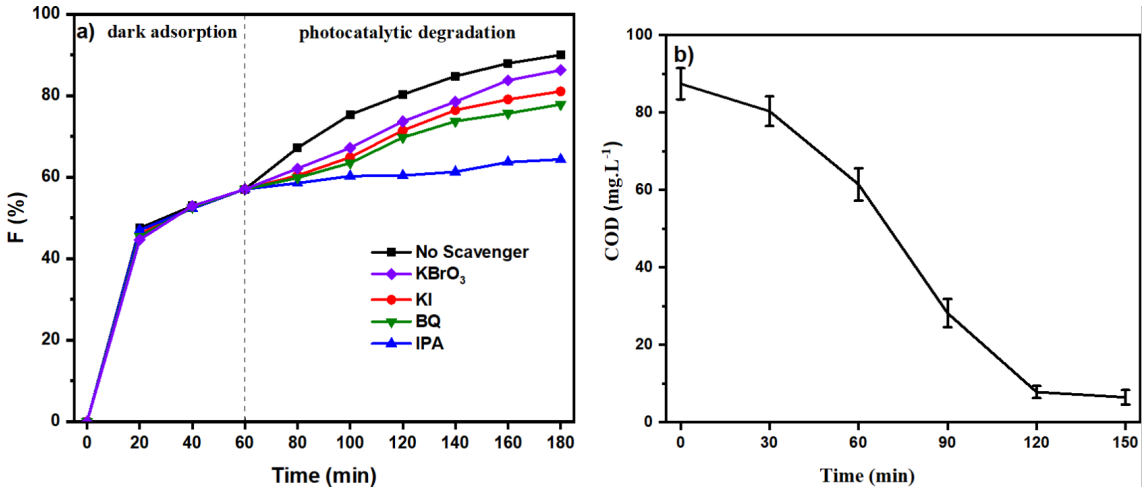
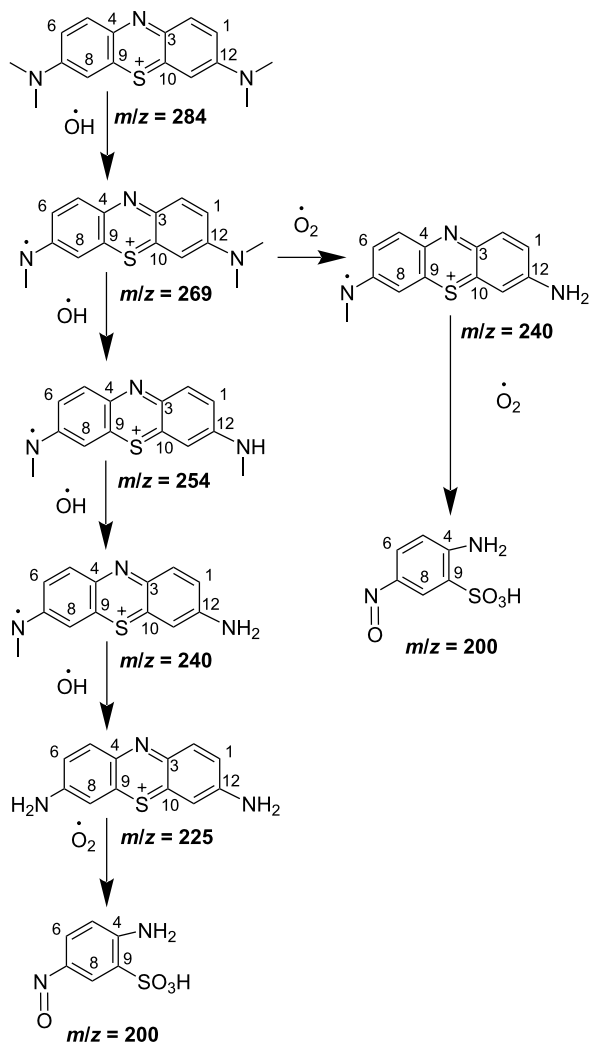


Figure 8: (a) Effects of addition of KI, IPA, $KBrO_3$, and BQ on the visible-light-driven photocatalytic degradation of MB with CF@GQDs; (b) dependence of the chemical oxygen demand on the reaction time.



Scheme 1: Proposed intermediates in MB degradation monitored by liquid chromatography coupled with tandem mass spectrometry recorded at 180 min (tested concentration: 10 ppm).

no significant loss of activity over three cycles. The CF/GQDs-200 photocatalyst used in the cycling tests was characterised by using XRD before and after the cycling experiments. The result indicates that the as-obtained CF/GQDs-200 does not suffer from photocorrosion and exhibits excellent reusability for the degradation process.

The mechanism of MB degradation over the CF/GQDs catalyst is illustrated in Scheme 2. Under visible light irradiation, photogenerated holes (h^+) are created in the valence bands via the transfer of photogenerated electrons (e^-) from the valence band to the conduction band (Equation 1). Hence, photoinduced electron transfer possibly takes place from CF to GQDs, which are excellent acceptors [39] (Equation 2). This retards the recombination of electrons and holes in the nanocomposites [40]. The photoinduced holes are, therefore, available to react with H_2O to produce $^{\bullet}OH$ radicals. The electrons in the CB band directly reduce MB to its degradation products or interact with oxygen in the aqueous solution to form peroxy anion radicals ($^{\bullet}O_2^-$). A part of h^+ oxidizes water to form hydroxyl radicals ($^{\bullet}OH$), or it can oxidize directly MB to its degradation products (Equations 4–6). Finally, the degradation products decompose into CO_2. The reactions are illustrated as follows:

$$\mathrm{CF} + h\nu \rightarrow \mathrm{CF}\left(\mathrm{e}^-_{\mathrm{CB}} + \mathrm{h}^+_{\mathrm{VB}}\right) \quad (1)$$

$$\mathrm{CF}\left(\mathrm{e}^-_{\mathrm{CB}}\right) \rightarrow \mathrm{GQDs}\left(\mathrm{e}^-_{\mathrm{CB}}\right) \quad (2)$$

$$\mathrm{GQDs}\left(\mathrm{e}^-_{\mathrm{CB}}\right) + \mathrm{MB} \rightarrow \text{degradation products} \quad (3)$$

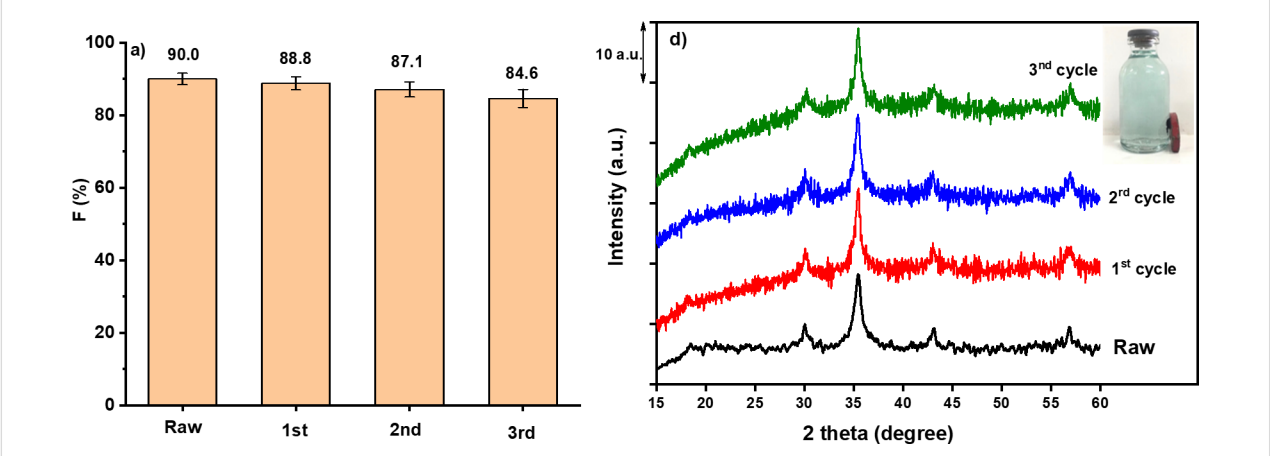
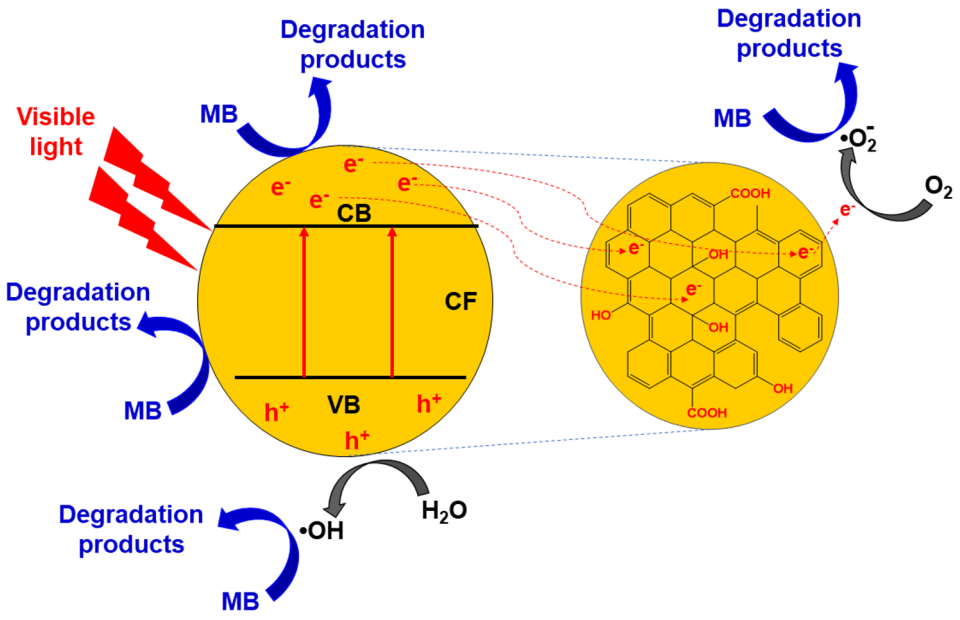


Figure 9: (a) Cyclic photocatalytic degradation experiments of MB with CF/GQDs-200 photocatalyst; (b) XRD pattern of CF/GQDs and reused CF/GQDs.



Scheme 2: Mechanism of MB degradation over the CF/GQDs catalyst.

$$h^{+}_{VB} + H_2O \rightarrow {}^{\cdot}OH + H^{+} \quad (4)$$

$${}^{\cdot}OH + MB \rightarrow \text{degradation products} \quad (5)$$

$$h^{+}_{VB} + MB \rightarrow \text{degradation products} \quad (6)$$

$$\text{degradation products} + \text{radicals}\left(e^{-}_{CB}, h^{+}_{VB}, {}^{\cdot}OH, {}^{\cdot}O_2^{-}\right) \rightarrow CO_2 + H_2O \quad (7)$$

Conclusion

$CoFe_2O_4$/GQDs were successfully synthesized in a thermal hydrolysis process from $Co(NO_3)_2$, $Fe(NO_3)_3$, and starch. The $CoFe_2O_4$ nanoparticles of around 20 nm are highly dispersed in GQDs. The $CoFe_2O_4$/GQDs exhibit superparamagnetic properties and are separable by applying an external magnetic field after the reaction. The mineralisation of MB via photocatalytic degradation is complete. The remarkable enhancement of the $CoFe_2O_4$/GQDs is attributed to active sites of GQDs and excellent heterojunctions between $CoFe_2O_4$ and GQDs. The former is favourable for more MB molecules to adsorb on the active sites of the photocatalysts, and the latter can facilitate the GQDs layers acting as electron acceptors, which are beneficial for suppressing the recombination of photogenerated electrons and holes. These results suggest that the $CoFe_2O_4$/GQD nanocomposite is a potential catalyst for methylene blue degradation and various environmental applications.

Supporting Information

Fragmentation spectrum of MB and HPLC spectrum of MB at initial and photocatalytic degradation after 180 min.

Supporting Information File 1

Detailed information on MS spectra and HPLC diagram.
[https://www.beilstein-journals.org/bjnano/content/supplementary/2190-4286-15-43-S1.pdf]

Funding

This work was financially supported by Hue University, Vietnam, under project code DHH2023-04-201 and by the Master and PhD Scholarship Programme of Vingroup Innovation Foundation (VINIF), code VINIF.2023.ThS.142.

Competing Interests

The authors have no relevant financial or non-financial interests to disclose.

Author Contributions

All authors contributed to the study conception and design. Material preparation, data collection and analysis were performed by V.C.N.A., L.T.T.N., L.T.K.D., D.T.N.H., N.T.S., N.T.T.U., N.N.U.T., L.V.T.S., L.T.H., T.N.T., and D.Q.K. The first draft of the manuscript was written by D.Q.K and all authors commented on previous versions of the manuscript. All authors read and approved the final manuscript.

ORCID® iDs

Vo Chau Ngoc Anh - https://orcid.org/0009-0007-2657-3682
Le Thi Thanh Nhi - https://orcid.org/0009-0007-5078-6151
Le Thi Kim Dung - https://orcid.org/0000-0002-2674-4900
Dang Thi Ngoc Hoa - https://orcid.org/0000-0003-4180-9351
Nguyen Truong Son - https://orcid.org/0009-0002-2259-1908
Nguyen Thi Thao Uyen - https://orcid.org/0009-0009-8719-6918
Nguyen Ngoc Uyen Thu - https://orcid.org/0009-0002-5454-4807
Le Van Thanh Son - https://orcid.org/0000-0002-2061-6983
Le Trung Hieu - https://orcid.org/0000-0001-8519-8236
Tran Ngoc Tuyen - https://orcid.org/0000-0003-1477-0471
Dinh Quang Khieu - https://orcid.org/0000-0003-3473-6377

Data Availability Statement

The data that supports the findings of this study is available from the corresponding author upon reasonable request.

References

1. Li, Y.; Hu, Y.; Zhao, Y.; Shi, G.; Deng, L.; Hou, Y.; Qu, L. *Adv. Mater. (Weinheim, Ger.)* **2011,** *23,* 776–780. doi:10.1002/adma.201003819
2. Dong, Y.; Shao, J.; Chen, C.; Li, H.; Wang, R.; Chi, Y.; Lin, X.; Chen, G. *Carbon* **2012,** *50,* 4738–4743. doi:10.1016/j.carbon.2012.06.002
3. Li, L.; Wu, G.; Yang, G.; Peng, J.; Zhao, J.; Zhu, J.-J. *Nanoscale* **2013,** *5,* 4015–4039. doi:10.1039/c3nr33849e
4. Inah, B. E.; Eze, J. F.; Louis, H.; Edet, H. O.; Gber, T. E.; Eno, E. A.; Etim, A. N.; Adeyinka, A. S. *Chem. Phys. Impact* **2023,** *7,* 100265. doi:10.1016/j.chphi.2023.100265
5. Revathy, R.; Sajini, T.; Augustine, C.; Joseph, N. *Results Eng.* **2023,** *18,* 101114. doi:10.1016/j.rineng.2023.101114
6. Gaikwad, R. S.; Chae, S.-Y.; Mane, R. S.; Han, S.-H.; Joo, O.-S. *Int. J. Electrochem.* **2011,** *2011,* 729141. doi:10.4061/2011/729141
7. Refat, N. M.; Nassar, M. Y.; Sadeek, S. A. *RSC Adv.* **2022,** *12,* 25081–25095. doi:10.1039/d2ra03345c
8. Ansari, S. M.; Sinha, B. B.; Sen, D.; Sastry, P. U.; Kolekar, Y. D.; Ramana, C. V. *Nanomaterials* **2022,** *12,* 3015. doi:10.3390/nano12173015
9. Jacinto, M. J.; Ferreira, L. F.; Silva, V. C. *J. Sol-Gel Sci. Technol.* **2020,** *96,* 1–14. doi:10.1007/s10971-020-05333-9
10. Ramachandran, S.; Sathishkumar, M.; Kothurkar, N. K.; Senthilkumar, R. *IOP Conf. Ser.: Mater. Sci. Eng.* **2018,** *310,* 012139. doi:10.1088/1757-899x/310/1/012139
11. Naghshbandi, Z.; Arsalani, N.; Zakerhamidi, M. S.; Geckeler, K. E. *Appl. Surf. Sci.* **2018,** *443,* 484–491. doi:10.1016/j.apsusc.2018.02.283
12. Chandrika, M.; Ravindra, A. V.; Wang, S. Y.; Ju, S. *J. Mater. Sci.* **2022,** *57,* 2610–2626. doi:10.1007/s10853-021-06701-8
13. Kumar, Y.; Shirage, P. M. *J. Mater. Sci.* **2017,** *52,* 4840–4851. doi:10.1007/s10853-016-0719-5
14. Mendelson, M. I. *J. Am. Ceram. Soc.* **1969,** *52,* 443–446. doi:10.1111/j.1151-2916.1969.tb11975.x
15. Zi, Z.; Sun, Y.; Zhu, X.; Yang, Z.; Dai, J.; Song, W. *J. Magn. Magn. Mater.* **2009,** *321,* 1251–1255. doi:10.1016/j.jmmm.2008.11.004
16. Chen, W.; Li, D.; Tian, L.; Xiang, W.; Wang, T.; Hu, W.; Hu, Y.; Chen, S.; Chen, J.; Dai, Z. *Green Chem.* **2018,** *20,* 4438–4442. doi:10.1039/c8gc02106f
17. Mei, Q.; Chen, J.; Zhao, J.; Yang, L.; Liu, B.; Liu, R.; Zhang, Z. *ACS Appl. Mater. Interfaces* **2016,** *8,* 7390–7395. doi:10.1021/acsami.6b00791
18. Lin, L.; Rong, M.; Luo, F.; Chen, D.; Wang, Y.; Chen, X. *TrAC, Trends Anal. Chem.* **2014,** *54,* 83–102. doi:10.1016/j.trac.2013.11.001
19. Fan, X.; Guan, J.; Cao, X.; Wang, W.; Mou, F. *Eur. J. Inorg. Chem.* **2010,** *2010,* 419–426. doi:10.1002/ejic.200900681
20. Bose, S.; Kuila, T.; Uddin, M. E.; Kim, N. H.; Lau, A. K. T.; Lee, J. H. *Polymer* **2010,** *51,* 5921–5928. doi:10.1016/j.polymer.2010.10.014
21. Hafeez, H. Y.; Lakhera, S. K.; Narayanan, N.; Harish, S.; Hayakawa, Y.; Lee, B.-K.; Neppolian, B. *ACS Omega* **2019,** *4,* 880–891. doi:10.1021/acsomega.8b03221
22. Chandramohan, P.; Srinivasan, M. P.; Velmurugan, S.; Narasimhan, S. V. *J. Solid State Chem.* **2011,** *184,* 89–96. doi:10.1016/j.jssc.2010.10.019
23. Cedeño-Mattei, Y.; Perales-Perez, O.; Tomar, M. S.; Roman, F.; Voyles, P. M.; Stratton, W. G. *J. Appl. Phys.* **2008,** *103,* 07E512. doi:10.1063/1.2838215
24. Sabnis, R. W. *Handbook of Biological Dyes and Stains;* John Wiley & Sons, Inc., 2010. doi:10.1002/9780470586242
25. Bensedira, A.; Haddaoui, N.; Doufnoune, R.; Meziane, O.; Labidi, N. S. *Polym. Polym. Compos.* **2022,** *30,* 096739112211417. doi:10.1177/09673911221141747
26. Chahar, D.; Taneja, S.; Bisht, S.; Kesarwani, S.; Thakur, P.; Thakur, A.; Sharma, P. B. *J. Alloys Compd.* **2021,** *851,* 156878. doi:10.1016/j.jallcom.2020.156878
27. Kalam, A.; Al-Sehemi, A. G.; Assiri, M.; Du, G.; Ahmad, T.; Ahmad, I.; Pannipara, M. *Results Phys.* **2018,** *8,* 1046–1053. doi:10.1016/j.rinp.2018.01.045
28. Jangam, K.; Patil, K.; Balgude, S.; Patange, S.; More, P. *RSC Adv.* **2020,** *10,* 42766–42776. doi:10.1039/d0ra08172h
29. Cao, Z.; Zhang, J.; Zhou, J.; Ruan, X.; Chen, D.; Liu, J.; Liu, Q.; Qian, G. *J. Environ. Manage.* **2017,** *193,* 146–153. doi:10.1016/j.jenvman.2016.11.039
30. Mandal, B.; Panda, J.; Paul, P. K.; Sarkar, R.; Tudu, B. *Vacuum* **2020,** *173,* 109150. doi:10.1016/j.vacuum.2019.109150
31. Sanad, M. M. S.; Farahat, M. M.; El-Hout, S. I.; El-Sheikh, S. M. *J. Environ. Chem. Eng.* **2021,** *9,* 105127. doi:10.1016/j.jece.2021.105127
32. Vavilapalli, D. S.; Peri, R. G.; Sharma, R. K.; Goutam, U. K.; Muthuraaman, B.; Ramachandra Rao, M. S.; Singh, S. *Sci. Rep.* **2021,** *11,* 19639. doi:10.1038/s41598-021-99020-6
33. Dojcinovic, M. P.; Vasiljevic, Z. Z.; Pavlovic, V. P.; Barisic, D.; Pajic, D.; Tadic, N. B.; Nikolic, M. V. *J. Alloys Compd.* **2021,** *855,* 157429. doi:10.1016/j.jallcom.2020.157429
34. Buxton, G. V.; Greenstock, C. L.; Helman, W. P.; Ross, A. B. *J. Phys. Chem. Ref. Data* **1988,** *17,* 513–886. doi:10.1063/1.555805
35. Li, Y.; Wang, J.; Yao, H.; Dang, L.; Li, Z. *J. Mol. Catal. A: Chem.* **2011,** *334,* 116–122. doi:10.1016/j.molcata.2010.11.005
36. Zhao, X.; Liu, H.; Shen, Y.; Qu, J. *Appl. Catal., B* **2011,** *106,* 63–68. doi:10.1016/j.apcatb.2011.05.005
37. Palominos, R.; Freer, J.; Mondaca, M. A.; Mansilla, H. D. *J. Photochem. Photobiol., A* **2008,** *193,* 139–145. doi:10.1016/j.jphotochem.2007.06.017
38. de Oliveira Guidolin, T.; Possolli, N. M.; Polla, M. B.; Wermuth, T. B.; Franco de Oliveira, T.; Eller, S.; Klegues Montedo, O. R.; Arcaro, S.; Cechinel, M. A. P. *J. Cleaner Prod.* **2021,** *318,* 128556. doi:10.1016/j.jclepro.2021.128556

39. Zhao, D. F.; Yang, H.; Li, R. S.; Ma, J. Y.; Feng, W. J. *Mater. Res. Innovations* **2014,** *18,* 519–523. doi:10.1179/1433075x13y.0000000178
40. Zhang, D.; Yang, J.; Wang, J.; Yang, J.; Qiao, G. *Opt. Mater. (Amsterdam, Neth.)* **2020,** *100,* 109612. doi:10.1016/j.optmat.2019.109612

License and Terms

This is an open access article licensed under the terms of the Beilstein-Institut Open Access License Agreement (https://www.beilstein-journals.org/bjnano/terms), which is identical to the Creative Commons Attribution 4.0 International License (https://creativecommons.org/licenses/by/4.0). The reuse of material under this license requires that the author(s), source and license are credited. Third-party material in this article could be subject to other licenses (typically indicated in the credit line), and in this case, users are required to obtain permission from the license holder to reuse the material.

The definitive version of this article is the electronic one which can be found at:
https://doi.org/10.3762/bjnano.15.43

BEILSTEIN JOURNAL OF NANOTECHNOLOGY

Simultaneous electrochemical determination of uric acid and hypoxanthine at a TiO_2/graphene quantum dot-modified electrode

Vu Ngoc Hoang[1,2], Dang Thi Ngoc Hoa[3], Nguyen Quang Man[3], Le Vu Truong Son[4], Le Van Thanh Son[4], Vo Thang Nguyen[4], Le Thi Hong Phong[5], Ly Hoang Diem[6], Kieu Chan Ly[7], Ho Sy Thang[*7] and Dinh Quang Khieu[*1]

Full Research Paper

Open Access

Address:
[1]University of Sciences, Hue University, Vietnam, [2]Tan Hiep High School, Kien giang, Vietnam, [3]University of Medicine and Pharmacy, Hue University, Vietnam, [4]The University of Danang, University of Science and Education, Vietnam, [5]Institute of Materials Science, Vietnam Academy of Science and Technology, Vietnam, [6]Kien Giang University, Vietnam and [7]Dong Thap University, Vietnam

Email:
Ho Sy Thang[*] - hsthang@dthu.edu.vn; Dinh Quang Khieu[*] - dqkhieu@hueuni.edu.vn

* Corresponding author

Keywords:
graphene quantum dots; hypoxanthine; peroxo titanium complexes; uric acid

Beilstein J. Nanotechnol. **2024,** *15,* 719–732.
https://doi.org/10.3762/bjnano.15.60

Received: 24 February 2024
Accepted: 22 May 2024
Published: 20 June 2024

This article is part of the thematic issue "Recent advances in synthesis and applications of organometallic nanomaterials".

Guest Editor: B. T. Huy

© 2024 Ngoc Hoang et al.; licensee Beilstein-Institut.
License and terms: see end of document.

Abstract

A TiO_2/graphene quantum dots composite (TiO_2/GQDs) obtained by in situ synthesis of GQDs, derived from coffee grounds, and peroxo titanium complexes was used as electrode modifier in the simultaneous electrochemical determination of uric acid and hypoxanthine. The TiO_2/GQDs material was characterized by photoluminescence, X-ray diffraction, Raman spectroscopy, high-resolution transmission electron microscopy, and energy-dispersive X-ray mapping. The TiO_2/GQDs-GCE exhibits better electrochemical activity for uric acid and hypoxanthine than GQDs/GCE or TiO_2/GCE in differential pulse voltammetry (DPV) measurements. Under optimized conditions, the calibration plots were linear in the range from 1.00 to 15.26 μM for both uric acid and hypoxanthine. The limits of detection of this method were 0.58 and 0.68 μM for uric acid and hypoxanthine, respectively. The proposed DPV method was employed to determine uric acid and hypoxanthine in urine samples with acceptable recovery rates.

Introduction

Uric acid (7,9-dihydro-1*H*-purine-2,6,8(3*H*)-trione, URI) is the primary final product of the purine metabolism in humans. High concentrations of URI in serum and urine are a sign of several diseases, such as gout, Lesch–Nyan disease, obesity, diabetes, high cholesterol levels, and kidney diseases [1,2]. Hypoxanthine (6-hydroxypurine, HYP), a purine derivative, is an indi-

cator of hypoxia [3]. A lower HYP concentration in the cerebrospinal fluid of patients compared to healthy individuals is related to Parkinson's disease [4]. The oxidation of HYP yields xanthine, which can be further oxidized to URI. Meat from shrimp, fish, and some other animals contain large amounts of HYP. High consumption of these foods has been considered to result in elevated levels of URI, associated with the risk of gout [5]. Hence, simple and selective methods to determine the purine content in food and dietary products are of interest among researchers [6,7]. At the present time, several techniques for the determination of URI and HYP are available, such as high-performance liquid chromatography [8], liquid chromatography–tandem mass spectrometry [9], and gas chromatography/mass spectrometry [10]. These approaches require complex handling procedures. Electrochemical techniques have been considered as a robust alternative for URI and HYP sensing because of their simplicity, cost-effectiveness, and reliability. The use of modified electrodes has shown to improve significantly electrocatalytic activity and electrical conductivity of electrodes.

Graphene, with sp^2-hybridized carbon atoms in a single layer, has gained much attention because of its unique physicochemical properties. Graphene quantum dots (GQDs) are zero-dimensional graphene derivatives consisting of one to few layers of graphene sheets with a size of less than 20 nm in width [11]. The missing bandgap results in an absence of luminescence in pristine graphene. However, a bandgap can be generated in GQDs through edge effects. Edge-functionalized GQDs have oxygen-containing functional groups such as hydroxy, carboxyl, carbonyl, and epoxy groups, which can conjugate to various biological/organic/inorganic molecules such as proteins, antibodies, or metal ions [12]. The capability of electron transfer/energy storage derived from their conjugate structure makes them effectively utilizable over the full light spectrum [13,14]. GQDs can be prepared through solvothermal/hydrothermal processes or carbonization from suitable organic molecules (polymers or biomass) [15]. Biomass waste (e.g., agricultural residues and food waste) is a renewable resource for the preparation of high-value carbon materials. Among food wastes, coffee grounds are a promising precursor to prepare GQDs with new functionalities regarding a more sustainable materials industry [16]. Considering the fields of catalysis and electrochemistry, combining GQDs with semiconductors, especially TiO_2, has been of interest. For example, GQDs have been successfully introduced into TiO_2 [17] to enhance its photocatalytic activity. John Peter et al. reported TiO_2/GQDs as anodes for enhancing the short-circuit current in solar cells [18]. The lithium-ion storage performance of C-GQDs/α-Fe_2O_3 composites in lithium batteries presented excellent cyclability and rate capability [19]. Among several chemical approaches for the synthesis of titania, sol–gel processes have been commonly used for practical application. In these sol–gel methods, titanium alkoxides and halides are extensively used as precursors [20,21]. Because of their high reactivity, a complicate control over the reaction conditions is critical to achieve the desired crystalline structures and morphology [22]. Recently, a synthesis using stable water-soluble titanium complexes has been developed to overcome the disadvantages of these precursors and to easily obtain fine titania particles with a controlled shape [23]. The synthesis of TiO_2/GQDs from water-soluble titanium complexes is expected to form a homogeneous suspension that is convenient for developing modified electrodes used in electrochemical analysis. To the best of our knowledge, there are only few reports on TiO_2/GQDs for electrochemical analysis.

In the present work, TiO_2/GQDs were prepared from coffee grounds and peroxo titanium complexes by a hydrothermal process. The simultaneous determination of URI and HYP using a TiO_2/GQDs-modified electrode were addressed.

Experimental

Materials

Coffee grounds were collected from the local area. Anatase (98%), hydrogen chloride (39%), hydrogen peroxide (30%), boric acid (99%), phosphoric acid (85%), acetic acid (99%), uric acid (99%), and hypoxanthine (99%) were provided by the Merck company, Germany. Stock solutions of URI and HYP were prepared prior to use.

Equipment

The X-ray diffraction patterns of the suspensions of GQDs, peroxo titanium complexes, and TiO_2/GQDs were recorded on a D8 Advance, Bruker, Germany with background subtraction. The morphologies of GQDs were observed by using a JEM 2100 high-resolution transmission electron microscopy (HRTEM), Joel, Japan. Raman spectroscopy measurements were performed on a WiTec, Alpha 300R with a 532 nm laser. Surface analyses of the obtained materials were carried out using a S-4800 scanning electron microscope (SEM), Hitachi (Japan). UV–vis absorption spectroscopy measurements was carried out on an 8453 UV–vis spectrophotometer, Agilent, USA. Photoluminescence (PL) spectroscopy measurements were performed on a FL3C-22 spectrophotometer, Horiba, USA.

Synthesis of TiO_2/GQDs

Peroxo titanium complexes were synthesized in a hydrothermal process. 0.25 g of TiO_2 and 12.5 mL of 10 M NaOH were mixed under ultrasonic stirring. The suspension was then transferred to a teflon-lined stainless steel autoclave and heated to 130 °C for 10 h. The resulting white solid was separated by

centrifugation and rinsed several times with 0.1 M HCl and distilled water until a supernatant with neutral pH was obtained. The solid was dried at 80 °C for 2 h. This product was then mixed with 30 mL of H_2O_2 (35%, d = 1.11 g·cm^3) at 90 °C under magnetic stirring for 1 h to obtain a clear yellow solution of peroxo titanium complexes. The concentration of TiO_2 in the complexes was found as 0.745% (w/w) (0.25 g of TiO_2 in 30 mL of H_2O_2).

GQDs were synthesized from coffee grounds. Coffee grounds (0.2 g) were first suspended in water (50 mL). The suspension was sonicated for 1 h before being transferred to the autoclave and heated up to 180 °C for 10 h. The resulting product was then cooled to room temperature and separated by centrifugation at 4000 rpm to obtain a dark brown solid. The concentration of GQDs calculated after subtracting the insoluble part was 0.249% (w/w) (0.125 g of coffee grounds in 50 mL of water).

TiO_2/GQDs suspensions with different TiO_2/GQDs ratios were prepared by mixing different volumes of GQDs and peroxo titanium complex suspensions under stirring at 50 °C for 1 h. The samples are denoted as (0:4)TiO_2/GQDs; (1:4)TiO_2/GQDs; (2:4)TiO_2/GQDs; (4:4)TiO_2/GQDs; (4:2)TiO_2/GQDs; (4:1)TiO_2/GQDs; (4:0)TiO_2/GQDs. The numbers in parentheses stand for the volume ratio of peroxo titanium complex to GQDs solutions.

Electrochemical studies

Voltammetric measurements were performed at room temperature using a CPA-HH5 electrochemical workstation, Vietnam. A conventional three-electrode cell with a glassy carbon working electrode (GCE, 3 mm diameter), a platinum wire auxiliary electrode, and a Ag/AgCl reference electrode was used. Electrolyte solutions were prepared using doubly distilled water. Britton–Robinson (BR) buffer solutions with pH between 2 and 6 were prepared by mixing boric acid solution, phosphoric acid solution, and acetic acid solution in appropriate ratios.

To prepare a TiO_2/GQDs-modified glassy carbon electrode (TiO_2/GQDs-GCE), 5 mL of TiO_2/GQDs suspension in water (0.1 mg/mL) was cast onto the surface of the bare GCE. The modified electrode was allowed to dry naturally for some hours at ambient temperature.

The urine samples for electrochemical measurement were prepared by first diluting 1 mL urine to 20 mL with distilled water. 1.5 mL of this urine solution was added to 2 mL of 0.25 M pH 3 buffer and was diluted to 10 mL with distilled water in an electrolysis cell. The solution was spiked with 10 µL of 500 µM URI and 20 µL of 500 µM HYT before dilution to 10 mL.

Results and Discussion

Characterization of materials

The mixtures of GQDs and TiO_2/GQDs suspensions were exposed to visible and UV light to confirm their fluorescence behavior. Under visible light, the aqueous suspension of GQDs is transparent and brown in color, while the suspension of the peroxo titanium complex is opaque yellow. The prepared TiO_2/GQD aqueous suspensions, in contrast, display a light yellow color, which gets darker as the ratio of TiO_2/GQD in the complex increases (Figure 1a). Under 365 nm UV irradiation (Figure 1b), the GQDs displays green luminescence, while the TiO_2/GQDs samples exhibit different levels of fluorescence. Figure 1c presents the emission spectra of GQDs and TiO_2/GQDs. GQDs exhibits an emission maximum at 450 nm corresponding to the blue luminescence. The luminous intensity at an emission wavelength of ca. 450 nm decreases with increasing ratio of TiO_2/GQDs in the material until it almost disappears when the fraction of GQDs is lower than that of TiO_2. This indicates that mainly GQDs contribute to the luminescence of all samples. Figure 1d presents the UV–vis spectra of the obtained suspensions. The UV–vis spectra show absorbance bands from 200–400 nm that are typical for the colloidal systems with nanoscale particles [24,25]. The UV–vis spectrum of GQDs shows a characteristic feature of GO at ≈300 nm due to the absorption of the graphitic structure [26], while that of titanium complexes presents an absorption band at 240 nm. The combination of titanium complexes with GQDs resulted in higher adsorption λ_{max} values.

XRD patterns of the obtained samples in suspension form are presented in Figure 2. The XRD patterns of TiO_2 and TiO_2/GQDs suspensions show broad peaks of TiO_2 at 2θ = 26°, corresponding to the (101) plane of the anatase phase (JCPDS file 73-1764) (Figure 2a). As the XRD measurements were made in liquids instead of solid powders, the diffraction peaks are found to be broad and weak. The diffraction peaks of the GQDs at 2θ = 30.4° can be assigned to the (002) plane of graphene. The broad nature of the diffraction peak is due to the structure of GQDs containing only few layers of graphene sheets [27]. The XRD pattern of TiO_2/GQDs in solid form (dried at 100 °C for 3 h) exhibits characteristic peaks of anatase at 2θ = 25.6°, 38.1°, and 48.3°, corresponding to the (101), (004), and (200) planes, respectively. This confirms that the (1:4)TiO_2/GQDs suspension contains fine anatase nanoparticles. The broadening of XRD peaks in suspension was employed to evaluate the size (D_{hkl}) of the crystal domains. It was calculated from the full width at half maximum (B) using the Scherrer equation $D_{(101)} = \frac{K\lambda}{B\cos\theta}$, where λ is the X-ray wavelength (1.5406 Å), θ is the Bragg angle, and K is a constant (ca. 0.9). The average crystallite size of the synthesized TiO_2 nanoparticles was found to be 7.1 nm. It is notable that no typical peaks for GQDs can be

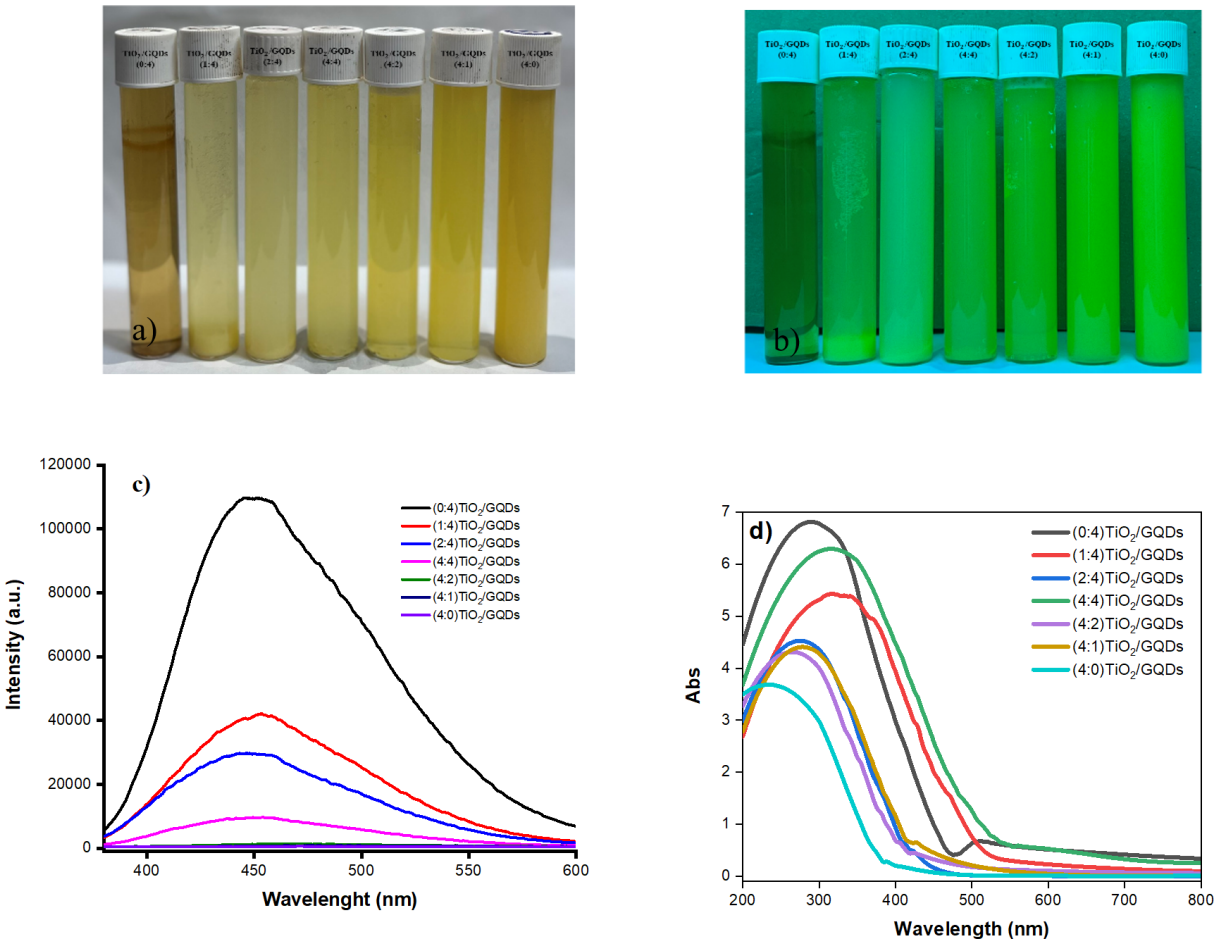


Figure 1: Images of aqueous suspension of TiO_2/GQDs samples (a) under white light and (b) under UV light. (c) Photoluminescence spectra excited at a wavelength of 365 nm. (d) UV–vis adsorption spectra of TiO_2, GQDs, and TiO_2/GQDs suspensions.

found in the XRD pattern of solid TiO_2/GQDs. This is possibly because of the low content of GQDs in the composites, which clearly indicates that GQDs do not affect significantly TiO_2 crystal structure.

Figure 2c presents the Raman spectra of the obtained materials. Four characteristic Raman-active E_g, $B1_g$, $A1_g$, and E_g modes of anatase TiO_2 are seen at 144, 395, 516, and 639 cm^{-1}, respectively [28]. In the Raman spectrum of GQDs, the peak at 1353 cm^{-1} can be attributed to the D band, which can be assigned to the vibrations of carbon atoms because of the presence of structural defects. The peak at 1576 cm^{-1} can be assigned to the G band due to the vibrations of sp^2-hybridized carbon atoms in graphene. The ratio of I_D/I_G is characteristic for the disorder of the graphene structure [29]. The characteristic vibrations for anatase are also observed in the Raman spectrum of the TiO_2/GQDs sample. However, the D and G bands of GQDs shift to 1357 and 1593 cm^{-1}, respectively, in the TiO_2/GQDs spectrum. The difference in I_D/I_G ratio, 0.94 for GQDs and 0.71 for TiO_2/GQDs, may be due to the interaction between TiO_2 and GQDs.

Figure 3 presents TEM observations of the obtained materials. The morphology of TiO_2 shows agglomerates of around 50–80 nm that consist of fine nanoparticles (Figure 3a), while that of GQDs shows fine spherical particles around 3–5 nm with high depression. In the composite sample, TiO_2 nanoparticles of around 100 nm can be seen to be highly dispersed in the GQDs matrix (Figure 3c). The TiO_2 particles in TiO_2/GQDs in Figure 3d were identified by HRTEM with an interplanar distance of (101) planes of 0.251 nm, which has also been revealed by XRD of TiO_2 in anatase form.

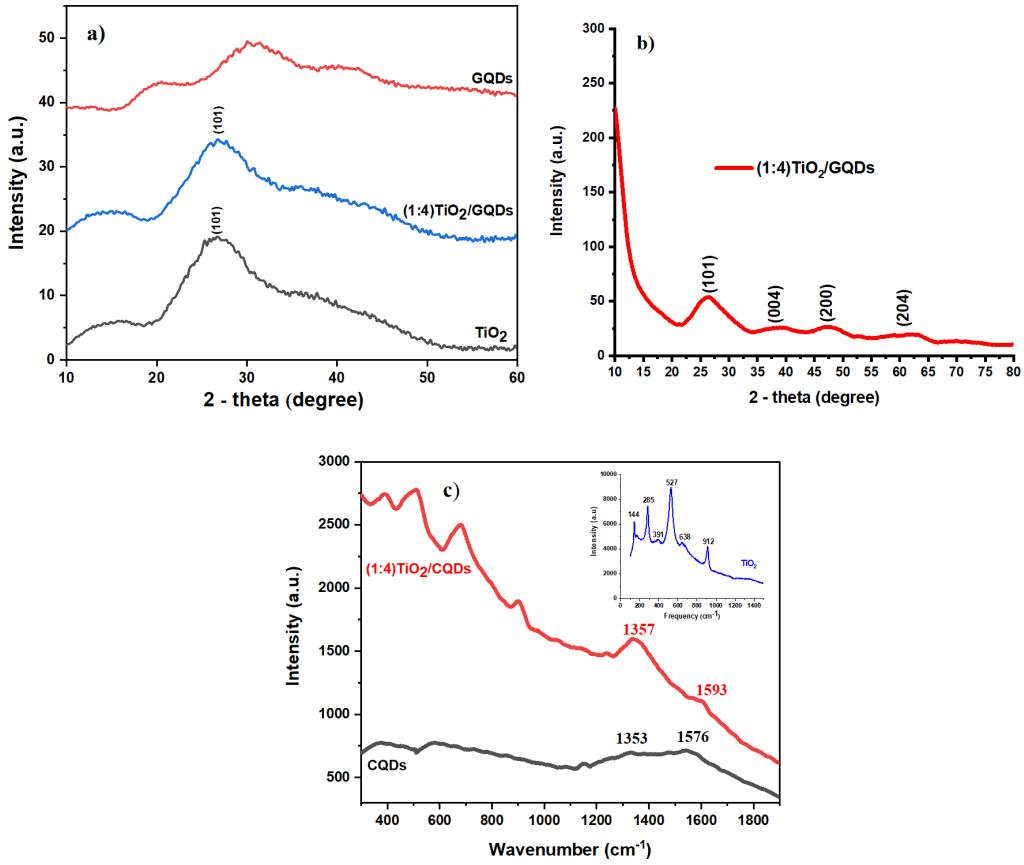


Figure 2: (a) XRD patterns of TiO_2, GQDs, and (1:4)TiO_2/GQDs in suspension form. (b) XRD pattern of (1:4)TiO_2/GQDs in solid form. (c) Raman spectra of TiO_2, GQDs, and (1:4)TiO_2/GQDs in solid form.

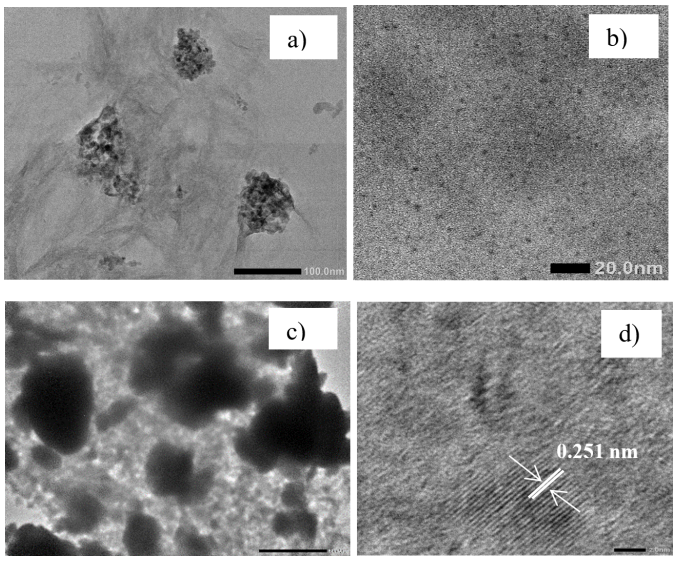


Figure 3: HRTEM images of (a) TiO_2, (b) GQDs, (c) (1:4)TiO_2/GQDs, and (d) of (1:4)TiO_2/GQDs with high magnification.

To further determine the composition of the prepared TiO_2/GQDs composites, EDX mapping was used (Figure 4). The obtained results reveal that TiO_2/GQDs contain C (30.6%), O (55.3%), and Ti (14.1%), evenly distributed across the sample. This is in agreement with the XRD, Raman, and HRTEM observations.

Simultaneous voltammetric determination of uric acid (URI) and hypoxanthine (HYP)

Cyclic voltammetric behavior of different electrodes

The cyclic voltammetric (CV) behaviors of different electrodes are presented in Figure 5a. The CV curve of the bare GCE shows broad and weak anodic peaks of URI and HYP oxida-

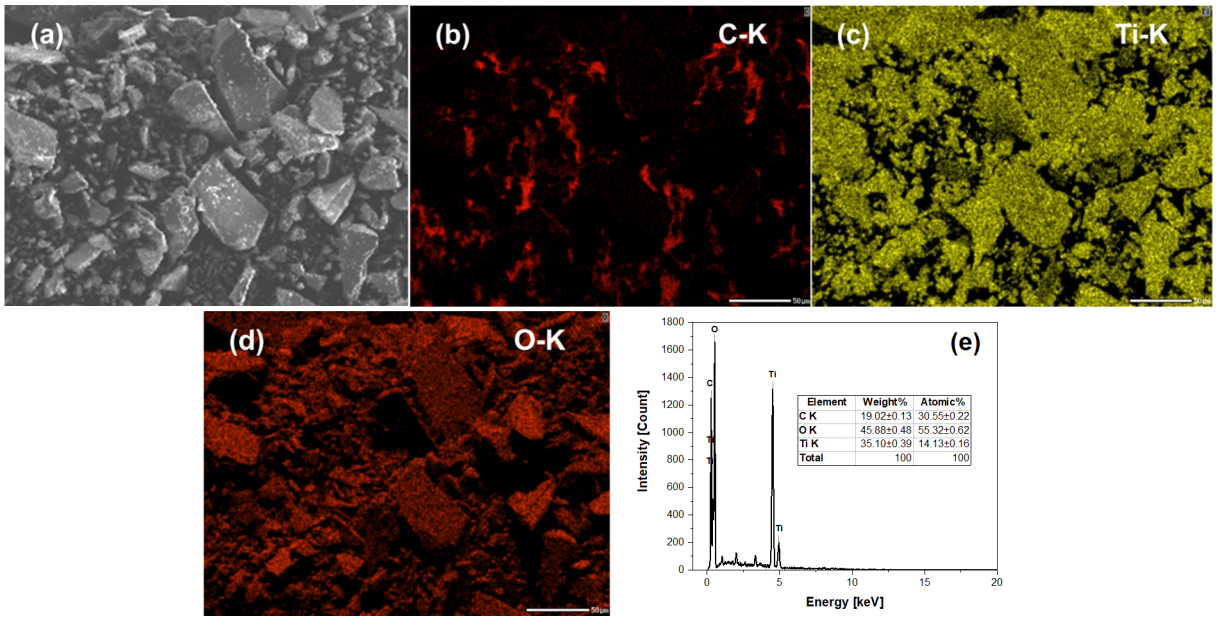


Figure 4: EDX mapping of (1:4)TiO_2/GQDs.

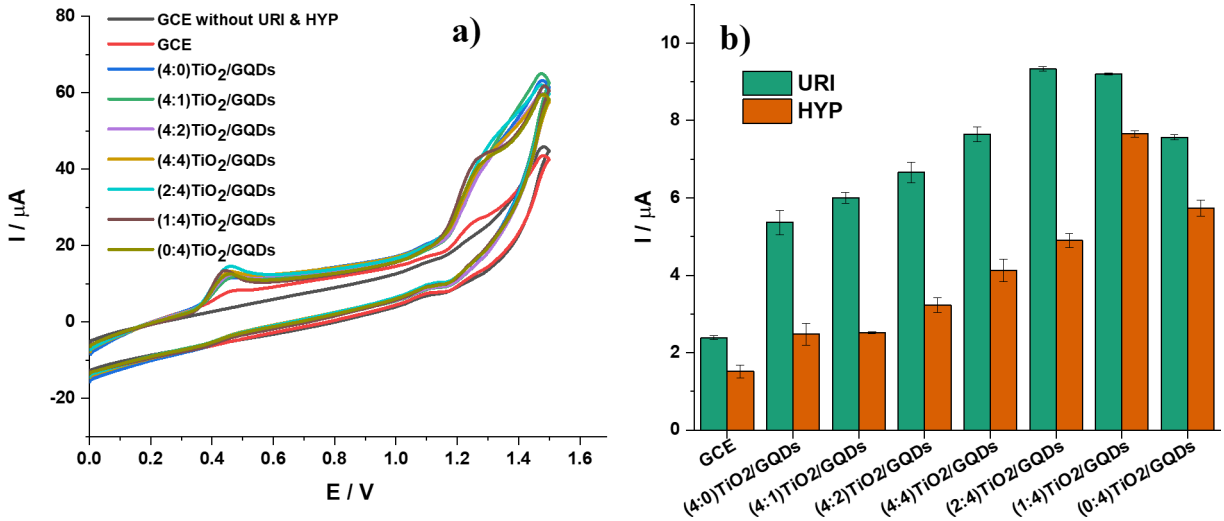


Figure 5: (a) CV curves at different electrodes in a solution (0.05 M BR buffer, pH 4) containing $C_{URI} = C_{HYP} = 25$ μM at a potential scan rate $v = 0.1$ V·s^{-1}. (b) Oxidation peak current of URI and HYP at different electrodes (the error bar represents the standard deviation of three measurements).

tion. The electrochemical signals are significantly enhanced when the electrode is modified with TiO_2/GQDs. A well-defined oxidation peak appears at 0.45 V for URI and at 1.26 V for HYP at the TiO_2/GQDs-GCE. It is notable that the electrochemical response is a function of the TiO_2/GQDs composition (Figure 5b). The oxidation peak currents of URI and HYP increase with increasing amount of GQDs in TiO_2/GQDs. However, the peak current of URI reaches its maximum when the GQDs reach 67% in mass (2:4)TiO_2/GQDs and decreases at higher amounts of GQDs. Meanwhile, the HYP oxidation peak current is highest when the amount of GQDs reaches 80% in mass in (1:4)TiO_2/GQDs. To balance between the peak currents of URI and HYP, the electrode modified by (1:4)TiO_2/GQDs was chosen for further investigation. At the (1:4)TiO_2/GQDs-GCE, the oxidation peak currents for URI and HYP are, respectively, 3.8 times and 5.1 times higher than those obtained at the bare GCE. URI is a weak diprotic acid with pK_{a1} = 5.4 and pK_{a2} = 9.8 [30]. HYP contains an ionizable group with pK_a = 8.7 [31]. The improved reversibility and sensitivity of the modified electrode may be due to the electrostatic interaction between positively charged URI and HYP and negatively charged GQD at remaining COO^- groups, the complexation of titanium to nitrogen or oxygen, or π–π interactions between the phenyl structure of purine and the planar hexagonal carbon structure of graphene.

Effect of pH

Figure 6a presents the pH dependence of the electrochemical response. The values of E_p and I_p vary as a function of pH, indicating that the oxidation process involves the transfer of protons. The oxidation peak current of both analytes peaks at pH 3 then decreases with further increase of pH. Therefore,

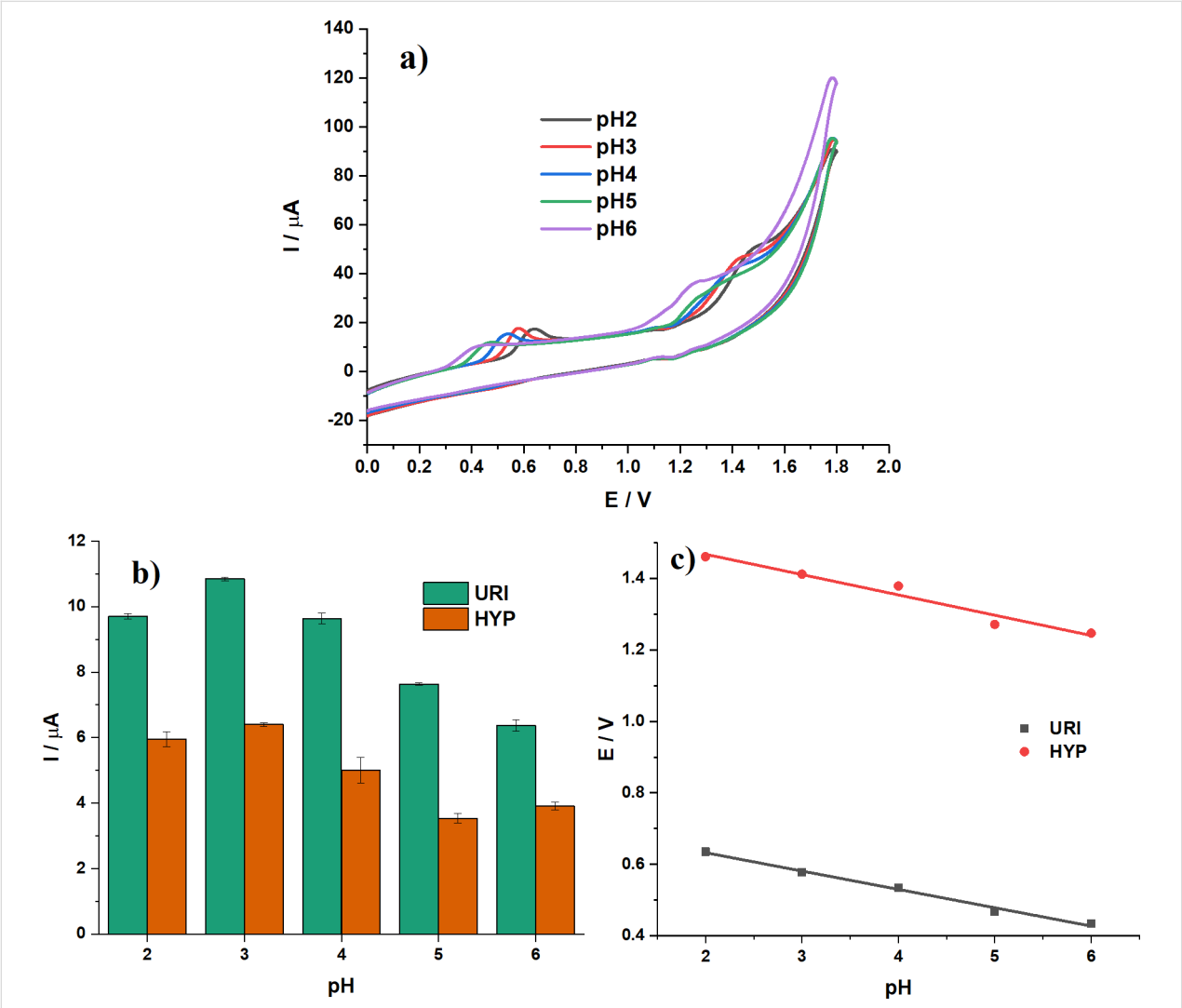


Figure 6: (a) CV curves of URI and HYP at equal concentrations of 25 µM in 0.05 M BR pH 2–6 at the (1:4)TiO_2/GQDs-GCE; potential scan rate v = 0.1 V·s^{-1}. (b) Oxidation peak current of URI and HYP at different pH values. (c) Linear plots of peak potential vs pH.

pH 3 was chosen for further experiments (Figure 6b). At the same time, the peak potential of both analytes shifts towards positive values with a linear relationship described by the following equations (Figure 6c):

$$E_{URI} = (0.7354 \pm 0.0109) + (-0.0514 \pm 0.0026)\text{pH};\ R^2 = 0.9925$$

$$E_{HYP} = (1.5818 \pm 0.0290) + (-0.0569 \pm 0.0068)\text{pH};\ R^2 = 0.9585$$

The slopes of the E_{URI} vs pH and E_{HYP} vs pH plots are close to the theoretical value of the Nernst equation (0.0599), indicating that the oxidation process involves the transfer of an equal number of protons and electrons.

Effect of scan rate

The effect of the scan rate on the electrochemical signals is illustrated in Figure 7a. The linear relationship between peak current and square root of scan rate is presented in Figure 7b with the following linear equations:

$$I_{URI} = (1.0832 \pm 0.3680) + (32.8361 \pm 0.9462)v^{1/2};\ R^2 = 0.9950$$

$$I_{HYP} = (0.3592 \pm 0.2316) + (18.2315 \pm 0.5955)v^{1/2};\ R^2 = 0.9936$$

The lines do not pass the origin, indicating that the oxidation process of both URI and HYP are controlled by adsorption processes [32].

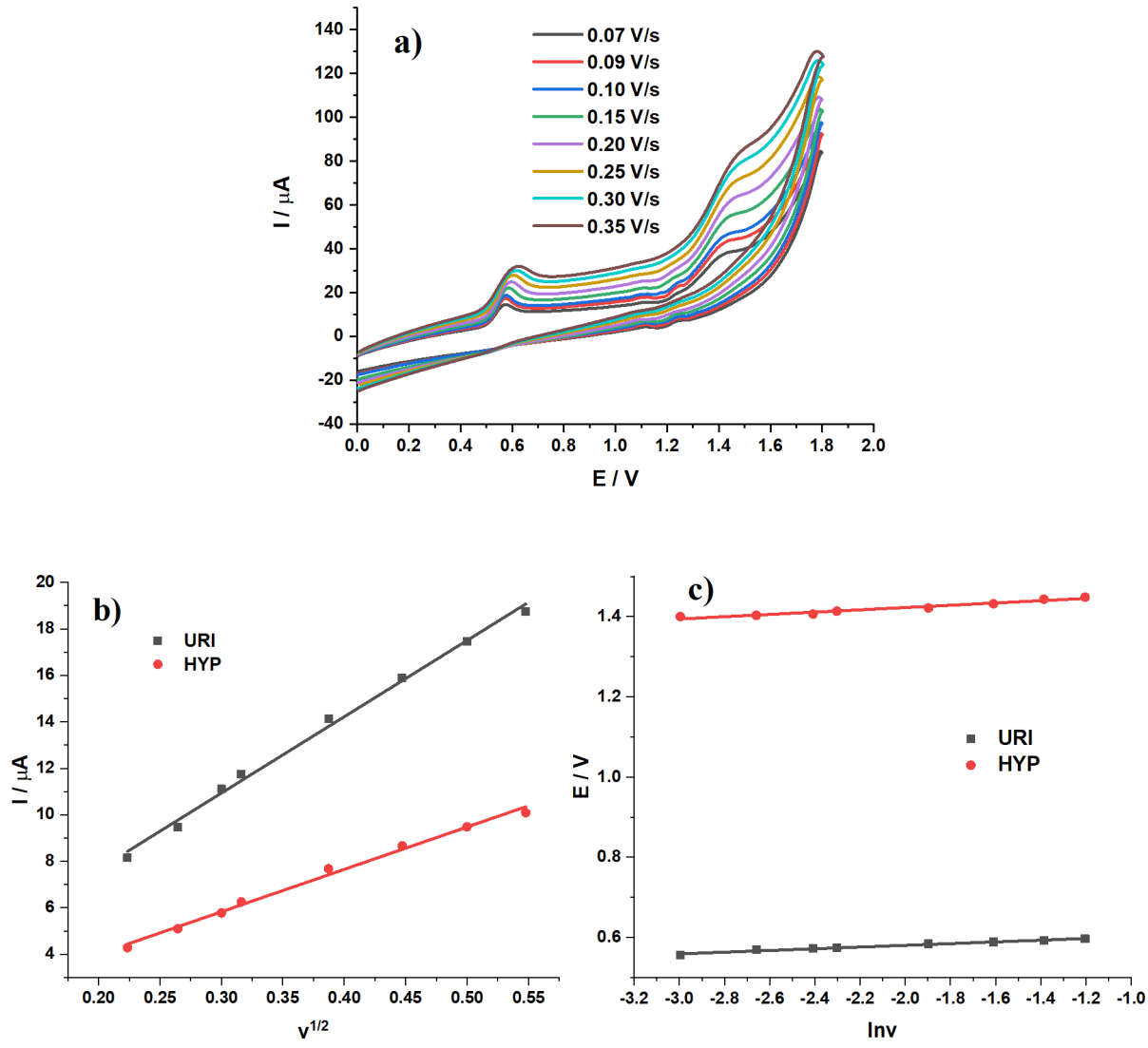
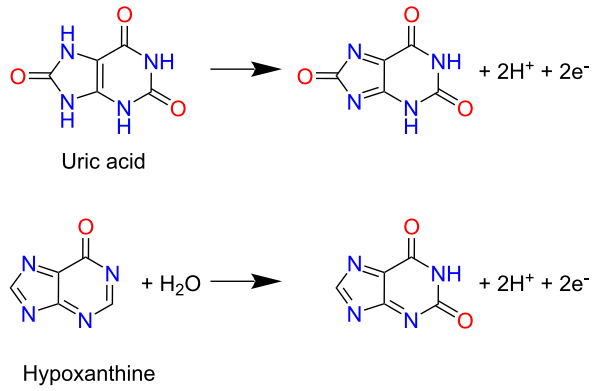


Figure 7: (a) CV curves of (1:4)TiO_2/GQDs-GCE in 0.05 M BR buffer (pH 3) with $C_{URI} = C_{HYP} = 25$ µM; scanning rate v = 0.07–0.35 V·s^{-1}. (b) Linear curves of peak intensity as a function of $v^{1/2}$. (c) Linear curves of peak potential of URI or HYP as a function of ln v.

The relationship between peak potential and natural logarithm of scan rate is described by the Laviron equation [33] (Figure 7c).

$$E_{URI} = (0.6228 \pm 0.0028) + (0.0214 \pm 0.0013) \ln v;\ R^2 = 0.9776$$
$$E_{HYP} = (1.4798 \pm 0.0051) + (0.0285 \pm 0.0024) \ln v;\ R^2 = 0.9600$$

The product $n\alpha$ was found as 1.2 for URI and 0.9 for HYP. For an irreversible system, α is assumed to be 0.5 [34]; therefore, n = 2.4 or 2 for URI and n = 1.8 or 2 for HYP, which indicates that the oxidation of URI and HYP involves the transfer of two electrons and two protons. Based on the above observations, plausible mechanisms for the electrooxidation of URI and HYP are proposed (Scheme 1), which are in good agreement with previous reports, where the oxidation of URI generates a bisimine [35], and the oxidation of HYP forms 6,8-dioxypurine at the N7=C8 double bond [36].



Scheme 1: Proposed oxidation mechanisms of URI and HYP at the (1:4)TiO_2/GQDs-GCE.

Relevant operational parameters

In the present work, the operational parameters accumulation potential (E_{acc}), accumulation time (t_{acc}), pulse amplitude (ΔE), and potential step (U_{step}) were optimized. E_{acc} does not significantly affect the oxidation signals (E_P and I_P) of URI and HYP (Supporting Information File 1, Figure S1a,b) when it is varied from −0.2 V to +0.4 V (vs Ag/AgCl|KCl 3 M). Specifically, E_P and I_P for the oxidation of URI remain constant at 0.510 ± 0.000 V and 13.43 ± 0.25 µA (n = 7), respectively; while the values for HYP are 1.341 ± 0.004 V and 7.204 ± 0.055 µA (n = 7), respectively. This shows that the TiO_2/GQDs material interacts well with URI and HYP during the accumulation step. An E_{acc} value of +0.1 V with low relative standard deviation (RSD) values for I_P of URI and HYP of 0.81% and 2.92%, respectively, was chosen to avoid any potential interference effect in real samples. The variation of the potential scan rate during DPV measurement reveals that the electrochemical reactions of URI and HYP are determined by adsorption. Therefore, even at t_{acc} = 0, the I_P values for URI and HYP are 3.787 ± 0.535 µA (n = 3) and 4.193 ± 0.318 µA (n = 3), respectively (Supporting Information File 1, Figure S1c,d). This phenomenon shows that URI and HYP quickly adsorb on the surface of the modified electrode at the beginning of the measurement. Therefore, when the accumulation time increases from 5 to 20 s, the I_P values of URI and HYP are not statistically different. However, it is possible that the high concentration of URI and HYP in the solution might saturate on the modified electrode surface. Therefore, an accumulation time of 15 s was chosen for further studies.

The effect of pulse amplitude (ΔE) was also studied (Supporting Information File 1, Figure S2a,b). When ΔE gradually increases from 0.04 to 0.08 V, the I_P of URI gradually increases, reaches the highest value at 0.10 V, and then remains constant up to ΔE of 0.12V. In contrast, the I_p of HYP rises with the increase of ΔE, peaks at 0.08 V, and then slightly decreases at higher pulse amplitudes. Furthermore, the HYP oxidation peak broadens with an increase of the peak half-width from 0.167 to 0.180 V as the pulse amplitude increases (Supporting Information File 1, Figure S2a). The oxidation peak of URI shifts positively as the pulse amplitude increases. This behavior might reduce the selectivity of the analytical method. Therefore, a pulse amplitude of 0.08 V was chosen for further studies. U_{step} in differential pulse anodic stripping voltammetry affects the potential scan rate and the stripping signal. The influence of U_{step} was studied in the range from 0.004 to 0.010 V corresponding to a potential scan rate from 13.3 $mV{\cdot}s^{-1}$ to 33.3 $mV{\cdot}s^{-1}$ with t_{step} = 0.3 s. It is clear that U_{step} slightly changes the oxidation potential of both HYP and URI. Theoretically, increasing the potential step might lead to an increase of I_p. However, a high U_{step} might also trigger the oxidation of other substances with similar oxidation potential, which greatly affects the simultaneous quantification of substances with stripping peaks close to each other. Therefore, a U_{step} value of 0.008 V was chosen for further studies.

Linear range and limit of detection

DPV curves for mixtures containing equal concentrations of URI and HYP are shown in Figure 8a. The peak current increases linearly when the concentration of both analytes increases from 1.00 to 15.26 µM (Figure 8b). The regression equations are as follows:

$$I_{URI} = (2.8804 \pm 0.0722) + (1.0818 \pm 0.0106) C_{URI};\ R^2 = 0.9984$$
$$I_{HYP} = (0.3161 \pm 0.0511) + (0.6520 \pm 0.0075) C_{HYP};\ R^2 = 0.9978$$

The limit of detection (LOD) is described as $3S/M$, where S is the standard deviation and M is the slope obtained from the cali-

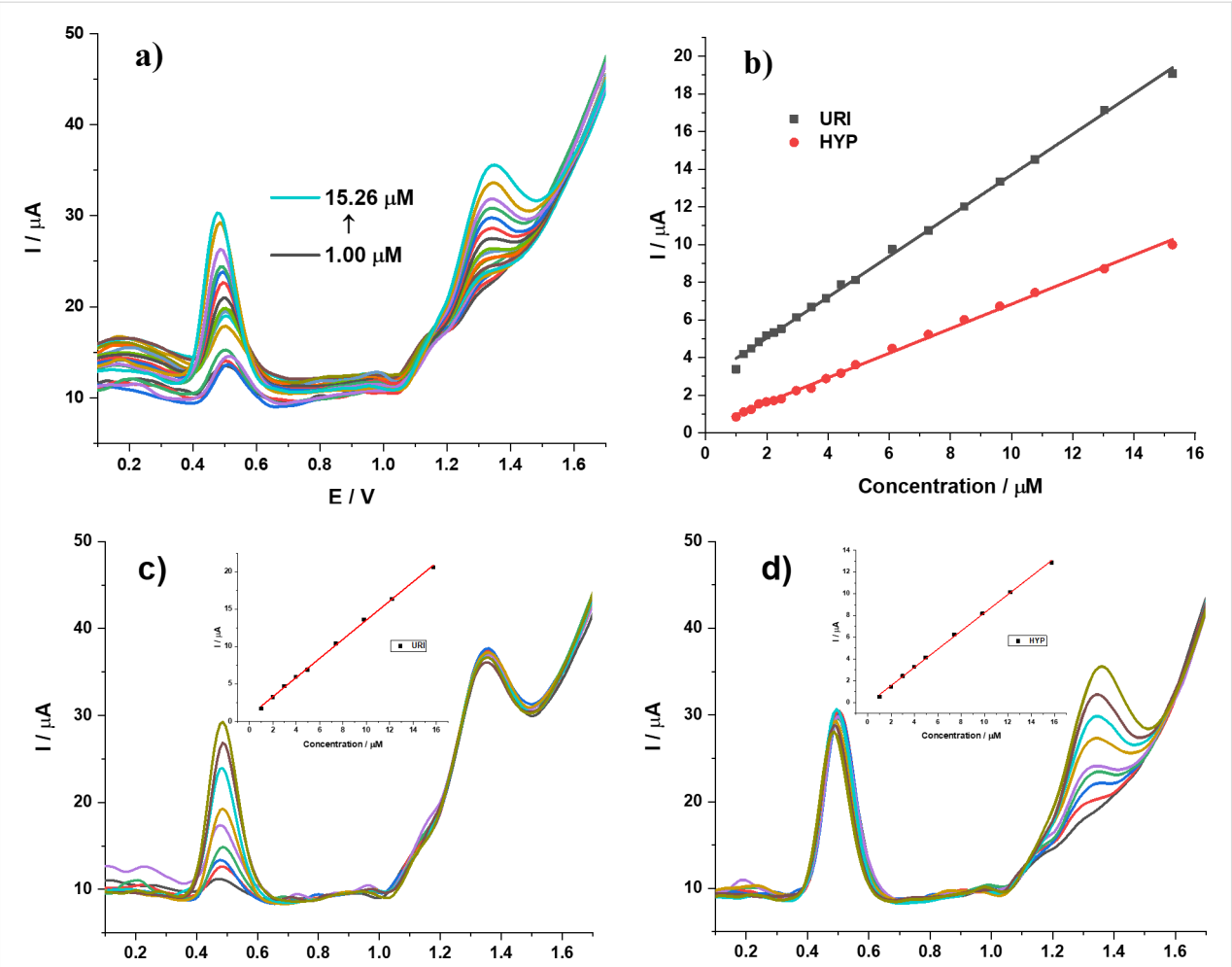


Figure 8: DPV curves at the (1:4)TiO_2/GQDs-GCE. (a) 0.05 M BR pH 3 with C_{URI} = C_{HYP} = 1.00–15.26 µM. (b) Linear plots of peak current vs URI and HYP concentration. (c) 0.05 M BR buffer (pH 3) with C_{URI} = 1.00–15.74 µM, C_{HYP} = 15.74 µM, the inset presents a linear plot of peak current vs URI concentration. (d) 0.05 M BR buffer (pH 3) with C_{HYP} = 1.00–15.74 µM, C_{HYP} = 15.74 µM, the inset presents a linear plot of peak current vs HYP concentration.

bration plot. The LOD values are 0.58 µM for URI and 0.68 µM for HYP. The cross-effect is a key factor for the simultaneous determination of analytes in a mixture. Figure 8c presents the effect of HYP concentration, which was kept constant at 15.74 µM, on the peak current intensity of different concentrations of URI. A linear response (the inset) is still found in the range of 1.00–15.74 µM with the regression equation of I_{URI} = (0.7538 ± 0.1356) + (1.2783 ± 0.0166)C_{URI} (R^2 = 0.9988) (LOD_{URI} = 0.61 µM). A similar behavior can be observed for the oxidation of an increasing amount of HYP (1.00–15.74 µM) (inset) in the presence of 15.74 µM URI. A linear calibration curve with a regression equation of I_{HYP} = (−0.1160 ± 0.0830) + (0.8376 ± 0.0102)C_{HYP} (R^2 = 0.9990) with LOD_{HYP} = 0.57 µM (Figure 8d) was found. These results indicate that the determination of URI in the presence of HYP and vice versa at the TiO_2/GQDs-GCE can be achieved with acceptable selectivity and sensitivity. A comparison with previously reported data is shown in Table 1. It is noticed that the performance of TiO_2/GQDs-GCE is better than or comparable with other electrodes with low detection limit.

Repeatability, stability and reproducibility

The parameters for validity of the proposed approaches are the within-run precision (repeatability), reproducibility, and the within-laboratory precision (long term-stability). The repeatability of the method was evaluated by comparing the RSD of the measurement to the RSD of the Horwitz function (RSD_H). If RSD is less than half of RSD_H, the repeatability is acceptable. The repeatability of this method was determined by analyzing ten replicate measurements on four different mixtures containing equal concentrations of URI and HYP (2.5, 5.0, 7.5, and 10 µM). The results show that all RSDs are smaller than 5% and 0.5·RSD_H (Figure 9a,b) indicating an acceptable repeatability. The reproducibility was estimated by measuring electrochemi-

Table 1: Comparison of URI and HYP determination at the TiO_2/GQDs-GCE with the literature.

Electrode	Method	Linear range (μM)		LOD (μM)		Applicability	Ref
		URI	HYP	URI	HYP		
Nf–{RuDMSO–Cl–H_2O}–MME/GCE	SWV	100–700	50–300	0.372	2.37	human urine samples	[37]
$Co_2Fe_2O_4$/rGO/GCE	DPV	2–10	2–10	0.767	0.506	urine samples	[38]
GCE/rGO/CS/Cr_2O_3/GCE	DPV	10–500	2–300	0.8	0.85	fish meat	[39]
PDAox–PTCA/GCE	DPV	1.8–238	3.8–293	1.50	1.25	biologically species	[40]
β-cyclodextrin/GCE	DPV	10–225	10–270	5	5	human urine samples	[41]
TiO_2/GQDs	DPV	1.0–15.3	1.0–15.3	0.58	0.68	urine samples	this work

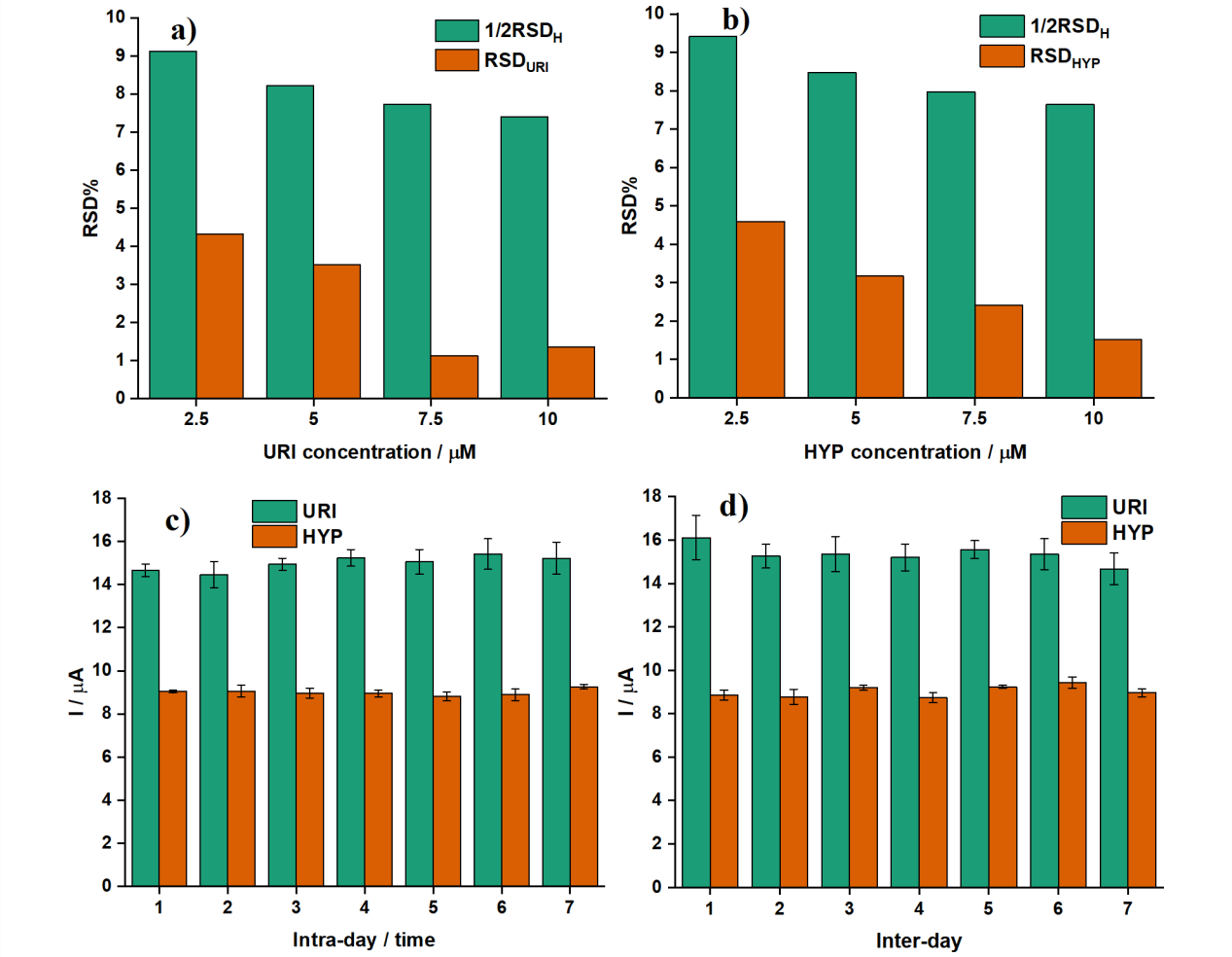


Figure 9: The RSD of ten replicate measurements of (a) URI and (b) HYP at the (1:4)TiO_2/GQDs-GCE in 0.05 M BR buffer pH 3 with C_{URI} = C_{HYP} = 2.5, 5.0, 7.5, and 10 μM. (c) I_p of URI and HYP (C_{URI} = C_{HYP} = 12 μM) in 0.05 M BR buffer pH 3 at seven different (1:4)TiO_2/GQDs-GCEs fabricated using the same procedure. (d) I_p of URI and HYP (C_{URI} = C_{HYP} = 12 μM) in 0.05 M BR buffer pH 3 at the (1:4)TiO_2/GQDs-GCE measured once a week.

cal signals of URI and HYP with seven modified electrodes fabricated using the same procedure. The peak currents (three consecutive measurements) of equal concentrations of URI and HYP (C_{URI} = C_{HYP} = 12 μM) at each modified electrode are given in Figure 9c. The peak currents were found as I_{URI} = 14.99 ± 0.34 (μA) with RSD = 2.26% and I_{HYP} = 9.00 ± 0.14 (μA) with RSD = 1.59%. An RSD smaller than 5% indicates that the proposed technique is reproducible. Stability is a

critical characteristic of electrochemical sensors; it can be determined by comparing electrochemical signals from a single electrode, which is kept at 4 °C in the BR buffer pH 3 between the measurements, for a definite period. DPV measurements were periodically performed once a week. Peak currents with RSD smaller than 5% were found as I_{URI} = 15.36 ± 0.43 (μA) (RSD = 2.82%) and I_{HYP} = 9.03 ± 0.26 (μA) (RSD = 2.93%) indicating good long-term stability of the (1:4)TiO_2/QGDs-GCE (Figure 9d).

In order to study the selectivity of the (1:4)TiO_2/GQDs-modified electrode, common co-existing substances, namely, NH_4Cl, KCl, Na_2SO_4, NH_4NO_3, $CaCl_2$, $ZnCl_2$, glucose (GLC), glutamic acid (GLA), urea (URE), L-cysteine (LCY) and xanthine (XTE), have been added to the analysis mixture containing URI (10 μM) and HYP (10 μM) to investigate the interference effect on the electrochemical responses (Figure 10 and Supporting Information File 1, Table S1). The results show that, except LCY and XTE affecting the measurement of URI and HYP at 40 and 60-fold excess, the other possible interferents exhibit no interference effect (with less than ±5% relative error) at 100-fold excess. This indicates that the designed modified electrode is a highly selective sensor for URI and HYP.

A human urine sample was used as real sample to investigate the reliability of the proposed method. The urine sample was diluted 130 times with 0.05 M BR buffer pH 3 before measurement. No other pretreatment process was required. The standard addition method was employed to test the recovery. The results show an exceptional recovery range from 96.57% to 103.58%, which clearly indicates the applicability and reliability of the proposed method (Table 2).

Conclusion

TiO_2/GQDs were prepared from peroxo titanium complexes, and GQDs were derived from ground coffee as precursor, which offers several advantages such as easy dispersion and functionalization during the synthesis. A simple strategy employing TiO_2/GQDs was used to fabricate a sensitive voltammetric sensor for the determination of URI and HYP in real samples. The decoration of nanoscale TiO_2 with GQDs can provide excellent electrode modification because of the combination of

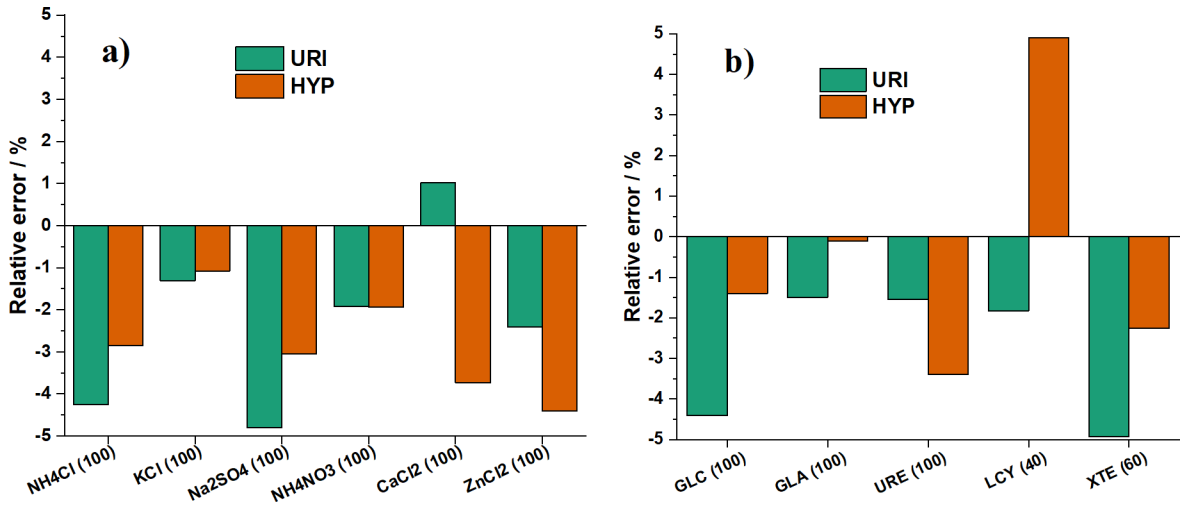


Figure 10: Effect of possible interferents. (a) Inorganic compounds and (b) organic compounds.

Table 2: Determination of URI and HYP in real samples (n = 5) with the (1:4)TiO_2/GQDs-GCE.

Sample	Analyte	Content ± SD (μM/)	Spiked (μg)	Found* ± SD (μg)	Recovery (%)
human urine 1	URI	2.633 ± 0.072	0.841	0.814 ± 0.029	96.84
	HYP	—	1.361	1.332 ± 0.030	97.88
human urine 2	URI	2.793 ± 0.066	0.841	0.860 ± 0.027	102.30
	HYP	—	1.361	1.341 ± 0.018	98.53
human urine 3	URI	4.493 ± 0.117	0.841	0.812 ± 0.023	96.57
	HYP	—	1.361	1.410 ± 0.030	103.58

enlarged active surface area and strong adsorptive capability of the nanomaterials. Low LODs, high reproducibility, and simple procedures for surface modification and analysis can be considered as the advantages of the proposed DPV method.

Supporting Information

Supporting Information File 1

Additional figures and tables.
[https://www.beilstein-journals.org/bjnano/content/supplementary/2190-4286-15-60-S1.pdf]

Competing Interests

The authors have no relevant financial or non-financial interests to disclose.

Author Contributions

Vu Ngoc Hoang: conceptualization; writing – original draft; writing – review & editing. Dang Thi Ngoc Hoa: formal analysis; investigation. Nguyen Quang Man: formal analysis; project administration; validation. Le Vu Truong Son: formal analysis; investigation. Le Van Thanh Son: investigation; validation. Vo Thang Nguyen: project administration; resources; validation. Le Thi Hong Phong: investigation; validation. Ly Hoang Diem: formal analysis; project administration. Kieu Chan Ly: formal analysis; validation. Ho Sy Thang: project administration; validation. Dinh Quang Khieu: conceptualization; writing – original draft; writing – review & editing.

ORCID® iDs

Vu Ngoc Hoang - https://orcid.org/0009-0004-4485-0258
Dang Thi Ngoc Hoa - https://orcid.org/0000-0003-4180-9351
Nguyen Quang Man - https://orcid.org/0000-0001-6511-1236
Le Vu Truong Son - https://orcid.org/0000-0002-1724-0137
Le Van Thanh Son - https://orcid.org/0000-0002-2061-6983
Vo Thang Nguyen - https://orcid.org/0000-0001-9224-8510
Le Thi Hong Phong - https://orcid.org/0000-0001-8825-6243
Ly Hoang Diem - https://orcid.org/0009-0004-0793-8509
Kieu Chan Ly - https://orcid.org/0009-0006-1291-3976
Ho Sy Thang - https://orcid.org/0000-0002-9660-3935
Dinh Quang Khieu - https://orcid.org/0000-0003-3473-6377

Data Availability Statement

All data that supports the findings of this study is available in the published article and/or the supporting information to this article.

References

1. Alderman, M.; Aiyer, K. J. V. *Curr. Med. Res. Opin.* **2004,** *20,* 369–379. doi:10.1185/030079904125002982
2. Liberopoulos, E.; Christides, D.; Elisaf, M. *J. Hypertens.* **2002,** *20,* 347. doi:10.1097/00004872-200202000-00027
3. Saugstad, O. D. *Pediatr. Res.* **1988,** *23,* 143–150. doi:10.1203/00006450-198802000-00001
4. Tohgi, H.; Abe, T.; Takahashi, S.; Kikuchi, T. *J. Neural Transm.: Parkinson's Dis. Dementia Sect.* **1993,** *6,* 119–126. doi:10.1007/bf02261005
5. Choi, H. K.; Atkinson, K.; Karlson, E. W.; Willett, W.; Curhan, G. *N. Engl. J. Med.* **2004,** *350,* 1093–1103. doi:10.1056/nejmoa035700
6. Azizpour Moallem, Q.; Beitollahi, H. *Microchem. J.* **2022,** *177,* 107261. doi:10.1016/j.microc.2022.107261
7. Dervisevic, M.; Dervisevic, E.; Şenel, M. *Microchim. Acta* **2019,** *186,* No. 749. doi:10.1007/s00604-019-3842-6
8. Sato, N.; Hirano, M.; Itoh, H.; Lu, P.; Okuda, S.; Nagata, K.; Okamoto, K. *Gout Uric Nucleic Acids* **2023,** *47,* 157–168. doi:10.14867/gnamtsunyo.47.2_157
9. Jia, Q.; Yang, Z.; Wang, Q.; Yang, H.; Tang, X.; Zhang, H.; Cao, L.; Zhang, G. *J. Sep. Sci.* **2023,** *46,* No. 2300090. doi:10.1002/jssc.202300090
10. Kuhara, T.; Tetsuo, M.; Ohse, M.; Shirakawa, T.; Nakashima, Y.; Yoshiura, K.-i.; Tanaka, N.; Taya, T. *IJU Case Rep.* **2023,** *6,* 436–439. doi:10.1002/iju5.12642
11. Kalluri, A.; Debnath, D.; Dharmadhikari, B.; Patra, P. *Methods Enzymol.* **2018,** *609,* 335–354. doi:10.1016/bs.mie.2018.07.002
12. Sapsford, K. E.; Algar, W. R.; Berti, L.; Gemmill, K. B.; Casey, B. J.; Oh, E.; Stewart, M. H.; Medintz, I. L. *Chem. Rev.* **2013,** *113,* 1904–2074. doi:10.1021/cr300143v
13. Song, W.; Poyraz, A. S.; Meng, Y.; Ren, Z.; Chen, S.-Y.; Suib, S. L. *Chem. Mater.* **2014,** *26,* 4629–4639. doi:10.1021/cm502106v
14. Sun, L.; Wu, W.; Yang, S.; Zhou, J.; Hong, M.; Xiao, X.; Ren, F.; Jiang, C. *ACS Appl. Mater. Interfaces* **2014,** *6,* 1113–1124. doi:10.1021/am404700h
15. Chen, W.; Lv, G.; Hu, W.; Li, D.; Chen, S.; Dai, Z. *Nanotechnol. Rev.* **2018,** *7,* 157–185. doi:10.1515/ntrev-2017-0199
16. Abbas, A.; Mariana, L. T.; Phan, A. N. *Carbon* **2018,** *140,* 77–99. doi:10.1016/j.carbon.2018.08.016
17. Ni, D.; Shang, Q.; Guo, T.; Wang, X.; Wu, Y.; Guan, H.; Wang, D.; Zhang, M. *Appl. Catal., B* **2017,** *210,* 504–512. doi:10.1016/j.apcatb.2017.04.019
18. Peter, I. J.; Rajamanickam, N.; Vijaya, S.; Anandan, S.; Ramachandran, K.; Nithiananthi, P. *Sol. Energy Mater. Sol. Cells* **2020,** *205,* 110239. doi:10.1016/j.solmat.2019.110239
19. Zhang, Y.; Zhang, K.; Jia, K.; Liu, G.; Ren, S.; Li, K.; Long, X.; Li, M.; Qiu, J. *Fuel* **2019,** *241,* 646–652. doi:10.1016/j.fuel.2018.12.030
20. Aslan Çakır, M.; Yetim, T.; Yetim, A. F.; Çelik, A. *J. Mater. Eng. Perform.* **2024,** *33,* 1472–1484. doi:10.1007/s11665-023-08049-3
21. Khan, H.; Seth, M.; Samanta, S.; Jana, S. *J. Sol-Gel Sci. Technol.* **2020,** *94,* 141–153. doi:10.1007/s10971-019-05108-x
22. Truong, Q. D.; Dien, L. X.; Vo, D.-V. N.; Le, T. S. *J. Solid State Chem.* **2017,** *251,* 143–163. doi:10.1016/j.jssc.2017.04.017
23. Yang, M.; Liu, N.; Wang, P.; Zhao, T. *Inorg. Chem. Commun.* **2023,** *153,* 110795. doi:10.1016/j.inoche.2023.110795
24. López-Muñoz, G. A.; Balderas-López, J. A.; Ortega-Lopez, J.; Pescador-Rojas, J. A.; Salazar, J. S. *Nanoscale Res. Lett.* **2012,** *7,* 667. doi:10.1186/1556-276x-7-667
25. Kato, H.; Nakamura, A.; Takahashi, K.; Kinugasa, S. *Phys. Chem. Chem. Phys.* **2009,** *11,* 4946–4948. doi:10.1039/b904593g

26. Ran, C.; Wang, M.; Gao, W.; Yang, Z.; Shao, J.; Deng, J.; Song, X. *RSC Adv.* **2014,** *4,* 21772–21776. doi:10.1039/c4ra03542a
27. Kumar, S.; Ojha, A. K. *Mater. Chem. Phys.* **2016,** *171,* 126–136. doi:10.1016/j.matchemphys.2015.12.008
28. Su, W.; Zhang, J.; Feng, Z.; Chen, T.; Ying, P.; Li, C. *J. Phys. Chem. C* **2008,** *112,* 7710–7716. doi:10.1021/jp7118422
29. Qu, D.; Zheng, M.; Du, P.; Zhou, Y.; Zhang, L.; Li, D.; Tan, H.; Zhao, Z.; Xie, Z.; Sun, Z. *Nanoscale* **2013,** *5,* 12272–12277. doi:10.1039/c3nr04402e
30. Chong, D. P. *J. Theor. Comput. Sci.* **2013,** *1,* No. 1000104. doi:10.4172/jtco.1000104
31. Bai, B.; Wang, X.; Yang, L.; Song, H.; Yan, G.; Han, Y.; Fang, H.; Sun, H. *Biomed. Chromatogr.* **2023,** *37,* No. e5560. doi:10.1002/bmc.5560
32. Soleymani, J.; Hasanzadeh, M.; Shadjou, N.; Jafari, M. K.; Gharamaleki, J. V.; Yadollahi, M.; Jouyban, A. *Mater. Sci. Eng., C* **2016,** *61,* 638–650. doi:10.1016/j.msec.2016.01.003
33. Laviron, E. *J. Electroanal. Chem. Interfacial Electrochem.* **1979,** *101,* 19–28. doi:10.1016/s0022-0728(79)80075-3
34. Li, C. *Colloids Surf., B* **2007,** *55,* 77–83. doi:10.1016/j.colsurfb.2006.11.009
35. Huang, D.; Cheng, Y.; Xu, H.; Zhang, H.; Sheng, L.; Xu, H.; Liu, Z.; Wu, H.; Fan, S. *J. Solid State Electrochem.* **2015,** *19,* 435–443. doi:10.1007/s10008-014-2614-9
36. Mathew, M. R.; Kumar, K. G. *J. Electrochem. Soc.* **2020,** *167,* No. 047519. doi:10.1149/1945-7111/ab74c1
37. Kumar, A. S.; Swetha, P. *J. Electroanal. Chem.* **2010,** *642,* 135–142. doi:10.1016/j.jelechem.2010.02.031
38. Hoan, N. T. V.; Minh, N. N.; Trang, N. T. H.; Thuy, L. T. T.; Van Hoang, C.; Mau, T. X.; Vu, H. X. A.; Thu, P. T. K.; Phong, N. H.; Khieu, D. Q. *J. Nanomater.* **2020,** *2020,* 9797509. doi:10.1155/2020/9797509
39. Ghanbari, K.; Nejabati, F. *Anal. Methods* **2020,** *12,* 1650–1661. doi:10.1039/d0ay00161a
40. Liu, X.; Ou, X.; Lu, Q.; Zhang, J.; Chen, S.; Wei, S. *RSC Adv.* **2014,** *4,* 42632–42637. doi:10.1039/c4ra05853d
41. Wei, G.; Zhi-yu, D.; Li-li, C.; Da-jun, L.; Xing-quan, H. *Chem. Res. Chin. Univ.* **2012,** *28,* 1047–1053.

License and Terms

This is an open access article licensed under the terms of the Beilstein-Institut Open Access License Agreement (https://www.beilstein-journals.org/bjnano/terms), which is identical to the Creative Commons Attribution 4.0 International License (https://creativecommons.org/licenses/by/4.0). The reuse of material under this license requires that the author(s), source and license are credited. Third-party material in this article could be subject to other licenses (typically indicated in the credit line), and in this case, users are required to obtain permission from the license holder to reuse the material.

The definitive version of this article is the electronic one which can be found at:
https://doi.org/10.3762/bjnano.15.60

BEILSTEIN JOURNAL OF NANOTECHNOLOGY

Facile synthesis of Fe-based metal–organic frameworks from Fe_2O_3 nanoparticles and their application for CO_2/N_2 separation

Van Nhieu Le*[1], Hoai Duc Tran[1], Minh Tien Nguyen[1], Hai Bang Truong[2,3], Toan Minh Pham[4] and Jinsoo Kim[4]

Full Research Paper

Open Access

Address:
[1]Faculty of Chemical Engineering, Industrial University of Ho Chi Minh City, 12 Nguyen Van Bao, Go Vap, Ho Chi Minh City 70000, Vietnam, [2]Optical Materials Research Group, Science and Technology Advanced Institute, Van Lang University, Ho Chi Minh City 700000, Vietnam, [3]Faculty of Applied Technology, School of Technology, Van Lang University, Ho Chi Minh City 700000, Vietnam and [4]Department of Chemical Engineering (Integrated Engineering), Kyung Hee University, 1732 Deogyeong-daero, Giheung-gu, Yongin-si, Gyeonggi-do 17104, Korea

Email:
Van Nhieu Le* - levannhieu@iuh.edu.vn

* Corresponding author

Keywords:
CO_2/N_2 separation; Fe_2O_3 nanoparticles; hydrothermal reaction; IAST-predicted CO_2/N_2 selectivity; MIL-100(Fe)

Beilstein J. Nanotechnol. **2024,** *15,* 897–908.
https://doi.org/10.3762/bjnano.15.74

Received: 30 March 2024
Accepted: 04 July 2024
Published: 19 July 2024

This article is part of the thematic issue "Recent advances in synthesis and applications of organometallic nanomaterials".

Guest Editor: T.-D. Nguyen

© 2024 Le et al.; licensee Beilstein-Institut.
License and terms: see end of document.

Abstract

A facile approach was employed to fabricate MIL-100(Fe) materials from Fe_2O_3 nanoparticles through a conventional hydrothermal reaction without the presence of HF and HNO_3. Effects of trimesic acid content in the reaction system on the quality and CO_2/N_2 separation performance of the as-prepared MIL-100(Fe) samples were investigated. Using 1.80 g of trimesic acid in the reaction system yielded the sample M-100Fe@Fe_2O_3#1.80, which proved to be the optimal sample. This choice struck a balance between the amount of required trimesic acid and the quality of the resulting material, resulting in a high yield of 81% and an impressive BET surface area of 1365.4 $m^2 \cdot g^{-1}$. At 25 °C and 1 bar, M-100Fe@Fe_2O_3#1.80 showed a CO_2 adsorption capacity of 1.10 $mmol \cdot g^{-1}$ and an IAST-predicted CO_2/N_2 selectivity of 18, outperforming conventional adsorbents in CO_2/N_2 separation. Importantly, this route opens a new approach to utilizing Fe_2O_3-based waste materials from the iron and steel industry in manufacturing Fe-based MIL-100 materials.

Introduction

Metal-organic frameworks (MOFs) are well-ordered porous hybrid structures assembled from the fundamental components of metal ion clusters and organic linkers. MOFs are well known as multipurpose materials that serve a broad range of applications because of their unique construction variants, enormous surface areas, high thermal stability, changeable pore system

sizes, and customizable chemical surfaces [1-6]. The family tree of MOFs holds giant lineages such as Zeolitic Imidazolate Framework (ZIF), University of Olso (UiO), Material of Institute Lavoisier (MIL), Dresden University of Technology (DUT), and others. Among them, the Fe-based MIL-100(Fe) material stands out as an exceptional member of the MIL family because of its distinct properties [7,8]. MIL-100(Fe) offers a substantial number of unsaturated metal sites. These sites act as Lewis acid sites once ligands (–OH and water) are removed from the termini of iron octahedra in the secondary building units (SBUs) through an activated-thermal process in a vacuum-controlled environment [9,10]. Notably, density and oxidation states of the formed unsaturated Fe sites (Fe(II) and Fe(III)) are temperature-dependent, influencing the strength of the Lewis acid properties. Lower temperatures (approx. 150 °C) favor Fe(III), while higher temperatures up to 250 °C promote Fe(II) [9,10]. The MIL-100(Fe) structure is built from oxo-trimers of iron octahedra as SBUs together with bridges of benzene-1,3,5-tricarboxylate, yielding a hybrid supertetrahedral structure. Following that, the hybrid structures self-assemble in a certain sequence to form a topology resembling the MTN-type of zeolite seen in Zeolite Socony Mobil Thirty-Nine (ZSM-39) [11]. The MIL-100(Fe) structure has a cubic series containing two types of large chambers with average diameters of 2.5 and 2.9 nm, which may accommodate guest molecules entering through pentagon (0.47–0.55 nm) and hexagon (0.86 nm) apertures; this is an extremely porous channel system with immense surface area and pore volume [10,12]. Furthermore, MIL-100(Fe) is also widely recognized for its low manufacturing cost, environmental friendliness, and biodegradability. Because of the abovementioned advantages, MIL-100(Fe) has gained popularity as a candidate for gas separation of CO/CO_2 [9,13], CO/N_2 [14,15], CO_2/CH_4 [16], $CH_4/C_2H_6/C_3H_8$ [17], and SF_6/N_2 [18].

In the early stage, MIL-100(Fe) was produced using metallic iron and iron salts, along with HF and HNO_3, in a conventional hydrothermal reactor operated at high temperatures [9,10]. While HF and HNO_3 improve yield and quality of MIL-100(Fe), they are harmful to the environment because of their toxicity and corrosiveness. As a result, scientists are consistently working to eliminate HF, HNO_3, and other enhancing agents from the reaction process while maintaining the material quality. Initially, trimethyl benzene-1,3,5-tricarboxylate and iron(III) chloride hexahydrate ($FeCl_3{\cdot}6H_2O$) were combined to create MIL-100(Fe) without using HF and HNO_3. This method resulted in high-quality MIL-100(Fe) with a Langmuir surface area of 2800 $m^2{\cdot}g^{-1}$, but the yield was only 47%. In addition, it extended the reaction time to three days and significantly increased the cost because of the more expensive trimethyl benzene-1,3,5-tricarboxylate compared to trimesic acid [19]. These factors caused an immense rise in production cost. Further efforts were made to enhance both product quality and yield by using $FeCl_3{\cdot}6H_2O$ and iron(III) nitrate nonahydrate ($Fe(NO_3)_3{\cdot}9H_2O$) as iron precursors in a high-temperature reactor without HF and HNO_3. The findings revealed that a high $Fe(NO_3)_3{\cdot}9H_2O$ concentration in the MIL-100(Fe) preparation resulted in excellent outcomes, achieving approximately 80% yield and a BET surface area of 1800 $m^2{\cdot}g^{-1}$. These results closely matched those from the original recipe, which utilized metallic iron in the presence of HF and HNO_3, yielding 82% and a BET surface area of 2050 $m^2{\cdot}g^{-1}$ [20]. Since then, various green synthetic routes from ferric nitrate and metallic iron powder have been developed for generating MIL-100(Fe), including low-temperature synthesis [21], solvent-free synthesis [22], and dry gel conversion pathway [23]. It should be noted that the observed BET surface area fluctuates between 1100 and 2100 $m^2{\cdot}g^{-1}$, reflecting the quality of the obtained MIL-100(Fe); it depends on the iron precursors, synthetic pathways, and the purification procedure to eliminate unexpected components inside the pore system [20,24,25].

Additionally, iron oxides were considered as iron precursors required to make MIL-100(Fe). The first candidate Fe_3O_4 was used to successfully fabricate MIL-100(Fe) in a hydrothermal reactor in the absence of HF and HNO_3 [26,27]; it resulted in enhanced porosity of the obtained material when increasing the mass ratio between Fe_3O_4 and benzene-1,3,5-tricarboxylic acid in the reactor. Very recently, Freund et al. [28] employed Fe_2O_3 to produce successfully MIL-100(Fe) in a conventionally hydrothermal reaction at 150 °C for 27 h with the assistance of HF and HNO_3, which are hazardous chemicals to the environment. In contrast to metallic iron and iron salts, iron oxides are acknowledged for their easy storage and abundant availability in raw materials derived from natural iron oxidation processes and steelmaking industry waste [29,30]. These characteristics play a crucial role in the selection of economical raw materials for the large-scale production of MIL-100(Fe). Utilizing iron oxide as an iron precursor for manufacturing MIL-100(Fe) contributes to the expansion of raw material options. According to what we know, until now, there has been no report on a pathway for generating MIL-100(Fe) from Fe_2O_3 without the assistance of HF and HNO_3.

In this study, MIL-100(Fe) nanoparticles were successfully made utilizing a green synthetic route to convert Fe_2O_3 in a traditional hydrothermal reaction with the assistance of trimesic acid. A variety of analytical methods were employed to estimate quality and yield of the as-prepared MIL-100(Fe) materials, including thermogravimetric analysis (TGA), Fourier-transform infrared (FTIR) spectroscopy, powder X-ray diffraction (PXRD) measurements, determination of textural properties,

scanning electron microscopy (SEM), and X-ray photoelectron spectroscopy (XPS). Subsequently, the gas separation performance of the as-prepared MIL-100(Fe) samples was assessed by studies regarding CO_2 and N_2 adsorption isotherms at various temperatures with pressures up to 1 bar.

Experimental

Materials

Iron(III) oxide (Fe_2O_3, 96%) and benzene-1,3,5-tricarboxylic acid (H_3BTC, 95%) were supplied from Sigma-Aldrich. Anhydrous ethanol (EtOH, 99.5%) was acquired from Daejung Chemicals (Korea). Deionized (DI) water was generated using the Aqua Max ultra 360 system from Young-Lin (Korea). No further purification was performed on the chemicals before use.

Preparation of M-100Fe@Fe_2O_3 and MIL-100(Fe) materials

The Fe-based metal-organic framework (MIL-100) was fabricated through a hydrothermal reaction system using iron(III) oxide as the precursor and H_3BTC as linker for Fe ion clusters. The procedure was adapted from the method described by Aslam and coworkers [26]. Typically, 0.9 g Fe_2O_3 and different amounts of H_3BTC, alongside 45 mL of DI water, were introduced into a Teflon beaker and gently stirred for 15 min at room temperature. The mixture was then carefully sealed inside an autoclave made of stainless steel before being placed inside an electrically heated oven operated at 160 °C for 12 h. Once the resultant slurry had cooled to ambient temperature, it was washed with DI water and EtOH at 60 °C three times. Finally, the solid powder was collected after centrifugation and drying at 70 °C for 12 h. The resulting products were marked as M-100Fe@Fe_2O_3#0.90, M-100Fe@Fe_2O_3#1.35, M-100Fe@Fe_2O_3#1.80, and M-100Fe@Fe_2O_3#2.25, corresponding to H_3BTC amounts of 0.90, 1.35, 1.80, and 2.25 g, respectively.

A MIL-100(Fe) reference sample was prepared in accordance with the protocol described in Horcajada's report [11], with additional details provided in Supporting Information File 1.

Characterizations

The materials' crystalline structure was identified via room-temperature powder X-ray diffraction (PXRD) patterns from a MiniFlex600 system (Rigaku, Japan). The scan covered a 2θ range of 3–40° at a speed of 6°·min^{-1}. Information regarding the morphologies of Fe_2O_3 and M-100Fe@Fe_2O_3 materials was collected using a field-emission scanning electron microscope Leo-Supra 55 (Carl Zeiss STM, Germany). An attenuated total reflectance (ATR) setup was adopted to record the Fourier-transform infrared (FTIR) spectra of all samples on a Frontier spectrometer (PerkinElmer, USA) in the wavenumber range of 4000–400 cm^{-1}. The thermal stability of the as-prepared materials was investigated over a temperature range of 30–650 °C, employing an acceleration rate of 5 °C·min^{-1} in an air stream, using a Q50 thermogravimetric analyzer (TA Instruments, New Castle, USA). The chemical states of Fe and O in the materials were examined using a K-Alpha photoelectron spectrometer (ThermoFisher Scientific, USA). The isotherms for N_2 adsorption and desorption at 77 K over the materials were measured using a BELSORP-max apparatus (BEL, Japan). This allowed for calculating the surface area, using the Brunauer–Emmett–Teller (BET) model, and the total pore volume and pore size distribution, using the Horvath–Kawazoe (HK) model. The samples were activated under vacuum at 150 °C for 12 h before being introduced into the porosity analyzer.

CO_2 and N_2 adsorption test

The characteristic adsorption of CO_2 and N_2 on the as-prepared materials was investigated in the range of 0–100 kPa at different temperatures using a static adsorption system (BELSORP-min II, BEL, Japan). Prior to implementation, approximately 250 mg of M-100Fe@Fe_2O_3 and MIL-100(Fe) samples were degassed under vacuum at 50 °C for 2 h, followed by an additional 12 h at 150 °C in a glass tube before naturally cooling to ambient temperature. To assess the adsorbent's reusability, five cycles of CO_2 adsorption and desorption were conducted at 25 °C. The adsorbent was refreshed for 2 h at 100 °C under vacuum for each cycle.

Estimation of CO_2/N_2 selectivity via ideal adsorbed solution theory (IAST)

The IAST is widely recognized as a predictive means to evaluate the adsorption selectivity of an adsorbent towards a gas mixture without experimental data for the gas mixture. Herein, a binary mixture of CO_2 and N_2 containing 10 vol % CO_2 is used to anticipate the CO_2/N_2 selectivity of the as-prepared materials. Initially, the experimental adsorption data for the single components CO_2 and N_2 were measured in a range of 0–100 kPa at 25 °C, which were then described using the Langmuir–Freundlich model [31,32]. The fitted parameters are given in Supporting Information File 1, Table S1 with high correlation coefficient values ($R^2 \geq 0.9998$) for all samples. Subsequently, the CO_2/N_2 selectivity over all samples was anticipated using IAST alongside the fitted parameters of the model. All Langmuir–Freundlich and IAST-CO_2/N_2 selectivity equations are detailed in Supporting Information File 1.

Results and Discussion

Material characterizations

A range of M-100Fe@Fe_2O_3 samples was prepared from iron oxide (Fe_2O_3) nanoparticles as precursor with H_3BTC as

organic linker through a hydrothermal reaction as shown in Figure 1. The H_3BTC concentration was incrementally introduced into the reaction system to control the quality of the as-prepared samples.

As shown in Figure 2, reflections of crystalline Fe_2O_3 were detected in the p-Fe_2O_3 XRD pattern, which are in absolute agreement with the simulated data, including the (220) and (311) planes in the examined region (JCPDS 39-1346). After the Fe_2O_3 nanoparticles underwent a highly conditional reaction, the characteristic peaks of MIL-100(Fe) were verified in the XRD profiles of the as-prepared M-100Fe@Fe_2O_3 samples. The XRD data of the reference MIL-100(Fe) sample and the simulated data from CCDC 640536 were aligned, demonstrating the successful preparation of MIL-100(Fe) crystals from Fe_2O_3 nanoparticles under the studied conditions. A further examination revealed that the measured peaks of MIL-100(Fe) gradually increased, whereas those of Fe_2O_3 decreased in intensity with increasing amounts of H_3BTC from 0.9 to 1.80 g. However, even after increasing the H_3BTC amount to 2.25 g in the reaction system, the characteristic peaks of MIL-100(Fe) and Fe_2O_3 were still preserved. This demonstrates that Fe_2O_3 nanoparticles were partially converted into MIL-100(Fe) material, with the quality of the obtained MIL-100(Fe) depending on the H_3BTC concentration.

To further reinforce this statement, the morphology of all materials was examined via SEM analysis. Figure 3 reveals that Fe_2O_3 nanoparticles appeared in spherical shapes, while MIL-100(Fe) crystals displayed an octahedral morphology with sizes around 1 µm. The SEM images of M-100Fe@Fe_2O_3 samples showed polyhedral nanoparticles, indicating the successful preparation of MIL-100(Fe) crystals. It is important to note that the morphology of the obtained MIL-100(Fe) crystals depends on both the source of Fe-based precursor

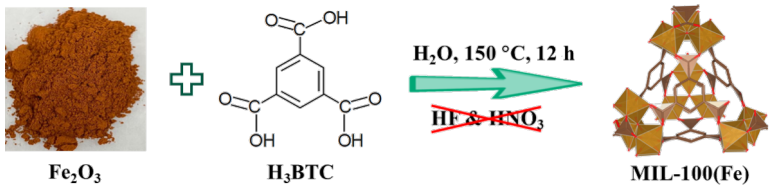


Figure 1: Pathway for preparing M-100Fe@Fe_2O_3 samples.

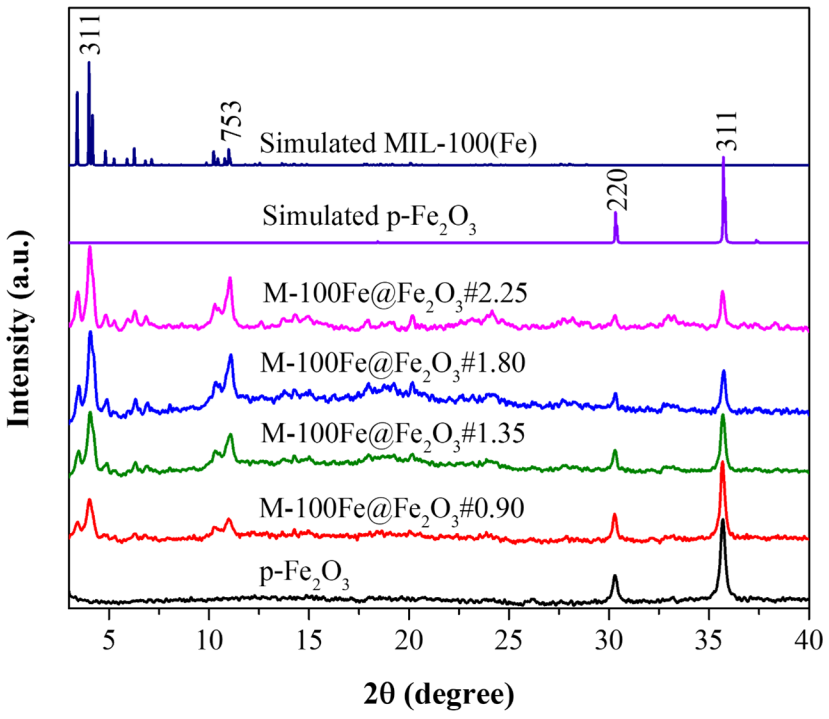


Figure 2: PXRD patterns of Fe_2O_3, MIL-100(Fe), and M-100Fe@Fe_2O_3 samples.

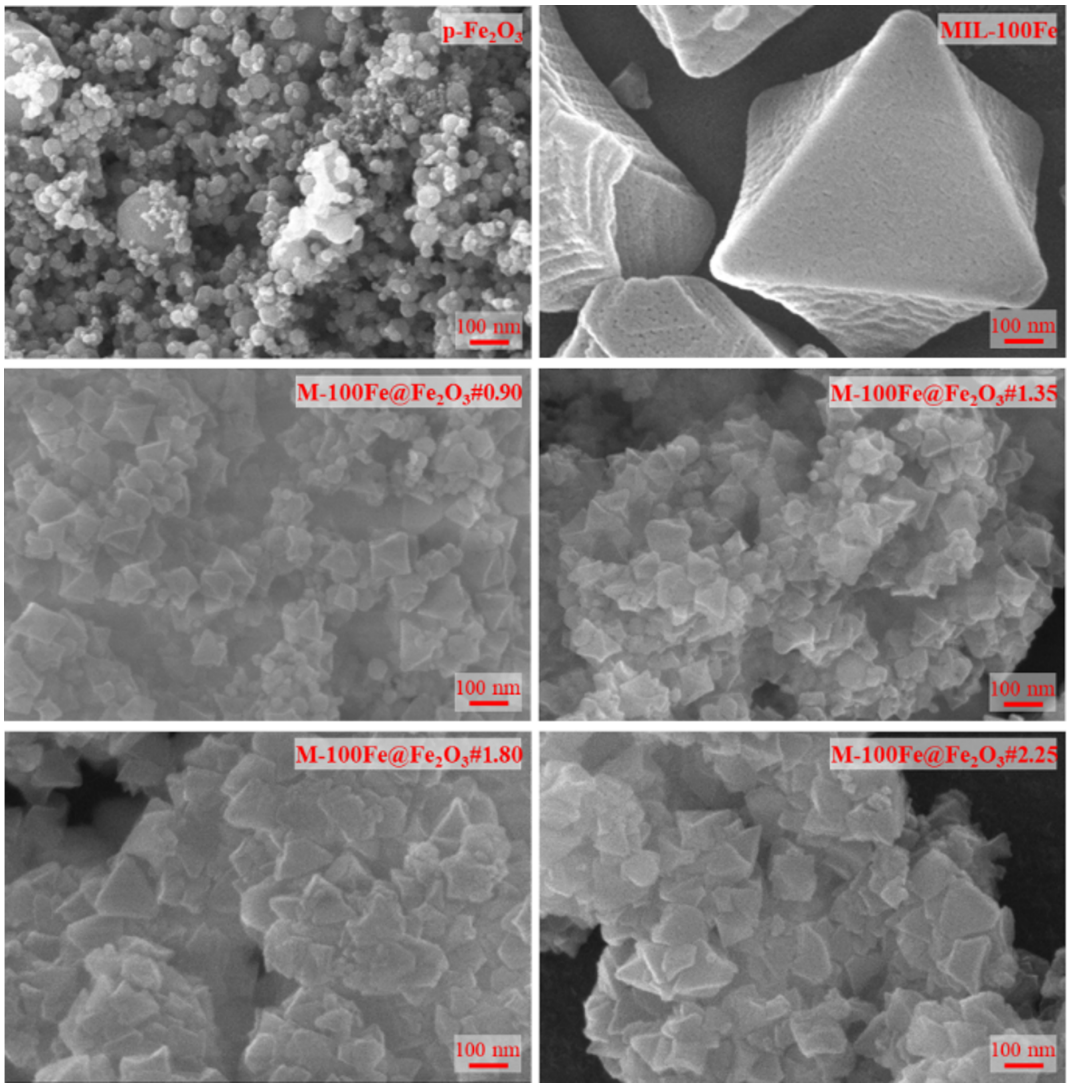


Figure 3: SEM images of Fe_2O_3, MIL-100(Fe), and M-100Fe@Fe_2O_3 samples.

and the synthetic approaches employed [24,25]. Additionally, the SEM images showed that spherical nanoparticles were easily observed in the M-100Fe@Fe_2O_3#0.90 and M-100Fe@Fe_2O_3#1.35 samples, whereas they were harder to detect in the M-100Fe@Fe_2O_3#1.80 and M-100Fe@Fe_2O_3#2.25 samples. This suggests that the concentration of MIL-100(Fe) crystals in the prepared M-100Fe@Fe_2O_3 samples increases in the following order: M-100Fe@Fe_2O_3#0.90 < M-100Fe@Fe_2O_3#1.35 < M-100Fe@Fe_2O_3#1.80 < M-100Fe@Fe_2O_3#2.25. This result aligns well with the XRD data shown in Figure 2.

Figure 4 exhibits ATR-FTIR spectra of Fe_2O_3, MIL-100(Fe), and as-prepared M-100Fe@Fe_2O_3 samples. Characteristic peaks, including vibration bands in the region of 550 to 630 cm^{-1}, were assigned to Fe–O bonds in the Fe_2O_3 structure [33], and a signal at 620 cm^{-1} was attributed to the vibration of Fe(III)–O bonds in oxo-centered trinuclear iron complexes (Fe_3–O) within the MIL-100(Fe) framework [32]. Besides, the vibrations at 712 and 760 cm^{-1} as well as in the region of 1380–1620 cm^{-1}, which were only detected on the FTIR spectra of M-100(Fe)@Fe_2O_3 samples, are well known as characteristic signals of MIL-100(Fe) [9,32]. It is noteworthy that the distinctive signals of MIL-100(Fe) displayed increasing intensity, while the signals associated with Fe_2O_3 (specifically at 420, 440, 680, and 730 cm^{-1}, as depicted in Figure 4) gradually weakened as the H_3BTC content was elevated from 0.90 to 1.80 g. These combined observations provide strong evidence of the successful synthesis of MIL-100(Fe) from Fe_2O_3 nanoparticles; the proportion of MIL-100(Fe) in the final material depends on the quantity of H_3BTC introduced into the reaction system.

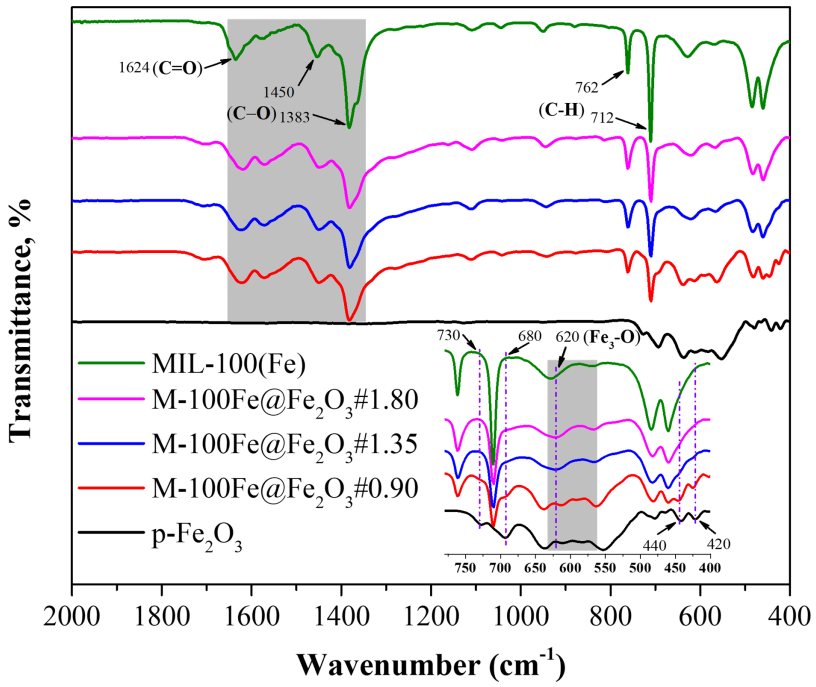


Figure 4: FTIR spectra of Fe_2O_3, MIL-100(Fe), and M-100Fe@Fe_2O_3 samples.

The textural properties of all materials were determined through analysis of N_2 adsorption and desorption isotherms. Figure 5a illustrates a dense structure for Fe_2O_3 nanoparticles, with isotherms exhibiting a type-III profile according to IUPAC. It reflects a limited BET surface area and a pore volume of 36.3 $m^2 \cdot g^{-1}$ and 0.118 $cm^3 \cdot g^{-1}$, respectively (Table 1). In contrast, the reference MIL-100(Fe) sample exhibited N_2 adsorption/desorption isotherms characteristic of type I. Additionally, a pore size distribution was observed with three prominent peaks at approximately 0.62, 1.30, and 1.75 nm within the micropore region defined by IUPAC (less than 2.0 nm), as depicted in Figure 5b. These observations confirm that the reference sample has a microporous structure with a BET surface area and a total pore volume of 1825.4 $m^2 \cdot g^{-1}$ and 0.772 $cm^3 \cdot g^{-1}$, respectively. Similarly, the micropore structures were also determined in the obtained M-100Fe@Fe_2O_3 samples by examining the profiles of isotherms and pore size distributions. Notably, the adsorbed amount of N_2 (Figure 5a) and the pore volume of the three primary peaks (Figure 5b) exhibited a gradual increase from M-100Fe@Fe_2O_3#0.90 to M-100Fe@Fe_2O_3#2.25 samples. The BET surface area and the total pore volume reached 858.9 $m^2 \cdot g^{-1}$ and 0.451 $cm^3 \cdot g^{-1}$ for M-100Fe@Fe_2O_3#0.90, respectively. Subsequently increasing the H_3BTC amount up to 1.80 g caused an improvement in BET surface area to 1365.4 $m^2 \cdot g^{-1}$ and total pore volume to 0.642 $cm^3 \cdot g^{-1}$ for M-100Fe@Fe_2O_3#1.80. There was a further slight enhancement in the porosity of the obtained material when increasing the H_3BTC amount from 1.80 to 2.25 g, corresponding to 1433.8 $m^2 \cdot g^{-1}$ and 0.671 $cm^3 \cdot g^{-1}$ for BET surface area and total pore volume of M-100Fe@Fe_2O_3#2.25, respectively. Considering the trade-off between required H_3BTC amount and porosity of the obtained materials and within

Table 1: Textural properties of Fe_2O_3 and the as-prepared samples.

Samples	BET surface area ($m^2 \cdot g^{-1}$)	Total pore volume ($cm^3 \cdot g^{-1}$)
p-Fe_2O_3	36.3	0.118
M-100Fe@Fe_2O_3#0.90	858.9	0.451
M-100Fe@Fe_2O_3#1.35	1065.1	0.526
M-100Fe@Fe_2O_3#1.80	1365.4	0.642
M-100Fe@Fe_2O_3#2.25	1433.8	0.671
MIL-100(Fe)	1825.4	0.772

the scope of our investigation, M-100Fe@Fe_2O_3#1.8 stands out as the optimal sample, exhibiting a BET surface area of 1365.4 $m^2 \cdot g^{-1}$, which surpasses the values of 730 $m^2 \cdot g^{-1}$ [26] and 1244.6 $m^2 \cdot g^{-1}$ [27] observed in MIL-100(Fe) samples prepared from Fe_3O_4.

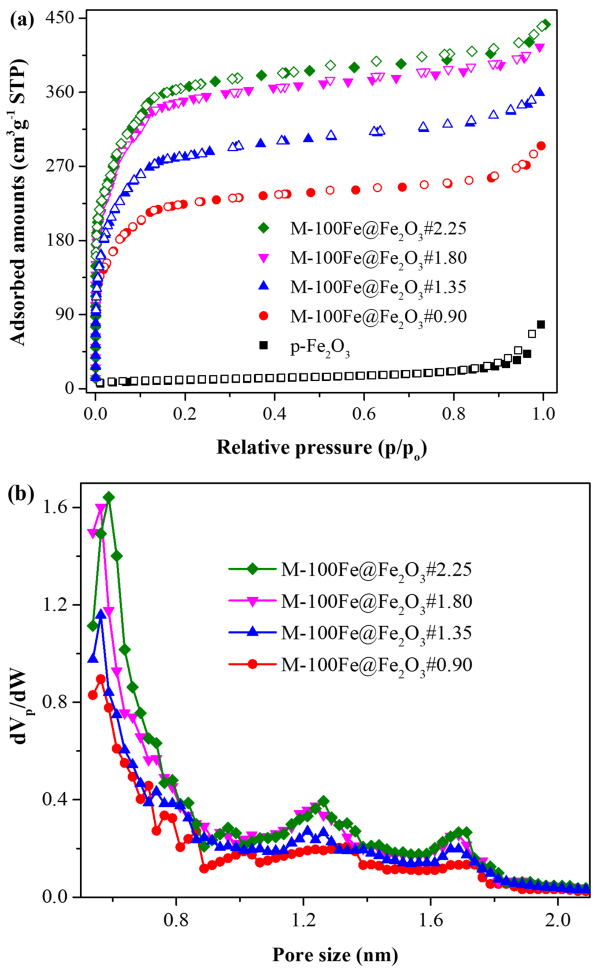


Figure 5: (a) N_2 adsorption and desorption isotherms over Fe_2O_3, MIL-100(Fe), and M-100Fe@Fe_2O_3 samples obtained at 77 K. (b) Pore size distribution of M-100Fe@Fe_2O_3 and reference MIL-100(Fe) samples calculated using the HK model.

Thermogravimetric analyses were performed on Fe_2O_3 and M-100Fe@Fe_2O_3 samples to confirm the presence of the MIL-100(Fe) phase in the resulting materials and to estimate the conversion of Fe_2O_3 into MIL-100(Fe) material. The TGA profile of Fe_2O_3 (Figure 6) showed only a very small weight loss in the investigated temperature range due to a small quantity of absorbed moisture in the sample. Contrarily, the TGA profiles of M-100Fe@Fe_2O_3#0.90, M-100Fe@Fe_2O_3#1.35, and M-100Fe@Fe_2O_3#1.80 samples revealed similar mechanisms in weight loss over a temperature range of 30 to 650 °C, coinciding with three stages of weight loss observed in the reference sample MIL-100(Fe). Initially, the trapped molecules (ethanol and water) inside the pore system were released at low temperature around 100 °C. Subsequently, the ligands (water and/or –OH ligands) connected to Fe sites of the iron oxo-clusters were removed, leaving unsaturated metal sites inside the framework. Finally, a significant weight loss (approx. 41.8%) occurred due to the decomposition of the organic linkers in the framework at high temperatures between 300 and 650 °C. The process continued until the sample's mass stabilized at 26.3 wt % of Fe_2O_3 at 600 °C [9,11,34]. As a result, the mass percentage of MIL-100(Fe) was calculated to be 65.5% based on the formula of MIL-100(Fe) ($Fe_3O[C_6H_3(COO)_3]_2$) after the removal of –OH and H_2O at 300 °C. This result matches with the value of 68.1% attained from the TGA profile of MIL-100(Fe) at 300 °C. Similarly, at 600 °C, the mass percentage of Fe_2O_3 reached 56.6%, 37.7%, and 34.5% for the M-100Fe@Fe_2O_3#0.90, M-100Fe@Fe_2O_3#1.35, and M-100Fe@Fe_2O_3#1.80 samples, respectively (Figure 6). As discussed, Fe_2O_3 was only partially converted into MIL-100(Fe); hence, the obtained Fe_2O_3 from TGA curves included both Fe_2O_3 derived from M-100(Fe)@Fe_2O_3 and the original Fe_2O_3 reactant. Combining the obtained data from the reference sample MIL-100(Fe), the mass percentages of Fe_2O_3 reactant were inferred to be 35.8%, 15.2%, and 6.6%, corresponding to conversion rates of 36.7%, 59.6%, and 81% for M-100Fe@Fe_2O_3#0.90, M-100Fe@Fe_2O_3#1.35, and M-100Fe@Fe_2O_3#1.80 samples, respectively.

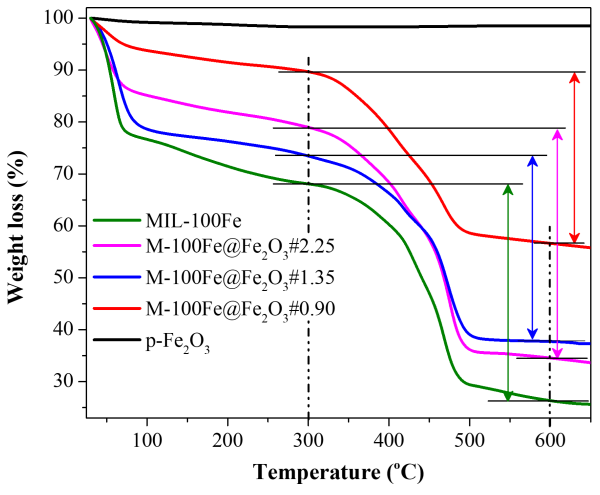


Figure 6: TGA curves of Fe_2O_3, MIL-100(Fe), and M-100Fe@Fe_2O_3 samples.

Figure 7 displays the oxidation states of Fe and O in both Fe_2O_3 and M-100Fe@Fe_2O_3#1.80 samples. In both cases, the Fe 2p spectra feature two prominent peaks at approximately 710 and

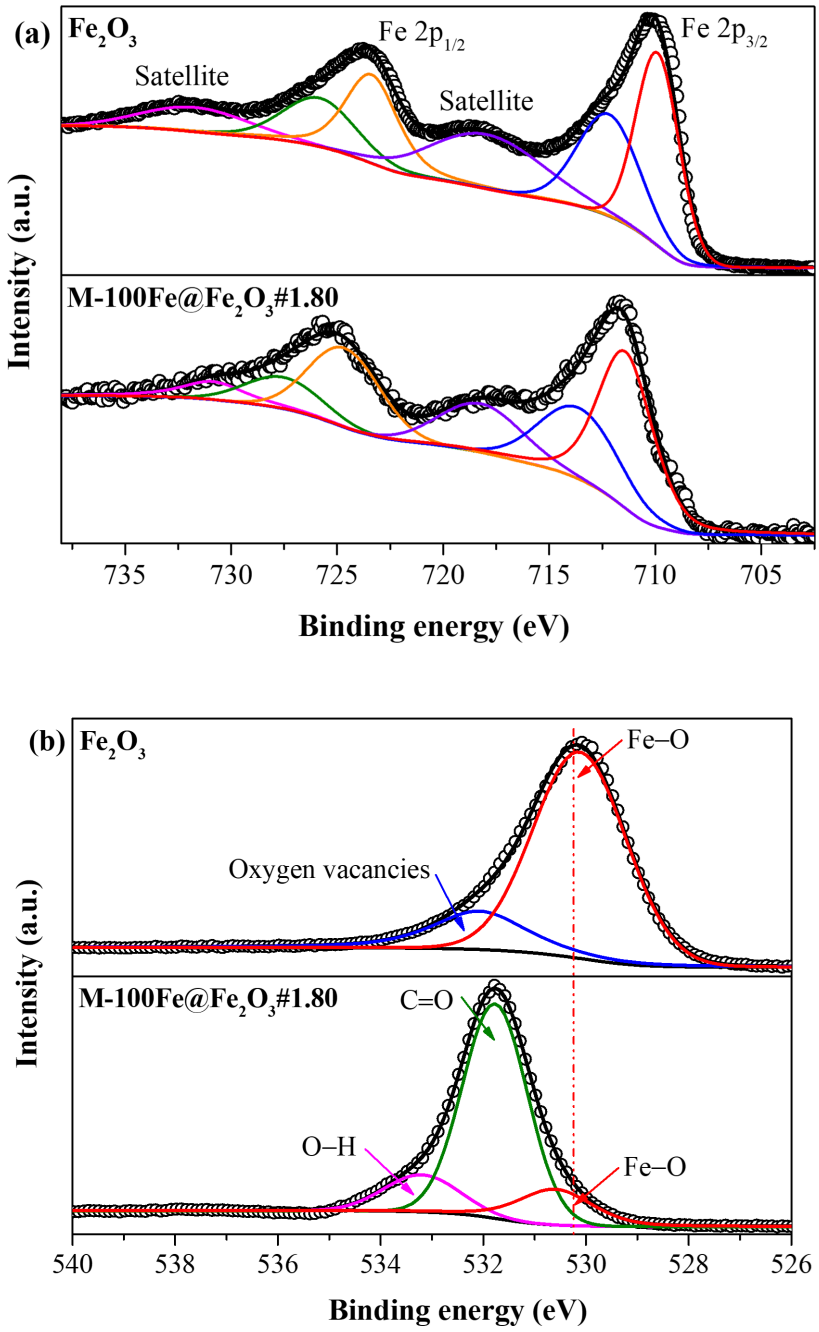


Figure 7: XPS spectra of Fe_2O_3 and M-100Fe@Fe_2O_3#1.80 samples: (a) Fe 2p region and (b) O 1 s region.

725 eV, accompanied by two shoulder peaks at around 718 and 731 eV. These peaks were attributed to Fe(III), corresponding to the Fe $2p_{3/2}$ and Fe $2p_{1/2}$ states, respectively [24,32]. Nevertheless, a substantial difference regarding the oxygen constituents was observed when examining the deconvoluted spectra of O 1s in Fe_2O_3 and M-100Fe@Fe_2O_3#1.80 samples. As shown in Figure 7b, the O 1s spectrum of the Fe_2O_3 sample exhibits two peaks, that is, a major peak at 530.1 eV standing for Fe–O bonds and a minor peak at 532 eV assigned to oxygen-related vacancies within the framework of Fe_2O_3 [35]. In contrast, the O 1s spectrum of the M-100Fe@Fe_2O_3#1.80 sample was composed of three peaks, namely, a major peak at 531.6 eV for C=O bonds and two minor peaks, one at 530.1 eV for Fe–O bonds and the other at 533.5 eV for O–H bonds [32,36]. It is noteworthy that Fe–O predominates in the Fe_2O_3 structure, whereas in the M-100Fe@Fe_2O_3#1.80 sample, the C=O is predominant. This difference is due to the presence of O atoms in the M-100Fe@Fe_2O_3#1.80 sample, which primarily

correspond to bridges of benzene-1,3,5-tricarboxylate in the MIL-100(Fe) framework.

CO_2/N_2 separation performance

To evaluate the effectiveness of CO_2/N_2 separation in the as-prepared samples, the adsorption behavior of CO_2 and N_2 was investigated at pressures ranging from 0 to 100 kPa at 298 K. As exhibited in Figure 8, a series of the as-prepared samples was arranged in the order of M-100Fe@Fe_2O_3#0.90 < M-100Fe@Fe_2O_3#1.35 < M-100Fe@Fe_2O_3#1.80 < M-100Fe@Fe_2O_3#2.25 < MIL-100(Fe) (reference sample) with a gradual increment in adsorption capacity for both CO_2 and N_2 due to the increasing BET surface area (Table 1). It is well known that the MIL-100(Fe) framework contains an abundance of active sites, including unsaturated metal sites, and –OH and free –COOH groups, which perhaps form adsorptive interactions with CO_2 molecules [32]. Consequently, the samples showed outstanding CO_2 uptake in comparison with N_2. Additionally, in Figure 9, the CO_2/N_2 separation performance of samples is depicted through IAST prediction of the CO_2/N_2 adsorptive selectivity (Supporting Information File 1). These predictions are based on a gas mixture containing 10% CO_2 and 90% N_2 by volume at 298 K. As displayed in Figure 9, all samples showed high potential for CO_2/N_2 separation at low pressure; at higher pressures, the separation performance gradually declined and reached plateau values. However, at the same bulk pressure, the adsorptive selectivity for CO_2 over N_2 of the adsorbents increased gradually because of the rising BET surface area resulting from an increase in the H_3BTC amount in the reaction system from 0.90 to 2.25 g. A similar trend was observed in the porosity analysis when increasing the H_3BTC amount from 1.80 to 2.25 g. It corresponds to a negligible improvement in CO_2 uptake, changing from 1.10 to 1.18 mmol·g^{-1} at 25 °C and 100 kPa. Taking into account the balance between CO_2 adsorption performance and the quantity of H_3BTC consumed, M-100Fe@Fe_2O_3#1.80 stands out as the preferred sample, exhibiting a CO_2 uptake capacity of 1.1 mmol·g^{-1} and a CO_2/N_2 selectivity of 18 at 25 °C and 100 kPa. These findings have been compared with the CO_2 uptake capacities of MIL-100(Fe)-based adsorbents created through different methods, as well as other MOFs and conventional materials, all of which are detailed in Table S2 (Supporting Information File 1).

Isosteric enthalpy of CO_2 adsorption over M-100Fe@Fe_2O_3#1.80 and its reusability

To explore the inherent relationship between the target gas and the adsorbent, the adsorption behavior of CO_2 over the M-100Fe@Fe_2O_3#1.80 sample was studied in a temperature range from 5 to 35 °C. As observed in the isotherms in Figure S1 (Supporting Information File 1), the CO_2 uptake was propor-

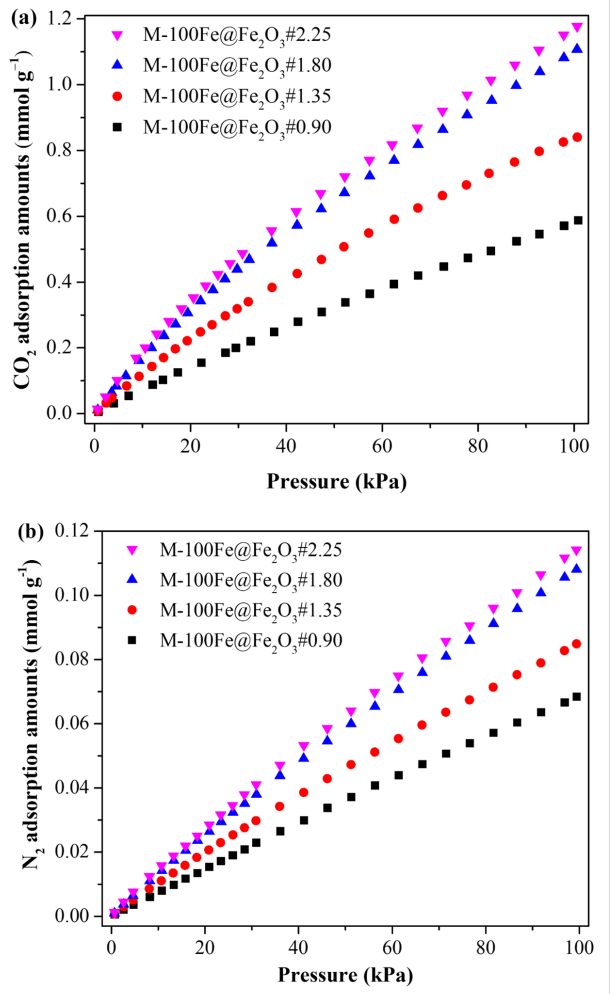


Figure 8: Adsorption isotherms of M-100Fe@Fe_2O_3 and reference MIL-100(Fe) samples at 298 K: (a) CO_2 adsorption isotherms, (b) N_2 adsorption isotherms.

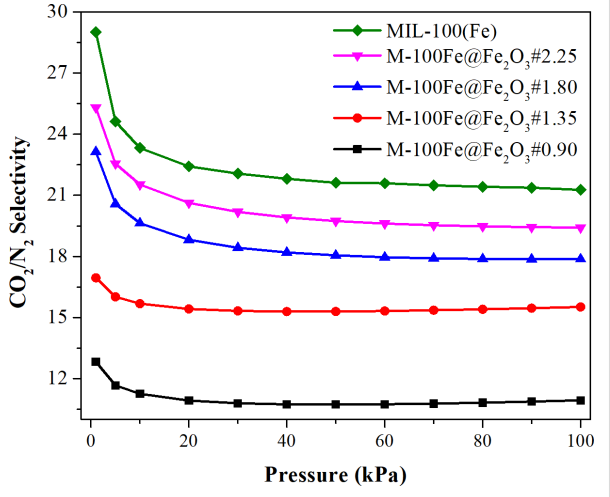


Figure 9: IAST-derived CO_2/N_2 selectivities over M-100Fe@Fe_2O_3 samples for a mixture with 10% N_2 and 90% CO_2 at 298 K.

tional to the pressure and inversely proportional to temperature, suggesting that adsorptive interactions based on physical bonds took place between CO_2 molecules and M-100Fe@Fe_2O_3#1.80 [31,37]. To support this assertion, the Clausius–Clayperon equation was employed to determine the isosteric enthalpy of CO_2 adsorption (Supporting Information File 1). As anticipated, the capture of CO_2 molecules using M-100Fe@Fe_2O_3#1.80 releases approximately 20 to 17 kJ·mol^{-1} when the CO_2 uptake is increased up to 1.0 mmol·g^{-1} (Figure 10). The obtained results fall within the value range defined for the physisorption regime [37,38], implying that a spent M-100Fe@Fe_2O_3#1.80 sample could be easily refreshed under soft conditions for reuse, thus, extending the material's life cycle. To affirm this aspect, a conservative trial of five cycles for CO_2 adsorption/desorption was carried out at 298 K as shown in Figure 11. The CO_2 uptake over the M-100Fe@Fe_2O_3#1.80 sample was maintained in comparison with the fresh sample after the five cycles.

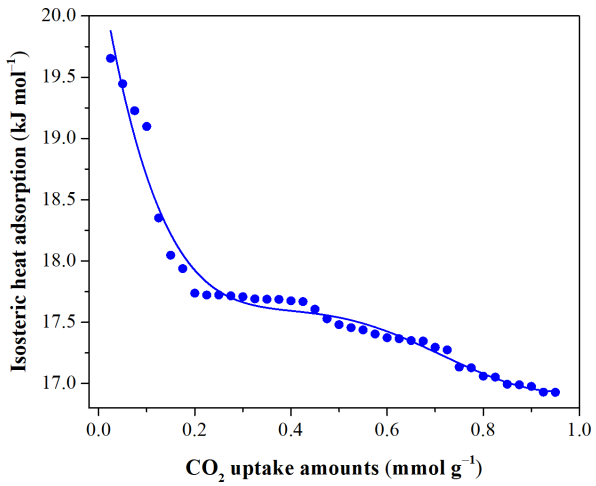


Figure 10: Enthalpy of CO_2 adsorption over M-100Fe@Fe_2O_3#1.80 sample.

Conclusion

For the first time, a facile synthetic method was employed to effectively fabricate MIL-100(Fe) from Fe_2O_3 using a typical hydrothermal process. By adjusting the mass ratio between Fe_2O_3 and H_3BTC in the reaction system, a continuous enhancement in the quality of the produced MIL-100(Fe) was achieved. The optimal conditions for producing MIL-100(Fe) material were determined to be 150 °C for 12 h, with a mass ratio of 0.9/1.80 (g/g) for Fe_2O_3/H_3BTC, as a trade-off between required H_3BTC amount and BET surface area. This resulted in an 81% conversion and a BET surface area of 1365.4 m^2·g^{-1} for the M-100Fe@Fe_2O_3#1.80 sample. Furthermore, M-100Fe@Fe_2O_3#1.80 demonstrated promising potential as an adsorbent for CO_2/N_2 separation, exhibiting a high CO_2 uptake of 1.1 mmol·g^{-1} and a CO_2/N_2 selectivity of 18 at 25 °C and

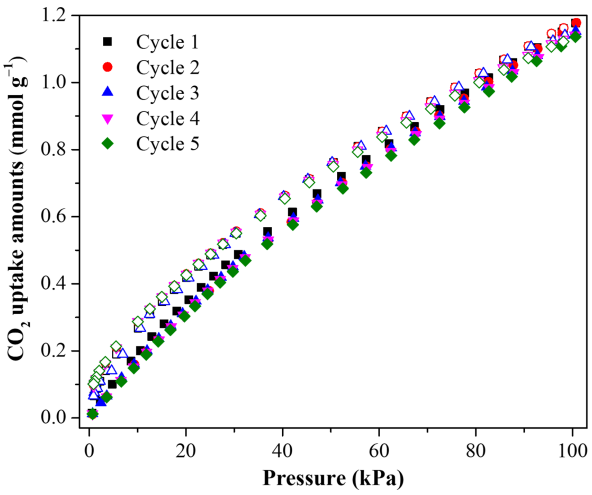


Figure 11: CO_2 adsorption/desorption isotherms over M-100Fe@Fe_2O_3#1.80 sample for five cycles at 298 K.

100 kPa. Importantly, it retained a significant CO_2 adsorption capacity even after five reuse cycles. The use of Fe_2O_3 in conjunction with an ecologically benign technology offers a new pathway for producing MIL-100(Fe), potentially utilizing a cheap and readily accessible raw material source from the iron and steel industry, thereby reducing production cost.

Supporting Information

Procedure to preparation of reference MIL-100(Fe). Langmuir–Freundlich model and the calculated IAST-CO_2/N_2 selectivity equations. The Clausius–Clayperon equation for calculating CO_2 heat adsorption. The characteristic parameters alongside correlation coefficients from fitting the Langmuir–Freundlich model (Table S1). CO_2 uptake capacity on various adsorbents at 1 bar (Table S2). CO_2 isotherms at several different temperature on M-100(Fe)@Fe_2O_3#1.80 sample (Figure S1). EDX mapping of elemental Fe and C on the M-100Fe@Fe_2O_3#1.80 sample (Figure S2).

Supporting Information File 1

Additional experimental data.
[https://www.beilstein-journals.org/bjnano/content/supplementary/2190-4286-15-74-S1.pdf]

Funding

This work was supported by a research grant no. 15/HĐ-ĐHCN with a code of 22/2HH02 from the Industrial University of Ho Chi Minh City, Vietnam.

Author Contributions

Van Nhieu Le: conceptualization; funding acquisition; project administration; validation; writing – original draft. Hoai Duc Tran: investigation; methodology; writing – original draft. Minh Tien Nguyen: investigation; methodology. Hai Bang Truong: conceptualization; visualization; writing – original draft. Toan Minh Pham: formal analysis; writing – original draft. Jinsoo Kim: writing – review & editing.

ORCID® iDs

Van Nhieu Le - https://orcid.org/0000-0001-7400-9639
Hoai Duc Tran - https://orcid.org/0000-0003-2595-7821
Hai Bang Truong - https://orcid.org/0000-0003-2906-7658

Data Availability Statement

The data that supports the findings of this study is available from the corresponding author upon reasonable request.

References

1. Le, V. N.; Kim, D.; Kim, J.; Othman, M. R. *ACS Appl. Nano Mater.* **2021,** *4,* 8863–8871. doi:10.1021/acsanm.1c01524
2. Le, V. N.; Phan, D.-P.; Kim, S.-S.; Lee, E. Y.; Kim, J. *Fuel Process. Technol.* **2022,** *238,* 107477. doi:10.1016/j.fuproc.2022.107477
3. Quijia, C. R.; Lima, C.; Silva, C.; Alves, R. C.; Frem, R.; Chorilli, M. *J. Drug Delivery Sci. Technol.* **2021,** *61,* 102217. doi:10.1016/j.jddst.2020.102217
4. Do, H. H.; Rabani, I.; Truong, H. B. *Beilstein J. Nanotechnol.* **2023,** *14,* 964–970. doi:10.3762/bjnano.14.79
5. Nguyen, M. K.; Gwag, J. S.; Nguyen-Dinh, L.; Truong, H. B.; Do, H. H.; Lee, Y.-C.; Tran, N. T.; Trung, L. G. *Nano Today* **2024,** *55,* 102211. doi:10.1016/j.nantod.2024.102211
6. Vo, T. K.; Kim, J.; Park, J.; Dao, D. Q.; Truong, H. B. *Chem. Eng. J.* **2024,** *481,* 148570. doi:10.1016/j.cej.2024.148570
7. Yang, S.; Li, X.; Zeng, G.; Cheng, M.; Huang, D.; Liu, Y.; Zhou, C.; Xiong, W.; Yang, Y.; Wang, W.; Zhang, G. *Coord. Chem. Rev.* **2021,** *438,* 213874. doi:10.1016/j.ccr.2021.213874
8. Zhong, G.; Liu, D.; Zhang, J. *Cryst. Growth Des.* **2018,** *18,* 7730–7744. doi:10.1021/acs.cgd.8b01353
9. Le, V. N.; Vo, T. K.; Lee, J. H.; Kim, J. C.; Kim, T.-H.; Oh, K. H.; Bae, Y.-S.; Kwak, S. K.; Kim, J. *Chem. Eng. J.* **2021,** *404,* 126492. doi:10.1016/j.cej.2020.126492
10. Yoon, J. W.; Seo, Y.-K.; Hwang, Y. K.; Chang, J.-S.; Leclerc, H.; Wuttke, S.; Bazin, P.; Vimont, A.; Daturi, M.; Bloch, E.; Llewellyn, P. L.; Serre, C.; Horcajada, P.; Grenèche, J.-M.; Rodrigues, A. E.; Férey, G. *Angew. Chem., Int. Ed.* **2010,** *49,* 5949–5952. doi:10.1002/anie.201001230
11. Horcajada, P.; Surblé, S.; Serre, C.; Hong, D.-Y.; Seo, Y.-K.; Chang, J.-S.; Grenèche, J.-M.; Margiolaki, I.; Férey, G. *Chem. Commun.* **2007,** 2820–2822. doi:10.1039/b704325b
12. Kim, A.-R.; Yoon, T.-U.; Kim, E.-J.; Yoon, J. W.; Kim, S.-Y.; Yoon, J. W.; Hwang, Y. K.; Chang, J.-S.; Bae, Y.-S. *Chem. Eng. J.* **2018,** *331,* 777–784. doi:10.1016/j.cej.2017.09.016
13. Le, V. N.; Kwon, H. T.; Vo, T. K.; Kim, J.-H.; Kim, W.-S.; Kim, J. *Mater. Chem. Phys.* **2020,** *253,* 123278. doi:10.1016/j.matchemphys.2020.123278
14. Peng, J.; Xian, S.; Xiao, J.; Huang, Y.; Xia, Q.; Wang, H.; Li, Z. *Chem. Eng. J.* **2015,** *270,* 282–289. doi:10.1016/j.cej.2015.01.126
15. Li, Y.-X.; Ji, Y.-N.; Jin, M.-M.; Qi, S.-C.; Li, S.-S.; Xue, D.-M.; Yue, M. B.; Liu, X.-Q.; Sun, L.-B. *ACS Appl. Mater. Interfaces* **2018,** *10,* 40044–40053. doi:10.1021/acsami.8b15913
16. Xian, S.; Peng, J.; Zhang, Z.; Xia, Q.; Wang, H.; Li, Z. *Chem. Eng. J.* **2015,** *270,* 385–392. doi:10.1016/j.cej.2015.02.041
17. Yuan, B.; Wang, X.; Zhou, X.; Xiao, J.; Li, Z. *Chem. Eng. J.* **2019,** *355,* 679–686. doi:10.1016/j.cej.2018.08.201
18. Kim, P.-J.; You, Y.-W.; Park, H.; Chang, J.-S.; Bae, Y.-S.; Lee, C.-H.; Suh, J.-K. *Chem. Eng. J.* **2015,** *262,* 683–690. doi:10.1016/j.cej.2014.09.123
19. Canioni, R.; Roch-Marchal, C.; Sécheresse, F.; Horcajada, P.; Serre, C.; Hardi-Dan, M.; Férey, G.; Grenèche, J.-M.; Lefebvre, F.; Chang, J.-S.; Hwang, Y.-K.; Lebedev, O.; Turner, S.; Van Tendeloo, G. *J. Mater. Chem.* **2011,** *21,* 1226–1233. doi:10.1039/c0jm02381g
20. Seo, Y.-K.; Yoon, J. W.; Lee, J. S.; Lee, U.-H.; Hwang, Y. K.; Jun, C.-H.; Horcajada, P.; Serre, C.; Chang, J.-S. *Microporous Mesoporous Mater.* **2012,** *157,* 137–145. doi:10.1016/j.micromeso.2012.02.027
21. Zhang, F.; Shi, J.; Jin, Y.; Fu, Y.; Zhong, Y.; Zhu, W. *Chem. Eng. J.* **2015,** *259,* 183–190. doi:10.1016/j.cej.2014.07.119
22. Han, L.; Qi, H.; Zhang, D.; Ye, G.; Zhou, W.; Hou, C.; Xu, W.; Sun, Y. *New J. Chem.* **2017,** *41,* 13504–13509. doi:10.1039/c7nj02975f
23. Ahmed, I.; Jeon, J.; Khan, N. A.; Jhung, S. H. *Cryst. Growth Des.* **2012,** *12,* 5878–5881. doi:10.1021/cg3014317
24. Lv, H.; Zhao, H.; Cao, T.; Qian, L.; Wang, Y.; Zhao, G. *J. Mol. Catal. A: Chem.* **2015,** *400,* 81–89. doi:10.1016/j.molcata.2015.02.007
25. Chávez, A. M.; Rey, A.; López, J.; Álvarez, P. M.; Beltrán, F. J. *Sep. Purif. Technol.* **2021,** *255,* 117660. doi:10.1016/j.seppur.2020.117660
26. Aslam, S.; Zeng, J.; Subhan, F.; Li, M.; Lyu, F.; Li, Y.; Yan, Z. *J. Colloid Interface Sci.* **2017,** *505,* 186–195. doi:10.1016/j.jcis.2017.05.090
27. Li, S.; Cui, J.; Wu, X.; Zhang, X.; Hu, Q.; Hou, X. *J. Hazard. Mater.* **2019,** *373,* 408–416. doi:10.1016/j.jhazmat.2019.03.102
28. Freund, R.; Lanza, A. E.; Canossa, S.; Gemmi, M.; Goscianska, J.; Cauda, V.; Oschatz, M.; Wuttke, S. *Chem. Mater.* **2023,** *35,* 1891–1900. doi:10.1021/acs.chemmater.2c02946
29. Sayadi, M. H.; Mansouri, B.; Shahri, E.; Tyler, C. R.; Shekari, H.; Kharkan, J. *Chemosphere* **2020,** *247,* 125900. doi:10.1016/j.chemosphere.2020.125900
30. Kargin, J.; Valladares, L. D. L. S.; Borja-Castro, L. E.; Xize, J.; Mukhambetov, D. G.; Konyukhov, Y. V.; Moreno, N. O.; Dominguez, A. G. B.; Barnes, C. H. W. *Hyperfine Interact.* **2022,** *243,* 14. doi:10.1007/s10751-022-01800-7
31. Le, V. N.; Vo, T. K.; Yoo, K. S.; Kim, J. *Sep. Purif. Technol.* **2021,** *274,* 119079. doi:10.1016/j.seppur.2021.119079
32. Le, V. N.; Nguyen, V. C.; Nguyen, H. T.; Tran, H. D.; Tu, T. N.; Kim, W.-S.; Kim, J. *Microporous Mesoporous Mater.* **2023,** *360,* 112716. doi:10.1016/j.micromeso.2023.112716
33. Sallam, S. A.; El-Subruiti, G. M.; Eltaweil, A. S. *Catal. Lett.* **2018,** *148,* 3701–3714. doi:10.1007/s10562-018-2569-z
34. Koo, J.; Hwang, I.-C.; Yu, X.; Saha, S.; Kim, Y.; Kim, K. *Chem. Sci.* **2017,** *8,* 6799–6803. doi:10.1039/c7sc02886e
35. Zhu, H.; Zhang, H.; Yang, T.; Zhou, L.; Wang, H.; Li, S.; Lan, Y. *Proc. Inst. Mech. Eng., Part L* **2022,** *236,* 2317–2325. doi:10.1177/14644207211022773

36. Huang, W.; Liu, N.; Zhang, X.; Wu, M.; Tang, L. *Appl. Surf. Sci.* **2017,** *425,* 107–116. doi:10.1016/j.apsusc.2017.07.050
37. Le, V. N.; Tu, T. N.; Kim, J. *Sep. Purif. Technol.* **2023,** *306,* 122718. doi:10.1016/j.seppur.2022.122718
38. Khan, M. A.; Kim, S.-w.; Rao, R. A. K.; Abou-Shanab, R. A. I.; Bhatnagar, A.; Song, H.; Jeon, B.-H. *J. Hazard. Mater.* **2010,** *178,* 963–972. doi:10.1016/j.jhazmat.2010.02.032

License and Terms

This is an open access article licensed under the terms of the Beilstein-Institut Open Access License Agreement (https://www.beilstein-journals.org/bjnano/terms), which is identical to the Creative Commons Attribution 4.0 International License (https://creativecommons.org/licenses/by/4.0). The reuse of material under this license requires that the author(s), source and license are credited. Third-party material in this article could be subject to other licenses (typically indicated in the credit line), and in this case, users are required to obtain permission from the license holder to reuse the material.

The definitive version of this article is the electronic one which can be found at:
https://doi.org/10.3762/bjnano.15.74

BEILSTEIN JOURNAL OF NANOTECHNOLOGY

Photocatalytic methane oxidation over a TiO_2/SiNWs p–n junction catalyst at room temperature

Qui Thanh Hoai Ta[1], Luan Minh Nguyen[1,2], Ngoc Hoi Nguyen[1,2], Phan Khanh Thinh Nguyen[*3] and Dai Hai Nguyen[*1,2]

Full Research Paper

Open Access

Address:
[1]Institute of Chemical Technology, Vietnam Academy of Science and Technology, 1A TL29 Street, Thanh Loc Ward, District 12, Ho Chi Minh City 700000, Vietnam, [2]Graduate University of Science and Technology, Vietnam Academy of Science and Technology, 18 Hoang Quoc Viet Street, Cau Giay District, Hanoi 100000, Vietnam and [3]Department of Chemical and Biological Engineering, Gachon University, 1342 Seongnamdaero, Sujeong-gu, Seongnam-si, Gyeonggi-do 13120, Republic of Korea

Email:
Qui Thanh Hoai Ta - tathanhhoaiqui2292@gmail.com;
Luan Minh Nguyen - nguyenminhluan.work@gmail.com;
Ngoc Hoi Nguyen - hoi83bmt@gmail.com;
Phan Khanh Thinh Nguyen* - thinhnpk@gachon.ac.kr;
Dai Hai Nguyen* - nguyendaihai0511@gmail.com

* Corresponding author

Keywords:
photocatalysis; photocatalytic CH_4 oxidation; p–n heterojunction; TiO_2/SiNWs

Beilstein J. Nanotechnol. **2024,** *15,* 1132–1141.
https://doi.org/10.3762/bjnano.15.92

Received: 18 May 2024
Accepted: 13 August 2024
Published: 02 September 2024

This article is part of the thematic issue "Recent advances in synthesis and applications of organometallic nanomaterials".

Guest Editor: B. T. Huy



© 2024 Ta et al.; licensee Beilstein-Institut.
License and terms: see end of document.

Abstract

Rapid recombination of charge carriers in semiconductors is a main drawback for photocatalytic oxidative coupling of methane (OCM) reactions. Herein, we propose a novel catalyst by developing a p–n junction titania–silicon nanowires (TiO_2/SiNWs) heterostructure. The structure is fabricated by atomic layer deposition of TiO_2 on p-type SiNWs. The TiO_2/SiNWs heterostructure exhibited an outstanding OCM performance under simulated solar light irradiation compared to the single components. This enhanced efficiency was attributed to the intrinsic electrical field formed between n-type TiO_2 and p-type SiNWs, which forces generated charge carriers to move in opposite directions and suppresses charge recombination. Besides, surface morphology and optical properties of the the p–n TiO_2/SiNWs catalyst are also beneficial for the photocatalytic activity. It is expected that the results of this study will provide massive guidance in synthesizing an efficient photocatalyst for CH_4 conversion under mild conditions.

Introduction

Methane (CH_4), which can take the form of liquefied natural gas, is one of the crucial sources of industrial chemicals and energy. However, CH_4 is a major precursor for tropospheric ozone, causing severe air pollution. Because of its rising atmospheric concentration, CH_4 poses a global warming potential approximately thirty fold larger than that of carbon dioxide

(CO_2) [1-3]. Therefore, it is a challenging mission to eliminate CH_4 from the atmosphere. Conventionally, CH_4 activation is carried out at high temperatures (>650 °C) via thermal methane conversion to value-added products. However, combustion of CH_4 for energy production usually generates great amounts of carbon dioxide as well as coke deposition on catalyst surfaces [4-7]. Therefore, sustainable strategies for both green conversion and atmospheric removal of CH_4 are urgently necessary [8-11]. Semiconductor-based photocatalysis has been attracting scientists' attention because of its environmental friendliness and easy handling [12-14]. Photocatalytic metal oxide semiconductor materials have been utilized for converting solar energy into valuable chemical energy in the field of CH_4 conversion [15-17]. Methane oxidation presents a particularly promising strategy. The primary objective is to convert methane into valuable products such as formaldehyde (HCHO), methanol (CH_3OH), and other value-added oxygenates, which serve as essential precursors in various manufacturing and production processes [18,19].

The n-type semiconductor titanium dioxide (TiO_2) has been discovered as a potential photocatalyst material because of its high stability, good dispersibility, and narrow energy bandgap. However, pristine TiO_2 shows only low photocatalytic efficiency because of the high recombination rate between holes and electrons and the low visible-light harvesting ability [20-22]. The rapid recombination of charge carriers prior to their participation in reactions significantly reduces the efficiency of methane oxidation reactions [23,24]. To address these issues of TiO_2 nanomaterials, many scientists have developed TiO_2-based nanostructure composites as advanced photocatalysts [25-30]. The recombination of charge carriers is mainly attributed to the anisotropic movement of generated electron–hole pairs in semiconductors. Therefore, the implementation of a driving force could remarkably accelerate the oriented motion of electrons and holes, which could suppress recombination and eventually improve photocatalytic efficiency. For years, doping of metal nanoparticles (NPs) into a semiconductor matrix has been extensively studied to enhance photocatalytic CH_4 oxidation performance. Metal NPs in, for example, Au/TiO_2, Au@Pd/ZnO, and Pt@Cu/TiO_2 composites act as electron scavenger centers and own more free electrons for reactions [25-27]. However, the generated electron affinity of metal NPs is sometimes insufficient and cannot prevent recombination or maintain electrons for further reactions.

As an advanced solution for catalysis modification, p–n junction photocatalysts with an intrinsic electric field formed at the interface have emerged, which effectively force charge carriers to move in opposite directions and hinder recombination [31-33]. Very recently, $Cu_2O/BiVO_4$, $Ag_2O/Bi_{12}O_{17}Cl_2$ and $CuFe_2O_4/Bi_4Ti_3O_{12}$ composite powders have shown improved efficiencies in water treatment based on p–n configuration advantages [34-36]. However, the wetness impregnation synthesis of those powder co-catalysts faces the issues of low surface area, low reproducibility, and difficult control of large-scale production. Therefore, the development of novel catalysts with unique morphologies by using precise tools is extremely essential and important [37-39].

Herein, we constructed a robust p–n junction catalyst by atomic layer deposition (ALD) of TiO_2 thin films on a p-type SiNW substrate for enhancing the photocatalytic efficiency in CH_4 oxidation. Pristine p-Si wafers have limited surface area and are highly susceptible to mechanical failure because of their brittle nature; in contrast, the etched SiNW arrays exhibit superior optical absorption and enhanced surface catalytic reaction properties. The intimate contact between 1D Si NWs and thin TiO_2 layers reduces the recombination rate of electron–hole pairs. Additionally, TiO_2/SiNWs offer flexibility, improved bandgap energy, and enhanced light harvesting across a broad spectrum, leading to higher photocatalytic efficiency. Combining SiNWs and TiO_2 presents an opportunity to leverage the strengths of both materials while mitigating their respective limitations. This study offers new insights into the design of an efficient system for OCM.

Results and Discussion

Structural and morphological properties

For understanding the crystalline structure of TiO_2 and SiNWs, X-ray diffraction patterns were recorded as displayed in Figure 1. The XRD pattern of a pure Si wafer and p-type SiNWs display a main peak at 2θ of 33.2°, which was attributed to the reflection from (200) planes. Despite being etched with concentrated acid and Ag^+ ions, there was no significant

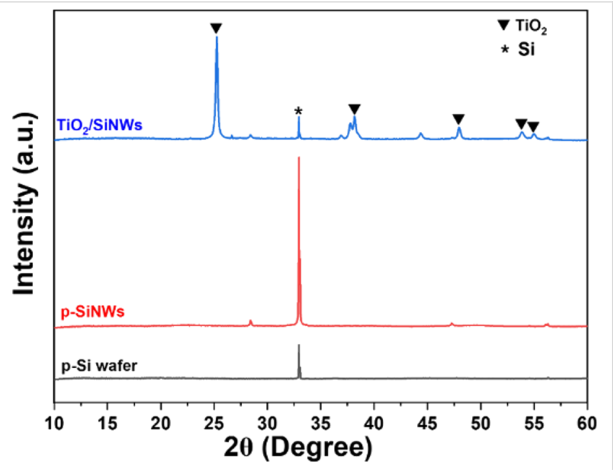


Figure 1: XRD patterns of p-Si, p-type SiNWs, and the TiO_2/SiNWs sample.

change in the peak position of p-type SiNWs, which corresponds to the original Si phase (JCPDS No.27-1402) [40,41]. In the case of the as-synthesized composite, the favored growth of TiO_2(101) on the surface of p-Si NWs has been noticed [42]. The minor (112), (200), (105), and (211) peaks at 2θ = 38.2°, 48.5°, 53.3°, and 55.1° indicate the formation of anatase TiO_2 (JCPDS No.21-1272) [43,44]. As expected, the crystal orientation of the TiO_2/SiNWs catalyst obviously led to the creation of a robust p–n junction photocatalyst.

The SEM analysis further confirms the morphological evolution during etching and TiO_2 ALD. As revealed in Supporting Information File 1, Figure S1, the morphology of SiNWs is characterized by individual nanowires that bunch together in a highly ordered manner, resulting in well-oriented Si NW arrays perpendicular to the Si bulk surface. Figure 2 shows cross-sectional- and top-view SEM images of the as-prepared TiO_2/SiNWs sample. The TiO_2/SiNWs arrays were well prepared with an average length of 4 µm. Moreover, the surface of the SiNWs was fully decorated by the TiO_2 passivation layer and became blurry. The active pure 25 nm TiO_2 layer exhibits flake-like morphology as displayed in Figure 2c,d.

Optical properties

Nanowire arrays offer a better optical absorption than planar Si wafers because of the specific morphology [45]. The optical absorption of the as-prepared catalyst is shown in Figure 3a. The UV–vis diffuse reflection spectrum of TiO_2/SiNWs catalyst is drastically reduced in comparison to the pure SiNWs. The superior antireflection property of the TiO_2/SiNWs catalyst may be attributed to the vertical wires, which enable strong light scattering leading to enhancement in light harvesting. The optical bandgap values of SiNWs and TiO_2/SiNWs are estimated at around 3.8 and 3.3 eV, respectively. Figure 3b displays the current–voltage (*I*–*V*) curves of the photocatalyst under dark and light conditions. The current of the sample under light conditions is higher than that under dark conditions. The slope of the *I*–*V* characteristic starts to increase, showing that generated electrons strongly influence the electrical properties of the samples.

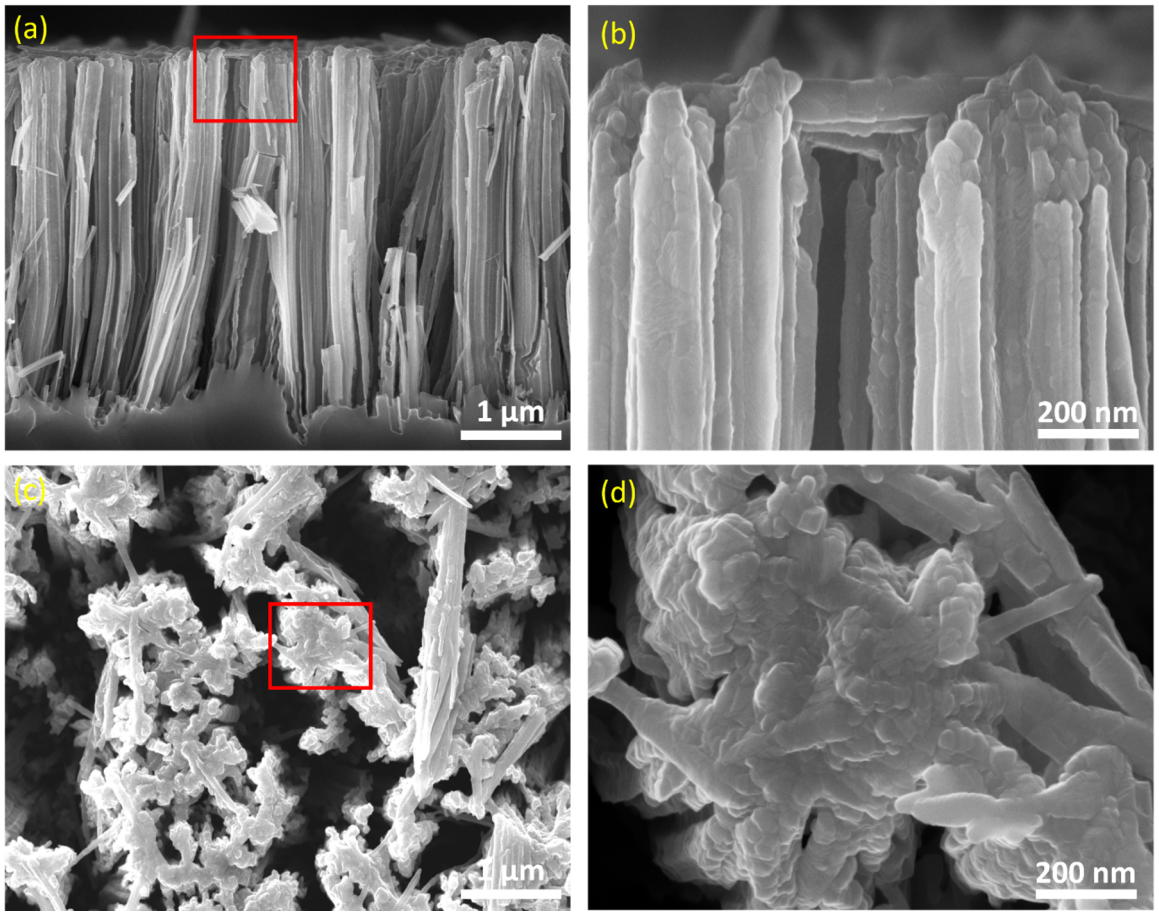


Figure 2: Cross-sectional view (a, b) and top view (c, d) SEM images of the TiO_2/SiNWs device with a higher-magnification view of the red rectangles on the right-hand side. A thin layer of TiO_2 (estimated at 25 nm) was deposited on the SiNWs by using ALD with 500 deposition cycles.

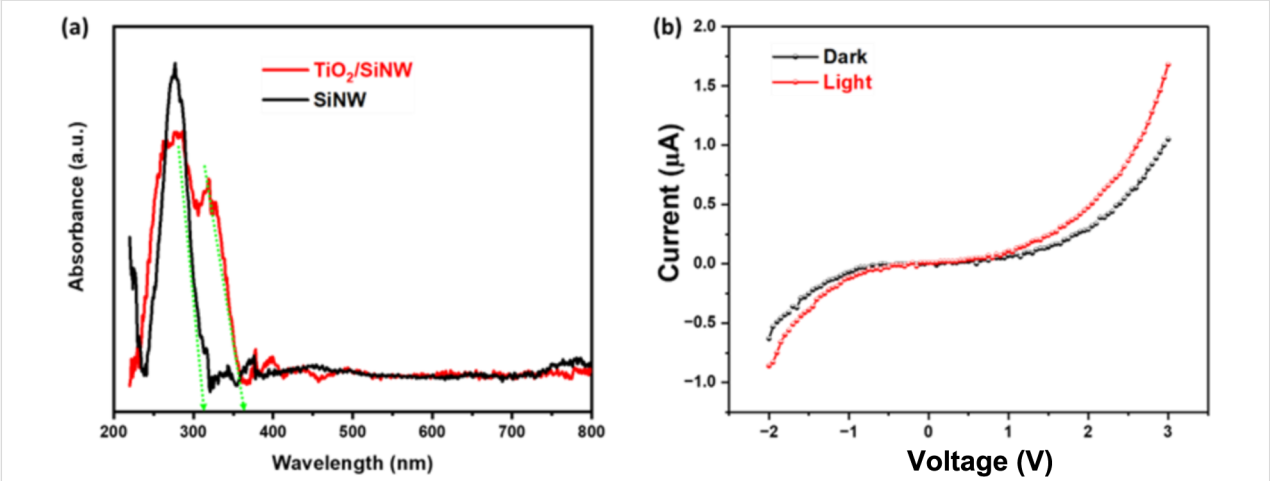


Figure 3: The UV–visible diffuse reflectance spectra (a) and *I–V* curve under light/dark conditions (b) of the TiO_2/SiNWs sample.

The surface interaction with gases during photocatalytic oxidative coupling can be analyzed using water contact angle analysis (as shown in Supporting Information File 1, Figure S2). The wettability of pure p-Si and the p-Si NW array are illustrated in Figure S3 (Supporting Information File 1). Pure p-Si had a water contact angle of 50.24°. Because of the nanowire array morphology, the p-Si NWs were more hydrophilic nature with a water contact angle of 3.36°, which manifests superior photocatalytic oxidative coupling.

Raman spectra were conducted to confirm the surface composition of the synthesized photocatalysts. As depicted in Figure 4a, the Raman spectrum of Si exhibits a single peak located at 519 cm^{-1}, corresponding to the first-order transverse optical (TO) mode of Si [46]. For the TiO_2/Si photocatalyst, two distinct peaks were observed, namely, (i) the characteristic E_g vibration of TiO_2, located at 146 cm^{-1}, and (ii) the TO phonon mode of Si (Figure 4b) [47-49]. Consequently, the combined surface-sensitive Raman and bulk-sensitive XRD results reveal that the n-type TiO_2 coating layer on p-type SiNWs does not influence the crystalline structure.

Photocatalytic OCM

The photocatalytic OCM activity of TiO_2/SiNWs sample under aerobic conditions is described in Figure 5. In a batch reactor, the photocatalytic CH_4 oxidation progresses as a function of irradiation time. Besides ethane (C_2H_6), carbon dioxide (CO_2) was detected as a by-product. Moreover, propane (C_3H_8) and H_2 were observed as result of the oxidative cross-coupling of methane and ethane (Figure 5a). The conversion reaction of CH_4 can be described as follows:

$$2CH_4 \rightarrow C_2H_6 + H_2.$$

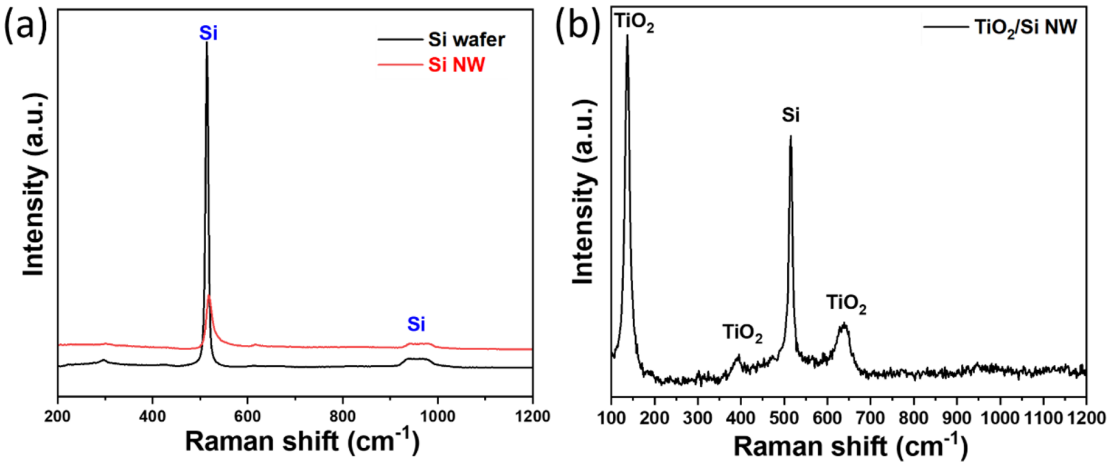


Figure 4: Raman spectra of pure p-Si and Si NW (a), and the TiO_2/SiNWs thin film (b).

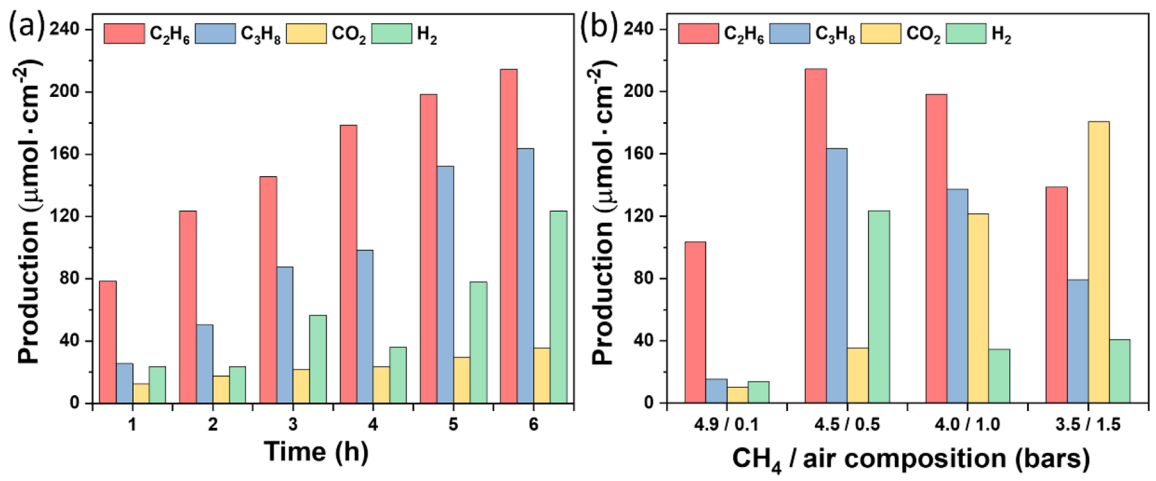


Figure 5: Photocatalytic CH_4 oxidation as a function of irradiation time (a) and different CH_4/air composition (b) over TiO_2/SiNWs. Reaction conditions: TiO_2/SiNWs chip (1 × 2 cm^2), total pressure of 5 bar, 20 °C, reaction time t = 6 h in (b).

To evaluate the reaction ratio-dependent photocatalytic OCM efficiency, we varied the gas pressure ratios between CH_4 and air. As shown in Figure 5b, more CO_2 was measured at lower CH_4-to-air ratios because of the higher O_2 content. Therefore, optimizing the CH_4/air ratio is important for improving the OCM reaction. The highest coupling selectivity was around 90% at CH_4/air ≈ 4.5:0.5, comparable to or higher than that of typical reported photocatalysts (Table 1). Although the TiO_2/Si composite did not achieve the best results compared to other photocatalysts, it remains a viable option for methane oxidation processes.

In order to investigate the individual effects of p-type SiNWs and TiO_2 layer on the photocatalytic OCM efficiency, comparable samples were irradiated under the same conditions. The methane coupling was analyzed with different samples using pure p-type SiNW, TiO_2/SiNW, TiO_2/glass catalyst, as shown in Figure 6a. In fact, only negligible CH_4 conversion was discovered over p-type SiNWs, and TiO_2/glass under the same conditions. It can be explained that the superior wettability of TiO_2/SiNWs (hydrophilic surfaces) compared to TiO_2/glass (hydrophobic surfaces) enables partial adsorption of water molecules, which facilitates the generation of radicals necessary for photocatalytic reactions. Furthermore, the TiO_2 nanostructure and p-type SiNWs are crucial in photogenerated charge separation and adsorption enhancement under UV–vis light. In other words, the ethane productivity of TiO_2/Si NWs was five times higher (210 μmol/cm^2) than that of pure p-Si NWs (20 μmol/cm^2) and glass/TiO_2 (30 μmol/cm^2).

Photocatalytic OCM over TiO_2/Si NWs catalysts was recorded in a batch reactor under different wavelengths of light. As

Table 1: Comparison of the OCM performance of the TiO_2/Si composite with previous photocatalysts.

Photocatalysts	Amount of catalyst	Reaction conditions	Light	Productivity (μmol·g^{-1}·h^{-1}) and selectivity	Ref.
Au@$Zn_2Ti_3O_8$	0.03 g	CH_4/O_2 = 15:1, mild conditions	50 W LED	C_2H_6: 1219 Sel.: 81%	[50]
Pt@TiO_2	0.075 g	CH_4 and water	UV lamp	C_2H_6: 57 Sel.: 62%	[51]
AuZnO@TiO_2	0.02 g	CH_4/air = 69:1, mild conditions	300 W Xe lamp	C_2H_6: 5020 Sel.: 90%	[30]
Ag HPW@TiO_2	0.1 g	CH_4 and air, 0.3 MPa	400 W Xe lamp	C_2H_6: 21 Sel.: 90%	[52]
Au@ZnO	0.005 g	CH_4/O_2 = 99:1, mild conditions	2 LEDs	C_2-C_4:684 Sel.: 83%	[53]
TiO_2/Si	1 × 2 cm^2	CH_4/air = 4.5:0.5, 0.5 MPa	300 W Xe lamp	C_2H_6: 210 μmol/cm^2 in 6 h Sel.: 90%	this work

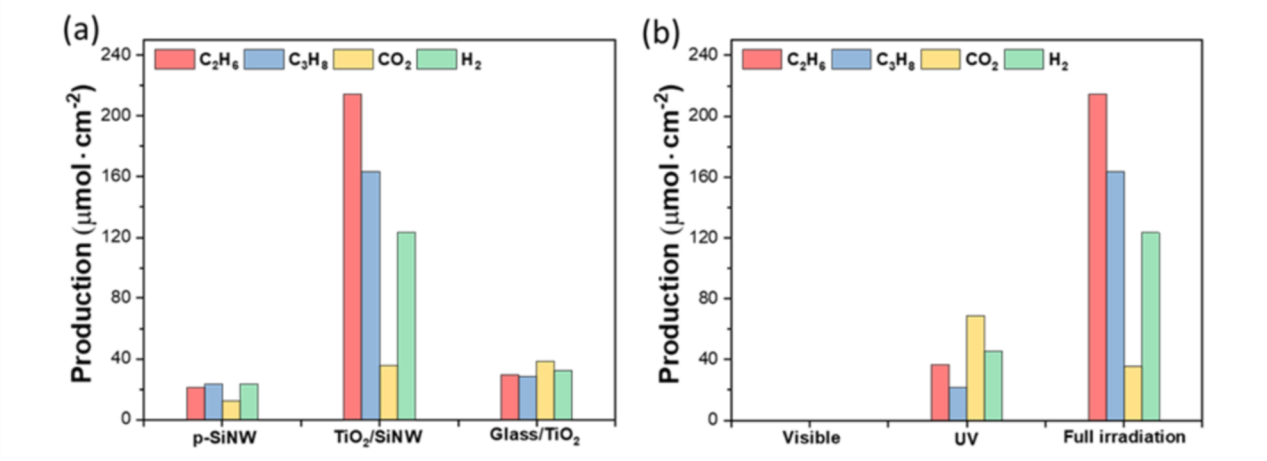


Figure 6: Photocatalytic CH_4 oxidation over different types of catalyst (a), and under different types of irradiation (b). Note that only TiO_2/SiNWs was used in panel (b). Reaction conditions: 5 bar, 20 °C, t = 6 h.

shown in Figure 6b, no products were detected under the visible-light irradiation. The photocatalytic performance under UV illumination was significantly lower than that under full illumination.

Figure 7 shows the recyclability of the p–n TiO_2/SiNWs photocatalyst. Note that after each cycle, the reactor was completely evacuated, and fresh gases were refilled for the following run. The photocatalytic activity of p–n TiO_2/SiNWs remained almost unchanged after four consecutive reaction cycles, indicating a high recyclability in the batch reactor.

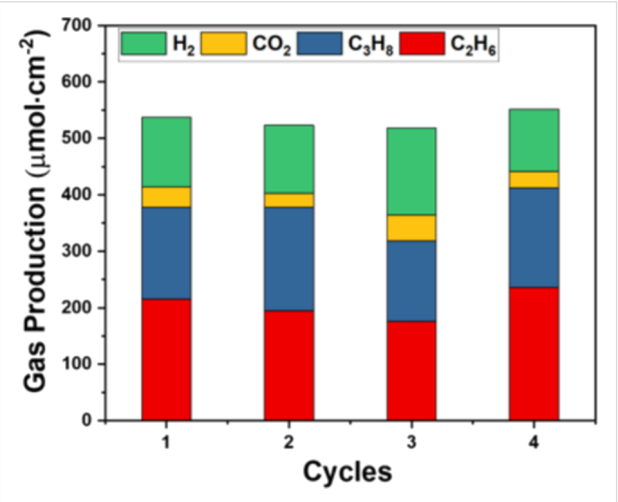


Figure 7: Stability of photocatalytic CH_4 oxidation reaction over the TiO_2/SiNWs sample.

Plausible charge transport mechanism

Figure 8 shows a schematic mechanism of the photocatalytic activity of the p–n TiO_2/SiNWs hierarchical structures. According to previous studies the energy bandgaps of p-Si and n-type TiO_2 were assumed to be 1.1 eV and 3.3 eV, respectively [54-56]. Because of the different electron affinities ($E_{ea,TiO2} \approx 4.10$ eV, $E_{ea,Si} \approx 4.05$ eV) [57,58] the electrons are excited and moved from the valance band minimum (VBM, 0.74V vs NHE) of SiNWs to the conduction band maximum (CBM, 0.35V vs NHE) of TiO_2 to enter the equilibrium state under irradiation following Aderson's model [39]. The photogenerated electrons tend to produce C_2H_6, C_3H_8, and H_2 from H^+. The photogenerated holes at the VBM of TiO_2 create oxidized intermediates and H^+ [59-61]. The whole process can be expressed by the S-scheme mechanism, as follows:

$$TiO_2/\text{Si NWs} \rightarrow TiO_2\left(h^+ + e^-\right) + \text{Si NWs}\left(h^+ + e^-\right),$$

at the CB of n-type TiO_2

$$O_2 + e^- + C^{\cdot} \rightarrow CO_2,$$

and at the VB of p-Si NW

$$CH_4 + h^+ \rightarrow H^+ + CH_2^{\cdot} + CH_3^{\cdot} + C^{\cdot} \rightarrow H_2 + C_2H_6 + C_3H_8.$$

Conclusion

A p–n junction TiO_2/SiNWs photocatalyst was synthesized via ALD and utilized for light-driven OCM. TiO_2/SiNWs revealed excellent performance owing to the smooth transport of photogenerated electrons in the p–n junction, which lowers the e–h recombination rate. The nanowire array structure of the catalyst provides a surface that can massively increase light absorption, achieving an efficient C_2H_6 yield of 210 μmol/cm^2 in 6 h with high selectivity under light illumination at room temperature. This research could offer new insights into composite photocatalysts for methane coupling.

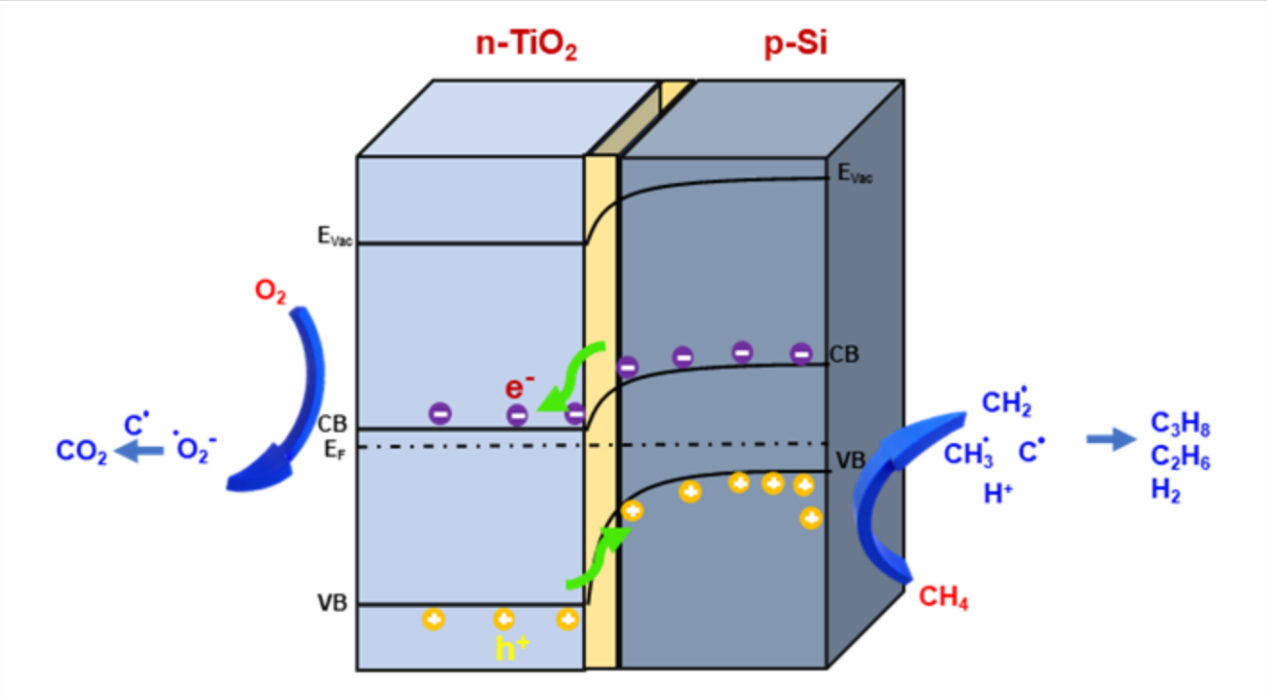


Figure 8: Proposed mechanism of photocatalytic CH_4 oxidation reaction over p–n junction TiO_2/SiNWs sample.

Experimental

Chemicals and materials

Commercial p-type Si 3-inch wafers (⟨100⟩ orientation, boron-doped, resistivity = 0.01–1 Ω·cm) were purchased from Silicon Mitus Corporation, South Korea. Silver nitrate ($AgNO_3$, 0.1 M), hydrofluoric acid HF (50 wt %), nitric acid (HNO_3, 63%), acetone, and ethanol were provided from Sigma-Aldrich. Deionized (DI) water was used for cleaning steps.

Si NWs and TiO_2/Si NWs preparation

First, a small piece (1 × 2 cm^2) was cut from a commercial p-type Si wafer and washed several times using DI water, ethanol, and acetone in a sonication bath. Etching solution containing $AgNO_3$ (0.1 M), HF (50 wt %) and H_2O (2:1:2 vol %) was prepared and kept at 56 °C for 20 min. The clean Si substrate was rapidly immersed in the etching medium and etched by the Ag^+ ions for 25 min to obtain 4 μm long SiNWs. Afterwards, remaining Ag on the Si surface was removed using HNO_3 (63 wt %) for 10 min. The etched p-Si NWs substrate was eventually washed with DI water and dried under N_2 flow, as shown in Figure 9.

Second, the as-prepared SiNWs sample was transferred to the chamber of an ALD system (R200 Advanced Picosun, 2013) for TiO_2 thin film deposition. The TiO_2 thin film deposition was carried out at 300 °C using $TiCl_4$ (98% purity, 0.2 s pulse time) and H_2O (0.1 s pulse time) as precursors. The vacuum level of

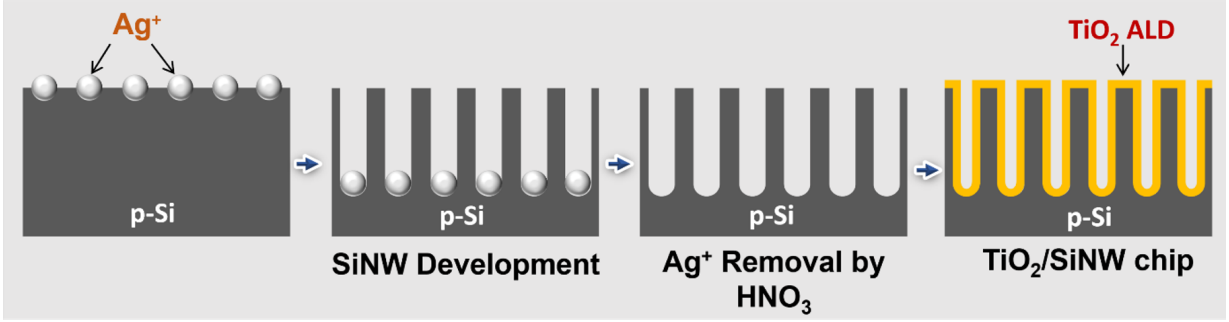


Figure 9: Schematic illustration of TiO_2/SiNWs chip fabrication starting from a p-type silicon wafer. A thin layer of TiO_2 was deposited on the Si NWs via ALD.

the chamber was kept at 8×10^{-3} bar, and the deposition rate was 0.051 nm/cycle. After cooling down to room temperature, the sample was taken out from chamber for photocatalytic experiments.

Photocatalytic tests

The as-synthesized catalyst was placed in a custom-made batch reactor with a small transparent quartz window, which was directly connected to a gas chromatograph (GC) with thermal conductivity and flame ionization detectors. A 300 W Xenon lamp was utilized as a light source (HAL-320). First, the reactor containing the photocatalytic thin film samples was evacuated using a vacuum pump for 10 min and filled with a mixture of CH_4/air (4.5/0.5 pressure ratio). The pressure ratio of the gas mixture was varied to study gas composition-dependent efficiency. The total pressure of gaseous reactants in batch reactor was established at 5 bar, and the photocatalytic system was kept in the dark (20 min) to reach equilibrium before exposure to simulated solar light. The temperature was kept at room temperature via a cooler.

Characterization

The crystalline structure and morphological properties of as-synthesized samples were analyzed using an X-ray diffraction system (XRD, Rigaku, SmartLab) with a 2θ range of 20–80° and a field-emission scanning electron microscope (FE-SEM, Hitachi, S-4700). The absorption properties of the thin films were analyzed using a diffuse reflectance UV–vis spectrometer (DRS-UV, Shimazu UV-2450). The chemical structure of the catalyst surface was analyzed using a Raman spectrometer (excitation of 532 nm, ANDOR Monora 500i). The surface wettability of the thin film sample was measured using a static contact angle system (Biosin Scientific), as shown in Supporting Information File 1, Figure S2. The contact angle between horizontal sample surface and the perimeter of the water drop was measured after 10 s of interaction. The in situ photocurrent measurements were carried out in the presence of gaseous reactants (CH_4/air = 4.5/0.5) ranging from −2 V to +3 V under dark and light conditions. Each measurement was scanned with 0.05 V intervals. The bias supply and current signals were provided and recorded by a Keithley system adapted with an amplifier.

Supporting Information

Supporting Information File 1

Additional figures.
[https://www.beilstein-journals.org/bjnano/content/supplementary/2190-4286-15-92-S1.pdf]

Acknowledgements

We acknowledge Material projects for using the TiO_2 and Si CIF files for the structures in the graphical abstract. The TiO_2 structure was reproduced from https://next-gen.materialsproject.org/materials/mp-1215, and the Si structure was reproduced from https://next-gen.materialsproject.org/materials/mp-165 (both published by The Materials Project and distributed under the terms of the Creative Commons Attribution 4.0 International License, https://creativecommons.org/licenses/by/4.0). Both structures were combined using the Vesta software (Momma, K.; Izumi, F. *J. Appl. Crystallogr.* **2011,** *44,* 1272–1276).

Funding

Ta Thanh Hoai Qui was funded by the Postdoctoral Scholarship Programme of Vingroup Innovation Foundation (VINIF), code VINIF.2023.STS.62.

Competing Interest

The authors declare that they have no known competing financial interests or personal relationships that could have appeared to influence the work reported in this paper.

Author Contributions

Qui Thanh Hoai Ta: supervision; validation; visualization; writing – original draft. Luan Minh Nguyen: data curation; formal analysis. Ngoc Hoi Nguyen: resources; software. Phan Khanh Thinh Nguyen: supervision; validation; visualization. Dai Hai Nguyen: writing – original draft; writing – review & editing.

ORCID® iDs

Qui Thanh Hoai Ta - https://orcid.org/0000-0002-0387-6281
Luan Minh Nguyen - https://orcid.org/0000-0003-3981-2084
Phan Khanh Thinh Nguyen - https://orcid.org/0000-0002-8204-6701
Dai Hai Nguyen - https://orcid.org/0000-0003-3501-7390

Data Availability Statement

The data that supports the findings of this study is available from the corresponding author upon reasonable request.

References

1. Reay, D.; Smith, P.; van Amstel, A. Methane Sources and the Global Methane Budget. In *Methane and Climate Change,* 1st ed.; Reay, D.; Smith, P., Eds.; Routledge: Abingdon-on-Thames, United Kingdom, 2010; pp 1–13. doi:10.4324/9781849775090
2. Lai, D. Y. F. *Pedosphere* **2009,** *19,* 409–421. doi:10.1016/s1002-0160(09)00003-4
3. Van Amstel, A. *J. Integr. Environ. Sci.* **2012,** *9,* 5–30. doi:10.1080/1943815x.2012.694892
4. Zamri, A. A.; Ong, M. Y.; Nomanbhay, S.; Show, P. L. *Environ. Res.* **2021,** *197,* 111204. doi:10.1016/j.envres.2021.111204

5. Biernat, K.; Malinowski, A.; Gnat, M. *The Possibility of Future Biofuels Production Using Waste Carbon Dioxide and Solar Energy;* Biofuels - Economy, Environment and Sustainability; InTech: Rijeka, Croatia, 2013. doi:10.5772/53831
6. Soeder, D. J. *Adv. Geo-Energy Res.* **2021,** *5,* 274–285. doi:10.46690/ager.2021.03.04
7. Benson, S. M. In *Carbon Dioxide Capture for Storage in Deep Geologic Formations – Results from the CO2 Capture Project: Vol 1-Capture and Separation of Carbon Dioxide from Combustion, Vol 2-Geologic Storage of Carbon Dioxide with Monitoring and Verification;* Thomas, D. C., Ed.; Elsevier, 2005. doi:10.1016/b978-008044570-0/50126-4
8. Mar, K. A.; Unger, C.; Walderdorff, L.; Butler, T. *Environ. Sci. Policy* **2022,** *134,* 127–136. doi:10.1016/j.envsci.2022.03.027
9. Collins, W. J.; Webber, C. P.; Cox, P. M.; Huntingford, C.; Lowe, J.; Sitch, S.; Chadburn, S. E.; Comyn-Platt, E.; Harper, A. B.; Hayman, G.; Powell, T. *Environ. Res. Lett.* **2018,** *13,* 054003. doi:10.1088/1748-9326/aab89c
10. Song, H.; Meng, X.; Wang, S.; Zhou, W.; Wang, X.; Kako, T.; Ye, J. *J. Am. Chem. Soc.* **2019,** *141,* 20507–20515. doi:10.1021/jacs.9b11440
11. Jiang, Y.; Li, S.; Wang, S.; Zhang, Y.; Long, C.; Xie, J.; Fan, X.; Zhao, W.; Xu, P.; Fan, Y.; Cui, C.; Tang, Z. *J. Am. Chem. Soc.* **2023,** *145,* 2698–2707. doi:10.1021/jacs.2c13313
12. Zhu, J.; Liao, M.; Zhao, C.; Liu, M.; Han, A.; Zhu, C.; Sun, Y.; Zhao, M.; Ye, S.; Cao, H. *Nano Res.* **2023,** *16,* 6402–6443. doi:10.1007/s12274-023-5428-6
13. Kim, C.-M.; Jaffari, Z. H.; Abbas, A.; Chowdhury, M. F.; Cho, K. H. *J. Hazard. Mater.* **2024,** *465,* 132995. doi:10.1016/j.jhazmat.2023.132995
14. Mao, J.; Ta, Q. T. H.; Tri, N. N.; Shou, L.; Seo, S.; Xu, W. *Appl. Mater. Today* **2023,** *35,* 101939. doi:10.1016/j.apmt.2023.101939
15. Baharudin, L.; Rahmat, N.; Othman, N. H.; Shah, N.; Syed-Hassan, S. S. A. *J. CO2 Util.* **2022,** *61,* 102050. doi:10.1016/j.jcou.2022.102050
16. Zhou, Z.; Sun, Z.; Duan, L. *Curr. Opin. Green Sustainable Chem.* **2023,** *39,* 100721. doi:10.1016/j.cogsc.2022.100721
17. Taifan, W.; Baltrusaitis, J. *Appl. Catal., B* **2016,** *198,* 525–547. doi:10.1016/j.apcatb.2016.05.081
18. Tucci, F. J.; Rosenzweig, A. C. *Chem. Rev.* **2024,** *124,* 1288–1320. doi:10.1021/acs.chemrev.3c00727
19. Siang, T. J.; Jalil, A. A.; Liew, S. Y.; Owgi, A. H. K.; Rahman, A. F. A. *Catal. Rev.: Sci. Eng.* **2024,** *66,* 343–399. doi:10.1080/01614940.2022.2072450
20. Qamar, O. A.; Jamil, F.; Hussain, M.; Bae, S.; Inayat, A.; Shah, N. S.; Waris, A.; Akhter, P.; Kwon, E. E.; Park, Y.-K. *Chem. Eng. J.* **2023,** *460,* 141734. doi:10.1016/j.cej.2023.141734
21. Chen, S.; Hu, Y. H. *Catal. Rev.: Sci. Eng.* **2023,** 1–41. doi:10.1080/01614940.2023.2169451
22. Rafique, M.; Hajra, S.; Irshad, M.; Usman, M.; Imran, M.; Assiri, M. A.; Ashraf, W. M. *ACS Omega* **2023,** *8,* 25640–25648. doi:10.1021/acsomega.3c00963
23. Li, X.; Li, C.; Xu, Y.; Liu, Q.; Bahri, M.; Zhang, L.; Browning, N. D.; Cowan, A. J.; Tang, J. *Nat. Energy* **2023,** *8,* 1013–1022. doi:10.1038/s41560-023-01317-5
24. Wang, Z.; Zhang, Z.; Wang, Z.; Lu, H.; Wang, L. *Appl. Catal., A* **2023,** *654,* 119082. doi:10.1016/j.apcata.2023.119082
25. Meng, L.; Chen, Z.; Ma, Z.; He, S.; Hou, Y.; Li, H.-H.; Yuan, R.; Huang, X.-H.; Wang, X.; Wang, X.; Long, J. *Energy Environ. Sci.* **2018,** *11,* 294–298. doi:10.1039/c7ee02951a
26. Jiang, W.; Low, J.; Mao, K.; Duan, D.; Chen, S.; Liu, W.; Pao, C.-W.; Ma, J.; Sang, S.; Shu, C.; Zhan, X.; Qi, Z.; Zhang, H.; Liu, Z.; Wu, X.; Long, R.; Song, L.; Xiong, Y. *J. Am. Chem. Soc.* **2021,** *143,* 269–278. doi:10.1021/jacs.0c10369
27. Lang, J.; Ma, Y.; Wu, X.; Jiang, Y.; Hu, Y. H. *Green Chem.* **2020,** *22,* 4669–4675. doi:10.1039/d0gc01608j
28. Wu, X.; Zhang, H.; Xie, S.; Wang, Y. *Chem Catal.* **2023,** *3,* 100437. doi:10.1016/j.checat.2022.10.013
29. Li, X.; Xie, J.; Rao, H.; Wang, C.; Tang, J. *Angew. Chem., Int. Ed.* **2020,** *59,* 19702–19707. doi:10.1002/anie.202007557
30. Song, S.; Song, H.; Li, L.; Wang, S.; Chu, W.; Peng, K.; Meng, X.; Wang, Q.; Deng, B.; Liu, Q.; Wang, Z.; Weng, Y.; Hu, H.; Lin, H.; Kako, T.; Ye, J. *Nat. Catal.* **2021,** *4,* 1032–1042. doi:10.1038/s41929-021-00708-9
31. Kim, M.; Lee, J.; Je, M.; Heo, B.; Yoo, H.; Choi, H.; Choi, J.; Lee, K. *J. Mater. Chem. A* **2021,** *9,* 2239–2247. doi:10.1039/d0ta10062e
32. Ding, Y.; Zhang, J.; Yang, Y.; Long, L.; Yang, L.; Yan, L.; Kong, W.; Liu, F.; Lv, F.; Liu, J. *Int. J. Hydrogen Energy* **2021,** *46,* 36069–36079. doi:10.1016/j.ijhydene.2021.08.175
33. Zhang, J.; Chen, X.; Bai, Y.; Li, C.; Gao, Y.; Li, R.; Li, C. *J. Mater. Chem. A* **2019,** *7,* 10264–10272. doi:10.1039/c8ta08199a
34. Wang, W.; Huang, X.; Wu, S.; Zhou, Y.; Wang, L.; Shi, H.; Liang, Y.; Zou, B. *Appl. Catal., B* **2013,** *134–135,* 293–301. doi:10.1016/j.apcatb.2013.01.013
35. Liu, T.; Shi, L.; Wang, Z.; Liu, D. *Colloids Surf., A* **2022,** *632,* 127811. doi:10.1016/j.colsurfa.2021.127811
36. Zhao, W.; Jin, Y.; Gao, C. H.; Gu, W.; Jin, Z. M.; Lei, Y. L.; Liao, L. S. *Mater. Chem. Phys.* **2014,** *143,* 952–962. doi:10.1016/j.matchemphys.2013.10.026
37. Kashyap, V.; Kumar, C.; Chaudhary, N.; Saxena, K. *Silicon* **2023,** *15,* 1203–1210. doi:10.1007/s12633-022-02068-w
38. Sawal, M. H.; Jalil, A. A.; Khusnun, N. F.; Hassan, N. S.; Bahari, M. B. *Electrochim. Acta* **2023,** *467,* 143142. doi:10.1016/j.electacta.2023.143142
39. Chandra, A.; Ghosh, S.; Sarkar, R.; Sarkar, S.; Chattopadhyay, K. K. *Chemosphere* **2024,** *352,* 141249. doi:10.1016/j.chemosphere.2024.141249
40. Shao, M.-W.; Shan, Y.-Y.; Wong, N.-B.; Lee, S.-T. *Adv. Funct. Mater.* **2005,** *15,* 1478–1482. doi:10.1002/adfm.200500080
41. Ta, Q. T. H.; Tran, N. M.; Tri, N. N.; Sreedhar, A.; Noh, J.-S. *Chem. Eng. J.* **2021,** *425,* 131437. doi:10.1016/j.cej.2021.131437
42. Tesvara, C.; Yousuf, M. R.; Albrahim, M.; Troya, D.; Shrotri, A.; Stavitski, E.; Karim, A. M.; Sautet, P. *ACS Catal.* **2024,** *14,* 7562–7575. doi:10.1021/acscatal.4c01018
43. Nguyen, T. T. D.; Le, N. C. T.; Nguyen, D.; Huynh, V. T.; Nguyen, L. T. B.; Nguyen, P. T. *Vietnam J. Chem.* **2023,** *61,* 38–44. doi:10.1002/vjch.202300053
44. Masuda, Y.; Kato, K. *J. Ceram. Soc. Jpn.* **2009,** *117,* 373–376. doi:10.2109/jcersj2.117.373
45. Park, Y.-S.; Lee, J. S. *ACS Photonics* **2017,** *4,* 2587–2594. doi:10.1021/acsphotonics.7b01018
46. Elfiad, A.; Benredouane, S.; Naama, S.; Moulai, F.; Friha, S.-E.; Hadjersi, T. *J. Photochem. Photobiol., A* **2024,** *451,* 115503. doi:10.1016/j.jphotochem.2024.115503
47. Vemula, S. K.; Katta, V. S.; Ojha, S.; Singh, F.; Raavi, S. S. K. *Opt. Mater. (Amsterdam, Neth.)* **2024,** *148,* 114947. doi:10.1016/j.optmat.2024.114947
48. Chen, Q.; Wang, Z.; Liao, H.; Li, R.; Feng, Z.; Li, Z.; Lin, L.; Li, J.; Chen, G. *Chem. Eng. J.* **2024,** *493,* 152316. doi:10.1016/j.cej.2024.152316

49. Cai, J.; Wang, Z.; Jia, S.; Feng, Z.; Ren, Y.; Lin, L.; Chen, G.; Zheng, Z. *ACS Appl. Mater. Interfaces* **2022,** *14,* 13703–13712. doi:10.1021/acsami.1c23939
50. Huang, Q.; Cai, J.; Wei, F.; Fan, Y.; Liang, Z.; Liu, K.; Lu, X. F.; Ding, Z.; Wang, S. *J. Mater. Chem. A* **2024,** *12,* 21334–21340. doi:10.1039/d4ta02049a
51. Yu, L.; Shao, Y.; Li, D. *Appl. Catal., B* **2017,** *204,* 216–223. doi:10.1016/j.apcatb.2016.11.039
52. Yu, X.; Zholobenko, V. L.; Moldovan, S.; Hu, D.; Wu, D.; Ordomsky, V. V.; Khodakov, A. Y. *Nat. Energy* **2020,** *5,* 511–519. doi:10.1038/s41560-020-0616-7
53. Yang, X.; Chen, M.; Weng, C.; Zhuge, D.; Jin, F.; Xiao, Y.; Tian, D.; Yin, Q.; Li, L.; Zhang, X.; Shi, G.; Lu, X.; Yan, L.; Wang, L.; Wen, B.; Zhao, Y.; Lin, J.; Wang, F.; Zhang, W.; Chen, Y. *Adv. Sci.* **2024,** *11,* 2470173. doi:10.1002/advs.202470173
54. Somvanshi, D.; Jit, S. *IEEE Trans. Nanotechnol.* **2014,** *13,* 62–69. doi:10.1109/tnano.2013.2290553
55. Tran Huu, H.; Ngo Van, N.; Vo, V.; Nguyen Thi, L. *Vietnam J. Catal. Adsorpt.* **2021,** *10,* 56–62. doi:10.51316/jca.2021.090
56. Rawat, G.; Somvanshi, D.; Kumar, H.; Kumar, Y.; Kumar, C.; Jit, S. *IEEE Trans. Nanotechnol.* **2016,** *15,* 193–200. doi:10.1109/tnano.2015.2512565
57. Sze, S. M.; Li, Y.; Ng, K. K. *Physics of Semiconductor Devices,* 4th ed.; John Wiley & Sons, 2021. doi:10.1002/0470068329
58. Chen, J.-Z.; Chen, T.-H.; Lai, L.-W.; Li, P.-Y.; Liu, H.-W.; Hong, Y.-Y.; Liu, D.-S. *Materials* **2015,** *8,* 4273–4286. doi:10.3390/ma8074273
59. Liu, Y.; Ji, G.; Dastageer, M. A.; Zhu, L.; Wang, J.; Zhang, B.; Chang, X.; Gondal, M. A. *RSC Adv.* **2014,** *4,* 56961–56969. doi:10.1039/c4ra10670a
60. Gulati, S.; Mulvehill, M. C.; Thompson, T. C.; Spurgeon, J. M. *Energy Fuels* **2023,** *37,* 8573–8582. doi:10.1021/acs.energyfuels.3c00568
61. Yao, X.; Chen, L.; Liu, M.; Feng, D.; Wang, C.; Lu, F.; Wang, W.; Wang, X.; Cheng, Y.; Liu, H.; Chen, H.; Wang, W. *Appl. Catal., B* **2018,** *221,* 70–76. doi:10.1016/j.apcatb.2017.08.087

License and Terms

This is an open access article licensed under the terms of the Beilstein-Institut Open Access License Agreement (https://www.beilstein-journals.org/bjnano/terms), which is identical to the Creative Commons Attribution 4.0 International License (https://creativecommons.org/licenses/by/4.0). The reuse of material under this license requires that the author(s), source and license are credited. Third-party material in this article could be subject to other licenses (typically indicated in the credit line), and in this case, users are required to obtain permission from the license holder to reuse the material.

The definitive version of this article is the electronic one which can be found at: https://doi.org/10.3762/bjnano.15.92

BEILSTEIN JOURNAL OF NANOTECHNOLOGY

Enhanced catalytic reduction through in situ synthesized gold nanoparticles embedded in glucosamine/alginate nanocomposites

Chi-Hien Dang[1,2], Le-Kim-Thuy Nguyen[1], Minh-Trong Tran[1], Van-Dung Le[1], Nguyen Minh Ty[1], T. Ngoc Han Pham[3], Hieu Vu-Quang[3], Tran Thi Kim Chi[4], Tran Thi Huong Giang[4], Nguyen Thi Thanh Tu[5] and Thanh-Danh Nguyen[*1,2]

Full Research Paper

Open Access

Address:
[1]Institute of Chemical Technology, Vietnam Academy of Science and Technology, 1A, TL29, Thanh Loc Ward, District 12, Ho Chi Minh City, Vietnam, [2]Graduate University of Science and Technology, Vietnam Academy of Science and Technology, 18 Hoang Quoc Viet, Cau Giay District, Hanoi, Vietnam, [3]NTT Hi-Tech Institute, Nguyen Tat Thanh University, Ho Chi Minh City 700000, Vietnam, [4]Institute of Materials Science, Vietnam Academy of Science and Technology, 18 Hoang Quoc 14 Viet, Cau Giay District, Hanoi 11000, Vietnam and [5]Faculty of Applied Technology, School of Technology, Van Lang University, Ho Chi Minh City, Vietnam

Email:
Le-Kim-Thuy Nguyen - danh5463bd@yahoo.com;
Nguyen Thi Thanh Tu - tu.ntt@vlu.edu.vn; Thanh-Danh Nguyen* - danh5463bd@yahoo.com

* Corresponding author

Keywords:
catalysis; gold nanoparticles; organic dyes; organometallic nanocomposites; reduction

Beilstein J. Nanotechnol. **2024,** *15,* 1227–1237.
https://doi.org/10.3762/bjnano.15.99

Received: 12 April 2024
Accepted: 06 September 2024
Published: 04 October 2024

This article is part of the thematic issue "Recent advances in synthesis and applications of organometallic nanomaterials".

Associate Editor: C. T. Yavuz

© 2024 Dang et al.; licensee Beilstein-Institut.
License and terms: see end of document.

Abstract

This study introduces a highly efficient and straightforward method for synthesizing gold nanoparticles (AuNPs) within a glucosamine/alginate (GluN/Alg) nanocomposite via an ionotropic gelation mechanism in aqueous environment. The resulting nanocomposite, AuNPs@GluN/Alg, underwent thorough characterization using UV–vis, EDX, FTIR, SEM, TEM, SAED, and XRD analyses. The spherical AuNPs exhibited uniform size with an average diameter of 10.0 nm. The nanocomposites facilitated the recyclable reduction of organic dyes, including 2-nitrophenol, 4-nitrophenol, and methyl orange, employing $NaBH_4$ as the reducing agent. Kinetic studies further underscored the potential of this nanocomposite as a versatile catalyst with promising applications across various industrial sectors.

Introduction

Gold nanoparticles (AuNPs) have garnered significant attention because of their exceptional physicochemical properties and diverse potential chemical applications [1-3]. The conventional synthesis of AuNPs typically involves the chemical reduction of Au^{3+} ions using various reducing agents and stabilizers [4,5]. However, many of these chemicals are highly reactive, posing risks to both the environment and biological systems. Consequently, integrating green chemistry principles into nanotechnology has become a focus of nanoscience research [6,7]. Numerous studies have highlighted the use of natural compounds or natural sources in the green synthesis of AuNPs [8,9]. Polysaccharides, in particular, have demonstrated significant control over the nucleation and growth of metallic nanoparticles. Utilizing polysaccharide-mediated procedures for AuNP synthesis offers several advantages over conventional methods, including cost-effectiveness, energy efficiency, low toxicity, and eco-friendliness [10-12].

Sodium alginate, derived from marine algae, consists of β-D-mannuronic acid and its stereoisomer α-L-guluronic acid, forming a linear block copolymer with branched chains [13,14]. This biopolymer possesses metal-binding functional groups that readily cross-link through strong electrostatic bonds with multivalent metal cations (such as Ca^{2+}, Ba^{2+}, and Cu^{2+}) to create an extensive gel network in water [15,16]. The cross-linking of saccharide chains within alginate generates macromolecules ranging in size from micrometers to millimeters, resulting in gelispheres insoluble in water. While gelispheres enhance the physical and mechanical properties of sodium alginate, their poor solubility limits their applicability.

Recently, an ionotropic gelation method has been developed to produce nanoparticles from gelispheres through interaction between oligosaccharides (e.g., cyclodextrins) and the cross-linker [17]. These materials find wide applications in drug delivery [18] and the encapsulation of nanometals [19,20]. Reduction of metallic ions can be achieved using various agents, including plant extracts [21]. This reduction typically involves two steps, namely, the loading of metallic ions onto the nanogel and the subsequent reduction [22,23]. In recent studies, in situ reduction of metal nanoparticles (MNPs) has been explored to enhance synthetic efficiency and streamline procedures by employing disaccharides such as lactose [24,25]. However, the potential of monosaccharides (e.g., glucose, fructose, and glucosamine (GluN)) for the in situ synthesis of metallic nanoparticles onto alginate-based nanogels remains unexplored.

Toxic organic dyes, including nitrophenols and methyl orange (MO), pose a significant environmental threat because of their persistence in water. This challenge has spurred extensive research into various remediation methods. Recently, there has been growing interest in catalytic degradation using oxidizing agents such as H_2O_2 and iron in Fenton reactions [26], as well as reducing agents such as $NaBH_4$ with nanometal catalysts. Additionally, the reduction of dyes, such as 4-nitrophenol (4-NiP) to harmless 4-aminophenol, a precursor for the synthesis of drugs like paracetamol and phenacetin, shows promise for producing dyes, cosmetics, and pharmaceuticals [27]. Plasmonic MNPs enhance catalytic performance by absorbing both dye molecules and BH_4^- ions, offering a potent solution for dye remediation [28].

In our ongoing research, we synthesized for the first time AuNPs using GluN molecules, serving as both interaction agents to cross-link Ca-Alg gelispheres and reducing agents, thereby providing a novel material for the stabilization of AuNPs. The resulting nanocomposites were characterized using various analytical techniques and demonstrated efficacy in the catalytic reduction of nitrophenols and methyl orange. A comparative analysis of the reduction processes was carried out to confirm the enhanced efficiency of the nanocomposites.

Experimental

Materials

The study utilized reagents and chemicals without additional purification. Glucosamine, gold(III) chloride, calcium acetate hydrate, sodium alginate, sodium tetrahydroborate, 2-nitrophenol, 4-nitrophenol, and methyl orange were procured from Acros Scientific (Belgium). Distilled water was used throughout the experimentation.

Preparation of nanocomposites

The preparation of the blank GluN/Alg nanocomposite involved an ionotropic gelation as outlined in our recent work [25]. In brief, calcium acetate aqueous solution (7.18 mL; 583 mg·mL^{-1}) was gradually mixed with sodium alginate aqueous solution (20 mL; 7.0 mg·mL^{-1}) while stirring for 1 h at 1300 rpm. Following overnight settling, the Alg/Ca^{2+} gelispheres underwent centrifugation at 3000 rpm for 10 min and were washed three times with 10 mL of distilled water each time to remove any impurities. Next, an aqueous solution of GluN (12.0 mL; 1.6 mg·mL^{-1}) was added to the Alg/Ca^{2+} gelispheres and stirred for 1 h at 1300 rpm. The resulting GluN/Alg suspension underwent ultrasonication for 30 min and was left overnight to ensure the formation of a stable gel. The resulting nanocomposite mixture was centrifuged at 3000 rpm for 10 min and washed three times with 10 mL of water each time to obtain the blank GluN/Alg nanocomposite, which was also used as the standard sample for further characterization. To synthesize the AuNPs@GluN/Alg nanocomposite, aqueous $AuCl_3$ solution

(13 mL, 0.0061–0.0554 mg·mL^{-1}) was added to GluN/Alg suspension (8 mL, 1.0 g·mL^{-1}). The reduction process was initiated through heating the mixture and visually confirmed by a change in color of the reaction mixture indicating the formation of AuNPs on the GluN/Alg composite. UV–vis spectroscopy within the range of 300 to 600 nm was employed to monitor this process. Subsequently, the mixture underwent centrifugation at 3000 rpm for 10 min and was washed with distilled water to eliminate impurities and unreacted metal ions. The resulting AuNPs@GluN/Alg nanocomposite powder was dried overnight in an oven at 60 °C and stored for further analysis.

To optimize the reaction parameters, the synthesis of AuNPs@GluN/Alg was fine-tuned to determine the optimal conditions. The impact of the mass ratio between metallic ions and GluN/Alg gel was investigated at levels of 1%, 3%, 5%, 7%, and 9% (w/w). The reaction temperature ranged from 30 to 90 °C, while the reaction time varied from 0 to 140 min.

Physicochemical characterizations of AuNPs@GluN/Alg nanocomposite

The samples synthesized under optimal conditions underwent physicochemical characterization and were used for the catalytic reduction of organic dyes. FTIR spectra of blank GluN/Alg and AuNPs@GluN/Alg were acquired using a Bruker Tensor 27 FTIR spectrophotometer, which scanned wavelengths from 500 to 4000 cm^{-1}. KBr pellets were used for the measurements. For morphological investigations of the nanocomposites, scanning electron microscopy (SEM) was performed using a SEM-S4800 instrument; transmission electron microscopy (TEM) and selected area electron diffraction (SAED) were carried out using a JEOL JEM-2100 instrument. Crystal structure characterizations of AuNPs were carried out via XRD diffraction. Zeta potential and dynamic light scattering (DLS) measurements were carried out on gel solutions (1.0 mg·mL^{-1}) using a nanoPartica Horiba SZ-100 instrument. Thermal analysis through thermogravimetry (TGA) was performed using a LabSys evo S60/58988 Thermoanalyzer (Setaram, France). The oven-dried powder of both blank nanocomposite GluN/Alg and synthesized composite AuNPs@GluN/Alg underwent heating from 30 to 800 °C at a rate of 10 °C·min^{-1} in an airflow of 20 mL·min^{-1} for TGA analysis.

Catalytic activity in the reduction of organic dyes

To evaluate the catalytic effectiveness of the synthesized AuNPs@GluN/Alg, we examined their ability to reduce the organic dyes 2-nitrophenol (2-NiP), 4-NiP, and MO using an excess of $NaBH_4$. Initially, 3.0 mg of the AuNPs@GluN/Alg solid was placed in a quartz cell with 1 cm path length, along with an aqueous solution of the organic dyes (2.5 mL, 0.1 mM). Then, 0.5 mL of $NaBH_4$ solution (0.06 M) was added to start the reaction. The reduction process of the dyes was in situ tracked over time using a UV–vis spectrophotometer, covering the wavelength range of 200–600 nm at room temperature without delay. We examined the kinetics of catalytic degradation by monitoring changes in absorbance values at specific wavelengths.

Given the small quantity of nanocatalyst and the excessive amount of $NaBH_4$, we treated the catalytic reduction of these dyes as a pseudo-first-order reaction. The reaction kinetics are described by the equation $\ln(C_t/C_0) = -k \cdot t$, where k represents the rate constant, and C_0 and C_t denote the initial concentration and the concentration at time t, respectively. The rate constant was derived from the slope of the plots of $\ln(C_t/C_0)$ as function of the reaction time [29-31].

To assess the reusability of AuNPs@GluN/Alg, we carried out the dye reduction process re-using the nanocomposite. Following each run, the nanocomposite was recovered from the reaction solution, cleaned with ethanol, and then washed multiple times with distilled water before being used again.

Results and Discussion

In situ synthesis of AuNPs@Glu/Alg

AuNPs are incorporated into a nanocomposite composed of GluN/Alg following the process depicted in Figure 1. Initially, the blank nanocomposite GluN/Alg is synthesized using the ionotropic gelation method, a technique previously described in our research. GluN serves a dual purpose in this process; it imparts negative charges, disrupting some cross-links within the insoluble gelispheres of Ca–alginate, and acts as a reductant, converting Au^{3+} into Au(0) during the synthesis of the nanocomposite AuNPs@GluN/Alg without additional chemicals. Alginate serves as a stabilizing agent. In the ionotropic gelation mechanism, the cross-linking matrix of Ca–alginate, formed by Ca^{2+} ions and carboxyl groups in sodium alginate, becomes insoluble, while the sugar molecules of GluN interact with Ca^{2+} ions, resulting in the formation of nanostructured particles and forming a homogeneous gel solution of GluN/Alg [24,25]. To synthesize AuNPs@GluN/Alg, the blank nanocomposite is centrifuged to remove impurities before introducing gold ions into the gel solution. The resulting solution is heated to facilitate the in situ reduction of Au^{3+} to Au(0). The synthesis conditions for AuNPs@GluN/Alg were optimized, followed by physicochemical characterizations using various analytical techniques. Finally, the application of the nanocomposite in catalyzing the reduction of organic dyes is explored.

Optimizing the synthesis conditions is crucial for the formation of AuNPs@GluN/Alg. In this study, we focused on determining the most favorable parameters for nanocomposite syn-

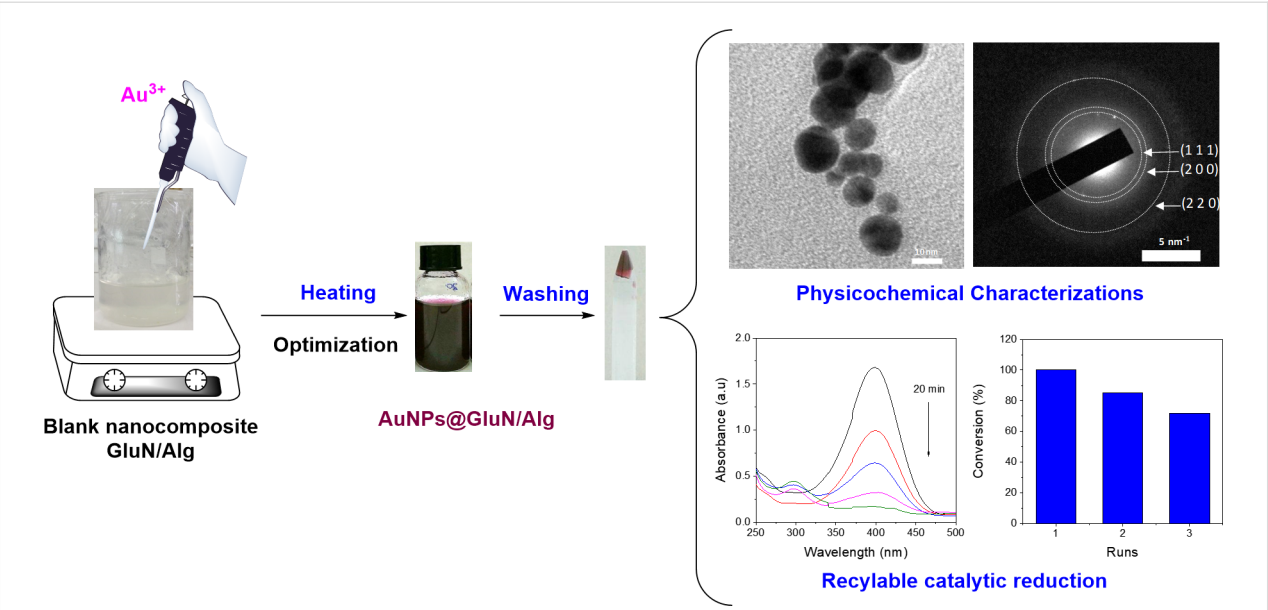


Figure 1: Schematic workflow illustration of the current study.

thesis, including the ratio of Au^{3+} ions to GluN/Alg gel, the reaction temperature, and the reaction time, by using UV–vis spectroscopy. Changes in the physicochemical properties, such as morphology and particle size of AuNPs, were monitored through absorbance and the λ_{max} values of the surface plasmon resonance (SPR) band. Figure 2 illustrates the impact of synthesis conditions on the formation of AuNPs@GluN/Alg. We explored the Au^{3+} ion-to-gel ratios ranging from 1% to 9% (w/w). The results indicate that the concentration of Au^{3+} ions profoundly influences the formation of stable AuNPs. An increase in Au^{3+} concentration led to a corresponding rise in the absorbance values at the SPR band, indicative of increased AuNP formation, while the λ_{max} values exhibited insignificant changes (Figure 2A,B). However, at higher Au^{3+}-to-gel ratios (9%), we observed the presence of solid material after synthesis, likely due to nanocomposite aggregation. Therefore, to achieve homogeneous nanoparticles, we opted for an Au^{3+}-to-gel ratio of 7% for further investigations.

Figure 2C,D illustrates the significant impact of the reaction temperature on the formation of nanocomposites. As the temperature increases, the UV–vis absorbance rises, reaching a peak at 70 °C, after which the absorbance declines again at higher temperatures (80 and 90 °C). This decrease in AuNP concentration in the colloidal solution is attributed to nanoparticle aggregation. Elevated temperatures can cause the detachment of the polysaccharide chains from the surface of the AuNPs, promoting the collision and attachment of nanoparticles to form larger aggregates, followed by coalescence [32,33]. Additionally, the morphology of AuNPs changes significantly at higher temperatures, as evidenced by a reduction in the λ_{max} values.

The optimization of reaction time was carried out within a range of 0 to 140 min. Figure 2E,F demonstrates the profound effect of the reaction time on AuNP formation under heating at 70 °C. The SPR band of the AuNPs only becomes evident after 40 min of heating, with the absorbance values peaking at 100 min, and the λ_{max} values stabilize after this duration. Thus, the optimal conditions for synthesizing AuNPs@GluN/Alg were determined to be a Au^{3+} ions-to-gel ratio of 7% and heating at 70 °C for 100 min. These optimal samples were further characterized and evaluated regarding their catalytic activity.

Characterization of AuNPs@GluN/Alg

Zeta potential analysis was employed to assess the stability of nanoparticles in the colloidal solution. Figure 3A shows that both the blank and AuNPs@GluN/Alg nanocomposites exhibit negative zeta potentials of −22 and −35 mV, respectively. The increased negativity in the zeta potential of AuNPs@GluN/Alg is attributed to the presence of AuNPs within the composite. The highly negative zeta potentials of both nanocomposites indicated their high stability in the aqueous solution.

The functional groups present in the nanocomposite were identified through FTIR spectroscopy, with the blank nanocomposite serving as a reference for the analysis of AuNPs@GluN/Alg. Figure 3B illustrates the similarity between the spectra. Peaks in the blank nanocomposite occur at specific wavenumbers (3447, 2924, 2854, 1748, 1632, and 1037 cm^{-1}), with slight shifts ob-

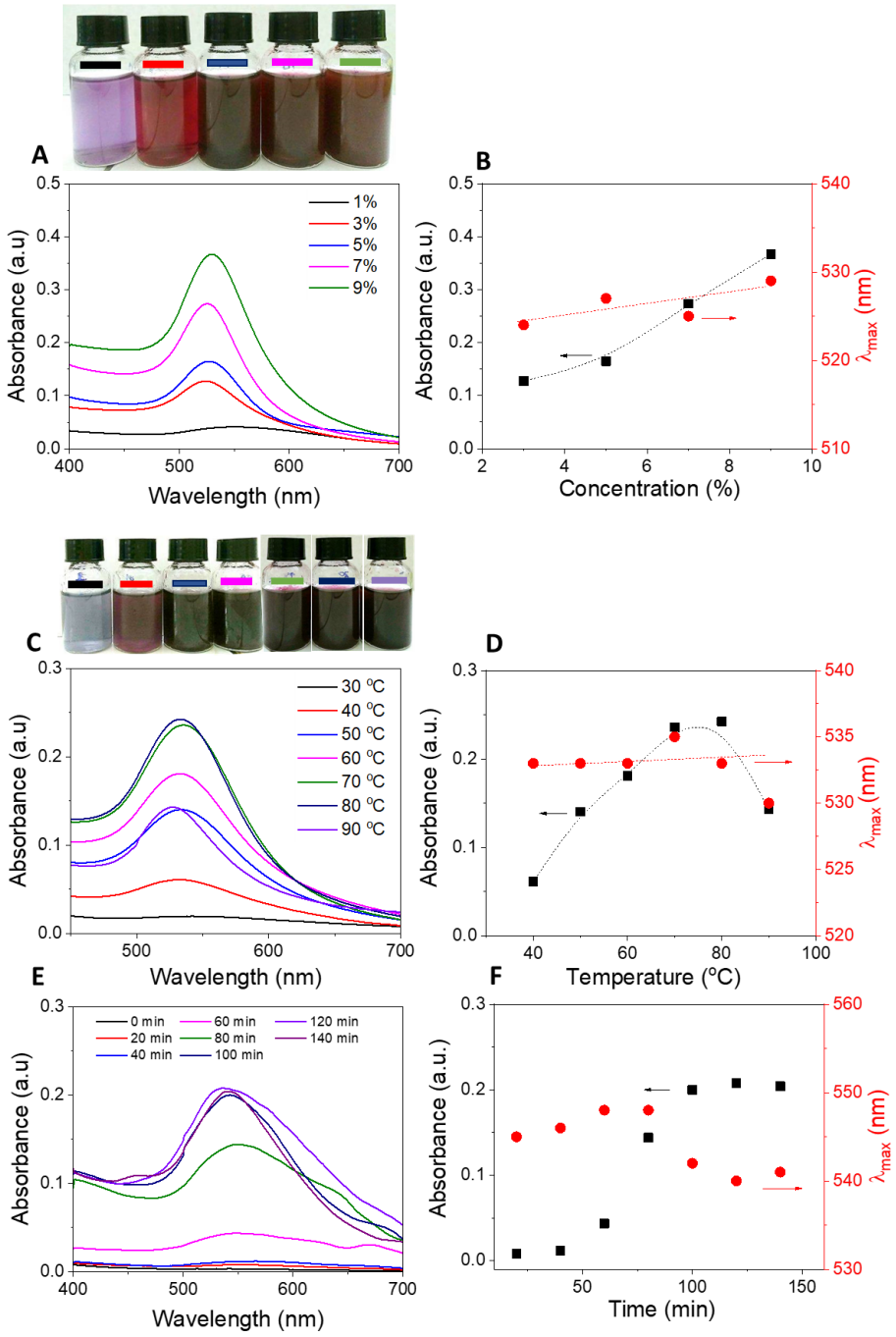


Figure 2: UV–vis spectra of AuNPs@GluN/Alg measured under varying reaction conditions (left) and plots of absorbance as function of various synthesis parameters (right). (A, B) Au^{3+} ions-to-gel ratio (w/w), (C, D) reaction temperature, and (E and F) reaction time. The upper photographs showing the corresponding color change.

served in the corresponding bands of AuNPs@GluN/Alg (3445, 2925, 2850, 1750, 1621, and 1035 cm^{-1}). The broad band around 3445 cm^{-1} corresponds to O–H groups of sugar molecules in the polysaccharides, while the vibrations at 2925 and 2850 cm^{-1} are attributed to symmetric stretching of C–H bonds. The peaks at 1750 and 1620 cm^{-1} signify carboxyl groups in alginate chains, with the peak at 1035 cm^{-1} indicating stretching vibrations of C–O bonds [34,35]. The FTIR spectra suggest the critical role of polysaccharides as stabilizing agents for AuNPs within the nanocomposite.

EDX analysis (Figure 3C) was conducted to determine the elemental composition of AuNPs@GluN/Alg. Strong signals at approximately 2.2 and 3.60 keV confirmed the presence of gold

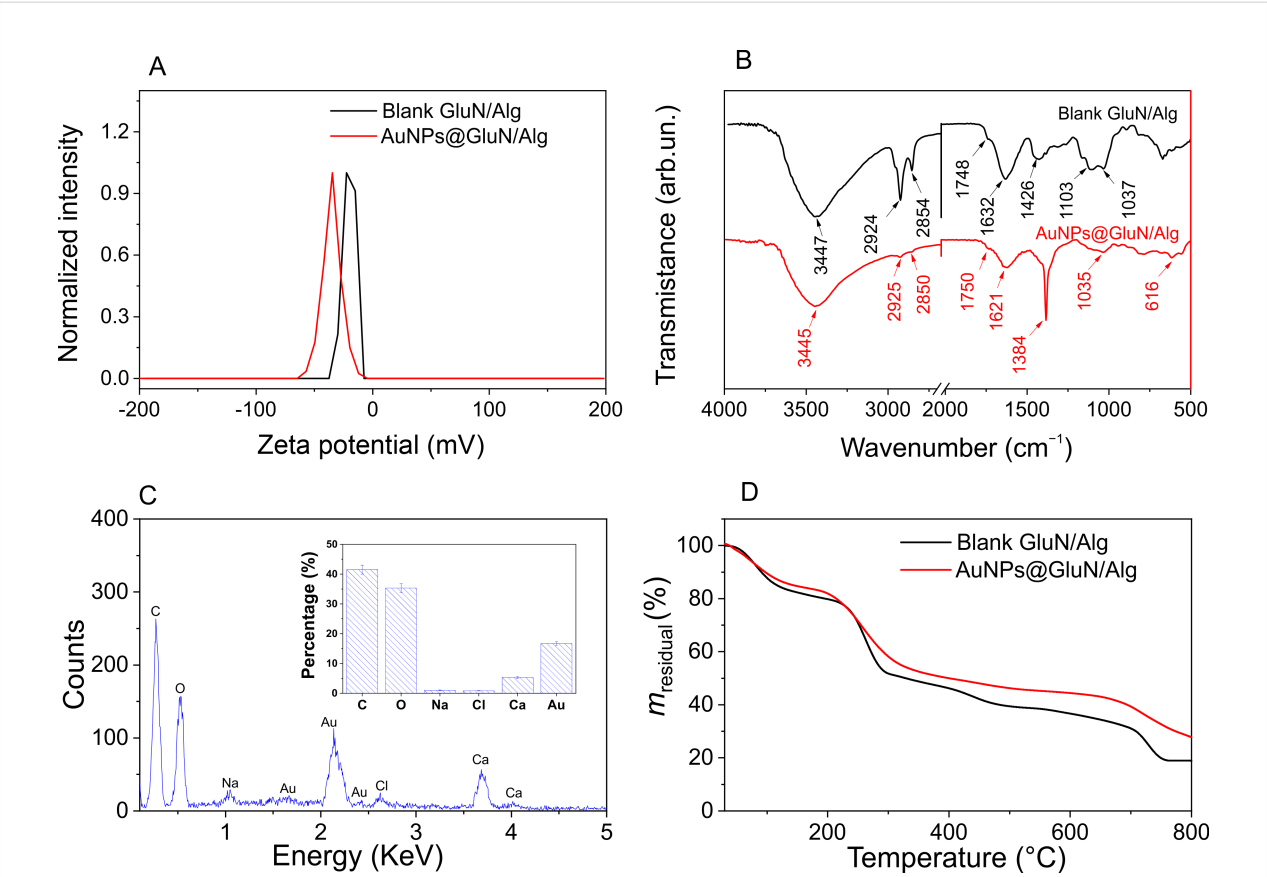


Figure 3: (A) Zeta potential curves, (B) FTIR spectra, (C) EDX spectrum and elemental composition (AuNPs@GluN/Alg only), and (D) TGA curves of GluN/Alg and AuNPs@GluN/Alg nanocomposites.

and calcium in the sample [36,37]. The identification of calcium reaffirms the formation of cross-links within the nanocomposite. Calculations revealed an average gold fraction of 17.4% (w/w) in the nanocomposite. This high concentration of gold nanoparticles is anticipated to impart excellent catalytic performance in the reduction of organic dyes.

Thermal properties of blank and AuNPs@GluN/Alg nanocomposites were assessed through TGA measurements in an airflow of 20 mL/min and a heating rate of 10 °C/min (Figure 3D). Similar kinds of thermal behavior were observed for both samples, characterized by three stages. At the initial stage, both nanocomposites exhibited a weight loss of approximately 17% in the temperature range of 30–100°C, attributed to the desorption of water absorbed during storage [38]. This showed that the dried nanocomposites can absorb moisture from the ambient environment well. The second stage revealed a slightly higher thermal stability of AuNPs@GluN/Alg (25% mass loss in the range of 210–290 °C) compared to blank GluN/Alg (31% mass loss in the range of 210–320 °C), indicating that AuNPs enhance the thermal stability of the polysaccharides. In the final stage, the weight loss of AuNPs@GluN/Alg was significantly lower than that of the blank nanocomposite in the temperature range of ca. 300–800 °C). Consequently, the ash residual of the AuNPs@GluN/Alg nanocomposite (30% of the initial mass) exceeded that of the blank sample (20% of the initial mass), suggesting the presence of inorganic components within the nanocomposite.

SEM and TEM analyses were performed to determine the morphology, and XRD and SAED patterns were used to evaluate the crystalline structure of AuNPs@GluN/Alg, as illustrated in Figure 4. The SEM images show that the AuNPs are uniform spherical particles with a size below 30 nm (Figure 4A,B). TEM images of AuNPs@GluN/Alg indicate an even geometry of the spherical particles (Figure 4C,D). A narrow size distribution of AuNPs was observed in the range of 3–27 nm with the highest frequency at 10 nm.

The crystalline structure of AuNPs was determined through XRD and SAED analysis. The XRD pattern showed Bragg reflections at 2θ values of 38.1°, 44.1°, and 64.5°, associated to,

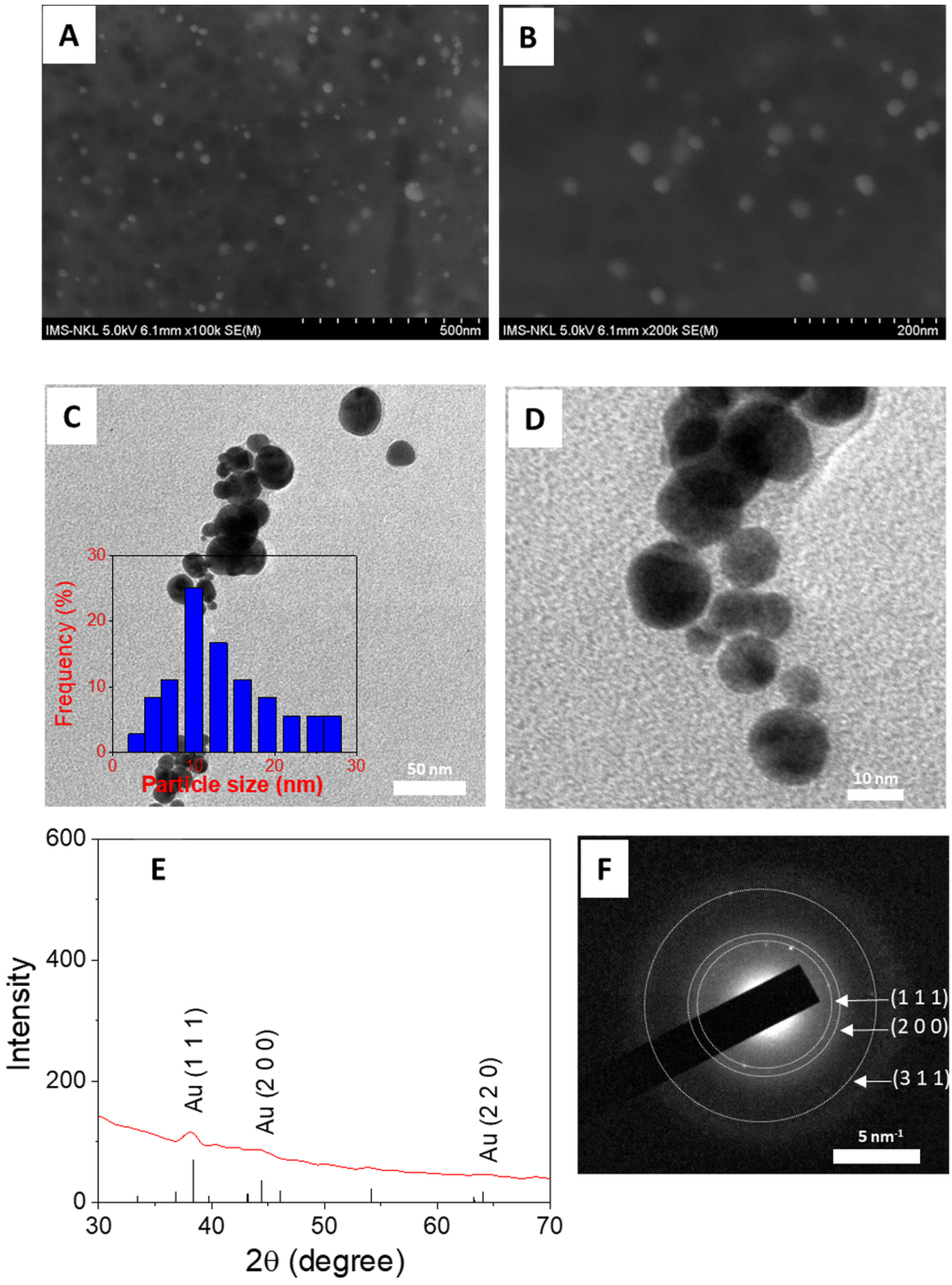


Figure 4: (A, B) SEM images with different magnifications, (C, D) TEM images with different magnifications, and (E) XRD and (F) SAED patterns of the AuNPs@GluN/Alg nanocomposite.

respectively, the (111), (200), and (220) planes of face-centered cubic (fcc) Au (card no. 96-901-1613) [39,40]. Moreover, the SAED pattern revealed rings of atoms with a d-spacing of 2.38 ± 0.12 Å, 2.92 ± 0.09 Å, and 1.22 ± 0.02 Å, corresponding to, respectively, the (111), (200), and (311) planes of fcc Au. Both analyses confirmed the presence of crystalline AuNPs in the synthesized nanocomposite.

Catalytic reduction of organic dyes

We investigated the catalytic efficiency of the AuNPs@GluN/Alg nanocomposite in reducing organic dyes using $NaBH_4$ as a model reaction. The persistence of toxic organic dyes poses a significant environmental hazard because of their poor biodegradability in aqueous environments [41]. The reduction mechanism involves the transfer of electrons from BH_4^- (the

electron donor) to the dye (the electron acceptor) facilitated by the surface of the metal nanoparticles [42,43]. Prior to electron transfer, dye and BH_4^- are adsorbed onto the catalyst surface, as depicted in Figure 5. Consequently, the effectiveness of this reaction hinges on the catalytic surface, influenced by both reagent adsorption and product desorption. We monitored the in situ reduction of organic dyes using the nanocatalyst via time-dependent UV–vis absorption measurements at ambient temperature. Confirmation of reduction was evidenced by the discoloration of the dye solution and the corresponding decrease in absorbance.

Figure 6 illustrates the results of the reduction of organic dyes. Initial experiments were conducted without the nanocatalyst and monitored over one week (Figure 6A,E,I). The findings revealed a gradual reduction in the concentration of 2-NiP by approximately 15% within the first hour and around 30% over the course of one week. The reduction of the other dyes was minimal in the absence of the nanocatalyst over the same period of time. Intriguingly, when the nanocomposite was introduced, a rapid decrease in absorbance values at specific wavelengths (413 nm for 2-NiP, 400 nm for 4-NiP, and 463 nm for MO) was observed, indicating efficient reduction. The varying reduction rates can be attributed to the structural differences among the dyes. The reduction of 2-NiP reached approximately 65% after the initial 5 min and was nearly complete (ca. 99%) after 9 min. The reduction of 4-NiP and MO took longer, with about 50% reduction after the initial 5 min and reaching near completion (ca. 99%) after 20 and 15 min, respectively. This variance underscores the different rates of dye adsorption and product desorption on the surface of the gold nanoparticles. Additionally, the polysaccharides can interact with functional groups within the dye structure, further influencing the adsorption/desorption dynamics of organic dyes on the surface of the AuNPs [44].

Regarding the reaction kinetics, the plots depicting $\ln(C_t/C_0)$ as function of the reaction time exhibit strongly linear correlations, with high determination coefficients, indicating pseudo-first-order kinetics for the degradation of organic dyes (Figure 6C,G,K). The rate constant for the reduction of 2-NiP (4.26×10^{-3} s^{-1}, $R^2 = 0.994$) surpassed that for the reduction of 4-NiP (2.05×10^{-3} s^{-1}, $R^2 = 0.995$). This variance may stem from the hindrance caused by the interaction between the hydroxy group in 4-NiP and functional groups in the polysaccharide chains, impeding the adsorption/desorption dynamics on the surface of the AuNPs. The rate constant for MO reduction was determined to be 4.04×10^{-3} s^{-1}, with $R^2 = 0.998$. Additionally, the recyclability study revealed that the highest recyclability was achieved after the reduction of 2-NiP, with over 98% retention after three cycles, while the recyclability regarding 4-NiP and MO notably declined in the third cycle, with 70% and 80% retention, respectively. These findings underscore the effectiveness of AuNPs@GluN/Alg in facilitating the recyclable reduction of 2-NiP. A comparison of MNPs–alginate-based catalysts shows that the AuNPs@GluN/

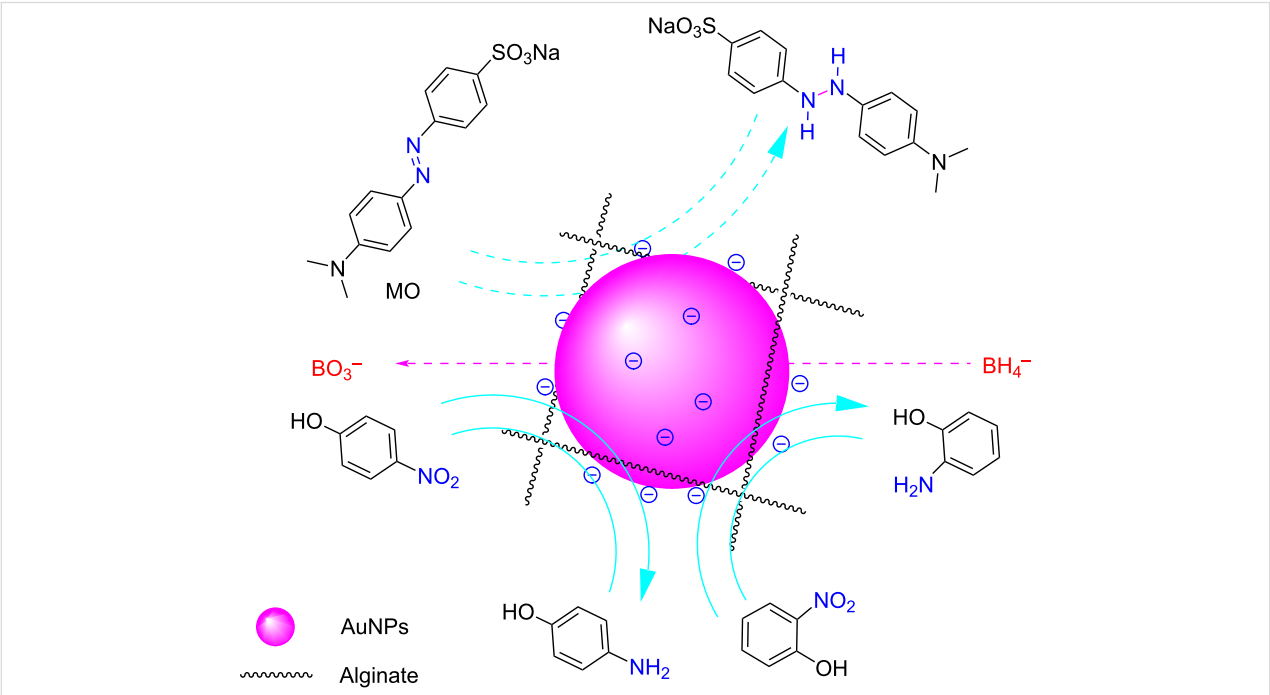


Figure 5: Proposed mechanism of the reduction of 2-NiP, 4-NiP, and MO using $NaBH_4$ in the presence of AuNPs@GluN/Alg catalyst.

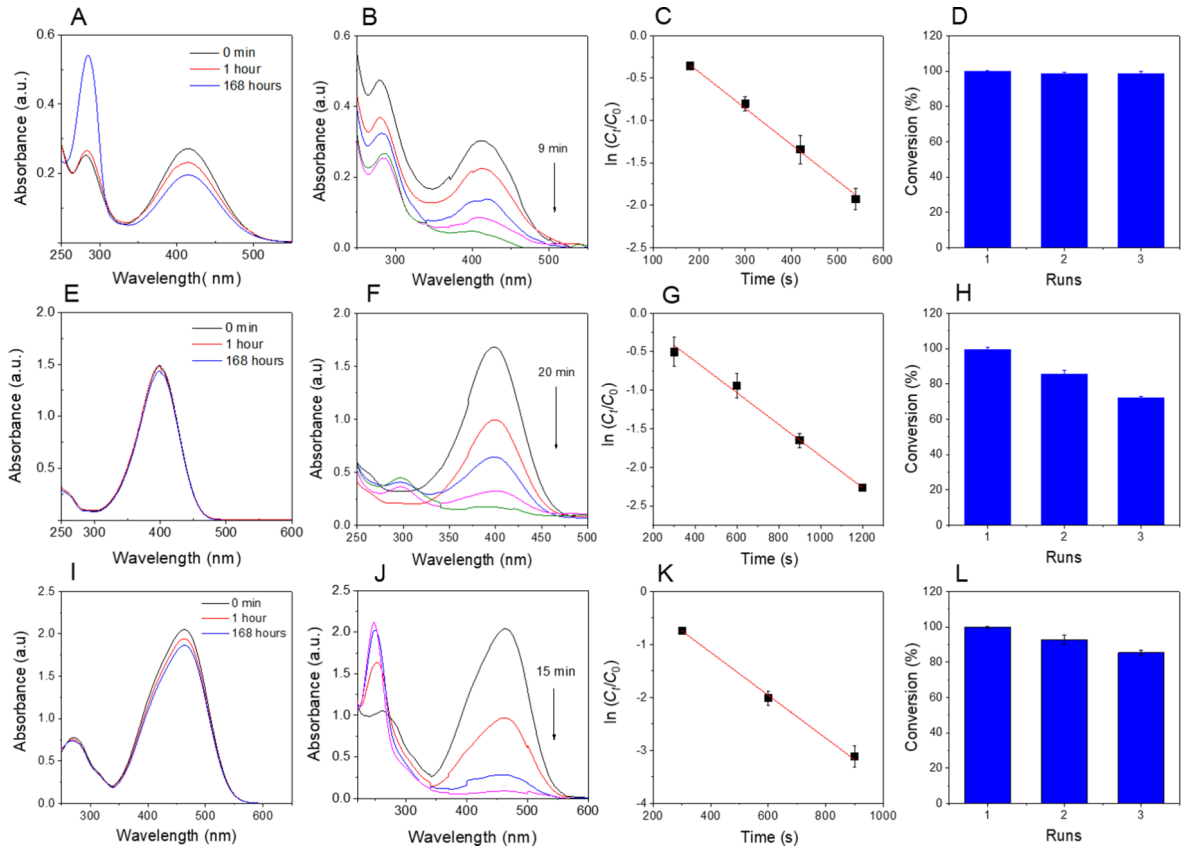


Figure 6: UV–vis spectra during the reduction of 2-NiP (A, B), 4-NiP (E, F), and MO (I, J) without and with nanocatalyst and plots of kinetic data and recyclability regarding 2-NiP (C, D), 4-NiP (G, H), and MO (K, L).

Alg nanocatalyst significantly enhanced catalytic performance in the reduction of organic dyes (Table 1).

Conclusion

This study introduces a novel approach for synthesizing gold nanoparticles within glucosamine/alginate nanocomposites via an in situ method. Comprehensive characterization using various analytical techniques was performed, revealing crystalline gold nanoparticles with an average diameter of 10.0 nm. The recyclable catalytic potential of the nanocomposite was then assessed for the reduction of 2-nitrophenol, 4-nitrophenol, and methyl orange utilizing $NaBH_4$. Remarkably, the reactions exhibited rapid kinetics, with pseudo-first-order rate constants ranging from 2.05×10^{-3} to 4.26×10^{-3} s^{-1}. Notably, the nano-

Table 1: Comparison of the catalytic activity of alginate-based nanocomposites in the reduction of organic dyes.

Dye	Catalyst	Catalyst mass	Time (min)	Rate constant (s^{-1})	Ref.
2-NiP	TiO_2–Ag@Alg	10.0 mg	40	0.5×10^{-3}	[45]
	CeO_2-SnO@Alg	10.0 mg	9	0.57×10^{-3}	[46]
	AuNPs@GluN/Alg	3.0 mg	9	4.26×10^{-3}	this work
4-NiP	AgNPs@PVP/ Alg	—	8	1.23×10^{-4}	[47]
	AgNPs@HPCD/ Alg	3.0 mg	25	1.51×10^{-3}	[21]
	PdNPs@HPCD/Alg	5.0 mg	24	1.78×10^{-3}	[22]
	AuNPs@GluN/Alg	3.0 mg	20	2.05×10^{-3}	this work
MO	AgNPs@HPCD/ Alg	3.0 mg	22	1.79×10^{-3}	[21]
	AuNPs@Lac/Alg	3.0 mg	22	2.86×10^{-3}	[24]
	Cu/Alg-CNBs	3.6 mg	17	2.25×10^{-3}	[48]
	AuNPs@GluN/Alg	3.0 mg	15	4.04×10^{-3}	this work

composite demonstrated excellent recyclability in the reduction of 2-nitrophenol. Consequently, this innovative nanocomposite emerges as a promising catalyst for organic dye reduction, offering considerable potential for diverse industrial applications.

Conflicts of Interest

The authors declare that they have no conflicts of interest.

Funding

The work is supported by Vietnam Academy of Science and Technology with number NCVCC15.02/24-25.

Author Contributions

Chi-Hien Dang: formal analysis; investigation; project administration; validation; writing – original draft. Le-Kim-Thuy Nguyen: formal analysis; investigation; validation; visualization. Minh-Trong Tran: data curation; formal analysis; investigation; validation. Van-Dung Le: formal analysis; investigation; validation; visualization. Nguyen Minh Ty: formal analysis; investigation; validation. T. Ngoc Han Pham: formal analysis; investigation; validation; visualization. Hieu Vu-Quang: data curation; formal analysis; validation. Tran Thi Kim Chi: formal analysis; investigation; visualization. Tran Thi Huong Giang: formal analysis; investigation; software; validation. Nguyen Thi Thanh Tu: formal analysis; investigation; validation; visualization. Thanh-Danh Nguyen: conceptualization; data curation; methodology; supervision; visualization; writing – review & editing.

ORCID® iDs

Le-Kim-Thuy Nguyen - https://orcid.org/0009-0008-3004-0018
T. Ngoc Han Pham - https://orcid.org/0000-0002-9080-5982
Hieu Vu-Quang - https://orcid.org/0000-0002-3468-5816
Tran Thi Kim Chi - https://orcid.org/0000-0002-5676-2472
Tran Thi Huong Giang - https://orcid.org/0009-0006-7385-8237
Nguyen Thi Thanh Tu - https://orcid.org/0000-0002-8299-4429
Thanh-Danh Nguyen - https://orcid.org/0000-0001-6330-8916

Data Availability Statement

All data that supports the findings of this study is available in the published article and/or the supporting information to this article.

References

1. Sadanandan, S.; Ramkumar, K.; Pillai, N. P.; Anuvinda, P.; Devika, V.; Ramanunni, K.; Sreejaya, M. *Food Control* **2023,** *148,* 109510. doi:10.1016/j.foodcont.2022.109510
2. Ganesh, K. M.; Bhaskar, S.; Cheerala, V. S. K.; Battampara, P.; Reddy, R.; Neelakantan, S. C.; Reddy, N.; Ramamurthy, S. S. *Nanomaterials* **2024,** *14,* 111. doi:10.3390/nano14010111
3. Chiang, M.-C.; Yang, Y.-P.; Nicol, C. J. B.; Wang, C.-J. *Int. J. Mol. Sci.* **2024,** *25,* 2360. doi:10.3390/ijms25042360
4. Santhosh, P. B.; Genova, J.; Chamati, H. *Chemistry* **2022,** *4,* 345–369. doi:10.3390/chemistry4020026
5. Elmi, G. R.; Saleem, K.; Baig, M. M. F. A.; Aamir, M. N.; Wang, M.; Gao, X.; Abbas, M.; Rehman, M. U. *Magnetochemistry* **2022,** *8,* 38. doi:10.3390/magnetochemistry8040038
6. Quinson, J. *J. Chem. Educ.* **2023,** *100,* 3612–3619. doi:10.1021/acs.jchemed.3c00492
7. Sakore, P.; Bhattacharya, S.; Belemkar, S.; Prajapati, B. G.; Elossaily, G. M. *Results Chem.* **2024,** *7,* 101264. doi:10.1016/j.rechem.2023.101264
8. Sargazi, S.; Laraib, U.; Er, S.; Rahdar, A.; Hassanisaadi, M.; Zafar, M. N.; Díez-Pascual, A. M.; Bilal, M. *Nanomaterials* **2022,** *12,* 1102. doi:10.3390/nano12071102
9. Zuhrotun, A.; Oktaviani, D. J.; Hasanah, A. N. *Molecules* **2023,** *28,* 3240. doi:10.3390/molecules28073240
10. Zvereva, M. V.; Aleksandrova, G. P.; Fadeeva, T. V. *Nanobiotechnol. Rep.* **2023,** *18,* 902–909. doi:10.1134/s2635167623600700
11. Gaikwad, D.; Sutar, R.; Patil, D. *Int. J. Biol. Macromol.* **2024,** *261,* 129547. doi:10.1016/j.ijbiomac.2024.129547
12. Barui, A. K.; Das, S.; Patra, C. R. Biomedical applications of green-synthesized metal nanoparticles using polysaccharides. *Functional Polysaccharides for Biomedical Applications;* Elsevier: Amsterdam, Netherlands, 2019; pp 329–355. doi:10.1016/b978-0-08-102555-0.00010-8
13. Younes, S.; Arnold, N.; Paper, M.; Keil, L.; Awad, D.; Brueck, T. Algal-based Biopolymers. *Value-added Products from Algae: Phycochemical Production and Applications;* Springer, 2023; pp 403–459. doi:10.1007/978-3-031-42026-9_13
14. Jin, M.; Shi, J.; Zhu, W.; Yao, H.; Wang, D.-A. *Tissue Eng., Part B* **2021,** *27,* 604–626. doi:10.1089/ten.teb.2020.0208
15. Choonara, Y. E.; Pillay, V.; Khan, R. A.; Singh, N.; du Toit, L. C. *J. Pharm. Sci.* **2009,** *98,* 2059–2072. doi:10.1002/jps.21590
16. Kumar, P.; Choonara, Y. E.; Du Toit, L. C.; Singh, N.; Pillay, V. *Pharmaceutics* **2018,** *10,* 233. doi:10.3390/pharmaceutics10040233
17. Nguyen, T.-D.; Hong-Ngan Tran, T.; Nguyen, C.-H.; Im, C.; Dang, C.-H. *Chem. Biochem. Eng. Q.* **2015,** *29,* 429–435. doi:10.15255/cabeq.2014.2092
18. Nguyen, C.-H.; Banh, K.-S.; Dang, C.-H.; Nguyen, C.-H.; Nguyen, T.-D. *Arabian J. Chem.* **2022,** *15,* 103814. doi:10.1016/j.arabjc.2022.103814
19. Leong, J.-Y.; Lam, W.-H.; Ho, K.-W.; Voo, W.-P.; Lee, M. F.-X.; Lim, H.-P.; Lim, S.-L.; Tey, B.-T.; Poncelet, D.; Chan, E.-S. *Particuology* **2016,** *24,* 44–60. doi:10.1016/j.partic.2015.09.004
20. Smrdel, P.; Bogataj, M.; Mrhar, A. *Sci. Pharm.* **2008,** *76,* 77–90. doi:10.3797/scipharm.0611-07
21. Nguyen, T.-D.; Dang, C.-H.; Mai, D.-T. *Carbohydr. Polym.* **2018,** *197,* 29–37. doi:10.1016/j.carbpol.2018.05.077
22. Nguyen, T.-D.; Vo, T.-T.; Nguyen, C.-H.; Doan, V.-D.; Dang, C.-H. *J. Mol. Liq.* **2019,** *276,* 927–935. doi:10.1016/j.molliq.2018.12.138
23. Nguyen, T.-D.; Vo, T.-T.; Huynh, T. T.-T.; Nguyen, C.-H.; Doan, V.-D.; Nguyen, D.-T.; Nguyen, T.-D.; Dang, C.-H. *New J. Chem.* **2019,** *43,* 16841–16852. doi:10.1039/c9nj04730a
24. Ho, T. T.-T.; Dang, C.-H.; Huynh, T. K.-C.; Hoang, T. K.-D.; Nguyen, T.-D. *Carbohydr. Polym.* **2021,** *251,* 116998. doi:10.1016/j.carbpol.2020.116998
25. Tu, N. T. T.; Vo, T. L.-A.; Ho, T. T.-T.; Dang, K.-P. T.; Le, V.-D.; Minh, P. N.; Dang, C.-H.; Tran, V.-T.; Dang, V.-S.; Chi, T. T. K.; Vu-Quang, H.; Fajgar, R.; Nguyen, T.-L.-H.; Doan, V.-D.; Nguyen, T.-D. *Beilstein J. Nanotechnol.* **2023,** *14,* 781–792. doi:10.3762/bjnano.14.64

26. Huang, C.-P.; Huang, Y.-H. *Appl. Catal., A* **2008,** *346,* 140–148. doi:10.1016/j.apcata.2008.05.017
27. Ogemdi, I. K. *Int. J. Pharm. Chem. (N. Y., NY, U. S.)* **2019,** *5,* 31–35. doi:10.11648/j.ijpc.20190503.12
28. Hamza, A.; Ho, K. C.; Chan, M. K. *Environ. Sci. Pollut. Res.* **2024,** *31,* 40873–40902. doi:10.1007/s11356-024-33798-6
29. Garg, N.; Bera, S.; Rastogi, L.; Ballal, A.; Balaramakrishna, M. V. *Spectrochim. Acta, Part A* **2020,** *232,* 118126. doi:10.1016/j.saa.2020.118126
30. Lin, C.; Tao, K.; Hua, D.; Ma, Z.; Zhou, S. *Molecules* **2013,** *18,* 12609–12620. doi:10.3390/molecules181012609
31. Ren, Z.; Li, H.; Li, J.; Cai, J.; Zhong, L.; Ma, Y.; Pang, Y. *Int. J. Biol. Macromol.* **2023,** *229,* 732–745. doi:10.1016/j.ijbiomac.2022.12.282
32. Dutta, A.; Paul, A.; Chattopadhyay, A. *RSC Adv.* **2016,** *6,* 82138–82149. doi:10.1039/c6ra17561a
33. Yue, K.; Jin, X.; Tang, J.; Tian, X.; Tan, H.; Zhang, X. *J. Nanosci. Nanotechnol.* **2019,** *19,* 3762–3771. doi:10.1166/jnn.2019.16315
34. Vandanjon, L.; Burlot, A.-S.; Zamanileha, E. F.; Douzenel, P.; Ravelonandro, P. H.; Bourgougnon, N.; Bedoux, G. *Mar. Drugs* **2023,** *21,* 482. doi:10.3390/md21090482
35. Soto-Vásquez, M. R.; Alvarado-García, P. A. A.; Youssef, F. S.; Ashour, M. L.; Bogari, H. A.; Elhady, S. S. *Mar. Drugs* **2022,** *21,* 36. doi:10.3390/md21010036
36. Soliman, M. K. Y.; Salem, S. S.; Abu-Elghait, M.; Azab, M. S. *Appl. Biochem. Biotechnol.* **2023,** *195,* 1158–1183. doi:10.1007/s12010-022-04199-7
37. Yan, K.; Yan, L.; Kuang, W.; Kaffash, A.; Mahdavi, B.; Baghayeri, M.; Liu, W. *Environ. Res.* **2023,** *238,* 117081. doi:10.1016/j.envres.2023.117081
38. Han, X.; Zhong, L.; Zhang, L.; Zhu, L.; Zhou, M.; Wang, S.; Yu, D.; Chen, H.; Hou, Y.; Zheng, Y. *Small* **2023,** *19,* 2303358. doi:10.1002/smll.202303358
39. Asal, Y. M.; Mohammad, A. M.; Abd El Rehim, S. S.; Al-Akraa, I. M. *J. Saudi Chem. Soc.* **2022,** *26,* 101508. doi:10.1016/j.jscs.2022.101508
40. Zayed, M.; Nasser, N.; Shaban, M.; Alshaikh, H.; Hamdy, H.; Ahmed, A. M. *Nanomaterials* **2021,** *11,* 2338. doi:10.3390/nano11092338
41. Tkaczyk, A.; Mitrowska, K.; Posyniak, A. *Sci. Total Environ.* **2020,** *717,* 137222. doi:10.1016/j.scitotenv.2020.137222
42. Alshammari, K. Heterogeneous catalysis using supported metal nanoparticles for environmental applications. Ph.D. Thesis, Cardiff University, Cardiff, UK, 2018.
43. Mazhani, M. Development of silver-magnetite nanocomposites for cysteine sensing and dye degradation. Master Thesis, Botswana International University of Science and Technology, Palapye, Botswana, 2020.
44. Gavade, N. L.; Kadam, A. N.; Babar, S. B.; Gophane, A. D.; Garadkar, K. M.; Lee, S.-W. *Ceram. Int.* **2020,** *46,* 11317–11327. doi:10.1016/j.ceramint.2020.01.161
45. Fadl, F. I. A. E.; Taleb, M. F. A. *J. Inorg. Organomet. Polym. Mater.* **2023,** *33,* 2142–2153. doi:10.1007/s10904-023-02651-7
46. Bakhsh, E. M.; Akhtar, K.; Fagieh, T. M.; Asiri, A. M.; Khan, S. B. *Int. J. Biol. Macromol.* **2021,** *191,* 243–254. doi:10.1016/j.ijbiomac.2021.09.029
47. Gao, Y.; Ding, X.; Zheng, Z.; Cheng, X.; Peng, Y. *Chem. Commun.* **2007,** 3720–3722. doi:10.1039/b706490j
48. Khan, S. B.; Ahmad, S.; Kamal, T.; Asiri, A. M.; Bakhsh, E. M. *Int. J. Biol. Macromol.* **2020,** *164,* 1087–1098. doi:10.1016/j.ijbiomac.2020.07.091

License and Terms

This is an open access article licensed under the terms of the Beilstein-Institut Open Access License Agreement (https://www.beilstein-journals.org/bjnano/terms), which is identical to the Creative Commons Attribution 4.0 International License (https://creativecommons.org/licenses/by/4.0). The reuse of material under this license requires that the author(s), source and license are credited. Third-party material in this article could be subject to other licenses (typically indicated in the credit line), and in this case, users are required to obtain permission from the license holder to reuse the material.

The definitive version of this article is the electronic one which can be found at:
https://doi.org/10.3762/bjnano.15.99

BEILSTEIN JOURNAL OF NANOTECHNOLOGY

Various CVD-grown ZnO nanostructures for nanodevices and interdisciplinary applications

The-Long Phan*[1], Le Viet Cuong‡[1], Vu Dinh Lam‡[2] and Ngoc Toan Dang‡[3,4]

Full Research Paper

Open Access

Address:
[1]Faculty of Engineering Physics and Nanotechnology, VNU University of Engineering and Technology, 144 Xuan Thuy, Cau Giay, Hanoi, Vietnam, [2]Graduate University of Science and Technology, Vietnam Academy of Science and Technology, Hanoi, Vietnam, [3]Institute of Research and Development, Duy Tan University, Da Nang 550000, Vietnam and [4]Faculty of Environmental and Natural Sciences, Duy Tan University, Da Nang 550000, Vietnam

Email:
The-Long Phan* - ptlong2512@vnu.edu.vn

* Corresponding author ‡ Equal contributors

Keywords:
chemical vapour deposition; electron microscopy; Raman and photoluminescent spectra; ZnO nanostructures

Beilstein J. Nanotechnol. **2024,** *15,* 1390–1399.
https://doi.org/10.3762/bjnano.15.112

Received: 24 July 2024
Accepted: 11 October 2024
Published: 11 November 2024

This article is part of the thematic issue "Recent advances in synthesis and applications of organometallic nanomaterials".

Guest Editor: T.-D. Nguyen

© 2024 Phan et al.; licensee Beilstein-Institut.
License and terms: see end of document.

Abstract

This work presents a simple chemical vapour deposition (CVD) method to grow ZnO nanostructures. By annealing Zn powder under atmospheric pressure conditions, we collected nanocrystals with various morphologies, including rods, pencils, sheets, combs, tetrapods, and multilegs. Raman scattering study reveals that the samples are monophasic with a hexagonal structure, and fall into the $P6_3mc$ space group. Depending on the morphology and crystal quality, their photoluminescence spectra have only a strong UV emission associated with the exciton radiative recombination, or both UV and defect-related visible emissions with their relative intensity ratio varying with the excitation power density. The obtained results prove that ZnO exhibits many novel nanostructures that can foster the development of next-generation optoelectronic nanodevices and new applications in biological and biomedical fields.

Introduction

In recent decades, nanomaterials whose diameters are in the range of 1–100 nm have been of intensive interest because they exhibit dimension-dependent intriguing behaviours that are different from their bulk counterparts. These special behaviours come from quantum confinement and surface effects dependent on the surface-to-volume ratio, which directly influences the electronic structure and the crystal structure symmetry. Thus, the study and fabrication of nanomaterials not only aim at exploring novel approaches of quantum physics, but also at realizing new multifunctional electronic/optoelectronic devices,

energy storage/generation systems, and renewable energy conversion devices with high performance and low-power consumption [1-3].

In comparison to semiconductors, ZnO has attracted much more attention. This is due to ZnO having outstanding semiconductor behaviours in comparison to other compounds [4-6]. Specifically, its large bandgap energy $E_g \approx 3.4$ eV is comparable to GaN – a typical material for blue-light-emitting diode (LED) technology [7,8]. Also, its exciton binding energy is higher than the thermal energy at 300 K, and it has high-quality optical microcavities [9]. Additionally, it is a transparent semiconductor with significant piezoelectricity [10]. These noble characteristics suggest ZnO to be a potential material in the fabrication of UV/blue/green LEDs, solid-state random lasers, UV-absorption devices, and nanogenerators [9,11-13]. Magnetic ordering can also be established in ZnO lattices upon doping with transition-metal and/or rare-earth elements (known as magnetic semiconductors, DMSs). This is expected to enable the development of next-generation spintronic devices [14] applicable to quantum and neuromorphic computing for artificial intelligence and internet of things [15-17].

Particularly during material fabrication processes, it has been discovered that ZnO exhibits many interesting structures in the nanoscale, such as rods, wires, rings, tubes, helixes, stars, bows, propellers, and cages [18-24]. Together with DMSs, these nanostructures will be beneficial to the development of new ZnO-based materials for photocatalytic [25], biomedical [26], gas sensing [27,28], and flexible electronic/optoelectronic applications [29,30]. They are usually fabricated by chemical vapour deposition (CVD) or solid-vapour phase thermal sublimation [18,23], thermal evaporation [21], hydrothermal method [31-33], and other facile chemical/physical routes [34]. The changes in fabrication and processing conditions will influence the shape and size of ZnO nanostructures.

When using CVD, vapour sources can be Zn powder or a mixture of powdered ZnO and C that are placed in the centre of the tube furnace. They are heated to high temperatures to create Zn vapours, which will be transported by a carrier gas and deposited onto substrates arranged at the downstream/upstream end with a suitable temperature range to form nanostructures [23,35,36]. Our current work uses this simple method to grow ZnO nanostructures. After fabrication, the crystal quality of nanostructures is assessed through Raman scattering (RS) and photoluminescent (PL) measurements at room temperature.

Experimental

As mentioned above, CVD was utilized to prepare ZnO nanostructures. A commercial Zn powder was used as the starting material (a vapour source) which was loaded in a ceramic bath. Clean Au-coated Si(001) substrates were arranged upstream on an alumina plate that was placed on the bath, nearby the vapour source. This system was placed in the centre of a horizontal quartz tube furnace, see [37] for more detail. The furnace tube was also connected with a gas line and a rotary vacuum pump oil. Before the growth, air was sucked out of the tube by back-filling it with argon (Ar) gas, and then pumped out until the base pressure went to $\approx 2 \times 10^{-3}$ Torr. After that, the gas mixture of $Ar/O_2 \approx 4{:}1$ at a flow rate of ≈300 sccm was introduced and used as a transport gas, which ensured the growth condition to be at atmospheric pressure. The growth was executed at a temperature range of T = 600–700 °C. After growth for 6–10 h, the CVD system was cooled down to collect white products formed on Si substrates. They were characterized by scanning electron microscopy (SEM, JEOL-6330F) and energy-dispersive X-ray (EDX) spectroscopy. Renishaw's RS and PL spectrometers operating with laser wavelengths of 488 and 325 nm were also employed to study phonon vibrational and emission spectra, respectively, of typical nanostructures.

Results and Discussion

We performed multiple experiments of growth of nanostructured ZnO materials by CVD under temperature and gas conditions as aforementioned described. After each growth, we obtained white products deposited on Si substrates. The analysis of their EDX spectra in the energy range of E = 0–20 keV shows the presence of Zn and O only, as representatively shown in Figure 1. It means that ZnO crystals were formed, and no impurity was generated during the material fabrication.

Recorded SEM images indicate the products grown on Au-coated Si substrates with various sizes and interesting morphologies. In general, these structures were sensitive to temperature change and were usually formed at temperatures in the range of T = 620–650 °C. Hereafter, we shall in turn present nanostructures obtained by CVD.

Figure 2a–f show SEM micrographs of some 1D-type nanostructures. They were grown at temperatures T = 620–630 °C. The first structure is typical of hexagonal-prism-shaped nanorods, named R_1 and R_2 in Figure 2a,b. Their diameter can be of several tens to hundreds of nanometres, and their length is about 10–15 μm. The second type of nanostructure has a shape which resembles that of matches or drumsticks, which was mixed with several hexagonal prism-shaped nanorods, named M in Figure 2c. We also collected images of nanopencils, named P_1 and P_2 in Figure 3d,e, which have hexagonal prism-shaped bodies with sharp tips similarly to pencils. Their tip lengths can be of several hundreds of manometers [38] or several micrometres – see Figure 2e. Nanopencils with sharp

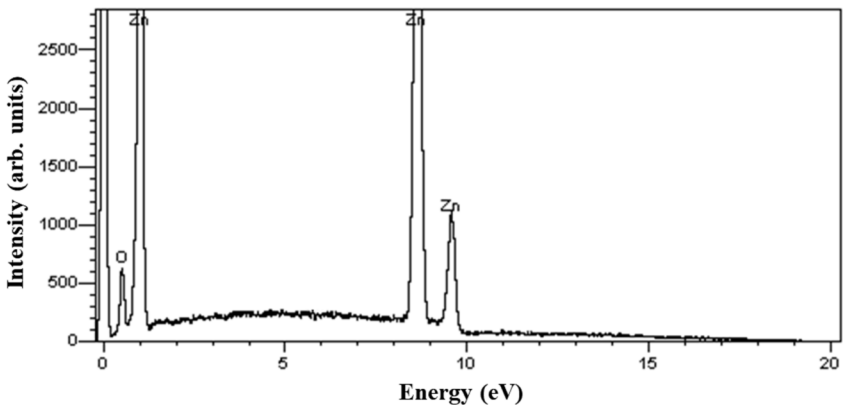


Figure 1: A representative EDX spectrum recorded from ZnO nanorods showing the presence of Zn and O in the product.

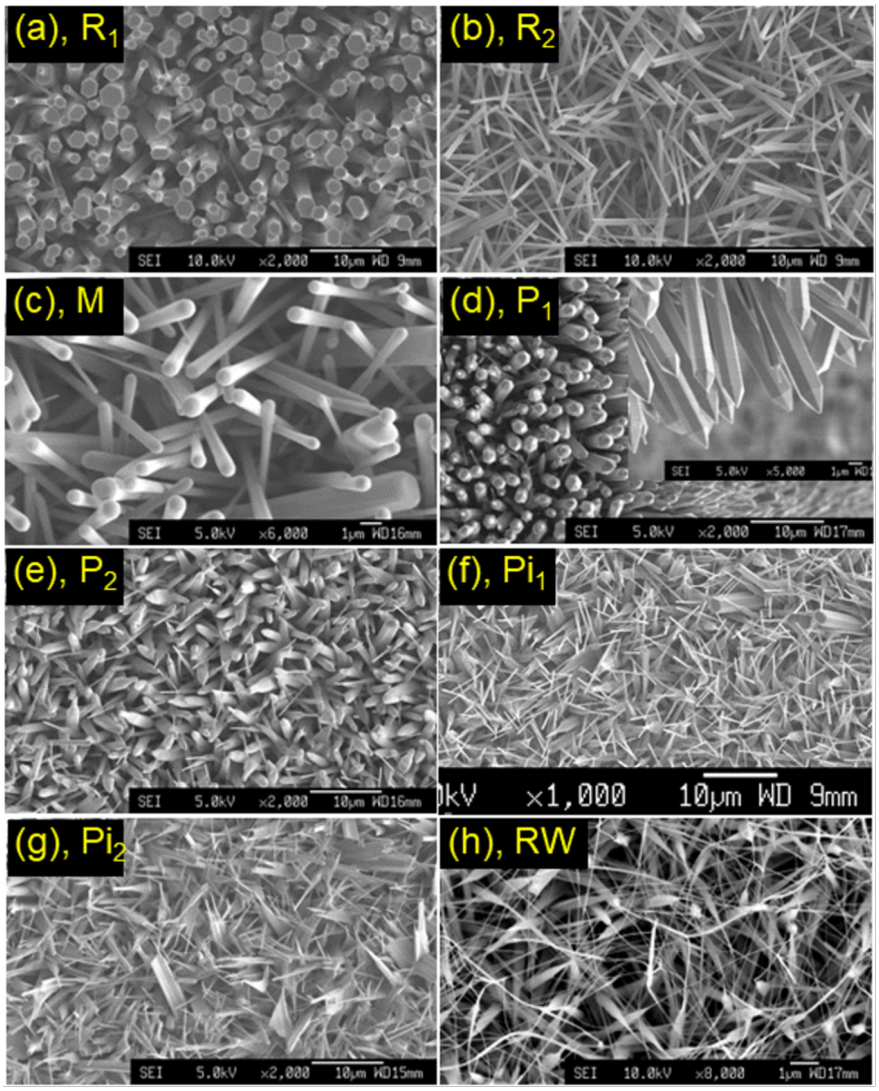


Figure 2: SEM micrographs of some nanostructures: (a, b) rods (R_1 and R_2), (c) matches or drumsticks (M), (d, e) pencils (P_1 and P_2), (f, g) pins (Pi_1 and Pi_2), and (h) rods with wires (RW).

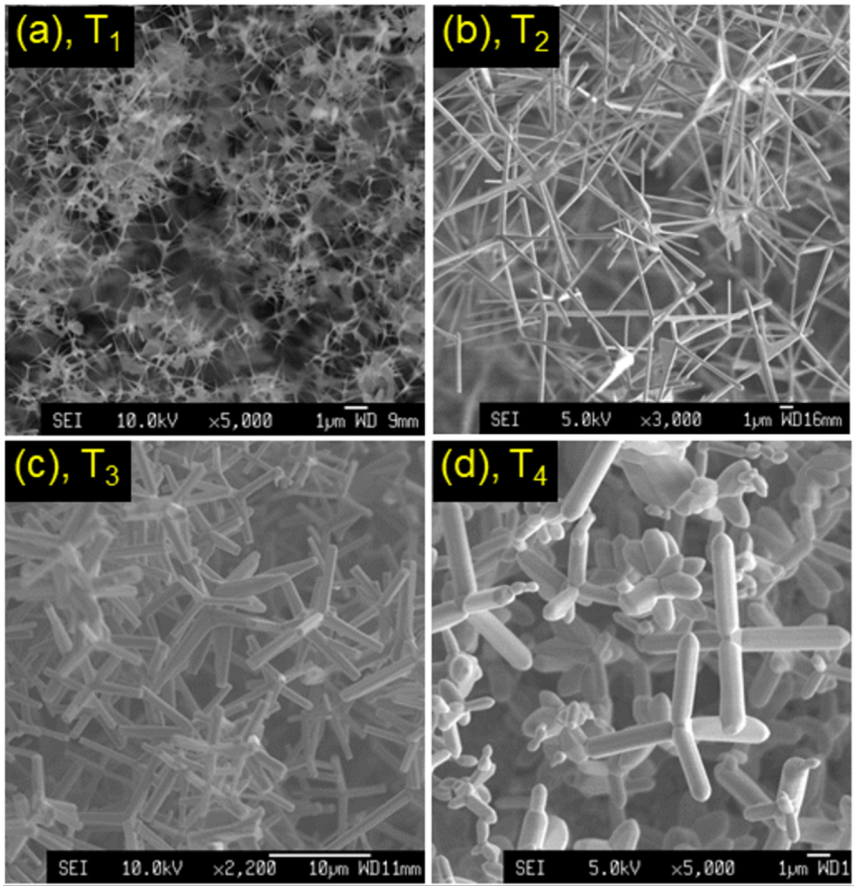


Figure 3: (a–d) SEM pictures of nanoscale tetrapods (T_1–T_4) with different morphologies.

tips can be called nanopins [39], denoted as Pi_1 in Figure 2f. During the growth, we could collect images of rods with two or three pins, named Pi_2 as shown in Figure 2g. In this case, rods are usually combined from several single rods. Apart from these structures, we collected images of cylindrical rods with long wires, named RW in Figure 2h. It has been demonstrated that all of these 1D-type structures are single crystals developing along the $c = \langle 0001 \rangle$ direction [39]. Top and bottom sides/surfaces of these structures are terminated with Zn and O atoms forming positively charged Zn-terminated (0001) and negatively charged O-terminated planes, respectively. Such 1D-type structures have many potential applications in optoelectronic devices [5,39,40], photocatalytic degradation [41], and water splitting for hydrogen technologies [38].

Figure 3a–d show SEM images of ZnO tetrapods. These various morphologies were grown at approx. 625–650 °C. The first one, named T_1 in Figure 3a, has needle-like arms of ≈1 μm of length. The dimeter of the arms is less than 50 nm. They converge at the origin with a size of ≈100 nm. For the second morphology, named T_2 in Figure 3b, the tetrapods have long arms of 8–10 μm, where arms are nanorods with diameters of 200–500 nm. Another tetrapod type shown in Figure 3c, named T_3, has a morphology similar to that of T_2 but with shorter arms of ≈5 μm. The other tetrapods shown in Figure 3d, named T_4, have pestle-like/cylindrical arms with unchanged diameter sizes of ≈800 nm, which were mixed with some multi-arm structures. According to the octa-twin model [42], the central nucleus is an octahedral multi-inversion twin that has eight trigonal pyramidal crystals with three $\{11\bar{2}2\}$ twin planes and a {0001} basal plane [43,44]. Thus, the arms of the tetrapod grow along the $\langle 0001 \rangle$ *c*-axis directions, starting from the central nucleus with $\{11\bar{2}2\}$ planes. Depending on the growth conditions, not only tetrapods but also octapods and multipods/multilegs (as shown in Figure 4) with different shapes and sizes of arms were also obtained [43,45].

Figure 5a,b show SEM micrographs of nanosheets (named S_1) recorded under different magnifications. They were developed at a temperature $T \approx 600$ °C. Their length and width are approx. 10–20 and 5–10 μm, respectively. Meanwhile, their thickness is less than 50 nm. Apart from these sheets, we have also collected

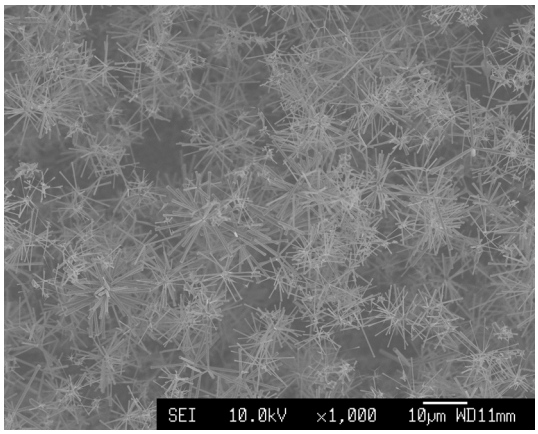


Figure 4: A micrograph showing ZnO multipods grown via CVD.

images of sheets glued with long nanorods that grew along the sheet width, named S_2 in Figure 5c. Such two-dimensional structures of ZnO are different from those prepared by hydrothermal process [46], radio-frequency magnetron sputtering [47], pulsed laser ablation [48], and electrodeposition methods [49]. They have many application potentials in dye-sensitized solar cells [46], self-powered energy-harvesting devices [47], photocatalysts [48], and turbid lenses [50]. It has been suggested that the preferential growth direction along the length of ZnO sheets is $\langle 10\bar{1}0\rangle$, while that along the width is the $\langle 0001\rangle$ direction [51]. This result is similar to the case of comb ribbons found in single-sided tooth combs, as shown below.

We also collected a mixture of single- and double-sided tooth combs that were developed at temperatures of T = 630–640 °C. Their length is several to tens of micrometres and the diameter of the teeth is about 50 nm, as shown in Figure 6a–c. As partially shown in [37], electron diffraction analyses indicated all combs to be single crystals. For single-sided tooth combs, named C_1 in Figure 6a,b, comb ribbon and teeth grew along the $\langle 10\bar{1}0\rangle$ and $\langle 0001\rangle$ directions, respectively. Meanwhile, for double-sided tooth combs, named C_2 in Figure 6c, comb ribbons are formed from two crystals interfaced at $\{10\bar{1}3\}$ planes, and teeth still grew along the $\langle 0001\rangle$ directions. Besides single- and double-sided tooth combs, there is also a sword-like nanocrystal, see Figure 6c. It is the comb ribbon formed before the teeth are constituted and developed. Combs reported by research groups have various morphologies and sizes, remarkably depending on fabrication conditions [46,52-57]. They are highly sensitive in gas-sensing applications [58,59], and can be used to tune second harmonic polaritons coupling with nanocavity modes and generating polariton cavity modes [60].

The aforementioned results indicate the variety of ZnO nanostructures as well as complex physical mechanisms occurring during their growth. Basically, these structures are formed according to the following processes [61]:

$$\mathrm{Zn(solid)} \rightarrow \mathrm{Zn(vapour)}\ \text{evaporation},$$

$$\mathrm{Zn(vapour)} + \mathrm{O_2} \rightarrow \mathrm{ZnO(seed)}\ \text{combustion},$$

$$\mathrm{Zn(seed)} \rightarrow \mathrm{ZnO(crystal)}\ \text{growth},$$

where the oxygen source was from the carrier-gas mixture. For the ZnO hexagonal structure, surface planes {0001},

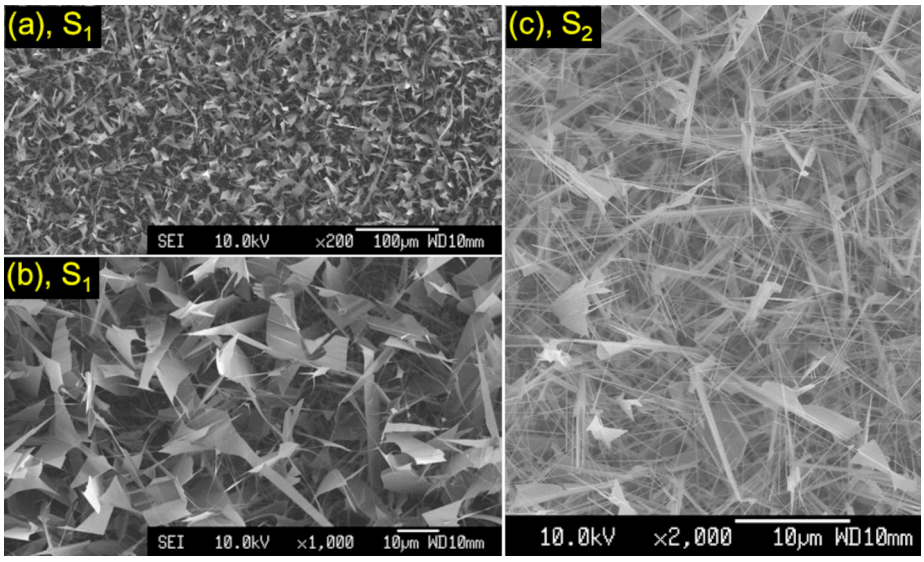


Figure 5: SEM pictures of (a, b) CVD-grown nanosheets, and (c) sheets glued with long nanorods.

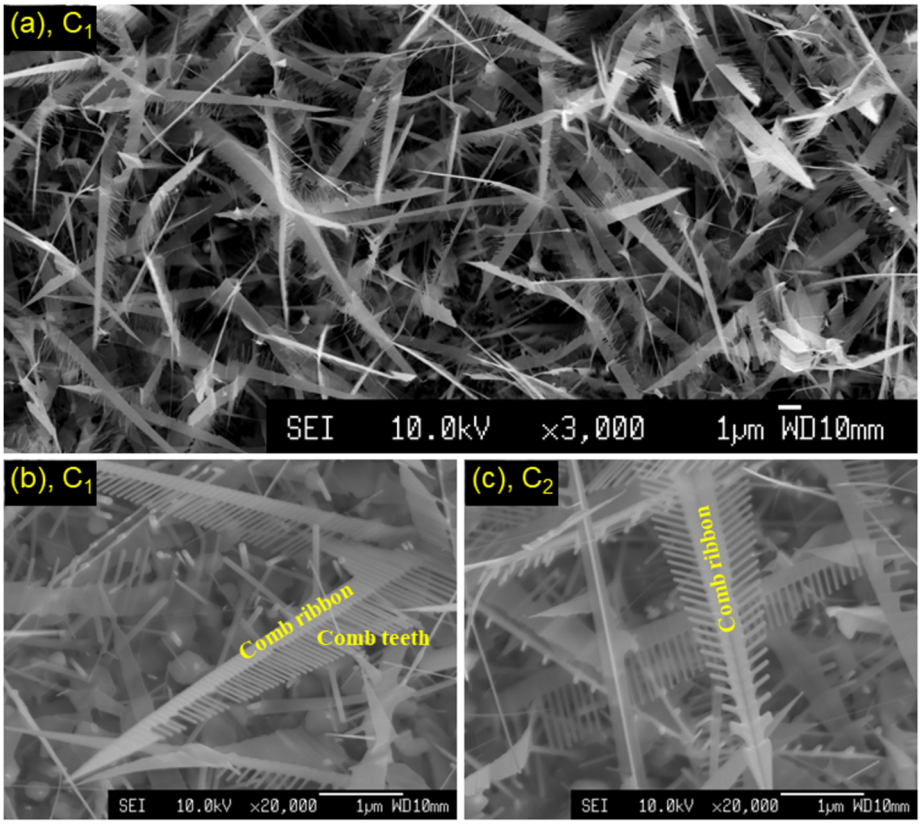


Figure 6: SEM pictures of (a, b) single- and (c) double-sided tooth combs.

$\{11\bar{2}0\}$, and $\{10\bar{1}0\}$ are known as referential and fast growth directions $\langle 0001\rangle$, $\langle 11\bar{2}0\rangle$, and $\langle 10\bar{1}0\rangle$, respectively, with the surface energy values in the following order: $E_{\{0001\}} > E_{\{11\bar{2}0\}} > E_{\{10\bar{1}0\}}$ [51]. At temperature and saturated vapour pressure values suitable for referential growth directions, ZnO crystals develop from Zn droplets working as nuclei/seeds, which react with oxygen in order to develop characteristic nanostructures.

Following morphological characterizations, we performed RS spectroscopy to check the crystal structure and quality of fabricated ZnO nanostructures. Figure 7 shows RS spectra of typical samples (namely R_1, P, Pi, T_2, T_3, M, and S labelled in the SEM images) recorded in the wavenumber range of 250–800 cm^{-1}. All spectra include vibration modes centred at approx. 331, 380, 409, 437, and 582 cm^{-1}. They are known as characteristic modes of the $P6_3mc$ hexagonal structure of ZnO [17,62]. It has been assigned the strongest mode at ≈437 cm^{-1} to E_2(L) while the others 331, 380, 409, and 582 cm^{-1} are in turn associated with E_2(H)-E_2(L), A_1(TO), E_1(TO), and E_1(LO) processes [62], as labelled in Figure 7. Spectral features recorded from these samples are almost the same. There are no anomalous modes induced by lattice defects, structural disorders, and impurities [17,63,64]. For some nanostructures, however, there are differences in RS intensity of some peaks, which could be due to different crystal orientations and thicknesses. Such results show that our fabricated ZnO nanostructures have a high quality and are single phase in the hexagonal structure.

We also measured PL spectra of typical samples under an excitation wavelength of 325 nm, which were measured at wavelengths of 350–700 nm. In this investigation, the maximum excitation laser-power density (I_o) was maintained at ≈170 kW/cm^2, and filters were utilized to tune the excitation density on experimental samples [65]. Recorded results revealed two main features of PL spectra which can be based on to classify the ZnO nanostructures into two sample groups. The first group gives only a UV emission at approx. 384–390 nm, such as P_1, T_2, M, and S shown in Figure 8a. Here, the UV emission is associated with the exciton radiative recombination [66]. An excitation-density increase would remarkably enhance the UV-emission intensity and cause a slight redshift and broadening of the UV line (due to the Coulomb interaction among carriers and exciton–exciton collision processes [67]), see Figure 8b.

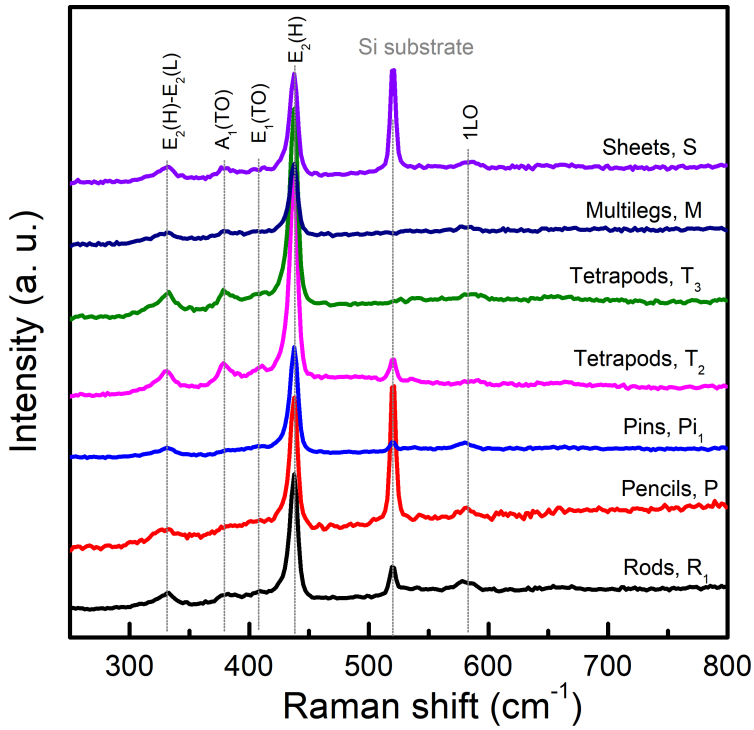


Figure 7: Raman scattering data of some ZnO nanostructures excited at a wavelength of λ = 488 nm. Apart from a Raman mode of Si substrates at ≈520 cm^{-1}, all other modes are from ZnO nanostructures.

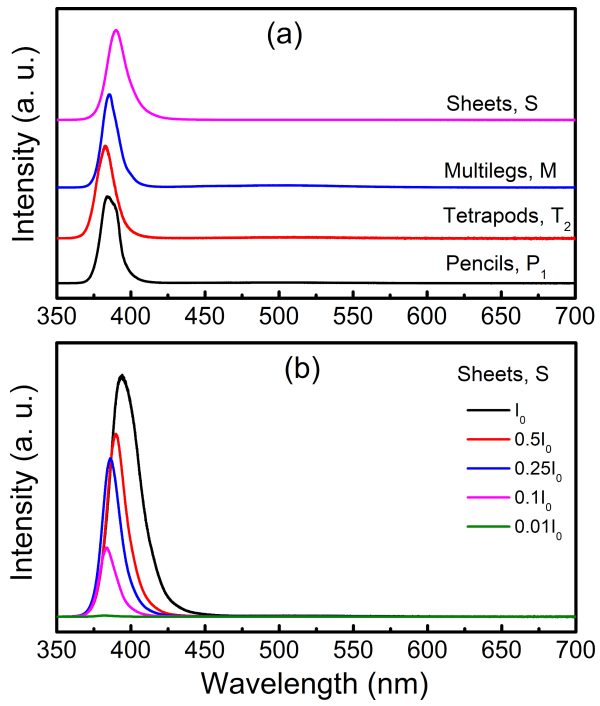


Figure 8: (a) PL spectra of some typical nanostructures (namely P_1, T_2, M, and S) showing only a UV emission with laser intensity of $0.1I_0$, and (b) spectra of nanosheets (namely S) excited by different laser power densities.

However, the PL spectra of the second group consist of both UV and visible emissions, typically the samples named R_1, R_2, and RW, as shown in Figure 9a. The UV emission peaks at ≈384 nm while the visible one peaks at approx. 510–525 nm – corresponding to the green emission that is usually assigned to donor (V_O)/acceptor (V_{Zn}) recombination [68], O_i defects [69], or V_O defects [70,71]. These defects are intrinsic and nonavoidable during the fabrication of ZnO nanostructures, and are usually dependent on a surface area-to-volume ratio of nanoparticles. Because of this reason, the relative intensity ratio of UV to visible lines can be used to evaluate the ZnO crystal quality [65]. By changing the excitation density, the intensity ratio of these two emissions could also be changed, as illustrated in Figure 9b and its inset for the case of nanorods R_2. In these samples, after laser excitation, the exciton-related UV emission is partially absorbed by defect centres occupying lower energy levels in the forbidden region. Different from the samples belonging to the first group, defects are insignificant due to their good crystal quality. Their exciton-related UV emission is not massively absorbed by defect centres playing a role as carrier traps, and always give a strong intensity.

Conclusion

We used CVD to grow ZnO nanostructures, such as rods, pencils, pins, sheets, combs, tetrapods, and multilegs. Their size

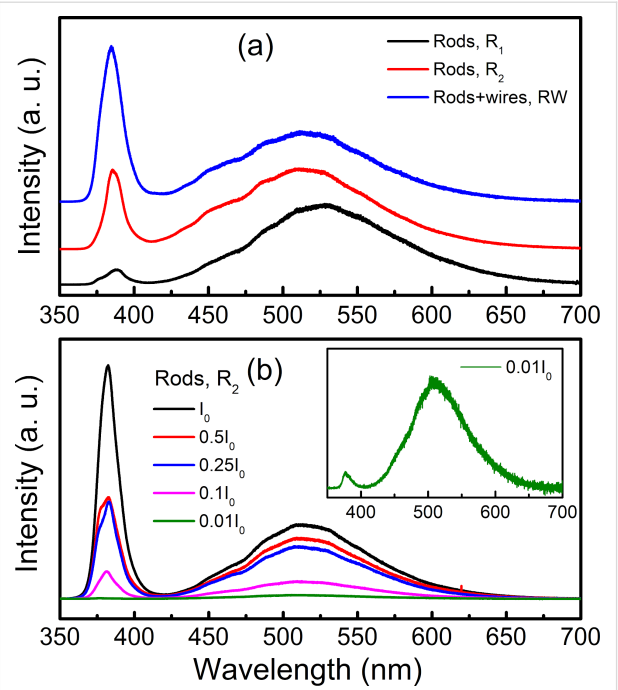


Figure 9: (a) PL spectra of nanorods (R_1 and R_2) showing only two UV and visible emissions with laser intensity of $0.1I_0$, and (b) spectra of nanorods R_2 excited by different laser-power densities – the inset is the spectrum for an excitation density of $0.01I_0$.

can be changed in the range from several tens to hundreds of nanometres. These structures usually grow at a temperature range of T = 600–650 °C. Raman spectra analysis for characteristic vibration modes proved that the collected ZnO nanostructures are single phase in the $P6_3mc$ hexagonal structure. The study of characteristic PL spectra revealed that the fabricated samples could be classified into two groups with different crystal qualities. The first one with a better crystal quality introduced only a UV emission due to the exciton recombination taking place near the band edge. Meanwhile, the other group introduced a PL spectra consisting of both UV and visible/green emissions. Here, the green emission at ≈525 nm is associated with point defects induced during growth. The intensity ratio of these two emissions is strongly dependent on the excitation density of the laser power. We believe that the successful fabrication of single-phase ZnO nanostructures with such optical characteristics will be important for the development of electronic/optoelectronic nanodevices. They also have potential applications in biological, biomedical, and environmental fields.

Author Contributions

The-Long Phan: conceptualization; investigation; visualization; writing – original draft. Le Viet Cuong: formal analysis; writing – review & editing. Vu Dinh Lam: formal analysis; writing – review & editing. Ngoc Toan Dang: formal analysis; writing – review & editing.

ORCID® iDs

The-Long Phan - https://orcid.org/0000-0001-8163-028X
Ngoc Toan Dang - https://orcid.org/0000-0003-3480-1888

Data Availability Statement

Data generated and analyzed during this study is available from the corresponding author upon reasonable request.

References

1. Rajalakshmi, M.; Sohila, S.; Ramya, S.; Divakar, R.; Ghosh, C.; Kalavathi, S. *Opt. Mater. (Amsterdam, Neth.)* **2012,** *34,* 1241–1245. doi:10.1016/j.optmat.2012.01.021
2. Jiang, K.; Pinchuk, A. O. Noble Metal Nanomaterials. In *Solid State Physics;* Camley, R. E.; Stamps, R. L., Eds.; Academic Press, 2015; pp 131–211. doi:10.1016/bs.ssp.2015.02.001
3. Kugarajah, V.; Hadem, H.; Ojha, A. K.; Ranjan, S.; Dasgupta, N.; Mishra, B. N.; Dharmalingam, S. Fabrication of nanomaterials. *Food, Medical, and Environmental Applications of Nanomaterials;* Elsevier: Amsterdam, Netherlands, 2022; pp 1–39. doi:10.1016/b978-0-12-822858-6.00001-7
4. Krishnan, B.; Shaji, S.; Acosta-Enríquez, M. C.; Acosta-Enríquez, E. B.; Castillo-Ortega, R.; Zayas, M. E.; Castillo, S. J.; Palamà, I. E.; D'Amone, E.; Pech-Canul, M. I.; D'Amone, S.; Cortese, B. Group II–VI Semiconductors. *Semiconductors;* Springer International Publishing: Cham, Switzerland, 2019; pp 397–464. doi:10.1007/978-3-030-02171-9_7
5. Nahhas, A. M. *Am. J. Nanomater.* **2018,** *6,* 15–23. doi:10.12691/ajn-6-1-2
6. Özgür, Ü.; Alivov, Y. I.; Liu, C.; Teke, A.; Reshchikov, M. A.; Doğan, S.; Avrutin, V.; Cho, S.-J.; Morkoç, H. *J. Appl. Phys.* **2005,** *98,* 041301. doi:10.1063/1.1992666
7. Dong, L.; Yadav, S. K.; Ramprasad, R.; Alpay, S. P. *Appl. Phys. Lett.* **2010,** *96,* 202106. doi:10.1063/1.3431290
8. Wang, X.; Zhao, X.; Takahashi, T.; Ohori, D.; Samukawa, S. *Nat. Commun.* **2023,** *14,* 7569. doi:10.1038/s41467-023-43472-z
9. Dong, H.; Zhou, B.; Li, J.; Zhan, J.; Zhang, L. *J. Materiomics* **2017,** *3,* 255–266. doi:10.1016/j.jmat.2017.06.001
10. Lu, Y.; Emanetoglu, N. W.; Chen, Y. ZnO Piezoelectric Devices. *Zinc Oxide Bulk, Thin Films and Nanostructures;* Elsevier: Amsterdam, Netherlands, 2006; pp 443–489. doi:10.1016/b978-008044722-3/50013-0
11. Nour, E. S.; Nur, O.; Willander, M. *Semicond. Sci. Technol.* **2017,** *32,* 064005. doi:10.1088/1361-6641/aa6bde
12. Sharma, D. K.; Shukla, S.; Sharma, K. K.; Kumar, V. *Mater. Today: Proc.* **2022,** *49,* 3028–3035. doi:10.1016/j.matpr.2020.10.238
13. Wang, Z. L.; Song, J. *Science* **2006,** *312,* 242–246. doi:10.1126/science.1124005
14. Chen, B.; Zeng, M.; Khoo, K. H.; Das, D.; Fong, X.; Fukami, S.; Li, S.; Zhao, W.; Parkin, S. S. P.; Piramanayagam, S. N.; Ter Lim, S. *Mater. Today* **2023,** *70,* 193–217. doi:10.1016/j.mattod.2023.10.004
15. Avrutin, V.; Izyumskaya, N.; Özgür, Ü.; Silversmith, D. J.; Morkoç, H. *Proc. IEEE* **2010,** *98,* 1288–1301. doi:10.1109/jproc.2010.2044966
16. Phan, T.-L.; Yu, S. C. *J. Phys. Chem. C* **2013,** *117,* 6443–6453. doi:10.1021/jp312080v

17. Petrov, D. N.; Dang, N. T.; Co, N. D.; Tu, B. D.; Lam, N. D.; Quang, T. V.; Nguyen, V. Q.; Lee, J. H.; Huy, B. T.; Yang, D. S.; Khan, D. T.; Phan, T. L. *J. Mater. Sci.* **2024,** *59,* 9217–9236. doi:10.1007/s10853-024-09724-z
18. Wang, Z. L. *Mater. Today* **2004,** *7,* 26–33. doi:10.1016/s1369-7021(04)00286-x
19. Davis, K.; Yarbrough, R.; Froeschle, M.; White, J.; Rathnayake, H. *RSC Adv.* **2019,** *9,* 14638–14648. doi:10.1039/c9ra02091h
20. Wisitsoraat, A.; Pimtara, I.; Phokharatkul, D.; Jaruwongrangsee, K.; Tuantranont, A. *Curr. Nanosci.* **2010,** *6,* 45–53. doi:10.2174/157341310790226315
21. ARJMAND, Y.; ESHGHI, H. *Bull. Mater. Sci.* **2014,** *37,* 1663–1668. doi:10.1007/s12034-014-0736-4
22. Mishra, Y. K.; Adelung, R. *Mater. Today* **2018,** *21,* 631–651. doi:10.1016/j.mattod.2017.11.003
23. Modeshia, D. R.; Dunnill, C. W.; Suzuki, Y.; Al-Ghamdi, A. A.; El-Mossalamy, E. H.; Obaid, A. Y.; Basahel, S. N.; Alyoubi, A. O.; Parkin, I. P. *Chem. Vap. Deposition* **2012,** *18,* 282–288. doi:10.1002/cvde.201206998
24. Zhang, B. P.; Binh, N. T.; Wakatsuki, K.; Segawa, Y.; Yamada, Y.; Usami, N.; Kawasaki, M.; Koinuma, H. *Appl. Phys. Lett.* **2004,** *84,* 4098–4100. doi:10.1063/1.1753061
25. Ong, C. B.; Ng, L. Y.; Mohammad, A. W. *Renewable Sustainable Energy Rev.* **2018,** *81,* 536–551. doi:10.1016/j.rser.2017.08.020
26. Zhang, Y.; Nayak, T.; Hong, H.; Cai, W. *Curr. Mol. Med.* **2013,** *13,* 1633–1645. doi:10.2174/15665240130666131111130058
27. Kang, Y.; Yu, F.; Zhang, L.; Wang, W.; Chen, L.; Li, Y. *Solid State Ionics* **2021,** *360,* 115544. doi:10.1016/j.ssi.2020.115544
28. Franco, M. A.; Conti, P. P.; Andre, R. S.; Correa, D. S. *Sens. Actuators Rep.* **2022,** *4,* 100100. doi:10.1016/j.snr.2022.100100
29. *NPG Asia Mater.* **2010**. doi:10.1038/asiamat.2010.142
30. Ho Kim, J.; Hwan Lee, J.; Kim, S.-W.; Yoo, Y.-Z.; Seong, T.-Y. *Ceram. Int.* **2015,** *41,* 7146–7150. doi:10.1016/j.ceramint.2015.02.031
31. Basnet, P.; Chatterjee, S. *Nano-Struct. Nano-Objects* **2020,** *22,* 100426. doi:10.1016/j.nanoso.2020.100426
32. Gu, C.; Shanshan, L.; Huang, J.; Shi, C.; Liu, J. *Sens. Actuators, B* **2013,** *177,* 453–459. doi:10.1016/j.snb.2012.11.044
33. Godse, P. R.; Mane, A. T.; Navale, Y. H.; Navale, S. T.; Mulik, R. N.; Patil, V. B. *SN Appl. Sci.* **2021,** *3,* 360. doi:10.1007/s42452-021-04357-2
34. Babayevska, N.; Przysiecka, Ł.; Iatsunskyi, I.; Nowaczyk, G.; Jarek, M.; Janiszewska, E.; Jurga, S. *Sci. Rep.* **2022,** *12,* 8148. doi:10.1038/s41598-022-12134-3
35. Lee, G.-H. *Jpn. J. Appl. Phys.* **2011,** *50,* 01BJ14. doi:10.1143/jjap.50.01bj14
36. Lupan, O.; Emelchenko, G. A.; Ursaki, V. V.; Chai, G.; Redkin, A. N.; Gruzintsev, A. N.; Tiginyanu, I. M.; Chow, L.; Ono, L. K.; Roldan Cuenya, B.; Heinrich, H.; Yakimov, E. E. *Mater. Res. Bull.* **2010,** *45,* 1026–1032. doi:10.1016/j.materresbull.2010.03.027
37. Phan, L. T.; Sun, Y.; Vincent, R. *J. Korean Phys. Soc.* **2011,** *59,* 60–64. doi:10.3938/jkps.59.60
38. Wang, T.; Lv, R.; Zhang, P.; Li, C.; Gong, J. *Nanoscale* **2015,** *7,* 77–81. doi:10.1039/c4nr03735a
39. Ahmad, U.; Hahn, Y. B. *Metal Oxide Nanostructures and Their Applications;* American Scientific Publishers, 2010.
40. Fujiwara, H.; Suzuki, T.; Niyuki, R.; Sasaki, K. *New J. Phys.* **2016,** *18,* 103046. doi:10.1088/1367-2630/18/10/103046
41. Muruganandam, L.; ALSharyani, A. K. *Desalin. Water Treat.* **2024,** *317,* 100288. doi:10.1016/j.dwt.2024.100288
42. Iwanaga, H.; Fujii, M.; Takeuchi, S. *J. Cryst. Growth* **1993,** *134,* 275–280. doi:10.1016/0022-0248(93)90136-k
43. Qiu, Y.; Luo, Q.; Liang, Z.; Cheng, Z.; Guo, B.; Fan, H.; Yang, S. *Mater. Lett.* **2015,** *154,* 103–106. doi:10.1016/j.matlet.2015.02.043
44. Mishra, Y. K.; Modi, G.; Cretu, V.; Postica, V.; Lupan, O.; Reimer, T.; Paulowicz, I.; Hrkac, V.; Benecke, W.; Kienle, L.; Adelung, R. *ACS Appl. Mater. Interfaces* **2015,** *7,* 14303–14316. doi:10.1021/acsami.5b02816
45. Ashok Kumar, E.; Riswana Barveen, N.; Wang, T.-J.; Kokulnathan, T.; Chang, Y.-H. *Microchem. J.* **2021,** *170,* 106660. doi:10.1016/j.microc.2021.106660
46. Park, J.-H.; Park, J.-G. *Appl. Phys. A: Mater. Sci. Process.* **2005,** *80,* 43–46. doi:10.1007/s00339-004-2936-z
47. Wang, Q.; Yang, D.; Qiu, Y.; Zhang, X.; Song, W.; Hu, L. *Appl. Phys. Lett.* **2018,** *112,* 063906. doi:10.1063/1.5012950
48. Ryu, Y. Y.; Kim, T.; Han, H. *Catalysts* **2019,** *9,* 787. doi:10.3390/catal9100787
49. Yang, J.; Wang, Y.; Kong, J.; Jia, H.; Wang, Z. *Opt. Mater. (Amsterdam, Neth.)* **2015,** *46,* 179–185. doi:10.1016/j.optmat.2015.04.016
50. Khokhra, R.; Kumar, M.; Rawat, N.; Barman, P. B.; Jang, H.; Kumar, R.; Lee, H.-N. *J. Opt. (Bristol, U. K.)* **2013,** *15,* 125714. doi:10.1088/2040-8978/15/12/125714
51. Zhu, Y.; Yang, H.; Sun, F.; Wang, X. *Nanoscale Res. Lett.* **2016,** *11,* 175. doi:10.1186/s11671-016-1379-8
52. Mousavi, S. H.; Haratizadeh, H.; de Oliveira, P. W. *Mater. Lett.* **2012,** *70,* 86–88. doi:10.1016/j.matlet.2011.11.042
53. Mohammadzadeh, A.; Azadbeh, M.; Shokriyan, B.; Khalil Abad, S. N. *Ceram. Int.* **2020,** *46,* 2552–2557. doi:10.1016/j.ceramint.2019.09.112
54. Al-Ruqeishi, M. S.; Mohiuddin, T. *Arabian J. Chem.* **2019,** *12,* 2774–2781. doi:10.1016/j.arabjc.2015.06.007
55. Yang, S.; Wang, Y.; Wang, L.; Zhang, G.; Vazinishayan, A.; Duongthipthewa, A. *AIP Adv.* **2016,** *6,* 065209. doi:10.1063/1.4954031
56. Liu, C. L.; Gao, H.; Li, L.; Liu, X.; Gao, Q.; Cuo, H. X.; Chen, T. T.; Miao, G. Q. *RSC Adv.* **2013,** *3,* 26149. doi:10.1039/c3ra43538e
57. Peng, D.; Huang, Y.; Yu, K.; Li, L.; Zhu, Z. *J. Nanomater.* **2010,** *2010,* 560409. doi:10.1155/2010/560409
58. Faisal, A. D. *Bull. Mater. Sci.* **2017,** *40,* 1061–1068. doi:10.1007/s12034-017-1461-6
59. Pan, X.; Zhao, X. *Sensors* **2015,** *15,* 8919–8930. doi:10.3390/s150408919
60. Capeluto, M. G.; Grinblat, G.; Tirado, M.; Comedi, D.; Bragas, A. V. *Opt. Express* **2014,** *22,* 5341. doi:10.1364/oe.22.005341
61. Jia, F.; Shih, Y.-L.; Pui, D. Y. H.; Li, Z.-Y.; Tsai, C.-J. *J. Nanopart. Res.* **2021,** *23,* 58. doi:10.1007/s11051-021-05145-0
62. Cuscó, R.; Alarcón-Lladó, E.; Ibáñez, J.; Artús, L.; Jiménez, J.; Wang, B.; Callahan, M. J. *Phys. Rev. B* **2007,** *75,* 165202. doi:10.1103/physrevb.75.165202
63. Phan, T.-L.; Zhang, Y. D.; Yang, D. S.; Nghia, N. X.; Thanh, T. D.; Yu, S. C. *Appl. Phys. Lett.* **2013,** *102,* 072408. doi:10.1063/1.4793428
64. Phan, T.-L.; Yu, S. C.; Vincent, R.; Bui, H. M.; Thanh, T. D.; Lam, V. D.; Lee, Y. P. *J. Appl. Phys.* **2010,** *108,* 044910. doi:10.1063/1.3478709
65. Phan, T.-L.; Yu, S. C.; Vincent, R.; Dan, N. H.; Shi, W. S. *J. Lumin.* **2010,** *130,* 1142–1146. doi:10.1016/j.jlumin.2010.02.010
66. Senthilkumar, K.; Yoshida, T.; Fujita, Y. *J. Mater. Sci.* **2018,** *53,* 11977–11985. doi:10.1007/s10853-018-2498-7
67. Suzuki, K.; Inoguchi, M.; Fujita, K.; Murai, S.; Tanaka, K.; Tanaka, N.; Ando, A.; Takagi, H. *J. Appl. Phys.* **2010,** *107,* 124311. doi:10.1063/1.3425783

68. Heo, Y. W.; Norton, D. P.; Pearton, S. J. *J. Appl. Phys.* **2005,** *98,* 073502. doi:10.1063/1.2064308
69. Wen, F.; Li, W.; Moon, J.-H.; Kim, J. H. *Solid State Commun.* **2005,** *135,* 34–37. doi:10.1016/j.ssc.2005.03.066
70. Musa, I.; Qamhieh, N.; Mahmoud, S. T. *Results Phys.* **2017,** *7,* 3552–3556. doi:10.1016/j.rinp.2017.09.035
71. Marković, S.; Stojković Simatović, I.; Ahmetović, S.; Veselinović, L.; Stojadinović, S.; Rac, V.; Škapin, S. D.; Bajuk Bogdanović, D.; Janković Častvan, I.; Uskoković, D. *RSC Adv.* **2019,** *9,* 17165–17178. doi:10.1039/c9ra02553g

License and Terms

This is an open access article licensed under the terms of the Beilstein-Institut Open Access License Agreement (https://www.beilstein-journals.org/bjnano/terms), which is identical to the Creative Commons Attribution 4.0 International License (https://creativecommons.org/licenses/by/4.0). The reuse of material under this license requires that the author(s), source and license are credited. Third-party material in this article could be subject to other licenses (typically indicated in the credit line), and in this case, users are required to obtain permission from the license holder to reuse the material.

The definitive version of this article is the electronic one which can be found at:
https://doi.org/10.3762/bjnano.15.112

BEILSTEIN JOURNAL OF NANOTECHNOLOGY

Electrochemical nanostructured CuBTC/FeBTC MOF composite sensor for enrofloxacin detection

Thi Kim Ngan Nguyen[1,2], Tien Dat Doan[1,3], Huy Hieu Luu[4], Hoang Anh Nguyen[3], Thi Thu Ha Vu[3], Quang Hai Tran[4], Ha Tran Nguyen[5], Thanh Binh Dang[6], Thi Hai Yen Pham[*1,3] and Mai Ha Hoang[1,3]

Full Research Paper

Open Access

Address:
[1]Graduate University of Science and Technology, Viet Nam Academy of Science and Technology, Ha Noi, Vietnam, [2]Faculty of Chemistry, TNU-University of Sciences, Tan Thinh Ward, Thai Nguyen City, Vietnam, [3]Institute of Chemistry, Vietnam Academy of Science and Technology, 18 Hoang Quoc Viet Street, Cau Giay District, Ha Noi, Vietnam, [4]Hanoi University of Industry, 298 Cau Dien Street, Bac Tu Liem District, Ha Noi, Vietnam, [5]National Key Laboratory of Polymer and Composite Materials, Ho Chi Minh City University of Technology, Vietnam National University, Ho Chi Minh City, 70000, Vietnam and [6]Center for High Technology Research and Development, Vietnam Academy of Science and Technology, 18 Hoang Quoc Viet Street, Cau Giay District, Ha Noi, Vietnam

Email:
Thi Hai Yen Pham* - haiyen25986@gmail.com

* Corresponding author

Keywords:
CuBTC; electrochemical sensor; enrofloxacin; FeBTC; metal-organic framework

Beilstein J. Nanotechnol. **2024,** *15,* 1522–1535.
https://doi.org/10.3762/bjnano.15.120

Received: 30 July 2024
Accepted: 05 November 2024
Published: 28 November 2024

This article is part of the thematic issue "Recent advances in synthesis and applications of organometallic nanomaterials".

Guest Editor: B. T. Huy



© 2024 Nguyen et al.; licensee Beilstein-Institut.
License and terms: see end of document.

Abstract

A novel electrochemical sensor for the detection of enrofloxacin (ENR) in aqueous solutions has been developed using a carbon paste electrode modified with a mixture of metal-organic frameworks (MOFs) of CuBTC and FeBTC. These MOFs were successfully synthesized via a solvothermal method and characterized using various techniques, including X-ray diffraction, Fourier-transform infrared spectroscopy, Brunauer–Emmett–Teller analysis, and X-ray photoelectron spectroscopy. The MOF mixture exhibited a particle size ranging from 40 to 100 nm, a high surface area of 1147 m^2/g, a pore volume of 0.544 cm^3/g, and a capillary diameter of 1.50 nm. Additionally, energy-dispersive X-ray mapping demonstrated the uniform distribution of the two MOFs within the electrode composition. The synergistic effect of the electrocatalytic properties of CuBTC and the high conductivity of FeBTC significantly enhanced the electrochemical response of ENR, increasing the signal by more than ten times compared to the unmodified electrode. Under optimal analytical conditions, the sensor exhibited three dynamic ranges for ENR detection, that is, 0.005 to 0.100 µM, 0.1 to 1.0 µM, and 1 to 13 µM, with coefficients of determination of 0.9990, 0.9954, and 0.9992, respectively, depending on the accumulation duration. The sensor achieved a low detection limit of 3 nM and demonstrated good reproducibility, with a relative standard deviation of 3.83%. Furthermore, the sensor demonstrated effective performance in analysing tap and lake water samples, with recovery rates ranging from 90.2% to 121.3%.

Introduction

Enrofloxacin (ENR) is a quinolinemonocarboxylic acid and a third-generation fluoroquinolone. This antibiotic is extensively used in livestock and aquaculture as an antibacterial agent, showing high activity against both Gram-negative and Gram-positive bacteria [1,2]. ENR, like other fluoroquinolones, is used to treat susceptible bacteria responsible for infections of the skin and soft tissue. The overuse of ENR causes severe adverse effects, including skeletal, reproductive, immune, and digestive disorders; moreover, ENR cannot be completely absorbed by most animals, it easily enters the environment through the excrement of organisms, also in the form of metabolites [3,4]. Nowadays, the concentration of ENR in products, especially animal products intended for human consumption is limited in the USA, the EU, and China [1,4]; the FDA also bans the use of ENR in both poultry and livestock [5]. Therefore, the determination of ENR residues is an urgent requirement. Various analytical techniques and methods have been developed to detect ENR, including microbiological methods, such as enzyme-linked immunosorbent assay (ELISA) [6], chromatography-mass spectrometry (LC-MS), chromatography (HPLC, UPLC), [3,7,8], flow immunochromatographic assays [9], and fluorescence measurements [10]. However, these methods have high requirements regarding instruments, chemicals, time consumption, and preparation of the samples. Electrochemical methods to detect ENR have attracted great attention because of benefits including high accuracy, simplicity, and environmental friendliness [11-14]. Electrochemical methods exhibited high efficacy in the detection of ENR with quick response, low cost, and simple handling; hence, these methods are promising to quantify ENR [15,16].

Noble metals and metal-organic frameworks (MOFs) are the most typical electrode materials to detect antibiotics [17,18]. MOFs emerged as the outstanding material for electrochemical sensor applications because of their high loading quantity and surface area, defined structures, and chemical stability [19,20]. Since the first report by Yaghi and his group in 1994 [21], MOFs have attracted great attention. The first publication related to a fluorescent sensor was presented by You et al. in 2002 [22]. MOFs are crystalline hybrid materials with network structures formed by the self-assembly of metal ions or metal clusters and organic ligands, which give them ultrahigh porosity and enormous internal surface area. However, using MOFs for electrochemical sensors has some limitations associated with the low conductivity of MOFs. Therefore, the coupling with conducting materials, such as carbon-based materials, metal nanoparticles, and polymers, has been performed to enhance the electron charge transfer of MOFs [23,24]; single MOFs combined with carbon-based materials have been extensively studied [12,25-28]. A sensitive and simplified electrochemical sensor using a $Cu_3(BTC)_2$-modified carbon paste electrode for detecting 2,4-dichlorophenol was reported by Dong and his group [29]. Owing to the large specific surface area, high absorption capacity, and an acceptable efficacy of the electron transfer, $Cu_3(BTC)_2$ exhibited a good sensitivity to 2,4-dichlorophenol in the range from 0.04 to 1.00 μM with a limit of detection (LOD) of 9 nM in differential pulse voltammetry measurements. Moreover, the combination of metal oxides and MOFs showed better electrochemical detection ability than pristine MOFs. For example, Wang et al. developed a MOF/TiO_2 composite to quantify chlorogenic acid in a range from 0.01 to 1.00 μM with a low LOD of 7 nM [30]. Utilizing carbon-based materials can provide not only enhanced electron transfer but also catalytic functions for the MOFs. A sensor for simultaneously detecting hydroquinone and catechol in water using a Cu-MOF–graphene composite was developed by Li and colleagues. Measurement ranges beginning at 1.0×10^{-6} and 1.0×10^{-3} M were achieved, with LODs of 5.9×10^{-7} M and 3.3×10^{-7} M for hydroquinone and catechol, respectively [31]. In addition, the coupling of MOFs with conducting polymers was investigated to modulate their electrical properties. Conducting poly(3,4-ethylenedioxythiophene) nanotubes were coated with porphyrin-based MOFs to detect dopamine in the range of 2×10^{-6} to 270×10^{-6} M with a LOD of 0.04×10^{-6} M [32]. The combination of two types of MOFs has been rarely investigated for the detection of antibiotics.

To our current knowledge, no reports have been made on the use of electrodes modified with a mixture of MOFs for the detection of enrofloxacin. In this study, a sensor was developed using a mixture of CuBTC and FeBTC to modify carbon paste electrodes for the determination of enrofloxacin. The characterization and properties of the fabricated electrode, including molecular structure, morphology, and electrochemical characteristics, were thoroughly investigated using various analytical techniques. The synergistic effects of CuBTC and FeBTC are considered promising for enhancing the performance of enrofloxacin sensors in aqueous solutions.

Results and Discussion

Characterization of (Cu)(Fe)BTC

In the XRD pattern in Figure 1a, the FeBTC sample shows peaks at 2θ values of 6.26°, 10.34°, 10.85°, 19.10°, 20.12°, 24.07°, and 27.82°, which are associated with the crystalline structure of FeBTC (CCDC card No. 640536). The CuBTC sample exhibits reflection peaks at 2θ values of 6.77° (200), 9.65° (220), 11.73° (222), 13.57° (400), 14.76° (331), 15.24° (420), 16.6° (422), 17.56° (500), 19.16° (440), 20.36° (600), 21.40° (620), 23.55° (444), 24.27° (551), 26.11° (731), 29.47° (751), 35.30° (773), and 39.21° (882), characteristic for the

CuBTC phase (CCDC card No. 112954) [28,33,34]. The XRD pattern of (Cu)(Fe)BTC exhibits a characteristic peak at 2θ of 10.85° assigned to the (842) crystal planes of the Fe-BTC phase, and all characteristic peaks of CuBTC appear. It can be observed that the characteristic peaks of pure FeBTC have a much lower intensity than those of pure CuBTC; therefore, the intensity of the characteristic peaks of the CuBTC phase predominates in the (Cu)(Fe)BTC pattern. The simultaneous presence of FeBTC and CuBTC phases in the (Cu)(Fe)BTC sample indicates the successful synthesis of (Cu)(Fe)BTC composite.

The N_2 adsorption/desorption isotherms of the (Cu)(Fe)BTC sample are of type I with H4 hysteresis ring according to IUPAC classification (Figure 1b) [35]. The N_2 adsorption isotherm for (Cu)(Fe)BTC shows rapid adsorption of nitrogen in the low-pressure range ($P/P_0 < 0.1$), suggesting a predominance of micropores [36]. Surface area, pore volume, and capillary diameters of the (Cu)(Fe)BTC sample are 1147 m^2/g, 0.544 cm^3/g, and 1.50 and 1.90 nm, respectively. Total pore volume, average pore diameter, and surface area of FeBTC are 1.46 cm^3/g, 2.38 nm, and 1211 m^2/g, respectively [37]. Surface area, total pore volume, and average pore diameter of CuBTC are 1134 m^2/g, 0.49 cm^3/g, and 1.74 nm, respectively [38].

The full-scan XPS spectrum of (Cu)(Fe)BTC (Figure 2a) shows the existence of C (284 eV), O (532 eV), Fe (712 and 726 eV), and Cu (935 eV). The C 1s XPS spectrum of the (Cu)(Fe)BTC sample (Figure 2b) reveals four peaks attributed to C=C/C–C (284.78 eV), C–O (285.42 eV), C=O (286.11 eV), and O–C=O (288.62 eV) [39]. The high-resolution O 1s XPS spectrum (Figure 2c) can be decomposed into oxygen in carboxyl groups (531.74 eV) and physically adsorbed –OH groups (533.30 eV) [40].

In the Fe 2p XPS spectra (Figure 2d), the binding energy peaks of Fe $2p_{3/2}$ correspond to Fe^{2+} and Fe^{3+} with peak positions at 711.42 and 713.35 eV, respectively. The Fe $2p_{1/2}$ peaks correspond to Fe^{2+} and Fe^{3+} with central peak positions at 724.20 and 726.31 eV, respectively. In addition, there are two shake-up satellites at 718.08 and 732.04 eV (denoted as sat.). The Fe^{2+} and Fe^{3+} components account for 51.62% and 48.38% in the (Cu)(Fe)BTC determined by peak area. In the Cu 2p XPS spectrum (Figure 2e), the binding energy peak of Cu $2p_{3/2}$ (934.9 eV) can be attributed to Cu^{2+}.

Characterization of (Cu)(Fe)BTC@CPE

Morphology

The TEM image of the (Cu)(Fe)BTC sample shows unevenly distributed particles with different particle sizes fluctuating in the range of 40 to 100 nm (Figure 3).

After mixing the electrode blend, SEM and EDX mapping were used to investigate the distribution of CuBTC and FeBTC on the electrode surface (Figure 4). Figure 4a clearly shows the scattering of bright CuBTC and FeBTC particles on the graphite flakes. Figure 4b confirms the homogenous distribution of Fe, Cu, and O in the electrode material.

Electrochemical property

The Nyquist diagrams in Figure 5 were obtained using electrochemical impedance spectroscopy (EIS) in a 0.1 M KCl solution containing 5 mM $[Fe(CN)_6]^{3-/4-}$. Based on the EIS analysis, the charge transfer resistances (R_{ct}) of CPE, CuBTC@CPE,

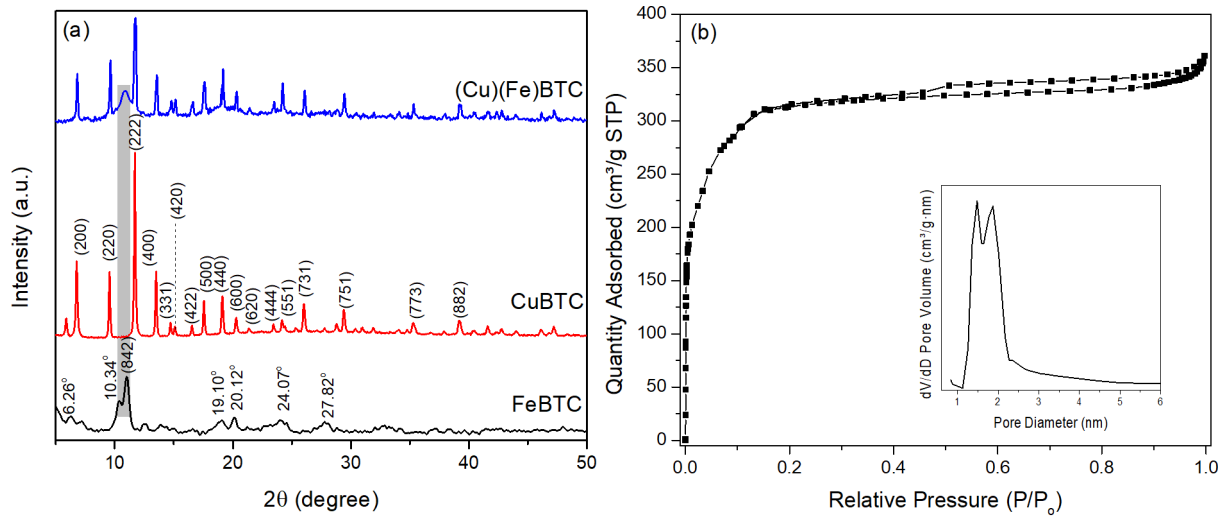


Figure 1: (a) XRD pattern and (b) N_2 adsorption/desorption isotherms of the (Cu)(Fe)BTC sample.

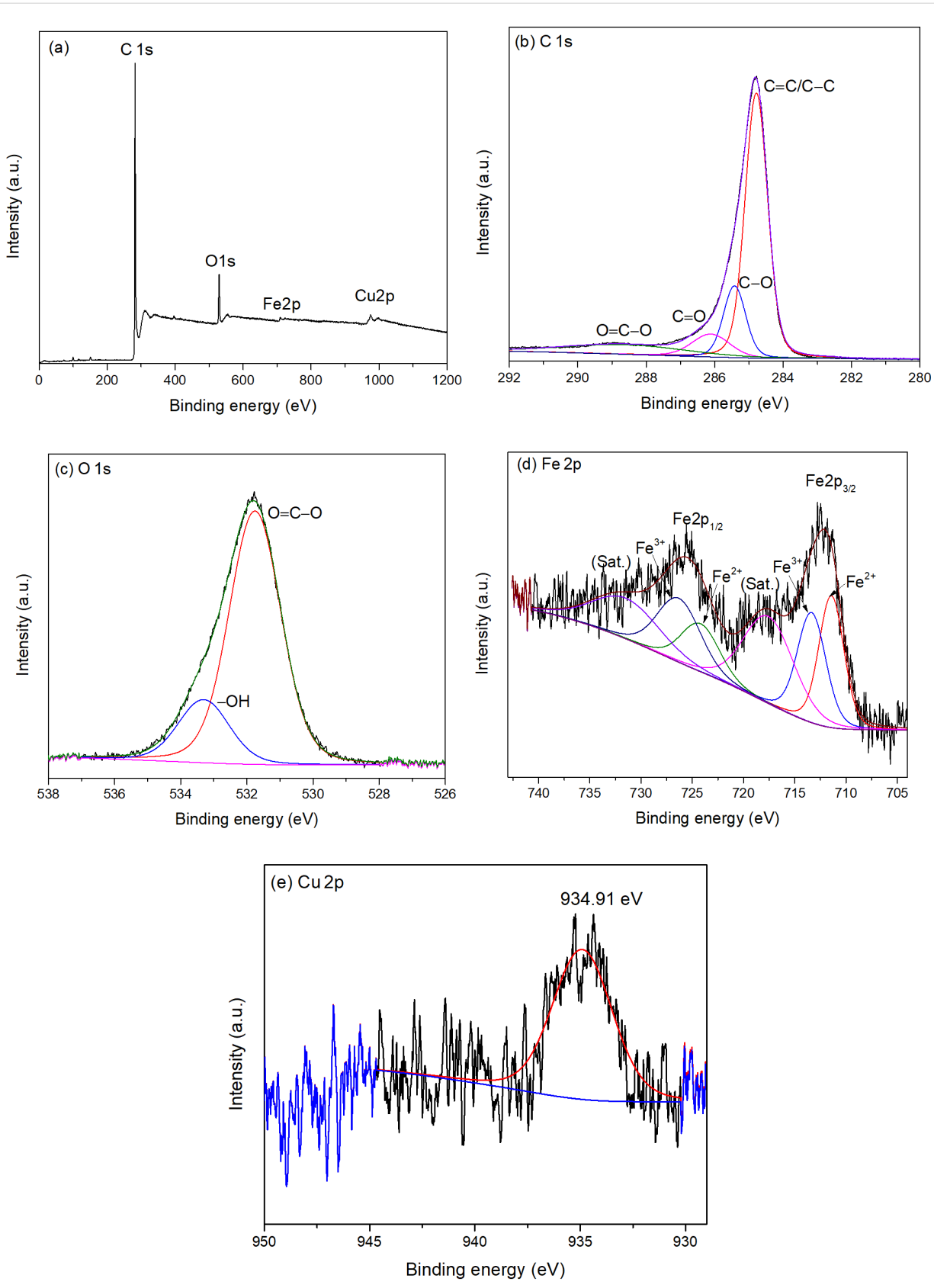


Figure 2: Full-scan (a) and high-resolution C 1s (b), O 1s (c), Fe 2p (d), and Cu 2p (e) XPS spectra of the (Cu)(Fe)BTC sample.

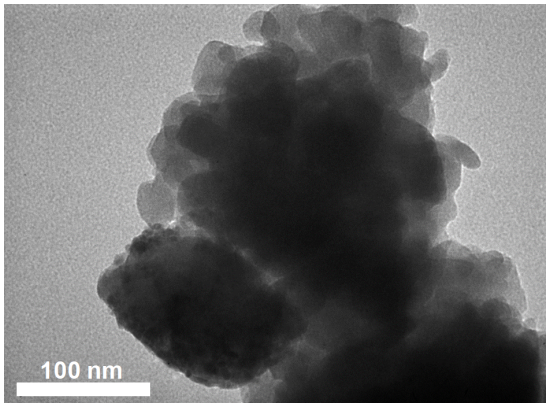


Figure 3: TEM image of (Cu)(Fe)BTC sample.

and (Cu)(Fe)BTC@CPE were calculated to be 742, 1710, and 547 Ω, respectively. It is evident that CuBTC increased the R_{ct} of the CuBTC@CPE electrode more than twofold compared to the CPE electrode, likely because of its low electron conductivity [41,42]. However, the addition of FeBTC, which has a low R_{ct} of 220 Ω and significantly better conductivity [37], to the (Cu)(Fe)BTC@CPE led to reduction to about a third in R_{ct}. This reduction in charge transfer resistance is advantageous for the enhancement of electrochemical oxidation on the electrode surface.

Electrochemical behaviour of enrofloxacin on the (Cu)(Fe)BTC@CPE electrode

The electrochemical behaviour of ENR was studied on both CPE and modified electrodes using cyclic voltammetry in the

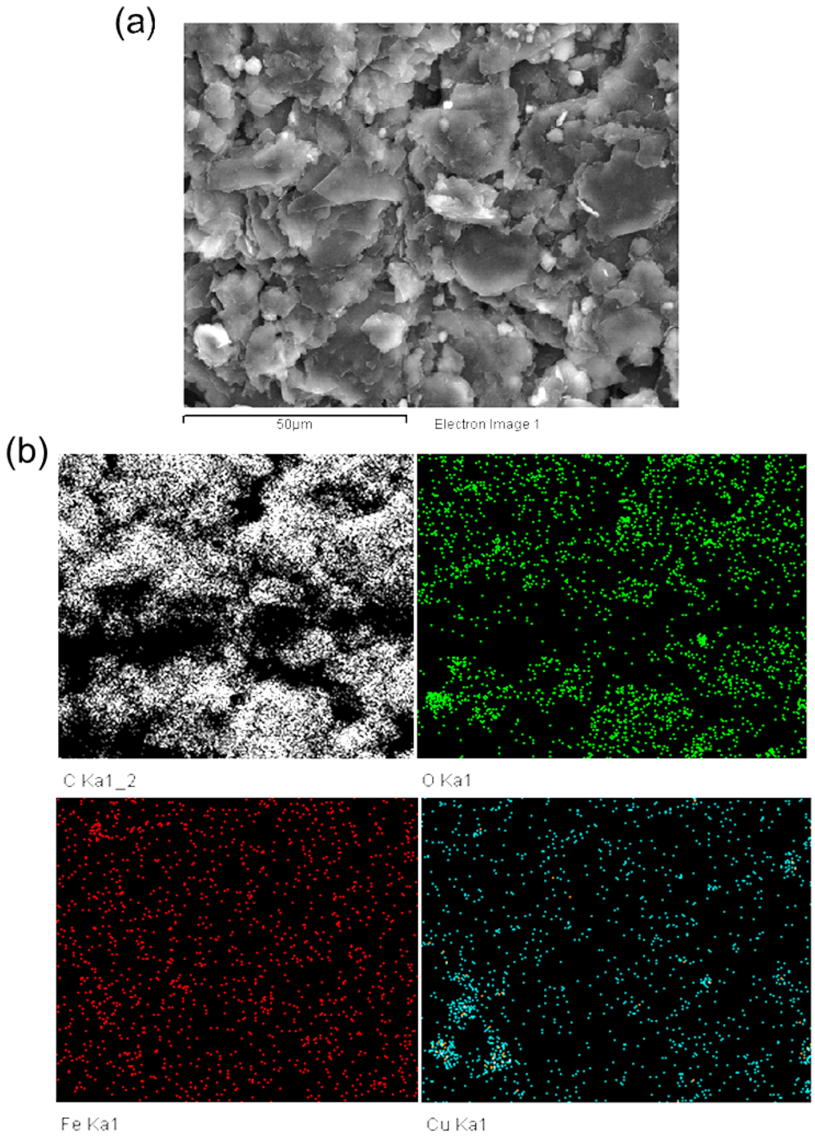


Figure 4: SEM images of (Cu)(Fe)BTC@CPE (a) and EDX maps of (Cu)(Fe)BTC@CPE (b).

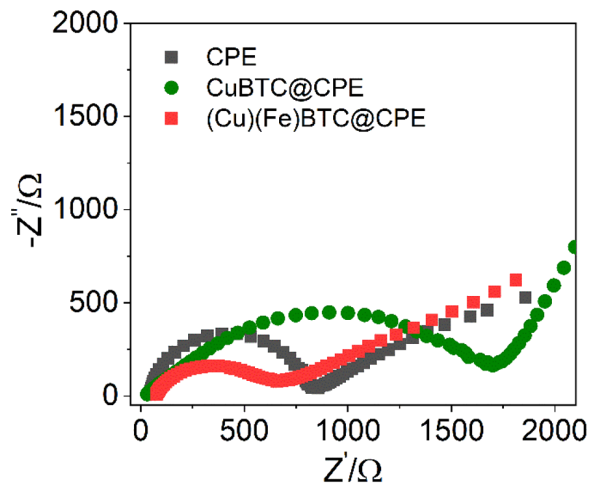


Figure 5: Nyquist plots of the modified electrodes in 0.1 M KCl solution containing 5 mM $[Fe(CN)_6]^{3-/4-}$.

potential window from 0.4 to 1.2 V. A modified electrode containing 5% CuBTC and 5% FeBTC was used for the investigation. The green line in Figure 6a shows the voltammogram in ENR-free blank solution with no electrochemical response for ENR. In phosphate-buffered saline (PBS) containing ENR, there is a peak at 0.85 V on all four electrodes, attributed to the oxidation of ENR during the anodic scanning. No reduction peak was observed, revealing that the electrochemical reaction mechanism of ENR is irreversible. The experimental results are consistent with previous studies [16,43,44]. Besides, the ENR peak obtained on (Cu)(Fe)BTC was much higher than those on CPE, CuBTC@CPE, and FeBTC@CPE, likely because of the catalytic properties of two MOF materials in the electrode composition.

For the determination of ENR, square wave adsorptive stripping voltammetry (SW-AdSV) was employed because of its superior performance in comparison to the cyclic voltammetric method. Figure 6b illustrates the square wave voltammograms (SWVs) depicting the electrochemical response of ENR in PBS solution containing 1 µM ENR. These SWVs reveal distinct, well-defined, and sharp peaks corresponding to the electrochemical oxidation of ENR. The peak height recorded on the (Cu)(Fe)BTC-modified electrodes is approximately ten times higher than that on the unmodified electrode, and the peak position shifted to more negative values compared to the CPE. This phenomenon highlights the significantly enhanced catalytic activity of the modified electrode. Additionally, the (Cu)(Fe)BTC@CPE electrode exhibited a significantly sharper, more symmetric, and higher peak than both the CuBTC@CPE and FeBTC@CPE electrodes. These observations support the conclusion regarding the synergistic effects of the catalytic activity of CuBTC and the good conductivity of FeBTC, which together contribute to the enhanced performance of the electrode.

Effect of MOF content on the enrofloxacin signal

The electrode has three components, namely, CuBTC, FeBTC, and carbon paste. The carbon paste content was maintained at 90%, resulting in the total of CuBTC and FeBTC being 10%. By altering the proportions of CuBTC and FeBTC in the electrode composition, significant variations in the ENR signal were observed (Figure 7). Specifically, an electrode composition with 0% CuBTC and 10% FeBTC produced an ENR signal of only 1.5 µA. Increasing the CuBTC content to 3% resulted in an ENR signal of 3 µA. The balanced composition of 5% each of CuBTC and FeBTC generated the highest ENR signal of nearly

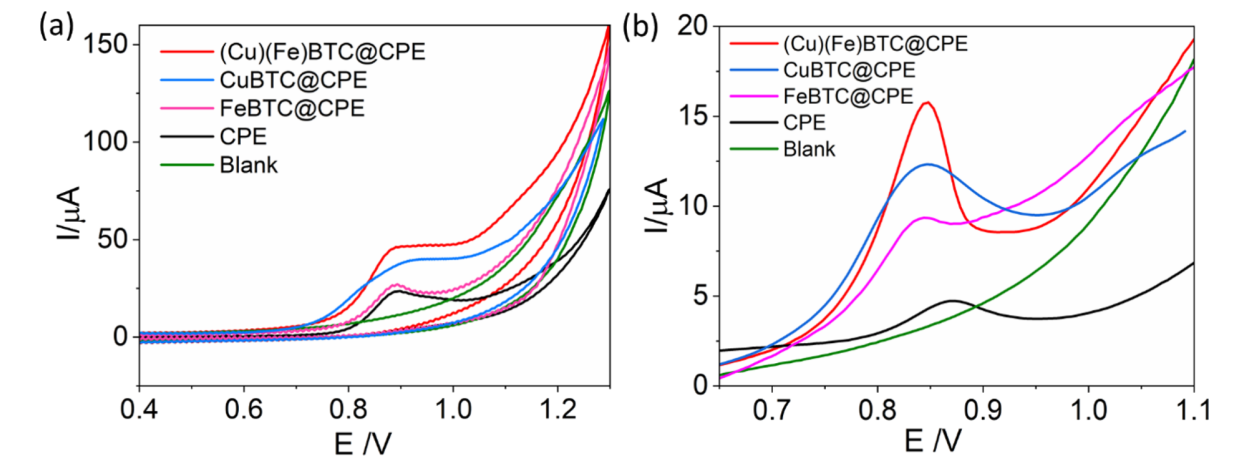


Figure 6: (a) Cyclic voltammograms of (Cu)(Fe)BTC@CPE and CPE electrodes in a 200 µM ENR solution in PBS at scan rate of 0.1 V/s The green line shows a voltammogram measured in ENR-free solution. (b) Square wave voltammograms of the studied electrodes in 1 µM ENR solution at an accumulation time of 90 s. The green line shows a voltammogram measured in ENR-free solution.

8 µA among all tested formulations, underscoring the significance of optimizing the ratio of these two components for effective electrochemical detection of ENR. Further increasing the CuBTC content to 7% resulted in a diminished ENR signal of 5 µA. Finally, a composition with 10% CuBTC and 0% FeBTC yielded a peak ENR current of approximately 6 µA. Therefore, the optimal weight percentages of 5% CuBTC and 5% FeBTC were chosen for electrode fabrication in the subsequent experiments.

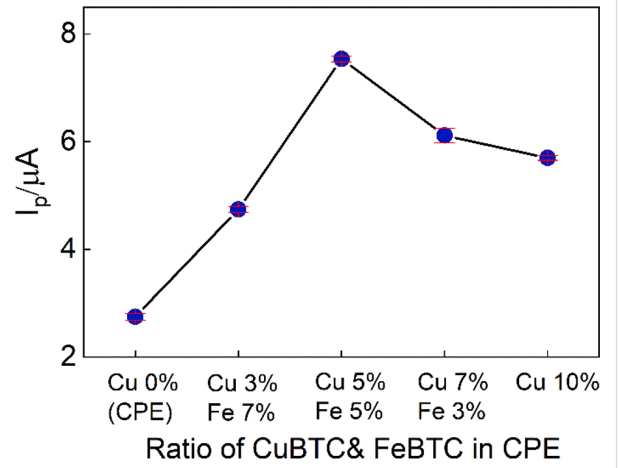


Figure 7: The impact of electrode composition the peak current of 1 µM enrofloxacin.

Effect of supporting electrolyte on the ENR signal

The electrolyte plays a crucial role in the oxidation reaction of ENR. Four electrolytes, that is, PBS, Britton–Robinson (BR), KCl, and $NaNO_3$, were tested to determine the most suitable environment for ENR oxidation. The voltammograms in Figure 8 show no clear SWV peak in KCl and $NaNO_3$ electrolytes. In contrast, PBS and BR yielded well-defined peaks at 0.85 and 0.88 V, respectively. The ENR peak in PBS is higher, sharper, and more symmetric compared to that in BR. Therefore, PBS was selected as the optimal electrolyte for subsequent experiments.

Effect of pH of the electrolyte on the ENR signal

The effect of pH on the ENR signal was investigated by performing SW-AdSV using the (Cu)(Fe)BTC@CPE electrode in a 1 µM ENR solution in PBS at different pH values (Figure 9a). The height of the ENR peak was significantly affected, as shown in Figure 9b. The ENR peak current increased significantly while the pH changed from 5 to 7 and reached the highest value at pH 7. As the pH value increased further, the peak current gradually decreased to nearly a half at pH 9.

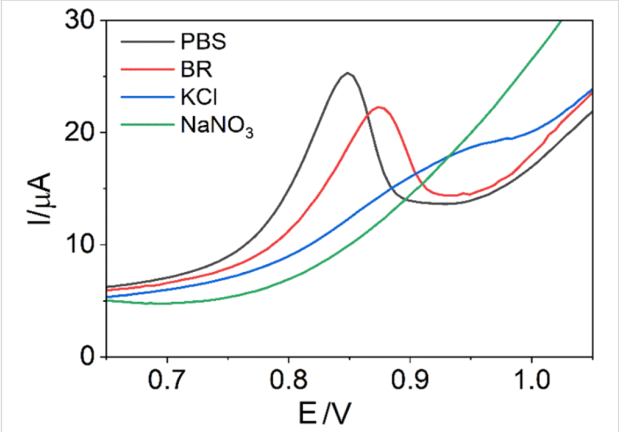


Figure 8: Square wave voltammograms of 1 µM ENR in different electrolytes.

Therefore, PBS solution with pH 7 was selected for the experiments in the next section.

The Nernst equation describes the relationship between the peak potential E_p and pH as follows: E_p (V) = 0.059(m/n) pH + b, where n and m denote the quantities of electrons and protons involved in the electrochemical reaction, and b is the intercept. Figure 9c shows that, in the pH range from 5 to 7, there is a linear relationship between E_p and pH value described by the equation E_p = −0.052 pH + 1.229 with a correlation coefficient of 0.952. The slope of the curve of 0.052 (close to 0.059) indicates that the ratio of protons to electrons participating in the oxidation reaction is 1 to 1, which is in accordance with previous publications [44,45].

Adsorption time

The accumulation time (t_{acc}) of enrofloxacin on the electrode surface is a critical factor in optimizing the ENR signal. In this study, ENR concentrations ranging from 0.02 to 2 µM were studied with adsorption times varying from 0 to 600 s, as illustrated in Figure 10. At the lowest concentration of 0.02 µM, no peak was observed for t_{acc} shorter than 240 s. However, from 240 to 600 s, the peak height increased linearly with the adsorption duration. This indicates that sufficient time is necessary for the ENR molecules to adsorb onto the electrode surface at this low concentration, and the signal improves with longer accumulation times within this range.

For a concentration of 0.2 µM, the peak current increased gradually and reached a steady state at t_{acc} exceeding 300 s. This suggests that, at this intermediate concentration, the electrode surface reaches saturation after 300 s of accumulation, beyond which the peak current stabilizes. At the highest concentration tested (2 µM), the peak current experienced a significant increase with increasing t_{acc} up to 120 s, followed by a gradual

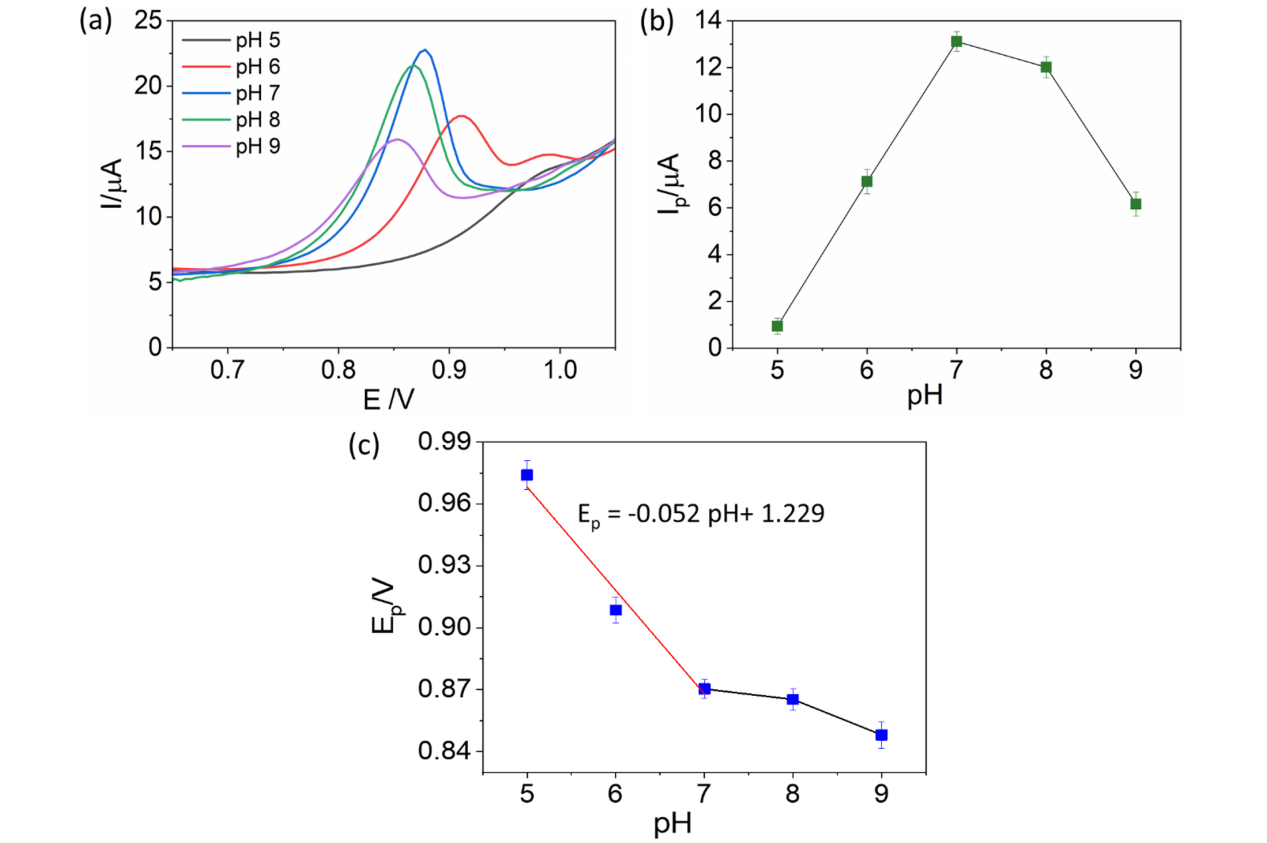


Figure 9: (a) SW-AdSV measurements of (Cu)(Fe)BTC@CPE in 1 μM ENR/PBS solution at different pH values from 6 to 9. (b) Plot of peak current vs pH. (c) Plot of peak potential vs pH.

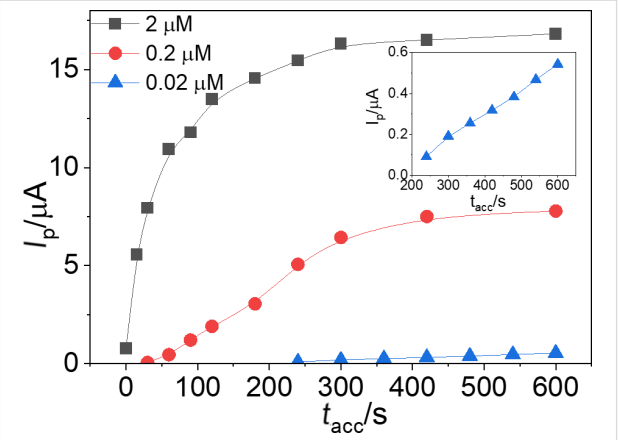


Figure 10: The relationship between ENR peak currents and accumulation time at different concentrations of ENR of 0.02, 0.2, and 2 μM. Inset: rescaled plot for 0.02 μM ENR.

rise, until it reached equilibrium at t_{acc} from 300 to 600 s. This behaviour indicates a rapid initial adsorption at high ENR concentration, with the surface reaching almost saturation relatively quickly, and then a slower adsorption to full saturation. These observations highlight the importance of optimizing t_{acc} for different ENR concentrations to achieve the best analytical signal. Longer accumulation times are beneficial at lower concentrations, while higher concentrations require shorter times to reach equilibrium.

Repeatability and reproducibility of the (Cu)(Fe)BTC@CPE electrode

Figure 11a depicts eight successive measurements conducted in 0.20 μM ENR solution using a single electrode without renewing the electrode surface. Clearly, in the second measurement, the ENR response decreased dramatically by over 50%. In the seventh and eighth measurements, the peak current of ENR remained at only about 15%. This phenomenon arises from the reaction product covering the active working area of the electrode, resulting in the low peak current observed in these measurements.

The electrode reproducibility performance was evaluated by comparing SWV signals in 0.2 μM ENR solution obtained on an electrode whose surface was renewed before each measurement (Figure 11b). The data indicated slight fluctuations in peak currents among eight measurements, with a relative standard deviation (RSD) of 3.83%. These results demonstrate good reproducibility of the developed electrodes.

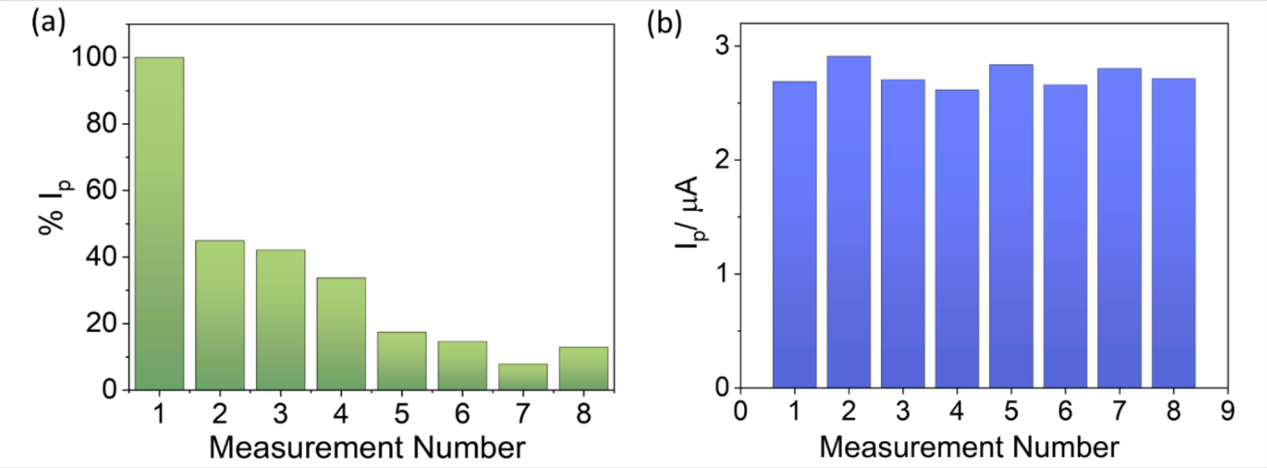


Figure 11: SW-AdSV measurements of successive measurements obtained in 0.20 µM ENR solution using electrodes (a) without renewal of the electrode surface and (b) with renewal of the electrode surface.

Calibration curve

Under the above optimal conditions, a calibration curve was established in the ENR concentration range from 0.005 to 0.100 µM at t_{acc} of 600 s (Figure 12a). Increasing SWV peaks as a function of the concentration were observed, and a linear relationship was established, described by the regression equation I_p (µA) = 56.136 × C_{ENR} (µM) + 0.340. SW-AdSV measurements were carried out with ENR concentrations from 0.1 to 1.0 µM to build the calibration curve at t_{acc} of 90 s. The obtained signals, as shown in Figure 12b, exhibit a linear correlation between the ENR oxidation peak height and ENR concentration, described by the regression equation I_p (µA) = 11.373 × C_{ENR} (µM) + 0.128 (R^2 = 0.9954). Figure 12c illustrates the calibration curve established for ENR in the concentration range from 1 to 13 µM at an accumulation time of 0 s. The linear relationship obtained is represented by the regression equation I_p (µA) = 1.225 × C_{ENR} (µM) + 0.557 (R^2 = 0.9992). The consistently high correlation coefficients indicate the robust performance of the developed sensor.

From the calibration curve at the lowest concentration range from 0.005 to 0.100 µM, a detection limit for ENR of 3 nM was calculated through the formula LOD = 3σ/b, where σ is the standard deviation of blank signals, and b is the slope of the regression line. The LOD is quite comparable to those in previous studies [16,46-49]. Additionally, the sensitivity of the sensor was calculated to be 56.14 µA/µM.

Anti-interference study

This study aimed to investigate the influence of organic and inorganic substances on the performance of a sensor by evaluating the changes in the ENR signal when these substances were present in the analytical solution. Figure 13 illustrates that, at a concentration 100 times higher than that of ENR, ions including K^+, Na^+, Ca^{2+}, Mg^{2+}, Zn^{2+}, Ni^{2+}, Cl^-, NO_3^-, SO_4^{2-}, HCO_3^-, and CH_3COO^- had a negligible impact on the ENR signal, leading to a reduction in the ENR signal of less than 5%. Regarding the influence of organic substances, when their concentration was 10 times higher than that of ENR, the impact on the ENR signal was small for ascorbic acid (AA), erythromycin (ERY), chloramphenicol (CAP), paracetamol (PARA), and amoxicillin (AMX). In contrast, cephalosporin (CEF), oxalic acid (OXA), and glucose (GLU) significantly reduced the signal, bringing it down to approximately 30%. At a 50-fold concentration, CAP and PARA still had no noticeable effect on ENR analysis. However, the presence of AA and CAP substantially affected the ENR signal, decreasing it to around 60% (data not shown here). It is worth noting that, within this concentration range, no ENR signal was detectable in the presence of CEF, OXA, or GLU. The experimental findings indicate that the sensor demonstrated good performance in detecting ENR in samples with a complex matrix.

Analysis in real sample matrices

The performance of the developed sensor was assessed by quantifying ENR levels in tap water and lake water. Different amounts of ENR were added to samples, ranging from 0.2 to 3.0 µM. ENR concentrations were determined using the standard addition method (Table 1). Notably, no ENR was initially detected in the original samples. However, in the spiked samples, the sensor yielded favourable results with recoveries ranging from 90.2% to 121.3%, indicating the reliability of the sensor and its effectiveness in real-world applications.

Conclusion

CuBTC and FeBTC metal-organic frameworks (MOFs) were successfully synthesized using a solvothermal method. The mixture of these MOFs demonstrated a high surface area, sub-

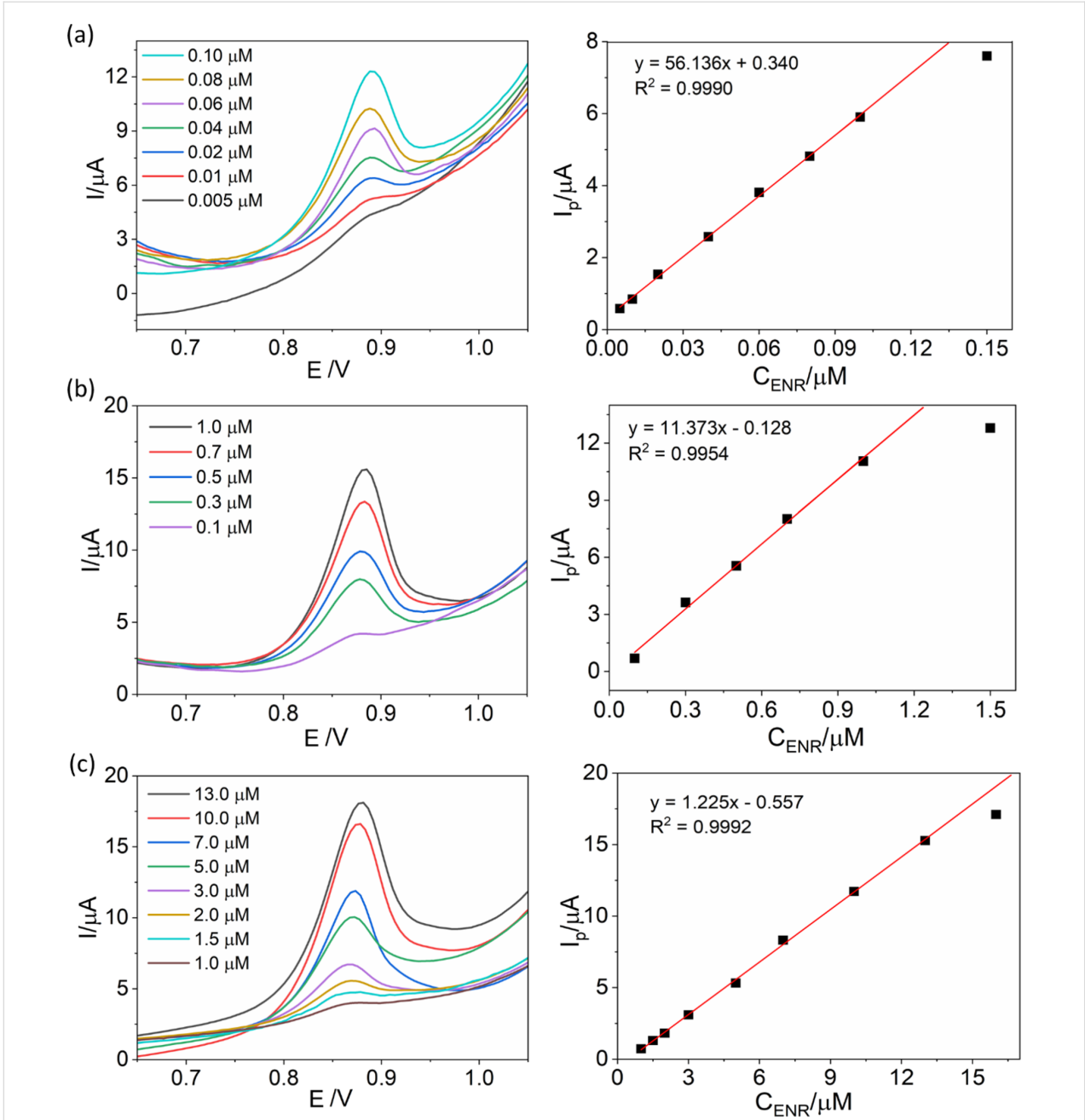


Figure 12: SW-AdSV measurements of ENR and calibration curves for (a) 0.005–0.100 μM (t_{acc} of 600 s), (b) 0.1–1.0 μM (t_{acc} of 90 s), and (c) 1–13 μM (t_{acc} of 0 s).

stantial total pore volume, and small capillary diameters. This hybrid material was then utilized as an electrode material for an electrochemical sensor designed to detect enrofloxacin through adsorptive stripping square wave voltammetry. The sensor fabricated with an optimal weight ratio between CuBTC and FeBTC (5:5) exhibited the highest signal for enrofloxacin detection. Notably, the sensor showed excellent performance with good reproducibility (RSD = 3.83%), a large dynamic range from 0.05 to 13 μM, a low detection limit of 3 nM, and high selectivity. Under the experimental conditions, the sensor provided satisfactory recoveries ranging from 90.2% to 121.3% in both tap water and lake water samples.

Experimental

Reagents and apparatus

Reagents

Enrofloxacin (ENR, $C_{19}H_{22}FN_3O_3$, 98%) was purchased from Thermo Fisher Scientific. Graphite powder and paraffin oil

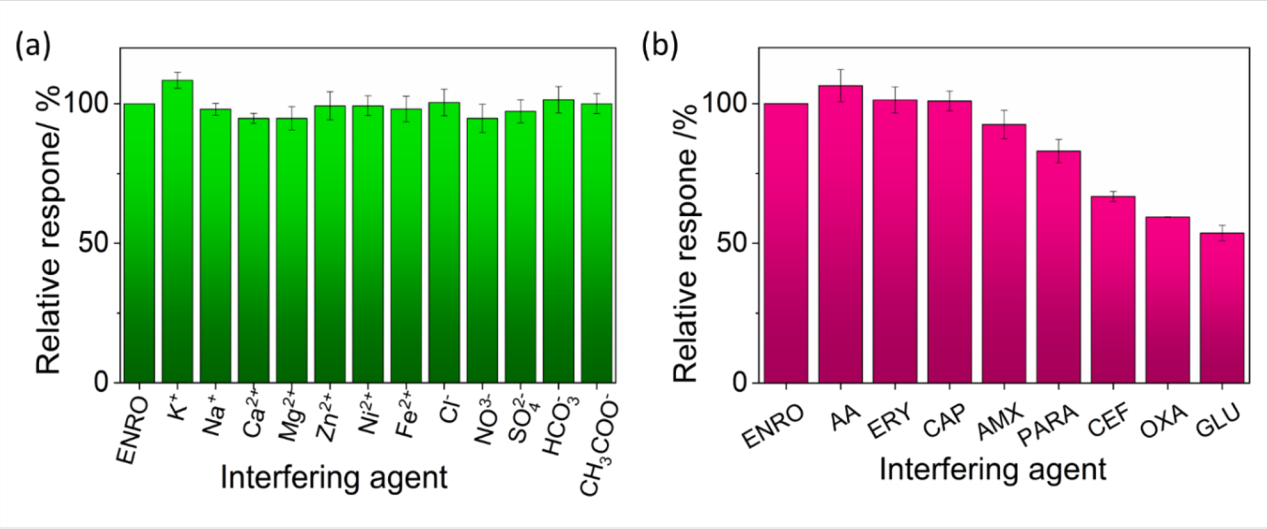


Figure 13: Influence of (a) inorganic ions and (b) organic compounds on the ENR signal.

Table 1: Analysis of ENR in spiked samples conducted with the (Cu)(Fe)BTC@CPE sensor.

Sample	C_{ENR} (μM)		Recovery (%)
	added concentration	found concentration	
tap water	0	not detected	—
	0.2	0.229	114.5
	0.4	0.434	108.5
	0.6	0.634	105.6
	1.0	1.108	110.8
	2.0	2.029	101.5
	3.0	3.639	121.3
lake water	0	not detected	—
	0.2	0.181	90.5
	0.4	0.392	98.0
	0.6	0.606	101.0
	1.0	0.923	92.3
	2.0	1.854	92.7
	3.0	2.706	90.2

were supplied by Thermo Scientific Acros. Trimesic acid (H_3BTC, 98%), $CuCl_2{\cdot}2H_2O$ (≥99%), $FeCl_3{\cdot}6H_2O$ (98%), *N*,*N*-dimethylformamide (DMF, 98%) and C_2H_5OH (96%), H_3PO_4 (85%), KOH (≥85.0%), KH_2PO_4 (≥99.5%), K_2HPO_4 (≥98.0%), KCl (>99.5%), and HCl (37%) were bought from Fisher and Sigma-Aldrich. All chemicals and reagents were of analytical grade and used without further purification. $K_3[Fe(CN)_6]$ (≥99.5%) and $K_4[Fe(CN)_6]$ (≥99.5%) were purchased from China. Phosphate-buffered saline (PBS) was prepared by mixing 0.2 M KH_2PO_4 and 0.2 M K_2HPO_4 in double-distilled water. The pH of the solution used for the optimization of electrolyte solution was changed from 6.0 to 9.0 by controlling the amount of these phosphate salts. Enrofloxacin stock solution was prepared by dissolving ENR powder in double-distilled water. The ENR solutions with desired concentrations were prepared daily by diluting the ENR stock solution in with PBS solution.

Apparatus

The electrochemical properties of the developed electrode and enrofloxacin were evaluated through cyclic voltammetry by using a custom-made potentiogalvanostat (supplied by Laboratory of Informatics in Chemistry, Institute of Chemistry, Vietnam Academy of Science and Technology). Electrochemical impedance spectroscopy (EIS) was performed by using an Autolab PGSTAT 302 in a frequency range of 100 kHz to 0.01 Hz. A three-electrode electrochemical setup was used including a platinum wire counter electrode, an Ag/AgCl/saturated KCl reference electrode, and a carbon paste electrode (CPE) or MOF-modified electrodes as working electrodes.

Physical and chemical properties of MOFs were characterized by using field-emission scanning electron microscopy (FESEM, Hitachi S-4800, Japan), energy-dispersive X-ray spectroscopy (EDX, Horiba 7593-H, England), and X-ray photoelectron spectroscopy (XPS, Thermo VG Multilab 2000).

Synthesis of CuBTC, FeBTC MOFs

CuBTC and FeBTC were synthesized using the solvothermal method as described in our previous reports [37,38]. Specifically, 12 mmol of trimesic acid was fully dissolved in 120 mL of *N*,*N*-dimethylformamide (DMF) (solution 1), and 12 mmol of the chloride salt of the corresponding metal was dissolved in 40 mL of water (solution 2). Solution 1 was then slowly added to solution 2 under vigorous stirring for 30 min before being transferred to a Teflon bottle. The mixture was heated at 150 °C for 12 h and stirred continuously to facilitate the MOF formation process. Finally, the synthesized powder was separated from the solution using a centrifuge at 6000 rpm, washed several times with DMF and ethanol, and dried to obtain CuBTC and FeBTC MOFs.

Preparation of (Cu)(Fe)BTC@CPE

Modified electrodes were prepared using a standardized procedure. CuBTC and FeBTC were carefully mixed to obtain a mixture called (Cu)(Fe)BTC. Then, paraffin oil, graphite powder, and (Cu)(Fe)BTC powder were combined in various weight ratios (as specified in Table 2) and thoroughly mixed in an agate mortar. The resulting mixture was then tightly packed into a Teflon electrode body (inner diameter 5 mm) to create the modified electrode named (Cu)(Fe)BTC@CPE with a geometrical surface area of 19.63 mm^2. Prior to experimentation, the electrode surface was polished using a balance paper to achieve a smooth surface. Carbon paste-modified electrodes containing either CuBTC or FeBTC were also fabricated for comparison and labelled as CuBTC@CPE and FeBTC@CPE, respectively.

Table 2: Components of the studied electrodes.

Electrode	Electrode component (wt. %)		
	CuBTC	FeBTC	Carbon paste
1	0	0	100
2	3	7	90
3	5	5	90
4	7	3	90
5	10	0	90

Detection of enrofloxacin

Enrofloxacin was electrochemically detected by using square wave adsorptive stripping voltammetry (SW-AdSV) in PBS. Briefly, the modified electrode was immersed in the analytical solution for different accumulation times (0, 90, and 600 s) under stirring for enrofloxacin adsorption on electrode surface. Then, the SW-AdSV response of enrofloxacin was recorded in the potential window of 0.6–1.1 V.

Spiked samples of tap water and lake water were used to evaluate the performance of the modified electrode. After spiking known concentrations of enrofloxacin into the water samples, the added concentration was determined using the standard addition method. All experimental work was performed at room temperature (25 ± 1 °C).

Funding

This research was financially supported by the Vietnam Academy of Science and Technology under grant TĐPTCB.04/24-26.

Author Contributions

Thi Kim Ngan Nguyen: formal analysis; investigation; writing – original draft. Tien Dat Doan: formal analysis; investigation; writing – original draft. Huy Hieu Luu: formal analysis; investigation. Hoang Anh Nguyen: methodology; validation; writing – original draft; writing – review & editing. Thi Thu Ha Vu: project administration; resources. Quang Hai Tran: methodology; validation. Ha Tran Nguyen: resources; writing – original draft. Thanh Binh Dang: formal analysis. Thi Hai Yen Pham: conceptualization; formal analysis; methodology; project administration; supervision; writing – review & editing. Mai Ha Hoang: funding acquisition; project administration; resources; supervision.

ORCID® iDs

Thanh Binh Dang - https://orcid.org/0009-0009-6870-8973
Thi Hai Yen Pham - https://orcid.org/0000-0003-3835-9580

Data Availability Statement

All data that supports the findings of this study is available in the published article and/or the supporting information of this article.

References

1. Trouchon, T.; Lefebvre, S. *Open J. Vet. Med.* **2016,** *6,* 40–58. doi:10.4236/ojvm.2016.62006
2. Papich, M. G. Enrofloxacin. In *Saunders Handbook of Veterinary Drugs,* Elsevier, 2016; pp 287–289. doi:10.1016/b978-0-323-24485-5.00240-0
3. Chen, J.; Ying, G.-G.; Deng, W.-J. *J. Agric. Food Chem.* **2019,** *67,* 7569–7586. doi:10.1021/acs.jafc.9b01334
4. Grabowski, Ł.; Gaffke, L.; Pierzynowska, K.; Cyske, Z.; Choszcz, M.; Węgrzyn, G.; Węgrzyn, A. *Int. J. Mol. Sci.* **2022,** *23,* 3648. doi:10.3390/ijms23073648
5. U.S. Food and Drug Administration. Withdrawal of enrofloxacin for use in poultry. 2005; https://www.fda.gov/animal-veterinary/recalls-withdrawals/withdrawal-enrofloxacin-poultry.
6. Kumar, K.; Thompson, A.; Singh, A. K.; Chander, Y.; Gupta, S. C. *J. Environ. Qual.* **2004,** *33,* 797. doi:10.2134/jeq2004.797a
7. Wang, G. N.; Yang, K.; Liu, H. Z.; Feng, M. X.; Wang, J. P. *Anal. Methods* **2016,** *8,* 5511–5518. doi:10.1039/c6ay00810k

8. Pearce, J. N.; Burns, B. G.; van de Riet, J. M.; Casey, M. D.; Potter, R. A. *Food Addit. Contam.: Part A* **2009,** *26,* 39–46. doi:10.1080/02652030802189757
9. Alhammadi, M.; Yoo, J.; Sonwal, S.; Park, S. Y.; Umapathi, R.; Oh, M.-H.; Huh, Y. S. *Front. Nutr.* **2022,** *9,* 1036826. doi:10.3389/fnut.2022.1036826
10. Li, S.; Nie, L.; Han, L.; Wen, W.; Wang, J.; Wang, S. *Foods* **2022,** *12,* 62. doi:10.3390/foods12010062
11. Yan, C.; Zhang, R.; Chen, Y.; Wang, G. *J. Electroanal. Chem.* **2017,** *806,* 130–135. doi:10.1016/j.jelechem.2017.10.047
12. Song, Y.; Xu, M.; Liu, X.; Li, Z.; Wang, C.; Jia, Q.; Zhang, Z.; Du, M. *Electrochim. Acta* **2021,** *368,* 137609. doi:10.1016/j.electacta.2020.137609
13. Chen, J.; Tan, L.; Qu, K.; Cui, Z.; Wang, J. *Microchim. Acta* **2022,** *189,* 95. doi:10.1007/s00604-022-05205-9
14. Phi Van, T.; Nguy, T. P.; Truong, L. T. N. *Anal. Methods* **2022,** *14,* 2195–2203. doi:10.1039/d2ay00192f
15. Lv, L.; Zhang, B.; Tian, P.; Xie, L.; Wei, W.; He, J.; Lin, M.; Zhu, H.; Chen, H.; He, B. *J. Electroanal. Chem.* **2022,** *911,* 116251. doi:10.1016/j.jelechem.2022.116251
16. Lu, S.; Wang, S.; Wu, P.; Wang, D.; Yi, J.; Li, L.; Ding, P.; Pan, H. *Adv. Powder Technol.* **2021,** *32,* 2106–2115. doi:10.1016/j.apt.2021.04.025
17. Lu, M.; Cao, C.; Wang, F.; Liu, G. *Mater. Des.* **2020,** *199,* 109409. doi:10.1016/j.matdes.2020.109409
18. Xi, L. L.; Zhang, P. M.; Zhu, Y. *Chin. Chem. Lett.* **2009,** *20,* 1245–1247. doi:10.1016/j.cclet.2009.04.025
19. Li, M.; Zhang, G.; Boakye, A.; Chai, H.; Qu, L.; Zhang, X. *Front. Bioeng. Biotechnol.* **2021,** *9,* 797067. doi:10.3389/fbioe.2021.797067
20. Kreno, L. E.; Leong, K.; Farha, O. K.; Allendorf, M.; Van Duyne, R. P.; Hupp, J. T. *Chem. Rev.* **2012,** *112,* 1105–1125. doi:10.1021/cr200324t
21. Yaghi, O. M.; Sun, Z.; Richardson, D. A.; Groy, T. L. *J. Am. Chem. Soc.* **1994,** *116,* 807–808. doi:10.1021/ja00081a067
22. Wang, Z.; Jin, C.-M.; Shao, T.; Li, Y.-Z.; Zhang, K.-L.; Zhang, H.-T.; You, X.-Z. *Inorg. Chem. Commun.* **2002,** *5,* 642–648. doi:10.1016/s1387-7003(02)00515-4
23. Schäfer, P. Electrochemical Growth of CuBTC Improving the Synthesis Toolkit through Mechanistic Understanding. Ph.D. Thesis, Universitätsmedizin der Johannes Gutenberg-Universität, Mainz, 2017.
24. Yap, M. H.; Fow, K. L.; Chen, G. Z. *Green Energy Environ.* **2017,** *2,* 218–245. doi:10.1016/j.gee.2017.05.003
25. Wang, B.; Lv, X.-L.; Feng, D.; Xie, L.-H.; Zhang, J.; Li, M.; Xie, Y.; Li, J.-R.; Zhou, H.-C. *J. Am. Chem. Soc.* **2016,** *138,* 6204–6216. doi:10.1021/jacs.6b01663
26. Rani, R.; Deep, A.; Mizaikoff, B.; Singh, S. *J. Electroanal. Chem.* **2022,** *909,* 116124. doi:10.1016/j.jelechem.2022.116124
27. Song, J.; Huang, M.; Lin, X.; Li, S. F. Y.; Jiang, N.; Liu, Y.; Guo, H.; Li, Y. *Chem. Eng. J.* **2022,** *427,* 130913. doi:10.1016/j.cej.2021.130913
28. Nguyen, M. B.; Hong Nhung, V. T.; Thu, V. T.; Ngoc Nga, D. T.; Pham Truong, T. N.; Giang, H. T.; Hai Yen, P. T.; Phong, P. H.; Vu, T. A.; Thu Ha, V. T. *RSC Adv.* **2020,** *10,* 42212–42220. doi:10.1039/d0ra06700h
29. Dong, S.; Suo, G.; Li, N.; Chen, Z.; Peng, L.; Fu, Y.; Yang, Q.; Huang, T. *Sens. Actuators, B* **2016,** *222,* 972–979. doi:10.1016/j.snb.2015.09.035
30. Wang, Y.; Chen, H.; Hu, X.; Yu, H. *Analyst* **2016,** *141,* 4647–4653. doi:10.1039/c6an00727a
31. Li, J.; Xia, J.; Zhang, F.; Wang, Z.; Liu, Q. *Talanta* **2018,** *181,* 80–86. doi:10.1016/j.talanta.2018.01.002
32. Huang, T.-Y.; Kung, C.-W.; Liao, Y.-T.; Kao, S.-Y.; Cheng, M.; Chang, T.-H.; Henzie, J.; Alamri, H. R.; Alothman, Z. A.; Yamauchi, Y.; Ho, K.-C.; Wu, K. C.-W. *Adv. Sci.* **2017,** *4,* 1700261. doi:10.1002/advs.201700261
33. Cheng, J.; Xuan, X.; Yang, X.; Zhou, J.; Cen, K. *RSC Adv.* **2018,** *8,* 32296–32303. doi:10.1039/c8ra05964k
34. Varghese, A. M.; Reddy, K. S. K.; Karanikolos, G. N. *Ind. Eng. Chem. Res.* **2022,** *61,* 6200–6213. doi:10.1021/acs.iecr.1c04710
35. Liao, M.; Qin, H.; Guo, W.; Gao, P.; Liu, J.; Xiao, H. *Int. J. Hydrogen Energy* **2022,** *47,* 35136–35148. doi:10.1016/j.ijhydene.2022.08.125
36. Tao, Y.; Yang, B.; Wang, F.; Yan, Y.; Hong, X.; Xu, H.; Xia, M.; Wang, F. *Sep. Purif. Technol.* **2022,** *300,* 121825. doi:10.1016/j.seppur.2022.121825
37. Nguyen, T. K. N.; Nguyen, T. H.; Nguyen, M. B.; Nguyen, H. A.; Vu, T. T. H.; Le, Q. H.; Tran, Q. H.; Pham, T. H. Y. *J. Electrochem. Soc.* **2023,** *170,* 056505. doi:10.1149/1945-7111/acced6
38. Tien, N. N.; Dat, N. T.; Manh, N. B.; Hieu, N. D.; Tu, V. C.; Ngan, N. T. T.; Ha, V. T. T.; Decorse, P.; Piro, B.; Thu, V. T. *J. Mater. Sci.* **2023,** *58,* 16699–16713. doi:10.1007/s10853-023-09083-1
39. Nguyen, M. B.; Le, G. H.; Nguyen, T. D.; Nguyen, Q. K.; Pham, T. T. T.; Lee, T.; Vu, T. A. *J. Hazard. Mater.* **2021,** *420,* 126560. doi:10.1016/j.jhazmat.2021.126560
40. Nguyen, M. B.; Nguyen, L. H. T.; Lai, H. T.; Doan, H. V.; Tran, N. Q.; Mai, N. X. D.; Tran, L. D.; Krisbiantoro, P. A.; Wu, K. C.-W.; Doan, T. L. H. *Chem. Eng. J.* **2024,** *497,* 154479. doi:10.1016/j.cej.2024.154479
41. Chang, M.; Meng, X. X.; Wang, Y.; Zhang, W. *Int. J. Hydrogen Energy* **2019,** *44,* 29583–29589. doi:10.1016/j.ijhydene.2019.05.012
42. Meng, C.; Chen, H.; Hu, P.; Yuan, A. *ChemistrySelect* **2020,** *5,* 15049–15054. doi:10.1002/slct.202003872
43. Wu, S.; Mao, J.; Zhang, Y.; Wang, S.; Huo, M.; Guo, H. *Food Chem.* **2023,** *413,* 135579. doi:10.1016/j.foodchem.2023.135579
44. Antilén, M.; Valencia, C.; Peralta, E.; Canales, C.; Espinosa-Bustos, C.; Escudey, M. *Electrochim. Acta* **2017,** *244,* 104–111. doi:10.1016/j.electacta.2017.05.104
45. Martínez-Mejía, M. J.; Sato, I.; Rath, S. *Environ. Sci. Pollut. Res.* **2017,** *24,* 15995–16006. doi:10.1007/s11356-017-9210-3
46. Karuppusamy, N.; Mariyappan, V.; Chen, S.-M.; Ramachandran, R. *Nanoscale* **2022,** *14,* 1250–1263. doi:10.1039/d1nr06343j
47. Do, T. N. Q.; Vu, T. T. H.; Le, Q. H.; Pham, T. P. N.; Ta, T. T.; Nguyen, T. L.; Pham, T. H. Y. *Anal. Lett.* **2024,** *57,* 1989–2003. doi:10.1080/00032719.2023.2284222
48. Aymard, C.; Kanso, H.; Serrano, M. J.; Pagán, R.; Noguer, T.; Istamboulie, G. *Food Chem.* **2022,** *370,* 131016. doi:10.1016/j.foodchem.2021.131016
49. Yu, Q.; Yang, H.; Yang, Y. *J. Food Meas. Charact.* **2024,** *18,* 87–94. doi:10.1007/s11694-023-02149-3

License and Terms

This is an open access article licensed under the terms of the Beilstein-Institut Open Access License Agreement (https://www.beilstein-journals.org/bjnano/terms), which is identical to the Creative Commons Attribution 4.0 International License (https://creativecommons.org/licenses/by/4.0). The reuse of material under this license requires that the author(s), source and license are credited. Third-party material in this article could be subject to other licenses (typically indicated in the credit line), and in this case, users are required to obtain permission from the license holder to reuse the material.

The definitive version of this article is the electronic one which can be found at:
https://doi.org/10.3762/bjnano.15.120

BEILSTEIN JOURNAL OF NANOTECHNOLOGY

Facile synthesis of size-tunable L-carnosine-capped silver nanoparticles and their role in metal ion sensing and catalytic degradation of *p*-nitrophenol

Akash Kumar[1,2], Ridhima Chadha[3,4], Abhishek Das[3,4], Nandita Maiti[*3,4] and Rayavarapu Raja Gopal[*1,2]

Full Research Paper

Open Access

Address:
[1]Nanomaterial Toxicology Laboratory, Drug and Chemical Toxicology Group, Food, Drug and Chemical, Environment and Systems Toxicology (FEST) Divison, CSIR-Indian Institute of Toxicology Research (CSIR-IITR), Vishvigyan Bhawan, 31 Mahatma Gandhi Marg, Lucknow 226001, India, [2]Academy of Scientific and Innovative Research (AcSIR), Ghaziabad 201002, India, [3]Radiation & Photochemistry Division, Bhabha Atomic Research Centre, Mumbai-400085, India and [4]Homi Bhabha National Institute, Anushaktinagar, Mumbai-400085, India

Email:
Nandita Maiti[*] - nanditab@barc.gov.in;
Rayavarapu Raja Gopal[*] - rajagopal@iitr.res.in

* Corresponding author

Keywords:
catalysis; heavy metals; L-carnosine; *p*-nitrophenol; silver nanoparticles

Beilstein J. Nanotechnol. **2024,** *15,* 1576–1592.
https://doi.org/10.3762/bjnano.15.124

Received: 20 July 2024
Accepted: 22 November 2024
Published: 06 December 2024

This article is part of the thematic issue "Recent advances in synthesis and applications of organometallic nanomaterials".

Guest Editor: T.-D. Nguyen

© 2024 Kumar et al.; licensee Beilstein-Institut.
License and terms: see end of document.

Abstract

L-Carnosine is a dipeptide with notable antioxidant, antiglycation, metal chelating, and neuroprotective properties. Despite its many biological roles, applying L-carnosine as a capping agent in nanoparticle synthesis has remained underexplored. This study explores the potential of L-carnosine in synthesizing tunable plasmonic silver nanoparticles (L-car-AgNPs). The formation of L-car-AgNPs was confirmed via UV–vis optical absorption spectroscopy, showing single and double plasmonic peaks, depending on the synthesis conditions. Physicochemical characterization using TEM, FTIR, and Raman spectroscopy, as well as EDX and XRD revealed controlled aggregation, successful capping, and crystalline growth of the L-car-AgNPs. The L-car-AgNPs exhibited promising sensing capabilities with limits of detection of 141.79 ppb (1.2 μM) for Cd^{2+}, 131.33 ppb (0.63 μM) for Pb^{2+}, 215.35 ppb (2.8 μM) for As^{3+}, and 245.49 ppb (4.7 μM) for Cr^{3+}. Additionally, these nanoparticles demonstrated catalytic activity regarding the degradation of *p*-nitrophenol (P-NP), achieving complete degradation of 0.25 and 1 mM solutions within 5 and 10 min, respectively. This study reveals the potential of L-car-AgNPs for both heavy metal ion detection and catalytic degradation of P-NP, indicating their suitability for environmental monitoring and remediation applications. Further optimization and research are needed to expand their environmental applications and to understand their interaction mechanisms with various contaminants.

Introduction

The persistent rise in environmental pollution, notably from heavy metal ions and organic pollutants, has propelled the development of innovative and efficient environmental monitoring and remediation methods. Five heavy metals, namely, mercury (Hg^{2+}), lead (Pb^{2+}), cadmium (Cd^{2+}), chromium (Cr^{3+}), and arsenic (As^{3+}), pose severe risks to human health and ecological systems because of their non-biodegradable nature and long biological half-lives, leading to bioaccumulation and biomagnification [1]. Similarly, organic pollutants such as *p*-nitrophenol (P-NP), from agricultural and industrial processes, are of significant concern because of their toxicity and resistance to degradation [2]. Consequently, detection and removal of these contaminants have become crucial for environmental sustainability and public health.

Silver nanoparticles (AgNPs) have attracted the interest of researchers worldwide in recent years because of their promising use in environmental chemistry. The unique optochemical properties of AgNPs, including high surface area to volume ratio, optical absorbance, excellent conductivity, and potent catalytic activity, make them ideal candidates for environmental monitoring and remediation [3]. Modifying silver nanoparticles with various biological molecules, peptides, proteins, and enzymes has further enhanced their functionality, stability, and selectivity towards specific pollutants [4-6]. Biomolecule-capped silver nanoparticles, particularly those stabilized by naturally occurring peptides such as L-carnosine, have shown exceptional sensing and catalytic degradation capabilities. L-Carnosine, a dipeptide consisting of β-alanine and histidine, stabilizes the nanoparticle structure and imparts functional attributes such as metal ion chelation and catalytic enhancement. These features make L-carnosine-capped AgNPs an ideal candidate for environmental applications. It was also reported that pristine AgNPs significantly interact with L-carnosine [7].

Traditional methods for heavy metal ion monitoring in environmental samples involve complex analytical instrumental techniques such as atomic absorption spectroscopy, inductively coupled plasma mass spectrometry, and high-performance liquid chromatography [8,9]. Environmental remediation of P-NP requires processes such as Fenton-like oxidation or ozonation [10]. These techniques require expensive equipment, specialized operational skills, and extensive sample preparation, making them less practical for on-site testing, frequent monitoring, and remediation.

In response to these challenges, recent advancements in nanotechnology have ushered in the development of nanoparticle-based systems that offer promising alternatives because of their simplicity, cost-effectiveness, and potential for real-time applications. Plasmonic nanoparticles, such as silver, have been widely explored for their unique plasmonic and catalytic properties [3,11,12]. These include localized surface plasmon resonance (LSPR), which can be utilized to detect heavy metal ions. The catalytic properties can be applied to degrade nitrophenolic compounds such as P-NP. Also, it is well documented that the properties of silver nanoparticles can be modulated through surface chemistry and other parameters such as size and shape [13]. Kästner and Thünemann described the catalytic degradation of P-NP using silver nanoparticles with the activity depending on the capping agents [14]. To design a dual-functional system for environmental applications, a potential capping and stabilizing agent is required for silver nanoparticle synthesis.

Maiti et al. demonstrated that the dipeptide L-carnosine interacted highly with pristine silver nanospheres [6]. However, its role as a stabilizing/capping agent was never explored for nanoparticle synthesis and advanced environmental applications. Current research has paved the way for developing L-carnosine-capped AgNPs (L-car-AgNPs) enabling environmental monitoring and remediation applications. In addition, L-carnosine is a natural compound widely present in the human brain and meat products. Also, it was reported that grafting magnetic nanoparticles with L-carnosine significantly enhanced the catalytic performance of the nanoparticles [15]. In another study, metal-organic framework nanoparticles fabricated with L-carnosine were employed for arsenic removal via an adsorption mechanism. The maximum removal of arsenic was 94.33 mg/g at a pH of 8.5 and 0.4 g/L adsorbent [16]. These studies confirmed that L-carnosine adsorbed on metal surfaces has widespread environmental applications. However, magnetic nanoparticles or MOFs coated with L-carnosine were applicable only for environmental remediation but were incapable of detecting heavy metal ions. This drawback was overcome by using L-carnosine in combination with silver nanoparticles, as their strong interaction was reported previously. Silver nanoparticles with other capping agents can also be used for either heavy metal sensing or degradation of P-NP. A study explored the potential of gelatine-embedded silver nanoparticles in the degradation of P-NP, but it was not used for heavy metal ion sensing [17]. Similarly, citrate-stabilized silver nanospheres were used for the colorimetric detection of Ni^{2+} with a threshold limit of 0.75 mM without any catalytic activity [18]. Therefore, it was hypothesized that the synthesis of silver nanoparticles capped with L-carnosine may provide two functionalities, that is, monitoring heavy metal ions and degradation of P-NP. Another challenge in sensing heavy metals with capped silver nanoparticles is to detect multiple metals simultaneously via ionic interactions between the exposed functional groups of the capping agent and

metal ions. This issue can be addressed using L-carnosine-capped nanosilver because the interaction of L-carnosine with different metal ions has already been reported [19]. The electrochemical detection of Hg^{2+}, Pb^{2+}, and Cd^{2+} was achieved via L-carnosine–metal interaction [20,21]. With this study, an attempt has been made to address the issues associated with traditional environmental monitoring and remediation systems. This article aims to develop a metal ion sensing and catalyst platform with in situ synthesized L-carnosine-capped silver nanoparticles. The metal ion selectivity (regarding Cd^{2+}, Pb^{2+}, As^{3+}, and Cr^{3+}) was monitored via colorimetric and spectrophotometric approaches. Furthermore, the catalytic activity was assessed using P-NP as a reagent. Through this study, we aim to contribute to the advancement of nanoparticle-based technologies to tackle some of the most pressing environmental challenges of our times.

Materials and Methods

Materials

L-Carnosine (cat. no. 29825, purity ≥95%), silver nitrate ($AgNO_3$, cat. no. 1.93200.0027, purity ≥99.5%), and sodium borohydride ($NaBH_4$, cat. no. 480886, purity 99.99%) were obtained from Cayman Chemical, Merck, and Sigma Aldrich, respectively. *p*-Nitrophenol (P-NP, cat. no. 144956, purity 99.5%) and sodium chloride (NaCl, cat. no. 41721, purity 99.9%) were purchased from SRL Chemicals, India. Sodium hydroxide (NaOH, cat. no. TC1460, purity 99.0%), along with a NIST-grade metal standard including arsenic (As^{3+}), aluminum (Al^{3+}), cadmium (Cd^{2+}), zinc (Zn^{2+}), mercury (Hg^{2+}), nickel (Ni^{2+}), copper (Cu^{2+}), chromium (Cr^{3+}), iron (Fe^{3+}), molybdenum (Mo^{2+}), and lead (Pb^{2+}) were acquired from CDH Fine Chemicals. The chemicals were used without further purification. Before the experiment, glassware was cleaned with aqua regia and rinsed twice with double distilled (DD) water.

Methods

Tunable plasmonic silver nanoparticle synthesis using L-carnosine

Silver nanoparticles with tunable plasmon wavelength were synthesized using a wet-chemical reduction approach. L-Carnosine-capped silver nanoparticles were prepared in the presence of $NaBH_4$, a strong reductant. The synthesized L-carnosine-capped silver nanoparticles were named according to their increasing order of plasmon peaks, that is, L-car-AgNP1, L-car-AgNP2, L-car-AgNP3, L-car-AgNP4, and L-car-AgNP5.

L-car-AgNP1 was synthesized at room temperature (RT = 25 °C), with the addition of 1 mL L-carnosine (0.01 M) to 5 mL DD water followed by sequential additions of 100 µL NaOH (1 M), 1 mL $AgNO_3$ (0.01 M), and 1 mL $NaBH_4$ (0.001 M). The other samples, L-car-AgNP2, L-car-AgNP3, L-car-AgNP4, and L-car-AgNP5, were synthesized at temperatures of 40, 60, and 80 °C and at boiling temperature, respectively. The synthesis procedure for L-car-AgNP2 to L-car-AgNP5 was similar, with the reaction mixture comprising 1 mL L-carnosine (0.01 M) added to 5 mL DD water, followed by sequential additions of 50 µL NaOH (1 M), 1 mL $AgNO_3$ (0.01 M), and 2 mL $NaBH_4$ (0.001 M). The term "L-car-AgNPs" is used throughout the article to refer to the synthesized silver nanoparticles collectively. Furthermore, nanopowders of the samples were prepared using 1 M NaCl solution via the precipitation method, and the obtained precipitate was air-dried.

Characterization of L-carnosine-capped silver nanoparticles

The spectral absorbance of L-car-AgNPs was recorded using an Epoch2 spectrophotometer (BioTek, USA) in the 300–900 nm range. Zeta potentials and average hydrodynamic diameters of L-car-AgNPs were determined using a Zetasizer (Nano ZS, Malvern, UK). The hydrodynamic size of L-car-AgNPs was measured by placing them in 1 mL disposable cuvettes (DTS0012), while the zeta potential was measured using zeta cuvettes (ZEN1020). The L-car-AgNPs samples were observed under a transmission electron microscope (TEM, 120 kV, FEI Tecnai, Netherlands) for a detailed examination of size and morphology. The crystalline structure of L-car-AgNP1 was determined using X-ray diffraction (XRD, Rigaku Smartlab, Japan) within a 2θ range of 35° to 80°. Nanoparticle solutions were air-dried, and the obtained nanopowders (20 mg) were used for measurements. The functionalization of AgNPs with L-carnosine was validated through Fourier-transform infrared spectroscopy (FTIR, Thermo Scientific Nicolet iS5, USA). For this, 10 mg of air-dried nanopowder was placed over a diamond, and the software (OMNIC™) was run over the spectral range of 400–4000 cm^{-1}.

The Raman spectra of L-carnosine-capped silver nanoparticles, as well as L-carnosine, as solid and in aqueous solution, were recorded at RT using an excitation source of 532 nm. The light source was a diode-pumped solid-state Nd^{3+}:YAG laser (Cobolt Samba 0532-01-0500-500, Cobolt AB, Sweden). For solid L-carnosine and L-car-AgNPs, powdered samples were placed on glass slides, and the Raman signal was collected in a backscattering geometry using a 50× long working distance objective. The incident laser of approximately 10 mW power had a spot size of approximately 50 µm on the sample surface. Aqueous L-carnosine solutions were analyzed using a standard cuvette (1 cm), and the Raman-scattered light was collected at an angle of 180°. The Raman signal detection was achieved with a charge-coupled device (CCD, Synapse, Horiba Jobin Yvon) attached to a monochromator (LabRAM HR800, Horiba Jobin Yvon, France) and edge filter using 532 nm as an excita-

tion source. The Raman signal of the silicon wafer at 520 cm^{-1} was considered the reference point for spectrometer calibration, ensuring a spectral measurement accuracy better than 1 cm^{-1}. The Raman spectra acquisition times were approximately 25 s for solid L-carnosine and L-car-AgNPs and 100 s for L-carnosine in aqueous solution.

DFT calculations

Theoretical insights into the FTIR and Raman measurements were obtained through molecular structure optimization of L-carnosine, its anionic form, and probable L-carnosine–$(Ag)_4$ complexes. The structure optimization was performed in vaccum and water as solvent using the SCRF (CPCM) model to account for the effect of the environment. The computations were performed using density functional theory (DFT) with the B3LYP functional [22] and split basis sets 6-31+G* for all atoms (C, O, N, and H), and LANL2DZ for Ag atoms. Calculations were executed using Gaussian 09, Revision A.02 software [23]. The optimization process was conducted without symmetry restrictions. The convergence criteria were an energy change of less than 1.0×10^{-6} Hartree and a gradient of less than 3.0×10^{-4} atomic units. The vibrational frequencies of L-carnosine, its anion, and the probable Ag_4 complexes were computed at the optimized geometries. Subsequently, the theoretical vibrational spectra were compared with the experimental Raman spectra of L-carnosine in various forms, namely, in the solid state, in aqueous solution, in alkaline solution, and as capping agents in silver nanoparticles (L-car-AgNPs).

Sensing of heavy metals

Metal standards (NIST grade, 1000 ppm) of As^{3+}, Al^{3+}, Cd^{2+}, Zn^{2+}, Hg^{2+}, Ni^{2+}, Cu^{2+}, Cr^{3+}, Pb^{2+}, Mo^{2+}, and Fe^{3+} were diluted to a concentration of 10 ppm. A uniform concentration of nanoparticles in terms of optical density (OD) was maintained throughout the experiment. The L-car-AgNPs were fixed at an optical density of 1 ± 0.2 OD for the sensing experiment. The final volume of L-car-AgNPs and the corresponding metal ions was 1 mL. In a typical sensing experiment, the metal ions were spiked in water to an end concentration of 0.5 ppm, followed by the addition of L-car-AgNPs as a sensing probe. The dispersion was then examined for colorimetric/spectrophotometric changes. Finally, the limit of detection (LOD) and the limit of quantification (LOQ) of the developed nanosensors were estimated through a linear plot of the absorption as a function of the concentration of the detected metal ions.

L-carnosine-capped silver nanoparticles as the catalytic agent

L-car-AgNPs were evaluated regarding their catalytic performance in the degradation of P-NP as a model substrate. P-NP is reduced and forms *p*-aminophenol (P-AP) in the presence of nanoparticle catalyst and $NaBH_4$. All catalysis experiments were performed at RT in a 3.5 mL quartz cuvette. The reagents were introduced in the sequence of 2 mL P-NP (0.25 mM or 1 mM), 1 mL of $NaBH_4$ (100 mM), and 50 µL of L-carnosine-capped AgNPs (1 ± 0.2 OD). The degradation of P-NP and the formation of P-AP were monitored by recording UV–vis spectra in the 300–900 nm range. The disappearance of the yellow color, characteristic of the nitrophenolate ion, was observed upon the addition of the AgNP catalyst, accompanied by a concomitant decrease in the absorbance intensity. The catalytic efficiency was quantified using the following equation:

$$\%\ \text{efficiency} = \left(\frac{C_0 - C_t}{C_0}\right) \cdot 100,$$

where C_0 represents the initial concentration at $t = 0$ and C_t denotes the concentration at time t.

Results and Discussion

Synthesis of L-carnosine-capped tunable silver nanoparticles

L-car-AgNPs were synthesized using a wet-chemical reduction approach. The precursor metal salt was reduced in the presence of the stabilizing or capping agent. Figure 1 shows a schematic representation of the L-car-AgNP synthesis. The sample L-car-AgNP1 was synthesized at room temperature by sequentially mixing water, NaOH, L-carnosine, $AgNO_3$, and $NaBH_4$. The obtained nanoparticles were bright yellow in color, confirming their spherical shape, as reported in previous studies. For the synthesis of the tunable L-car-AgNP2 to L-car-AgNP5 samples, a slightly modified protocol was used compared to L-car-AgNP1. The modifications in terms of temperature and the ratio of $NaBH_4$ to NaOH led to the formation of L-car-AgNPs with different colors. The color of the obtained nanoparticles suggested that they were in a controlled aggregated state. Further characterization was performed to analyze the physicochemical properties of the synthesized L-carnosine-capped silver nanoparticles.

Optical spectroscopy of L-carnosine-capped silver nanoparticles

The synthesized silver nanoparticles capped with L-carnosine were assessed regarding their absorption peaks, as illustrated in Figure 2. The sample L-car-AgNP1 exhibited a single absorption peak at 410 nm (Figure 2a). All other samples displayed two absorption peaks, that is, the first near 400 nm and the second at 500 nm (L-car-AgNP2), 530 nm (L-car-AgNP3), 590 nm (L-car-AgNP4), and 650 nm (L-car-AgNP5) (Figure 2b). The observed absorption bands are attributed to LSPR. This

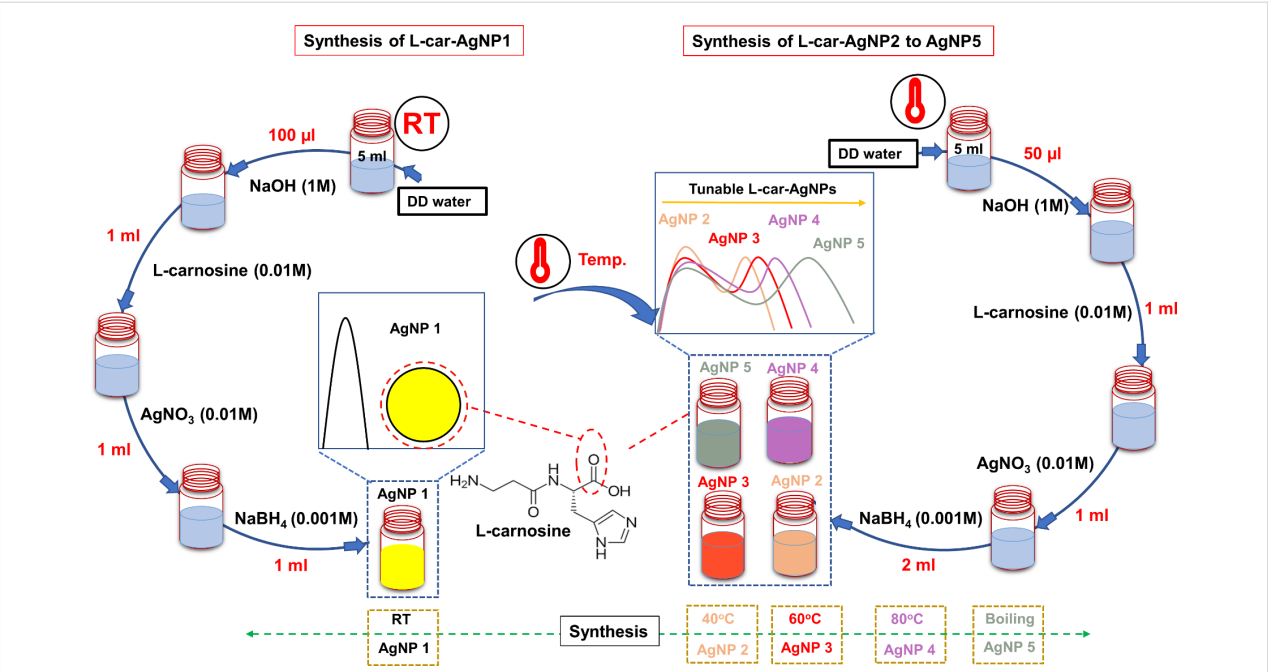


Figure 1: Schematic representation of the synthesis of tunable L-carnosine-capped silver nanoparticles (L-car-AgNPs) along with the critical parameters. The samples L-car-AgNP1, AgNP2, AgNP3, AgNP4, and AgNP5 were synthesized at RT, 40, 60, and 80 °C and at boiling temperature, respectively.

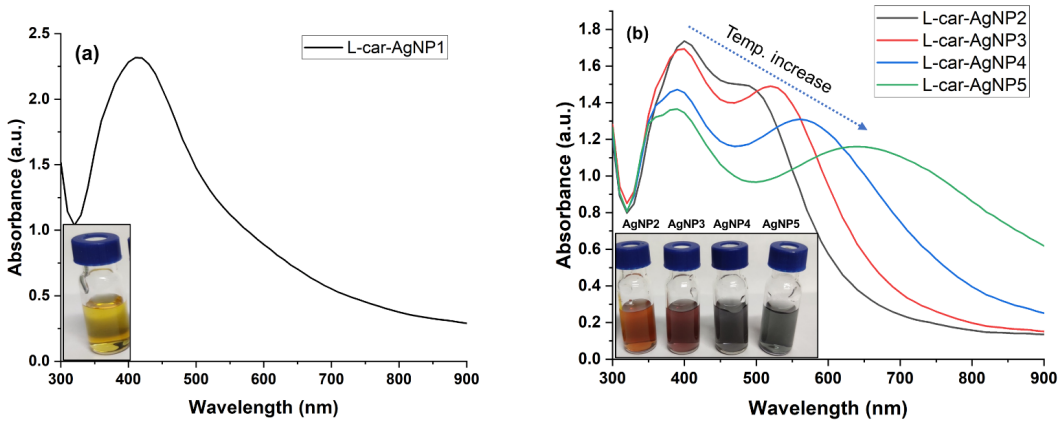


Figure 2: Optical absorbance of (a) L-carnosine-capped AgNP1 and (b) L-carnosine-capped AgNP2–AgNP5. The insets of the figure show photographs of the synthesized nanoparticle suspensions.

phenomenon is an intrinsic property of noble metal nanoparticles [3]. The inset in Figure 2 shows a change in color from bright yellow (L-car-AgNP1) to dark yellow, ruby red, blue, and blackish blue for L-car-AgNP2, AgNP3, AgNP4, and AgNP5, respectively. The sample L-car-AgNP1 shows a single absorption peak and a bright yellow color, which confirms that the nanoparticles are spherical and monodispersed. However, silver nanoparticles with anisotropic shape were reported to have two absorption bands, namely transverse and longitudinal [24]. Furthermore, the color of the anisotropic nanosilver is different from yellow, which is also observed in the samples L-car-AgNP2 to L-car-AgNP5. The transverse and longitudinal absorption bands might be correlated to the formation of polydisperse nanoparticles prepared at higher temperatures because it has been reported that Ostwald ripening occurs faster at higher temperatures [25]. Therefore, it is assumed that the higher temperature, along with the ratio of NaOH to $NaBH_4$, led to the formation of aggregated L-car-AgNPs. These results contradict earlier reports and confirm the formation of aggregated L-car-AgNPs with two absorption bands. However,

despite the different shapes, absorption bands and colors of the L-car-AgNPs samples are similar to those published on CTAB-capped silver nanorods [24]. The formation of aggregated nanoparticles in the current study is probably due to the capping of L-carnosine instead of CTAB. In addition, L-carnosine induces a second absorption peak in the pristine silver nanospheres upon interaction. The appearance of the redshifted peak might be due to charge transfer or aggregation [7]. An increased nanoparticle size leads to a further redshift of the plasmonic peak [26]. Hydrodynamic size, zeta potential, and morphology of the L-car-AgNPs are shown in Figure 3.

Information on average hydrodynamic size and distribution of nanoparticles in colloidal solution was obtained from DLS measurements. The hydrodynamic sizes of L-car-AgNP1, L-car-AgNP2, L-car-AgNP3, L-car-AgNP4, and L-car-AgNP5 were 36.26, 43.05, 70.09, 127.3, and 483.6 nm, respectively (Figure 3a and Supporting Information File 1, Figure S1). The sequential increase in nanoparticle size confirms nanoparticle aggregation or formation of bigger particles and is consistent with the absorption spectra in Figure 2.

The polydispersity index (PDI) is a dimensionless value that measures the width of the size distribution of particles in a sample. The PDI values of L-car-AgNP1, L-car-AgNP2, L-car-AgNP3, L-car-AgNP4, and L-car-AgNP5 were 0.113, 0.250, 0.299, 0.397, and 0.268, respectively (Figure 3a). A PDI value below 0.3 typically indicates a relatively narrow and well-controlled size distribution [27]. L-Carnosine forms a monolayer around the nanoparticles, providing a consistent and uniform surface coverage. This uniformity in surface passivation contributes to the narrow size distribution of the nanoparticles. The formation of stable silver nanoparticles capped with L-carnosine was confirmed via zeta potential measurements. The zeta potential values of L-car-AgNP1, L-car-AgNP2, L-car-AgNP3, L-car-AgNP4, and L-car-AgNP5 were −40.9 ± 3.42, −39.5 ± 3.43, −40.9 ± 3.94, −38.6 ± 4.58, and −40.9 ± 4.80, respectively. Zeta potentials beyond ±30 mV indicate excellent colloidal stability due to strong repulsive forces among the nanoparticles (Figure 3a and Supporting Information File 1, Figure S2) [28]. The highly negative zeta potential values are probably due to the exposed functional group of L-carnosine molecules. The negatively charged carboxyl groups (COO^-) of L-carnosine are attracted towards the positively charged surfaces of silver.

The morphology and size of silver nanoparticles capped with L-carnosine were measured using TEM (Figure 3b–f). The TEM micrograph of L-car-AgNP1 (Figure 3b) indicates the formation of spherical particles with high monodispersity and is consistent with the optical absorbance and DLS measurements. However, L-car-AgNP2–5 (Figure 3c–f) show L-carnosine-induced controlled aggregation (formation of bigger size particles) upon increasing the temperature, which is also consistent with the

(a)

Nanoparticles	Hydrodynamic size (nm)	PDI	Zeta potential (mV)
L-car-AgNP1	36.26	0.113	-40.9±3.42
L-car-AgNP2	43.05	0.250	-39.5±3.43
L-car-AgNP3	70.09	0.299	-40.0±3.94
L-car-AgNP4	127.3	0.397	-38.6±4.58
L-car-AgNP5	483.6	0.268	-40.8±4.80

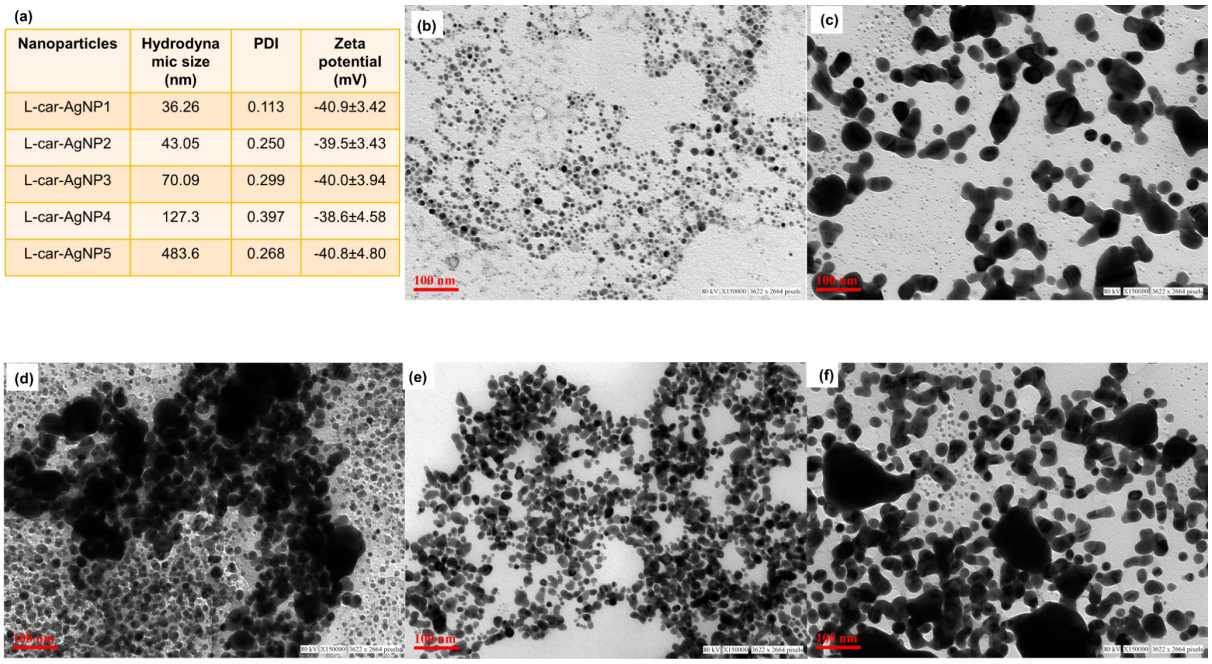


Figure 3: (a) Hydrodynamic size and zeta potential of L-carnosine-capped silver nanoparticles and TEM micrographs of (b) L-car-AgNP1, (c) L-car-AgNP2, (d) L-car-AgNP3, (e) L-car-AgNP4, and (f) L-car-AgNP5.

optical absorption and DLS measurements. The micrograph of samples with two absorption peaks indicates that the nanoparticles aggregated. The results confirm that L-car-AgNP2–5 nanoparticles are polydisperse.

FTIR, Raman spectroscopy and X-ray diffraction

In addition to TEM analysis, the interaction between functional groups of L-carnosine and silver, the elemental composition, and the diffraction pattern of L-car-AgNPs were assessed using FTIR, Raman, EDX, and XRD, as shown in Figure 4.

Figure 4a shows the FTIR analysis of pure L-carnosine and its interaction with the silver nanoparticles in L-car-AgNPs. In the case of pure L-carnosine, a characteristic NH_2 asymmetric stretching frequency at ca. 3243 cm^{-1} overlaps with the broad OH peak of H_2O. The imidazole (C=C) stretching and carboxylate (COO^-) asymmetric stretching frequencies are observed at

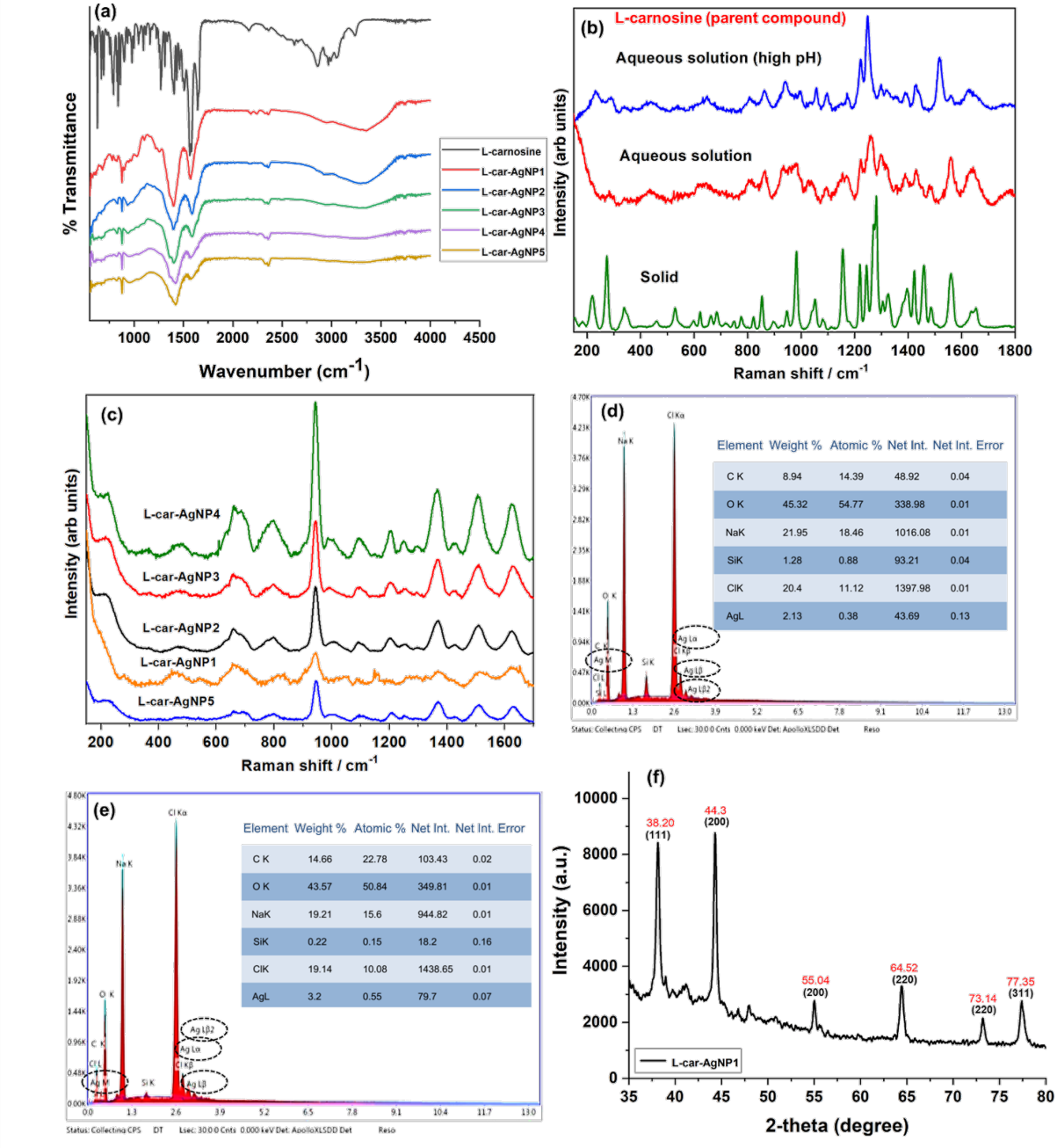


Figure 4: (a) FTIR spectra of L-carnosine and L-car-AgNPs. Raman spectra of (b) L-carnosine (solid and aqueous solution) and (c) L-car-AgNPs. SEM-EDX data confirms the presence of silver in (d) L-car-AgNP1 and (e) L-car-AgNP2. (f) XRD pattern of L-carnosine AgNP1.

1568 and 1404 cm^{-1}, respectively [7]. However, in the case of L-car-AgNPs, the peak at 3243 cm^{-1} disappeared, which might be due to the interaction of the NH_2 groups with silver nanoparticles or their proximity to the nanoparticles' surface. Several prominent overlapping peaks were observed at 1576 cm^{-1} (imidazole C=C stretching), 1404 cm^{-1} (carboxylate, COO^- asymmetric stretching), and 878 cm^{-1} (asymmetric NH_2 wagging) in L-car-AgNPs. This suggests that the nanoparticles were capped with L-carnosine.

Figure 4b shows the Raman spectrum of pure L-carnosine in solid and aqueous phases at normal and alkaline pH values. The prominent Raman bands in solid L-carnosine are observed at 3204 cm^{-1} (symmetric NH_2 stretching), 3082 cm^{-1} (imidazole (imz) ring CH stretching), 2906 cm^{-1} (symmetric CH_2 stretching), 1560 cm^{-1} (imz ring C=C stretching), 1458 cm^{-1} (imz ring C–N stretching), 1422 cm^{-1} (amide NH bend), 1281 cm^{-1} (imz ring breathing), 1219 cm^{-1} (CH_2 twist), 1156 cm^{-1} (NH_2 twist), 1051 cm^{-1} (CH_2 rock), 982 cm^{-1} (imz ring deformation), 854 cm^{-1} (NH_2 wag), 623 cm^{-1} (amide NH out of plane bend), 528 cm^{-1} (amide NCO bend), 339 cm^{-1} (CO_2 bend) and 273 cm^{-1} (imz ring rotation). The Raman spectra of a saturated solution of L-carnosine at normal (and alkaline) pH shown in Figure 4b display strong peaks at 3265 (3266), 2903 (2909), 1639 (1628), 1560 (1577), 1481 (1516), 1428 (1428), 1298 (1299), 1260 (1249), 1223 (1222), 1037 (1057), 981 (997), 935 (941), and 863 (862) cm^{-1}, which are assigned to symmetric NH_2 stretching, symmetric CH_2 stretching, amide C=O stretching, imz ring C=C stretching, CH_2 scissoring, amide NH bend, imz ring breathing, imz ring C–N stretching, CH_2 twist, CH_2 rock, imz ring deformation, C–CO_2 stretching, and NH_2 wagging, respectively. The symmetric CO_2 stretching vibration in L-carnosine at normal (alkaline) pH appears weakly at 1388 (1391) cm^{-1}. The observed shift in the Raman bands of L-carnosine in aqueous solution compared to those in the solid is probably due to solvent effects.

Figure 4c shows surface-enhanced Raman spectra (SERS) of L-carnosine-capped silver nanoparticles. The signal-to-noise (S/N) ratio follows the order L-car-AgNP4 > L-car-AgNP3 > L-car-AgNP2 > L-car-AgNP1 > L-car-AgNP5. Therefore, the results show maximum SERS enhancement for AgNP4. This is probably because of the greater surface roughness of the nanoparticles, leading to maximum electromagnetic enhancement in AgNP4. The SERS spectra of the L-car-AgNPs are almost similar and show Raman bands at 1623 cm^{-1} (amide C=O stretching), 1505 cm^{-1} (imz ring C=C stretching), 1365 cm^{-1} (CO_2 symmetric stretching), 1204 cm^{-1} (CH_2 twist), 1092 cm^{-1} (C–NH_2 stretching), 994 cm^{-1} (imz ring deformation), 943 cm^{-1} (C-CO_2 stretching), 792 cm^{-1} (imz ring NH bend), 685 cm^{-1} (CO_2 bend), 660 cm^{-1} (amide NH bend), 473 cm^{-1} (NH_2 twist) and 215 cm^{-1} (Ag–O stretching). The observation of the abovementioned prominent peaks in the SERS spectra confirms the capping of silver nanoparticles with L-carnosine. The SERS enhancement observed in various vibrations associated with imidazole ring, CO_2, and NH_2 groups suggests that, at alkaline pH, the anionic form of L-carnosine is bound to the AgNPs surface through the carboxylate group and the imidazole as well as amino groups remain close to the silver nanoparticles' surface. The optimized structure of the L-carnosine–$(Ag)_4$ complex (Supporting Information File 1, Figure S4c) supports the experimental results well.

FTIR and Raman spectroscopy confirm the successful capping of silver nanoparticles with L-carnosine. The presence of Ag in L-carnosine-capped AgNPs was also assessed using SEM-EDX. Figure 4d and Figure 4e confirm that Ag is present in L-car-AgNP1 and L-car-AgNP2, respectively. The insets of Figure 4d and Figure 4e indicate 2.13 and 3.2 wt % of silver in L-car-AgNP1 and L-car-AgNP2, respectively. However, apart from silver, high fractions of sodium and chlorine were observed. This is probably due to the preparation of the nanopowders using the precipitation method with NaCl. In addition, NaOH used in the synthesis process acts as a source of sodium in the EDX spectrum.

Crystalline structures of L-car-AgNPs were analyzed using X-ray diffraction. The XRD pattern of one sample representative of all synthesized L-carnosine-capped silver nanospheres is given here (Figure 4f). There are prominent peaks at 38.2°, 44.3°, 64.5°, and 77.4°, attribtuted to the (111), (200), (220), and (311) crystal planes, respectively, of face-centered cubic silver. These results are consistent with [29]. However, two minor peaks are also observed at 55.04° and 73.14°, which have also been observed in another study regarding nanoparticles. The peaks are attributed to the (200) and (220) planes of silver oxide [30]. The characterization of L-car-AgNPs confirms that L-carnosine caps the silver nanoparticles and, thus, can be utilized as a sensing and catalytic agent against environmental contaminants.

DFT results

The optimized geometries of L-carnosine are shown in Supporting Information File 1, Figure S3. L-Carnosine may exist in two H-bonded forms (Supporting Information File 1, Figure S3a,b) where the carboxylic acid and amino groups remain close, and the O–H moiety of the carboxyl group forms a H-bond with the N atom of the amino group. L-Carnosine may also exist in forms where the carboxylic acid and amino groups are far apart (Supporting Information File 1, Figure S3c,d). From the optimized energies, it is observed that the conformation in Figure S3a is the most stable, followed by the ones in Figure S3b, Figure S3c,

and Figure S3d, with relative stabilization energies of 0, 1.093, 4.779, and 5.473 kcal/mol, respectively. The optimized geometries of the anionic form of L-carnosine in water are shown in Supporting Information File 1, Figure S4a,b. The optimized energies of the two forms suggest that the form in Figure S4a is more stable than the form in Figure S4b by 2.242 kcal/mol. The optimized geometries of the L-carnosine–$(Ag)_4$ complexes are shown in Figure S4c,d. The optimized energies of the L-carnosine–$(Ag)_4$ complexes suggest that the form in Figure S4c is more stable than the one in Figure S4d by 1.713 kcal/mol. The infrared and Raman frequencies were computed for all possible forms of L-carnosine, its anionic form, and the L-carnosine–$(Ag)_4$ complexes. The observed FTIR and Raman peaks are assigned based on the theoretical (B3LYP/6-31+G*)-computed frequencies.

Detection of $Cd^{2+}$and Pb^{+2} using L-car-AgNP1

The L-carnosine-capped AgNPs were evaluated regarding the detection of heavy metals via UV–vis spectrophotometry. A series of metal ions, namely As^{3+}, Al^{3+}, Cd^{2+}, Zn^{2+}, Hg^{2+}, Ni^{2+}, Cu^{2+}, Cr^{3+}, Pb^{2+}, Mo^{2+}, and Fe^{3+}, was used for the sensing experiment. Figure 5 shows the absorption spectra of L-car-AgNP1 mixed with various metal ions. The concentration of L-car-AgNP1 was fixed in terms of optical density at 1 ± 0.2. Figure 5a shows the optical absorbance spectra of L-car-AgNP1 after adding Cd^{2+} and Pb^{2+} and all other metals at a concentration of 0.5 ppm. Figure 5b confirms the specificity of L-car-AgNP1 towards Cd^{2+} and Pb^{2+} compared to the control. The plasmon peak with λ_{max} = 410 nm gradually decreases upon adding Cd^{2+} and Pb^{2+} ions. This is accompanied by a redshift of the absorbance wavelength or the formation of a new peak. Also, L-car-AgNP1 shows a significant color change (yellow to brownish-yellow) in the presence of Cd^{2+} and Pb^{2+} (Figure 5c). The color and absorption spectra change can be attributed to the nanoparticles' aggregation [31]. A slight increase in the intensity of L-car-AgNPs after the addition of Cr^{3+} ions was also observed, possibly due to the metal–AgNP complex that decreases the interparticle distance followed by a plasmonic and colorimetric change [32]. The L-carnosine structure has amine or carboxyl functional groups. However, zeta potential measurements confirmed that L-car-AgNPs are negatively charged, and the overlapping peaks in FTIR suggested that carboxyl is the exposed functional group. Based on the earlier reports, free $–NH_2$ and carboxyl groups are believed to participate in cross-linking and forming complexes between L-car-AgNP1 and Cd^{2+}/Pb^{2+} ions. The Cd^{2+} and Pb^{2+} ions interact with lone electron pairs of these exposed groups. We hypothesize that the complexation between L-car-AgNP1 and Cd^{2+}/Pb^{2+} decreases the distance between the nanoparticles. This results in a redshift

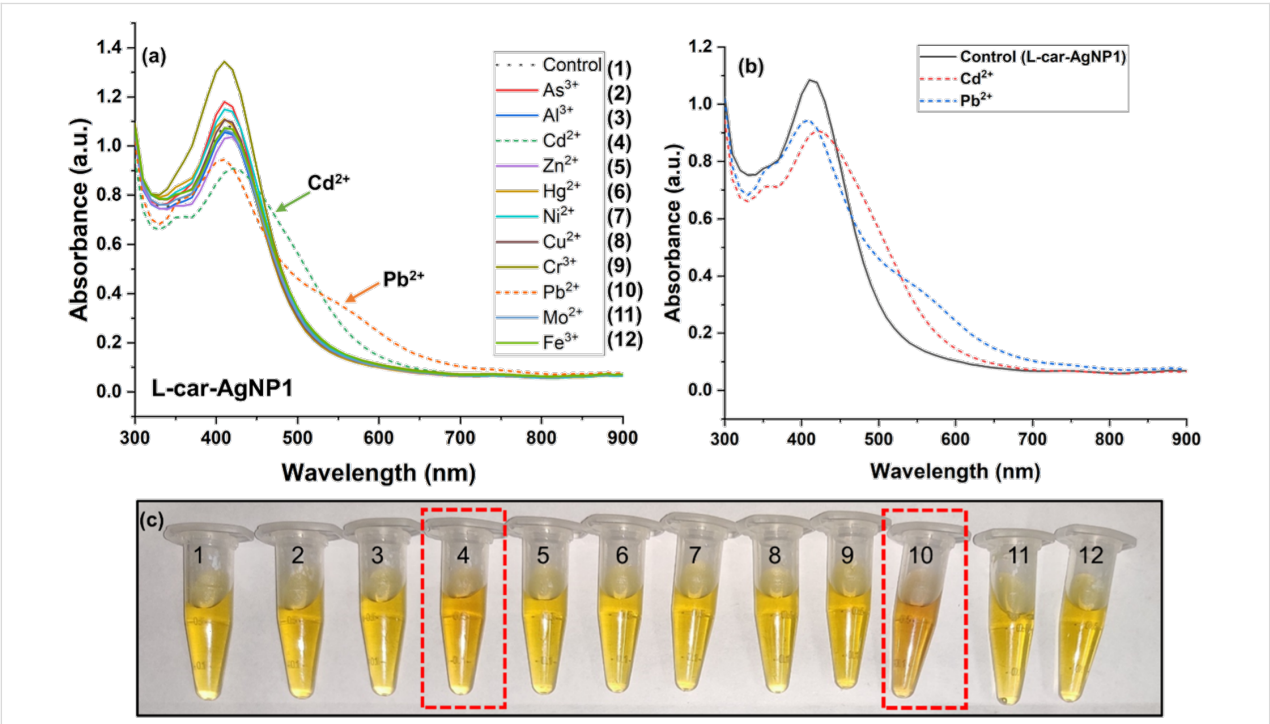


Figure 5: Heavy metal ion sensing using L-car-AgNP1. (a) UV–vis spectrophotometric determination of Cd^{2+}, Pb^{2+}, and the other metal ions. (b) Optical absorbance of L-car-AgNP1 with and without Cd^{2+} and Pb^{2+}. (c) Colorimetric detection of Cd^{2+} and Pb^{2+} using L-car-AgNP1 compared to control (no. 1, without metal ions). The dashed line and the red dashed boxes show the spectrophotometric and colorimetric change upon adding Cd^{2+} (no. 4) and Pb^{2+} (no. 10).

and the emergence of shoulder peaks in the absorption spectra, followed by a decrease in absorption intensity compared to the control. Abate et al. showed that L-carnosine can interact with bivalent ions, including Cd^{2+} [19]. This study also confirms that the bivalent metal ions Pb^{2+} and Cd^{2+} prominently interact with L-car-AgNP1.

Detection of As^{3+} and Cr^{3+}, using L-car-AgNP2 and L-car-AgNP5

As^{3+} and Cr^{3+} were detected using L-car-AgNPs that showed a dual absorption bands (transverse and longitudinal). The samples L-car-AgNP2, L-car-AgNP3, and L-car-AgNP4 could detect As^{3+} and Cr^{3+} via colorimetric and spectrophotometric observations (Figure 6a,b,d and Supporting Information File 1, Figure S5). In contrast, L-car-AgNP5 did not detect any metal ions, which might be due to the formation of larger aggregates of silver nanoparticles (Figure 6c). L-car-AgNP2 exhibited a prominent colorimetric and spectrophotometric sensing ability towards As^{3+} and Cr^{3+} (Figure 6a). The concentration of L-car-AgNP2 was fixed at an optical density of 1 ± 0.2, and the concentration of added metal ions was 0.5 ppm. The results show that only the tubes containing As^{3+} and Cr^{3+} display a prominent color change from ruby red (control) to dark yellow (Figure 6d). This implies that L-car-AgNP2 has strong selectivity towards As^{3+} and Cr^{3+}. Figure 6b shows the UV–vis absorption spectra of L-car-AgNP2 without metal ions and with As^{3+} and Cr^{3+}. The absorption curves reveal that As^{3+} and Cr^{3+} lead to hypsochromic (530 nm) and hyperchromic (400 nm) shifts, respectively, of the plasmon peak. The interaction between negatively charged L-car-AgNP2 and positively charged As^{3+} and Cr^{3+} leads to changes in AgNPs depending on the metal ion concentration, resulting in the deformation of anisotopic to isotropic particles. A similar plasmonic shift has been observed in the literature, where As^{3+} induced the formation of spherical silver nanoparticles after being added to silver nanoprisms [33]. In addition, negatively charged silver nanoparticles are prone to interaction with As^{3+} and Cr^{3+} under basic conditions (pH 10). Earlier reports have confirmed the interaction of Cr^{3+} with metal nanoparticles at basic pH [34]. Therefore, it is assumed that L-car-AgNP2, L-car-AgNP3, and L-car-AgNP4 can stabilize the AgNPs under alkaline conditions (pH 10) and can detect As^{3+} and Cr^{3+} in all samples. This is due to the interaction of As^{3+} and Cr^{3+} with the exposed functional groups on the surface of the silver nanoparticles. In the case of L-car-AgNP5, the nanoparticles lose the ability to interact with the trivalent metal ions because of the formation of bigger particles, which was confirmed by TEM and DLS measurements.

Interference study and quantification of the detection limit for Cd^{2+} and Pb^{2+} using L-car-AgNP1

The ability of L-car-AgNP1 as a probe for the selective detection of Cd^{2+} and Pb^{2+} in the presence of multiple metal ions was assessed using an interference study, where several groups of metal mixtures were prepared (Figure 7). The metal ions, namely As^{3+}, Al^{3+}, Zn^{2+}, Hg^{2+}, Ni^{2+}, Cu^{2+}, Cr^{3+}, Mo^{2+}, and Fe^{3+}, were mixed in a volume of 1 mL with a final concentration of 0.5 ppm for each metal. The metal ion mixtures were

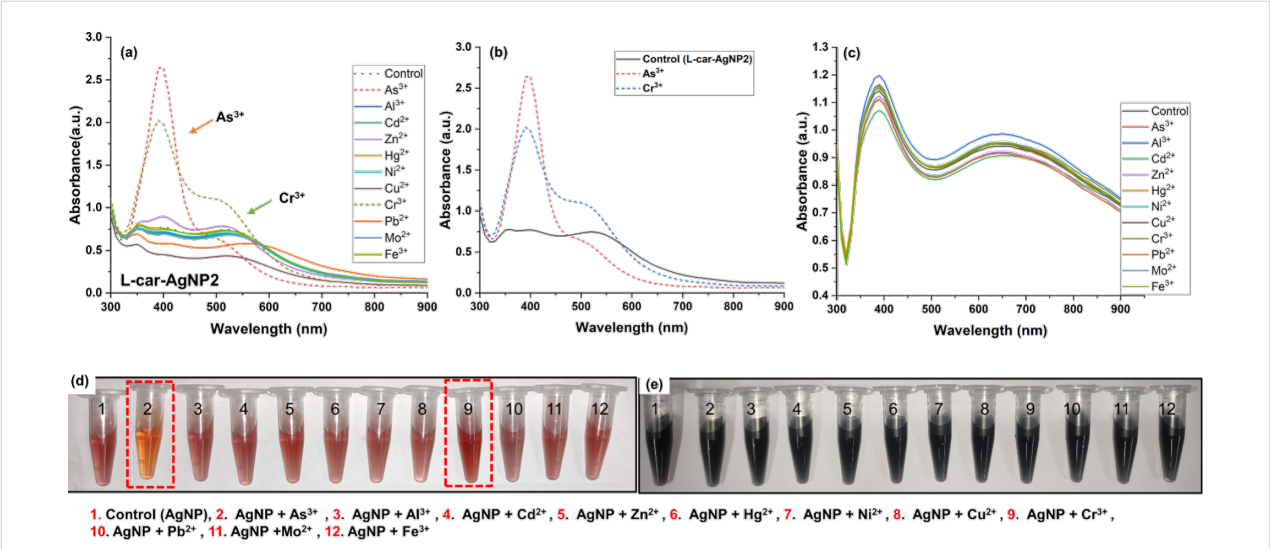


Figure 6: Heavy metal ion sensing using L-car-AgNP2 and L-car-AgNP5. (a) UV–vis spectrophotometric determination of As^{3+} and Cr^{3+} (marked by arrows). (b) Optical absorbance of L-car-AgNP2 with and without As^{3+} and Cr^{3+}. (c) Optical spectrometry confirmed no metal ion interaction with L-car-AgNP5. (d) Colorimetric detection of As^{3+} and Cr^{3+} using L-car-AgNP2 compared to the control without metal ions. (e) No colorimetric change was observed in L-car-AgNP5 with or without the metal ions. The dashed lines and the red dashed boxes show the spectrophotometric and colorimetric change upon adding As^{3+} and Cr^{3+}.

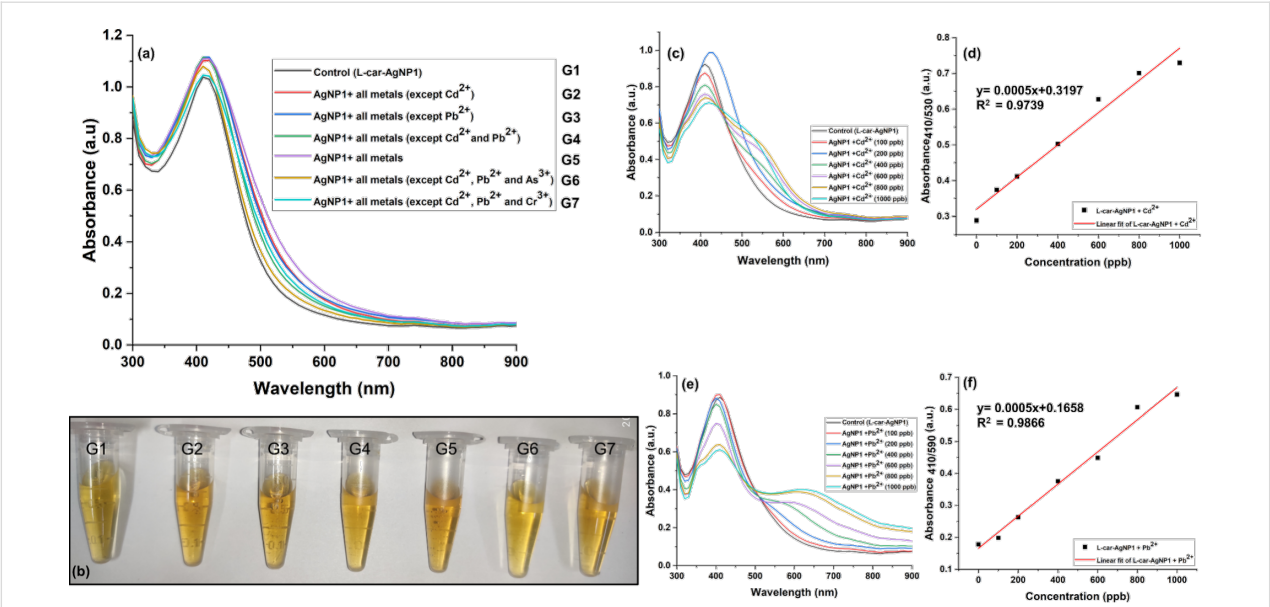


Figure 7: Interference study regarding the metal ion selectivity of L-car-AgNP1. (a) Optical absorbance of different groups 2–7 (G2–G7) and the control sample (G1). (b) Colorimetric observation of metal ion selectivity in the presence of groups 1–7. (c) UV–vis spectral absorbance of L-car-AgNP1 with different Cd^{2+} concentrations (100–1000 ppb) and (d) the corresponding linear curve. (e) UV–vis spectral absorbance of L-car-AgNP1 with different Pb^{2+} concentrations (100–1000 ppb) and (f) the corresponding linear curve.

grouped as groups G1–7, where G1 included no metal ions (control group). G2 and G3 included all metal ions except either Cd^{2+} or Pb^{2+}, respectively. G4 included all metal ions except both Cd^{2+} and Pb^{2+}. G5 contained all metal ions including Cd^{2+} and Pb^{2+}. After adequate mixing of the metal ions, L-car-AgNP1 was dispersed into the test system and underwent colorimetric and spectrophotometric investigations. The slight color changes in G2, G3, and G5 indicate the detection of Cd^{2+} and Pb^{2+} even when mixed with other metal ions (Figure 7a). In G2, a slight increase and shift in peak intensity in the presence of different metals (λ_{max} = 420 nm, 1.11 OD) compared to the control (λ_{max} = 410 nm, 1.0 OD) was observed, possibly because of Pb^{2+}. A similar behavior was noticed in the case of G3, because of Cd^{2+}. G5 exhibited a peak value of λ_{max} = 420 nm and 1.11 OD, because of the presence of both Cd^{2+} and Pb^{2+}. The value did not shift much, possibly because of the presence of a metal mixture instead of single metal ions. Similarly, no prominent color change in the different groups was observed, in accordance with the optical absorbance measurements (Figure 7a,b). However, a slight change in color and absorbance in group 4 was observed, which consists of all metal ions except Cd^{2+} and Pb^{2+}. This suggests that other metal ions also interfere with the nanoparticles. Therefore, G6 and G7 were included in the study, including all metal ions except Cd^{2+} and Pb^{2+} and either As^{3+} or Cr^{3+}, respectively. No prominent color change was observed in G6 and G7. An increase in absorption intensity in G6 was observed, which was not the case for G7. This confirmed that As^{3+} slightly interferes in a metal ion mixture. After successful qualitative detection and development of a sensing probe, quantification of the detection limit for Cd^{2+} and Pb^{2+} using

L-car-AgNP1 was carried out, and LOD and LOQ were calculated. In Figure 7c and Figure 7e, only a single metal (i.e., Cd^{2+} or Pb^{2+}) was added to L-car-AgNP1, and the changes as functions of the metal ion concentration were measured. The changes in absorbance were plotted as functions of the concentrations of Cd^{2+} and Pb^{2+} (Figure 7d,f). The linear fit for Cd^{2+} showed an excellent R^2 value of 0.9739 with LOD and LOQ values of 141.79 ppb (1.2 µM) and 238.56 ppb (2.12 µM), respectively. In the case of Pb^{2+}, LOD and LOQ were found to be 131.33 ppb (0.63 µM) and 397.99 ppb (1.92 µM) with an R^2 value of 0.9866. In Table 1, recent studies on the colorimetric detection of Cd^{2+} and Pb^{2+} using nanoparticles are summarized, along with their detection limits.

Interference study and quantification of the detection limit for As^{3+} and Cr^{3+} using L-car-AgNP2

The usability of L-car-AgNP2 as a probe for the selective detection of As^{3+} and Cr^{3+} was assessed in an interference study, where several groups of metal mixtures were prepared (Figure 8). For the interference study, metal ions, namely, Al^{3+}, Cd^{2+} Zn^{2+}, Hg^{2+}, Ni^{2+}, Cu^{2+}, Pb^{2+}, Mo^{2+}, and Fe^{3+}, were mixed in a volume of 1 mL with a final concentration of 0.5 ppm for the metal ions. The metal ion mixtures were grouped as sample groups S1–7, where S1 included no metal

Table 1: Recent studies on sensitive colorimetric metal detection using various nanoparticles.

Nanoparticles	Metal detected	Detection method	LOD	Ref.
cysteine- and methionine-capped AgNPs	arsenic	paper-based colorimetric	0.0005 ppm	[33]
glutathione-capped AuNPs	arsenic	RGB colorimetric	0.12 ppb	[35]
citrate-capped AgNPs	arsenic	colorimetric	5.3 ppb	[36]
Boswellia sacra extract-stabilized AgNPs	arsenic	colorimetric	0.143 ppm	[37]
starch-stabilized AgNPs	chromium	colorimetric	0.93 μM	[38]
chlorophyll-coated AgNPs	chromium	colorimetric	0.62 μM	[39]
morin + PVP-capped AgNPs	chromium	colorimetric	4×10^{-5} M	[40]
secnidazole functionalized AgNPs	cadmium	colorimetric	0.07 μM	[41]
grape juice-stabilized AgNPs	cadmium	colorimetric	4.95 μM	[42]
Annona muricata extract-stabilized AuNPs	cadmium	colorimetric	4.45×10^{-8} M	[43]
orange peel extract-stabilized AuNPs	lead	colorimetric	13.31 μM	[44]
curcumin AgNPs	lead	colorimetric	13.6 μM	[45]
maltol-capped AgNPs	lead	colorimetric	0.067 μM	[46]
L-carnosine-capped AgNP1	cadmium and lead	colorimetric	141.79 ppb (1.2 μM) and 131.33 ppb (0.63 μM)	this work
L-carnosine-capped AgNP2	arsenic and chromium	colorimetric	215.35 ppb (2.8 μM) and 245.49 ppb (4.7 μM)	this work

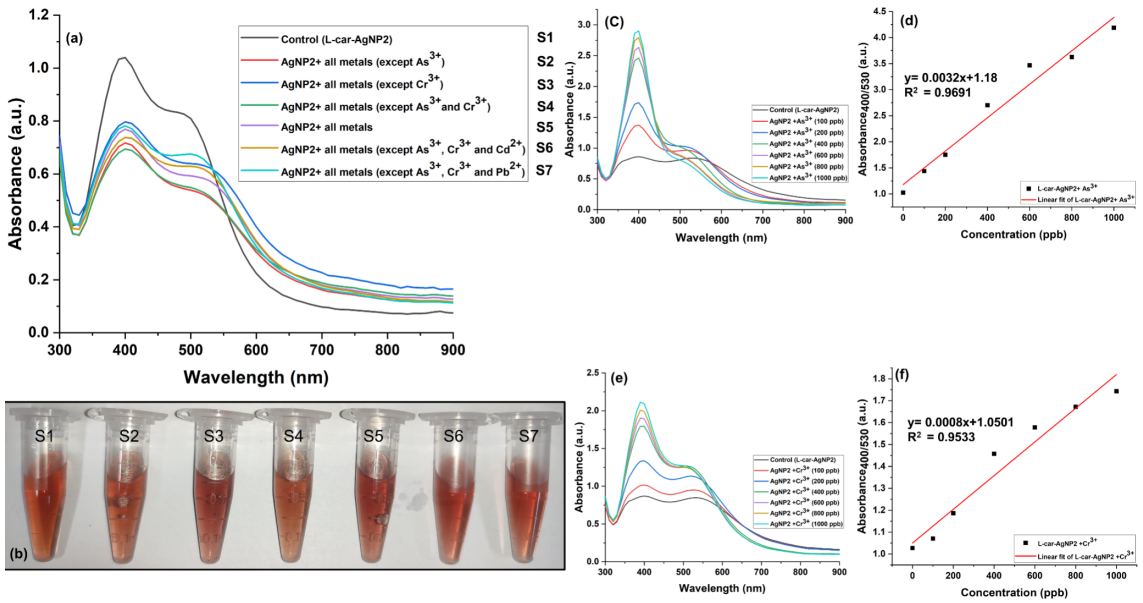


Figure 8: Interference study regarding the metal ion selectivity of L-car-AgNP2. (a) Optical absorbance of different groups S2–7 and the control sample (S1). (b) Colorimetric observation of metal ion selectivity in the presence of groups S1–7. (c) UV–vis spectral absorbance of L-car-AgNP2 with different As^{3+} concentrations (100–1000 ppb) and (d) the corresponding linear curve. (e) UV–vis spectral absorbance of L-car-AgNP2 with different Cr^{3+} concentrations (100–1000 ppb) and (f) the corresponding linear curve.

ions (control group). S2 and S3 included all metal ions except either As^{3+} or Cr^{3+}, respectively. S4 included all metal ions except both As^{3+} and Cr^{3+}. S5 contained all metal ions, including As^{3+} and Cr^{3+}. After adequately mixing the metal ions, L-car-AgNP2 was dispersed into the test system and underwent colorimetric and spectrophotometric investigations. The slight color change observed in S2, S3, and S5 indicated the successful detection of As^{3+} and Cr^{3+}, even in the presence of other metal ions. The colorimetric detection was further validated through optical spectrometry, which showed increased absorbance (Figure 8a) in S2 (λ_{max} = 515 nm, 0.52 OD), S3 (λ_{max} = 530 nm, 0.62 OD), and S5 (λ_{max} = 530 nm, 0.56 OD) compared to S1 (control, λ_{max} = 500 nm, 0.8 OD). However, a slight change in color and plasmon peak was observed in S4

(λ_{max} = 510 nm, 0.53 OD) (Figure 8b). This suggested that other metals also interfere with the nanoparticles. Therefore, S6 (λ_{max} = 505 nm, 0.62 OD) and S7 (λ_{max} = 500 nm, 0.67 OD) were included in the study, which included of all metal ions except As^{3+} and Cr^{3+} and either Cd^{2+} or Pb^{2+}, respectively. However, no prominent color change was observed in S6 and S7, but an increase in the plasmon peak intensity in S6, but not in S7. This confirmed that Cd^{2+} slightly interferes with detecting As^{3+} and Cr^{3+}. This is probably due to the interaction of L-car-AgNPs with bivalent metal ions, as reported elsewhere [19].

After successful qualitative detection and the development of a sensing probe, quantification of the detection limit for As^{3+} and Cr^{3+} using L-car-AgNP2 was carried out, and LOD and LOQ were calculated. In Figure 8c and Figure 8e, only a single metal (i.e., As^{3+} or Cr^{3+}, respectively) was added to L-car-AgNP2, and the changes as functions of the metal ion concentration were measured. The changes in absorbance were plotted as functions of the concentrations of As^{3+} and Cr^{3+} (Figure 8d,f). The linear fit for As^{3+} showed an R^2 value of 0.9691 with LOD and LOQ values of 215.35 ppb (2.8 µM) and 591.42 ppb (7.8 µM), respectively. In the case of Cr^{3+}, the obtained values of LOD and LOQ were 245.49 ppb (4.7 µM) and 743.92 ppb (14.2 µM), respectively, with an R^2 value of 0.9533. In Table 1, recent studies on the colorimetric detection of As^{3+} and Cr^{3+} using nanoparticles and their detection limits are summarized.

Catalytic potential of L-car-AgNPs in degradation of *p*-nitrophenol

The catalytic efficacy of L-car-AgNPs was evaluated using the degradation of P-NP and the formation of P-AP as a model reaction. This transformation, catalyzed by noble metal nanoparticles in the presence of $NaBH_4$ as reducing agent, is widely utilized to assess the catalytic performance of nanomaterials [14]. All catalytic experiments were performed in a standard quartz cuvette, and the spectral changes were monitored as the reaction progressed. The reaction mixture consisted of an aqueous solution of P-NP (0.25 and 1 mM) and 0.1 M $NaBH_4$ to which L-car-AgNPs were added. It was noticed that, upon introducing $NaBH_4$, the light yellow color changes to intense yellow-green, accompanied by an absorption shift from 317 to 400 nm, indicating the formation of *p*-nitrophenolate ions (an intermediate) in the basic reaction medium [47]. These intermediate ions were further degraded in the presence of L-car-AgNPs as a nanocatalyst to the stable product P-AP. The conversion of P-NP to P-AP was monitored through UV–vis spectroscopy. In UV–vis measurements, there was a decrease in absorption intensity at 400 nm, and a minor peak around 300 nm was observed due to the formation of P-AP (Figure 9).

Figure 9 illustrates the P-NP degradation at 0.25 mM using L-car-AgNPs (1 ± 0.2 OD). L-car-AgNP1 led to the degradation of 0.25 mM P-NP within 90 s of the reaction, achieving a degradation efficiency of 95.5% (Figure 9a). In comparison, L-car-

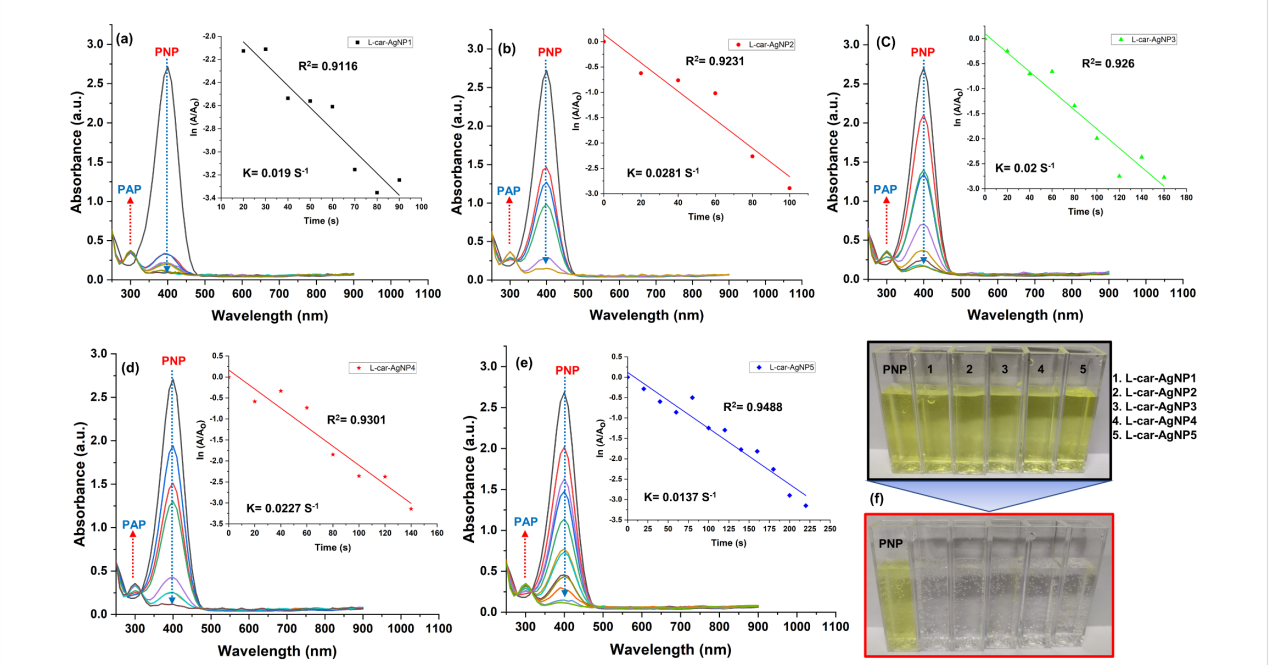


Figure 9: (a–e) UV–vis absorption measurements showing the catalytic degradation of 0.25 mM P-NP using L-carnosine-capped AgNP1–5. The inset graphs show pseudo-first-order kinetics for the degradation of P-NP. (f) Color change in P-NP solutions before and after the addition of L-car-AgNPs. The dashed red and blue arrows indicate the formation of P-AP and the degradation of P-NP, respectively.

AgNP2, L-car-AgNP3, L-car-AgNP4, and L-car-AgNP5 achieved complete P-NP degradation within 100, 160, 140, and 220 s, respectively, with catalytic efficiencies of 96.18%, 96.52%, 94.61% and 95.71% (Figure 9b–e). The color change from yellow to colorless indicates complete degradation of P-NP and, thus, the catalytic potential of the nanoparticles (Figure 9f). Increasing the P-NP concentration to 1 mM required longer times until full degradation, as documented in Supporting Information File 1 (Figure S6). The degradation times for 1 mM P-NP using L-car-AgNP1, L-car-AgNP2, L-car-AgNP3, L-car-AgNP4, and L-car-AgNP5 were 270, 330, 300, 270, and 420 s, respectively (Supporting Information File 1, Figure S6). The different degradation times might be attributed to differences in particle sizes and monodispersity. TEM and DLS measurements revealed that L-car-AgNP1 nanoparticles were spherical and monodisperse, whereas the other nanoparticles (L-car-AgNP2–5) exhibited polydispersity and non-spherical shapes. This is in accordance with results from Jiji et al., where different shapes of gold nanoparticles had varying efficiencies in the catalytic degradation of nitrophenol compounds, with spherical nanoparticles being highly effective [48]. Kinetic analysis was performed based on pseudo-first-order reaction kinetics for the concentration of 0.25 mM P-NP. The spectral absorbance at a concentration of 1 mM P-NP exceeded 4 OD, necessitating a dilution factor of 10 to achieve an observable OD of 1.2 (Supporting Information File 1, Figure S6). Given the excess $NaBH_4$ used in the reaction, the borohydride concentration was assumed to remain constant. The rate constants (k) were computed from the linear plots of $\ln(A/A_0)$ as a function of time, where A and A_0 denote the absorbances at time t and $t = 0$, respectively. The calculated rate constants were 0.019, 0.028, 0.020, 0.023, and 0.014 s^{-1} for L-car-AgNP1, L-car-AgNP2, L-car-AgNP3, L-car-AgNP4, and L-car-AgNP5 respectively, at 25 ± 2 °C. This suggests that the catalytic activity of the nanoparticles is in the order of AgNP5 < AgNP1 < AgNP3 < AgNP4 < AgNP2. Interestingly, the catalytic activity of L-car-AgNPs does not depend on the hydrodynamic size of the nanoparticles obtained from DLS. These results confirmed that the catalytic activity of metal nanoparticles does not necessarily increase with decreasing size, potentially because of the strong curvature of the surface of very small particles, which has also been reported [14,49]. In addition, the obtained rate constants for L-car-AgNP4, L-car-AgNP3, and L-car-AgNP2 are nearly the same, but the lower rate constant in case of AgNP5 might be due to the formation of larger aggregates, which was confirmed by optical spectroscopy and TEM analysis. The high efficiency of AgNP2 might be due to its quasi-spherical shape.

The catalytic degradation of P-NP by L-car-AgNPs can be attributed to the unique optical and catalytic properties of AgNPs, which are enhanced by their high surface-to-volume ratio and plasmonic effects. The observed pseudo-first-order kinetics suggest that the rate-determining step involves the adsorption of P-NP onto the nanoparticle surface, followed by the electron transfer from $NaBH_4$ to the adsorbed P-NP molecules facilitated by the AgNPs. The obtained rate constants indicate that L-carnosine-capped AgNPs are comparable to or more efficient than other noble metal nanoparticles (Table 2), underscoring their potential as cost-effective catalysts for the degradation of nitroaromatic compounds, which are prevalent in industrial effluents and pose significant environmental risks.

Conclusion

Silver nanoparticles with tunable absorption bands were synthesized for the first time using L-carnosine as a capping agent. This novel approach has facilitated the development of nanoparticles that exhibit controlled size and stability, which is crucial for various applications. L-carnosine-capped silver nanoparticles, designated as L-car-AgNPs, were extensively characterized using UV–vis absorbance, DLS, zeta potential, FTIR, Raman spectroscopy, TEM, SEM-EDX, and XRD. This comprehensive analysis elucidates the optical absorbance, sizes, surface charges, functional group interactions, elemental compositions, and diffraction patterns of L-car-AgNPs. Furthermore, different sizes of L-car-AgNPs (L-car-AgNP1 to L-car-AgNP5) were explored regarding their potential as metal ion sensors. Among them, L-car-AgNP1 showed selective detection of Cd^{2+} and Pb^{2+}. In contrast, L-car-AgNP2, L-car-AgNP3, and L-car-

Table 2: Comparative study of the degradation of P-NP using various nanoparticles.

Nanoparticles	Time of degradation (min)	Catalyst concentration	P-NP concentration	Ref.
Acacia nilotica (stem)-stabilized AgNPs	10	5 mg	0.1 mM	[50]
citrate-capped Au- NPs	14	200 µL	0.2 mM	[51]
citrate-capped AgNPs	120	0.54 mg	0.1 mM	[52]
cobalt (Co)-doped ZnO NPs	180	30 mg	30 mg/L (30 ppm)	[53]
cobalt oxide nanocomposites	15	200 µL (1 mg/mL)	9.03 mg/L (9.030 ppm)	[54]
L-car-AgNPs	<5	50 µL (1 ± 0.2 OD)	0.25 mM (34.75 ppm)	this work
	<10		1 mM (139 ppm)	

AgNP4 showed affinity towards As^{3+} and Cr^{3+} detection. Interestingly, L-car-AgNP5 did not detect any metal ions. The quantitative limits of detection (LODs) of Cd^{2+}, Pb^{2+}, As^{3+}, and Cr^{3+} were 141.79, 131.33, 215.35, and 245.49 ppb, respectively. These values suggest a competitive sensitivity compared to other nanoparticle-based sensors reported in the literature.

Additionally, the catalytic activity of L-car-AgNPs was studied regarding the degradation of 0.25 and 1 mM concentrations of *p*-nitrophenol (P-NP) within 5 and 10 min, respectively. The catalytic efficiencies for 0.25 mM P-NP were 95.5%, 96.18%, 96.52%, 94.61%, and 95.71% achieved with L-car-AgNP1, L-car-AgNP2, L-car-AgNP3, L-car-AgNP4, and L-car-AgNP5, respectively. The rapid degradation demonstrates the catalytic prowess of L-car-AgNPs and highlights their potential in environmental remediation applications. The successful synthesis of L-car-AgNPs with tunable plasmon resonance has paved the way for their application as colorimetric sensors for heavy metal detection and as efficient catalysts for the degradation of nitroaromatic compounds. The selectivity regarding metal ions based on the nanoparticle size demonstrates the potential for developing tailored sensors for specific applications. The catalytic activity of the nanoparticles in the degradation of *p*-nitrophenol highlights their potential as cost-effective and environmentally friendly catalysts for the remediation of industrial effluents. Future studies will focus on optimizing these nanoparticles for broader applications and understanding their interaction mechanisms at the molecular level.

Supporting Information

The file contains six figures. Figures S1 and S2 show hydrodynamic sizes and zeta potentials obtained from DLS measurements. Figures S3 and S4 show optimized geometries of L-carnosine and the L-carnosine–AgNPs complex, respectively. Figure S5 shows the colorimetric and spectrophotometric detection of metal ions using L-car-AgNP3 and L-car-AgNP4. Figure S6 shows the catalytic degradation of 1 mM *p*-nitrophenol using L-car-AgNPs.

Supporting Information File 1

Additional figures.
[https://www.beilstein-journals.org/bjnano/content/supplementary/2190-4286-15-124-S1.pdf]

Acknowledgements

The authors acknowledge Mr Jai Shankar for TEM imaging and Mr Joel Saji for XRD and FTIR measurement. The authors are grateful to CSIR-IITR, Lucknow, for providing the platform and facilities for this research work. The CSIR-IITR publication committee approved this paper, and the communication number is IITR/SEC/MS/2024/39.

Funding

This research work was supported by the CSIR-Indian Institute of Toxicology Research (Major Laboratory Project-MLP-001) approved by the competent authority of CSIR-IITR, Lucknow, India. Akash Kumar is thankful to CSIR for providing fellowship.

Conflict of Interest

The authors declare that there is no conflict of interest.

Author Contributions

Akash Kumar: formal analysis; investigation; methodology; validation; writing – review & editing. Ridhima Chadha: data curation; formal analysis. Abhishek Das: investigation; methodology. Nandita Maiti: methodology; supervision; visualization; writing – review & editing. Rayavarapu Raja Gopal: conceptualization; formal analysis; investigation; methodology; supervision; validation; visualization; writing – review & editing.

Data Availability Statement

All data that supports the findings of this study is available in the published article and/or the supporting information of this article.

References

1. Balali-Mood, M.; Naseri, K.; Tahergorabi, Z.; Khazdair, M. R.; Sadeghi, M. *Front. Pharmacol.* **2021,** *12,* 643972. doi:10.3389/fphar.2021.643972
2. Toxicological profile for nitrophenols. https://stacks.cdc.gov/view/cdc/128698 (accessed Nov 21, 2024).
3. Galatage, S. T.; Hebalkar, A. S.; Dhobale, S. V.; Mali, O. R.; Kumbhar, P. S.; Nikade, S. V.; Killedar, S. G. Silver Nanoparticles: Properties, Synthesis, Characterization, Applications and Future Trends. In *Silver Micro-Nanoparticles - Properties, Synthesis, Characterization, and Applications;* Kumar, S.; Kumar, P.; Shakher Pathak, C., Eds.; IntechOpen: London, U.K., 2021. doi:10.5772/intechopen.99173
4. Boas, D.; Remennik, S.; Reches, M. *J. Colloid Interface Sci.* **2023,** *631,* 66–76. doi:10.1016/j.jcis.2022.10.154
5. Samuel, V. R.; Rao, K. J. *Chem. Phys. Impact* **2023,** *6,* 100161. doi:10.1016/j.chphi.2023.100161
6. Chadha, R.; Das, A.; Lobo, J.; Meenu, V. O.; Paul, A.; Ballal, A.; Maiti, N. *Colloids Surf., A* **2022,** *641,* 128558. doi:10.1016/j.colsurfa.2022.128558
7. Thomas, S.; Biswas, N.; Malkar, V. V.; Mukherjee, T.; Kapoor, S. *Chem. Phys. Lett.* **2010,** *491,* 59–64. doi:10.1016/j.cplett.2010.03.059
8. Mohammed, H.; Sadeek, S.; Mahmoud, A. R.; Zaky, D. *Microchem. J.* **2016,** *128,* 1–6. doi:10.1016/j.microc.2016.04.002
9. Okano, G.; Igarashi, S.; Yamamoto, Y.; Saito, S.; Takagai, Y.; Ohtomo, T.; Kimura, S.; Ohno, O.; Oka, Y. *Int. J. Environ. Anal. Chem.* **2015,** *95,* 135–144. doi:10.1080/03067319.2014.994619

10. Trapido, M.; Kallas, J. *Environ. Technol.* **2000,** *21,* 799–808. doi:10.1080/09593330.2000.9618966
11. Chadha, R.; Maiti, N.; Kapoor, S. *J. Phys. Chem. C* **2014,** *118,* 26227–26235. doi:10.1021/jp509190f
12. Kumar, N.; Thomas, S.; Rao, R.; Maiti, N.; Kshirsagar, R. J. *J. Phys. Chem. A* **2019,** *123,* 9770–9780. doi:10.1021/acs.jpca.9b07367
13. Amirjani, A.; Koochak, N. N.; Haghshenas, D. F. *J. Chem. Educ.* **2019,** *96,* 2584–2589. doi:10.1021/acs.jchemed.9b00559
14. Kästner, C.; Thünemann, A. F. *Langmuir* **2016,** *32,* 7383–7391. doi:10.1021/acs.langmuir.6b01477
15. Panahi, F.; Bahrami, F.; Khalafi-Nezhad, A. *J. Iran. Chem. Soc.* **2017,** *14,* 2211–2220. doi:10.1007/s13738-017-1157-2
16. Keykhaee, M.; Razaghi, M.; Dalvand, A.; Salehian, F.; Soleimani, H.; Samzadeh-Kermani, A.; Shamsollahi, H. R.; Foroumadi, A.; Ramazani, A.; Khoobi, M.; Alimohammadi, M. *J. Environ. Health Sci. Eng.* **2020,** *18,* 1163–1174. doi:10.1007/s40201-020-00535-3
17. Kamal, T.; Khan, M. S. J.; Khan, S. B.; Asiri, A. M.; Chani, M. T. S.; Ullah, M. W. *J. Polym. Environ.* **2020,** *28,* 399–410. doi:10.1007/s10924-019-01615-8
18. Almaquer, F. E. P.; Ricacho, J. S. Y.; Ronquillo, R. L. G. *Sustainable Environ. Res.* **2019,** *29,* 23. doi:10.1186/s42834-019-0026-3
19. Abate, C.; Aiello, D.; Cordaro, M.; Giuffrè, O.; Napoli, A.; Foti, C. *J. Mol. Liq.* **2022,** *368,* 120772. doi:10.1016/j.molliq.2022.120772
20. Abate, C.; Piperno, A.; Fragoso, A.; Giuffrè, O.; Mazzaglia, A.; Scala, A.; Foti, C. *Dalton Trans.* **2023,** *52,* 3699–3708. doi:10.1039/d2dt04093j
21. Sarkar, A. R.; Sarkar, M. *J. Chem. Res., Synop.* **1997,** 304–305. doi:10.1039/a605510i
22. Becke, A. D. *J. Chem. Phys.* **1993,** *98,* 1372–1377. doi:10.1063/1.464304
23. *Gaussian 09,* Revision A.02; Gaussian, Inc.: Wallingford, CT, USA, 2016.
24. Hormozi-Nezhad, M. R.; Jalali-Heravi, M.; Robatjazi, H.; Ebrahimi-Najafabadi, H. *Colloids Surf., A* **2012,** *393,* 46–52. doi:10.1016/j.colsurfa.2011.10.023
25. Madras, G.; McCoy, B. J. *Chem. Eng. Sci.* **2004,** *59,* 2753–2765. doi:10.1016/j.ces.2004.03.022
26. Kumar, A.; Das, N.; Satija, N. K.; Mandrah, K.; Roy, S. K.; Rayavarapu, R. G. *Nanomaterials* **2019,** *10,* 45. doi:10.3390/nano10010045
27. Danaei, M.; Dehghankhold, M.; Ataei, S.; Hasanzadeh Davarani, F.; Javanmard, R.; Dokhani, A.; Khorasani, S.; Mozafari, M. R. *Pharmaceutics* **2018,** *10,* 57. doi:10.3390/pharmaceutics10020057
28. Joseph, E.; Singhvi, G. Multifunctional nanocrystals for cancer therapy: a potential nanocarrier. In *Nanomaterials for Drug Delivery and Therapy;* Grumezescu, A. M., Ed.; Elsevier, 2019; pp 91–116. doi:10.1016/b978-0-12-816505-8.00007-2
29. Bhattacharyya, A.; Prasad, R.; Buhroo, A. A.; Duraisamy, P.; Yousuf, I.; Umadevi, M.; Bindhu, M. R.; Govindarajan, M.; Khanday, A. L. *J. Nanosci.* **2016,** 4679410. doi:10.1155/2016/4679410
30. Iqbal, S.; Fakhar-e-Alam, M.; Akbar, F.; Shafiq, M.; Atif, M.; Amin, N.; Ismail, M.; Hanif, A.; Farooq, W. A. *J. Mol. Struct.* **2019,** *1189,* 203–209. doi:10.1016/j.molstruc.2019.04.041
31. Iarossi, M.; Schiattarella, C.; Rea, I.; De Stefano, L.; Fittipaldi, R.; Vecchione, A.; Velotta, R.; Ventura, B. D. *ACS Omega* **2018,** *3,* 3805–3812. doi:10.1021/acsomega.8b00265
32. Ghosh, S. K.; Pal, T. *Chem. Rev.* **2007,** *107,* 4797–4862. doi:10.1021/cr0680282
33. Saadati, A.; Farshchi, F.; Hasanzadeh, M.; Liu, Y.; Seidi, F. *RSC Adv.* **2022,** *12,* 21836–21850. doi:10.1039/d2ra02820d
34. Jain, P.; Kumari, A.; Manna, A. K.; De, A. *Mater. Today: Proc.* **2022,** *49,* 3147–3150. doi:10.1016/j.matpr.2020.11.084
35. Zheng, B.; Li, J.; Zheng, Z.; Zhang, C.; Huang, C.; Hong, J.; Li, Y.; Wang, J. *Opt. Laser Technol.* **2021,** *133,* 106522. doi:10.1016/j.optlastec.2020.106522
36. Bali, S.; Goswami, S.; Halder, A.; Mondal, A. *Anal. Methods* **2024,** *16,* 170–174. doi:10.1039/d3ay01701j
37. Al-aqbi, Z. T.; Abdulsahib, H. T.; Al-Doghachi, F. A. J. *Plasmonics* **2024,** 2237. doi:10.1007/s11468-024-02237-0
38. Sapyen, W.; Toonchue, S.; Praphairaksit, N.; Imyim, A. *Spectrochim. Acta, Part A* **2022,** *274,* 121094. doi:10.1016/j.saa.2022.121094
39. Sharma, S.; Sharma, S. K.; Tiwari, A.; Jaiswal, A.; Uttam, K. N. *Anal. Lett.* **2024,** *57,* 940–952. doi:10.1080/00032719.2023.2233034
40. Dang-Bao, T.; Nguyen, T.-S.; Tran-Dinh, N.-T.; Lam, H.-H.; Phan, H.-P. *Chem. Phys. Impact* **2023,** *6,* 100245. doi:10.1016/j.chphi.2023.100245
41. Arain, M.; Nafady, A.; Haq, M. A. U.; Asif, H. M.; Ahmad, H. B.; Soomro, R. A.; Shah, M. R.; Mujeeb-Ur-Rehman; Sirajuddin. *Optik (Munich, Ger.)* **2024,** *299,* 171620. doi:10.1016/j.ijleo.2024.171620
42. Jabariyan, S.; Zanjanchi, M. A. *Appl. Phys. A: Mater. Sci. Process.* **2019,** *125,* 872. doi:10.1007/s00339-019-3167-7
43. Singh, K.; Kumar, V.; Kukkar, B.; Kim, K.-H.; Sharma, T. R. *Int. J. Environ. Sci. Technol.* **2022,** *19,* 4673–4690. doi:10.1007/s13762-021-03331-0
44. Zannotti, M.; Piras, S.; Remia, L.; Appignanesi, D.; Giovannetti, R. *Chemosensors* **2024,** *12,* 33. doi:10.3390/chemosensors12030033
45. Chanajaree, R.; Ratanatawanate, C.; Ruangchaithaweesuk, S.; Lee, V. S.; Wittayanarakul, K. *J. Mol. Liq.* **2021,** *343,* 117629. doi:10.1016/j.molliq.2021.117629
46. Naqvi, S. S.; Anwar, H.; Ahmed, B.; Siddiqui, A.; Shah, M. R.; Ali, S. A. *Mater. Chem. Phys.* **2024,** *318,* 129220. doi:10.1016/j.matchemphys.2024.129220
47. Satapathy, S.; Mohanta, J.; Si, S. *ChemistrySelect* **2016,** *1,* 4940–4948. doi:10.1002/slct.201600985
48. Jiji, S. G.; Gopchandran, K. G. *Colloid Interface Sci. Commun.* **2019,** *29,* 9–16. doi:10.1016/j.colcom.2018.12.003
49. Fenger, R.; Fertitta, E.; Kirmse, H.; Thünemann, A. F.; Rademann, K. *Phys. Chem. Chem. Phys.* **2012,** *14,* 9343–9349. doi:10.1039/c2cp40792b
50. Shah, Z.; Hassan, S.; Shaheen, K.; Khan, S. A.; Gul, T.; Anwar, Y.; Al-shaeri, M. A.; Khan, M.; Khan, R.; Haleem, M. A.; Suo, H. *Mater. Sci. Eng., C* **2020,** *111,* 110829. doi:10.1016/j.msec.2020.110829
51. Berahim, N.; Basirun, W. J.; Leo, B. F.; Johan, M. R. *Catalysts* **2018,** *8,* 412. doi:10.3390/catal8100412
52. Mahy, J. G.; Kiendrebeogo, M.; Farcy, A.; Drogui, P. *Catalysts* **2023,** *13,* 842. doi:10.3390/catal13050842
53. Akhtar, A.; Akram, K.; Aslam, Z.; Ihsanullah, I.; Baig, N.; Bello, M. M. *Environ. Prog. Sustainable Energy* **2023,** *42,* e13984. doi:10.1002/ep.13984
54. Bukhamsin, H. A.; Hammud, H. H.; Awada, C.; Prakasam, T. *Catalysts* **2024,** *14,* 89. doi:10.3390/catal14010089

License and Terms

This is an open access article licensed under the terms of the Beilstein-Institut Open Access License Agreement (https://www.beilstein-journals.org/bjnano/terms), which is identical to the Creative Commons Attribution 4.0 International License (https://creativecommons.org/licenses/by/4.0). The reuse of material under this license requires that the author(s), source and license are credited. Third-party material in this article could be subject to other licenses (typically indicated in the credit line), and in this case, users are required to obtain permission from the license holder to reuse the material.

The definitive version of this article is the electronic one which can be found at:
https://doi.org/10.3762/bjnano.15.124